Composite Repair

Theory and Design

Cong N. Duong and
Chun Hui Wang

Composite Repair

To my parents, my wife Thanh,
my children, Clara and Nathan,
my sister San, and my two nieces,
Hannah and Tanya

Cong N. Duong

To my wife Zoe Zhuqing and
children, Esther and Jeremy

Chun Hui Wang

Composite Repair

Theory and Design

Cong N. Duong
Associate Technical Fellow
The Boeing Company

and

Chun Hui Wang
Head of Composites and Low-Observable Structures
Air Vehicles Division
Defence Science and Technology Organisation
Australia

ELSEVIER

AMSTERDAM • BOSTON • HEIDELBERG • LONDON
NEW YORK • OXFORD • PARIS • SAN DIEGO
SAN FRANCISCO • SINGAPORE • SYDNEY • TOKYO

The Boulevard, Langford Lane, Kidlington, Oxford OX5 1GB, UK
Radarweg 29, PO Box 211, 1000 AE Amsterdam, The Netherlands

First edition 2007

British Library Cataloguing in Publication Data
A catalogue record for this book is available from the British Library

Library of Congress Cataloging-in-Publication Data
A catalog record for this book is available from the Library of Congress

ISBN–13: 978-0-08-045146-6
ISBN–10: 0-08-045146-2

For information on all Elsevier publications
visit our web site at books.elsevier.com

Printed and bound in The Netherlands

07 08 09 10 11 10 9 8 7 6 5 4 3 2 1

Contents

This Page Intentionally Left Blank

Preface

Bonded composite repairs are efficient and cost-effective means of repairing cracks and corrosion grind-out cavity in metallic structures, and composite structures sustained impact and ballistic damages, especially in aircraft structures. Currently there are two edited books available on this topic (*Bonded Repair of Aircraft Structures*, ed. Baker and Jones, 1988, Martinus Nijhoff Publisher; *Advances in Bonded Composite Repair of Metallic Structure*, Baker et al., 2002, Elsevier). However, none has been dedicated to the comprehensive mathematical analysis of the fundamentals of bonded composite repair technology. Our objective in this book is therefore to fill in that gap.

This book devotes entirely its content to the design and analysis of bonded repairs, focusing on the mathematical techniques and analysis approaches that are critical to the successful implementation of bonded repairs. It grew out of recent research we conducted at the Boeing Company and the Defence Science and Technology Organisation (DSTO, Australia) over the past ten years. The topics addressed herein are developed to the extent that the presentation is sufficiently self-explanatory, and hence it could serve as a state-of-the-art reference guide to engineers, scientists, researchers, and practitioners interested in the underpinning design methodology and the modeling of composite repairs. Furthermore, it can be used as a companion reference book to the United States Air Force (USAF) bonded repair guidelines (Guidelines for Composite Repair of Metallic Structure-CRMS, AFRL-WP-TR-1998-4113) and the Royal Australian Air Force (RAAF) Design Standard DEF(AUST)9005 that are currently used by most practitioners and field repair engineers throughout the world, as well as for the new software called CRAS (Composite Repair of Aircraft Structures) developed by the Boeing Company and funded by the USAF.

We have organized the book into 14 chapters. An introduction to the composite repair process is presented in Chapter 1. To set the scene for the latter development, Chapter 2 provides some background information and basic concepts and characteristics of bonded joints and bonded doublers. Chapter 3 presents the foundation of the mechanics of crack-patching technology, focusing particularly on elliptical patches and geometrically linear analyses. Chapters 4 and 5 deal respectively with the stress and fracture analysis of polygonal patches in fully supported one-sided or two-sided repairs and an unsupported one-sided repair. Extension of the crack-patching model developed in Chapters 3 and 4 to corrosion repairs is described in Chapter 6. In Chapter 7, a stress analysis of the peel and shear deformation of adhesive near patch ends is presented for both untapered and tapered patches. Chapter 8 outlines a crack-closure-based methodology to model

the growth behavior of repaired cracks. Design algorithms for repairs to cracks and corrosion damage are described respectively in Chapters 9 and 10, with experimental verifications of the analytical methods presented in Chapter 11. Application of the composite repairs to sonic fatigue cracks is discussed in Chapter 12. Chapter 13 deals with some miscellaneous issues concerning secondary effects, such as multiple patches in proximity, thick composite patch, and tapered patch. The book finally ends with concluding remarks in Chapter 14.

We would like to express our thanks to a number of colleagues. In 1999, the Boeing Company was awarded a multiple-million contract by the United States Air Force Research Laboratory (AFRL) to develop new technologies for Composite Repair of Aircraft Structures (CRAS) including a software application. A bulk of the first author research on the composite repairs would have been impossible without the financial support from the CRAS program. He is, therefore, grateful to the financial support by the AFRL through the CRAS program under the management of Dr David Stargel and to the permission of AFRL to include selective materials from the CRAS final reports in this book. He is also indebted to his colleagues for their contributions and supports to the composite repair researches. In particular, he would like to thank Drs John Hart-Smith, Jin Yu, and John Tracy, the rest of the CRAS team and the management of the Boeing Company. In addition, he had been privileged to pursue his graduate studies at MIT and Caltech under the guidance of Professors John Dugundji and Wolfgang Knauss. He, therefore, would like to take this opportunity to thank his two former advisors for their generous financial support and their hospitality during his time at these two institutions.

Since 1995 the second author has been privileged of being mentored by Drs Francis Rose and Alan Baker, both widely recognized as the leading pioneers in the field of bonded repairs. The research results presented in this book would have been impossible without the guidance and help from his DSTO colleagues, including Dr Richard Chester, Mr. Richard Callinan, and Dr Steve Galea. Last, but not the least, we are grateful to our families for their love, encouragement, patience, and support while this book was being written.

Cong N. Duong
Huntington Beach, California, USA
Chun Hui Wang
Melbourne, Australia

Acknowledgements

With kind permissions of Springer Science and Business Media and the American Society of Mechanical Engineers (ASME), the followings of authors' previous journal articles and book chapter publication have been reused in the present book: (1) "The stress intensity factor for a cracked stiffened sheet repaired with an adhesively bonded composite patch," by Duong and Yu, *International Journal of Fracture*, 84, 37–60 (1997); (2) "Stress analysis and failure assessment of lap joints," by Wang and Rose, Chapter 1, in *Recent Advances in Structural Joints and Repairs for Composite Materials* (Tong and Soutis, eds, 2000); (3) "Analysis of a plate containing a polygon-shaped inclusion with a uniform eigencurvature," by Duong and Yu, *ASME Journal of Applied Mechanics*, 70, 404–407 (2003); and (4) On the characterization of fatigue crack growth in a plate with a single sided repair," by Duong and Wang, *ASME Journal of Engineering Materials and Technology*, 126, 192–198 (2004). The authors gratefully acknowledge their permission.

Disclaimer

While the publisher and authors have used their best efforts in preparing this book, they make no representations or warranties with respect to the accuracy or completeness of its contents. The authors, their employers, the sponsored US Government, and the publisher do not warrant the merchantability of the methods nor their fitness for a particular use. In no instance will they be liable for any damages sustained by the user, or any third party, caused by or attributed to the use of the methods set forth in this book.

CHAPTER 1

Introduction

When today's aircraft reach the end of their service life, fatigue cracks are found to have developed along rivet holes and other highly stressed regions of the aircraft. In order to extend the life of these aircraft, repairs have been made to arrest these cracks. Composite doublers or repair patches provide an innovative repair technique, which can enhance the way aircraft are maintained. Instead of riveting multiple steel or aluminum plates to facilitate an aircraft repair, a single composite doubler is bonded to the damaged structure. Adhesively bonded composite repairs have many advantages over mechanically fastened repairs (Baker and Jones, 1988): (i) no new stress concentration created by new rivet holes; (ii) high stiffness-to-weight and strength-to-weight ratios of the patch, thus reducing drag; (iii) patches are readily formed into complex shapes, permitting the repair of irregular components; (iv) high fatigue and corrosion resistance of the composite; and (v) potential time savings in installation. This repair technique has been primarily used in the area of military aviation. Examples of military application (CRMS Guidelines, 1998) are the repairs of the cracked weep-holes on the C-141 fleet, cracked fuel-vent holes on F16, cracked splices of the upper wing of B-52 G/H models, cracked fuel-access doorframe of B-52, cracked upper (crown) section of the fuselage on C-5A fleet, and F-111 lower-wing skin crack. In this chapter, the objectives of the bonded repairs and an overview of their repair process will be given in Section 1.1. The objectives of this book are stated in Section 1.2. This follows by a review of the past and current work on the design and analysis of bonded repairs in Section 1.3. The chapter is finally concluded by a brief review of the basic elements of the fracture mechanics theory in Section 1.4.

1.1 Objectives of Bonded Repairs and an Overview of the Repair Process

Bonded repair of metallic aircraft structure is used to extend the life of flawed or under-designed components at reasonable cost. Such repairs generally have one of three objectives: fatigue enhancement, crack patching or corrosion repair (Composite Repair of Aircraft Structures [CRAS] Design Manual, 2003).

(1) Fatigue enhancement: Under-designed metallic structure does not necessarily display cracking or other damage at the time a repair action is desired. The concern may stem from observed damage in fleet-leading aircraft or from insufficient analytical crack growth life in the presence of an assumed 1.27 mm flaw, required by United States Air Force (USAF) durability criteria (Joint Service Specification Guide [JSSG], 1998). However, the remedy for such conditions are costly in that they may require either re-design or performance of costly inspections, necessitating the removal of skin panels, at intervals more frequent than desired. Fatigue enhancement refers to the application of composite doublers to such under-designed components to reduce the stress levels, enhancing fatigue life and/or minimizing repeated inspections.

(2) Crack patching: Repair of cracked structure may be performed, by bonding an external patch to the structure, to either stop or slow crack growth.

(3) Corrosion repair: Corrosion damage is removed by grinding out material in the area of the damage. Grind-out areas may be reinforced with fill material and a bonded patch to restore the original load-carrying capability.

The process for repair of damage to aircraft structure is divided into three phases:

(1) Structural assessment of the damage

(2) Repair design and analysis

(3) Installation and inspection of the repair.

Assessment of the flawed structure is required before designing the repair. The flaw can be either under-design or actual damage, such as cracking or corrosion. Such assessment takes into account not only the structural design details but also an understanding of the natural and induced environments to which the structure is subjected during its lifetime and of the cause of the damage. A repair should satisfy all the expected conditions that the original structure must satisfy. These conditions include, but are not limited to, ultimate loads, durability, damage tolerance, environment, fit, function and aerodynamic and electromagnetic performance. However, a repair may be used to get a part to some limited life based on an upcoming retirement. In that case, reduced capability from the original life requirement might be acceptable. This information is essential to design a repair that will have the appropriate performance characteristics.

Once knowledge of the structure is obtained, the design of the repair can start. The design of the repair must address all the expected conditions that the original structure must satisfy. Two additional areas of consideration during repair design are the source of the damage and installation of the repair. If installation of the repair, as well as inspection requirements, were considered part of the design process, problems with installation should be minimized. A properly designed repair, if not installed properly, is unlikely to meet performance criteria. The final step in the process is inspection of the installation.

1.1.1 Structural assessment

The starting point for repair design is knowledge of the structure, i.e., understanding load paths, stresses, geometry, environment and function, as well as the flaw to be repaired. The following list includes information that may be needed to design a proper repair:

- Material type and geometry of the structure being repaired
- Aerodynamic and/or electromagnetic constraints
- Size constraints
- Additional structure or systems present
- Location constraints
- Flammability requirements
- Weight and balance
- Thermodynamic constraints
- Avionics or electronic constraints
- Environment
- Stress levels
- Loading
- Surface preparation constraints
- Availability and compatibility of repair materials, equipment and facilities

Structural flaws can be either basic under-design conditions or actual damage. Under-designed structure necessitates more frequent inspections and/or re-design or repair to meet life criteria. Damage can occur as the structure ages, resulting in fatigue cracks and corrosion pitting, or can be induced by specific events such as acid spills, lightning strikes, bird strikes, miss-drilled holes and tool marks.

The cause of the damage must be addressed or subsequent damage may occur. For example, a corrosive environment may create additional damage to the repair or the surrounding structure. The cause must be determined. If the damage can occur on any aircraft in the fleet, it may be beneficial to survey other aircraft. Once the cause of damage is known, steps can be taken to prevent the damage from recurring in the same area.

1.1.2 Repair design

The repair design must address static strength, durability, function, fit and inspection, as well as satisfy any applicable damage tolerance considerations. Structural and non-structural constraints must also be addressed.

Structural constraints include items like how the repair fits or if there is existing structure that must be accounted for during the design. The initial patch design must conform to geometry of the structure to be repaired. If possible, the patch should not cover existing fasteners that may require future removal. The location of fasteners (rivets) should be considered. Fasteners should not be partially covered or just outside the patch. The USAF Composite Repair to Metallic Structure (CRMS) Guidelines (1998) recommends that the patch edge be at least three times the fastener diameter away from the uncovered fasteners, to avoid stress concentration at the patch edge. The location of the patch relative to substructure should be considered. Locating a single-sided patch over substructure reduces out-of-plane bending. However, the patch should not end just outside the substructure, resulting in a discontinuity in the neutral axis and potential for more bending in that area. Extending a patch over a joint should be avoided as bending at joints is a concern.

Non-structural constraints may deal with the avionics systems or aerodynamic performance. Additional factors that are pertinent to the design of a repair are time constraints for accomplishing the repair, available repair facilities and available materials.

The foundations of the design process for repairs over flawed skin structure are basic design criteria. Patch design criteria, in their simplest form, are to minimize stress in the structure near the defect and at the edge of the patch and to maximize load carried by the patch, decreasing that carried by the structure. Minimizing stress, near a crack, stops or impedes further growth. Detailed design criteria account for operational loads and environments to which the repaired structure will be subjected.

(a) Bonded vs mechanically fastened repairs

Once the decision has been made that a defective structure may be repaired rather than replaced, the next choice is the method of repair. The two primary methods for attaching a repair patch to the damaged structure are mechanical fasteners and adhesive bonding. The method of attachment must be capable of transferring stresses into the repair material from the original structure to retard crack growth and to minimize stress concentration.

A key difference between mechanically fastened and adhesively bonded patches for crack repair is that the former is so flexibly attached that the crack continues to grow under the patch, unless it is first cleaned out by removal of sufficient material to reduce stress concentration at the crack tip. This may entail removal of large amounts of intact structure, converting sharp cracks into round holes. When bonded repairs can be applied, however, the interface between patch and structure is so stiff that it is possible to remove little or no material. Even a hole drilled through the crack tips may not be desirable because it would remove the zone of cold-worked material that itself impedes further crack growth.

The repair must be designed such that stress concentrations, from the method of attachment, are kept to a minimum. Bonded repairs introduce stress concentration from load attraction to the stiffened area. Mechanically fastened repairs introduce stress concentrations from the fastener hole as well as from load attraction. Bonded repairs offer several advantages over mechanically fastened – riveted or bolted – repairs. Adhesive bonding

provides more uniform and efficient load transfer into the repair patch and less stress concentration than mechanical fastening.

In some situations, bonded repairs may not be recommended. The USAF only permits bonded repairs to primary or flight critical components when cracks are not critical at limit load (CRMS Guidelines, 1998). Similarly, for cutouts and grind-outs, bonded repairs are only allowed if the skin stress in the remaining structure is below the material ultimate strength at limit load.

The major disadvantage of bonded repairs is their complexity. Installation process controls are very stringent; advanced materials and processes are required; and the design itself is more complex. Technicians generally do not need special training or experience to install mechanically fastened repairs. Such training and experience is a requisite for bonded repairs. Consequently, bonded repairs are not generally recommended when

- Stringent cleaning and processing steps cannot be adhered to, within a controlled environment.
- The structure to be repaired cannot withstand the high cure temperatures required for bonded repairs.
- The structure to be repaired is subjected to very high loads for which mechanical joints may be more efficient.
- The repair will be exposed to high humidity that can prevent achievement and maintenance of a good quality bond.

There are exceptions to these guidelines. For example, Warner Robin Air Logistic Center (WR-ALC) has considerable experience installing bonded repairs in high humidity conditions.

(b) Size and shape of the bonded patch

The size of the repair is governed by the required space for proper load transfer through the adhesive into the composite patch, and the physical limitations of the area to be repaired. The termination point of the repair patch, with respect to existing structure, can influence the durability of the repaired area. A check for possible interference, from patch overlap with adjacent structure and systems, is required to ensure their continued proper operation. The plan shape of the repair patch is typically octagonal, although other shapes are utilized. Deviations to simple shapes are used to account for changes in the shape of the damaged structure and for specific design elements of a repair, such as the need to keep the high stress at the edge of the patch away from other structural details. The patch may need to wrap around an opening in the structure or another structural member. The thickness of the patch must account for the required strength, stiffness, fit, and functional constraints. The patch is usually tapered to reduce stress concentrations induced by load transfer at the edge of the patch.

(c) Choice of repair material

The selected material must be able to withstand the expected conditions in the damaged area and to withstand ultimate and fatigue stresses. Fatigue stresses will determine the durability of the repair from a strength standpoint. The operating environment will determine the longevity of the repair. The repair material must be able to withstand applicable natural and induced environments. Heat, vibration, cold, hydraulic fluid, moisture, fuel, and oil can cause degradation of the material. The repair configuration itself must not create an adverse environment. For example, the repair should not create a situation for galvanic corrosion. The material should also be selected on the basis of any damage tolerance requirements and the potential need for through-the-patch inspections using eddy current, ultrasonic or thermographic non-destructive inspection (NDI) techniques.

Coefficient of thermal expansion (CTE) compatibility between the repair material and the structure to be repaired is an essential consideration. Differences in CTE can create patch disbond or structural failure outside the repair. Repair design should account for thermally induced stresses from heating during the adhesive cure process and from temperature variances associated with aircraft flight operations.

The material generally used for composite patches is Boron/epoxy (B/ep) because it has high stiffness (Young's modulus about three times that of aluminum) and strength, is fatigue-resistant and immune to corrosion. It also has low electrical conductivity, unlike carbon materials. However, in cases where the patch is required to follow significant curvature, use of carbon materials may be desirable. Modified epoxy film adhesives, such as FM-73, are most commonly used to bond the patch to metallic structure. Special pre-bonding surface treatments, based on use of silane coupling agents, ensure durable bonds.

(d) Analysis of the repair design

The repair should be evaluated against all criteria during the design phase of the repair. Analysis should only provide the final check that the design of the repair is adequate. The analyses required might include consideration of static ultimate load, fatigue, fail-safe, damage tolerance, durability, heat transfer, vibration, aerodynamics, aesthetics, fit and function. Finite element (FE) and/or appropriate closed-form analyses must be performed for that purpose.

(e) Pre-installation check

A check to determine if the repair can be installed is required. This check is necessary to ensure that the repair, as designed, can be installed. The initial design process should account for how the repair will be installed. Considerations should, as a minimum, include heating and temperature distribution methods, temperature measurement and control techniques, pressurization methods, the cure process, and quality control and inspection aspects. Prior to attempting the repair installation, a thermal survey must be conducted, during which the vicinity of the repair is brought to and maintained at the required cure temperature. For cracked structure, leak checks should also be made and

the crack sealed. If both sides of the crack are accessible, the backside is dammed and the crack flooded with solvent. A vacuum is pulled, the backside surface cleaned and sealant applied under vacuum.

1.1.3 Installation of the repair

Primary considerations for bonded repair installation are surface preparation, heating methods, pressurization methods, the cure process and inspections. The CRMS Guidelines (1998) should be consulted to determine further details of the installation process.

Good adhesion of a bonded patch to the structural surface is critical to the durability of a repair and surface preparation, compatible with the repair materials and installation procedures, is essential. Phosphoric acid anodizing (PAA) and grit blast silane (GBS), or grit blast solgell, are aluminum surface preparations that are most effective. Prior to either method, surface contaminants (sealants, paint, grease, etc.) are removed by use of abrasives and cleaning agents. PAA consists of an electrical current-induced surface electro-chemical change to increase the adhesive surface area and to increase moisture resistance. GBS involves a light blasting with aluminum oxide grit and an application of a water-soluble silane-coupling agent that bonds to both the metal and the adhesive primer.

Temperatures required during cure cycles are generally developed by heater blanket, heating blocks, oven, autoclave, forced air, or infrared lamp systems. The most common source is the heater blanket in which resistance-heating wires are imbedded in a flexible heat-resistant medium, which is placed over the repair area. Choosing a heating method is based on several considerations:

- Power requirements dependent on the emissivity of the materials, area to be heated, thickness of heated zone and required temperature.
- Location of heat source, usually determined by thermal surveys.
- Required temperature distribution, as determined by thermocouples, prior to and during the repair.
- Temperature measurement and control.

Pressure, applied during curing, minimizes voids in the bond line and ensures contact between the patch, adhesive, and structure. Vacuum bags, mechanical devices or autoclaves develop pressure. The most common pressurization technique is the vacuum bag method in which an airtight bag is placed over the repair and evacuated.

Patches are either pre-cured or co-cured. Pre-cured patches are laid up on molds of the component, allowing for high quality control and pre-installation inspections. These patches are cured independently and then bonded to the structure in a separate operation, usually at a somewhat lower temperature. Lower cure temperature equates to lower thermal stress due to CTE mismatch. The alternative is to cure the patch and adhesive in place over the area to be repaired. These co-cured patches require compatible adhesive and patch materials.

Non-destructive inspection of the completed repair is used to ensure that the repair does not contain any unexpected anomalies and the damage in the structure has not grown. NDI techniques include eddy current, dye penetrant, ultrasonic, x-ray, and thermographic inspections.

1.2 Objectives of This Book

This book deals primarily with the analysis and design aspect of the bonded repair process. As mentioned in Section 1.1, the repair process requires assessment of the damage or under-design condition, design of repair details and installation of the repair. In this book, it is assumed that the defect or design flaw has been detected, classified and identified as a candidate for a bonded repair. No information on this pre-repair structural evaluation is presented in this book. Furthermore, the installation procedures are also omitted since the primary purpose of this book is to provide engineers, practitioners, researchers, and scientists the theoretical foundations of the design and analysis of bonded repairs. In the last several decades, new advances in analytical methods for designing and analyzing a composite patch have been made. Simple and explicit results of some of these methods have been incorporated into the engineering guidelines or standards such as the USAF CRMS Guidelines (1998) and the Royal Australian Air Force (RAAF) Engineering Standard C5003 (Davis, 1995) for use by practitioners and depot repair engineers. In contrast, more complex analytical models as well as the iterative patch design process have been implemented in various software formats. Among these, the USAF Composite Repair of Aircraft Structures (CRAS) software is considered to be the most capable bonded repair code, which integrates various simple and complex analytical models for the design and analysis of a composite patch together with a very-easy-to-use graphical user interface (GUI) (CRAS Software User Manual, 2003). The analysis methods and design process described in this book are generally consistent with those of the CRAS software as well as the engineering guidelines mentioned above. This book therefore can also be used as a good reference to the CRAS software as well as to the USAF CRMS Guidelines and RAAF C5003 Engineering Standard. In addition, engineers, scientists, and researchers can also learn from this book many powerful mathematical techniques or methods that can be developed into a design and analysis software tool for a composite patch repair.

1.3 Review of Past and Current Work on Design and Analysis of Bonded Repair

There are several methods for the analysis of crack patching and corrosion repair. They can be broadly classified as either analytical or numerical. Numerical analysis such as the conventional FE analysis requires a considerable amount of modeling and computing efforts since a very fined mesh must be used near the two crack tips due to the stress singularity there. The numerical method is therefore too laborious for parametric studies in design calculations and for crack growth analysis. On the other hand, the analytical method uses basic elasticity solutions, which provides accurate solutions with minimum

inputs from the user, and the values of these inputs can be easily changed without any major modeling effort. For that reason, only analytical work will be discussed in this book.

Analytical work has been done in both academia and industry. In the earliest work, the analysis involved an infinite composite patch adhesively bonded to an infinite cracked plate (Erdogan and Arin, 1972; Ratwani, 1974; Keer et al., 1976). The adhesive was treated as a two-dimensional shear spring. The problem was reduced to a pair of integral equations that were solved by numerical integration with the discretization of the bonded interface. The effect of the finite size of the patch was ignored in that analysis. However, that analysis included the effects of disbond and the out-of-plane bending due to load path eccentricity near the crack on the crack-tip behavior. The size of the disbond was determined by calculating the shear strain in the adhesive and comparing these values to the shear strain allowable in the adhesive. Those regions surpassing the allowable were considered to be debonded. Nevertheless, the bending analysis considered by Ratwani (1974) has been found later to be deficient (Arendt and Sun, 1994). Extension of this early approach to complex repair configurations such as repairs on a stiffened sheet or thin strip repairs had also been considered by Ratwani (1980) and Ratwani and Kan (1982). However, he did not solve these problems through exact analyses. He used the compounding technique for the analysis of repairs on a stiffened sheet. Since the load transfers between the patch and the sheet and between the sheet and the stiffeners depend on the relative stiffnesses of these three components, the compounding technique may not be appropriate for this problem. Furthermore, his account for an infinite strip patch also may be inaccurate since the strip was treated as a one-dimensional elastic rod.

The effect of a finite two-dimensional patch is first treated analytically by Rose (1981, 1982, 1988). By dividing the crack patching analysis into two stages, each with different simplified assumptions, simple formula for estimating physical field quantities critical to the repair can be derived. Rose's analysis was based on the linear superposition of two problems, each problem corresponding to one stage of the analysis. The first problem involved an elliptical composite patch rigidly bonded to an *uncracked* metallic sheet. The stresses at the prospective location of the crack for the second problem were calculated. In the second problem, a semi-infinite crack in an infinite patched sheet was considered. The semi-infinite crack was loaded on its surfaces by the same stresses found in the first problem but in a reversed fashion. Rose's analysis included the effect of thermal stresses because of the thermal mismatch between the patch and the damaged structures due to either low operating temperature or curing of the adhesive. The effect of finite crack length and the influence of debonding were examined in Rose (1987a,b) via a simple distributed spring model. No mention was made as to the incorporation of stiffener and crack asymmetry. The bending analysis given by Rose (1988) was also found subsequently to be incorrect (Arendt and Sun, 1994). Since these original works, Rose and his colleagues at Defense Science and Technology Organization (DSTO) in Australia, especially Wang, had expanded the analysis capabilities to include the effect of structural constraint on thermal stresses due to curing (Wang and Erjavec, 2000; Wang et al., 2000), and the effect of the out-of-plane bending on the crack-tip behavior (Wang and Rose, 1999). However, most of these works were limited to either plane stress analysis or geometrically linear analysis. The Rose's analytical model was

later incorporated into a Windows-based repair program entitled CALCUREP (2001) by Fredell (1994) of the U.S. Air Force Academy. Other contributions to the design and analysis of bonded repairs were made by Atluri (1992), Bottega and Loia (1996, 1997). Atluri (1992) solved the problem of a cracked sheet reinforced by an infinite composite strip parallel to a crack by using the Fourier integral transform method. His work, however, did not include the effects of a disbond, thermal stresses, and stiffeners. In contrast, Bottega and Loia (1996, 1997) addressed the issue of debonding at the patch edge, which may compromise the performance of repairs on flat and cylindrical panels. Even though this edge debonding issue is important when considering a bonded repair, it is beyond the scope of this book. Parallel efforts in the development of analytical methods for composite repairs to composite structures also have been conducted in the past decades. Among them, the works by Soutis and Hu (1997), Soutis et al. (1999), Engels and Becker (2002), Barut et al. (2002), Oterkus et al. (2005) for repairs of a composite panel with a cutout are worthy to mention.

Under the sponsorship of the U.S. Air Force Research Laboratory (AFRL), Duong and his colleagues at the Boeing Company have expanded the design and analysis capabilities for bonded composite repairs beyond the existing capabilities and incorporated these new developments along with those developed at DSTO into a software called CRAS (2003). Under this sponsorship, they have made five major contributions to the field of bonded technology (Duong, 2003a,b; Duong et al., 2003). First, robust algorithms have been developed for the initial patch designs of cracking and corrosion repairs. In the past, an initial patch design capability existed; however, that capability was available only for crack patching and it was relatively primitive (Jones, 1988). Secondly, theoretical analysis of a non-elliptical patch has been made possible using inclusion model with eigenstrain theory. Thirdly, the analytical method for crack patching analysis has been extended to the analyses of corrosion pits repaired with a polygon-shaped patch. Fourthly, the analysis of the out-of-plane bending for thermal stresses and thermo-mechanical stresses has been significantly improved by including the effects of geometrically nonlinearity and non-elliptical shaped patch. Finally, a new bond-line analysis for tapered patches and doublers has been developed, which includes the coupling effects between the peel and the shear behavior of the adhesive as well as the effect of the geometrical and material nonlinearity.

1.4 Basic Elements of Fracture Mechanics Theory

The stresses distribution near the crack tip of a repaired structure is singular, i.e., the crack-tip stress fast reaches infinity. Therefore, unlike the case of holes or cutouts, the stress concentration approach is not applicable for measuring the severity of a cracked structure. In an elastically cracked structure, the amplitude of the singularity of the crack-tip stress, widely known as the stress intensity factor, is used to measure the structure's residual strength and the structure's capability to resist fatigue crack growth. Since the main basic assumption underlying the stress intensity factor approach is that the structure remains elastic during the whole fracture process, the approach is often referred to as the linear elastic fracture mechanics (LEFM) approach. According to

LEFM theory, the stress field near a crack tip is governed by the following expression (Broek, 1987):

$$\begin{Bmatrix}\sigma_x\\ \sigma_y\\ \tau_{xy}\end{Bmatrix} = \frac{K_I}{\sqrt{2\pi r}}\cos(\theta/2)\begin{Bmatrix}1-\sin(\theta/2)\sin(3\theta/2)\\ 1+\sin(\theta/2)\sin(3\theta/2)\\ \sin(\theta/2)\cos(3\theta/2)\end{Bmatrix}$$

$$+\frac{K_{II}}{\sqrt{2\pi r}}\begin{Bmatrix}-\sin(\theta/2)[2+\cos(\theta/2)\cos(3\theta/2)]\\ \sin(\theta/2)\cos(\theta/2)\cos(3\theta/2)\\ \cos(\theta/2)[1-\sin(\theta/2)\sin(3\theta/2)]\end{Bmatrix}+0(r^0) \qquad (1.1)$$

$$\begin{Bmatrix}\tau_{xz}\\ \tau_{yz}\end{Bmatrix} = \frac{K_{III}}{\sqrt{2\pi r}}\begin{Bmatrix}-\sin(\theta/2)\\ \cos(\theta/2)\end{Bmatrix}+0(r^0)$$

where K_I, K_{II}, and K_{III} are the stress intensity factors for three respective modes: opening, sliding or shear and tearing modes. These three modes describe three independent kinematic movements of the upper and lower crack surfaces with respect to each other as shown in Figure 1.1 for all possible modes of crack propagation in an elastic material. Depending on the loading and geometry of the cracked structure, one, two or all three modes of fracture can be operated simultaneously. Mode I is the most common mode found in practical applications. For reference, the crack-tip displacements for modes I and II are also given here as

$$\begin{Bmatrix}u_x\\ u_y\end{Bmatrix} = \frac{K_I}{2E_s}\sqrt{\frac{r}{2\pi}}(1+\nu_s)\begin{Bmatrix}(2\kappa_\varepsilon-1)\cos(\theta/2)-\cos(3\theta/2)\\ (2\kappa_\varepsilon+1)\sin(\theta/2)-\sin(3\theta/2)\end{Bmatrix}$$

$$+\frac{K_{II}}{2E_s}\sqrt{\frac{r}{2\pi}}(1+\nu_s)\begin{Bmatrix}(2\kappa_\varepsilon+3)\sin(\theta/2)+\sin(3\theta/2)\\ -(2\kappa_\varepsilon-3)\cos(\theta/2)+\cos(3\theta/2)\end{Bmatrix}+0(r^0) \qquad (1.2)$$

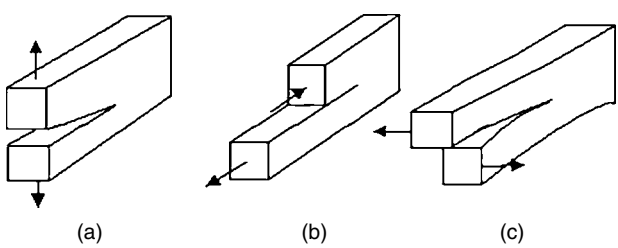

Fig. 1.1. Three basic modes of fracture: (a) mode I or opening mode, (b) mode II or shear mode; and (c) mode III or tearing mode.

where

$$\kappa_\varepsilon = \begin{cases} (3-\nu_s)/(1+\nu_s) & \text{for plane stress} \\ 3-4\nu_s & \text{for plane strain} \end{cases} \tag{1.3}$$

E_s and ν_s are the Young's modulus and Poisson's ratio of the cracked structure, respectively. Another important parameter which can also be used to characterize fracture of a cracked structure is the so-called 'energy release rate'. It is the energy released per unit extension of crack front per unit thickness of the structure, defined by

$$G = -\frac{\mathrm{d}\Pi}{\mathrm{d}a} = -\frac{\mathrm{d}\,(U_E - W)}{\mathrm{d}a} \tag{1.4}$$

which for a linearly elastic structure reduces to $G = \frac{1}{2}\frac{\mathrm{d}U_E}{\mathrm{d}a}$, where W is the external work done on the structure, U_E is the strain energy stored in the structure, and Π is the potential energy. For elastic structure and for mode I fracture, G is related to the stress intensity factors by

$$G = \begin{cases} \dfrac{K_I^2}{E_s} & \text{plane stress} \\ \dfrac{K_I^2}{E_s}\left(1-\nu_s^2\right) & \text{plane strain} \end{cases} \tag{1.5}$$

G is also referred to as the crack driving force. It remains now to show how to determine the residual strength and the fatigue crack growth of a cracked structure using the linear elastic fracture mechanics approach.

(a) Crack growth under static load or residual strength of a cracked structure

The principle of the linear elastic fracture mechanics approach is that at the onset of fracture the crack-tip stress intensity factor or the strain energy release rate of a given fracture mode is constant. In other words, for all different geometries and loading configurations, the stress intensity factors or strain energy release rates of all different specimens are the same at fracture. Thus, at fracture K_I or G of a cracked structure reaches a unique value for a given material. This critical stress intensity factor or strain energy release rate is a material property and often referred to as the fracture toughness. For metallic materials, fracture toughness is a function of material thickness, orientation, alloy, temper and form, as well as temperature. Figure 1.2 shows schematically the typical effect of thickness or stress state (plane stress vs plane strain) on fracture toughness. This variation of the fracture toughness with respect to the material thickness is attributed in part due to the crack-tip plasticity, which inevitably always exists at the crack tip in metals. Values of plane-strain fracture toughness for opening mode (mode I) denoted by K_{IC} for various aluminum alloys can be obtained from MIL-HNBK 5 and they are listed in Table 1.1 for reference.

Most, if not all, metallic materials used on aircraft structures exhibit elastic-plastic behavior. In order to use the LEFM approach for metallic cracked structure with thin

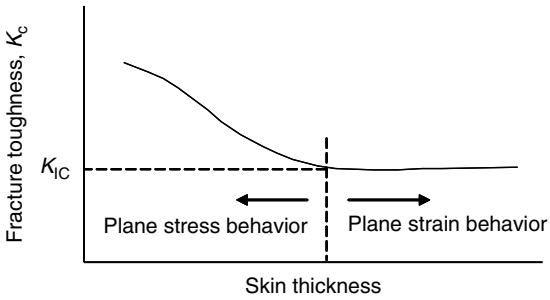

Fig. 1.2. Typical effect of skin thickness on fracture toughness in ductile materials.

Table 1.1. Plane-strain fracture toughness (K_{IC}) for selective skin aluminum materials.

Material	Thickness (mm)	Orientation	Plain Strain K_{IC}(MPa$\sqrt{m}$)
2014-T651 Plate	12.7–25.4	L-T	24.2
		T-L	23.1
2014-T652 Hand forging	20.3–50.8	L-T	34.1
		T-L	23.1
2024-T351 Plate	20.3–50.8	L-T	34.1
	35.6–76.2	L-S	27.5
2024-T851 Plate	≥12.7	L-T	25.3
	10.2–101.6	T-L	24.2
2124-T851 Plate	≥20.3	L-T	31.9
	15.2–152.4	T-L	27.5
	≥12.7	S-L	23.1
7050-T7351 Plate	25.4–152.4	L-T	38.5
	50.8–152.4	T-L	36.3
	20.3–38.1	S-L	30.8
7050-T74 Die forging	15.2–180.3	S-L	26.4
7050-T7451 Plate		L-T	35.2
	≥25.4	T-L	30.8
	17.8–50.8	S-L	25.3
7050-T7452 Hand forging	88.9–139.7	L-T	34.1
	88.9–190.5	T-L	23.1
	88.9–190.5	S-L	20.9
7050-T76511 Extrusion		L-T	34.1
7075-T651 Plate	≥15.2	L-T	28.6
	≥12.7	T-L	24.2
		S-L	19.8
7075-T7351 Plate	≥25.4	L-T	33
	≥12.7	T-L	29.7
	≥12.7	S-L	24.2
7075-T73511 Extrusion	≥22.9	L-T	38.5
	25.4–177.8	T-L	22
	≥17.8	T-L	25.3
	≥12.7	S-L	22

(*Continued*)

Table 1.1. (Continued)

Material	Thickness (mm)	Orientation	Plain Strain K_{IC}(MPa$\sqrt{m}$)
7075-T7352 Hand forging		L-T	36.3
	≥20.3	T-L	28.6
7075-T7651 Plate	≥20.3	L-T	31.9
	≥12.7	T-L	25.3
	≥12.7	S-L	19.8
7075-T7651 Clad plate	12.7–15.2	L-T	27.5
	12.7–15.2	T-L	26.4
7075-T76511 Extrusion	33–177.8	L-T	38.5
	30.5	T-L	25.3
7175-T651 Plate		L-T	28.6
		T-L	24.2
7175-T7351 Plate		L-T	36.3
		T-L	29.7
7175-T73511 Extrusion	≥17.8	L-T	36.3
	≥12.7	T-L	27.5
7175-T7651 Clad plate		L-T	35.2
		T-L	29.7
7175-T7651 Plate		L-T	35.2
		T-L	27.5
7475-T651 Plate		L-T	41.8
	15.2–50.8	T-L	37.4
	≥15.2	S-L	30.8
7475-T7351 Plate	33–101.6	L-T	51.6
	≥33	T-L	40.6
	≥17.8	S-L	33
7475-T7651 Plate	25.4–50.8	L-T	45.1
	≥25.4	T-L	39.6

sheet thickness, an engineering concept of apparent plane stress fracture toughness will be used. Fracture of thin metallic structure involves a stable tearing phase before an unstable crack growth leading to the final catastrophic failure. As the crack grows, the material becomes tougher due to a requirement of higher plastic energy dissipation at the crack tip. As a result, the applied load and thus the applied stress intensity factor must be increased to continue to drive the fracture beyond the initial onset of fracture. If the applied load or stress intensity remains the same beyond the initial onset of fracture, the crack propagation will be stopped. The apparent fracture toughness is determined as the critical stress intensity factor at the final failure load (or the load when the crack becomes unstable) and based on the original crack length.

(b) Fatigue crack growth

Crack growth under cyclic fatigue loads can be also predicted by using the stress intensity factor. Two different cracks will have equal rate of growth if they experience the same stress and environmental conditions at the crack tip. Thus, besides the environmental

effect, cracks of the same stress intensity factor history will grow in the same manner. In general, the fatigue crack growth rate is a function of both the stress intensity factor range ΔK and the cyclic stress ratio R, i.e.,

$$\frac{\mathrm{d}a}{\mathrm{d}N} = \mathrm{f}\,(\Delta K,\ R) \tag{1.6}$$

In Equation (1.6), ΔK is defined as the difference of the stress intensity factors at the maximum (or peak) and the minimum (or valley) of the loading cycle while R is the ratio of the minimum stress intensity factor to the maximum stress intensity factor. For an un-patched crack or a patched crack without thermally induced residual stress, $R = \dfrac{K_{\text{min-load}}}{K_{\text{max-load}}} = \dfrac{\sigma_{\infty-\text{max load}}}{\sigma_{\infty-\text{min load}}}$. The effect of R-ratio can be explained by a phenomenon called the plasticity-induced closure. Even though there are other forms of crack closure such as roughness and oxide-induced closure, the plasticity-induced closure appears to be more relevant to the R-ratio effect. As the crack grows under cyclic loading, residual plastic deformed material (sometimes also called residual plastic stretch) is left on the crack surfaces. During unloading, these surfaces contact each other at the minimum applied load. As the result of this contact (closure), during reloading, the crack will not fully open at the minimum load even when this minimum load is tension. The crack will start to fully open at a higher load than the minimum load during reloading. Since only the crack-opening portion of the loading cycle will contribute to the fatigue crack growth and if the crack opening during reloading accounts for the closure effect, the stress intensity factor range based on the stresses at the maximum loading and at the first crack opening during reloading, but not the actual stress intensity factor range, should be used in the $\mathrm{d}a/\mathrm{d}N$ relation. This newly defined stress intensity factor range is commonly referred to as the effective stress intensity factor range, i.e., ΔK_{eff}. When the plasticity-induced closure is accounted for in the crack growth model, $\mathrm{d}a/\mathrm{d}N$ data for different R-ratios can be collapsed onto a unique $\mathrm{d}a/\mathrm{d}N$ vs ΔK_{eff} curve.

Analytical models for crack closure were developed first by Dill and Saff (1976), Budiansky and Hutchinson (1978), and Newman (1981, 1982, 1992). These models were all based on the Dugdale model for the crack-tip plasticity (Dugdale, 1960). These models were used to calculate the load at the first crack opening during reloading. It is beyond the scope of this book to discuss these models in details. Only an extension of the Budiansky and Hutchinson's crack closure model to large-scale yielding is briefly reviewed in Chapter 8, in relevance to the topic of fatigue crack growth in a repaired structure.

CHAPTER 2

Theory of Bonded Doublers and Bonded Joints

2.1 Introduction

One of the keys to understanding the analysis and design of patches is the relative displacements between the patch and the skin in the immediate vicinity of a damage and around the edge of the patch. In many instances, these relative displacements are calculated approximately using the conventional one-dimensional theory of bonded doublers or joints for reasons of simplicity or another. The theories of bonded doublers and joints are therefore presented in this chapter.

Since a bonded doubler or joint represents a multiplayer structure involving two substrates and a thin adhesive layer, the stress states that exist at various levels in a bonded doubler or joint are very complex. Considerable effort has been devoted to develop simple yet accurate analytical estimates for bonded doublers and joints. Consequently, many theories exist. However, in this chapter, theories that provide the same level of fidelity in the models as have been employed by Volkensen (1938) and Goland and Reissner (1944) for bonded joints are presented. These theories are essentially based on the work of Hart-Smith (1973a,b,c, 1974, 1982, 1999, 2005b), and they are applied to doubler and joint configurations that are representative of a bonded repair. They also include an elastic-plastic representation for the adhesive. Using these relatively simple theories, explicit solutions can be derived and all features of prime importance can be studied. Other important effects that are not considered in these theories, except for the coupling effect between peel and shear behavior in an unbalanced doubler or joint which will be covered separately in Chapter 7 when dealing with tapered joint and doubler, will be augmented in the second part of the chapter. As a final note, all analyses in this chapter are conducted for plane strain condition, which results will be used extensively in some latter chapters.

2.2 Stress Analysis of Two-Sided Doublers and Double-Strap Joints

As mentioned in Section 2.1, the analysis presented in this section follows that provided by Volkensen (1938) and Hart-Smith (1973b). The analysis with the elastic adhesive representation is delineated first and followed by the one with elastic-plastic characterization of the adhesive.

2.2.1 Elastic analysis of two-sided doublers and double-strap joints

Referring to Figure 2.1, the basic differential equations are

Horizontal force equilibrium

$$\begin{aligned} \frac{\mathrm{d}N_{\mathrm{p}}}{\mathrm{d}x} - \tau^{(\mathrm{A})} &= 0 \\ \frac{\mathrm{d}N_{\mathrm{s}}}{\mathrm{d}x} + \tau^{(\mathrm{A})} &= 0 \end{aligned} \tag{2.1}$$

Adherend stress–strain relations

$$\begin{aligned} \frac{\mathrm{d}u_{\mathrm{p}}}{\mathrm{d}x} &= \frac{N_{\mathrm{p}}}{E'_{\mathrm{p}} t_{\mathrm{p}}} + \alpha_{\mathrm{p}} \Delta T \\ \frac{\mathrm{d}u_{\mathrm{s}}}{\mathrm{d}x} &= \frac{N_{\mathrm{s}}}{E'_{\mathrm{s}} t_{\mathrm{s}}} + \alpha_{\mathrm{s}} \Delta T \\ E'_{\mathrm{s,p}} &= \frac{E_{\mathrm{s,p}}}{1 - \nu^2_{\mathrm{s,p}}} \end{aligned} \tag{2.2}$$

Adhesive elastic stress–strain relation

$$\tau^{(\mathrm{A})} = G_{\mathrm{A}} \gamma^{(\mathrm{A})} = -\frac{G_{\mathrm{A}}}{t_{\mathrm{A}}} \left(u_{\mathrm{s}} - u_{\mathrm{p}} \right) \tag{2.3}$$

where u is the longitudinal displacement of the adherend; N is the load per unit width; τ and γ are the shear stress and strain; E, α, t, and G are the extensional modulus, thermal expansion coefficient, thickness and shear modulus, respectively; the subscripts and superscripts s, p and A denote the skin, patch (doubler or strap) and adhesive, respectively; ΔT is the temperature change measured from the stress free temperature. Differentiating Equation (2.3) once and substituting (2.2) into the resulting equation yield

$$\begin{aligned} \frac{\mathrm{d}\tau^{(\mathrm{A})}}{\mathrm{d}x} &= -\frac{G_{\mathrm{A}}}{t_{\mathrm{A}}} \left(\frac{\mathrm{d}u_{\mathrm{s}}}{\mathrm{d}x} - \frac{\mathrm{d}u_{\mathrm{p}}}{\mathrm{d}x} \right) \\ &= -\frac{G_{\mathrm{A}}}{t_{\mathrm{A}}} \left[\frac{N_{\mathrm{s}}}{E'_{\mathrm{s}} t_{\mathrm{s}}} - \frac{N_{\mathrm{p}}}{E'_{\mathrm{p}} t_{\mathrm{p}}} + \left(\alpha_{\mathrm{s}} - \alpha_{\mathrm{p}} \right) \Delta T \right] \end{aligned} \tag{2.4}$$

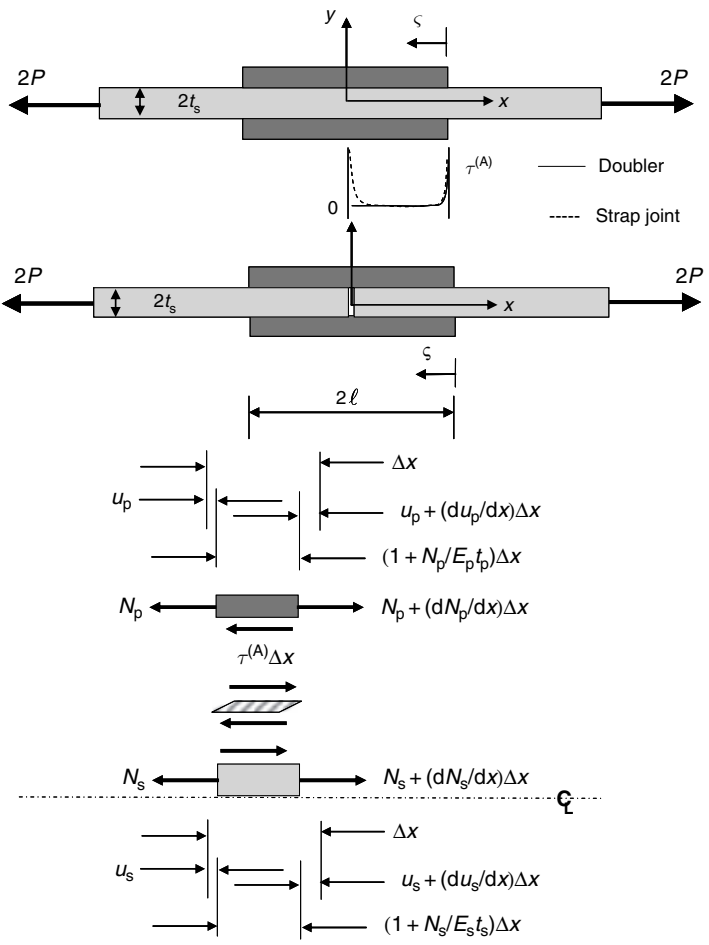

Fig. 2.1. Geometry of a two-sided doubler and a double strap joint, and terminologies used in their analyses.

The differential equation governing the adhesive shear–strain distribution follows by differentiation of Equation (2.4) and elimination of $\frac{dN_s}{dx}$ and $\frac{dN_p}{dx}$ from the resulting equation using (2.1).

$$\frac{d^2\tau^{(A)}}{dx^2} - \beta_A^2 \tau^{(A)} = 0 \tag{2.5}$$

where

$$\beta_A^2 = \frac{G_A}{t_A}\left(\frac{1}{E'_p t_p} + \frac{1}{E'_s t_s}\right)$$

$$= \frac{G_A}{t_A}\left(\frac{1+S}{S}\right)\frac{1}{E'_s t_s} \tag{2.6}$$

and S is the ratio of the patch (doubler or strap) stiffness to the skin stiffness, i.e.,

$$S = \frac{E'_{\mathrm{p}} t_{\mathrm{p}}}{E'_{\mathrm{s}} t_{\mathrm{s}}} \tag{2.7}$$

The general solution of Equation (2.5) is

$$\tau^{(\mathrm{A})} = A \sinh(\beta_{\mathrm{A}} x) + B \cosh(\beta_{\mathrm{A}} x) \tag{2.8}$$

The constants A and B are evaluated from the boundary conditions on $\frac{\mathrm{d}\tau^{(\mathrm{A})}}{\mathrm{d}x}$ and $\tau^{(\mathrm{A})}$.

Choosing the origin of the x-coordinate as the middle of the doubler or joint, it is clear that for a doubler

$$\tau^{(\mathrm{A})}(0) = 0 \tag{2.9}$$

$$\begin{aligned} N_{\mathrm{s}}(\ell) &= P \\ N_{\mathrm{p}}(\ell) &= 0 \end{aligned} \tag{2.10}$$

Condition (2.9) implies $B = 0$. Evaluating Equation (2.4) at $x = \ell$, invoking condition (2.10), and utilizing the results $B = 0$ and $\tau^{(\mathrm{A})}$ given by (2.8) provide

$$\begin{aligned} A &= -\frac{G_{\mathrm{A}}}{\beta_{\mathrm{A}} t_{\mathrm{A}} \cosh(\beta_{\mathrm{A}} \ell)} \left[\frac{P}{E'_{\mathrm{s}} t_{\mathrm{s}}} + \left(\alpha_{\mathrm{s}} - \alpha_{\mathrm{p}}\right) \Delta T \right] \\ &= -\frac{G_{\mathrm{A}}}{\beta_{\mathrm{A}} t_{\mathrm{A}} \cosh(\beta_{\mathrm{A}} \ell)} \left[\frac{\sigma_\infty}{E'_{\mathrm{s}}} + \left(\alpha_{\mathrm{s}} - \alpha_{\mathrm{p}}\right) \Delta T \right] \end{aligned} \tag{2.11}$$

noting that $P = \sigma_\infty t_{\mathrm{s}}$. Hence, Equation (2.8) becomes

$$\tau^{(\mathrm{A})} = -\frac{G_{\mathrm{A}} \sinh(\beta_{\mathrm{A}} x)}{\beta_{\mathrm{A}} t_{\mathrm{A}} \cosh(\beta_{\mathrm{A}} \ell)} \left[\frac{\sigma_\infty}{E'_{\mathrm{s}}} + \left(\alpha_{\mathrm{s}} - \alpha_{\mathrm{p}}\right) \Delta T \right] \tag{2.12}$$

The negative sign on the right-hand side of (2.12) signifies that the adhesive shear stress $\tau^{(\mathrm{A})}$ is in opposite direction to that shown in Figure 2.1, as expected.

In contrast, for a double-strap joint, the boundary conditions will be given by

$$\begin{aligned} N_{\mathrm{s}}(0) &= 0 \\ N_{\mathrm{p}}(0) &= P \end{aligned} \tag{2.13}$$

$$\begin{aligned} N_{\mathrm{s}}(\ell) &= P \\ N_{\mathrm{p}}(\ell) &= 0 \end{aligned} \tag{2.14}$$

Evaluating Equation (2.4) at $x = 0$ and $x = \ell$, respectively, noting $\tau^{(A)}$ given by (2.8), and making use of Equations (2.13)–(2.14) yield

$$\begin{aligned} A &= -\frac{G_A}{\beta_A t_A}\left[-\frac{P}{E'_p t_p} + \left(\alpha_s - \alpha_p\right)\Delta T\right] \\ &= -\frac{G_A}{\beta_A t_A}\left[-\frac{\sigma_\infty t_s}{E'_p t_p} + \left(\alpha_s - \alpha_p\right)\Delta T\right] \\ &= -\frac{G_A}{\beta_A t_A}\left[-\frac{\sigma_\infty}{E'_s S} + \left(\alpha_s - \alpha_p\right)\Delta T\right] \end{aligned} \tag{2.15}$$

$$\begin{aligned} B &= -\frac{G_A}{\beta_A t_A \sinh\left(\beta_A \ell\right)}\left[\frac{\sigma_\infty}{E'_s} + \left(\alpha_s - \alpha_p\right)\Delta T\right] - A\frac{\cosh\left(\beta_A \ell\right)}{\sinh\left(\beta_A \ell\right)} \\ &= -\frac{G_A}{\beta_A t_A \sinh\left(\beta_A \ell\right)}\left[\frac{\sigma_\infty}{E'_s} + \left(\alpha_s - \alpha_p\right)\Delta T + \frac{\sigma_\infty}{E'_s S}\cosh\left(\beta_A \ell\right)\right. \\ &\quad \left. - \left(\alpha_s - \alpha_p\right)\Delta T \cosh\left(\beta_A \ell\right)\right] \end{aligned} \tag{2.16}$$

or

$$B = -\frac{G_A}{\beta_A t_A \sinh\left(\beta_A \ell\right)}\left\{\frac{\sigma_\infty}{E'_s}\left[1 + \frac{\cosh\left(\beta_A \ell\right)}{S}\right] + \left(\alpha_s - \alpha_p\right)\Delta T\left[1 - \cosh\left(\beta_A \ell\right)\right]\right\}$$

where S is again the doubler or strap stiffness to skin stiffness ratio.

Thus,

$$\begin{aligned} \tau^{(A)} &= -\frac{G_A \sinh\left(\beta_A x\right)}{\beta_A t_A}\left[-\frac{\sigma_\infty}{S \cdot E'_s} + \left(\alpha_s - \alpha_p\right)\Delta T\right] \\ &\quad - \frac{G_A \cosh\left(\beta_A x\right)}{\beta_A t_A \sinh\left(\beta_A \ell\right)}\left\{\frac{\sigma_\infty}{E'_s}\left[1 + \frac{\cosh\left(\beta_A \ell\right)}{S}\right] + \left(\alpha_s - \alpha_p\right)\Delta T\left[1 - \cosh\left(\beta_A \ell\right)\right]\right\} \end{aligned} \tag{2.17}$$

for a double-strap joint.

For a long overlap bonded doubler or strap joint, $\beta_A \ell \gg 1$. In that case, Equations (2.12) and (2.17) reduce to the same following equation for points near the end of the doubler or strap, i.e., for $x = \ell - |\varsigma|$ and $|\varsigma| \ll 1$,

$$\tau^{(A)} = -\frac{G_A e^{-\beta_A \varsigma}}{\beta_A t_A}\left[\frac{\sigma_\infty}{E'_s} + \left(\alpha_s - \alpha_p\right)\Delta T\right] \tag{2.18}$$

In deriving Equation (2.18), the following approximations had been used in the simplification

$$\begin{aligned} &\sinh(\beta_A \ell) \approx \cosh(\beta_A \ell) \approx \frac{e^{\beta_A \ell}}{2} \\ &\frac{1}{\sinh(\beta_A \ell)} \approx \frac{1}{\cosh(\beta_A \ell)} \approx 0 \end{aligned} \tag{2.19}$$

for $\beta_A \ell \gg 1$.

Several conclusions can be made from examination of this special case $\beta_A \ell \gg 1$. First, the solutions near the end of the doubler or strap are the same for both doubler and joint configurations, provided that their overlaps are sufficiently long. The interruption of the skin in the joint configuration has no effect to the solution near the end of the strap in a long overlap joint. In a similar manner, the adhesive shear–stress distribution near the break of the skin in the long overlap joint can be obtained from Equation (2.17) as

$$\begin{aligned} \tau^{(A)} &\approx -\frac{G_A \sinh(\beta_A x)}{\beta_A t_A}\left[-\frac{\sigma_\infty}{S \cdot E'_s} + (\alpha_s - \alpha_p)\Delta T\right] \\ &\quad - \frac{G_A \cosh(\beta_A x)}{\beta_A t_A}\left[\frac{\sigma_\infty}{S \cdot E'_s} - (\alpha_s - \alpha_p)\Delta T\right] \\ &\approx -\frac{G_A e^{-\beta_A |x|}}{\beta_A t_A}\left[\frac{\sigma_\infty}{S \cdot E'_s} - (\alpha_s - \alpha_p)\Delta T\right] \end{aligned} \tag{2.20}$$

for $|x| \ll 1$ and $\ell \gg 1$, and noting that $\beta_A \ell \gg 1$ so that Equation (2.19) holds. Equations (2.18) and (2.20) suggest that the doubler or strap and skin strain together throughout the interior of the doubler or strap, except for load transfer zones near the break of the skin in the joint configuration and near the end of the overlap in both joint and doubler configurations. This is because the adhesive shear stress $\tau^{(A)}$ decays exponentially within these transfer zones and becomes zero outside them. The load transfer between the skin and the doubler or strap effectively occurs over a length of order β_A^{-1}. A second conclusion drawn from the special case $\beta_A \ell \gg 1$ is that an adhesively bonded skin and a rigidly bonded skin will have approximately the same overall stiffness with the percentage difference proportional to the order of $1/\beta_A \ell$ (Rose, 1981, 1982, 1988). Consequently, the redistribution of stress due to a bonded patch can be computed using a rigid bond assumption. This inclusion analogy for such stress computation was first exploited by Rose (1981, 1982, 1988). Thirdly, from Equations (2.18) and (2.20), the maximum shear adhesive stress $\tau_{max}^{(A)}$ at the end of the doubler or strap is given by $-\frac{G_A}{\beta_A t_A}\left[\frac{\sigma_\infty}{E'_s} - (\alpha_s - \alpha_p)\Delta T\right]$ and it is equal to $-\frac{G_A}{\beta_A t_A}\left[\frac{\sigma_\infty}{S \cdot E'_s} - (\alpha_s - \alpha_p)\Delta T\right]$ at the break of the skin in the joint configuration. Thus, the maximum adhesive shear stress is inversely proportional to the square root of the adhesive thickness, i.e., $\tau_{max}^{(A)} \propto \frac{1}{\sqrt{t_A}}$, recalling that β_A is given by Equation (2.6). Finally, by noting that the thermal terms in Equations (2.18) and (2.20) are equal and opposite, it is clear that the net adhesive shear stress $\tau^{(A)}$ for the case of purely thermal loading will be zero, as expected.

It will be shown in Chapter 3 that the skin stress in the overlap of a rigidly bonded doubler configuration and the displacement of the skin at the break point in a joint configuration are also of interest. The skin stress in the overlap of a doubler configuration can be determined from the same strain condition between the doubler and the skin, and from the horizontal force equilibrium equation. In the absence of thermal loading, i.e., $\Delta T = 0$, this skin stress denoted by σ_0 is derived as follows

$$\begin{aligned} \varepsilon_s &= \varepsilon_p \\ E'_s \varepsilon_s t_s + E'_p \varepsilon_p t_p &= \sigma_\infty t_s \end{aligned} \tag{2.21}$$

Thus,

$$\begin{aligned} \varepsilon_s &= \frac{\sigma_\infty t_s}{E'_s t_s + E'_p t_p} \\ \sigma_0 = \sigma_s(0) &= E'_s \varepsilon_s = \frac{\sigma_\infty E'_s t_s}{E'_s t_s + E'_p t_p} = \frac{\sigma_\infty}{1+S} \end{aligned} \tag{2.22}$$

On the other hand, the displacement of the skin at the break point of a double-strap joint can be evaluated from Equation (2.3) for $x = 0$, using the result of Equation (2.20) and noting that $u_p = 0$ at $x = 0$ due to symmetry. Hence,

$$\begin{aligned} u_s(x=0) &= -\tau^{(A)}(x=0) \cdot \frac{t_A}{G_A} \\ &= \frac{1}{\beta_A}\left[\frac{\sigma_\infty}{S \cdot E'_s} - (\alpha_s - \alpha_p)\Delta T\right] \end{aligned} \tag{2.23}$$

For the special case $\Delta T = 0$, Equation (2.23) can be rewritten as

$$\begin{aligned} u_s(x=0) &= \frac{1}{\beta_A}\left(\frac{\sigma_\infty}{S \cdot E'_s}\right) \\ &= \frac{\beta_A}{\beta_A^2}\left(\frac{\sigma_\infty}{S \cdot E'_s}\right) \\ &= \frac{\beta_A t_A t_s}{G_A} \cdot \frac{\sigma_\infty}{1+S} \end{aligned} \tag{2.24}$$

where the term β_A^2 in the denominator has been substituted by Equation (2.6). The above equation can also be expressed in terms of σ_0 as

$$u_s(x=0) = \frac{\beta_A t_A t_s}{G_A}\sigma_0 \tag{2.25}$$

by virtue of Equation (2.22).

2.2.2 Elastic-plastic analysis of two-sided doublers and double-strap joints

In this case, the adhesive stress–strain relation (2.3) must be modified. As before, the adhesive shear strain is given by

$$\gamma^{(\mathrm{A})} = -\frac{u_\mathrm{s} - u_\mathrm{p}}{t_\mathrm{A}} \tag{2.26}$$

while the adhesive shear stress within the elastic region (of length d of Figure 2.2) is given by Equation (2.3). However, through the remaining plastic region, the adhesive shear stress is taken as

$$\tau^{(\mathrm{A})} = -\tau_\mathrm{Y}^{(\mathrm{A})} = \text{constant} \tag{2.27}$$

where $\tau_\mathrm{Y}^{(\mathrm{A})}$ is the yield strength of the adhesive and the adhesive is characterized by an elastic-perfectly-plastic model (Figure 2.3). In Equation (2.27), $\tau^{(\mathrm{A})}$ has been set equal to negative $\tau_\mathrm{Y}^{(\mathrm{A})}$ since $\tau^{(\mathrm{A})}$ as found in Section 2.2.1 will be in opposite direction with that shown in Figure 2.1. The equilibrium equation and the adherend stress–strain relations for this case of elastic-plastic adhesive are still specified by Equations (2.1)–(2.2). Differentiating Equation (2.26) once and substituting Equation (2.2) into the resulting equation yield

$$\frac{\mathrm{d}\gamma^{(\mathrm{A})}}{\mathrm{d}x} = -\frac{1}{t_\mathrm{A}}\left[\frac{N_\mathrm{s}}{E_\mathrm{s}' t_\mathrm{s}} - \frac{N_\mathrm{p}}{E_\mathrm{p}' t_\mathrm{p}} + \left(\alpha_\mathrm{s} - \alpha_\mathrm{p}\right)\Delta T\right] \tag{2.28}$$

The differential equation governing the adhesive shear–strain distribution follows by differentiation of Equation (2.28) and elimination of $\frac{\mathrm{d}N_\mathrm{s}}{\mathrm{d}x}$ and $\frac{\mathrm{d}N_\mathrm{p}}{\mathrm{d}x}$ from the resulting equation using (2.1).

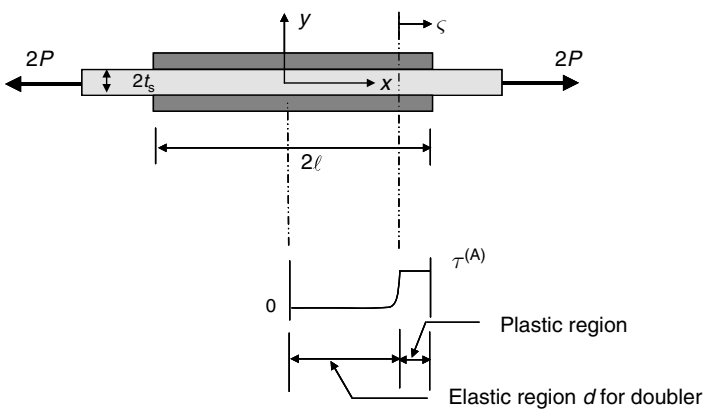

Fig. 2.2. Geometry for elastic-plastic analysis of a two-sided doubler.

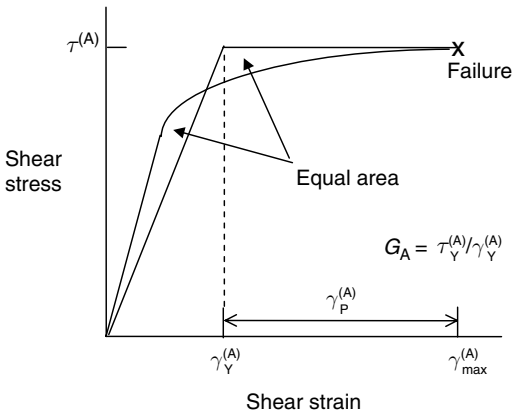

Fig. 2.3. A typical shear stress–strain curve for an adhesive. For simplicity, the adhesive is idealized as an elastic-perfectly-plastic material as shown.

$$\frac{\mathrm{d}^2\gamma^{(\mathrm{A})}}{\mathrm{d}x^2} - \frac{\tau^{(\mathrm{A})}}{t_\mathrm{A}}\left(\frac{1}{E'_\mathrm{s}t_\mathrm{s}} - \frac{1}{E'_\mathrm{p}t_\mathrm{p}}\right) = 0$$

$$\frac{\mathrm{d}^2\gamma^{(\mathrm{A})}}{\mathrm{d}x^2} - \frac{G_\mathrm{A}}{t_\mathrm{A}}\left(\frac{1}{E'_\mathrm{s}t_\mathrm{s}} - \frac{1}{E'_\mathrm{p}t_\mathrm{p}}\right)\frac{\tau^{(\mathrm{A})}}{G_\mathrm{A}} = 0 \tag{2.29}$$

$$\frac{\mathrm{d}^2\gamma^{(\mathrm{A})}}{\mathrm{d}x^2} - \beta_\mathrm{A}^2\frac{\tau^{(\mathrm{A})}}{G_\mathrm{A}} = 0$$

It should be noted that Equation (2.29) will be the same as (2.4) when the adhesive remains elastic since the latter equation can be obtained from the former by multiplying both sides of the equation by a constant G_A. Equation (2.29) has the general solution

$$\begin{aligned}\gamma^{(\mathrm{A})} &= A\sinh(\beta_\mathrm{A}x) + B\cosh(\beta_\mathrm{A}x) \quad \text{if } \left|\tau^{(\mathrm{A})}\right| < \tau_\mathrm{Y}^{(\mathrm{A})} \\ \gamma^{(\mathrm{A})} &= -\frac{\beta_\mathrm{A}^2\tau_\mathrm{Y}^{(\mathrm{A})}}{2G_\mathrm{A}}x^2 + Cx + F \quad \text{if } \left|\tau^{(\mathrm{A})}\right| = \tau_\mathrm{Y}^{(\mathrm{A})}\end{aligned} \tag{2.30}$$

As in Section 2.2.1, the solution of a double-sided bonded doubler will be derived first due to its simplicity. In the case of bonded doubler, all high load transfer zone will occur near the end of the overlap. Referring to Figure 2.2, the plastic region is assumed to occur near the end of the overlap, i.e., $|x| > d$, while the elastic region is within length d where d is also part of the sought solution. For algebraic manipulation, the general solution (2.30) will be rewritten as following for the doubler configuration

$$\gamma^{(\mathrm{A})} = A\sinh(\beta_\mathrm{A}x) \quad |x| \le d \tag{2.31}$$

and

$$\gamma^{(\mathrm{A})} = -\frac{\beta_{\mathrm{A}}^2 \tau_{\mathrm{Y}}^{(\mathrm{A})}}{2G_{\mathrm{A}}}\varsigma^2 + C\varsigma + F \quad |x| > d \text{ or } 0 \le \varsigma < \ell - d \tag{2.32}$$

where $\varsigma = x - d$ from Figure 2.2, and the constant B has been set to zero due to anti-symmetry requirement for the elastic adhesive shear stress. The boundary conditions are expressible in the form

$$\gamma^{(\mathrm{A})} = -\frac{\tau_{\mathrm{Y}}^{(\mathrm{A})}}{G_{\mathrm{A}}} = -\gamma_{\mathrm{Y}}^{(\mathrm{A})} \quad \text{at } x = d \text{ and } \varsigma = 0 \tag{2.33}$$

$$\frac{d\gamma^{(\mathrm{A})}}{dx} = \frac{d\gamma^{(\mathrm{A})}}{d\varsigma} \quad \text{at } x = d \text{ and } \varsigma = 0 \tag{2.34}$$

and

$$\frac{\mathrm{d}\gamma^{(\mathrm{A})}}{\mathrm{d}\varsigma} = -\frac{1}{t_{\mathrm{A}}}\left[\frac{\sigma_\infty}{E'_{\mathrm{s}}} + \left(\alpha_{\mathrm{s}} - \alpha_{\mathrm{p}}\right)\Delta T\right] \quad \text{at } \varsigma = \ell - d \tag{2.35}$$

via Equation (2.28) with $N_{\mathrm{s}}(\varsigma = \ell - d) = P = \sigma_\infty t_{\mathrm{s}}$ and $N_{\mathrm{p}}(\varsigma = \ell - d) = 0$. From this

$$A = -\frac{\gamma_{\mathrm{Y}}^{(\mathrm{A})}}{\sinh(\beta_{\mathrm{A}} d)} \tag{2.36}$$

$$F = -\gamma_{\mathrm{Y}}^{(\mathrm{A})} \tag{2.37}$$

$$C = -\frac{\beta_{\mathrm{A}}\gamma_{\mathrm{Y}}^{(\mathrm{A})}}{\tanh(\beta_{\mathrm{A}} d)} \tag{2.38}$$

$$\frac{\beta_{\mathrm{A}} \cdot d \cdot \tanh(\beta_{\mathrm{A}} d) - 1}{\tanh(\beta_{\mathrm{A}} d)} = \beta_{\mathrm{A}}\ell - \frac{1}{\beta_{\mathrm{A}} t_{\mathrm{A}} \gamma_{\mathrm{Y}}^{(\mathrm{A})}}\left[\frac{\sigma_\infty}{E'_{\mathrm{s}}} + \left(\alpha_{\mathrm{s}} - \alpha_{\mathrm{p}}\right)\Delta T\right] \tag{2.39}$$

Thus,

$$\gamma^{(\mathrm{A})} = -\frac{\gamma_{\mathrm{Y}}^{(\mathrm{A})}}{\sinh(\beta_{\mathrm{A}} d)}\sinh(\beta_{\mathrm{A}} x) \quad |x| \le d \tag{2.40}$$

$$\gamma^{(\mathrm{A})} = -\gamma_{\mathrm{Y}}^{(\mathrm{A})}\left[1 + \frac{\beta_{\mathrm{A}}}{\tanh(\beta_{\mathrm{A}} d)}\varsigma + \frac{\beta_{\mathrm{A}}^2}{2}\varsigma^2\right] \quad 0 \le \varsigma < \ell - d \tag{2.41}$$

where d is determined from the transcendental Equation (2.39). When d as determined from Equation (2.39) for a given applied stress σ_∞ is negative, what it means is that

the far-field-applied stress is not high enough to induce plastic deformation at the end of doubler or strap. For a sufficiently long overlap, $\tanh(\beta_A d) \to 1$ since $\beta_A d \gg 1$, and the maximum load per unit width which can be applied to the structure before bond failure can be evaluated from Equation (2.41) at the peak end of the adhesive shear strain distribution, i.e., $\varsigma = \ell - d$, which can be expressed in terms of the adhesive shear strain allowable as

$$\frac{P_{\max}\beta_A}{\tau_Y^{(A)}} = \left(1 + \frac{1}{S}\right)\left[\sqrt{1 + \frac{2\gamma_p^{(A)}}{\gamma_Y^{(A)}}} + \frac{\beta_A\left(\alpha_p - \alpha_s\right)\Delta T}{\tau_Y^{(A)}\left(\frac{1}{E_s' t_s} + \frac{1}{E_p' t_p}\right)}\right] \tag{2.42}$$

where $\gamma_p^{(A)}$ is the maximum allowable plastic strain of the adhesive as defined in Figure 2.3.

The solution of a double-strap joint can be derived in a similar manner as that for a doubler configuration. However, new boundary conditions must be employed and they are given by (Figure 2.4)

$$\gamma^{(A)} = -\gamma_Y^{(A)} \quad \text{at } x = -\frac{d}{2} \text{ or } \varsigma_1 = 0 \tag{2.43}$$

$$\gamma^{(A)} = -\gamma_Y^{(A)} \quad \text{at } x = +\frac{d}{2} \text{ or } \varsigma_2 = 0 \tag{2.44}$$

$$\frac{d\gamma^{(A)}}{dx} = -\frac{d\gamma^{(A)}}{d\varsigma_1} \quad \text{at } x = -\frac{d}{2} \text{ or } \varsigma_1 = 0 \tag{2.45}$$

$$\frac{d\gamma^{(A)}}{dx} = \frac{d\gamma^{(A)}}{d\varsigma_2} \quad \text{at } x = +\frac{d}{2} \text{ or } \varsigma_2 = 0 \tag{2.46}$$

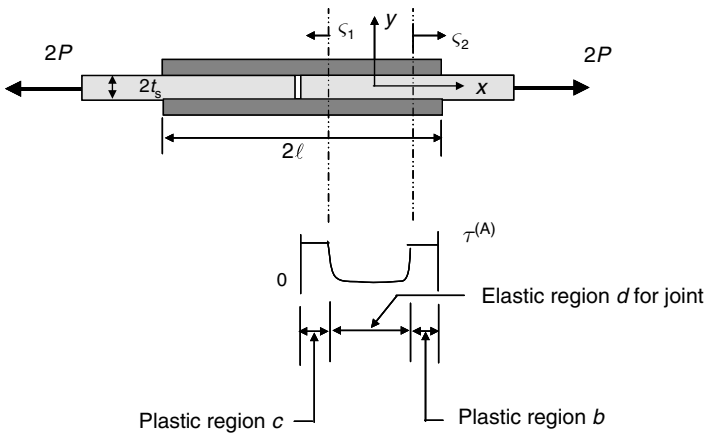

Fig. 2.4. Geometry for elastic-plastic analysis of a double strap joint.

$$-\frac{\mathrm{d}\gamma^{(\mathrm{A})}}{\mathrm{d}\varsigma_1} = -\frac{1}{t_\mathrm{A}}\left[-\frac{\sigma_\infty t_\mathrm{s}}{E'_\mathrm{p} t_\mathrm{p}} + \left(\alpha_\mathrm{s} - \alpha_\mathrm{p}\right)\Delta T\right] \quad \varsigma_1 = c \tag{2.47}$$

$$\frac{\mathrm{d}\gamma^{(\mathrm{A})}}{\mathrm{d}\varsigma_2} = -\frac{1}{t_\mathrm{A}}\left[\frac{\sigma_\infty t_\mathrm{s}}{E'_\mathrm{s} t_\mathrm{s}} + \left(\alpha_\mathrm{s} - \alpha_\mathrm{p}\right)\Delta T\right] \quad \varsigma_2 = b \tag{2.48}$$

$$c + d + b = \ell \tag{2.49}$$

From Equation (2.30), the solution of the adhesive shear strain in these zones of Figure 2.4 can be expressed as

$$\gamma^{(\mathrm{A})} = A\,\sinh\left(\beta_\mathrm{A} x\right) + B\,\cosh\left(\beta_\mathrm{A} x\right) \quad -\frac{d}{2} \le x \le \frac{d}{2} \tag{2.50}$$

$$\gamma^{(\mathrm{A})} = -\frac{\beta_\mathrm{A}^2 \tau_\mathrm{Y}^{(\mathrm{A})}}{2G_\mathrm{A}}\varsigma_1^2 + C\varsigma_1 + F \quad 0 \le \varsigma_1 < c \tag{2.51}$$

$$\gamma^{(\mathrm{A})} = -\frac{\beta_\mathrm{A}^2 \tau_\mathrm{Y}^{(\mathrm{A})}}{2G_\mathrm{A}}\varsigma_2^2 + H\varsigma_2 + J \quad 0 \le \varsigma_2 < b \tag{2.52}$$

where $\gamma_\mathrm{Y}^{(\mathrm{A})} = \frac{\tau_\mathrm{Y}^{(\mathrm{A})}}{G_\mathrm{A}}$ has been used in the simplification. From this

$$F = -\gamma_\mathrm{Y}^{(\mathrm{A})} \tag{2.53}$$

$$J = -\gamma_\mathrm{Y}^{(\mathrm{A})} \tag{2.54}$$

$$B = -\frac{\gamma_\mathrm{Y}^{(\mathrm{A})}}{\cosh\left(\frac{\beta_\mathrm{A} d}{2}\right)} \tag{2.55}$$

$$A = 0 \tag{2.56}$$

$$C = -\beta_\mathrm{A}\gamma_\mathrm{Y}^{(\mathrm{A})}\tanh\left(\frac{\beta_\mathrm{A} d}{2}\right) \tag{2.57}$$

$$H = -\beta_\mathrm{A}\gamma_\mathrm{Y}^{(\mathrm{A})}\tanh\left(\frac{\beta_\mathrm{A} d}{2}\right) \tag{2.58}$$

$$c = \frac{1}{t_\mathrm{A}\beta_\mathrm{A}^2\gamma_\mathrm{Y}^{(\mathrm{A})}}\left[\frac{\sigma_\infty t_\mathrm{s}}{E'_\mathrm{p} t_\mathrm{p}} + \left(\alpha_\mathrm{p} - \alpha_\mathrm{s}\right)\Delta T\right] - \frac{\tanh\left[\frac{\beta_\mathrm{A}(\ell - b - c)}{2}\right]}{\beta_\mathrm{A}} \tag{2.59}$$

$$b = \frac{1}{t_\mathrm{A}\beta_\mathrm{A}^2\gamma_\mathrm{Y}^{(\mathrm{A})}}\left[\frac{\sigma_\infty}{E'_\mathrm{s}} - \left(\alpha_\mathrm{p} - \alpha_\mathrm{s}\right)\Delta T\right] - \frac{\tanh\left[\frac{\beta_\mathrm{A}(\ell - b - c)}{2}\right]}{\beta_\mathrm{A}} \tag{2.60}$$

It is clear from Equations (2.53)–(2.60) that in order to have the explicit solution one must first solve iteratively (2.59) and (2.60) simultaneously for the plastic zone sizes b and c since some of the unknown coefficients in (2.50)–(2.52) are given in terms of d which in turn depends on b and c via (2.49). Depending on the level of the far-field-applied stress σ_∞, c and b as determined from (2.59) and (2.60) may be both positive, both negative, or one positive and the other negative. A negative value of b and c means that σ_∞ is not sufficiently high to induce the plastic deformation in the adhesive at these two ends of the overlap. For a long overlap, there is no interaction between the overlap end and the skin interruption end. In that case, the solution near the end of the overlap of a joint configuration is given by the same formula as that for a doubler configuration. However, the solution near the skin interruption end must be determined from Equation (2.51) with the constants C, F and c given by (2.57), (2.53) and (2.59), respectively. Since $\tanh\left[\frac{\beta_A(\ell-b-c)}{2}\right] = \tanh\left(\frac{\beta_A d}{2}\right) \to 1$ for $\ell \gg b$, c and for $\beta_A d \gg 1$, therefore, from Equation (2.59), $c = \frac{1}{t_A\beta_A^2\gamma_Y^{(A)}}\left[\frac{\sigma_\infty t_s}{E_p' t_p} + \left(\alpha_p - \alpha_s\right)\Delta T\right] - \frac{1}{\beta_A}$. Similarly, for large ℓ, Equation (2.57) is simplified to $C = -\beta_A\gamma_Y^{(A)}$. Hence, from Equation (2.26) with $u_p = 0$ (due to the symmetry) and from (2.51) with c and C given above while F given by (2.53), a straightforward algebraic manipulation yields the displacement of the skin at the interruption end when $\Delta T = 0$ as

$$u_s(s_1 = c) = \frac{t_A\gamma_Y^{(A)}}{2}\left[1 + \left(\frac{\sigma_\infty t_s}{t_A\beta_A E_p' t_p \gamma_Y^{(A)}}\right)^2\right] \tag{2.61}$$

By noting from Equation (2.6) that $\beta_A^2 = \frac{G_A}{t_A}\left(\frac{1+S}{S}\right)\frac{1}{E_s' t_s}$, Equation (2.61) can also be cast into the following form

$$u_s(s_1 = c) = \frac{t_A\tau_Y^{(A)}}{2G_A}\left[1 + \left(\frac{\sigma_0}{\sigma_{0Y}}\right)^2\right] \tag{2.62}$$

where σ_0 is defined previously by (2.22) as $\sigma_0 = \frac{\sigma_\infty}{1+S}$, $\sigma_{oY} = \frac{\tau_Y^{(A)}}{\beta_A t_s}$, and $\tau_Y^{(A)}$ is again the yield strength of the adhesive. The result of Equation (2.62) will be utilized in Chapter 3 for computing the stress intensity factor of a crack after patching.

2.2.3 Peel stresses in two-sided doublers and double-strap joints

For thick patches the bond may fail in peel before its shear strength potential could be reached. This section therefore presents an analysis that deals with the peel stresses in the bond line. The geometry and nomenclature for this analysis are illustrated in Figure 2.5. The differential equations for the outer patch are

Moment equilibrium

$$\frac{dM_p}{dx} = V_p - \frac{\tau^{(A)} t_p}{2} \tag{2.63}$$

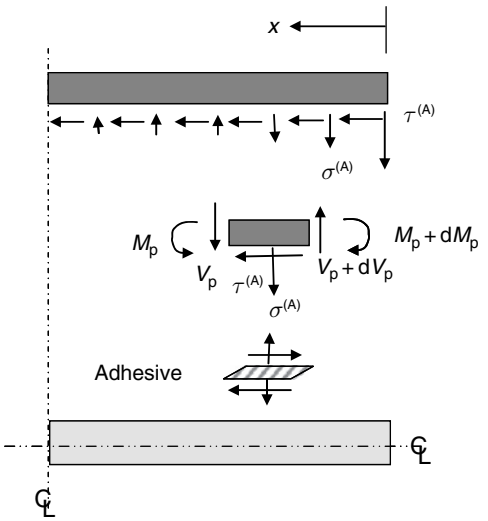

Fig. 2.5. Geometry for analysis of peel stress in a two-sided doubler.

Force equilibrium

$$\frac{dV_p}{dx} = \sigma^{(A)} \tag{2.64}$$

Moment–curvature relation

$$\frac{d^2 w_p}{dx^2} = -\frac{M_p}{D_p} \tag{2.65}$$

Adhesive stress–strain relation

$$\varepsilon^{(A)} = \frac{\sigma^{(A)}}{E_A} = \frac{w_p - w_s}{t_A} = \frac{w_p}{t_A} \tag{2.66}$$

where w_s is set equal to zero since the doubler or joint configuration is symmetric with respect to the middle plane of the skin, E_A is the extensional modulus of the adhesive, D_p is the bending rigidity of the patch, i.e., $D_p = \frac{E'_p t_p^3}{12}$, V_p is the vertical shear force acting on the cross section plane of the patch, and the rest are previously defined.

To uncouple the differential equations governing the peel and shear stress, the shear stress $\tau^{(A)}$ in Equation (2.63) is set constant. This simplification is justified whenever the loads are so high as to induce plastic deformation and thus constant shear stress $\tau_Y^{(A)}$ in the adhesive over significant distance from the critical end at which the peel stress peaks. From Equations (2.63)–(2.66), differentiation and elimination yield the governing differential for the transverse deflection of the patch as

$$\frac{d^4 w_p}{dx^4} + \frac{E_A}{D_p t_A} w_p = 0 \tag{2.67}$$

It should be emphasized that since (2.67) has been derived approximately, the peel stress solution obtained in this section may not satisfy all the required boundary conditions exactly.

To simplify the algebraic manipulation, it is appropriate to assume that the overlap is long since it is always the case in practice to preclude inadequate shear strength. For a sufficiently long overlap, the peel stresses at the end of the overlap are identical to those at the interruption end of the skin, provided that the adhesive undergoes plastic deformation at these both ends due to shears. The peel solution therefore will be derived particularly for points near the end of the overlap. Under the long overlap assumption, the solution of Equation (2.67) is given by

$$w_{\mathrm{p}} = A\mathrm{e}^{-\hat{\upsilon}x}\cos(\hat{\upsilon}x) + B\mathrm{e}^{-\hat{\upsilon}x}\sin(\hat{\upsilon}x) \tag{2.68}$$

where

$$\hat{\upsilon} = \left(\frac{E_{\mathrm{A}}}{4D_{\mathrm{p}}t_{\mathrm{A}}}\right)^{1/4} \tag{2.69}$$

and x is now measured from the end of the overlap as shown in Figure 2.5. The boundary conditions defining the constants A and B are

$$M_{\mathrm{p}} = -D_{\mathrm{p}}\frac{\mathrm{d}^2 w_{\mathrm{p}}}{\mathrm{d}x^2} = 0 \quad \text{at } x = 0 \tag{2.70}$$

and $V_{\mathrm{p}} = 0$ at $x = 0$, whence from Equations (2.63) and (2.65)

$$\frac{\mathrm{d}M_{\mathrm{p}}}{\mathrm{d}x} = -\frac{\tau_{\mathrm{Y}}^{(\mathrm{A})}t_{\mathrm{p}}}{2} = -D_{\mathrm{p}}\frac{\mathrm{d}^3 w_{\mathrm{p}}}{\mathrm{d}x^3} \quad \text{at } x = 0 \tag{2.71}$$

where $\tau^{(\mathrm{A})}$ in Equation (2.63) has been set equal to the adhesive yield strength $\tau_{\mathrm{Y}}^{(\mathrm{A})}$ due to plastic deformation occurring at the overlap end. Of these, condition (2.70) requires that

$$\left.\frac{\mathrm{d}^2 w_{\mathrm{p}}}{\mathrm{d}x^2}\right|_{\mathrm{x}=0} = 2\hat{\upsilon}^2\mathrm{e}^{-\hat{\upsilon}x}\left[A\sin(\hat{\upsilon}x) - B\cos(\hat{\upsilon}x)\right]\big|_{\mathrm{x}=0} = 0 \tag{2.72}$$

or

$$B = 0 \tag{2.73}$$

In contrast, condition (2.71) provides

$$\left.\frac{\mathrm{d}^3 w_{\mathrm{p}}}{\mathrm{d}x^3}\right|_{\mathrm{x}=0} = 2A\hat{\upsilon}^3\left[-\sin(\hat{\upsilon}x) + \cos(\hat{\upsilon}x)\right]\mathrm{e}^{-\hat{\upsilon}x} + 2B\hat{\upsilon}^3\left[\cos(\hat{\upsilon}x) + \sin(\hat{\upsilon}x)\right]\mathrm{e}^{-\hat{\upsilon}x}\big|_{\mathrm{x}=0}$$

$$= \frac{\tau_{\mathrm{Y}}^{(\mathrm{A})}t_{\mathrm{p}}}{2D_{\mathrm{p}}} = 2\hat{\upsilon}^3(A + B) \tag{2.74}$$

Substituting (2.73) into (2.74) yields

$$A = \frac{\tau_{\mathrm{Y}}^{(\mathrm{A})} t_{\mathrm{p}}}{4 D_{\mathrm{p}} \hat{\upsilon}^3} \tag{2.75}$$

and from Equation (2.68)

$$w_{\mathrm{p}} = \frac{\tau_{\mathrm{Y}}^{(\mathrm{A})} t_{\mathrm{p}}}{4 D_{\mathrm{p}} \hat{\upsilon}^3} \cos(\hat{\upsilon} x)\, \mathrm{e}^{-\hat{\upsilon} \mathrm{x}} \tag{2.76}$$

Hence, the maximum peel stress in the adhesive can be determined by evaluating Equation (2.66) at $x = 0$ with w_{p} given by (2.76) as

$$\begin{aligned} \sigma_{\max}^{(\mathrm{A})} &= \frac{\tau_{\mathrm{Y}}^{(\mathrm{A})} t_{\mathrm{p}}}{4 D_{\mathrm{p}} \hat{\upsilon}^3} \cdot \frac{E_{\mathrm{A}}}{t_{\mathrm{A}}} \\ &= \tau_{\mathrm{Y}}^{(\mathrm{A})} \left(\frac{3 E_{\mathrm{A}} t_{\mathrm{p}}}{E_{\mathrm{p}}' t_{\mathrm{A}}} \right)^{1/4} \end{aligned} \tag{2.77}$$

Even though Equation (2.77) has been derived under the assumption that significant plastic deformation occurs at the ends of the overlap, it is also used by Hart-Smith for the case that the adhesive shear stress is still below its yield strength as

$$\sigma_{\max}^{(\mathrm{A})} = \tau_{\max}^{(\mathrm{A})} \left(\frac{3 E_{\mathrm{A}} t_{\mathrm{p}}}{E_{\mathrm{p}}' t_{\mathrm{A}}} \right)^{1/4} \tag{2.78}$$

where $\tau_{\max}^{(\mathrm{A})}$ is the maximum shear stress in the adhesive at the end of the overlap which is equal to $\tau_{\mathrm{Y}}^{(\mathrm{A})}$ if the adhesive undergoes plastic deformation there.

2.3 Stress Analysis of One-Sided Bonded Doublers and Single-Strap Joints

The analysis of the one-sided bonded doublers and single-strap joints proceeds in three stages, followed the Hart-Smith approach (1999, 2005b), which can be considered as an extension of the Goland–Reissner solution of a single-lap joint to the present doubler and joint configurations. The typical configurations of these doublers and joints are shown schematically in Figure 2.6(a). The first is the establishment of the bending moment in the adherends at the end of the overlap and also at the skin interruption end in the case of joint configuration. The second is the derivation of an expression for the peel stresses induced in the adhesive by the out-of-plane deflection (bending) due to the eccentricity in the load path. The third solution is for the adhesive shear stress distribution associated with transferring the load from one adherend to the other. Various approximations have been used in each stage so that the proposed solution process is analytically simple to apply. The analysis conducted here is rather limited to the case of uniform cooling and with tensile loads. Under such thermo-mechanical loading, the structure will

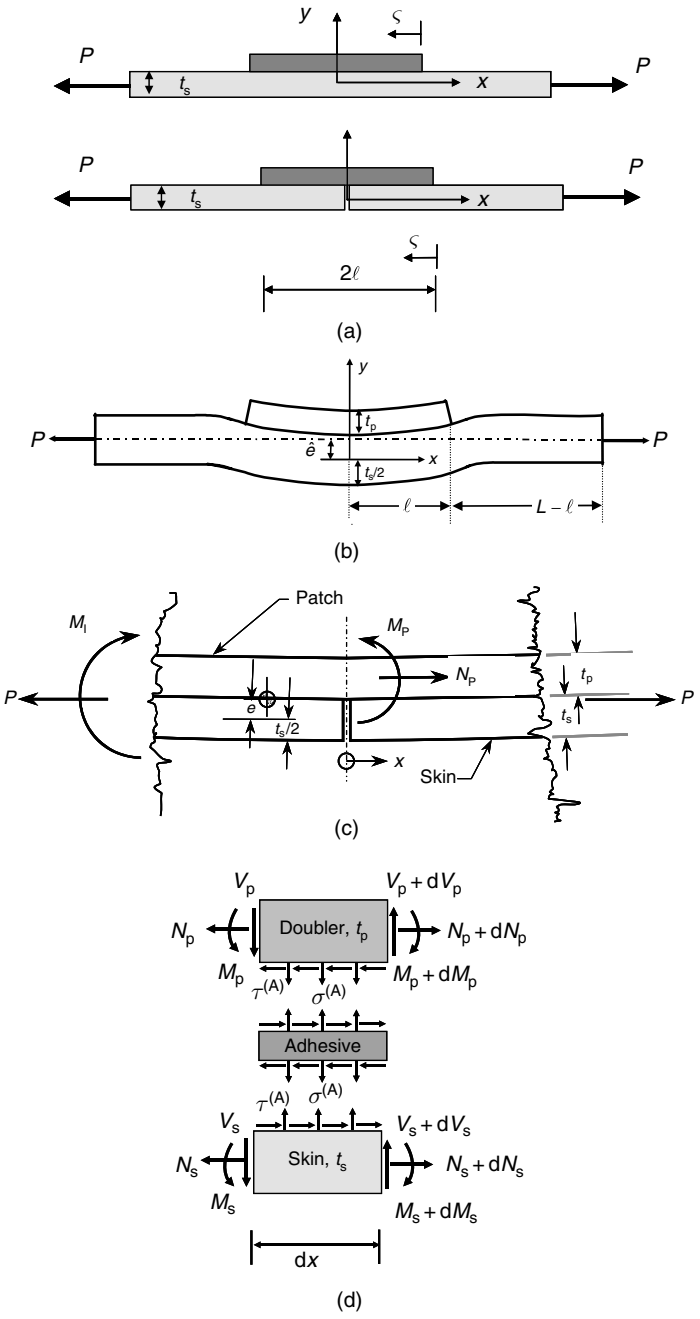

Fig. 2.6. Terminologies for analyses of a one-sided doubler and a single strap joint: (a) geometry of a doubler and joint; (b) deformed shape of a doubler in moment analysis; (c) moment distribution at the skin interruption end in stage I analysis of a strap joint; and (d) differential elements for analysis of adhesive shear and peel stresses.

exhibit geometrically nonlinear response but without experiencing buckling or global instability.

The Hart-Smith three-stage analysis approach will be described in Sections 2.3.1–2.3.3. It is worthy to note that the response of a patched beam subjected to a variety of thermo-mechanical loading (uniform heating/cooling with tensile/compressive loads) and support conditions (clamped or hinged ends) have been considered by Karlsson and Bottega (2000a,b). They employed a variational formulation which results in a self-consistent set of equations and conditions governing the response of the structural system. However, since the latter approach will yield identical results to those presented here for the combined uniform cooling and tensile loading and since it is much more complicated than the former Hart-Smith approach, that approach will not be discussed in this chapter. Furthermore, it is also found from their work and the Hart-Smith's work that the current solution will become indeterminate for a vanishing small tensile load. This degenerated solution for a case of purely thermal load will be treated separately in Section 5.3.1(a) of Chapter 5.

2.3.1 Stage I: Solution for bending moment at ends and middle of overlap

The equations governing the adhesive stresses require knowledge of the bending moment at the ends of the overlap as boundary conditions. Therefore, the analysis starts with a solution for these quantities (Figure 2.6(b)). It was shown in Section 2.1 that for a sufficiently long overlap, the load transfer between adherends are confined to narrow zones at the ends of the overlap and for joints also at the skin interruption end in joints, with only negligible adhesive shear stress throughout the elastic trough in between these load transfer zones. It is therefore appropriate to assume in this analysis portion for the adherend bending moments (except for the mentioned narrow load transfer zones) that the doubler or strap is rigidly bonded to the skin plate. As before, for simplicity, the bending moments are derived first for the doubler configuration. The bending moment M_{H} in the skin, outside the overlap, is expressed by

$$M_{\mathrm{H}} = -Pw_{\mathrm{H}} \quad |x| > \ell \tag{2.80}$$

where w_{H} is the transverse deflection outside the overlap and P is the applied longitudinal load per unit width. In contrast, the bending moment M_{I} in the overlap is given as follows.

$$\begin{aligned} M_{\mathrm{I}} &= -P\left(w_{\mathrm{I}} + \hat{e}\right) + M^{\mathrm{therm}} = -P\left(w_{\mathrm{I}} + \hat{e} - \frac{M^{\mathrm{therm}}}{P}\right) \quad |x| \le \ell \\ \hat{e} &= \frac{\left(\frac{t_{\mathrm{s}}+t_{\mathrm{p}}}{2}\right)S}{1+S} \\ M^{\mathrm{therm}} &= F^{\mathrm{therm}} \cdot \left(\frac{t_{\mathrm{s}}+t_{\mathrm{p}}}{2}\right) \\ F^{\mathrm{therm}} &= \frac{E'_{\mathrm{s}}t_{\mathrm{s}}E'_{\mathrm{p}}t_{\mathrm{p}}\left(\alpha_{\mathrm{p}}-\alpha_{\mathrm{s}}\right)\Delta T}{E'_{\mathrm{s}}t_{\mathrm{s}}+E'_{\mathrm{p}}t_{\mathrm{p}}} \end{aligned} \tag{2.81}$$

where w_I is defined as the transverse deflection inside the overlap, $\hat{e}$ is the eccentricity, S is the patch stiffness ratio, and the rest are previously defined. $\hat{e}$ is defined as the distance between the centroid of the skin layer alone and the centroid of the patch–skin combination in the rigidly bonded overlap. Similar to Equation (2.65), the classical plate-bending theory relate the curvature to the bending moment via the relation

$$M_H = -D_s \frac{d^2 w_H}{dx^2} \tag{2.82}$$

$$M_I = -D_I \frac{d^2 w_I}{dx^2} \tag{2.83}$$

in which

$$\begin{aligned} D_s &= \frac{E'_s t_s^3}{12} \\ D_I &= I_M \cdot D_s \end{aligned} \tag{2.84}$$

$$I_M = 1 + \frac{E'_s t_s^3}{E'_p t_p^3} + \frac{\left(1 + \frac{t_s}{t_p}\right)^2}{\left(1 + \frac{E'_p t_p}{E'_s t_s}\right)} \tag{2.85}$$

D_s and D_I are the bending stiffnesses of the skin and of the rigidly bonded overlap, respectively. Substituting Equation (2.82) into (2.80), and (2.83) into (2.81) yields

$$\frac{d^2 w_H}{dx^2} - \frac{P}{D_s} w_H = 0 \tag{2.86}$$

$$\frac{d^2 w_I}{dx^2} - \frac{P}{D_I} w_I = \frac{P \cdot \left(\hat{e} - \frac{M^{therm}}{P}\right)}{D_I} \tag{2.87}$$

The respective solutions of (2.86) and (2.87) are

$$w_H = A \cosh(\xi_H x) + B \sinh(\xi_H x) \quad |x| > \ell \tag{2.88}$$

$$w_I = C \cosh(\xi_I x) + F \sinh(\xi_I x) - \hat{e} + \frac{M^{therm}}{P} \quad |x| \le \ell \tag{2.89}$$

where

$$\xi_H = \sqrt{\frac{P}{D_s}} \tag{2.90}$$

$$\xi_I = \sqrt{\frac{P}{D_I}} \tag{2.91}$$

The four integration constants are determined from the following four boundary conditions

$$\left.\frac{\mathrm{d}w_{\mathrm{I}}}{\mathrm{d}x}\right|_{\mathrm{x}=0} = 0 \quad \text{(symmetry)} \tag{2.92}$$

$$w_{\mathrm{H}}(\ell) = w_{\mathrm{I}}(\ell) \quad \text{(displacement continuity)} \tag{2.93}$$

$$\frac{\mathrm{d}w_{\mathrm{H}}}{\mathrm{d}x}(\ell) = \frac{\mathrm{d}w_{\mathrm{I}}}{\mathrm{d}x}(\ell) \quad \text{(slope continuity)} \tag{2.94}$$

$$w_{\mathrm{H}}(L) = 0 \quad \text{(simply supported at the ends)} \tag{2.95}$$

Condition (2.92) requires that

$$F = 0 \tag{2.96}$$

On the other hand, condition (2.95) provides

$$A = -B\tanh(\xi_{\mathrm{H}}L) \tag{2.97}$$

The displacement compatibility (2.93) requires that

$$B\left[-\tanh(\xi_{\mathrm{H}}L)\cosh(\xi_{\mathrm{H}}\ell) + \sinh(\xi_{\mathrm{H}}\ell)\right] = C\cosh(\xi_{\mathrm{I}}\ell) - \left(\hat{e} - \frac{M^{\mathrm{therm}}}{P}\right) \tag{2.98}$$

whence

$$C = B\frac{\left[-\tanh(\xi_{\mathrm{H}}L)\cosh(\xi_{\mathrm{H}}\ell) + \sinh(\xi_{\mathrm{H}}\ell)\right]}{\cosh(\xi_{\mathrm{I}}\ell)} + \frac{\left(\hat{e} - \frac{M^{\mathrm{therm}}}{P}\right)}{\cosh(\xi_{\mathrm{I}}\ell)} \tag{2.99}$$

and the continuity of slope (2.94) requires that

$$\xi_{\mathrm{I}}C\sinh(\xi_{\mathrm{I}}\ell) = B\xi_{\mathrm{H}}\left[-\tanh(\xi_{\mathrm{H}}L)\sinh(\xi_{\mathrm{H}}\ell) + \cosh(\xi_{\mathrm{H}}\ell)\right] \tag{2.100}$$

Substitution of (2.99) into (2.100) gives

$$B = -\frac{\left(\hat{e} - \frac{M^{\mathrm{therm}}}{P}\right)}{\cosh(\xi_{\mathrm{H}}\ell)\left[\tanh(\xi_{\mathrm{H}}\ell) - \tanh(\xi_{\mathrm{H}}L)\right]\left\{1 - \frac{\xi_{\mathrm{H}}\left[1 - \tanh(\xi_{\mathrm{H}}L)\tanh(\xi_{\mathrm{H}}\ell)\right]}{\xi_{\mathrm{I}}\tanh(\xi_{\mathrm{I}}\ell)\left[\tanh(\xi_{\mathrm{H}}\ell) - \tanh(\xi_{\mathrm{H}}L)\right]}\right\}} \tag{2.101}$$

From Equation (2.99) with B given by (2.101), C is found to be

$$C = \frac{\left(\hat{e} - \frac{M^{\text{therm}}}{P}\right)}{\cosh(\xi_{\text{I}}\ell)} \left\{ \frac{1}{1 - \frac{\xi_{\text{I}} \tanh(\xi_{\text{I}}\ell)\left[\tanh(\xi_{\text{H}}\ell) - \tanh(\xi_{\text{H}}L)\right]}{\xi_{\text{H}}\left[1 - \tanh(\xi_{\text{H}}L)\tanh(\xi_{\text{H}}\ell)\right]}} \right\} \tag{2.102}$$

With the constants of integration A, B, C and F having been explicitly derived, the analysis of the adherend bending moment for a doubler configuration is completed. It is interesting to note from Equation (2.89) that the deflection at the center of the doubler is given by

$$\begin{aligned} w_{\text{I}}(x=0) &= C - \left(\hat{e} - \frac{M^{\text{therm}}}{P}\right) \\ &= \frac{\left(\hat{e} - \frac{M^{\text{therm}}}{P}\right)}{\cosh(\xi_{\text{I}}\ell)} \left\{ \frac{1}{1 - \frac{\xi_{\text{I}} \tanh(\xi_{\text{I}}\ell)\left[\tanh(\xi_{\text{H}}\ell) - \tanh(\xi_{\text{H}}L)\right]}{\xi_{\text{H}}\left[1 - \tanh(\xi_{\text{H}}L)\tanh(\xi_{\text{H}}\ell)\right]}} - \cosh(\xi_{\text{I}}\ell) \right\} \end{aligned} \tag{2.103}$$

This solution has been verified for a particular doubler configuration specified in Table 2.1, when $\Delta T = 0$ (and thus $M^{\text{therm}} = 0$) by comparing it to the corresponding FE result in Figure 2.7. Furthermore, for $L \gg 1$, it is very easy to show that $\tanh(\xi_{\text{H}}L) \to 1$, and $C \to \frac{\left(\hat{e} - \frac{M^{\text{therm}}}{P}\right)}{\cosh(\xi_{\text{I}}\ell) + \frac{\xi_{\text{I}}}{\xi_{\text{H}}}\sinh(\xi_{\text{I}}\ell)}$ so that w_{I} from (2.89) is reduced to the following simple form

$$w_{\text{I}}(x) = \frac{\left(\hat{e} - \frac{M^{\text{therm}}}{P}\right)\cosh(\xi_{\text{I}}x)}{\cosh(\xi_{\text{I}}\ell) + \frac{\xi_{\text{I}}}{\xi_{\text{H}}}\sinh(\xi_{\text{I}}\ell)} - \left(\hat{e} - \frac{M^{\text{therm}}}{P}\right) \quad \text{for } L \gg 1 \tag{2.104}$$

The form of w_{I} given by Equation (2.104) will be exploited in the next portion of this analysis as well as in the next two sections.

Table 2.1. Dimensions and material properties of a typical repair.

Layer	Young's modulus (GPa)	Poisson's ratio	Thickness (mm)
Skin	71	0.3	3.0
Patch	207	0.3	1.0
Adhesive	1.89	0.3	0.2

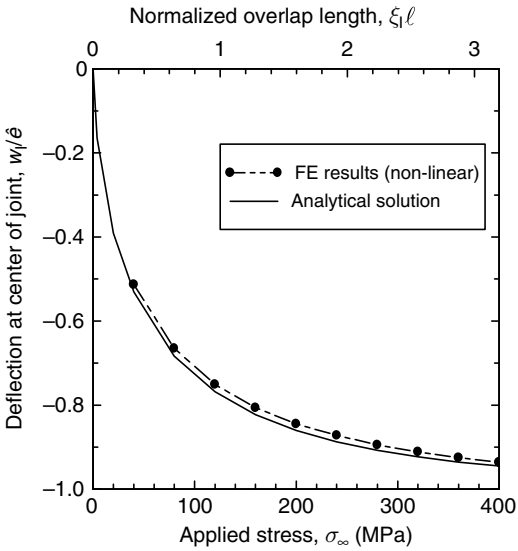

Fig. 2.7. Deflection of the one-sided doubler accounting for geometrically nonlinear deformation at the center of the overlap.

The bending moment inside the overlap follows from Equations (2.104) and (2.83) as

$$M_{\mathrm{I}}(x) = -\frac{P \cdot \left(\hat{e} - \dfrac{M^{\mathrm{therm}}}{P}\right)}{\cosh(\xi_{\mathrm{I}}\ell) + \dfrac{\xi_{\mathrm{I}}}{\xi_{\mathrm{H}}}\sinh(\xi_{\mathrm{I}}\ell)} \cosh(\xi_{\mathrm{I}} x) \quad \text{for } L \gg 1 \tag{2.105}$$

It is interesting to note from Equation (2.105) that for a combination of a long overlap and high load P, the bending moment vanishes at the middle of the doubler since $\cosh(\xi_4 c) \gg 1$, $\sinh(\xi_4 c) \gg 1$ for $\xi_{\mathrm{I}}\ell \gg 1$. Physically, for a high load P, the skin/patch combination tries to deflect sufficiently to align its centroid with the line of action of the applied load.

On the other hand, the bending moment outside the overlap is evaluated from Equations (2.82), (2.88) and (2.97) as

$$M_{\mathrm{H}}(x) = -D_{\mathrm{s}}\frac{d^2 w_{\mathrm{H}}}{dx^2} = -D_{\mathrm{s}}\xi_{\mathrm{H}}^2 B\left[-\tanh(\xi_{\mathrm{H}} L)\cosh(\xi_{\mathrm{H}} x) + \sinh(\xi_{\mathrm{H}} x)\right] \tag{2.106}$$

where B is given by (2.101). Again, by limiting to the case $L \gg 1$, Equation (2.106) can be re-expressed as

$$M_{\mathrm{H}}(x) = -\frac{P \cdot \left(\hat{e} - \dfrac{M^{\mathrm{therm}}}{P}\right) \cdot \left[\sinh(\xi_{\mathrm{H}} x) - \cosh(\xi_{\mathrm{H}} x)\right]}{\cosh(\xi_{\mathrm{H}}\ell)\left[1 - \tanh(\xi_{\mathrm{H}}\ell)\right]\left[1 + \dfrac{\xi_{\mathrm{H}}}{\xi_{\mathrm{I}}\tanh(\xi_{\mathrm{I}}\ell)}\right]} \tag{2.107}$$

Thus, the bending moment at the end of doubler is found to be equal to

$$M_{\mathrm{H}}(\ell) = \frac{P \cdot \left(\hat{e} - \dfrac{M^{\mathrm{therm}}}{P} \right) \cdot \dfrac{\xi_{\mathrm{I}}}{\xi_{\mathrm{H}}} \tanh\left(\xi_{\mathrm{I}} \ell\right)}{1 + \dfrac{\xi_{\mathrm{I}}}{\xi_{\mathrm{H}}} \tanh\left(\xi_{\mathrm{I}} \ell\right)} \tag{2.108}$$

The next portion of the analysis deals with the single-strap joint configuration. As long as the gap under the middle of the strap is close to zero extent parallel to the applied load and the overlap is sufficiently long, the presence of this gap has no effect on the derivation of expressions for the bending moments in the adherends, except for the existence of a locally concentrated bending moment of magnitude of $-P\left(\frac{t_{\mathrm{p}}+t_{\mathrm{s}}}{2} - \hat{e} + \frac{M^{\mathrm{therm}}}{P}\right)$ in the strap directly over the gap due to the shift in neutral axis of the applied load as shown in Figure 2.6(c). However, the curvature associated with this concentrated bending moment cannot be predicted accurately by the classical Kirchoff theory as presently assumed and this curvature is claimed to be insignificant by Hart-Smith. Thus, in the case of a single-strap joint, there would be a different bending moment in the continuous member (strap) at $x = 0$ than that for a doubler configuration. The magnitude of this moment can be deduced as a simple modification of the previous solution for the doubler configuration at $x = 0$. It should be remembered that the bending moment at $x = 0$ for a doubler configuration can be obtained from Equation (2.105) as

$$M_{\mathrm{I}}(x=0) = -\frac{P \cdot \left(\hat{e} - \dfrac{M^{\mathrm{therm}}}{P} \right)}{\cosh\left(\xi_{\mathrm{I}} \ell\right) + \dfrac{\xi_{\mathrm{I}}}{\xi_{\mathrm{H}}} \sinh\left(\xi_{\mathrm{I}} \ell\right)}$$

Thus, the bending moment at $x = 0$ for a strap joint configuration can be deduced as

$$M_{\mathrm{I}}^{\mathrm{p}}(x=0) = -\frac{P \cdot \left(\hat{e} - \dfrac{M^{\mathrm{therm}}}{P} \right)}{\cosh\left(\xi_{\mathrm{I}} \ell\right) + \dfrac{\xi_{\mathrm{I}}}{\xi_{\mathrm{H}}} \sinh\left(\xi_{\mathrm{I}} \ell\right)} - P\left(\frac{t_{\mathrm{p}} + t_{\mathrm{s}}}{2} - \hat{e} + \frac{M^{\mathrm{therm}}}{P} \right) \tag{2.109}$$

$$M_{\mathrm{I}}^{\mathrm{s}}(x=0) = 0$$

2.3.2 Stage II: Solution for induced adhesive peel stresses

The analysis technique of Section 2.2.3 will be used here, but for a one-sided bonded doubler or a single-strap joint, and with different boundary conditions. As in Section 2.2.3, it is assumed that the peel stresses are uncoupled from any effects of the adhesive shear stresses developed as the doubler or strap is strained to match the stretching of the skin. The coupling effect will be investigated by a method given in Chapter 7. The geometry and terminology for the peel stress analysis are identified in

Figure 2.6(d). In contrast to the preceding stage I analysis, the present analysis accounts for a thin layer of adhesive. Moment equilibrium requires that

$$\frac{\mathrm{d}M_{\mathrm{p}}}{\mathrm{d}x} = V_{\mathrm{p}} - \frac{\tau^{(\mathrm{A})} t_{\mathrm{p}}}{2} \tag{2.110}$$

$$\frac{\mathrm{d}M_{\mathrm{s}}}{\mathrm{d}x} = V_{\mathrm{s}} - \frac{\tau^{(\mathrm{A})} t_{\mathrm{s}}}{2} \tag{2.111}$$

where the subscripts p and s denote the patch (doubler or strap) and skin, respectively.

Longitudinal force equilibrium requires that

$$\frac{\mathrm{d}N_{\mathrm{p}}}{\mathrm{d}x} - \tau^{(\mathrm{A})} = 0 \tag{2.112}$$

$$\frac{\mathrm{d}N_{\mathrm{s}}}{\mathrm{d}x} + \tau^{(\mathrm{A})} = 0 \tag{2.113}$$

while transverse force equilibrium requires that

$$\frac{\mathrm{d}V_{\mathrm{p}}}{\mathrm{d}x} - \sigma^{(\mathrm{A})} = 0 \tag{2.114}$$

$$\frac{\mathrm{d}V_{\mathrm{s}}}{\mathrm{d}x} + \sigma^{(\mathrm{A})} = 0 \tag{2.115}$$

Plate-bending theory provides the equations

$$\frac{\mathrm{d}^2 w_{\mathrm{p}}}{\mathrm{d}x} = -\frac{M_{\mathrm{p}}}{D_{\mathrm{p}}} \tag{2.116}$$

$$\frac{\mathrm{d}^2 w_{\mathrm{s}}}{\mathrm{d}x} = -\frac{M_{\mathrm{s}}}{D_{\mathrm{s}}} \tag{2.117}$$

The adhesive peel and shear strains and stresses were established in Sections 2.2.3 and 2.2.1 via Equations (2.66) and (2.3) and they are repeated here for convenience

$$\varepsilon^{(\mathrm{A})} = \frac{\sigma^{(\mathrm{A})}}{E_{\mathrm{A}}} = \frac{w_{\mathrm{p}} - w_{\mathrm{s}}}{t_{\mathrm{A}}} \tag{2.118}$$

$$\gamma^{(\mathrm{A})} = \frac{\tau^{(\mathrm{A})}}{G_{\mathrm{A}}} = \frac{u_{\mathrm{p}} - u_{\mathrm{s}}}{t_{\mathrm{A}}} \tag{2.119}$$

In contrast to the case of no bending outlined in Section 2.2.1, the longitudinal displacements of the adherends are not uniform through their thickness. The longitudinal displacements u_{p} and u_{s} of the doubler or strap and skin defined as those on each side

of the bond line are related to the longitudinal forces and bending moments, all per unit width, by

$$\frac{\mathrm{d}u_\mathrm{p}}{\mathrm{d}x} = \frac{N_\mathrm{p}}{E'_\mathrm{p}t_\mathrm{p}} - \frac{M_\mathrm{p}t_\mathrm{p}}{2D_\mathrm{p}} + \alpha_\mathrm{p}\Delta T \tag{2.120}$$

$$\frac{\mathrm{d}u_\mathrm{s}}{\mathrm{d}x} = \frac{N_\mathrm{s}}{E'_\mathrm{s}t_\mathrm{s}} + \frac{M_\mathrm{s}t_\mathrm{s}}{2D_\mathrm{s}} + \alpha_\mathrm{s}\Delta T \tag{2.121}$$

The first term in the right-hand side of Equation (2.120) or (2.121) is the average longitudinal strain due to the axial load ($= \sigma/E' = N/tE'$) while the second term is the longitudinal strain due to the bending moment at the bottom of the doubler or top of the skin $\left[= \mathrm{d}^2w/\mathrm{d}x^2 \cdot (\pm t/2) = -\frac{M}{D} \cdot (\pm t/2)\right]$, and the last term represents thermal strain.

As in Section 2.2.3, to uncouple the differential equations governing the adhesive peel and shear stresses, the adhesive shear stresses in Equations (2.110) and (2.111) are again set constant. Thus, (2.110) and (2.111) can be differentiated once and subtracted from each other to produce

$$\frac{\mathrm{d}^2M_\mathrm{s}}{\mathrm{d}x^2} - \frac{\mathrm{d}^2M_\mathrm{p}}{\mathrm{d}x^2} = \frac{\mathrm{d}V_\mathrm{s}}{\mathrm{d}x} - \frac{\mathrm{d}V_\mathrm{p}}{\mathrm{d}x} \tag{2.122}$$

The transverse displacements w_p and w_s can be expressed alternately as, assuming that the overall length $L \gg 1$,

$$\begin{aligned} w_\mathrm{s} &= \frac{1}{2}\left(w_\mathrm{s} - w_\mathrm{p}\right) + \frac{1}{2}\left(w_\mathrm{s} + w_\mathrm{p}\right) = \frac{1}{2}\left(w_\mathrm{s} - w_\mathrm{p}\right) + w_\mathrm{I} \\ w_\mathrm{p} &= -\frac{1}{2}\left(w_\mathrm{s} - w_\mathrm{p}\right) + \frac{1}{2}\left(w_\mathrm{s} + w_\mathrm{p}\right) = -\frac{1}{2}\left(w_\mathrm{s} - w_\mathrm{p}\right) + w_\mathrm{I} \end{aligned} \tag{2.123}$$

where w_I is the average displacement of the skin and doubler which is given by Equation (2.104). It should be noted that w_I is obtained from stage I analysis, which includes the effect of geometrical nonlinearity. On the other hand, the difference $\frac{1}{2}\left(w_\mathrm{p} - w_\mathrm{s}\right)$ will be obtained from this stage II analysis portion which is strictly speaking geometrically linear. Such technique is verified by Hart-Smith (2005a,b) to be appropriate for analyzing bonded repairs. Using (2.114) and (2.115) to eliminate the transverse shear forces and introducing the moment–curvature relations (2.116)–(2.117) allow (2.122) to be re-expressed in the form

$$-D_\mathrm{s}\frac{\mathrm{d}^4w_\mathrm{s}}{\mathrm{d}x^4} + D_\mathrm{p}\frac{\mathrm{d}^4w_\mathrm{p}}{\mathrm{d}x^4} + 2\sigma^{(\mathrm{A})} = 0 \tag{2.124}$$

From which, in light of Equations (2.123) and (2.118), one finally arrives at

$$\frac{\left(D_\mathrm{s} + D_\mathrm{p}\right)}{2}\frac{\mathrm{d}^4}{\mathrm{d}x^4}\left(w_\mathrm{s} - w_\mathrm{p}\right) + \frac{2E_\mathrm{A}}{t_\mathrm{A}}\left(w_\mathrm{s} - w_\mathrm{p}\right) = -\left(D_\mathrm{s} - D_\mathrm{p}\right)\frac{\mathrm{d}^4w_\mathrm{I}}{\mathrm{d}x^4} \tag{2.125}$$

$$\frac{\mathrm{d}^4}{\mathrm{d}x^4}\left(\frac{w_\mathrm{s} - w_\mathrm{p}}{2}\right) + \frac{4E_\mathrm{A}}{t_\mathrm{A}\left(D_\mathrm{s} + D_\mathrm{p}\right)}\left(\frac{w_\mathrm{s} - w_\mathrm{p}}{2}\right) = -\frac{\left(D_\mathrm{s} - D_\mathrm{p}\right)}{\left(D_\mathrm{s} + D_\mathrm{p}\right)}\frac{\mathrm{d}^4w_\mathrm{I}}{\mathrm{d}x^4} \tag{2.126}$$

The complementary solution of (2.126) is

$$\frac{w_s - w_p}{2} = A\cosh(\upsilon x)\cos(\upsilon x) + B\sinh(\upsilon x)\sin(\upsilon x) + G\sinh(\upsilon x)\cos(\upsilon x) + H\cosh(\upsilon x)\sin(\upsilon x) \tag{2.127}$$

where

$$\upsilon^4 = \frac{E_A}{t_A\left(D_s + D_p\right)} \tag{2.128}$$

It is worthy to note that υ is different from $\hat{\upsilon}$ defined in Section 2.2.3. The particular solution of Equation (2.126) can be found by expressing the right-hand side of (2.126) explicitly using Equation (2.104) as

$$-\frac{\left(D_s - D_p\right)}{\left(D_s + D_p\right)}\frac{d^4 w_I}{dx^4} = -\frac{\left(D_s - D_p\right)\left(\hat{e} - \frac{M^{therm}}{P}\right)\xi_I^4\cosh(\xi_I x)}{\left(D_s + D_p\right)\left[\cosh(\xi_I \ell) + \frac{\xi_I}{\xi_H}\sinh(\xi_I \ell)\right]} \tag{2.129}$$

Upon substitution of (2.129) into (2.126), it is then clear that the particular solution of (2.126) can be determined as

$$\frac{w_s - w_p}{2} = J\cosh(\xi_I x) \tag{2.130}$$

with the coefficient J given by

$$J\left(\xi_I^4 + 4\upsilon^4\right) = -\frac{\left(D_s - D_p\right)\cdot\left(\hat{e} - \frac{M^{therm}}{P}\right)\xi_I^4}{\left(D_s + D_p\right)\left[\cosh(\xi_I \ell) + \frac{\xi_I}{\xi_H}\sinh(\xi_I \ell)\right]} \tag{2.131}$$

or

$$\begin{aligned} J &= -\frac{\left(D_s - D_p\right)\cdot\left(\hat{e} - \frac{M^{therm}}{P}\right)}{\left(D_s + D_p\right)\left(1 + \frac{4\upsilon^4}{\xi_I^4}\right)\left[\cosh(\xi_I \ell) + \frac{\xi_I}{\xi_H}\sinh(\xi_I \ell)\right]} \\ &= -\frac{\left(D_s - D_p\right)\cdot\left(\hat{e} - \frac{M^{therm}}{P}\right)}{\left[\left(D_s + D_p\right) + \frac{4E_A}{t_A \xi_I^4}\right]\left[\cosh(\xi_I \ell) + \frac{\xi_I}{\xi_H}\sinh(\xi_I \ell)\right]} \end{aligned} \tag{2.132}$$

As before, the solution for a doubler configuration will be proceeded first. To simplify the algebraic manipulation, only solution for all long doubler lengths $2\cdot\ell$ will be derived here. For a sufficiently long doubler and for points inside the overlap near the end of the doubler, Equation (2.130) can be simplified as

$$\begin{aligned} \frac{w_s - w_p}{2} &\approx -\frac{\left(D_s - D_p\right)\cdot\left(\hat{e} - \frac{M^{therm}}{P}\right)}{\left[\left(D_s + D_p\right) + \frac{4E_A}{t_A \xi_I^4}\right]\left(1 + \frac{\xi_I}{\xi_H}\right)} e^{-\xi_I s} \\ &= C_c e^{-\xi_I s} \end{aligned} \tag{2.133}$$

where $\varsigma = \ell - x$,

$$C_c = -\frac{\left(D_s - D_p\right)\left(\hat{e} - \frac{M^{\text{therm}}}{P}\right)}{\left[\left(D_s + D_p\right) + \frac{4E_A}{t_A \xi_I^4}\right]\left(1 + \frac{\xi_I}{\xi_H}\right)} \tag{2.134}$$

On the other hand, the complementary solution (2.127) is approximated by

$$\frac{w_s - w_p}{2} \approx e^{-\upsilon\varsigma}\left[A\cos\left(\upsilon\varsigma\right) + B\sin\left(\upsilon\varsigma\right)\right] \tag{2.135}$$

Thus the general solution in this long overlap case is given by

$$\frac{w_s - w_p}{2} = e^{-\upsilon\varsigma}\left[A\cos\left(\upsilon\varsigma\right) + B\sin\left(\upsilon\varsigma\right)\right] + C_c e^{-\xi_I\varsigma} \tag{2.136}$$

One boundary condition for determining the constants A and B is that the integral of the peel stress over the bonded area must be zero since the peel stresses cannot exert any net normal (vertical) force across the bond layer. Consequently, from (2.118),

$$\int_0^\infty \sigma^{(A)} \mathrm{d}x = -\frac{E_A}{t_A}\int_0^\infty \left(w_s - w_p\right)\mathrm{d}x = 0 \tag{2.137}$$

which upon substitution (2.136) yields

$$A + B + \frac{2\upsilon C_c}{\xi_I} = 0 \tag{2.138}$$

The other boundary condition involves the bending moment in the skin and doubler just inside the end of the overlap. They must be equal to the values just outside the overlap, where the moment in the doubler equals to zero while the moment in the skin equals to $M_H\left(x = \ell\right)$, and $M_H\left(x = \ell\right)$ is given by (2.108). From Equations (2.116), (2.117) and (2.136),

$$\begin{aligned}
\left.\frac{M_p}{D_p} - \frac{M_s}{D_s}\right|_{x=\ell \text{ or } \varsigma=0} &= \left.\frac{\mathrm{d}^2}{\mathrm{d}\varsigma^2}\left(w_s - w_p\right)\right|_{x=\ell \text{ or } \varsigma=0} \\
&= 4\upsilon^2 e^{-\upsilon\varsigma}\left[A\sin\left(\upsilon\varsigma\right) + B\cos\left(\upsilon\varsigma\right)\right] + 2\xi_I^2 C_c e^{-\xi_I\varsigma}\Big|_{\varsigma=0} \\
&= 4\upsilon^2 B + 2\xi_I^2 C_c \\
&= -\frac{M_H\left(\ell\right)}{D_s}
\end{aligned} \tag{2.139}$$

The coefficients A and B then follow as

$$\begin{aligned}
B &= -\frac{M_H\left(\ell\right)}{4D_s\upsilon^2} - \frac{\xi_I^2 C_c}{2\upsilon^2} \\
A &= \frac{M_H\left(\ell\right)}{4D_s\upsilon^2} + \frac{\xi_I^2 C_c}{2\upsilon^2} - \frac{2\upsilon C_c}{\xi_I}
\end{aligned} \tag{2.140}$$

which after appropriate substitutions produce

$$B = -\frac{P\left(\hat{e} - \frac{M^{\text{therm}}}{P}\right)\frac{\xi_{\text{I}}}{\xi_{\text{H}}}\tanh\left(\xi_{\text{I}}\ell\right)}{4D_{\text{s}}\upsilon^2\left[1+\frac{\xi_{\text{I}}}{\xi_{\text{H}}}\tanh\left(\xi_{\text{I}}\ell\right)\right]} + \frac{\xi_{\text{I}}^2\left(D_{\text{s}}-D_{\text{p}}\right)\left(\hat{e}-\frac{M^{\text{therm}}}{P}\right)}{2\upsilon^2\left[\left(D_{\text{s}}+D_{\text{p}}\right)+\frac{4E_{\text{A}}}{t_{\text{A}}\xi_{\text{I}}^4}\right]\left(1+\frac{\xi_{\text{I}}}{\xi_{\text{H}}}\right)} \tag{2.141}$$

$$A = \frac{P\left(\hat{e} - \frac{M^{\text{therm}}}{P}\right)\frac{\xi_{\text{I}}}{\xi_{\text{H}}}\tanh\left(\xi_{\text{I}}\ell\right)}{4D_{\text{s}}\upsilon^2\left[1+\frac{\xi_{\text{I}}}{\xi_{\text{H}}}\tanh\left(\xi_{\text{I}}\ell\right)\right]} - \left(\frac{\xi_{\text{I}}^2}{2\upsilon^2}-\frac{2\upsilon}{\xi_{\text{I}}}\right)\frac{\left(D_{\text{s}}-D_{\text{p}}\right)\left(\hat{e}-\frac{M^{\text{therm}}}{P}\right)}{\left[\left(D_{\text{s}}+D_{\text{p}}\right)+\frac{4E_{\text{A}}}{t_{\text{A}}\xi_{\text{I}}^4}\right]\left(1+\frac{\xi_{\text{I}}}{\xi_{\text{H}}}\right)} \tag{2.142}$$

The maximum peel stress is then calculated from Equations (2.118) and (2.136) at $\varsigma = 0$ with coefficients A, B and C_{c} defined above as

$$\begin{aligned}\sigma_{\max}^{(\text{A})} &= -\frac{E_{\text{A}}}{t_{\text{A}}}\left(w_{\text{s}}-w_{p}\right)\Big|_{\varsigma=0} = -2\frac{E_{\text{A}}}{t_{\text{A}}}\left\{e^{-\upsilon\varsigma}\left[A\cos\left(\upsilon x\right)+B\sin\left(\upsilon x\right)\right]+C_{\text{c}}e^{-\xi_{\text{I}}\varsigma}\right\}\Big|_{\varsigma=0} \\ &= -\frac{P\left(\hat{e}-\frac{M^{\text{therm}}}{P}\right)E_{\text{A}}\frac{\xi_{\text{I}}}{\xi_{\text{H}}}\tanh\left(\xi_{\text{I}}\ell\right)}{2D_{\text{s}}\upsilon^2 t_{\text{A}}\left[1+\frac{\xi_{\text{I}}}{\xi_{\text{H}}}\tanh\left(\xi_{\text{I}}\ell\right)\right]} \\ &\quad + \frac{E_{\text{A}}}{t_{\text{A}}}\left(\frac{\xi_{\text{I}}^2}{\upsilon^2}-\frac{4\upsilon}{\xi_{\text{I}}}+2\right)\frac{\left(D_{\text{s}}-D_{\text{p}}\right)\left(\hat{e}-\frac{M^{\text{therm}}}{P}\right)}{\left[\left(D_{\text{s}}+D_{\text{p}}\right)\quad+\frac{4E_{\text{A}}}{t_{\text{A}}\xi_{\text{I}}^4}\right]\left(1+\frac{\xi_{\text{I}}}{\xi_{\text{H}}}\right)}\end{aligned} \tag{2.143}$$

It should be noted that for balanced adherends, i.e., $E_{\text{s}} = E_{\text{p}}$ and $D_{\text{s}} = D_{\text{p}}$, the second term in the right-hand side of the last equation of (2.143) is identically zero. The maximum adhesive peel stress in this case is inversely proportional to the square of the adhesive thickness since $\sigma_{\max}^{(\text{A})} \propto \frac{1}{\upsilon^2 t_{\text{A}}} \propto \frac{1}{\sqrt{t_{\text{A}}}}$. Also, if numerical substitutions of patch and skin properties into (2.143) yield a negative value value of $\sigma_{\max}^{(\text{A})}$, what it means is that the peel stress is in opposite direction with the one shown in Figure 2.6.

As mentioned throughout previous sections, since the solutions near the end of the overlap will be nearly the same for both doubler and joint configuration as long as the overlap is sufficiently long, it remains now to derive the peel stresses near the interruption end of the skin in the single-strap joint configuration with long overlap. In Section 2.3.1, it was discussed that within the classical plate theory, the transverse deflections and curvatures of the doubler and joint configuration are also the same at the middle of the doubler or strap. This is because the net moments across the middle sections of these two configurations differ only by a concentrated moment of a magnitude of $-P\left(\frac{t_{\text{p}}+t_{\text{s}}}{2}-\hat{e}+\frac{M^{\text{therm}}}{P}\right)$, and this concentrated moment does not produce any additional curvature. In other words, the right-hand side of Equation (2.126) is still given by (2.129) even for the joint configuration. Since only the solution near the middle of the strap is considered now and since the particular solution (2.130) of Equation (2.126) with the constant coefficient J given by Equation (2.132) will be vanishing small for $x \to 0$ in a long overlap joint, this particular solution therefore will be ignored from the general solution in the present joint analysis. It should be emphasized that the particular solution

was retained in the previous derivation but not in the present one since in the former case $J \propto \frac{1}{\cosh(\xi_I \ell)}$ or $\frac{1}{\sinh(\xi_I \ell)}$ for $\xi_I \ell \gg 1$, thus $J \cdot \cosh(\xi_I x)$ is finite as x approaches ℓ, while in the present case, even though J is still given by the same expression as above for a long overlap but $\cosh(\xi_I x) \to 1$ as x goes to zero, whence $J \cdot \cosh(\xi_I x) \to 0$. Thus, the complete solution near the skin interruption of a joint configuration will be represented by Equation (2.135). The constants A and B of Equation (2.135) in the joint case can be found from the similar boundary conditions (2.137) and (2.139), but with $M_p = M_I^p(x=0)$ and $M_s = 0$ at the skin interruption end as indicated in Equation (2.109), and similar to (2.140), they are given by

$$B = \frac{M_p^I(0)}{4v^2 D_p} = -\frac{1}{4v^2 D_p}\left[\frac{P\left(\hat{e} - \frac{M^{\text{therm}}}{P}\right)}{\cosh(\xi_I \ell) + \frac{\xi_I}{\xi_H}\sinh(\xi_I \ell)} + P\left(\frac{t_p + t_s}{2} - \hat{e} + \frac{M^{\text{therm}}}{P}\right)\right] \tag{2.144}$$

$$A = -B = -\frac{M_p^I(0)}{4v^2 D_p} = \frac{1}{4v^2 D_p}\left[\frac{P\left(\hat{e} - \frac{M^{\text{therm}}}{P}\right)}{\cosh(\xi_I \ell) + \frac{\xi_I}{\xi_H}\sinh(\xi_I \ell)} + P\left(\frac{t_p + t_s}{2} - \hat{e} + \frac{M^{\text{therm}}}{P}\right)\right]$$

Thus,

$$\begin{aligned}\sigma_{\max}^{(A)} &= -2A\frac{E_A}{t_A} \\ &= -\frac{E_A}{2v^2 D_p t_A}\left[\frac{P\left(\hat{e} - \frac{M^{\text{therm}}}{P}\right)}{\cosh(\xi_I \ell) + \frac{\xi_I}{\xi_H}\sinh(\xi_I \ell)} + P\left(\frac{t_p + t_s}{2} - \hat{e} + \frac{M^{\text{therm}}}{P}\right)\right]\end{aligned} \tag{2.145}$$

Equation (2.145) indicates that the peak peel stress at the skin interruption end is also inversely proportional to the adhesive thickness t_A, i.e., $\sigma_{\max}^{(A)} \propto \frac{1}{\sqrt{t_A}}$.

We conclude this section by noting that the governing equation for the adhesive peel stress commonly takes a rather different form than (2.124). By again setting $\tau^{(A)}$ to be constant, this alternate form can be derived from Equations (2.110)–(2.117) as follows:

$$\frac{d^4 w_p}{dx^4} = -\frac{1}{D_p}\frac{d^2 M_p}{dx^2} = -\frac{1}{D_p}\frac{dV_p}{dx} = -\frac{\sigma^{(A)}}{D_p} = -\frac{E_A\left(w_p - w_s\right)}{D_p t_A} \tag{2.146}$$

$$\frac{d^4 w_s}{dx^4} = -\frac{1}{D_s}\frac{d^2 M_s}{dx^2} = -\frac{1}{D_s}\frac{dV_s}{dx} = \frac{\sigma^{(A)}}{D_s} = \frac{E_A\left(w_p - w_s\right)}{D_s t_A} \tag{2.147}$$

Hence,

$$\frac{d^4}{dx^4}\left(w_p - w_s\right) + \frac{E_A}{t_A}\left(\frac{1}{D_p} + \frac{1}{D_s}\right)\left(w_p - w_s\right) = 0 \tag{2.148}$$

or

$$\frac{d^4 \varepsilon^{(A)}}{dx^4} + \frac{E_A}{t_A}\left(\frac{1}{D_p} + \frac{1}{D_s}\right)\varepsilon^{(A)} = 0 \tag{2.149}$$

since $\frac{w_p - w_s}{t_A} = \varepsilon^{(A)}$. Equation (2.149) will be used in Chapter 5 for deriving the spring constants of the crack-bridging model.

2.3.3 Stage III: Solution for induced adhesive shear stresses

The differential equation governing the adhesive shear behavior follows from Equations (2.120), (2.121), (2.112), (2.113), (2.110) and (2.111).

$$\frac{d^2 u_p}{dx^2} = \frac{1}{E'_p t_p}\frac{dN_p}{dx} - \frac{t_p}{2D_p}\frac{dM_p}{dx}$$

$$= \frac{\tau^{(A)}}{E'_p t_p} - \frac{t_p}{2D_p}\left(V_p - \frac{\tau^{(A)} t_p}{2}\right) \tag{2.150}$$

$$\frac{d^2 u_s}{dx^2} = \frac{1}{E'_s t_s}\frac{dN_s}{dx} + \frac{t_s}{2D_s}\frac{dM_s}{dx}$$

$$= -\frac{\tau^{(A)}}{E'_s t_s} + \left(V_s - \frac{\tau^{(A)} t_s}{2}\right)\left(\frac{t_s}{2D_s}\right) \tag{2.151}$$

Subtracting Equation (2.151) from (2.150) and making use of (2.119) provide

$$\frac{d^2 u_p}{dx^2} - \frac{d^2 u_s}{dx^2} = \frac{t_A}{G_A}\frac{d^2 \tau^{(A)}}{dx^2}$$

$$= \left(\frac{1}{E'_p t_p} + \frac{1}{E'_s t_s}\right)\tau^{(A)} - \frac{V_p t_p}{2D_p} - \frac{V_s t_s}{2D_s} + \left(\frac{t_p^2}{4D_p} + \frac{t_s^2}{4D_s}\right)\tau^{(A)}$$

$$= \left(\frac{4}{E'_p t_p} + \frac{4}{E'_s t_s}\right)\tau^{(A)} - \left(\frac{V_p t_p}{2D_p} + \frac{V_s t_s}{2D_s}\right) \tag{2.152}$$

Differentiating (2.152) once and substituting (2.114) and (2.115) respectively for $\frac{dV_p}{dx}$ and $\frac{dV_s}{dx}$ yield

$$\frac{t_A}{G_A}\frac{d^3 \tau^{(A)}}{dx^3} = 4\left(\frac{1}{E'_p t_p} + \frac{1}{E'_s t_s}\right)\frac{d\tau^{(A)}}{dx} - \left(\frac{t_p}{2D_p}\frac{dV_p}{dx} + \frac{t_s}{2D_s}\frac{dV_s}{dx}\right)$$

$$= 4\left(\frac{1}{E'_p t_p} + \frac{1}{E'_s t_s}\right)\frac{d\tau^{(A)}}{dx} - \sigma^{(A)}\left(\frac{t_p}{2D_p} - \frac{t_s}{2D_s}\right) \tag{2.153}$$

or

$$\frac{d^3 \tau^{(A)}}{dx^3} - \frac{4G_A}{t_A}\left(\frac{1}{E'_p t_p} + \frac{1}{E'_s t_s}\right)\frac{d\tau^{(A)}}{dx} = -\frac{G_A}{t_A}\left(\frac{t_p}{2D_p} - \frac{t_s}{2D_s}\right)\sigma^{(A)} \tag{2.154}$$

From (2.154), the right-hand side will be identically equal to zero for balance adherends. Otherwise, for simplicity, Equation (2.154) will be approximated as

$$\frac{\mathrm{d}^3\tau^{(\mathrm{A})}}{\mathrm{d}x^3} - \frac{4G_{\mathrm{A}}}{t_{\mathrm{A}}}\left(\frac{1}{E'_{\mathrm{p}}t_{\mathrm{p}}} + \frac{1}{E'_{\mathrm{s}}t_{\mathrm{s}}}\right)\frac{\mathrm{d}\tau^{(\mathrm{A})}}{\mathrm{d}x} \approx 0 \tag{2.155}$$

Equation (2.155) can also be rewritten as

$$\frac{\mathrm{d}}{\mathrm{d}x}\left[\frac{\mathrm{d}^2\tau^{(\mathrm{A})}}{\mathrm{d}x^2} - \frac{4G_{\mathrm{A}}}{t_{\mathrm{A}}}\left(\frac{1}{E'_{\mathrm{p}}t_{\mathrm{p}}} + \frac{1}{E'_{\mathrm{s}}t_{\mathrm{s}}}\right)\tau^{(\mathrm{A})}\right] = 0 \tag{2.156}$$

or

$$\frac{\mathrm{d}^2\tau^{(\mathrm{A})}}{\mathrm{d}x^2} - \frac{4G_{\mathrm{A}}}{t_{\mathrm{A}}}\left(\frac{1}{E'_{\mathrm{p}}t_{\mathrm{p}}} + \frac{1}{E'_{\mathrm{s}}t_{\mathrm{s}}}\right)\tau^{(\mathrm{A})} = \text{constant} \tag{2.157}$$

Thus the general solution of (2.155) is given by

$$\tau^{(\mathrm{A})} = A\cosh(2\beta_{\mathrm{A}}x) + B\sinh(2\beta_{\mathrm{A}}x) + C \tag{2.158}$$

where $\beta_{\mathrm{A}} = \sqrt{\frac{G_{\mathrm{A}}}{t_{\mathrm{A}}}\left(\frac{1}{E'_{\mathrm{p}}t_{\mathrm{p}}} + \frac{1}{E'_{\mathrm{s}}t_{\mathrm{s}}}\right)}$ as defined in Equation (2.6). As in Section 2.2.1, the constant coefficients A, B and C are determined from the boundary conditions on $\frac{\mathrm{d}\tau^{(\mathrm{A})}}{\mathrm{d}x}$ and $\tau^{(\mathrm{A})}$. Differentiating (2.158) once and utilizing the results from (2.119)–(2.121) give

$$\begin{aligned}\frac{\mathrm{d}\tau^{(\mathrm{A})}}{\mathrm{d}x} &= 2\beta_{\mathrm{A}}\left[A\sinh(2\beta_{\mathrm{A}}x) + B\cosh(2\beta_{\mathrm{A}}x)\right] = \frac{G_{\mathrm{A}}}{t_{\mathrm{A}}}\left(\frac{\mathrm{d}u_{\mathrm{p}}}{\mathrm{d}x} - \frac{\mathrm{d}u_{\mathrm{s}}}{\mathrm{d}x}\right)\\ &= \frac{G_{\mathrm{A}}}{t_{\mathrm{A}}}\left[\frac{N_{\mathrm{p}}}{E'_{\mathrm{p}}t_{\mathrm{p}}} - \frac{M_{\mathrm{p}}t_{\mathrm{p}}}{2D_{\mathrm{p}}} - \frac{N_{\mathrm{s}}}{E'_{\mathrm{s}}t_{\mathrm{s}}} - \frac{M_{\mathrm{s}}t_{\mathrm{s}}}{2D_{\mathrm{s}}} + \left(\alpha_{\mathrm{p}} - \alpha_{\mathrm{s}}\right)\Delta T\right]\end{aligned} \tag{2.159}$$

As in all previous analyses, the analysis for the bonded doubler will be completed first. The boundary conditions for the doubler configurations are given by (similar to Equations (2.9) and (2.10))

$$\tau^{(\mathrm{A})}(0) = 0 \tag{2.160}$$

$$N_{\mathrm{s}}(\ell) = P \tag{2.161}$$

$$N_{\mathrm{p}}(\ell) = 0 \tag{2.162}$$

In addition,

$$\begin{aligned}M_{\mathrm{s}}(\ell) &= M_{\mathrm{H}}(\ell)\\ M_{\mathrm{p}}(\ell) &= 0\end{aligned} \tag{2.163}$$

where $M_H(\ell)$ is obtained from the stage I analysis, and given by Equation (2.108). Furthermore, the load in the doubler at $x = 0$ also must be equal to the integral of the shear stresses transferred through the adhesive, i.e.,

$$\int_0^{\ell} \tau^{(A)} dx = N_p(0) \tag{2.164}$$

For a long overlap doubler, it was shown in Section 2.3.1 that the overall bending moment will vanish at the middle of the doubler. In that case, $N_p(0)$ can be calculated by the simple method presented in Section 2.2.1 as follows. In Section 2.2.1, the stress in the skin at the middle of the doubler was calculated from the same strain condition between the doubler and the skin there and from the horizontal force equilibrium, and it is given by (2.22). From Equation (2.22),

$$\sigma_s(0) = \frac{\sigma_\infty}{1+S}$$

$$N_s(0) = t_s \sigma_s(0) = \frac{\sigma_\infty t_s}{1+S}$$

$$\varepsilon_s(0) = \frac{\sigma_s(0)}{E'_s} = \frac{\sigma_0}{E'_s} = \frac{\sigma_\infty}{E'_s(1+S)}$$

and by noting $\varepsilon_p(0) = \varepsilon_s(0)$ (same strain condition at the middle of the doubler), it then follows that

$$N_p(0) = t_p \sigma_p(0) = E'_p t_p \varepsilon_p(0) = E'_p t_p \varepsilon_s(0) = \frac{E'_p t_p \sigma_\infty}{E'_s(1+S)} = \frac{S\sigma_\infty t_s}{(1+S)}$$

The above results for $N_s(0)$ and $N_p(0)$ do not account for the effect of thermal mismatch between two adherends. When this thermal mismatch effect is included, the expressions for $N_s(0)$ and $N_p(0)$ will finally take the following form:

$$\begin{aligned} N_s(0) &= \frac{\sigma_\infty t_s}{(1+S)} + F^{\text{therm}} \\ N_p(0) &= \frac{S\sigma_\infty t_s}{(1+S)} - F^{\text{therm}} \end{aligned} \tag{2.165}$$

where F^{therm} is defined in Equation (2.81). Thus, (2.164) becomes

$$\int_0^{\ell} \tau^{(A)} dx = \frac{S\sigma_\infty t_s}{(1+S)} - F^{\text{therm}} \tag{2.166}$$

It is very easy to show that for a long overlap doubler, i.e., $\beta_A \ell \gg 1$, the adhesive shear stress $\tau^{(A)}$ near the end of the doubler can be approximated from Equation (2.158) as

$$\tau^{(A)} = Be^{-2\beta_A s} + C \tag{2.167}$$

where the coordinate ς is measured from the doubler's end. The constants B and C are determined as follows. From Equation (2.166) with $\tau^{(A)}$ defined by (2.167) and noting that $e^{-2\beta_s \ell} \approx 0$ for $\beta_A \ell \gg 1$, one obtains

$$\begin{aligned}\int_0^{\ell} \tau^{(A)} \mathrm{d}x = \int_0^{\ell} \tau^{(A)} \mathrm{d}\varsigma &= -\frac{B}{2\beta_A} e^{-2\beta_A \varsigma}\Big|_0^{\ell} + C\ell \\ &= -\frac{B}{2\beta_A} e^{-2\beta_A \ell} + \frac{B}{2\beta_A} + C\ell \approx \frac{B}{2\beta_A} + C\ell \\ &= \frac{S}{1+S}\sigma_\infty t_s - F^{\text{therm}} \end{aligned} \tag{2.168}$$

Evaluations of $\frac{\mathrm{d}\tau^{(A)}}{\mathrm{d}x}$ at $x = \ell$ or $\varsigma = 0$ via (2.159) with N_p, N_s, etc. given by conditions (2.161)–(2.163) and also via Equation (2.167), and equating the results yield

$$\left.\frac{\mathrm{d}\tau^{(A)}}{\mathrm{d}x}\right|_{x=\ell \text{ or } \varsigma=0} = \left[-\frac{P}{E_s' t_s} - \frac{t_s \cdot M_H(\ell)}{D_s} + (\alpha_p - \alpha_s)\Delta T\right]\frac{G_A}{t_A} = -2\beta_A B \tag{2.169}$$

It then follows that

$$B = \frac{G_A}{2\beta_A t_A}\left[\frac{t_s \cdot M_H(\ell)}{2D_s} + \frac{\sigma_\infty}{E_s'} + (\alpha_s - \alpha_p)\Delta T\right] \tag{2.170}$$

$$C = \frac{S}{1+S}\left(\frac{\sigma_\infty t_s}{\ell}\right) - \frac{1}{4\beta_A^2 \ell}\left[\frac{t_s \cdot M_H(\ell)}{2D_s} + \frac{\sigma_\infty}{E_s'} + (\alpha_s - \alpha_p)\Delta T\right]\left(\frac{G_A}{t_A}\right) - \frac{F^{\text{therm}}}{\ell}$$

Thus,

$$\begin{aligned}\tau_{\max}^{(A)} &= \frac{S}{1+S}\left(\frac{\sigma_\infty t_s}{\ell}\right) \\ &\quad + \frac{G_A}{2\beta_A t_A}\left[\frac{t_s M_H(\ell)}{2D_s} + \frac{\sigma_\infty}{E_s'} + (\alpha_s - \alpha_p)\Delta T\right]\left(1 - \frac{1}{2\beta_A \ell}\right) - \frac{F^{\text{therm}}}{\ell} \end{aligned} \tag{2.171}$$

provided that $\beta_A \ell \gg 1$.

On the other hand, for the long overlap bonded splice, the adhesive shear stress near the interruption end of the skin is given similarly by Equation (2.167) but with the coordinate ς being replaced by the coordinate x measured from the middle of the strap. The constants B and C are now determined from the boundary conditions

$$\int_0^{\ell} \tau^{(A)} \mathrm{d}x = \frac{\sigma_\infty t_s}{(1+S)} + F^{\text{therm}} \tag{2.172}$$

$$
\begin{aligned}
&N_{\mathrm{p}}(0) = P \\
&N_{\mathrm{s}}(0) = 0 \\
&M_{\mathrm{p}}(0) = M_{\mathrm{I}}^{\mathrm{p}}(0) \\
&M_{\mathrm{s}}(0) = 0
\end{aligned}
\tag{2.173}
$$

$$
\begin{aligned}
\left.\frac{\mathrm{d}\tau^{(\mathrm{A})}}{\mathrm{d}x}\right|_{x=0} &= \frac{G_{\mathrm{A}}}{t_{\mathrm{A}}}\left[\frac{N_{\mathrm{p}}}{E'_{\mathrm{p}}t_{\mathrm{p}}} - \frac{M_{\mathrm{p}}t_{\mathrm{p}}}{2D_{\mathrm{p}}} - \frac{N_{\mathrm{s}}}{E'_{\mathrm{s}}t_{\mathrm{s}}} - \frac{M_{\mathrm{s}}t_{\mathrm{s}}}{2D_{\mathrm{s}}} + \left(\alpha_{\mathrm{p}} - \alpha_{\mathrm{s}}\right)\Delta T\right]\Bigg|_{x=0} \\
&= \frac{G_{\mathrm{A}}}{t_{\mathrm{A}}}\left[\frac{\sigma_{\infty}t_{\mathrm{s}}}{E'_{\mathrm{p}}t_{\mathrm{p}}} - \frac{t_{\mathrm{p}}\cdot M_{\mathrm{I}}^{\mathrm{p}}(0)}{2D_{\mathrm{p}}} + \left(\alpha_{\mathrm{p}} - \alpha_{\mathrm{s}}\right)\Delta T\right]
\end{aligned}
$$

$$
\begin{aligned}
B &= \frac{G_{\mathrm{A}}}{2\beta_{\mathrm{A}}t_{\mathrm{A}}}\left[\frac{M_{\mathrm{I}}^{\mathrm{p}}(0)\cdot t_{\mathrm{p}}}{2D_{\mathrm{p}}} - \frac{\sigma_{\infty}t_{\mathrm{s}}}{E'_{\mathrm{p}}t_{\mathrm{p}}} + \left(\alpha_{\mathrm{s}} - \alpha_{\mathrm{p}}\right)\Delta T\right] \\
C &= \frac{1}{1+S}\left[\frac{\sigma_{\infty}t_{\mathrm{s}}}{\ell}\right] \\
&\quad - \frac{1}{4\beta_{\mathrm{A}}^2\ell}\left[\frac{M_{\mathrm{I}}^{\mathrm{p}}(0)\cdot t_{\mathrm{p}}}{2D_{\mathrm{p}}} - \frac{\sigma_{\infty}t_{\mathrm{s}}}{E'_{\mathrm{p}}t_{\mathrm{p}}} + \left(\alpha_{\mathrm{s}} - \alpha_{\mathrm{p}}\right)\Delta T\right]\left(\frac{G_{\mathrm{A}}}{t_{\mathrm{A}}}\right) + \frac{F^{\mathrm{therm}}}{\ell}
\end{aligned}
\tag{2.174}
$$

where $M_{\mathrm{I}}^{\mathrm{p}}(0)$ is the bending moment in the patch at its middle and it is given by the first equation of (2.109). Equation (2.172) corresponds to the condition that the integral of the shear stress through the adhesive near the skin interruption end is equal to the constant load in the skin throughout most of the skin interior as the skin and strap strain together. With constants B and C determined, the maximum adhesive shear stress at the skin interruption end is finally given by

$$
\begin{aligned}
\tau_{\max}^{(\mathrm{A})} &= \frac{1}{1+S}\left(\frac{\sigma_{\infty}t_{\mathrm{s}}}{\ell}\right) \\
&\quad + \frac{G_{\mathrm{A}}}{2\beta_{\mathrm{A}}t_{\mathrm{A}}}\left[\frac{t_{\mathrm{p}}M_{\mathrm{I}}^{\mathrm{p}}(0)}{2D_{\mathrm{p}}} - \frac{\sigma_{\infty}t_{\mathrm{s}}}{E'_{\mathrm{p}}t_{\mathrm{p}}} + \left(\alpha_{\mathrm{s}} - \alpha_{\mathrm{p}}\right)\Delta T\right]\left(1 - \frac{1}{2\beta_{\mathrm{A}}\ell}\right) + \frac{F^{\mathrm{therm}}}{\ell}
\end{aligned}
\tag{2.175}
$$

The reader is reminded that since the overlap is assumed to be sufficiently long in the present analysis so that there is no interaction between the interruption end of the skin and the doubler end, the shear stress in the adhesive near the strap end of a splice joint configuration, therefore, will be the same as that of the bonded doubler. This latter solution is already delineated in the preceding bonded doubler analysis, and therefore it will not be repeated here. It is evident from Equations (2.171) and (2.175) that $\tau_{\max}^{(\mathrm{A})} \propto \frac{1}{\sqrt{t_{\mathrm{A}}}}$.

It is interesting to note that, unlike in the case of a two-sided bonded doubler or a double-strap joint, both the peel stress and the shear stress in a one-sided configuration are proportional to the reciprocal of the square root of the bond-line thickness for long overlap length, i.e., $\beta_A \ell \gg 1$ and $\upsilon \ell \gg 1$.

2.4 Consideration of Other Important Effects in Bonded Doublers and Joints

The theories presented in Sections 2.2 and 2.3 treat the adhesive layer as infinite, unconnected shear and tensile springs. In these theories both the shear stress and the peel stress in the adhesive layer vary strongly over the length of the overlap, and attain their maximum values at the end of overlap or at the skin interruption end. Assuming the overlap length is sufficiently large as compared to the load transfer length, the maximum shear and peel stresses become independent of the length of overlap; see for instances Equations (2.18), (2.20) and (2.78) for two-sided bonded doublers and double-strap joints, Equations (2.171), (2.175) and (2.145), all with $\ell \to \infty$, for one-sided configurations.

As a consequence, these theories suffer from three major deficiencies. First, the adhesive shear stress solution does not satisfy the exact boundary condition of zero shear stress at the ends of the adhesive layer (Adams and Peppiatt, 1974; Gilbert and Rigolot, 1988; Roberts, 1989; Wang et al., 1998a). Secondly, these solutions do not capture the complex stress singularity at the termini of the adhesive layer (Hein and Erdogan, 1971; Groth, 1988; Reedy, 1990, 1993; Akisanya and Fleck, 1997; Wang and Rose, 2000). The third problem is that the stress state in the adherends is inevitably assumed to be uniform in the thickness direction, and hence stress concentrations are ignored (Wang et al., 1998a).

Attempts have been made to eradicate the first deficiency of the plate-spring approach by treating the adhesive layer as a two-dimensional continuum (Allman, 1977), while retaining the plate-theory approximation for the substrates. Although these refined theories permit satisfaction of the stress-free surface condition at the ends of a square-edged adhesive layer, the distance over which the adhesive shear stress attains its peak value appears to scale with the substrate thickness, instead of the adhesive layer thickness as indicated by FE analysis (Wang et al., 1998a).

Recent progresses in addressing the above-mentioned three major deficiencies will be presented in this section. First, a simple correction to the shear stress distribution along the mid-plane of the adhesive layer has been obtained using an eigen-function expansion method, which captured the boundary layer effect near the end of an adhesive layer. Secondly, the corner singularity will be determined using an asymptotic matching method. It will be shown that this corner singularity offers a very promising failure criteria of bonded joints under both static and fatigue loading conditions. The improved adhesive shear stress solution then permits determination of the stress concentration in adherends. In addition to addressing the three mentioned deficiencies, the triaxial stress-state in the adhesive layer and the implications on adhesive plastic yielding are also discussed.

2.4.1 Stress-free condition at the adhesive ends

According to the plate-spring theories for bonded joints, the adhesive shear stress distribution near the ends of adhesive layer can be expressed as follows, assuming that the overlap is sufficiently long so that the peaks at the two ends are isolated:

$$\tau^{(A)}(x) = \tau^{(A)}_{max} e^{-\beta_A x} \tag{2.176}$$

The reason that the plate-spring models predict a finite shear stress at the ends of adhesive layer stems from the assumption of spring laws being position independent, i.e., the shear stress is proportional to the relative longitudinal displacement between two substrates, even at a stress-free surface. Nevertheless, despite this deficiency and the large number of assumptions involved in the plate-spring models, solutions of the adhesive shear and peel stresses have been shown to correlate well with FE analysis except very close to the ends of adhesive layer.

Since the ends of the adhesive layer are stress-free, the shear stress near the ends must change from this simple distribution so as to satisfy the traction-free boundary conditions. According to St Venant's principle, the perturbation in the stress field is confined to a region near the ends (within a distance comparable in extent to the layer's thickness). This means that for the case of square edge the finite shear stress predicted by the plate-spring theories can be considered as residual stresses. It then follows that the problem with stress-free edge condition can be solved by superposing on the stress field derived based on plate-spring analogy a second stress field that just negates the traction on the ends.

Since the adhesive layer generally has a Young's modulus much lower than the substrates, it is not unreasonable to model the substrates as rigid clamps. Consequently the problem can be considered as a strip clamped at two long edges and subjected to a uniform shear traction and zero normal traction at $x = 0$, as depicted in Figure 2.8. From a theoretical viewpoint, rigorous calculation of the shear stress near the square ends of an adhesive layer requires a consideration of stress singularities at the corners of the interface between the adhesive layer and the substrates. However, since the field in which the stresses are dominated by a corner singularity is normally very small (Wang and Rose, 2000), the effect of corner singularity can be ignored when determining the shear stress at the mid-plane of the adhesive layer.

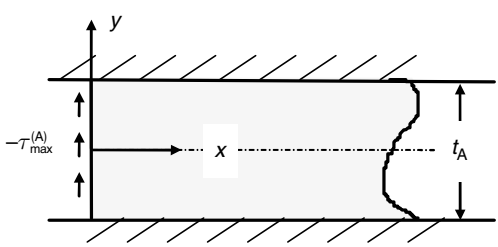

Fig. 2.8. A strip rigidly clamped along two long edges.

Table 2.2. First eigen root for different adhesive Poisson's ratio.

Root n	Poisson's ratio ν_A		
	0.25	0.3	0.35
1	$2.1752 + 0.74371i$	$2.1650 + 0.8032i$	$2.1535 + 0.8687i$

Using an eigen-function expansion method, the shear stress at the mid-plane of the adhesive layer has been found to be well approximated by the first-order solution (Wang et al., 1998a),

$$\tau^{(A)}(x, 0) = -\tau^{(A)}_{max} e^{-2\varpi x/t_A} \cos(2\varpi x/t_A) \tag{2.177}$$

where ϖ denotes the real part of the first eigen root (Table 2.2), which is equal to 2.1535 for a Poisson's ratio of 0.35.

Combining Equations (2.176) and (2.177) leads to the following improved solution of adhesive shear stress distribution in a bonded joint:

$$\tau^{(A)}(x) = \tau^{(A)}_{max} \left[e^{-\beta_A x} - e^{-2\varpi x/t_A} \cos(2\varpi x/t_A) \right] \tag{2.178}$$

which obviously satisfies the zero shear stress boundary condition at the end of adhesive layer ($x = 0$). This stress distribution is shown in Figure 2.9 together with the results of FE analysis detailed later, indicating a good agreement. This solution will be utilized in Section 2.4.3 to determine the stress concentration in adherend.

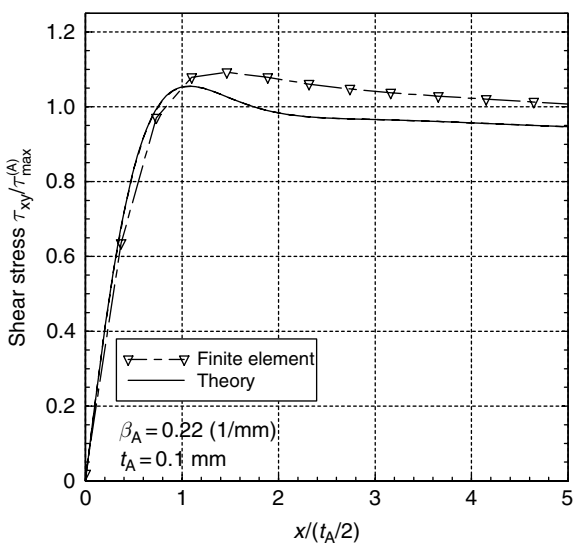

Fig. 2.9. Adhesive shear stress distribution including the end effect.

2.4.2 Corner singularity

Square edge

It is well recognized that stress singularity exists at a corner between the adhesive and the adherend (Williams, 1952; Hein and Erdogan, 1971; Groth, 1988; Akisanya and Fleck, 1997; Tong and Steven, 1999). Studies have also shown that for joints bonded with brittle adhesives the intensity of the stress singularity at the interface corner may be used to predict failure of bonded joints (Groth, 1988; Reedy, 1990).

For the adhesive joint shown in Figure 2.10, there are two corner singularities at points A and B. To apply the fracture mechanics approach, both the order and the intensity of the corner singularity must be quantified in terms of joint geometry and the applied load. While the order of singularity can be obtained from an asymptotic analysis (Williams, 1952; Bogy, 1971; Hein and Erdogan, 1971), the magnitude of the stress intensity factors requires matching the asymptotic solution with the outer solution. An efficient method of carrying out this asymptotic matching analysis is to employ the FE method.

Distributions of the three stress components, σ_{xx}, σ_{yy} and τ_{xy} are shown in Figure 2.11, indicating clearly the high stress elevations near the two corners.

In the case of square ends shown in Figure 2.12, the stress intensity factor K is defined as follows in terms of the stress component normal to the interface, $\sigma_{\theta\theta}$:

$$\sigma_{\theta\theta}(\theta = \pi) = \frac{K}{r^{\lambda}} \tag{2.179}$$

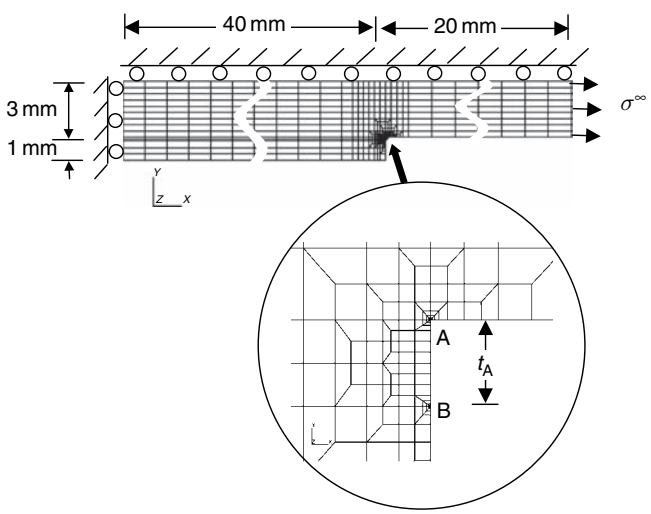

Fig. 2.10. Finite element mesh for a double-lap joint.

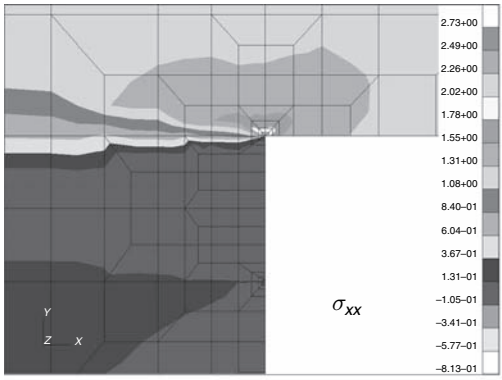

(a)

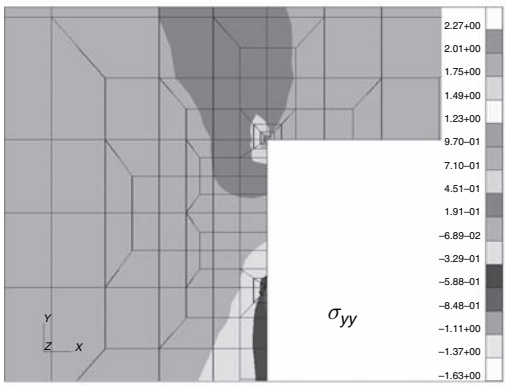

(b)

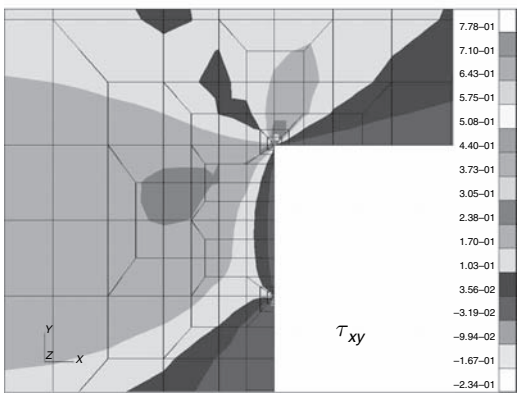

(c)

Fig. 2.11. Contour plots of normalized stresses: (a) axial stress σ_{xx}; (b) peel stress σ_{yy}; and (c) shear stress τ_{xy}.

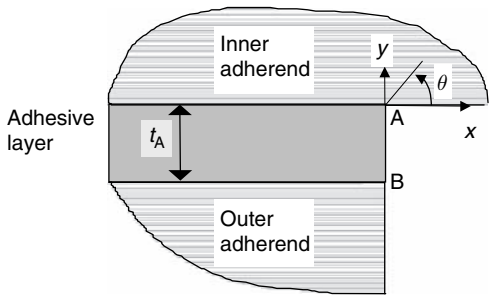

Fig. 2.12. Ends of adhesive layer, showing a square edge.

In this case, the shear stress distribution along the interface is (Wang and Rose, 2000)

$$\tau_{r\theta}(\theta = \pi) = -\frac{K}{r^{\lambda}}\nu_{\mathrm{A}} \tag{2.180}$$

where the parameter λ denotes the order of corner singularity, which is shown in Figure 2.13 for a square end, and ν_{A} is the Poisson's ratio of the adhesive layer.

The order of singularity at square end can be expressed as

$$\lambda = 1.29\nu_{\mathrm{A}}(1 - 0.768\nu_{\mathrm{A}}) \tag{2.181}$$

while the stress intensity factor is given by

$$K = [\hat{A}(\nu_{\mathrm{A}})\sigma_{\max}^{(\mathrm{A})} + \hat{B}(\nu_{\mathrm{A}})\tau_{\max}^{(\mathrm{A})}]t_{\mathrm{A}}^{\lambda} \tag{2.182}$$

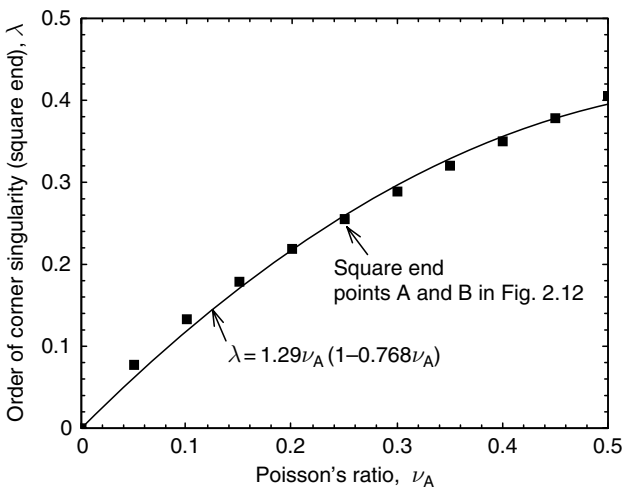

Fig. 2.13. Order of singularity at square end for various Poisson's ratios.

where $\sigma_{\max}^{(A)}$ and $\tau_{\max}^{(A)}$ are the maximum peel and shear stresses of the adhesive, which can be obtained by methods outlined in Sections 2.2 and 2.3 for a linear elastic adhesive. The parameters $\hat{A}$ and $\hat{B}$ depend solely on the Poisson's ratio of the adhesive via the following equations (Wang and Rose, 2000),

$$\hat{A}(\nu_A) = 0.836 - 2.23\nu_A + 6.29\nu_A^2 - 9.64\nu_A^3 \tag{2.183}$$

$$\hat{B}(\nu_A) = 3.12 - 15.8\nu_A + 40.1\nu_A^2 - 37.6\nu_A^3 \tag{2.184}$$

The stress intensity factors at two corner points shown by the insert of Figure 2.14(a) therefore can be expressed as follows, noting the difference in the sign of shear stress as indicated in the insert of Figure 2.14(b):

$$K_{C_1} = \tau_{\max}^{(A)} \hat{B}(\nu_A)\, t_A^{\lambda} \tag{2.185}$$

$$K_{C_4} = [\hat{A}(\nu_A)\sigma_{\max}^{(A)} - \hat{B}(\nu_A)\tau_{\max}^{(A)}]t_A^{\lambda} \tag{2.186}$$

Comparisons between FE results and predictions based on Equations (2.185) and (2.186) are shown in Figure 2.14. It is seen that there is a good agreement between the predictions and the FE results. It is also clear from Figure 2.14 that the corner singularity dominates a reasonably large region. For brittle adhesives whose process zone at failure is smaller than the singularity field, the strength of the joint would be entirely characterized by the stress intensity factors discussed above.

Spew fillet

Studies have shown that spew fillets formed during bonding at the ends of overlap may have an important influence on the joint strength (Adams and Harris, 1987; Groth, 1988; Kairouz and Matthews, 1993; Adams et al., 1997). Formation of the spew fillet not only modifies the stress distribution along the mid-plane of the adhesive layer (Adams and Peppiatt, 1974), but may also eliminate the corner singularity. Referring to Figure 2.15, while the stresses at corner C are singular, the stress-state at point A depends strongly on the angle θ. In the following these two points will be examined in turn.

Assuming that the Young's modulus of the adhesive is far smaller than the modulus of the adherend, the order of the stress singularity at corner A under plane-strain conditions can be obtained from the solution of Williams (1952), and the results are shown in Figure 2.16. It is clear that spew corners would be free of singularities when the fillet angle is less than a critical angle, which is dependent on the Poisson's ratio of the adhesive. The value of this critical angle is shown in Figure 2.17. The absolute maximum angle at which no corner singularity would exist for any Poisson's ratio is 45 degrees. Therefore, if the spew fillet angle can be controlled to be equal or less than 45 degrees, stresses at corners A and B in Figure 2.15 would be regular.

To verify the singularity associated with a spew fillet, a FE analysis has been carried out using the FE mesh shown in Figure 2.10, with a spew fillet shown in Figure 2.18.

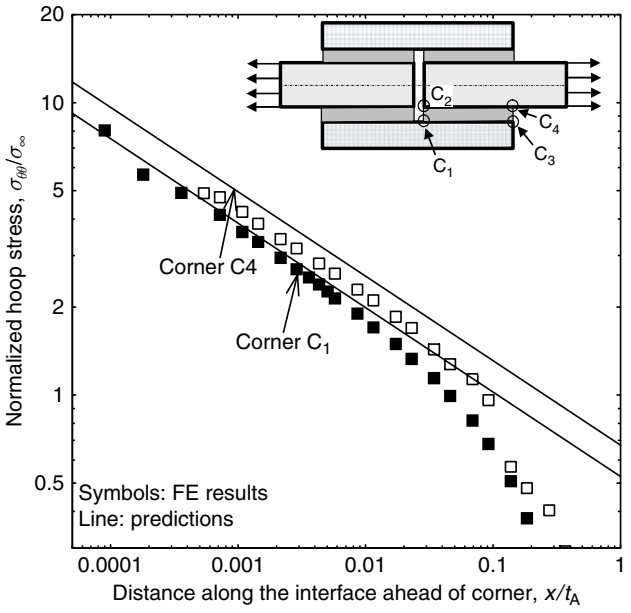

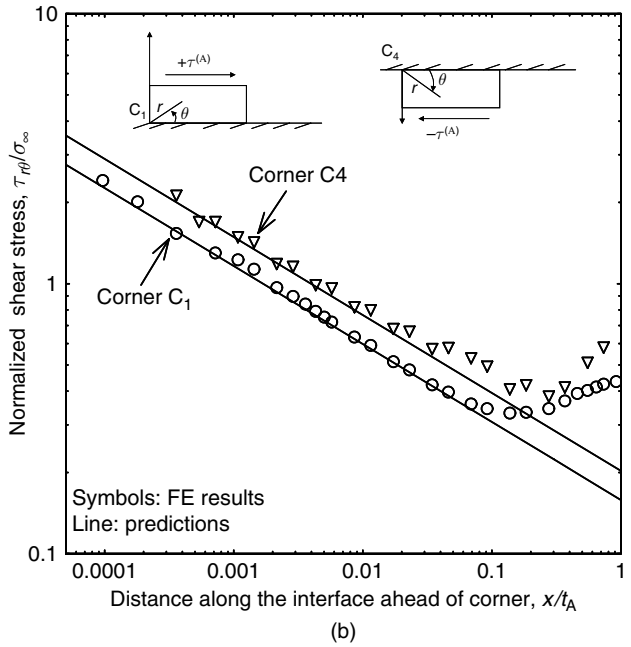

Fig. 2.14. Distribution of (a) normal stress and (b) shear stress along the interface ahead of the corners C_1 and C_4 in a double-lap joint.

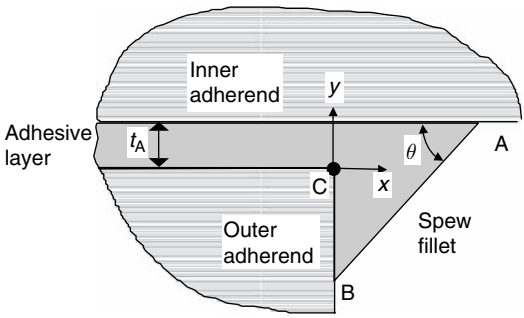

Fig. 2.15. Configuration of a spew fillet.

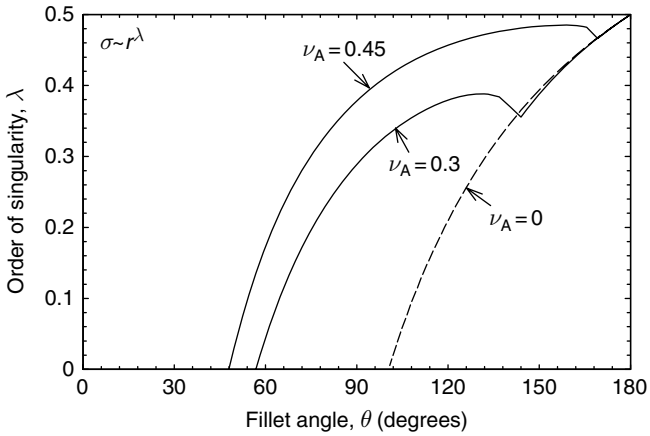

Fig. 2.16. Order of corner singularity at spew fillet (points *A* and *B* in Figure 2.15).

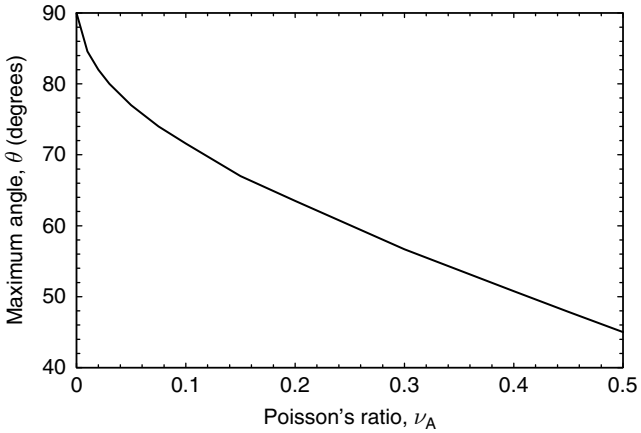

Fig. 2.17. Maximum fillet angle θ for zero corner singularity.

The spew fillet angle at both points A and B is equal to 45 degrees. Contours of the resulting stress components σ_{xx}, σ_{yy}, and τ_{xy} are shown in Figure 2.18, confirming that the stresses at points A and B are no long singular. Consequently, corner singularity exists only at corner C. Solutions of the order of singularity and the stress intensity factor for this corner can be found in Wang and Rose (2000). It is worth pointing out that this corner singularity can be removed by rounding of corner C (see Adams et al., 1997).

It is clear in Figure 2.18 that corner singularity exists only at point C of Figure 2.15. It has been found that there are two singular terms for the stresses at corner C (Wang and Rose, 2000). The order of the stronger singular term is approximately equal to 0.41 for typical Poisson's ratio of 0.35.

From the preceding analysis it is clear that corner singularities can be completely removed if the end of adhesive layer can be shaped so that all interface angles are less than 45 degrees. An example of such an end that would be free of corner singularity is shown in Figure 2.19. Further work is required to clarify the influence of adhesive layer thickness on the joint strength.

2.4.3 Stress concentration in adherends

Since the adhesive shear stress peaks at the end of adhesive layer, significant through-thickness stress concentrations exists in the loaded adherend (Cornell, 1953; Adams et al., 1986; Kairouz and Matthews, 1993; Wang et al., 1998a). This is schematically shown in Figure 2.20 for a double-strap joint. Such a stress concentration can be extremely detrimental to joint strength, especially when the overlap terminates near another stress concentration site, such as a fastener hole.

Quantitative methods for evaluating the stress concentration in adherends are often critical to the design and assessment of bonded joints. For example, to avoid adhesive failure and achieve the maximum strength, bonded joints are mostly designed so that the bonding strength is greater than the substrate strength (Hart-Smith, 1973b). In this case, it is paramount to be able to determine the strength of the substrates, taking into account the stress concentrations. Kairouz and Matthews (1993) reported that the load-carrying capacity of adhesively bonded joints with cross-ply substrates having 90° surface layer would be dictated by the maximum longitudinal stress occurring near the ends of overlap. There have been instances where unexpected fatigue failures of metallic substrates occurred immediately outside the end of a reinforcement patch, possibly caused by the interaction between the high stress concentration induced by bonded reinforcement and fastener holes situated near the ends of overlap.

According to Wang et al. (1998a), a first-order estimate of the maximum longitudinal stress (in the loaded adherend) at the end of overlap is given by the following integration, noting Equation (2.178):

$$\sigma_{xx,\max} = \int_0^\infty \frac{\tau^{(\mathrm{A})}(x)}{x}\mathrm{d}x = \frac{2}{\pi}\tau_{\max}^{(\mathrm{A})}\int_0^\infty \frac{\mathrm{e}^{-\beta_{\mathrm{A}}t_{\mathrm{A}}x} - \mathrm{e}^{-2\varpi x}\cos(2\varpi x)}{x}\mathrm{d}x \tag{2.187}$$

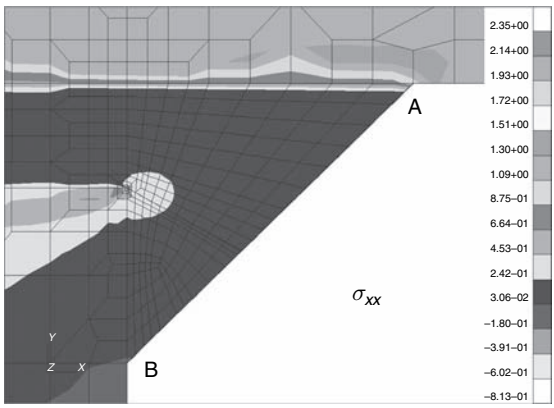

(a)

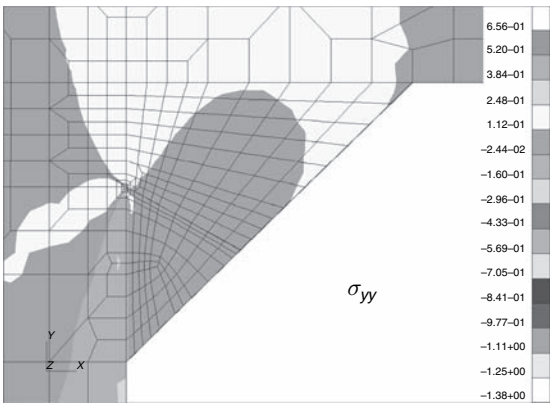

(b)

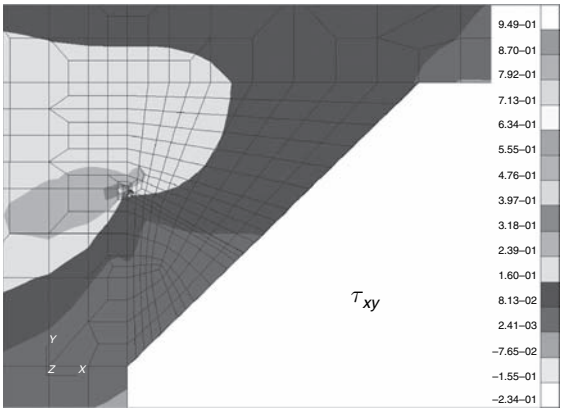

(c)

Fig. 2.18. Stress contours near spew fillet.

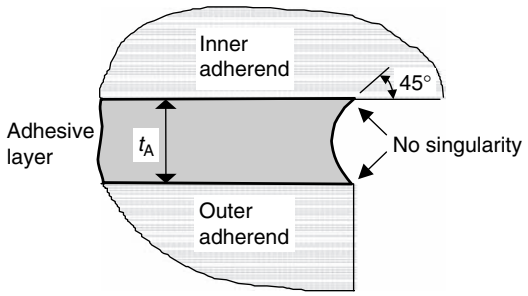

Fig. 2.19. Adhesive end free of corner singularity.

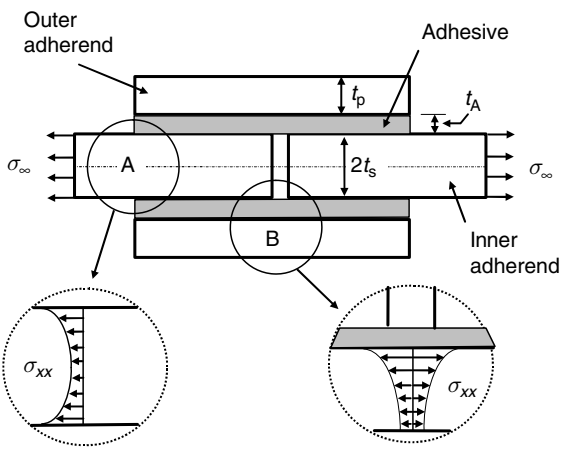

Fig. 2.20. Through-thickness stress concentrations in adherends of a double-strap joint.

For a typical Poisson's ratio of 0.35, the parameter ϖ is equal to 2.1535. In this case, the maximum longitudinal stress is dependent only on the value of $\beta_A t_A$. Equation (2.187) can be readily evaluated numerically, and the results are shown in Figure 2.21. It is clear that a considerable stress concentration exists in the loaded adherend as a result of the shear deformation in the adhesive layer.

As an example consider a double-strap joint representative of a unidirectional boron patch bonded to an aluminium plate. The thicknesses of the inner adherend, the outer adherend and the adhesive layer are respectively 6, 1.3 and 0.1 mm. The Young's moduli of the inner adherend and the outer adherend are 72 and 210 GPA, while the shear modulus and the Poisson's ratio of the adhesive layer are 700 MPa and 0.3, respectively. The load transfer parameter β_A is equal to $0.18\,\text{mm}^{-1}$, thus giving rise to a stress elevation of $3.27\tau_{\max}^{(A)}$. The normalized longitudinal stress along the adherend–adhesive interface from a FE analysis (with spew fillet) is shown in Figure 2.22, indicating a maximum stress concentration factor of 1.42. According to Equation (2.18), noting that

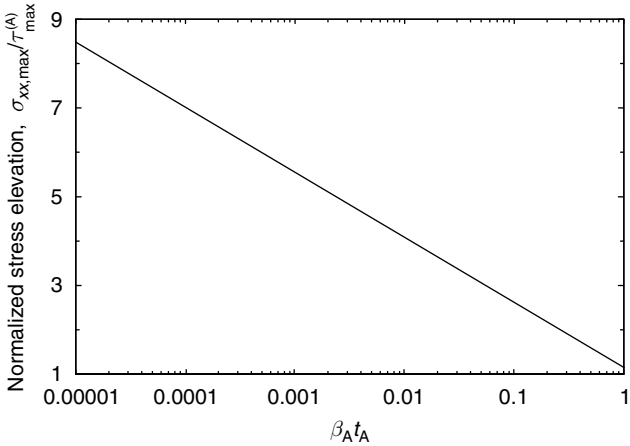

Fig. 2.21. Normalized longitudinal stresses in adherend.

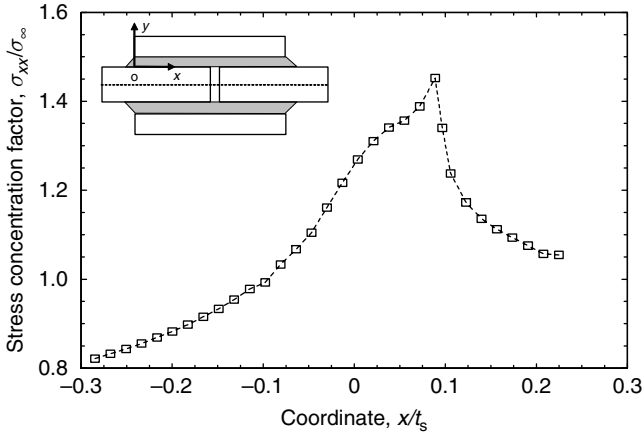

Fig. 2.22. Longitudinal stress along the plate–adhesive interface of a double-strap joint with a spew fillet. The coordinate x is measured from the square end of the adherend as shown in the insert.

$\Delta T = 0$, the maximum shear stress $\tau_{\max}^{(A)} = 0.536\sigma_\infty$. Consequently the stress concentration ($= \sigma_{xx,\max}/\sigma_\infty$) is estimated to be 1.75 from the theory, which is higher than the FE results. The first-order solution can be improved if the effect of spew fillet is taken into account. Assuming that the presence of spew fillet would reduce the peak shear stress by 20%, the analytical estimate would come very close to the FE solution.

2.4.4 Triaxial stresses and plastic yielding

In analyzing the stresses in bonded doublers or joints, often only two stress components, the peel stress and the shear stress, are considered. However, due to the constraint

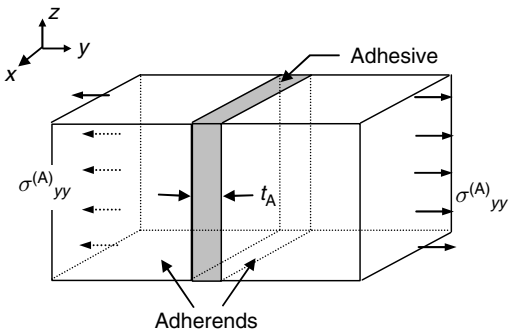

Fig. 2.23. A unit cell representing an adhesive layer sandwiched between substrates.

imparted by the stiff adherends, the stress state in an adhesive layer is truly triaxial (Adams et al., 1997; Wang and Rose, 1997a). The lateral stress components parallel to the interface give rise to a high hydrostatic tension. This hydrostatic stress is important in determining the plastic yield behavior of polymers (Wang and Chalkley, 2000), affecting both the crazing mechanism and also the glass transition temperature (Losi and Knauss, 1992; Duong and Knauss, 1995). In this section the triaxial stress state within an adhesive layer is first examined, and then the plastic yielding behavior of adhesive under triaxial stresses is discussed.

Referring to Figure 2.23 which shows a unit cell representing an adhesive layer sandwiched between two stiff adherends, the two lateral stress components, $\sigma^{(A)}_{xx}$ and $\sigma^{(A)}_{zz}$, can be expressed in terms of the peel stress $\sigma^{(A)} \equiv \sigma^{(A)}_{yy}$ (Adams et al., 1997; Wang and Rose, 1997a),

$$\sigma^{(A)}_{xx} \equiv \sigma^{(A)}_{zz} = \frac{\nu_A}{1-\nu_A}\sigma^{(A)}_{yy} = \frac{\nu_A}{1-\nu_A}\sigma^{(A)} \tag{2.188}$$

Consequently the hydrostatic stress is

$$p = \frac{1}{3}(\sigma^{(A)}_{xx} + \sigma^{(A)}_{yy} + \sigma^{(A)}_{zz}) = \frac{1+\nu_A}{3(1-\nu_A)}\sigma^{(A)} \tag{2.189}$$

To quantify the influence of hydrostatic stress on the plastic yielding behavior of polymer adhesive, a series of experiments have been carried out on a film adhesive (FM73), under various combination of tension, compression and shear loading (Wang and Chalkley, 2000). The results are shown in Figure 2.24, where the equivalent shear stress is defined as

$$6\tau^2_{eq} = \left(\sigma^{(A)}_{xx} - \sigma^{(A)}_{yy}\right)^2 + \left(\sigma^{(A)}_{yy} - \sigma^{(A)}_{zz}\right)^2 + \left(\sigma^{(A)}_{zz} - \sigma^{(A)}_{xx}\right)^2 + 6\tau^{(A)^2}_{xy} \tag{2.190}$$

It can be seen that when the hydrostatic stress is negative (in compression), the equivalent shear stress is approximately constant, indicating that the conventional von Mises yield criterion is applicable. However, under tensile hydrostatic stress, the equivalent shear

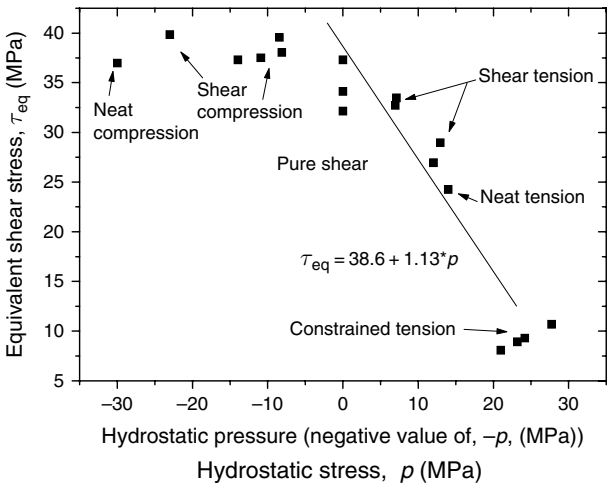

Fig. 2.24. Influence of hydrostatic stress on yield stress of FM73 adhesive.

stress decreases rapidly as the hydrostatic stress increases. These data suggest that the modified von Mises yield criterion (Bowden and Jukes, 1972) is applicable for positive hydrostatic stress:

$$\tau_{\text{eq}} - \tilde{\mu}\, p = \tau_{\text{Y}}^{(\text{A})} \tag{2.191}$$

where $\tau_{\text{Y}}^{(\text{A})}$ denotes the yield stress under shear (zero hydrostatic stress), and the experimental data shown in Figure 2.24 suggest that the coefficient $\tilde{\mu}$ is approximately 1.13 for FM73 adhesive.

One important implication of the triaxial stress state in an adhesive layer is that it would have a significant effect on the onset of plastic yielding. Denoting the shear stress and the peel stress as $\tau^{(\text{A})}$ and $\sigma^{(\text{A})}$, and recalling Equation (2.188), the equivalent shear stress from Equation (2.190) can be written as

$$\tau_{\text{eq}} = \tau^{(\text{A})} \left[1 + \frac{1}{3} \left(\frac{1-2\nu_{\text{A}}}{1-\nu_{\text{A}}} \frac{\sigma^{(\text{A})}}{\tau^{(\text{A})}} \right)^2 \right]^{1/2} \tag{2.192}$$

where $\sigma^{(\text{A})}$ and $\tau^{(\text{A})}$, thus the ratio $\sigma^{(\text{A})}/\tau^{(\text{A})}$, can be obtained by the conventional theories outlined in Sections 2.2 and 2.3 for bonded doublers and joints. Then the modified von Mises yield criterion can be expressed as

$$\tau^{(\text{A})} \left\{ \left[1 + \frac{1}{3} \left(\frac{1-2\nu_{\text{A}}}{1-\nu_{\text{A}}} \frac{\sigma^{(\text{A})}}{\tau^{(\text{A})}} \right)^2 \right]^{1/2} + \frac{1+\nu_{\text{A}}}{3(1-\nu_{\text{A}})} \tilde{\mu} \frac{\sigma^{(\text{A})}}{\tau^{(\text{A})}} \right\} = \tau_{\text{Y}}^{(\text{A})} \tag{2.193}$$

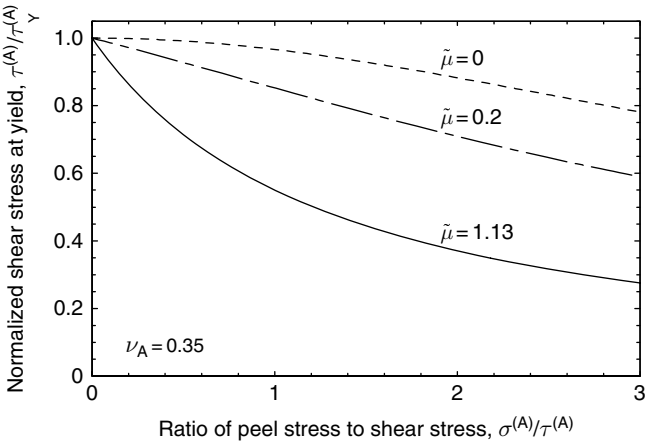

Fig. 2.25. Effect of triaxial stress on the value of shear stress at yielding.

which is shown by the solid curve in Figure 2.25 for FM73 adhesive ($\tilde{\mu} = 1.13$). For comparison purposes, two other cases corresponding to the original von Mises yield criterion $\tilde{\mu} = 0$ and an adhesive of lower pressure sensitivity are also plotted in the figure. It is clear that there is a substantial reduction of the shear stress at yielding due to the effect of hydrostatic tensile stress. This implies that if the design limit of a lap joint is the onset of plastic yielding, the effect of peel stress on the allowable shear stress has to be considered. Likewise, if the peel strength turns out to be the limiting factor, the design allowables for the peel stress should also take into account the effect of hydrostatic tension.

2.5 Failure Criteria for Bonded Doublers and Joints

Adhesive failure within a joint is usually assumed to be governed by a critical stress, or a critical strain, sometimes coupled with a characteristic length (Kinloch, 1987). Some examples include Hart-Smith (1973a,b), Adams (1989, 1992), and Bigwood and Crocombe (1990). Strain energy density (Hart-Smith, 1973b; Jones et al., 1993) and stress over a zone (Clark and Mcgregor, 1993) have also been suggested for predicting joint strength. However, it has long been noted (Adams and Peppiatt, 1974) that there is a large discrepancy between theoretical predictions and experimental data. As discussed in Sections 2.2 and 2.3, both the maximum adhesive shear and the peel stresses at the ends of a long overlap joint are inversely proportional to the square root of the adhesive thickness. Therefore, for a given applied load, the thicker the adhesive, the lower the stresses are. This means that the conventional strain- or stress-based failure criteria would predict an increase in joint strength (total failure load) with the increase in bond-line thickness. In other words, the remote applied stress at failure is proportional to the square root of the adhesive thickness,

$$\sigma_\infty^{\text{ult}} \propto \sqrt{t_A} \tag{2.194}$$

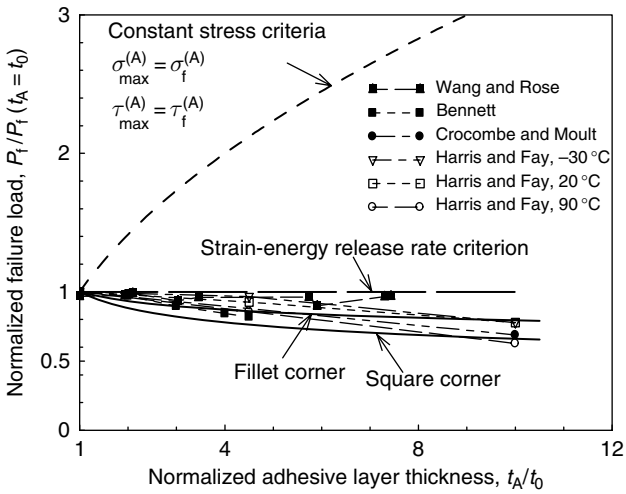

Fig. 2.26. Comparison of experimental results of joint strength and theoretical predictions. The variable t_0 denotes a baseline adhesive thickness.

Experimental results, however, exhibited exactly the opposite trend: the load-carrying capacity of joints decreases with bond-line thickness (Bennett, 1972; Hylands and Sidwell, 1980; Crocombe and Moult, 1988; Harris and Fay, 1992).

Five sets of experimental results on single-lap joints (Bennett, 1972; Crocombe and Moult, 1988; Harris and Fay, 1992) and one set of data on single-strap joints (Wang and Rose, 1997b) are shown in Figure 2.26, together with the predictions of stress-based failure criteria. It can be seen that with the increase in bond-line thickness, joint strengths decreased, contrary to the expectations of stress-based failure criteria. Also shown in the figure are predictions based on fracture mechanics approaches (strain-energy release rate and corner stress-intensity factor), which will be discussed in detail later.

Under fatigue loading, it has also been observed that fatigue crack growth rates and fatigue endurance (Imanaka et al., 1988; Harris and Fay, 1992; Krenk et al., 1996) also exhibited anomalous behavior with respect to adhesive thickness. These results showed that on the basis of the maximum (shear or normal) stress in the adhesive, joints with thinner adhesive lasted longer than joints with thicker adhesive. For a given applied load, although joints with thicker adhesive exhibited longer fatigue lives than joints of thinner adhesive, the increase in fatigue load is much less than what would be expected on the basis of constant stress. Therefore it is clear that the conventional failure criteria, be it stress-, strain-, or strain-energy-density-based, are not geometry independent, hence the data obtained from one configuration are not readily transferable to other types of joint, or the same joint with different bond-line thicknesses.

Fracture mechanics concepts have also been introduced for characterizing bonded joints (Mall et al., 1982; Johnson and Mall, 1985; Kinloch, 1987; Wang, 1997, 1998), but mainly to joints with crack-like defects, such as butt joints, edge-cracked cantilever beam

and cracked-lap-shear specimens (Johnson, 1986; Kinloch, 1987). The thickness of the adhesive is basically ignored and the disbond is treated as a crack, thus permitting the use of linear elastic fracture mechanics parameters. FE analysis and compliance approaches are the two main methods used in evaluating the energy release rate. An alternative method of calculating the strain energy release rate is through the J-integral (Fernlund and Spelt, 1991a,b; Edde and Verreman, 1992; Wang and Rose, 1997b), leading to expressions of the strain-energy release rate in terms of the maximum adhesive shear and peel stresses obtained from plate-spring theories of lap joints:

$$G_{\mathrm{I}} = \frac{\sigma_{\max}^{(\mathrm{A})2}}{2E_{\mathrm{A}}} t_{\mathrm{A}}$$
$$G_{\mathrm{II}} = \frac{\tau_{\max}^{(\mathrm{A})2}}{2G_{\mathrm{A}}} t_{\mathrm{A}} \tag{2.195}$$

and the total strain-energy release rate is the sum of the above two components.

Since the maximum adhesive shear and peel stresses are proportional to the reciprocal of the square root of the bond-line thickness, it can be readily shown that the strain-energy release rates given by (2.195) are independent of bond-line thickness, and are dependent only on the dimensions of the adherends and the applied load. Consequently, fracture mechanics–based failure criteria would predict that joint strength is independent of bond-line thickness, as indicated in Figure 2.26. When compared to the stress/strain-based failure criteria, this represents a considerable improvement, considering that joint strength has been observed to decrease with bond-line thickness. However, the fracture mechanics methods are applicable only to joints with large disbond of length greater than or comparable to substrate thickness. Since virtually all bonded joints are manufactured to be free of large disbonds, the physical basis of the above-mentioned fracture mechanics methods as applied to bonded joints is not clear.

For disbond-free bonded joints, the corner stress-intensity factor has been found to be a promising criterion that can unify the failure loads of butt joints of varying bond-line thicknesses (Reedy and Guess, 1997) and the failure loads of single-lap joints (Groth, 1988). Since the corner stress-intensity factor uniquely characterizes the deformation at an interface corner, it would serve as a failure criterion for bonded joints provided that the size of the process zone is comparable to the corner singularity zone. According to this failure criterion, failure will occur when the corner stress-intensity factor attains a critical value. Accordingly the joint strength would decrease as the adhesive thickness increases, i.e.,

$$\sigma_{\infty}^{\mathrm{ult}} \propto t_{\mathrm{A}}^{\lambda-0.5} \tag{2.196}$$

where λ is given by Equation (2.181), consistent with the various experimental findings shown in Figure 2.26. For Poisson's ratio of 0.35, the order of singularity λ is equal to 0.32. In this case, prediction of the corner stress-intensity factor criterion is shown in Figure 2.26. This prediction seems to provide a lower bound to all the experimental results. This is most likely due to the ignorance of the spew fillet.

It was found in Section 2.4.2 that for a spew fillet configurations shown in Figure 2.15, there are two singular terms for the stresses at corner C. The order of the stronger singular term is approximately equal to 0.41 for a typical Poisson's ratio of 0.35. Consequently the critical corner stress-intensity factor criterion would predict the joint strength to decrease with adhesive thickness via the following relation,

$$\sigma_{\infty}^{\text{ult}} \propto t_{\text{A}}^{-0.1} \tag{2.197}$$

which is also shown in Figure 2.26, indicating a good agreement with the experimental results.

2.6 Summary

This chapter presents various analytical models for determining stresses in bonded joints and doublers that are relevant to the repair geometries. The presented analytical models account for various important effects such as elastic-plastic adhesive, geometrically nonlinear deformation, triaxial stresses on plastic yielding, adherend stress concentration, and corner singularity at the termini of the adhesive layer. Several criteria for failure assessment of bonded joints and doublers are also discussed.

CHAPTER 3

Fundamental Concept of Crack Patching

3.1 Introduction

As discussed in Chapter 1, bonded repairs can be applied either as a precaution to reinforce undamaged structures or as a remedy to cracked structures so that the stress intensity factor of the crack being repaired has been significantly reduced to an appropriate level. The multiplayer nature of a bonded repair, which comprises three different layers of materials with vastly different properties, gives rise to very complicated stress states. Although in principal the problem can be analyzed by using numerical tools, such as the finite element method or the boundary element method, in many cases such an approach is not only cumbersome but also unnecessary. This is because inevitably stress transfer between the host structure and the patch occurs in two relatively small regions, one close to the outside boundary of the patch and one near the cracked region in the host structure; consequently, the problem can be more efficiently resolved analytically by using a boundary layer approach. Furthermore, the theoretical analyses presented in this chapter will provide a good conceptual understanding of the fundamental mechanics of bonded repairs and the associated key parameters that are important to design of repairs.

To focus on theoretical modeling of bonded repairs, we shall consider a relatively simple yet representative repair configuration, namely a centre-cracked plate (denoted as skin) being repaired by an elliptical patch, as illustrated in Figure 3.1. It is assumed that the repaired structure experiences no out-of-plane deformation, either because the skin is fully supported against out-of-plane deflection or because the skin is repaired with two identical patches bonded on both sides. The case of one-sided repairs that is not supported against out-of-plane deformation will be briefly introduced in this chapter within a context of geometrically linear analysis with a key stress intensity factor being simply estimated, as its formal analysis will be discussed in Chapter 5. It is worth noting that the primary function of a bonded repair is to sufficiently reduce the stress intensity factor of the crack being repaired so that the residual strength has been restored to an acceptable level, and the growth rate of the crack under fatigue condition is sufficiently slow to ensure an acceptable inspection interval. Therefore it is important to determine

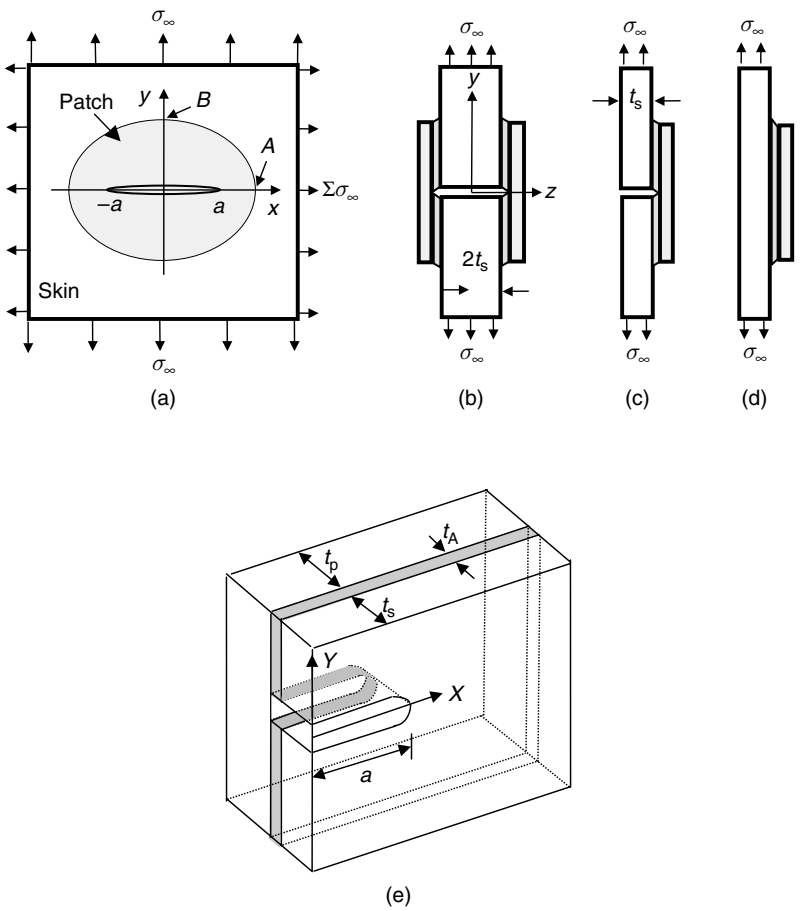

Fig. 3.1. Repair configurations and coordinates. (a) Plan view; (b) cross section along centre line ($x = 0$) with no bending deflection allowed, representing two-sided repair; (c) cross section of a one-sided repair along the centre line; (d) cross section at $x \to \infty$ for one-sided repair; and (e) near crack region.

the stress intensity factor of a repaired crack, as well as the stresses in the patch and the adhesive layer for given mechanical or thermal loading.

One very important concept in the analysis of bonded repairs for crack patching is the two-stage approach first employed by Rose (1981, 1982, 1988), which allows each stage to be solved by employing different theoretical methods with appropriate simplifying assumptions. In stage I, which is referred to as the load attraction problem, the redistribution of the stresses or strains in an un-cracked skin due to the presence of a patch is determined, assuming that the skin and the patch are rigidly bonded upon curing. This assumption is appropriate because the length of the load transfer zone around the edge of the patch is usually small compared to the overall dimension of the patch. Then in

stage II, the crack-tip stress intensity factor and the stresses in the patch and the adhesive layer close to the cracked region are determined by appealing to the superposition principle. This is achieved by pressurizing the crack faces with the prospective stresses (the stresses that would exist along the crack path) already determined in stage I. This two-stage approach will be used extensively in Chapters 4 and 5 in the development of generic algorithms for analyzing irregular-shaped repairs to supported and un-supported plate-like structures. Extension of this two-stage analysis approach to the repairs of corrosive damages will be presented in Chapter 6.

3.2 Formulation and Notation

Referring to Figure 3.1, the problem to be considered is a cracked skin plate with a patch adhesively bonded on one-side. The plate, which has a thickness of t_s for a one-sided repair and $2t_s$ for a symmetric repair, contains a through-thickness crack of length $2a$. The thickness of the patch and the adhesive layer are respectively t_p and t_A. The cross sections in the yz are depicted in Figure 3.1(b)–(d). The Young's modulus and the Poisson's ratio of each individual layer are denoted as E and ν; here and in the following, subscripts s, p, and A will be used to distinguish properties pertaining, respectively, to the skin plate, the patch, and the adhesive layer. In addition, the shear modulus of the adhesive will be denoted as G_A. The crack is along the line segment $|x| \le a,\ y = 0$, and the patch is over an elliptical region defined by

$$\left(\frac{x}{A}\right)^2 + \left(\frac{y}{B}\right)^2 \le 1 \tag{3.1}$$

which completely covers the crack ($A > a$). After this repair, the plate is subjected to a remote stress specified by

$$\sigma^s_{yy} = \sigma_\infty \quad \sigma^s_{xx} = \Sigma \cdot \sigma_\infty \quad \tau^s_{xy} = \tau_\infty \qquad (x^2 + y^2 \to \infty) \tag{3.2}$$

By using the superposition principle, it is easy to demonstrate that the above problem can be decomposed into a tensile mode ($\tau_\infty = 0$) and a shear mode ($\sigma_\infty = 0$). In this chapter we will focus on the tensile mode, while the shear mode (Wang and Rose, 1998) will be briefly discussed in Section 3.3.5.

From a geometrical consideration, bonded repairs, as illustrated in Figure 3.1, fall into two categories: two-sided (symmetric) and one-sided (asymmetric). In the former case, two identical reinforcements are bonded on the two surfaces of a cracked plate. This symmetric arrangement ensures that there is no out-of-plane deflection over the repaired region (see Figure 3.1(b)), provided the cracked plate is subjected to extensional loads given by Equation (3.2). In actual repairs, however, one-sided repair is often adopted in which composite patches are applied to only one side of the panel. This is because most often, only one face of a structure to be repaired is accessible and sometimes only one side of a structure is allowed to be patched, e.g., aircraft fuselage or wing sections. Provided the structure to be repaired is well supported against out-of-plane deflection, for instance, by stiffeners attached to one side, it is acceptable to ignore the out-of-plane bending, thus permitting the problem to be treated as being symmetric. However, in the

case of un-supported, one-sided repairs, the out-of-plane bending caused by the shift of the neutral plane away from that of the plate may considerably lower the repair efficiency.

By using the superposition principle it is easy to demonstrate that the problem depicted in Figure 3.1 is equivalent to solving the following perturbation problem: a patched crack subjected to an internal pressure, $-\sigma_0$, acting on the crack faces, as depicted in Figure 3.2. This allows the analysis to be divided into two stages (Rose, 1981, 1982). To determine the prospective stress σ_0, first we consider the re-distribution of stress which would be caused by the patch if it were bonded to an *uncracked plate* (Figure 3.3). The quantity of interest is the normal stress σ_0 along the prospective crack path in

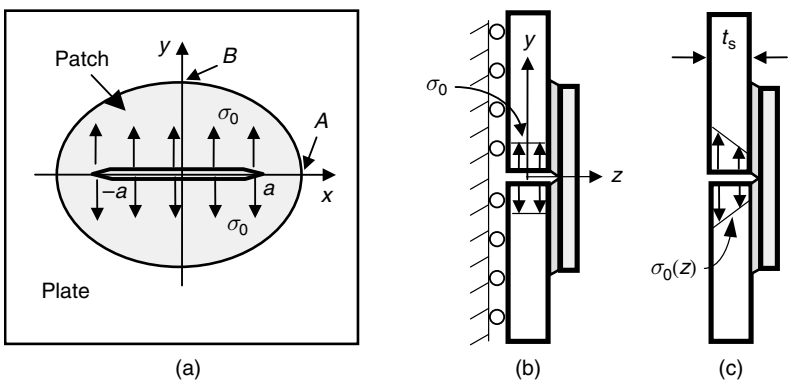

Fig. 3.2. A patched crack subjected to internal pressure.

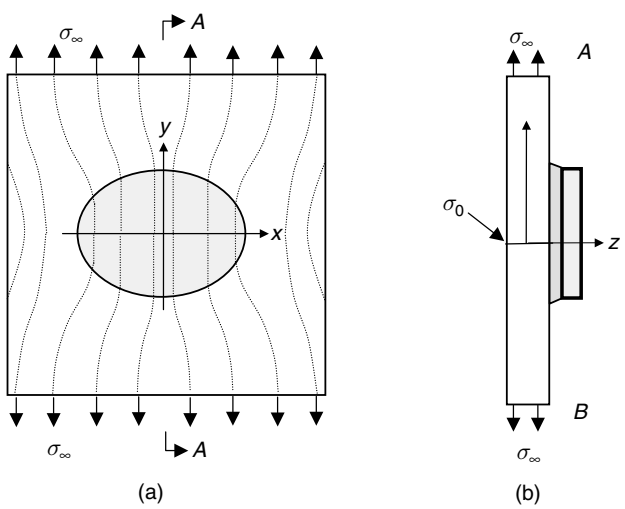

Fig. 3.3. Inclusion analogy for stage I analysis. (a) Flow of load lines into reinforced portions; (b) cross section along centre line.

the uncracked plate. For the case of symmetric repairs or fully supported one-sided repair (no out-of-plane bending), this *prospective* stress σ_0 is uniform through the plate thickness, whereas in the case of un-supported one-sided repairs, the prospective stress distributes linearly through the plate thickness (Wang et al., 1998b), as illustrated in Figure 3.2(b,c). At the second stage, we determine the stress distribution around the crack subjected to an internal pressure of $-\sigma_0$. Due to the presence of the crack, a stress singularity exists at the two crack tips at $x = \pm a$. Here the stress intensity factor K_{I} at the crack tip $x = a$ is defined as,

$$K_{\mathrm{I}}(z) = \lim_{x \to a+} \sqrt{2\pi(x-a)}\,\sigma^{\mathrm{s}}_{yy}(x, y = 0, z) \tag{3.3}$$

where the stress $\sigma^{\mathrm{s}}_{yy}(x, y = 0, z)$ is yet to be determined in terms of the internal stress σ_0 and the repair dimensions and constituent properties. Depending whether the repair is supported against out-of-plane bending, the stress intensity factor may vary through the plate thickness; details will be presented in Section 3.4.

In the absence of a reinforcing patch, the normal stress σ^{s}_{xx} parallel to the crack would not affect the stress intensity factor, but this is no longer true for the repaired plate. After the repair, K_{I} will depend on the applied stress ratio Σ defined by Equation (3.2) and also on the aspect ratio *B/A* of the patch. Provided the adhesive layer remains elastic, the main unknowns K_{I}, $\sigma^{(\mathrm{A})}_{\max}$, $\tau^{(\mathrm{A})}_{\max}$, $\sigma^{\mathrm{s}}_{\max}$, and $\sigma^{\mathrm{p}}_{\max}$ will depend linearly on the principal applied stress σ_∞ of Equation (3.2). The analytical results which will be derived in Sections 3.3 and 3.4 will show clearly the parametric dependence of these unknowns on the dimensions and material properties of a repair configuration.

Since a bonded repair represents a multiple layered structure with a crack being present in one layer only, an exact, analytical solution of this three-dimensional problem is an almost intractable task. Hence it is imperative to make appropriate simplifications to enable the derivation of analytical solutions. It should be noted that there is no fundamental difficulty in employing a fully three-dimensional FE method to estimate the stresses and stress intensity factors in a patched structure. It is, however, often impractical nor necessary to rely solely on time-consuming FE computations for routine engineering designs, especially if parametric analysis is required to optimize a design and to study the sensitivities of repairs to varying geometry dimensions and material properties. In this regard, analytical solutions would be preferred over numerical solutions.

3.3 Symmetric or Fully Supported One-Sided Repairs

The solution of the problem formulated in Section 3.2 will be derived, assuming the repaired structure is supported against out-of-plane bending or the cracked skin plate is repaired with two patched bonded on the two sides. The analysis will be divided into two stages as indicated in Section 3.2.

3.3.1 Stage I: Load attraction by patch

Consider first the re-distribution of stress in an *uncracked* skin plate due to the local stiffening produced by the bonded reinforcement. As illustrated in Figure 3.3(a), the

reinforced region will attract more load due to the increased stiffness, leading to a higher prospective stress than that predicted by one-dimensional analysis. The repair geometry that corresponds to a one-dimensional analysis is a patch spanning across the entire width of the skin plate. The one-dimensional theory of bonded joints and doublers (see Chapter 2) estimates the skin stress underneath the patch as

$$\sigma_0 = \frac{\sigma_\infty}{(1+S)} \tag{3.4}$$

where S is the patch stiffness to skin stiffness ratio, i.e., $S = \frac{E'_p t_p}{E'_s t_s} = \frac{E_p t_p}{E_s t_s}$ when $\nu_p = \nu_s$. This one-dimensional theory also provides an estimate of the load-transfer length β_A^{-1} for load transfer from the skin to the patch. If that transfer length is much less than the in-plane dimensions A and B of the patch, we may view the reinforced region as an inhomogeneity of higher stiffness than the surrounding skin, and proceed in the following three steps.

(i) Determine the elastic constants of the equivalent inhomogeneity in terms of those of the skin and the reinforcing patch.

(ii) Determine the stress in the equivalent inhomogeneity.

(iii) Determine how the load which is transmitted through the inhomogeneity is shared between the skin and the patch, from which the prospective stress σ_0 can be calculated.

Steps (i) and (iii) can be readily performed using classical composite plate theory. In the case of symmetric or fully supported one-sided repairs, the patch and skin have identical strains.

Step (ii) is greatly facilitated by the known results of ellipsoidal inhomogeneity (Eshelby, 1957; Mura, 1998) in an infinite sheet under uniform far-field-applied stress: the stress and strain within an ellipsoidal inhomogeneity is uniform, as indicated schematically in Figure 3.3(a). The uniform stress state can be determined analytically with the help of imaginary cutting, straining and welding operations. General solution methods were derived by Rose (1981) for the case where both the skin and the reinforcing patch are taken to be orthotropic, with their principal axes parallel to the $x-y$ axes. However, that method employed by Rose (1981) requires modification for the special case of *isotropic skin*, the case of most interest for repairs to metallic structures, because the resulting characteristic equation has coincident roots.

In the following we will present a simpler solution for the special case of isotropic skin repaired with an orthotropic patch. Although the following analysis is derived for a supported one-sided repair, pertinent solutions for a symmetric repair shown in Figure 3.1(c) will be the same by noting that the same symbol t_s will now represent the half thickness of the skin in the symmetric repair. The patch, the adhesive layer, and the reinforced portion of the skin can be replaced by an equivalent orthotropic plate, which can now be viewed as an "inhomogeneity" having different constitutive properties from the surrounding "matrix". For an isotropic skin and an orthotropic patch,

the stiffness matrix of the equivalent inhomogeneity, denoted as $\left[C^{\mathrm{I}}\right]$, is given by Rose (1981) for a supported one-sided repair,

$$\left[C^{\mathrm{I}}\right] = [C^{\mathrm{s}}] + \frac{t_{\mathrm{p}}}{t_{\mathrm{s}}}[C^{\mathrm{p}}] \tag{3.5}$$

with

$$[C^{\mathrm{s}}] = \frac{E_{\mathrm{s}}}{1-\nu_{\mathrm{s}}^2}\begin{bmatrix} 1 & \nu_{\mathrm{s}} \\ \nu_{\mathrm{s}} & 1 \end{bmatrix} \quad [C^{\mathrm{p}}] = \frac{E_{11}^{\mathrm{p}}}{1-\nu_{12}^{\mathrm{p}}\nu_{21}^{\mathrm{p}}}\begin{bmatrix} 1 & \nu_{12}^{\mathrm{p}}E_{22}^{\mathrm{p}}/E_{11}^{\mathrm{p}} \\ \nu_{12}^{\mathrm{p}}E_{22}^{\mathrm{p}}/E_{11}^{\mathrm{p}} & E_{22}^{\mathrm{p}}/E_{11}^{\mathrm{p}} \end{bmatrix}$$
$$\text{and} \quad \left[C^{\mathrm{I}}\right] = \frac{E_{11}^{\mathrm{I}}}{1-\nu_{12}^{\mathrm{I}}\nu_{21}^{\mathrm{I}}}\begin{bmatrix} 1 & \nu_{12}^{\mathrm{I}}E_{22}^{\mathrm{I}}/E_{11}^{\mathrm{I}} \\ \nu_{12}^{\mathrm{I}}E_{22}^{\mathrm{I}}/E_{11}^{\mathrm{I}} & E_{22}^{\mathrm{I}}/E_{11}^{\mathrm{I}} \end{bmatrix} \tag{3.6}$$

The elastic compliance matrix of the inhomogeneity is $\left[C^{\mathrm{I}}\right]^{-1}$.

According to the Eshelby inhomogeneity result, the stresses and strains inside an elliptical inhomogeneity are uniform. The x- and y-components of the stresses inside the inhomogeneity are denoted as p and q, respectively. Because of the traction continuity across the interface, the tractions at the boundary between the inhomogeneity and the surrounding skin plate along the x and y direction are related to the constant stresses p and q as illustrated in Figure 3.4.

The unknown stresses p and q are to be determined from the displacement continuity conditions along the interface between the inhomogeneity and the surround skin plate. Since the strains in the inhomogeneity are constant (independent of x and y), the displacement continuity implies that the y-strain is continuous at point A, and the x-strain is continuous at point B. This can be expressed as

$$\begin{aligned} \varepsilon_{xx,B}^{\mathrm{I}} &= \varepsilon_{xx,B}^{\mathrm{s}} \\ \varepsilon_{yy,A}^{\mathrm{I}} &= \varepsilon_{yy,A}^{\mathrm{s}} \end{aligned} \tag{3.7}$$

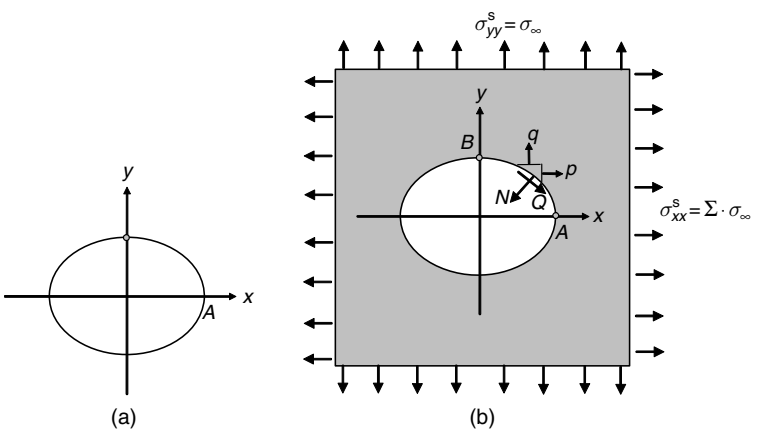

Fig. 3.4. Inclusion analogy approach for stage I analysis.

Within the inhomogeneity, referring to Figure 3.4(a), the strains at an arbitrary point (x, y) inside the inhomogeneity are given by

$$\begin{Bmatrix} \varepsilon^{\mathrm{I}}_{xx} \\ \varepsilon^{\mathrm{I}}_{yy} \end{Bmatrix} = \left[C^{\mathrm{I}}\right]^{-1} \begin{Bmatrix} p \\ q \end{Bmatrix} \tag{3.8}$$

For the plate with an elliptical cut-out as shown in Figure 3.4(b), the stresses can be determined by linear superposition of two problems: (i) an infinite plate without a hole under the stresses p and q applied at infinity; and (ii) an infinite plate with an elliptical hole under the far-field-applied stresses $\sigma^{\mathrm{s}}_{xx} = \Sigma \cdot \sigma_{\infty} - p$ and $\sigma^{\mathrm{s}}_{yy} = \sigma_{\infty} - q$. By noting that the solution of the first problem is trivial while the solution of the second problem is available and can be found in Timoshenko and Goodier (1970), the stresses for a plate with an elliptical cut-out as shown in Figure 3.4(b) can be derived as

$$\begin{Bmatrix} \sigma^{\mathrm{s}}_{xx} \\ \sigma^{\mathrm{s}}_{yy} \end{Bmatrix}_A = \begin{Bmatrix} p \\ p - 2\frac{A}{B}q - \sigma_{\infty xx} + \sigma_{\infty yy}(1 + 2A/B) \end{Bmatrix} \tag{3.9}$$

for point A and

$$\begin{Bmatrix} \sigma^{\mathrm{s}}_{xx} \\ \sigma^{\mathrm{s}}_{yy} \end{Bmatrix}_B = \begin{Bmatrix} -2\frac{B}{A}p + q - \sigma_{\infty yy} + \sigma_{\infty xx}(1 + 2B/A) \\ q \end{Bmatrix} \tag{3.10}$$

for point B, respectively.

Therefore the strains at points A and B are

$$\begin{Bmatrix} \varepsilon^{\mathrm{s}}_{xx,B} \\ \varepsilon^{\mathrm{s}}_{yy,A} \end{Bmatrix} = -\left[m_1\right] \begin{Bmatrix} p \\ q \end{Bmatrix} + \left[m_2\right] \begin{Bmatrix} \sigma_{\infty xx} \\ \sigma_{\infty yy} \end{Bmatrix} \tag{3.11}$$

where

$$\left[m_1\right] = \frac{1}{E_{\mathrm{s}}} \begin{bmatrix} 2\ B/A & -(1-\nu_{\mathrm{s}}) \\ -(1-\nu_{\mathrm{s}}) & 2\ A/B \end{bmatrix} \tag{3.12}$$

$$\left[m_2\right] = \frac{1}{E_{\mathrm{s}}} \begin{bmatrix} 1+2\ B/A & -1 \\ -1 & 1+2\ A/B \end{bmatrix} \tag{3.13}$$

Inserting Equations (3.8) and (3.11) into (3.7) leads to the unknown stresses p and q,

$$\begin{Bmatrix} p \\ q \end{Bmatrix} = \left[\left[C^{\mathrm{I}}\right]^{-1} + \left[m_1\right]\right]^{-1} \left[m_2\right] \begin{Bmatrix} \sigma_{\infty xx} \\ \sigma_{\infty yy} \end{Bmatrix} \tag{3.14}$$

which involves only elementary matrix algebra. The prospective stresses in the plate, along $y = 0$ ($|x| < A$), are,

$$\begin{Bmatrix} \sigma^{\mathrm{s}}_{xx} \\ \sigma^{\mathrm{s}}_{yy} \end{Bmatrix} = \left[C^{\mathrm{s}}\right]\left[C^{\mathrm{I}}\right]^{-1} \begin{Bmatrix} p \\ q \end{Bmatrix} \tag{3.15}$$

Another quantity which is also the primary interest in assessing the efficiency and the viability of the repair is the skin stress near the termination of the patch. For an elliptical patch, the skin stress around the patch is peaked at the tip of the patch. This peak skin stress is given in terms of q as

$$\sigma_{yy}^{s}\left(B^{+},0\right)=q \tag{3.16}$$

For simplicity, explicit results for the particular case where both the plate and patch are isotropic and have the same Poisson's ratio, $\nu_p=\nu_s$, will be presented here first. The prospective stress in the plate along $y=0$ within the patched region ($|x|<A$) is

$$\sigma_0=\phi\sigma_\infty \tag{3.17}$$

where

$$\phi=\frac{1}{Z}\left[4+2\frac{B}{A}+2\frac{A}{B}+S\left(3+\nu_s+2\frac{B}{A}\right)+S\cdot\Sigma\left(1-\nu_s-2\nu_s\frac{B}{A}\right)\right] \tag{3.18}$$

with

$$Z=3(1+S)^2+2(1+S)(B/A+A/B+\nu_s S)+1-\nu_s^2 S^2 \tag{3.19}$$

It is clear that the stress-reduction factor ϕ depends on three non-dimensional parameters: (i) the stiffness ratio S; (ii) the aspect ratio B/A; and (iii) the applied stress biaxiality Σ. The parameters characterizing the adhesive layer do not affect σ_0, but we recall that the idealization used to derive Equations (3.17) and (3.18) relies on $\beta_A^{-1}\ll A,\ B$, and β_A^{-1} is dependent on adhesive parameters as evident from Equation (2.6) of Chapter 2.

To illustrate the important features of Equation (3.18), we show in Figure 3.5(a) the variation of the stress-reduction factor ϕ with aspect ratio for three loading configurations: (i) uniaxial tension ($\Sigma=0$); (ii) equal biaxial tension ($\Sigma=1$); and (iii) pure shear ($\Sigma=-1$), setting $S=1$ and $\nu_s=1/3$ for all cases. It can be seen that there is little variation for aspects ratio ranging from $B/A=0$ (horizontal strip) to $B/A=1$ (circular patch), so that for preliminary design calculations, one can conveniently assume the patch to be circular, to reduce the number of independent parameters. It is also noted from Equation (3.18) that for $\nu_s=1/3$ and a circular patch ($A/B=1$), the stress-reduction factor ϕ becomes independent of the biaxiality ratio Σ. As illustrated in Figure 3.5(a) the curves for $\Sigma=0$ and $\lambda=-1$ cross over for $B/A=1$, indicating that, for a circular patch, the transverse stress $\sigma_{\infty x}=\Sigma\cdot\sigma_\infty$ does not contribute to the prospective stress, so that this parameter can also be ignored in preliminary design estimates. In this particular case, the stress-reduction factor ϕ depends only on the stiffness ratio S, as depicted in Figure 3.5(b), together with the one-dimensional result given by Equation (3.4) as $\phi=\sigma_\infty/(1+S)$. It can be seen that the one-dimensional solution ignoring the load attraction effect of composite patch overestimates the reduction in skin stress. For the special case of circular patch and Poisson's ratio being equal to 1/3, Equation (3.18) can be simplified to become,

$$\phi=\frac{3}{3+2S}\quad(B/A=1,\ \nu_s=1/3) \tag{3.20}$$

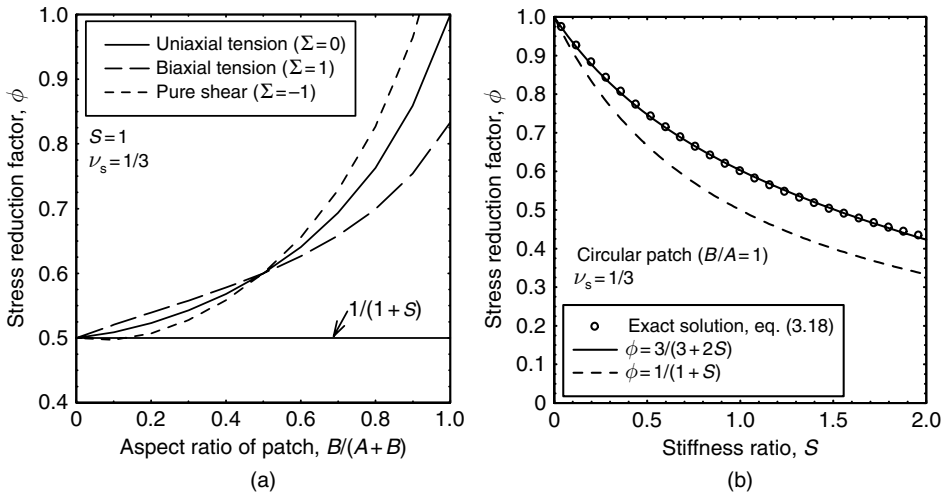

Fig. 3.5. Variation of stress reduction factor with (a) aspect ratio for an elliptical patch of semi-axes A and B under uniaxial tension, biaxial tension, and pure shear; (b) stiffness ratio S for a circular patch.

On the other hand, when both the skin and the patch are isotropic and have the same Poisson's ratio, the peak stress in the skin outside the patch can be expressed in terms of σ_0 as

$$\sigma_{yy}^{\mathrm{s}}\left(B^{+},0\right)=(1+S)\,\sigma_0$$
$$K_{\mathrm{t}}=\frac{\sigma_{yy}^{\mathrm{s}}\left(B^{+},0\right)}{\sigma_\infty}=(1+S)\,\frac{\sigma_0}{\sigma_\infty} \tag{3.21}$$

The results given above for an isotropic patch are explicit and simple, making it easy to perform parametric studies of the effects of patch stiffening ratio and the aspect ratio of elliptical patches. Equations (3.17) and (3.21) for a special case of uniaxial tensile load ($\Sigma=0$) have been plotted in the form of a design chart in Figure 3.6. Curves of constant K_{t} and constant S loci are shown in the figure. This chart, presented in Figure 3.6, makes it easy to understand the effects of various design variables. It is clear from Figure 3.6 that excessive stiffening ratios or long, skinny patches with high B/A ratios would result in high skin stress at the patch tip. Long patches are also shown to be less effective than wide patches in reducing the skin stress underneath the patch. Furthermore, there is no universal "best" point design. It appears that all possibly acceptable patch designs, i.e., $1\le S\le 2$ and $\frac{1}{5}\le\frac{B}{A}\le 7$, are confined to a region marked by the heavy line as indicated in the same figure.

It remains now is to show the effect of patch orthotropy $\left(E_{22}^{p}/E_{11}^{p}\right)$ on skin stresses underneath the patch and at the patch tip, i.e., σ_0 and K_{t}, based on implicit results derived above. It turns out that the patch's orthotropy has only very minor influence on the stress-reduction factor ϕ and K_{t}. To illustrate that effect, particular results for a

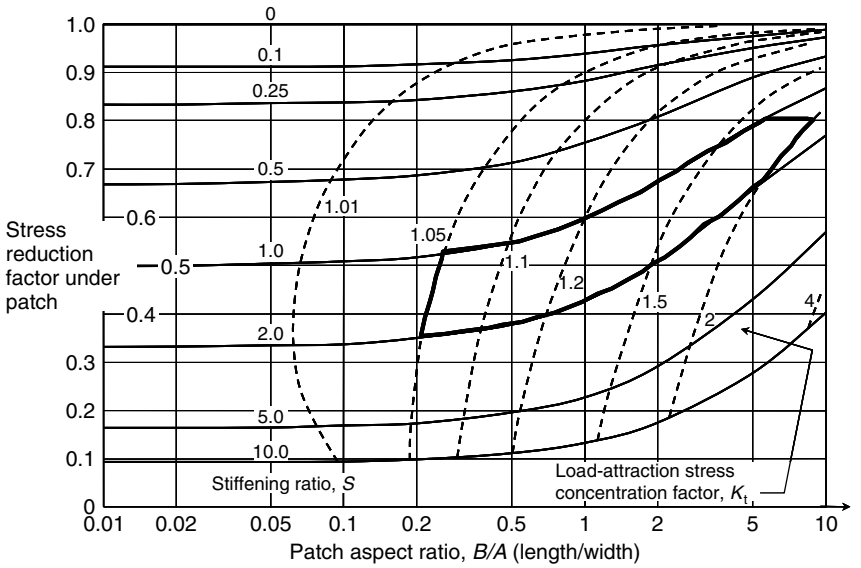

Fig. 3.6. Design chart for isotropic patches with $\nu_p = \nu_s$ under uniaxial tension.

repair under a uniaxial tensile load with orthotropic patches of a zero transverse stiffness are plotted in a chart form (Figure 3.7) similar to Figure 3.6. It is evident from a comparison between Figures 3.7 and 3.6 that, for close-to-circular patches, the solution for orthotropic patches predicts much the same stress level in the skin under the patch

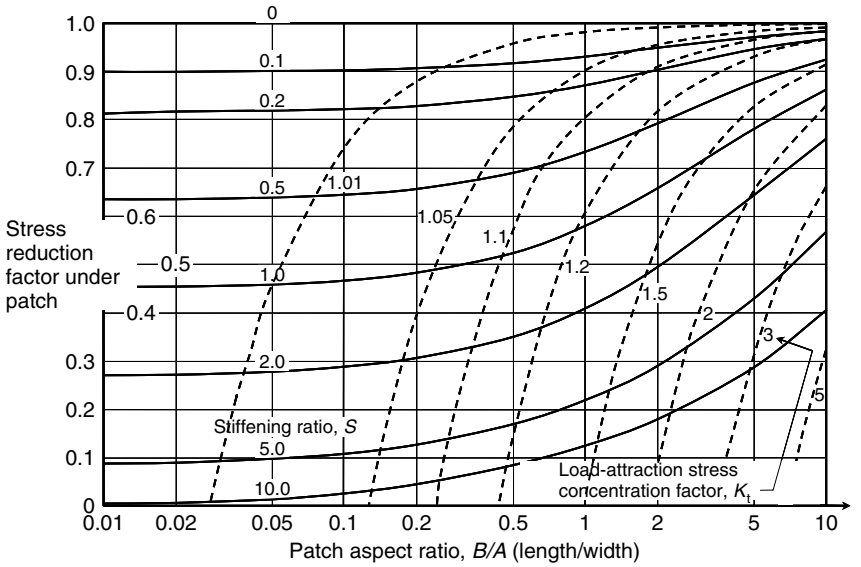

Fig. 3.7. Design chart for orthotropic patches with zero transverse stiffness under uniaxial tension.

as is predicted by formulas (3.17) and (3.18) for isotropic patches. The same is true for any configurations associated with high skin stresses under the patch. Only in the lower corner of Figure 3.7, for impractically wide and lightly stressed patch, is the difference significant. Moreover, even then, the use of equations for the isotropic analysis would always be conservative.

3.3.2 Stage II: Stress intensity factor

Once the stress at the prospective crack location is known, one can proceed to the second stage of the analysis in which the plate is cut along the line segment ($|x| < a,\ y = 0$), and pressure equal to σ_0 is applied internally to the faces of this cut to make these faces stress-free. Provided that the load transfer to the reinforcement during this second stage takes place in the immediate neighbourhood of the crack, the reinforcement may be assumed to be of infinite extent. Thus the problem at this stage is to determine the stress intensity factor K_{I} for the configuration shown in Figure 3.2(a).

Without the patch, the stress intensity factor would have the value $K_{\mathrm{I}0}$ given by the well-known formula (Broek, 1987),

$$K_{\mathrm{I}0} = \sigma_0 \sqrt{\pi a} \tag{3.22}$$

This provides an upper bound for K_{I}, since the restraining action of the patch would reduce the stress intensity factor. However, $K_{\mathrm{I}0}$ increases indefinitely as the crack length increases, whereas the crucial property of the reinforced plate of Figure 3.2(a) is that K_{I} does not increase beyond a limiting value, denoted by $K_{\mathrm{I}\infty}$, as will be confirmed later. That limiting value is the value of the stress intensity factor for a semi-infinite crack. It can be determined by deriving first the corresponding strain-energy release rate as follows. Before we proceed, let us first determine the deformation of the reinforced strips shown in Figure 3.2(b). In Chapter 2, the distribution of the adhesive shear stress $\tau^{(\mathrm{A})}$ near the skin interruption end of a long overlap double-strap joint takes the following form:

$$\tau^{(\mathrm{A})}(y) = \tau^{(\mathrm{A})}_{\max} \mathrm{e}^{-\beta_{\mathrm{A}} y} \tag{3.23}$$

where $\tau^{(\mathrm{A})}_{\max}$ can be determined from the simple equilibrium condition, $\sigma_0 t_{\mathrm{s}} = \int_0^{\infty} \tau^{(\mathrm{A})}(y)\mathrm{d}y$,

$$\tau^{(\mathrm{A})}_{\max} = \beta_{\mathrm{A}} t_{\mathrm{s}} \sigma_0 \tag{3.24}$$

Recalling Equation (2.25), the opening displacement of the plate at $y = 0$ can be readily determined,

$$u_{\mathrm{s}}(0) = \frac{\beta_{\mathrm{A}} t_{\mathrm{s}} t_{\mathrm{A}}}{G_{\mathrm{A}}} \sigma_0 \tag{3.25}$$

Let us denote the total opening as $\delta = 2u_{\mathrm{s}}(0)$. The above equation can be rewritten as,

$$\sigma_0 = \frac{1}{2} \Lambda E_{\mathrm{s}} \delta \tag{3.26}$$

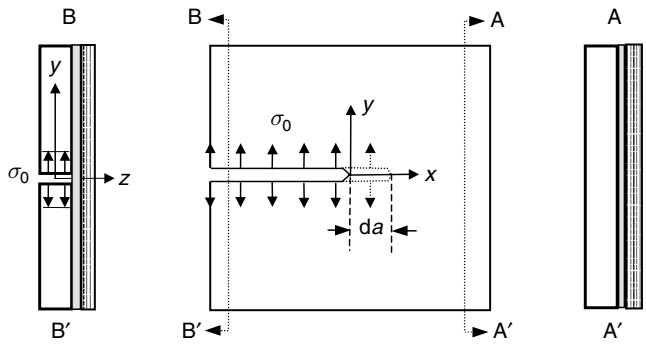

Fig. 3.8. A patched crack subjected to internal pressure.

with

$$\Lambda = \frac{G_{\mathrm{A}}}{\beta_{\mathrm{A}} t_{\mathrm{A}} t_{\mathrm{s}} E_{\mathrm{s}}} \equiv \frac{S\beta_{\mathrm{A}}}{(1+S)\,(1-\nu_{\mathrm{s}}^2)} \tag{3.27}$$

Consider the configuration shown in Figure 3.8. If the semi-infinite crack extends by a distance "da", the stress and displacement fields are simply shifted to the right by "da". The change in the strain energy U_{E} is that involved in converting a strip of width "da" from the state shown as section AA′ in Figure 3.8 to that shown in section BB′, as depicted in Figure 3.8. Consequently the change in the potential energy Π for a crack advancement δa, which is defined as the difference between the strain energy change $U_{\mathrm{E}}(=\frac{1}{2}\sigma_0 t_{\mathrm{s}}\delta)$ and the work performed by the external load $W\,(=\sigma_0 t_{\mathrm{s}}\delta = 2U_{\mathrm{E}})$,

$$\Pi = U_{\mathrm{E}} - W = -\frac{1}{2}\sigma_0 t_{\mathrm{s}}\delta \tag{3.28}$$

The crack extension force, i.e., the strain-energy release rate $G_{\mathrm{I}\infty}$ is given by

$$G_{\mathrm{I}\infty} t_{\mathrm{s}} = -\frac{\partial \Pi}{\partial a} = \frac{1}{2}\sigma_0 t_{\mathrm{s}}\delta \tag{3.29}$$

which can be re-written as, recalling Equation (3.26)

$$G_{\mathrm{I}\infty} = \frac{\sigma_0^2}{\Lambda E_{\mathrm{s}}} \tag{3.30}$$

From the above equation, assuming that the usual relation holds between the strain-energy release rate G_{I} and the stress intensity factor K_{I} (Broek, 1987), we obtain,

$$K_{\mathrm{I}\infty} = \frac{\sigma_0}{\sqrt{\Lambda}} \tag{3.31}$$

It is clear from this derivation that $K_{\mathrm{I}\infty}$ is an upper-bound for K_{I}. The validity of this formula will be substantiated by an independent FE analysis to be discussed later.

3.3.3 The effect of plastic adhesive

The stress intensity factor solution derived in Section 3.3.2 is valid only if the adhesive remains elastic. If the maximum adhesive shear stress does exceed the shear yield stress, the relationship between σ_0 and the crack-opening displacement δ will become non-linear, as illustrated in Figure 3.9(b), which also shows the correct area corresponding to $G_{I\infty}$. For an adhesive that is elastic-perfectly-plastic with a shear yield-stress $\tau_Y^{(A)}$, from Equation (3.24), the adhesive begins to yield at the following stress,

$$\sigma_{0Y} = \frac{\tau_Y^{(A)}}{\beta_A t_s} \tag{3.32}$$

It was shown in Chapter 2 that for $\sigma_0 \geq \sigma_{0Y}$ the crack opening-displacement δ is given by (see Equation (2.62)),

$$\delta = \frac{\tau_Y^{(A)} t_A}{G_A}\left[1+\left(\frac{\sigma_0}{\sigma_{0Y}}\right)^2\right] \equiv \frac{\sigma_{0Y}}{\Lambda E_s}\left[1+\left(\frac{\sigma_0}{\sigma_{0Y}}\right)^2\right] \quad (\sigma_0 \geq \sigma_{0Y}) \tag{3.33}$$

where $\frac{\tau_Y^{(A)} t_A}{G_A}$ has been expressed in terms of Λ and σ_{0Y} via Equations (3.32) and (3.27). Following the method outlined in the previous section, the strain-energy release rate $G_{I\infty}$ can be determined,

$$G_{I\infty} = \sigma_0\delta - \int_0^{\delta} \sigma_0 \mathrm{d}\delta = \int_0^{\sigma_{0Y}} \delta\, \mathrm{d}\sigma_0 + \int_{\sigma_{0Y}}^{\sigma_0} \delta\, \mathrm{d}\sigma_0$$

$$= \frac{\sigma_0^2}{\Lambda E_s}\left[\frac{(\sigma_0/\sigma_{0Y})^3 + 3(\sigma_0/\sigma_{0Y}) - 1}{3(\sigma_0/\sigma_{0Y})^2}\right] \quad (\sigma_0 \geq \sigma_{0Y}) \tag{3.34}$$

Then, the stress intensity factor for $\left(\sigma_0/\sigma_{0Y}\right) \geq 1$ can be expressed as

$$K_{I\infty} = \frac{\sigma_0}{\sqrt{\Lambda}}\left[\frac{(\sigma_0/\sigma_{0Y})^3 + 3(\sigma_0/\sigma_{0Y}) - 1}{3(\sigma_0/\sigma_{0Y})^2}\right]^{1/2} \quad [(\sigma_0/\sigma_{0Y}) \geq 1] \tag{3.35}$$

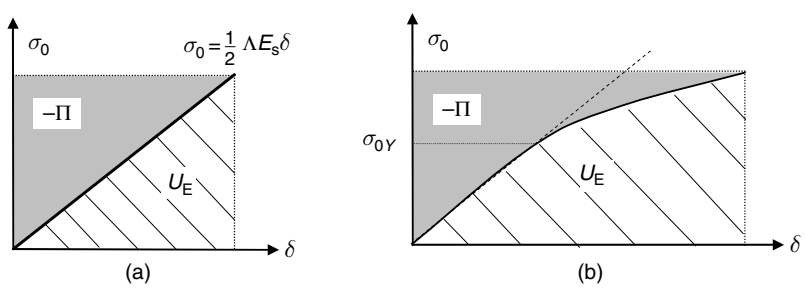

Fig. 3.9. Illustration of the interpretation of $G_{I\infty}$ as a complementary energy. (a) Elastic adhesive; and (b) elastic-plastic adhesive.

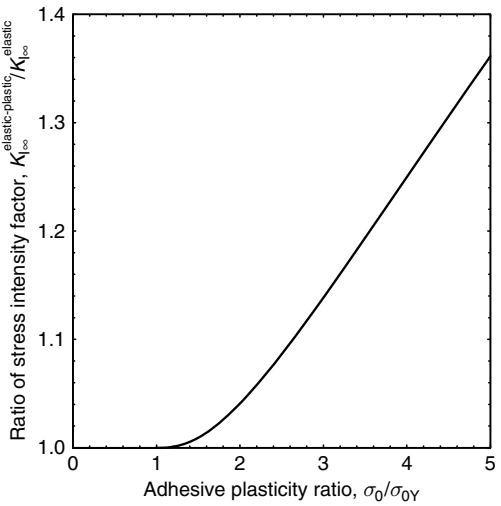

Fig. 3.10. Increase in stress intensity factor due to adhesive yielding.

where $\frac{\sigma_0}{\sqrt{\Lambda}}$ is the corresponding stress intensity factor when the plastic yielding in the adhesive is ignored. As can be seen from Equation (3.35) the increase in $K_{I\infty}$ due to adhesive yielding depends only on the plasticity ratio $\left(\sigma_0/\sigma_{0Y}\right)$ as shown in Figure 3.10.

3.3.4 The effect of finite crack size

For cracks of finite size, stress intensity factor K_I is apparently dependent on the crack length. For a small crack length, $a \leq 1/\sqrt{\Lambda}$, $\boldsymbol{K}_{I0} < \boldsymbol{K}_{I\infty}$, and the stress intensity factor varies between the lower bound $\boldsymbol{K}_{I0} = \boldsymbol{\sigma}_0\sqrt{\pi a}$ and the upper bound $\boldsymbol{K}_{I\infty} = \sigma_0/\sqrt{\Lambda}$. It becomes independent of crack length and equals to $\boldsymbol{K}_{I\infty}$ for $a > 1/\sqrt{\Lambda}$. In general the stress intensity factor $\boldsymbol{K}_I$ can be expressed as

$$K_I = F\sigma_0\sqrt{\pi a} \tag{3.36}$$

where F denotes the reduction in the stress intensity factor after repair. An exact solution of the function $K_I(a)$ or F can be obtained using the method developed by Keer et al. (1976) for the special case of an isotropic plate and reinforcement having identical Poisson's ratio. By idealizing the adhesive layer as shear springs and treating the stresses in the adhesive layer as body forces acting on the mid-plane of the plate and the reinforcement, the problem can be reduced to a single integral equation. An extensive parametric study (Wang and Rose, 1998) revealed that the reduction factor F depends strongly on the parameter Λ given by Equation (3.27) and to a lesser extent on the stiffness ratio S, as shown by the symbols in Figure 3.11. Based on

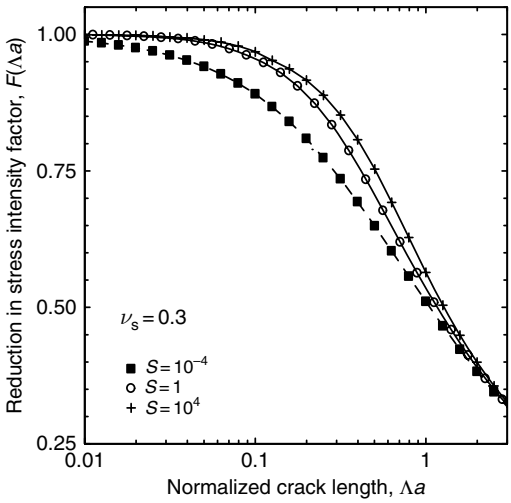

Fig. 3.11. Reduction in stress intensity factor for various patch configurations. Symbols denote the exact solutions by the Keer method, solid curves denote the interpolating function given by Equation (3.37), and dashed curve denotes the solution of crack bridging model for $S = 1$ as represented by Equation (3.42).

the solutions of the integral equation, the following interpolating function can be constructed,

$$F(\Lambda a) = \left[\frac{1}{\pi \Lambda a} \tanh \left(\frac{\pi \Lambda a}{1 + \hbar \pi \Lambda a} \right) \right]^{1/2} \tag{3.37}$$

where constant $\hbar$ has been determined by curve fitting the numerical solution of the integral equation, which gives $\hbar = 0.3$ for balanced repairs ($S = 1.0$) and $\hbar = 0.1$ for infinitely-rigid patch ($S \to \infty$). Plots of Equation (3.37) for $S = 1.0$ and $S \to \infty$ are denoted by solid curves in Figure 3.11. It is very easy to show from Equation (3.37) that $F(\Lambda a) \approx 1/\sqrt{\pi \Lambda a}$ for all $a > 1/\Lambda$. In other words, the stress intensity factor of a patched crack rapidly approaches the upper bound limit $K_{I\infty} = \sigma_0/\sqrt{\Lambda}$ and thus independent on the crack length for $a > 1/\Lambda$.

A simple yet more versatile method of determining the reduction in stress intensity factor after repair is the crack bridging model (Rose, 1987a), which has been recently extended to analyze the coupled in-plane stretching and out-of-plane bending of one-sided repairs (Wang and Rose, 1999). From the previous analysis it is clear that the essential reinforcing action at the second stage is the restraint on the crack opening due to the bonded reinforcements. The basic idea underlying the crack bridging model is that this restraining action can be represented by a continuous distribution of springs acting between the crack faces, as illustrated in Figure 3.12. This idealization reduces the problem at stage II to two parts: (i) determine the appropriate constitutive relation (i.e., stress–displacement relation) for the springs; and (ii) solve a one-dimensional integral equation for the crack opening,

$$\delta(x) = u_y^s(x, y \to 0^+) - u_y^s(x, y \to 0^-) = 2u_y^s(x, y \to 0^+) \quad |x| < a \tag{3.38}$$

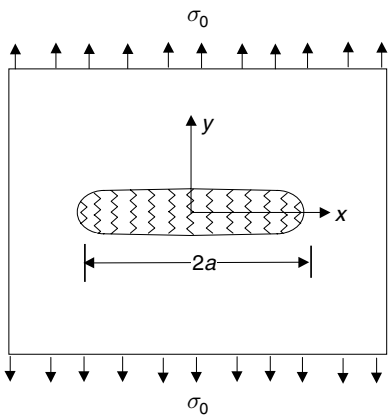

Fig. 3.12. Schematic representation of a centre-crack reinforced by distributed springs.

It is assumed that distributed linear springs act between the crack faces over the crack region so that the boundary conditions on $y = 0$ are

$$\begin{aligned} \sigma_{yy}(x) &= \Lambda E_s u_y(x) \quad |x| < a \\ u_y(x) &= 0 \quad |x| \geq a \end{aligned} \tag{3.39}$$

where Λ denotes a *normalized spring constant* which has dimension $length^{-1}$. It is worth noting that this normalized spring constant Λ has already been determined in Section 3.3.2 and is given by Equation (3.27). With these assumptions, the problem of determining the crack opening displacement $u_y(x)$ can be reduced to that of solving the following integral equation (Rose, 1987a; Wang and Rose, 1999),

$$\frac{E_s}{2\pi} \int_{-a}^{a} = \frac{u_y(t)}{(x-t)^2} \mathrm{d}t = -\sigma_0 + \Lambda E_s u_y(x) \tag{3.40}$$

The integral in the above equation is interpreted as a Hadamard finite part (1952) which can be viewed as the derivative, a Cauchy principal value integral. The above equation can be efficiently solved using either Galerkin's method or collocation methods. Once the crack-opening displacement $u_y(x)$ is determined, the stress intensity factor K_I can be calculated by

$$K_I = \lim_{x \to a} \frac{E_s \sqrt{2\pi}}{4} \frac{u_y(x)}{\sqrt{a-x}} \tag{3.41}$$

Detailed numerical results for K_I are available in Rose (1987a), which also provided the following interpolating function constructed based on the numerical results,

$$F(\Lambda a) = \left[\frac{1 + 2.23\Lambda a}{1 + 4.776\Lambda a + 7(\Lambda a)^2} \right]^{1/2} \tag{3.42}$$

Plot of Equation (3.42) for $S = 1$ is also shown in Figure 3.11 as a dashed curve. As compared to the exact solutions by the Keer formulation (as represented by Equation (3.37)), the crack-bridging model (as represented by Equation (3.42)) slightly over-estimates the reduction in stress intensity factor for balanced repair ($S = 1$) in the short crack limit. Both the two interpolating formulas, Equations (3.37) and (3.42) recover the asymptotic solution of (3.31) in the long crack limit as $a \to \infty$.

3.3.5 The effect of mixed mode loading

Although cracks that are likely to be encountered in practice are generally aligned in a direction perpendicular to the principal tensile stress (or strain), giving rise to mode I cracking, there are at least two circumstances where mixed mode cracking is a major concern in the context of bonded repair. First, application of bonded reinforcements, which are frequently anisotropic, may alter the local stress-state near the crack region so that the maximum principal stress may no longer remain perpendicular to the crack plane. Secondly, structures are frequently subjected to non-proportional loading in which the principal stress/strain axes rotate with time, thus cracks may experience a time-dependent mixed mode loading. If the bonded repair technique is used to repair mode II cracks, one important question remaining to be resolved is whether this method is still effective.

For simplicity let us consider the particular case of an isotropic circular patch ($A/B = 1$) with a Poisson's ratio $\nu_s = 1/3$. In this case, the prospective stress in the plate after repair can be determined using the general solution for biaxial tension presented in Section 3.3.1, namely Equation (3.20):

$$\tau_0 = \frac{3}{3+2S}\tau_\infty \quad (B/A = 1,\ \nu_s = 1/3) \tag{3.43}$$

Detailed solution of the mode-II stress intensity factor K_{II} can be found in Wang and Rose (1998). We shall not repeat here the intermediate details of the analysis but simply recall the results for the upper-bound and the interpolating function. The upper-bound solution of K_{II} is given by an equation similar to that for tensile mode:

$$K_{II} = \frac{\tau_0}{\sqrt{\Lambda_{II}}} \tag{3.44}$$

where the *normalized shear spring constant* Λ_{II} is given by

$$\Lambda_{II} = \frac{\beta_A^{II} S}{2(1+S)(1+\nu_s)} \tag{3.45}$$

with

$$\beta_A^{II} = \sqrt{\frac{G_A}{t_A}\left(\frac{1}{\mu_s t_s} + \frac{1}{\mu_p t_p}\right)} \tag{3.46}$$

It is evident that Λ_{II} is lower than the spring constant for that for mode I crack. For instance, in the case of isotropic patch, Λ_{II} is related to the spring constant Λ for mode I crack by

$$\Lambda_{II} = \sqrt{\frac{1-\nu_s}{2}}\Lambda = \frac{\Lambda}{\sqrt{3}} \quad \nu_s = 1/3 \tag{3.47}$$

An important implication arising from this difference is that when strongly anisotropic reinforcements with low in-plane shear moduli, such as unidirectional plastic reinforced composites, are used to repair a crack under shear loading (with the fibers being perpendicular to the crack), the repair efficiency will be much lower than that could be expected on the basis of mode I analysis.

For finite crack size, the stress intensity factor K_{II} can also be expressed as (Wang and Rose, 1998)

$$K_I = F(\Lambda_{II}a)\,\tau_0\sqrt{\pi a} \tag{3.48}$$

with $F(\Lambda_{II}a)$ being given by Equation (3.37) or Equation (3.42).

3.4 One-Sided Repairs

So far, we have ignored the tendency for out-of-plane bending that would result from bonding a reinforcing patch to only one face of an un-supported skin plate, so that, strictly speaking, the preceding analysis is more appropriate for the case of two-sided reinforcement in which patches bonded to both faces and to one-sided repairs which are supported against out-of-plane deflection. In the present analysis we shall consider the particular case where the patch covers the entire cracked plate. It is again convenient to divide the analysis into two stages. For simplicity, the stress reduction due to stage I will be analyzed within the framework of geometrically linear elasticity in this section. The stage I geometrically nonlinear analysis will be discussed later in Chapter 5. However, stage II is adequately analyzed using geometrically linear elasticity.

Consider first the effect of one-sided patch on an *un-cracked* skin plate which is subjected to a uniaxial tension. Assuming that the patch is far greater than the shear stress transfer length, we treat the patched region as a composite plate with a rigid bond line. The stress distribution in the plate and the reinforcement can be determined using the conventional theory of cylindrical bending of plates, i.e., we shall assume that the bending deformation of the reinforced portion satisfies the usual kinematic condition that plane sections remain plane. However, the stress intensity factor will be assumed to vary linearly through the plate thickness in accordance to the shear deformation (Reissner) plate theory as discussed later in Chapter 5, i.e.,

$$K_I(z) = K_{mean} + K_b\frac{2z}{t_s} \tag{3.49}$$

where K_{mean} and K_b denote respectively the membrane and bending stress intensity factors.

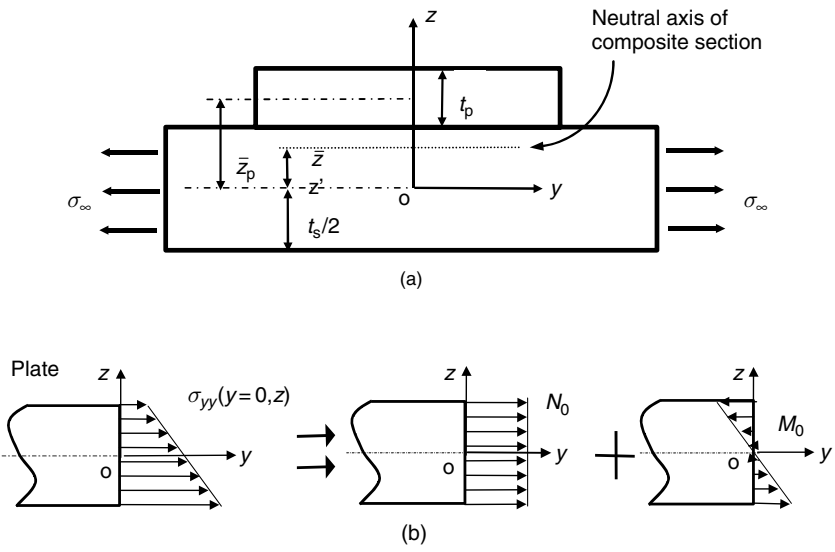

Fig. 3.13. Stress distribution in an un-cracked plate reinforced with a patch. (a) Composite plate subjected to uniaxial tension; and (b) stress distribution in the plate.

The position of the neutral plane of the composite skin consisting of the base skin and rigidly bonded patch is denoted by $\bar{z}$, referring to Figure 3.13,

$$\bar{z} = \frac{S(t_s + t_p + 2t_A)}{2(1+S)} \tag{3.50}$$

The moment of inertia of the reinforced region I_t is

$$I_t = I_s + I_p \frac{E'_p}{E'_s} \tag{3.51}$$

where

$$I_s = \frac{t_s^3}{12} + t_s \bar{z}^2 \tag{3.52}$$

$$I_p = \frac{t_p^3}{12} + \frac{t_p(t_s + t_p - 2\bar{z})^2}{4} \tag{3.53}$$

The stress distribution in the patched plate is assumed to be linear in the thickness direction, so that it can be specified in terms of the membrane force N_0 and a bending moment M_0 per unit length in the x-direction, as depicted in Figure 3.13 (Wang et al., 1998b; Wang and Rose, 1999),

$$N_0 = \int_{-t_p/2}^{t_p/2} \sigma_{yy}(y=0,z)\mathrm{d}z \equiv \frac{\sigma_\infty t_s}{1+S} + \frac{\sigma_\infty t_s^2 \bar{z}^2}{I_t} \tag{3.54}$$

$$M_0 = -\int_{-t_P/2}^{t_P/2} \sigma_{yy}(y=0,z) z \mathrm{d}z \equiv \frac{\sigma_\infty t_s^4 \bar{z}}{12 I_t} \tag{3.55}$$

Comparison between Equations (3.54) and (3.4), noting that $N_0 = \sigma_0 t_s$ in a symmetric repair, clearly shows that the plate in a one-sided repair is transferring more membrane stress than in an equivalent two-sided repairs. Therefore, due to out-of-plane bending induced by load eccentricity, the stress distribution along the prospective crack path before the crack appears is higher than for a corresponding two-sided reinforcement. In addition, there is a bending moment acting on the prospective crack faces. Consequently, due to the shift of neutral plane, one-sided repairs would experience not only an increase in the net force that the plate is transmitting, but also a secondary bending moment.

The strain-energy release rate can be determined following the method outlined in Section 3.3.2. For an elastic adhesive, the change in the potential energy is still given by Equation (3.28) as $\Pi = U_E - W$ where $W = 2U_E$ or $U_E = W/2$, and therefore $\Pi = -W/2$. However, the work done and thus the change in the potential energy now consist of two terms: work done by the membrane force and the bending moment (Wang et al., 1998b),

$$t_s G_{I\infty} = N_0 u_0 + M_0 \theta_0 \tag{3.56}$$

where u_0 and θ_0 denote the opening displacement and the angle of rotation of the crack face faces, which are related to the membrane force N_0 and M_0 via the following relation,

$$\begin{Bmatrix} u_0 \\ \theta_0 \end{Bmatrix} = \begin{bmatrix} c_{11}\ c_{12} \\ c_{21}\ c_{22} \end{bmatrix} \begin{Bmatrix} N_0 \\ M_0 \end{Bmatrix} \tag{3.57}$$

with

$$\begin{aligned}
c_{11} &= \frac{t_s(t_s+t_p)}{4\tilde{\nu} D_p} + \left[\frac{1}{E'_p t_p} + \frac{1}{E'_s t_s} + \frac{t_p(t_p+t_s)}{4D_p} \right] \left[\frac{1}{2\beta_A} - \frac{G_A t_s}{16\tilde{\nu}^2 \beta_A t_A} \left(\frac{t_p}{D_p} - \frac{t_s}{D_s} \right) \right] \\
c_{12} &= \frac{t_s}{2\tilde{\nu} D_p} \left(1 + \frac{D_p}{D_s} \right) + \left(\frac{t_p}{2D_p} - \frac{t_s}{2D_s} \right) \left[\frac{1}{2\beta_A} - \frac{G_A t_s}{16\tilde{\nu}^2 \beta_A t_A} \left(\frac{t_p}{D_p} - \frac{t_s}{D_s} \right) \right] \\
c_{21} &= \frac{t_p + t_s}{2\tilde{\nu} D_p} - \frac{G_A}{8\tilde{\nu}^2 \beta_A t_A} \left(\frac{t_p}{D_p} - \frac{t_s}{D_s} \right) \left[\frac{1}{E'_p t_p} + \frac{1}{E'_s t_s} + \frac{t_p(t_s+t_p)}{4D_p} \right] \\
c_{22} &= \frac{1}{\tilde{\nu} D_p} \left(1 + \frac{D_p}{D_s} \right) - \frac{G_A}{16\tilde{\nu}^2 \beta_A t_A} \left(\frac{t_p}{D_p} - \frac{t_s}{D_s} \right)^2
\end{aligned} \tag{3.58}$$

$$D_s = \frac{E'_s t_s^3}{12} \quad D_p = \frac{E'_p t_p^3}{12} \tag{3.59}$$

$$\tilde{\nu}^4 = \frac{E'_A}{4t_A} \left[\frac{1}{D_s} + \frac{1}{D_p} \right] \tag{3.60}$$

It is worthy to note that the first term in the right-hand side of Equation (3.56) is the same as the right-hand-side term of Equation (3.29) derived for a symmetric repair since $N_0 = \sigma_0 t_s$ for a symmetric repair and δ is defined there to be $2u_s(0) \equiv 2u_0$. Furthermore, the constant c_{11}, c_{12}, etc. can be considered as the compliances of the springs bridging the crack surfaces, and their detailed derivations will be given in Chapter 5 in connection to the crack bridging model.

Therefore the total strain-energy release rate can be expressed as

$$G_{I\infty} = \frac{1}{t_s}\left[c_{11}N_0^2 + (c_{12}+c_{21})N_0M_0 + c_{22}M_0^2\right] \tag{3.61}$$

which can be simplified to become

$$G_{I\infty} = \frac{(\sigma_\infty)^2}{(1+S)^2}\frac{\omega^2}{\Lambda} \tag{3.62}$$

where Λ is given by Equation (3.27), and the term ω is well approximated by the following expression (Wang et al., 1998b)

$$\omega^2 \approx 2 + \frac{3t_s}{2t_p} + \frac{3\beta_A t_s}{\tilde{\nu} t_p}\left(1+\frac{t_s}{t_p}\right) + (1+S)\left(2+\frac{3t_s}{2t_p}\right)\frac{\bar{z}^2 t_s}{I_t}$$
$$+ (1+S)\frac{\beta_A}{\tilde{\nu}}\left(1+\frac{t_s}{t_p}\right)\frac{\bar{z}t_s^3}{t_p I_t}\left(\frac{3\bar{z}}{t_s}-1\right) \tag{3.63}$$

Consequently, the root-mean-square stress intensity factor $K_{I\infty,rms}$ for one-sided repair can be expressed as

$$K_{rms,\infty} = \frac{\sigma_\infty}{1+S}\frac{\omega}{\sqrt{\Lambda}} \tag{3.64}$$

It is now possible to define a spring constant for one-sided repairs:

$$\Lambda_b = \frac{\Lambda}{\omega^2} \tag{3.65}$$

With this spring constant, the stress intensity factor for a one-sided repair can be expressed in a similar form as for two-sided repairs,

$$K_{rms}(a) = \frac{\sigma_\infty}{1+S}\sqrt{\pi a}F(\Lambda_b \cdot a) \tag{3.66}$$

where F again is given by either Equation (3.37) or (3.42). Figure 3.14 shows a comparison between Equation (3.66) and the results of three-dimensional FE analyses. The dimensions and material properties of the repair configuration being considered are summarized in Table 3.1. For this repair, we have the shear stress transfer length $\beta_A^{-1} = 5.634\,\text{mm}$, and the normalized spring constant $\Lambda = 0.096\,\text{mm}^{-1}$. In the FE analyses, three constituents – the patch, the adhesive, and the skin – are assumed to deform

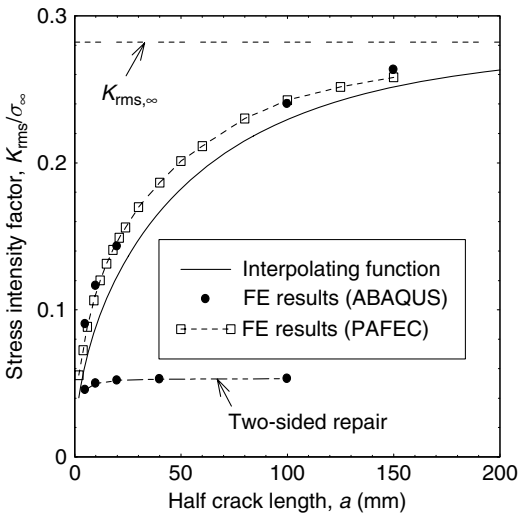

Fig. 3.14. Comparison between analytical solution and finite element results for one-sided repairs. Symbols denote the results of three-dimensional finite element analysis and the curves indicate the theoretical formulas.

Table 3.1. Dimensions and material properties of a typical repair.

Layer	Young's modulus (GPa)	Poisson's ratio	Thickness (mm)
Skin	71	0.3	3.0
Patch	207	0.3	1.0
Adhesive	1.89	0.3	0.2

elastically only, and are each modeled by 20-noded isoparametric brick elements. The same problem has been analyzed using two different FE codes, namely ABAQUS (1997) and PAFEC (1995); both yielded approximately the same results. It can be seen that the above formula is in good correlation with the FE results. For comparison, results from the corresponding symmetric repair are also obtained and presented in Figure 3.14. It is also worth noting that the results confirm that the stress intensity factor K_{rms} for a one-sided repair is much higher than that for an equivalent two-sided repair, indicating the importance of out-of-plane bending.

The root-mean-square stress intensity factor K_{rms} is related to the membrane and bending stress intensity factors (Wang et al., 1998b),

$$K_{rms}^2 = K_{mean}^2 + \frac{1}{3}K_b^2 \tag{3.67}$$

Although the root-mean-square of the stress intensity factor has been derived, the maximum and minimum stress intensity factors (through skin thickness) still remain

unresolved. It is apparent that the energy method alone is insufficient to determine the membrane and bending stress intensity factors, as an additional equation is required to partition K_{rms} into membrane and bending components. Therefore a crack-bridging model which is capable of analyzing the combined tensile-stretching and bending of one-sided repairs must be used. This model will be discussed in detail in Chapter 5.

3.5 Thermal Stresses

For the sake of simplicity the thermal stresses resulting from cure and service temperature fluctuations have not been considered so far. Often the resulting thermal residual stresses in the skin are tensile, owing to the increase in the stiffness of the patched region and the lower coefficient of thermal expansion of the composite patches. This tensile residual stress will increase the maximum stress intensity factor of the crack after repair, hence may enhance fatigue crack growth rate (see Chapters 8 and 11). Therefore thermal residual stresses represent a major factor in the design of repairs.

The process of adhesive bonding using high-strength structural adhesives (thermal-plastics) generally requires curing the adhesive above the ambient temperature. For instance, in a typical repair applied to an aircraft structure the reinforced region is initially heated to the curing temperature of the adhesive for certain duration. During this heating process, the patch is free to expand, hence experiences no thermal stress. The skin, however, may experience thermal stresses due to the localized heating. Once the adhesive is fully cured, the patch is bonded to the parent structure. The subsequent cooling to the ambient temperature will induce additional thermal stresses both in the patch and the skin, because the repaired region has a different thermal expansion coefficient. Thermal stresses may also arise when the patched structure experiences thermal cycling in service.

Solutions of the thermal residual stresses in symmetric repairs and one-sided repairs due to either curing of adhesive or low operating temperature with various degree of complexity will be derived in Chapters 4 and 5, respectively. In the following, as an introductory to the subject, only the results pertaining to supported repairs in an infinite skin due to low operating temperatures will be presented. Consider an isotropic plate that is reinforced by a circular "isotropic" patch of radius R_{i} and subjected to uniform temperature field of T_{oper}. The thermal expansion coefficient, the modulus, and Poisson's ratio of the patch are denoted by α_{p}, ν_{p}, and E_{p}, respectively. The objective here is to determine the thermal stresses in the patch and in the skin both outside and underneath the patch.

Changes in operating temperature will result in thermal stresses. In this case, the temperature distribution is essentially uniform. However, since the repaired region has a higher stiffness than the surrounding area, thermal stress would occur. As in Section 3.3.1, the x- and y- components of the thermal residual stress in the inhomogeneity are denoted as p^{oper} and q^{oper}. The displacement continuity condition at the boundary between the inhomogeneity and the surrounding skin plate can be expressed as

$$\varepsilon_r^{\text{I}}(r = R_{\text{i}}) = \varepsilon_r^{\text{s}}(r = R_{\text{i}}) \tag{3.68}$$

Because of the axisymmetry of the problem, $\varepsilon_r^{\text{s}}(r = R_{\text{i}}) = \varepsilon_{yy,B}^{\text{s}}(y = R_{\text{i}}) = \varepsilon_{xx,A}^{\text{s}}(y = R_{\text{i}})$ and $p^{\text{oper}} = q^{\text{oper}}$. Thus, from Equation (3.10), noting that $A/B = 1$, $\sigma_\infty = 0$, and

$p^{\text{oper}} = q^{\text{oper}}$, and by expressing stresses in terms of strains using the thermo-elastic constitutive relation (to account for thermal strains) for an isotropic skin,[1] the radial strain in the skin just outside the patch is determined to be

$$\varepsilon_r^{\text{s}}\left(r = R_{\text{i}}\right) = \varepsilon_{yy}^{\text{s}}\left(y = R_{\text{i}}\right) = -\frac{1+\nu_{\text{s}}}{E_{\text{s}}} p^{\text{oper}} + \alpha_{\text{s}}\left(T_{\text{oper}} - T_{\text{room}}\right) \tag{3.69}$$

In contrast, the strain of the inhomogeneity at $r = R_{\text{i}}$ is derived from Equation (3.8), after appropriate modification to account for the thermal strain,[2] as

$$\varepsilon_r^{\text{I}}\left(r = R_{\text{i}}\right) = \frac{1-\nu_{\text{I}}}{E_{\text{I}}} p^{\text{oper}} + \alpha_{\text{I}}\left(T_{\text{oper}} - T_{\text{room}}\right) \tag{3.70}$$

where E_{I}, ν_{I} and α_{I} are the equivalent elastic constants and equivalent thermal expansion coefficient of the patch–skin combination (inhomogeneity). By noting that E_{I}, ν_{I}, and α_{I} are defined respectively by Equation (3.5) in Section 3.3.1 and Equation (4.99) of Chapter 4, p^{oper} then can be readily determined from Equations (3.68), (3.69), and (3.70) as,

$$p^{\text{oper}} = -\frac{E_{\text{s}} S\ \left(1-\nu_{\text{s}}\right)\ \left(\alpha_{\text{p}} - \alpha_{\text{s}}\right)}{2\left(1-\nu_{\text{p}}\right) + \left(1-\nu_{\text{s}}^2\right)\ S}\left(T_{\text{oper}} - T_{\text{room}}\right)\left[\frac{\left(1-\nu_{\text{p}}\right)\ \left(1+\nu_{\text{s}}\right) + \left(1-\nu_{\text{s}}^2\right)\ S}{\left(1-\nu_{\text{p}}^2\right) + \left(1-\nu_{\text{s}}^2\right)\ S}\right] \tag{3.71}$$

Since skin stress just outside the repair is given by (3.16) and since $p^{\text{oper}} = q^{\text{oper}}$ in the present case, this skin stress is therefore also given by Equation (3.71).

The thermal residual stresses inside the repaired region resulting from the uniform temperature loading are

$$\begin{aligned}\sigma_{\text{s}}^{\text{oper}} &= \sigma_{xx,\text{s}}^{\text{oper}} = \sigma_{yy,\text{s}}^{\text{oper}} \\ &= -\alpha_{\text{s}} E_{\text{s}}\left(T_{\text{oper}} - T_{\text{room}}\right)\frac{\left(1-\alpha_{\text{p}}/\alpha_{\text{s}}\right)\ S}{2\left(1-\nu_{\text{p}}\right) + \left(1-\nu_{\text{s}}^2\right)\ S}\left[\frac{\left(1-\nu_{\text{p}}\right)\ \left(1+\nu_{\text{s}}\right) + \left(1-\nu_{\text{s}}^2\right)\ S}{\left(1-\nu_{\text{p}}^2\right) + \left(1-\nu_{\text{s}}^2\right)\ S}\right]\end{aligned} \tag{3.72}$$

for the skin, and

$$\begin{aligned}\sigma_{\text{p}}^{\text{oper}} &= \sigma_{xx,\text{p}}^{\text{oper}} = \sigma_{yy,\text{p}}^{\text{oper}} \\ &= \alpha_{\text{s}} E_{\text{p}}\left(T_{\text{oper}} - T_{\text{room}}\right)\frac{\left(2-\nu_{\text{s}}\right)\ \left(1-\alpha_{\text{p}}/\alpha_{\text{s}}\right)}{2\left(1-\nu_{\text{p}}\right) + \left(1-\nu_{\text{s}}^2\right)\ S}\left[\frac{\left(1-\nu_{\text{p}}\right)\ \left(1+\nu_{\text{s}}\right) + \left(1-\nu_{\text{s}}^2\right)\ S}{\left(1-\nu_{\text{p}}^2\right) + \left(1-\nu_{\text{s}}^2\right)\ S}\right]\end{aligned} \tag{3.73}$$

---

[1] The general thermo-elastic constitutive relation is given by $\varepsilon_{\text{ij}} = C_{\text{ijkl}}^{-1}\sigma_{\text{kl}} + \alpha_{\text{ij}}\Delta T$.

[2] In general, the thermal strain can be accounted for in the results presented in Section 3.3.1 by replacing the strain term ε_{ij} there with $\varepsilon_{\text{ij}} - \alpha_{\text{ij}}\Delta T$.

for the patch. It is interesting to note from Equations (3.71) and (3.72) that the skin stress is compressive outside the repair and tensile under the patch when $T_{oper} < T_{room}$ (for low operating temperature) since in general $\alpha_p < \alpha_s$. In addition, as shown later in Section 4.5 of Chapter 4, the above result of thermal stresses due to changes in operating temperature can also be used to evaluate thermal stresses due to adhesive curing of the repaired structure in a uniform temperature field. This is because curing of the repaired structure involves a heating phase followed by a cooling phase and the repaired structure will remain stress free during the heating phase if the curing takes place in a uniform temperature field. The curing of the repaired structure in a uniform temperature field therefore will have the same effect as changes in operating temperature. Consequently, thermal stresses due to a uniform temperature curing can be determined using the same Equations as (3.71)–(3.73), except that $\left(T_{oper} - T_{room}\right)$ is now replaced by $\left(T_{room} - T_{curing}\right)$ in those equations.

3.6 Summary

In this chapter, a fundamental concept of crack patching is introduced. The so-called two-stage solution procedure proposed by Rose that will be used throughout the book is described. Analytical solutions for determining load attraction and the crack-tip stress intensity factor of both symmetric and one-sided repairs are delineated. The effects of the nonlinear adhesive, out-of-plane bending, mixed mode loading and thermal stresses on the repair efficiency are also discussed.

CHAPTER 4

Mathematical Theory of Supported One-Sided Crack Patching or Two-Sided Crack Patching

4.1 Introduction

Analytical method for analyzing crack patching using the inclusion analogy was first proposed by Rose (1981, 1982, 1988) for an elliptical patch as mentioned in Chapter 3. Rose's fundamental idea is to divide the analysis into two stages (Figure 4.1). The merit of dividing the analysis into two stages is that each stage can be solved by a different analytical method employing a different set of appropriate simplifying assumptions. In stage I, the redistribution of stress in an *uncracked* skin due to the presence of the patch is determined, assuming that the skin and the patch are rigidly bonded. This assumption is appropriate in practice because the length of the load transfer zone around the edge of the patch is usually small compared with the overall dimension of the patch. Stage I problem is commonly referred to as a load attraction problem. For stage II, a problem of an infinite sandwiched plate consisting of a centered-cracked skin plate *adhesively* bonded to an uncracked patch is considered. This two-stage analytical procedure provides a practical method to estimate quantities of primary interests such as the stress concentration factors near the edge of the patch, the patch stresses, the crack-tip stress intensity factor, and the adhesive shear stresses.

In the following, we will present the analysis for a supported one-sided repair. Pertinent solutions for a two-sided repair can be readily obtained by taking t_s to be the half thickness of the skin when considering a latter repair case.

4.2 Stage I: Load Attraction

In Chapter 3, stage I analysis had been carried out only for certain simple shapes such as ellipses or circles. An approximate algorithmic solution is therefore derived in this section for the elastic fields in an infinite isotropic skin sheet rigidly bonded with an orthotropic, polygon-shaped patch. The approach presented here combines the equivalent

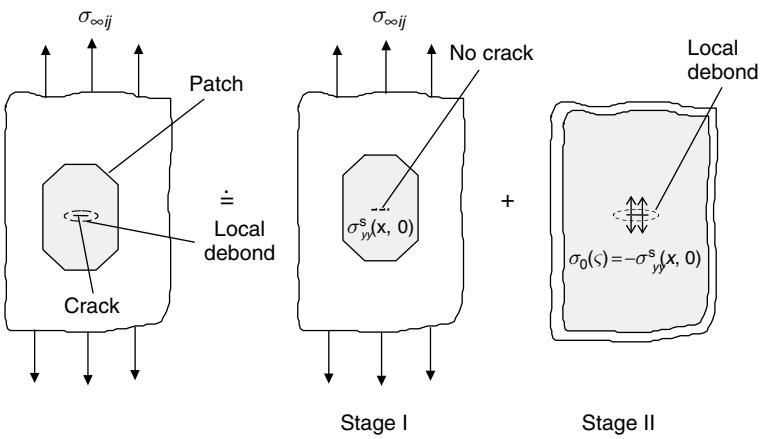

Fig. 4.1. The Rose's two-stage analysis procedure for crack patching: stage I, load attraction; and stage II, fracture analysis. In the figure, $\sigma^s_{yy}(x, 0)$ is the skin stress underneath the patch at the prospective crack location.

inclusion method by Eshelby (1957; Mura, 1998) and the algorithmic solutions for a polygonal inclusion (1996) with constant and polynomial eigenstrains (Rodin, 1996; Duong et al., 2001a).

The terminology "inclusion", which is mentioned throughout this book, may have been used in a slightly different context in the literature on the subject of bonded repairs so that perhaps it needs a clarification. When a finite subdomain Ω in a homogeneous material D is prescribed by an initial strain (or eigenstrain) field and this initial strain field is zero outside Ω, then Ω is called an inclusion. If a subdomain Ω in a material D has elastic moduli different from those outside Ω, then Ω is called an inhomogeneity. The present patching problem is therefore classified as an inhomogeneity problem. The solution of the load attraction problem in a bonded (patched) sheet will be solved by the Eshelby equivalent inclusion method combining with the algorithmic solutions for polygonal inclusions developed by Rodin (1996) and Duong et al. (2001a). This approach is preferred to other methods such as Muskhelishvili complex variable method since literature contains numerous solutions for inclusion problems. In contrast, the latter method requires a complex mapping for a non-elliptical patch and also an integration of a strain field resulting in multiple-valued functions.

As mentioned earlier, the elastic fields due to inclusions in an infinitely extended media have been investigated by many authors, following the pioneering work by Eshelby (1957). Since a list of references on this subject is extensive and can be found in a book by Mura (1998), not all of those works will be discussed here. Only references most relevant to the present development will be cited. Elastic fields due to an ellipsoidal inclusion with eigenstrain given in the form of polynomials of coordinates were obtained by Sendeckyj (1967) and Moschovidis (1975). Using these results, Moschovidis (1975; Moschovidis and Mura, 1975) employed the equivalent inclusion method to formulate the

solution for a number of ellipsoidal inhomogeneities in an infinitely extended isotropic material. Johnson et al. (1980a,b) used the same approach to study the stress field in cuboidal precipitates. On the other hand, elastic fields in a polygon-shaped inclusion with uniform eigenstrains in an infinitely extended isotropic media were studied by Rodin (1996) and Nozaki and Taya (1997). Duong et al. (2001a) extended the Rodin's approach to the case of polynomial eigenstrain and applied the obtained solution to the load attraction problem in a rigidly bonded sheet. Their approach for a general shaped inhomogeneity is foremost robust and therefore will be presented in the next section. It should be emphasized that the approach employed by Duong et al. gives only an approximate solution to the presently patched problem since the condition for equivalency, as shown later in the next section, can only be satisfied approximately using the first few terms of the Taylor's series.

4.2.1 Equivalent inclusion method

In this section, the equivalent inclusion method is briefly reviewed for latter discussion. In the equivalent inclusion method, the stress and strain fields induced by an inhogomeneity-occupied region Ω will be the same as those induced by the eigenstrain field ε_{ij}^{*} in the same region of a homogeneous material C_{ijkl}^{0} when ε_{ij}^{*} is selected appropriately as shown in Figure 4.2. The second problem in Figure 4.2 is an inclusion problem. The equivalency condition between the two problems requires that

$$\begin{aligned} \varepsilon_{ij}^{\mathrm{I}} &= \varepsilon_{ij}^{\mathrm{H}} \\ \sigma_{ij}^{\mathrm{I}} &= \sigma_{ij}^{\mathrm{H}} \end{aligned} \tag{4.1}$$

at each point in subregion Ω. For problem B, i.e., the inclusion problem, the induced strain field is commonly expressed in terms of the eigenstrain ε_{ij}^{*} and the far-field-applied strain $\varepsilon_{\infty ij}$ as (Mura, 1998)

$$\varepsilon_{ij}^{\mathrm{H}} = H_{ijkl}\varepsilon_{kl}^{*} + \varepsilon_{\infty ij} \tag{4.2}$$

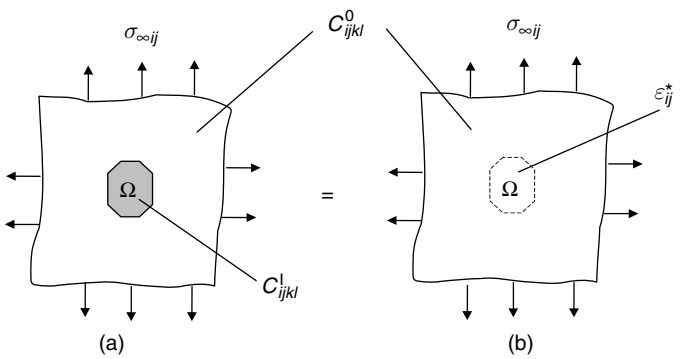

Fig. 4.2. An illustration of the equivalent inclusion method: (a) an inhomogeneity problem (problem A); and (b) an inclusion problem with eigenstrains ε_{ij}^{*} (problem B).

where H_{ijkl} is called Eshelby tensor. The next section of this chapter will be devoted to the calculation of this Eshelby tensor for a polygon-shaped domain Ω with eigenstrains given in the form of polynomials of position coordinates. Similar to the thermal or initial strain, the resulting stress inside Ω for problem B from Hook's law is

$$\sigma_{ij}^{\mathrm{H}} = C_{ijkl}^{0}\left(\varepsilon_{kl}^{\mathrm{H}} - \varepsilon_{kl}^{*}\right) \tag{4.3}$$

while the corresponding stress for the first problem, i.e., problem A, equals

$$\sigma_{ij}^{\mathrm{I}} = C_{ijkl}^{\mathrm{I}}\varepsilon_{kl}^{\mathrm{I}} \tag{4.4}$$

where C_{ijkl}^{I} is the elastic moduli of the inhomogeneity, C_{ijkl}^{0} is the elastic moduli of the material outside subregion Ω in problem A and also the elastic moduli of the homogeneous material in problem B. In Equations (4.1)–(4.4), the superscripts H and I denote the homogeneity (or inclusion) and inhomogeneity problems, respectively.

Substituting Equations (4.2)–(4.4) into Equation (4.1) yields the following equation for the eigenstrain ε_{ij}^{*}:

$$\begin{aligned} \Delta C_{ijkl}H_{klmn}\varepsilon_{mn}^{*} - C_{ijkl}^{0}\varepsilon_{kl}^{*} &= -\Delta C_{ijkl}\varepsilon_{\infty kl} \\ \Delta C_{ijkl} &= C_{ijkl}^{0} - C_{ijkl}^{\mathrm{I}} \end{aligned} \tag{4.5}$$

It should be noted that the above equation is nonlinear because H_{ijkl} is an implicit function of ε_{ij}^{*}.

Equation (4.5) will be solved approximately by the following procedure (Moschovidis, 1975; Moschovidis and Mura, 1975). First, ε_{ij}^{*} is assumed to be polynomials of the position coordinates with yet to be determined coefficients, i.e.,

$$\varepsilon_{ij}^{*} = F_{ij} + F_{ijk}x_k + F_{ijkl}x_k x_l + \cdots \tag{4.6}$$

In Equation (4.6), F_{ij}, F_{ijk}, $F_{ijkl}\ldots$, etc., are constants symmetric with respect to the free indices i, j and having value independent of the order in which the summation indices appear; i.e., $F_{ijkl} = F_{jikl}$, $F_{ijkl} = F_{ijlk}$. As shown in the next section, the strain fields induced by each term of the polynomial eigenstrain are given respectively by $S_{ijkl}F_{kl}$, $S_{ijklm}F_{klm}$, and $S_{ijklmn}F_{klmn}$, where $S_{ijkl}(\mathbf{x})$, $S_{ijklm}(\mathbf{x})$, and $S_{ijklmn}(\mathbf{x})$ are the Eshelby tensors that correspond to a constant, linear, and quadratic eigenstrains, respectively. It should be noted that these tensors in general are not constant tensors, even for the case with uniform eigenstrains. These Eshelby tensors for a polygonal inclusion Ω will be computed using the algorithmic approach developed by Rodin (1996) and Duong et al. (2001a). The details of these computations will be given in the next section, and let us assume for now that these Eshelby tensors are already obtained. With these in mind, Equation (4.2) then becomes

$$\varepsilon_{ij}^{\mathrm{H}} = \varepsilon_{\infty ij} + H_{ijkl}\varepsilon_{kl}^{*} = \varepsilon_{\infty ij} + S_{ijkl}F_{kl} + S_{ijklm}F_{klm} + S_{ijklmn}F_{klmn} + \cdots \tag{4.7}$$

and therefore

$$H_{ijkl}\varepsilon_{kl}^{*} = S_{ijkl}F_{kl} + S_{ijklm}F_{klm} + S_{ijklmn}F_{klmn} + \cdots \tag{4.8}$$

The next two steps are to expand the Eshelby tensors S's in Equation (4.8) into Taylor series, and to substitute the expanded form of Equation (4.8) into Equation (4.5) together with Equation (4.6). By setting the coefficient of each polynomial term of the resulting equation to zero, one obtains a system of algebraic equations with the unknowns F_{ij}, F_{ijk}, and F_{ijkl}.

To illustrate the above procedure, the solution for a polygon-shaped inhomogeneity that is symmetric with respect to two coordinate axes in an infinitely extended isotropic media with uniform applied normal strains at infinity will be formulated. The elastic moduli of the inhomogeneity are also assumed to be orthotropic with the material principal directions parallel to the coordinate axes. The double symmetry condition of this problem imposes that the normal component of the eigenstrains must be an even function of the coordinates while the shear component is an odd function. If the eigenstrain ε^*_{ij} is approximated by a second degree polynomial, then ε^*_{ij}, after taking into consideration the double symmetry condition, must presume the following form:

$$\begin{aligned}
\varepsilon^*_{11} &= F_{11} + x_1^2 F_{1111} + x_2^2 F_{1122} \\
\varepsilon^*_{22} &= F_{22} + x_1^2 F_{2211} + x_2^2 F_{2222} \\
\varepsilon^*_{12} &= x_1 x_2 F_{1212}
\end{aligned} \tag{4.9}$$

Furthermore, by observing the symmetric and anti-symmetric property of the normal and shear components of the induced strain field and by invoking the material orthotropy and isotropy, one can deduct from Equation (4.5) the following set of algebraic equations for the unknown coefficients F's (without summation on the subscript α):

$$\begin{aligned}
&\Delta C_{\alpha\alpha 11} L_{11}(\mathbf{0}) + \Delta C_{\alpha\alpha 22} L_{22}(\mathbf{0}) - C^0_{\alpha\alpha 11} F_{11} - C^0_{\alpha\alpha 22} F_{22} = -\Delta C_{\alpha\alpha 11}\varepsilon_{\infty 11} - \Delta C_{\alpha\alpha 22}\varepsilon_{\infty 22} \\
&\frac{1}{2}\Delta C_{\alpha\alpha 11}\frac{\partial^2}{\partial x_1^2} L_{11}(\mathbf{0}) + \frac{1}{2}\Delta C_{\alpha\alpha 22}\frac{\partial^2}{\partial x_1^2} L_{22}(\mathbf{0}) - C^0_{\alpha\alpha 11} F_{1111} - C^0_{\alpha\alpha 22} F_{2211} = 0 \\
&\frac{1}{2}\Delta C_{\alpha\alpha 11}\frac{\partial^2}{\partial x_2^2} L_{11}(\mathbf{0}) + \frac{1}{2}\Delta C_{\alpha\alpha 22}\frac{\partial^2}{\partial x_2^2} L_{22}(\mathbf{0}) - C^0_{\alpha\alpha 11} F_{1122} - C^0_{\alpha\alpha 22} F_{2222} = 0 \\
&\Delta C_{1212}\frac{\partial^2}{\partial x_1 \partial x_2} L_{12}(\mathbf{0}) - C^0_{1212} F_{1212} = 0
\end{aligned} \tag{4.10}$$

where

$$\begin{aligned}
L_{\alpha\beta}(\mathbf{x}) = {} & S_{\alpha\beta 11}(\mathbf{x}) F_{11} + S_{\alpha\beta 22}(\mathbf{x}) F_{22} + S_{\alpha\beta 1111}(\mathbf{x}) F_{1111} + S_{\alpha\beta 1122}(\mathbf{x}) F_{1122} \\
& + S_{\alpha\beta 2211}(\mathbf{x}) F_{2211} + S_{\alpha\beta 2222}(\mathbf{x}) F_{2222} + S_{\alpha\beta 1212}(\mathbf{x}) F_{1212} \quad (\alpha,\ \beta = 1,\ 2)
\end{aligned} \tag{4.11}$$

and the notation $L_{\alpha\beta}(\mathbf{0})$ and $\frac{\partial^2}{\partial x_1^2} L_{\alpha\beta}(\mathbf{0})$, etc., means that the L's and their second derivatives are evaluated at point $(0, 0)$, i.e., the origin of the coordinate system.

Once the coefficients F's, thus ε^*_{ij}, are determined, the elastic fields in the inhomogeneity problem (problem A) can be obtained from the corresponding results of the equivalent inclusion problem (problem B). In particular, the strain and stress fields in the inhomogeneity problem are given by

$$\varepsilon^{\mathrm{I}}_{ij} = \varepsilon^{\mathrm{H}}_{ij} = \varepsilon_{\infty ij} + S_{ijkl}F_{kl} + S_{ijklmn}F_{klmn} + \cdots \tag{4.12}$$

$$\sigma^{\mathrm{I}}_{ij}(\mathbf{x}) = \begin{cases} C^0_{ijkl}\left(\varepsilon^{\mathrm{H}}_{kl} - \varepsilon^*_{kl}\right) & \text{inside } \Omega \\ C^0_{ijkl}\varepsilon^{\mathrm{H}}_{kl} & \text{outside } \Omega \end{cases} \tag{4.13}$$

It should be emphasized that throughout this chapter and also throughout this book, within a context of the equivalent inclusion method, C^{I}_{ijkl} denotes the moduli of the inhomogeneity and therefore the moduli of the inhomogeneous region Ω, while $\varepsilon^{\mathrm{I}}_{ij}$ and σ^{I}_{ij} indicate the strain and the stress fields in the inhomogeneity problem. In other words, while C^{I}_{ijkl} only defines the moduli of points inside the inhomogeneous region, $\varepsilon^{\mathrm{I}}_{ij}$ and σ^{I}_{ij} describe the strain and the stress fields of points both inside and outside the inhomogeneous region.

4.2.2 Inclusion problem with polynomial eigenstrains

The Eshelby tensors S's mentioned in Section 4.2.1 for a polygon-shaped inclusion with polynomial eigenstrains and the complete elastic fields of the "equivalent" inclusion problem will be derived here, following the work of Rodin (1996) and Duong et al. (2001a).

(a) Formulation

Consider an infinite, elastic, homogeneous, and isotropic media having an inclusion Ω with an eigenstrain ε^*_{ij}, and stress free at the infinity, i.e., $\varepsilon_{\infty ij} = 0$. The eigenstrain is so defined that it assumes some functional value in Ω but vanishes outside Ω. The induced strain $\varepsilon^{\mathrm{H}}_{ij}$ and the resulting stress σ^{H}_{ij} are given by Mura (1998)

$$\varepsilon^{\mathrm{H}}_{ij}(\mathbf{x}) = \frac{1}{8\pi(1-\nu)}\left[\Psi_{kl,klij} - 2\nu\Phi_{kk,ij} - 2(1-\nu)\left(\Phi_{ik,kj} + \Phi_{jk,ki}\right)\right] \tag{4.14}$$

$$\sigma^{\mathrm{H}}_{ij}(\mathbf{x}) = \begin{cases} C^0_{ijkl}(\varepsilon^{\mathrm{H}}_{kl} - \varepsilon^*_{kl}) & \text{inside } \Omega \\ C^0_{ijkl}\varepsilon^{\mathrm{H}}_{kl} & \text{outside } \Omega \end{cases} \tag{4.15}$$

where

$$\Psi_{ij} = \iint_{\Omega} \varepsilon^*_{ij}\,|\mathbf{x} - \mathbf{x}'|\,\mathrm{d}\mathbf{x}'$$

$$\Phi_{ij} = \iint_{\Omega} \frac{\varepsilon^*_{ij}}{|\mathbf{x} - \mathbf{x}'|}\mathrm{d}\mathbf{x}' \tag{4.16}$$

$d\mathbf{x}' = dx_1' \cdot dx_2' \cdot dx_3'$, $|\mathbf{x}-\mathbf{x}'| = \sqrt{(x_1-x_1')^2+(x_2-x_2')^2+(x_3-x_3')^2}$, while the comma indicates partial differentiation, and ν is the Poisson's ratio of the homogeneous material. The functions Ψs and Φs are known as the bi-harmonic and harmonic potentials, respectively. It should be noted that the induced strain field given by Equation (4.14) is valid for both interior and exterior points of Ω.

Now, assuming that the eigenstrain ε_{ij}^* is given in the form of Equation (4.6), substitution of (4.6) into (4.16) yields

$$\begin{aligned}
\Psi_{ij} &= F_{ij}\psi + F_{ijk}\psi_k + F_{ijkl}\psi_{kl} + \cdots \\
\Phi_{ij} &= F_{ij}\phi + F_{ijk}\phi_k + F_{ijkl}\phi_{kl} + \cdots \\
\psi &= \iint_\Omega |\mathbf{x}-\mathbf{x}'|d\mathbf{x}' \\
\psi_{k\ldots l} &= \iint_\Omega x_k' \ldots x_l' |\mathbf{x}-\mathbf{x}'|d\mathbf{x}' \\
\phi &= \iint_\Omega \frac{1}{|\mathbf{x}-\mathbf{x}'|}d\mathbf{x}' \\
\phi_{k\ldots l} &= \iint_\Omega \frac{x_k' \ldots x_l'}{|\mathbf{x}-\mathbf{x}'|}d\mathbf{x}'
\end{aligned} \tag{4.17}$$

Substitution of (4.17) into (4.14) gives

$$\varepsilon_{ij}^{\mathrm{H}}(\mathbf{x}) = S_{ijkl}(\mathbf{x})F_{kl} + S_{ijklm}(\mathbf{x})F_{klm} + S_{ijklmn}(\mathbf{x})F_{klmn} + \cdots \tag{4.18}$$

where

$$\begin{aligned}
8\pi(1-\nu)S_{ijklm\ldots n} = {} & \psi_{m\ldots n,klij} - 2\nu\delta_{kl}\phi_{m\ldots n,ij} - (1-\nu)(\delta_{il}\phi_{m\ldots n,kj} + \delta_{jl}\phi_{m\ldots n,ki} \\
& + \delta_{ik}\phi_{m\ldots n,lj} + \delta_{jk}\phi_{m\ldots n,li})
\end{aligned} \tag{4.19}$$

ν is again the Poisson's ratio of the elastic homogeneous material, and δ_{kl} is the Kronecker delta, and the comma indicates partial differentiation. From Equation (4.18), it is clear that S_{ijkl}, S_{ijklm}, and S_{ijklmn} are the Eshelby tensors for an inclusion with eigenstrains given by constant, linear, and quadratic functions of the coordinates, respectively. In order to determine these tensors, ψ, $\psi_{m\ldots n}$, ϕ, $\phi_{m\ldots n}$ and their derivatives need to be evaluated. Rodin (1996) and Duong et al. (2001a) have proposed a simple algorithm to compute these quantities. A brief description of that algorithm will be presented in part (b) of this section.

So far all formulas are given for an infinite 3-D media. In relevance to the present load attraction problem, these formulas must be specialized to a two-dimensional elasticity. Since most of these formulas are quite general, they also apply well to the

two-dimensional case without any change, except for the expressions given in Equations (4.16) and (4.17). By considering the inclusion Ω as an infinite cylinder with a polygon-shaped cross-section, one can obtain formulas corresponding to Equations (4.16) and (4.17) for a plane strain case by integrating those equations in the third direction (Rodin, 1996; MacMillan, 1958; Duong et al., 2001a). These new formulas will be given explicitly in part (b).

(b) Computational algorithm

As before, the presentation will be restricted to the case of a polygon-shaped inclusion symmetric with respect to both coordinate axes and with eigenstrain given by Equation (4.9). For simplicity, all formulations presented in this part will be derived for plane strain condition. The formulation can be easily modified for the plane stress case by replacing the Young's modulus E with $E(1+2\nu)/(1+\nu)^2$ and the Poisson's ratio ν with $\nu/(1+\nu)$ while keeping the shear modulus μ unchanged.

The algorithm is implemented in three stages (Rodin, 1996; Duong et al., 2001a). First, the inclusion domain Ω is decomposed into a set of triangular elements (subregions) in such a way that **x**, the point where the solution is evaluated, is a common vertex of all the elements (Figure 4.3). Second, ψ, $\psi_{m\ldots n}$, ϕ, $\phi_{m\ldots n}$ and their derivatives are calculated for each element in its *local* coordinate system. Third, tensors S's are assembled from the elemental contributions after appropriate coordinate transformation from local to a common, global coordinate system. The triangular elements made up of domain Ω are called duplexes and they are referred to as simplexes for the case of right triangles. Since a duplex can be formed from two simplexes and the computation for the latter is more efficient than that for the former, only the elemental Eshelby tensors for a simplex in the local coordinate system will be derived here (Rodin, 1996; Duong et al., 2001a).

In all previous sections, only one coordinate system is kept referred to, i.e., the global coordinate x_1–x_2 system **X** with an origin at the center of Ω as shown in Figure 4.3. Referring to Figure 4.3, let us define the element coordinate system mentioned in the above paragraph as follows. It has the origin at **x**, basis vectors (**n, t**) where **n** is a unit vector outward normal to the edge and **t** is the tangent vector, and the corresponding coordinates (η, ζ). In these coordinates, the positions of vertices are represented by the pairs (b, c^+) and (b, c^-). For a convex polygon, b is positive when **x** is an interior point of Ω and becomes negative for otherwise.

Rodin (1996) showed that computations of the Eshelby tensors are simpler if they are carried out in this local coordinate system. In fact, all results given in the cited reference for a simplex with uniform eigenstrains are obtained in the local coordinate system. However, for inclusion with polynomial eigenstrains, computations along these lines for a simplex requires introducing a second local coordinate system y_1–y_2, i.e., **Y**, which is parallel to the element coordinate system but shares the same origin as that of the global coordinate system (see Figure 4.3). In the **Y**-coordinate system, point **x** where the solution is evaluated will be denoted as **y**. It should be remembered that the eigenstrains given in (4.9), however, are expressed in the form of polynomials of *global* coordinates. From the work of Rodin (1996) and Duong et al. (2001a), for a two-dimensional

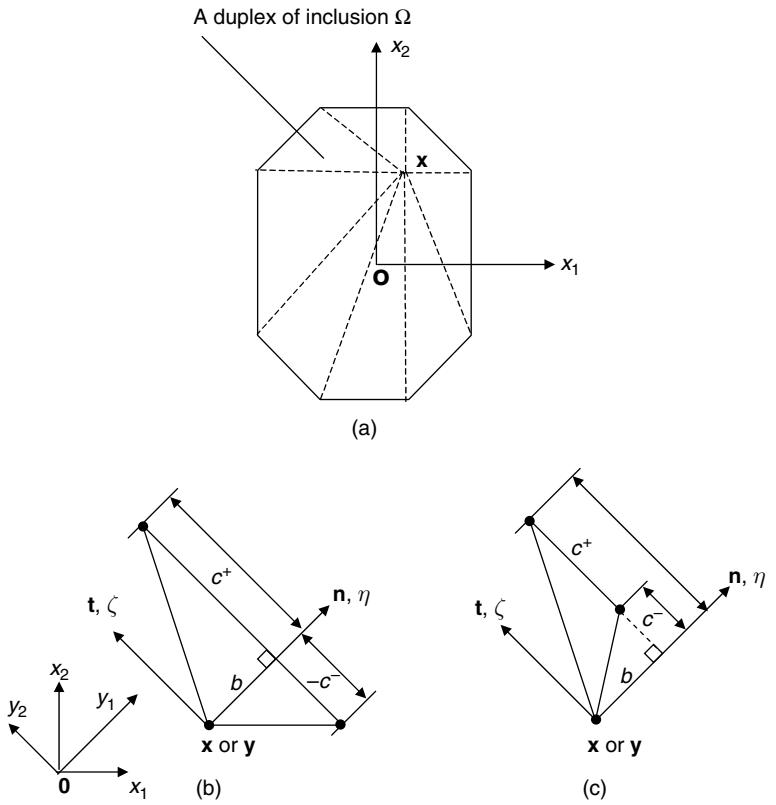

Fig. 4.3. Two-dimensional construction of duplexes used in the Rodin's and Duong et al.'s algorithms. Global, local, and elemental coordinate systems for a typical duplex are also defined in the figure: (a) shows inclusion Ω; (b) and (c) show typical duplexes, with vertices shown as filled circles. In the (η, ζ) coordinate system, for duplex (b) add the simplex with vertices $(0,0)$, (b, c^-), $(b, 0)$ to the simplex with vertices $(0,0)$, $(b, 0)$, (b, c^+), while for duplex (c) subtract the simplex with vertices $(0,0)$, $(b, 0)$, (b, c^-) from the simplex with vertices $(0,0)$, $(b, 0)$, (b, c^+). The minus sign in front of c^- emphasizes that in this particular geometry $c^- < 0$.

(plane strain) simplex with one of the vertices defined by $(b,\ c)$, $\psi, \psi_{m\ldots n}, \phi, \phi_{m\ldots n}$ in Equation (4.17) can be rewritten as

$$\psi = -\frac{1}{2}\int_0^b \mathrm{d}\eta \int_0^{c\eta/b} \left(\eta^2+\zeta^2\right)\ln\left(\eta^2+\zeta^2\right)\mathrm{d}\zeta$$
$$\psi_{m\ldots n} = -\frac{1}{2}\int_0^b \mathrm{d}\eta \int_0^{c\eta/b} \left(x'_m \ldots x'_n\right)\cdot\left(\eta^2+\zeta^2\right)\ln\left(\eta^2+\zeta^2\right)\mathrm{d}\zeta \tag{4.20}$$

$$\phi = -\int_0^b \mathrm{d}\eta \int_0^{c\eta/b} \ln\left(\eta^2+\zeta^2\right)\mathrm{d}\zeta$$

$$\phi_{m\ldots n} = -\int_0^b \mathrm{d}\eta \int_0^{c\eta/b} (x'_m \ldots x'_n)\ln\left(\eta^2+\zeta^2\right)\mathrm{d}\zeta$$

where

$$\begin{aligned} x'_1 &\equiv x'_1(\eta,\zeta) = (y_1+\eta)\cos\theta - (y_2+\zeta)\sin\theta \\ x'_2 &\equiv x'_2(\eta,\zeta) = (y_1+\eta)\sin\theta + (y_2+\zeta)\cos\theta \end{aligned} \tag{4.21}$$

x'_1 and x'_2 are global coordinates of a point (η, ζ) in the simplex, while y_1 and y_2 are the coordinates (in the **Y**-coordinate system) of the point **x** where S_{ijkl} is evaluated and it is also the origin of the elemental coordinate system. Angle θ and y_α are independent of η and ζ. The logarithmic terms appear in Equation (4.20) as a result of the integration of Equation (4.17) in the third direction as mentioned in part (a) of this section.

For the eigenstrains given by Equation (4.9), it needs to evaluate four potential pairs (ϕ, ψ), (ϕ_{11}, ψ_{11}), (ϕ_{22}, ψ_{22}), and (ϕ_{12}, ψ_{12}), which correspond to the eigenstrains F_{ij}, $x_1^2 \cdot F_{ij11}$, $x_2^2 \cdot F_{ij22}$, and $x_1 \cdot x_2 \cdot F_{ij12}$, respectively. It can be shown, after some lengthy algebra, that these potential pairs are given by (Rodin, 1996; Duong et al., 2001a)

$$\phi(b,c) = \frac{b}{2}\left[3c - 2b\tan^{-1}\left(\frac{c}{b}\right) - c\ln\left(b^2+c^2\right)\right]$$

$$\begin{aligned} \psi(b,c) = \frac{b}{144}\Big[&33b^2c + 7c^3 - 24b^3\tan^{-1}\left(\frac{c}{b}\right) - 18b^2c\ln\left(b^2+c^2\right) \\ &-6c^3\ln\left(b^2+c^2\right)\Big] \end{aligned}$$

$$\begin{aligned} -\phi_{11}(\mathbf{y},b,c) = {} & \left(y_1^2\cos^2\theta + y_2^2\sin^2\theta - 2y_1y_2\cos\theta\sin\theta\right)I_0^0 + I_0^2\cos^2\theta + I_2^0\sin^2\theta \\ & + (2y_1\cos^2\theta - 2y_2\cos\theta\sin\theta)I_0^1 + (2y_2\sin^2\theta - 2y_1\cos\theta\sin\theta)I_1^0 \\ & - 2\cos\theta\sin\theta I_1^1 \end{aligned} \tag{4.22}$$

$$\begin{aligned} -2\psi_{11}(\mathbf{y},b,c) = {} & \left(y_1^2\cos^2\theta + y_2^2\sin^2\theta - 2y_1y_2\cos\theta\sin\theta\right)(I_0^2+I_2^0) + (I_2^2+I_0^4)\cos^2\theta \\ & + (I_4^0+I_2^2)\sin^2\theta + (2y_1\cos^2\theta - 2y_2\cos\theta\sin\theta)(I_2^1+I_0^3) \\ & + (2y_2\sin^2\theta - 2y_1\cos\theta\sin\theta)(I_1^2+I_3^0) - 2\cos\theta\sin\theta(I_3^1+I_1^3) \end{aligned}$$

$$\begin{aligned} -\phi_{22}(\mathbf{y},b,c) = {} & \left(y_1^2\sin^2\theta + y_2^2\cos^2\theta + 2y_1y_2\cos\theta\sin\theta\right)I_0^0 + I_0^2\sin^2\theta + I_2^0\cos^2\theta \\ & + (2y_1\sin^2\theta + 2y_2\cos\theta\sin\theta)I_0^1 + (2y_2\cos^2\theta + 2y_1\cos\theta\sin\theta)I_1^0 \\ & + 2\cos\theta\sin\theta I_1^1 \end{aligned}$$

$$
\begin{aligned}
-2\psi_{22}(\mathbf{y}, b, c) = &\left(y_1^2 \sin^2\theta + y_2^2 \cos^2\theta + 2y_1 y_2 \cos\theta \sin\theta\right)\left(I_0^2 + I_2^0\right) \\
&+ \left(I_2^2 + I_0^4\right)\sin^2\theta + \left(I_4^0 + I_2^2\right)\cos^2\theta + \left(2y_1 \sin^2\theta + 2y_2 \cos\theta \sin\theta\right)\left(I_2^1 + I_0^3\right) \\
&+ \left(2y_2 \cos^2\theta + 2y_1 \cos\theta \sin\theta\right)\left(I_1^2 + I_3^0\right) + 2\cos\theta \sin\theta\left(I_3^1 + I_1^3\right) \\
-\phi_{12}(\mathbf{y}, b, c) = &\left[y_1^2 \cos\theta \sin\theta - y_2^2 \cos\theta \sin\theta + y_1 y_2\left(\cos^2\theta - \sin^2\theta\right)\right] I_0^0 + I_0^2 \cos\theta \sin\theta \\
&- I_2^0 \cos\theta \sin\theta + \left[2y_1 \cos\theta \sin\theta + y_2\left(\cos^2\theta - \sin^2\theta\right)\right] I_0^1 \\
&- \left[2y_2 \cos\theta \sin\theta - y_1\left(\cos^2\theta - \sin^2\theta\right)\right] I_1^0 + \left(\cos^2\theta - \sin^2\theta\right) I_1^1 \\
-\psi_{12}(\mathbf{y}, b, c) = &\left[y_1^2 \cos\theta \sin\theta - y_2^2 \cos\theta \sin\theta + y_1 y_2\left(\cos^2\theta - \sin^2\theta\right)\right]\left(I_0^2 + I_2^0\right) \\
&+ \left(I_2^2 + I_0^4\right)\cos\theta \sin\theta - \left(I_4^0 + I_2^2\right)\cos\theta \sin\theta \\
&+ \left[2y_1 \cos\theta \sin\theta + y_2\left(\cos^2\theta - \sin^2\theta\right)\right]\left(I_2^1 + I_0^3\right) \\
&- \left[2y_2 \cos\theta \sin\theta - y_1\left(\cos^2\theta - \sin^2\theta\right)\right]\left(I_1^2 + I_3^0\right) \\
&+ \left(\cos^2\theta - \sin^2\theta\right)\left(I_3^1 + I_1^3\right)
\end{aligned}
$$

where

$$
I_p^q(b, c) = \int_0^b \int_0^{c\eta/b} \eta^q \zeta^p \ln\left(\zeta^2 + \eta^2\right) \mathrm{d}\zeta \, \mathrm{d}\eta \quad (q = 0, 1, \ldots, 4;\ p = 0, 1, \ldots, 4) \tag{4.23}
$$

The integral $I_p^q(b, c)$ is straightforward to evaluate; however, its explicit form will be omitted here as it can be found in Gradshteyn and Ryzhik (1965). It is worthy to note that the potential pair (ϕ, ψ) for constant eigenstrain is only a function of b and c.

To obtain the Eshelby tensors S's in global coordinate system, the potentials must be differentiated with respect to $\mathbf{x}$ as indicated in Equation (4.19). However, as mentioned in the beginning of this part, it is more convenient to obtain these tensors in the y_1–y_2 local coordinate system, i.e., $\mathbf{Y}$. By denoting the Eshelby tensors S's in the local $\mathbf{Y}$-coordinate system as $\overline{S}$'s, $\overline{S}$'s are still defined by Equation (4.19); however, they must be obtained by differentiating the potentials appropriately with respect to $\mathbf{y}$. Since b and c are implicit functions of either $\mathbf{x}$ (and thus $\mathbf{y}$) or (η, ζ), their differentiations with respect to $\mathbf{y}$ or (η, ζ) must be obtained. By observing that $\frac{\partial b}{\partial \eta} = \frac{\partial c}{\partial \zeta} = -1$ and $\frac{\partial b}{\partial \zeta} = \frac{\partial c}{\partial \eta} = 0$ (Rodin, 1996), it follows that

$$
\begin{aligned}
\frac{\partial b}{\partial y_1} &= \frac{\partial c}{\partial y_2} = -1 \\
\frac{\partial b}{\partial y_2} &= \frac{\partial c}{\partial y_1} = 0
\end{aligned} \tag{4.24}
$$

since the **Y**-coordinate system is parallel to the elemental (η, ζ) coordinate system. Therefore, for any scalar function f(**y**, *b*, *c*),

$$\begin{aligned}\frac{\partial}{\partial y_1} f(\mathbf{y}, b, c) &= \frac{\partial f}{\partial y_1} + \frac{\partial f}{\partial b}\cdot\frac{\partial b}{\partial y_1} + \frac{\partial f}{\partial c}\cdot\frac{\partial c}{\partial y_1} = \frac{\partial f}{\partial y_1} - \frac{\partial f}{\partial b} \\ \frac{\partial}{\partial y_2} f(\mathbf{y}, b, c) &= \frac{\partial f}{\partial y_2} + \frac{\partial f}{\partial b}\cdot\frac{\partial b}{\partial y_2} + \frac{\partial f}{\partial c}\cdot\frac{\partial c}{\partial y_2} = \frac{\partial f}{\partial y_2} - \frac{\partial f}{\partial c}\end{aligned} \tag{4.25}$$

It is then clear that the differentiation of the potentials with respect to the local coordinates will be greatly simplified. That explains why the Eshelby tensors have been derived in the local coordinate system. Nevertheless, this task still involves extremely laborious calculation, except for the case of uniform eigenstrain. One therefore should rely on symbolic computations to carry out that task. In fact, all explicit expressions for $\overline{S}$'s have been derived with the aid of *Mathematica* (Wolfram, 1991). For the case of a constant eigenstrain, the Eshelby tensors $\overline{S}$'s (in the local coordinates) are given explicitly as follows (Rodin, 1996):

$$\begin{aligned}
\overline{S}_{\eta\eta\eta\eta} &= \frac{1}{8\pi(1-\nu)}\left[4(1-\nu)\hat{\alpha} - \frac{1-2\nu}{2}\sin 2\hat{\alpha} - \frac{1}{8}\sin 4\hat{\alpha}\right] \\
\overline{S}_{\eta\eta\zeta\zeta} &= \frac{1}{8\pi(1-\nu)}\left[4\nu\hat{\alpha} - \frac{(1+2\nu)}{2}\sin 2\hat{\alpha} + \frac{1}{8}\sin 4\hat{\alpha}\right] \\
\overline{S}_{\eta\eta\eta\zeta} &= \frac{1}{8\pi(1-\nu)}\left[-\frac{3}{2} - \nu\cos 2\hat{\alpha} + \frac{1}{8}\cos 4\hat{\alpha} + \frac{1-4\nu}{2}\ln(\sec\hat{\alpha})\right] \\
\overline{S}_{\zeta\zeta\eta\eta} &= \frac{1}{8\pi(1-\nu)}\left[-\frac{1-2\nu}{2}\sin 2\hat{\alpha} + \frac{1}{8}\sin 4\hat{\alpha}\right] \\
\overline{S}_{\zeta\zeta\zeta\zeta} &= \frac{1}{8\pi(1-\nu)}\left[\frac{3-2\nu}{2}\sin 2\hat{\alpha} - \frac{1}{8}\sin 4\hat{\alpha}\right] \\
\overline{S}_{\zeta\zeta\eta\zeta} &= \frac{1}{8\pi(1-\nu)}\left[-\frac{1}{2} + (1-\nu)\cos 2\hat{\alpha} - \frac{1}{8}\cos 4\hat{\alpha} + \frac{3-4\nu}{2}\ln(\sec\hat{\alpha})\right] \\
\overline{S}_{\eta\zeta\eta\eta} &= \frac{1}{8\pi(1-\nu)}\left[-\frac{3}{2} + \frac{1}{8}\cos 4\hat{\alpha} + \frac{1}{2}\ln(\sec\hat{\alpha})\right] \\
\overline{S}_{\eta\zeta\zeta\zeta} &= \frac{1}{8\pi(1-\nu)}\left[-\frac{1}{2} + \cos 2\hat{\alpha} - \frac{1}{8}\cos 4\hat{\alpha} + \frac{3}{2}\ln(\sec\hat{\alpha})\right] \\
\overline{S}_{\eta\zeta\eta\zeta} &= \frac{1}{8\pi(1-\nu)}\left[2(1-\nu)\hat{\alpha} - \frac{1}{2}\sin 2\hat{\alpha} + \frac{1}{8}\sin 4\hat{\alpha}\right]
\end{aligned} \tag{4.26}$$

where $\hat{\alpha} = \tan^{-1}\left(\frac{c}{b}\right)$. On the other hand, the expressions of $\overline{S}$'s for quadratic eigenstrains are too lengthy to be included in this book due to space limitation.

So far only the algorithm to compute Eshelby tensors $\overline{S}(\mathrm{y})$ and $S(\mathbf{x})$ have been outlined. However, as indicated in Equation (4.10) of Section 4.2.1, it is also necessary to compute the second derivative of $S(\mathbf{x})$'s with respect to $\mathbf{x}$. Two different methods can be been used to evaluate the second derivatives of $S(\mathbf{x})$'s. The first method involves numerical differentiation of $S(\mathbf{x})$'s using central-difference scheme with error of order h^4 where h is the spacing between grid points (James et al., 1977). In this method, $S(\mathbf{x})$'s must be computed at a number of points in a rectangular grid surrounding the point of interest. The second method is to use *Mathematica* (Wolfram, 1991) to derive $\partial\overline{S}/\partial\mathbf{y}$'s and $\partial^2\overline{S}/\partial\mathbf{y}^2$'s analytically and then to transform these derivatives into $\partial^2 S/\partial\mathbf{x}^2$'s through appropriate coordinate transformation. It turns out that both methods yield almost identical results for all illustrative examples considered in Section 4.4. However, the implementation of the former method is much simpler.

Stresses near the vertex of Ω are of practical importance in design and analysis of bonded repairs and therefore needed to be addressed. As pointed out by Rodin (1996), the stress field near the vertex of Ω under constant eigenstrain takes the following asymptotic form:

$$\boldsymbol{\sigma} \approx \frac{1}{8\pi(1-\nu)}\left(\hat{\mathbf{M}}_1 - \hat{\mathbf{M}}_2\right)\mathbf{F}\ln\left(\frac{\ell}{r}\right) \tag{4.27}$$

where

$$\boldsymbol{\sigma} = \begin{Bmatrix}\sigma_{11}\\ \sigma_{22}\\ \sigma_{12}\end{Bmatrix} \quad \mathbf{F} = \begin{Bmatrix}F_{11}\\ F_{22}\\ F_{12}\end{Bmatrix} \tag{4.28}$$

subscripts 1 and 2 of $\hat{\mathbf{M}}$ denote the edges forming the vertex; ℓ is a representative edge length (Figure 4.4); r is the distance from the vertex; $\hat{\mathbf{M}}_1$ and $\hat{\mathbf{M}}_2$ are represented by the same matrix in the basis $(\mathbf{n}_1,\ \mathbf{t}_1)$ and $(\mathbf{n}_2,\ \mathbf{t}_2)$, respectively. That matrix is

$$\hat{\mathbf{M}} = \frac{1}{2}\begin{bmatrix}0 & 0 & -1+4\nu\\ 0 & 0 & -3+4\nu\\ -1 & -3 & 0\end{bmatrix} \tag{4.29}$$

It can be shown that the stress field near the vertices of Ω with eigenstrains prescribed by Equation (4.9) also takes the same asymptotic form of Equation (4.27), except that $\mathbf{F}$ is now defined as (Duong et al., 2001a):

$$\mathbf{F} = \begin{Bmatrix}F_{11} + x_1^2F_{1111} + x_2^2F_{1122}\\ F_{22} + x_1^2F_{2211} + x_2^2F_{2222}\\ x_1x_2F_{1212}\end{Bmatrix} \tag{4.30}$$

4.2.3 Solution of the load attraction problem

The load attraction problem will be solved implicitly in this section using the equivalent inclusion method mentioned in Section 4.2.1 and the results for polygonal inclusions in Section 4.2.2.

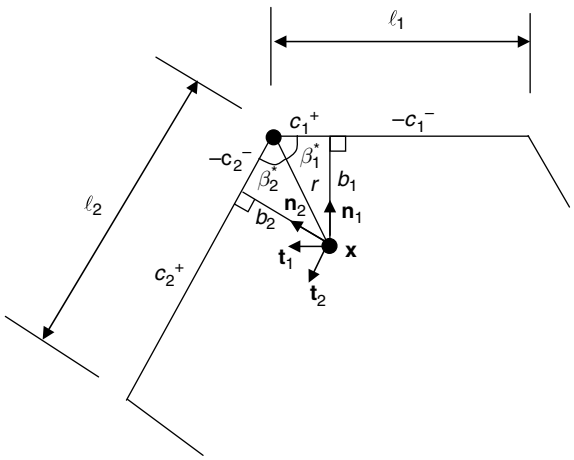

Fig. 4.4. Geometrical parameters of the duplexes for evaluating the asymptotic form of the vertex singularity (Rodin, 1996).

Consider an infinite isotropic skin sheet reinforced with a polygon-shaped, bonded patch and the sheet is subjected to remote biaxial stresses similar to that shown in Figure 4.2. This problem can be analyzed by the equivalent inclusion method mentioned in Section 4.2.1 with the following simplifying assumptions:

- All material behavior is linearly elastic.
- All sheet and patch materials are in a state of generalized plane stress.
- The patch is modeled as an integral part of the skin using inclusion analogy.

The effect of thermal stresses associated with the curing processing and the variation of operating temperatures can be superimposed on the results obtained from this basic model. However, for clarity, this effect will be treated later in Section 4.2.4 in a separate analysis.

In Section 4.2.1, a problem of an infinite isotropic sheet containing an inhomogeneity under remote biaxial stresses is considered. In order to apply the results obtained from that section to the present load attraction problem, one needs to establish the material properties of the inhomogeneity, which are equivalent to those of the patched skin. This had been done by Rose (1981, 1982, 1988) and also by Fredell (1994) with key results in matrix formulation summarized below for plane stress condition:

$$C_{11}^{\mathrm{I}} = \frac{C_{11}^{\mathrm{s}} t_{\mathrm{s}} + C_{11}^{\mathrm{p}} t_{\mathrm{p}}}{t_{\mathrm{I}}}$$

$$C_{22}^{\mathrm{I}} = \frac{C_{22}^{\mathrm{s}} t_{\mathrm{s}} + C_{22}^{\mathrm{p}} t_{\mathrm{p}}}{t_{\mathrm{I}}} \tag{4.31}$$

$$\nu_{12}^{\mathrm{I}} = \frac{\nu_{12}^{\mathrm{s}} C_{22}^{\mathrm{s}} t_{\mathrm{s}} + \nu_{12}^{\mathrm{p}} C_{22}^{\mathrm{p}} t_{\mathrm{p}}}{C_{22}^{\mathrm{s}} t_{\mathrm{s}} + C_{22}^{\mathrm{p}} t_{\mathrm{p}}}$$

$$\mu^{\mathrm{I}} = \frac{\mu_{\mathrm{s}} t_{\mathrm{s}} + \mu^{\mathrm{p}} t_{\mathrm{p}}}{t_{\mathrm{I}}}$$

where

$$\begin{aligned} C_{11}^{\mathrm{s}} = C_{22}^{\mathrm{s}} &\equiv \frac{E_s}{1-\nu_{\mathrm{s}}^2} \\ \nu_{12}^{\mathrm{s}} = \nu_{21}^{\mathrm{s}} &= \nu_{\mathrm{s}} \\ \mu_{\mathrm{s}} &= \frac{E_{\mathrm{s}}}{2\,(1+\nu_{\mathrm{s}})} \\ C_{11}^{\mathrm{p}} \equiv \frac{E_{11}^{\mathrm{p}}}{1-\nu_{12}^{\mathrm{p}}\nu_{21}^{\mathrm{p}}} \quad C_{22}^{\mathrm{p}} &\equiv \frac{E_{22}^{\mathrm{p}}}{1-\nu_{12}^{\mathrm{p}}\nu_{21}^{\mathrm{p}}} \end{aligned} \tag{4.32}$$

E, ν, μ, and t are the extensional modulus, Poisson's ratio, shear modulus, and thickness, respectively, while the superscripts or subscripts I, s, and p signify the inhomogeneity, skin, and patch. It should be remembered that the stress–strain relation for the isotropic or orthotropic material in a matrix form is given by (Jones, 1975)

$$\begin{Bmatrix} \sigma_{11} \\ \sigma_{22} \\ \sigma_{12} \end{Bmatrix} = \begin{bmatrix} C_{11} & \nu_{12}C_{22} & 0 \\ \nu_{12}C_{22} & C_{22} & 0 \\ 0 & 0 & \mu \end{bmatrix} \begin{Bmatrix} \varepsilon_{11} \\ \varepsilon_{22} \\ \gamma_{12} \end{Bmatrix} = [C] \begin{Bmatrix} \varepsilon_{11} \\ \varepsilon_{22} \\ \gamma_{12} \end{Bmatrix} \tag{4.33}$$

Also, in deriving Equation (4.31), the following two conditions have been used (Rose, 1981):

$$\begin{aligned} \sigma_{ij}^{\mathrm{I}} t_{\mathrm{I}} &= \sigma_{ij}^{\mathrm{s}} t_{\mathrm{s}} + \sigma_{ij}^{\mathrm{p}} t_{\mathrm{p}} \\ \varepsilon_{ij}^{\mathrm{I}} &= \varepsilon_{ij}^{\mathrm{s}} = \varepsilon_{ij}^{\mathrm{p}} \end{aligned} \tag{4.34}$$

The inhomogeneity thickness t_{I} can be chosen arbitrarily; however, t_{I} has been chosen to be the same as t_{s} to enable to apply directly the results established in Section 4.2.1. The stress field in the load attraction problem now can be determined by following the procedure outlined in Section 4.2.1, using constant or quadratic eigenstrain distribution approximation. However, to put C_{ijkl}^{0} and ν defined in Sections 4.2.1 and 4.2.2 in the present context, they should be identified with C_{ijkl}^{s} and ν_{s}, respectively. The stress field in the patched region is calculated by first solving, for instance, Equation (4.10) for the eigenstrains, then by computing the strains and stresses in the inclusion problem according to Equations (4.7) and (4.15), respectively, with the Eshelby tensors S's being evaluated using the computational algorithm discussed in part (b) of Section 4.2.2. These obtained stresses are also the stresses in the inhomogeneity problem as indicated by Equation (4.1). When the material at the point of evaluation is homogeneous through the thickness such as in the region outside Ω, the stresses obtained from the inhomogeneity

problem will be the final stresses at that point. On the other hand, if the material at the evaluated point is not homogeneous through the thickness, a further step is needed to distribute the obtained stresses to its material constituents using the conditions similar to Equation (4.34). For example, once σ_{ij}^{I} has been calculated, the stresses in the skin and patch inside the reinforced area can be determined from the conditions prescribed in Equation (4.34) as $\sigma_{ij}^{\mathrm{s}} = C_{ijkl}^{\mathrm{s}} \left(C_{klmn}^{\mathrm{I}}\right)^{-1} \sigma_{mn}^{\mathrm{I}}$ and $\sigma_{ij}^{\mathrm{p}} = C_{ijkl}^{\mathrm{p}} \left(C_{klmn}^{\mathrm{I}}\right)^{-1} \sigma_{mn}^{\mathrm{I}}$ since $\varepsilon_{ij}^{\mathrm{s}} = \varepsilon_{ij}^{\mathrm{p}} = \varepsilon_{ij}^{\mathrm{I}} = \left(C_{ijkl}^{\mathrm{I}}\right)^{-1} \sigma_{kl}^{\mathrm{I}}$, while the stress in the skin outside the patch is equal to σ_{ij}^{I}.

4.2.4 Load attraction with thermal effects

Repaired structures are usually subjected to two types of thermal loading: heating and cooling cycles associated with the curing process of the adhesive and the low operating temperature of the aircraft during high altitude cruising. Since the thermal expansion coefficients of the repaired skin and the patch are significantly different, these thermal loads may induce large residual thermal stresses and therefore affect the efficiency of the repair. The solution approach employed in Section 4.2.1 will be extended in this section to evaluate these thermal stresses. Even though the adhesive during bond formation is better characterized by a constitutive description which incorporates its dependence on the rate of mechanical deformation and on the thermal history (Duong and Knauss, 1995), for simplicity, the adhesive is modeled here as a linear elastic material with a zero stiffness and a glassy modulus at temperatures above and below its glass transition temperature, respectively.

For a two-sided bonded repair or a supported one-sided repair, no out-of-plane displacement will be induced when the repair is subjected to the thermo-mechanical loading. In the absence of the out-of-plane bending, since the skin and patch assume to behave as linearly elastic materials, the repair problem considered in this chapter will be linear. Thus, the total stress solution of the thermo-mechanical problem can be found by summing the individual contributions from the mechanical and thermal loads. Since the solution of the mechanical problem is already delineated in Section 4.2.3, this section therefore will be devoted entirely to the thermal stress problem.

It will be shown first that the thermal stress problem associated with a uniform cooling can be reformulated as an initial strain problem, in which the patch is subjected to a prescribed initial strain field (Duong and Yu, 2002a). Even though this equivalency is only demonstrated for the case of uniform cooling, it can be shown that the equivalency is also held for the case of curing of the adhesive. This way will allow us to solve the thermal stress problem directly within the context of the equivalent inclusion method.

(a) Determining the equivalent initial strain field prescribed in the patch

The equivalent initial strain field prescribed in the patch will be derived for two cases: uniform low operating temperature and the thermal cycle associated with adhesive curing.

Case 1: Uniform low operating temperature

In this case, the whole patched skin is cooled uniformly. Since the solution of this thermal stress problem within the framework of linear elasticity is independent of the cooling path, the cooling process can be arbitrarily assumed to take place in two steps. In the first step, the skin is cooled first to a low operating temperature while the patch is still at a stress-free (ambient) temperature. Furthermore, the patch is also subjected simultaneously to a fictitious uniform strain field of $\alpha_s \Delta T \delta_{ij}$ where α_s is the thermal expansion coefficient of the skin, $\Delta T = \left(T_{\text{operating}} - T_{\text{ambient}}\right)$, and δ_{ij} is the Kronecker delta. Since the patch is subjected to a uniform strain field of $\alpha_s \Delta T \delta_{ij}$ that is compatible with the thermal strain of the skin, the skin will contract freely during this cooling phase without experiencing any exerted forces from the patch, resulting in a stress-free skin. Thus, the strain field in the skin and patch at the end of the first step of cooling will be given by

$$\varepsilon_{ij}^{\text{s(step1)}}(\mathbf{x}) = \varepsilon_{ij}^{\text{p(step1)}}(\mathbf{x}) = \alpha_s \Delta T \delta_{ij} \tag{4.35}$$

In the second step of cooling, the patch is allowed to cool to a low operating temperature and also to relieve simultaneously the fictitious strain field $\alpha_s \Delta T \delta_{ij}$ imposed previously on it. The problem of the second-step cooling is then a problem of a patched skin with the following strain prescribed in the patch:[1]

$$\varepsilon_{ij}^{\text{(T)(p)}} = \left(\alpha_{ij}^{\text{p}} \Delta T - \alpha_s \Delta T \delta_{ij}\right) = \Delta \alpha_{ij} \cdot \Delta T \tag{4.36}$$

where α_{ij}^{p} is the thermal expansion coefficient tensor of the patch in the principal material directions, and the rest are previously defined. For the present discussion purpose, let us assume that the solution of this second-step cooling problem is already obtained with the strain solutions for the skin and patch denoted as

$$\varepsilon_{ij}^{\text{s(step2)}}(\mathbf{x}) = \varepsilon_{ij}^{\text{p(step2)}}(\mathbf{x}) = \varepsilon_{ij}^{\text{f}}(\mathbf{x}) \tag{4.37}$$

The total strains in the skin and patch at the end of the cooling process are then equal to the sum of individual contributions from the first and second steps of cooling, and they are given by

$$\varepsilon_{ij}^{\text{s}}(\mathbf{x}) = \varepsilon_{ij}^{\text{p}}(\mathbf{x}) = \varepsilon_{ij}^{\text{f}}(\mathbf{x}) + \alpha_s \Delta T \delta_{ij} \tag{4.38}$$

[1] This problem is similar but not exactly an initial strain problem, since the patch in this problem assumes to be stress-free when its total strain is equal to 0. In contrast, in a truly initial strain problem, the patch will be stress-free when its total strain is equal to $\varepsilon_{ij}^{\text{(T)(p)}}$.

On the other hand, the thermal stresses in the skin and patch after cooling are determined from the thermo-elastic constitutive relation as

$$\begin{aligned}
\sigma_{ij}^{\mathrm{s}}(\mathbf{x}) &= C_{ijkl}^{\mathrm{s}}\left[\varepsilon_{kl}^{\mathrm{s}}(\mathbf{x}) - \alpha_{\mathrm{s}}\Delta T\delta_{kl}\right] = C_{ijkl}^{\mathrm{s}}\varepsilon_{kl}^{\mathrm{f}}(\mathbf{x}) \\
\sigma_{ij}^{\mathrm{p}}(\mathbf{x}) &= C_{ijkl}^{\mathrm{p}}\left[\varepsilon_{kl}^{\mathrm{p}}(\mathbf{x}) - \alpha_{kl}^{\mathrm{p}}\Delta T\right] = C_{ijkl}^{\mathrm{p}}\left[\varepsilon_{kl}^{\mathrm{f}}(\mathbf{x}) - \left(\alpha_{kl}^{\mathrm{p}}\Delta T - \alpha_{\mathrm{s}}\Delta T\delta_{kl}\right)\right] \\
&= C_{ijkl}^{\mathrm{p}}\left[\varepsilon_{kl}^{\mathrm{f}}(\mathbf{x}) - \Delta\alpha_{kl}\Delta T\right] \\
&= C_{ijkl}^{\mathrm{p}}[\varepsilon_{kl}^{\mathrm{f}}(\mathbf{x}) - \varepsilon_{kl}^{(\mathrm{T})(\mathrm{p})}]
\end{aligned} \tag{4.39}$$

Let us consider now a truly initial strain problem in which the patch is prescribed by an initial strain field $\varepsilon_{ij}^{(\mathrm{T})(\mathrm{p})}$ given by Equation (4.36). The strain solution of the latter initial strain problem will be the same as that of the second-step cooling problem mentioned above due to their similarity, i.e., $\varepsilon_{ij}^{\mathrm{s}} = \varepsilon_{ij}^{\mathrm{p}} = \varepsilon_{ij}^{\mathrm{f}}$. However, the stresses in the skin and patch of the initial strain problem will be given, respectively, by $\sigma_{ij}^{\mathrm{s}} = C_{ijkl}^{\mathrm{s}}\varepsilon_{kl}^{\mathrm{f}}$ and $\sigma_{ij}^{\mathrm{p}} = C_{ijkl}^{\mathrm{p}}\left(\varepsilon_{kl}^{\mathrm{f}} - \varepsilon_{kl}^{(\mathrm{T})(\mathrm{p})}\right)$, which are in turn equal to the thermal stresses in the skin and patch of the original thermal stress problem after cooling as indicated by Equation (4.39). Thus, the considered thermal stress problem can be solved equivalently by an initial strain problem with an initial strain $\varepsilon_{ij}^{(\mathrm{T})(\mathrm{p})} = \Delta\alpha_{ij}\cdot\Delta T$ prescribed in the patch, as postulated earlier, since the stress fields in both the problems are the same. However, since the strain fields of these two problems differ by a constant amount of $\alpha_{\mathrm{s}}\Delta T\delta_{ij}$ over the whole domain (recalling that the strain fields of the initial strain problem and of the original thermal stress problem are given by $\varepsilon_{ij}^{\mathrm{f}}$ and Equation (4.38), respectively), this uniform strain field $\alpha_{\mathrm{s}}\Delta T\delta_{ij}$ must be added to the strain field $\varepsilon_{ij}^{\mathrm{f}}$ of the initial strain problem in order to obtain the corresponding strain solution of the original thermal stress problem.

Case 2: Thermal cycle associated with adhesive curing

Adhesive curing usually involves heating the reinforced region using a heater blanket to a high temperature above the adhesive's glass transition temperature under pressure for a few hours and then allowing the adhesive and adherends to cool to the ambient temperature. For simplicity, the temperature distribution around the heater blanket is assumed to be a step function with the inside region held at one constant temperature while the outside being held at a constant ambient temperature. This assumption for the temperature field may not be realistic due to the heat conduction; nevertheless, it still can be used in the analysis to provide a first-ordered estimate of the effect of curing on crack patching efficiency in the preliminary design phase. The effect of non-uniform thermal field has been addressed before by Rose (1988) and Wang et al. (2000) for a circular patch, the results of which can be used as correction factors for the results presented in this section. The Rose and Wang et al.'s models will be discussed in detail in Section 4.5.

During heating, the adhesive is assumed to be very soft so that the patch undergoes a free expansion while the skin is under thermal stresses because the skin material outside of the heated region is still cool. The thermal stresses in the skin during the heating phase can be easily calculated by using the algorithmic solution given in Section 4.2.2

for a polygon-shaped inclusion with a constant eigenstrain $\alpha_s \cdot \Delta T_{\text{heating}}$ where $\Delta T_{\text{heating}} = T_{\text{curing}} - T_{\text{ambient}} > 0$. The skin's total strain inside the heated region associated with these thermal stresses can then be calculated, which is smaller than $\alpha_s \cdot \Delta T_{\text{heating}}$ and will be denoted here by $\varepsilon_{ij}^{\text{s(heating)}}$. It should be noted that $\varepsilon_{ij}^{\text{s(heating)}}$ computed by the inclusion model will be independent of the size of the heated region.

The next step is to cool the whole repair down to the ambient temperature. This cooling step will be divided further into two substeps: (i) the patch is first held at a constant curing temperature and simultaneously subjected to a fictitious initial strain field $-\varepsilon_{ij}^{\text{s(heating)}}$ while the skin is cooled, and (ii) the patch is then allowed to cool and to relieve simultaneously the fictitious initial strain $-\varepsilon_{ij}^{\text{s(heating)}}$ imposed in (i). Since the patch is subjected to an initial strain $-\varepsilon_{ij}^{\text{s(heating)}}$ in substep (i), the skin will contract back to its original shape without experiencing any exerted forces from the patch, resulting in a stress-free skin at the end of substep (i). It is then clear that the described thermal stress problem is now reduced to an initial strain problem with the following initial strain prescribed in the patch:

$$\varepsilon_{ij}^{(\text{T})(\text{p})} = -\alpha_{ij}^{\text{p}} \Delta T_{\text{heating}} + \varepsilon_{ij}^{\text{s(heating)}} \tag{4.40}$$

(b) Solution of thermal stresses

With the equivalent initial strain prescribed in the patch having been determined for the two common types of thermal loading, the next step is to formulate a mathematical model for the thermal stress analysis. Since the patch is assumed to bond rigidly to a repaired skin over a polygonal region Ω, the patch is considered as an integral part of the skin inside Ω, and the skin with a patch incorporated is modeled as an inhomogeneity. The (thermo-elastic) constitutive relation for this inhomogeneity is given by

$$\begin{aligned} \sigma_{ij}^{\text{I}} &= C_{ijkl}^{\text{I}} \left(\varepsilon_{kl}^{\text{I}} - \varepsilon_{kl}^{(\text{T})} \right) \\ \varepsilon_{ij}^{(\text{T})} &= \frac{t_{\text{p}}}{t_{\text{s}}} C_{ijkl}^{\text{I}-1} C_{klmn}^{\text{p}} \varepsilon_{mn}^{(\text{T})(\text{p})} \end{aligned} \tag{4.41}$$

where C_{ijkl}^{I} is the stiffness of the inhomogeneity given by Equations (4.31) and (4.33) in Section 4.2.3, and $\varepsilon_{ij}^{(\text{T})(\text{p})}$ is already defined in part (a). Equation (4.41) obviously accounts for the initial strain field prescribed in the patch. With the above discussion in mind, the thermal stress problem then reduces to a problem of an infinite isotropic, linear elastic sheet (skin) with a stiffness C_{ijkl}^{s} containing a polygon-shaped inhomogeneity Ω with a stiffness C_{ijkl}^{I} and subjected to an initial strain field $\varepsilon_{ij}^{(\text{T})}$, and this latter problem will be solved by the equivalent inclusion method outlined in Section 4.2.1.

As in Section 4.2.1, the stress and strain fields induced by an inhomogeneity-occupied region Ω will be the same as those induced by the eigenstrain field ε_{ij}^{*} in the same region of a homogeneous material C_{ijkl}^{s} when ε_{ij}^{*} is selected appropriately. Following the procedure given in 4.2.1 for an inhomogeneity symmetric with respect to both coordinate

axes, by approximating ε_{ij}^{*} as a second-ordered polynomial of the position coordinates with yet to be determined coefficients, i.e.,

$$\varepsilon_{ij}^{*} = F_{ij} + F_{ijkl} x_k x_l \tag{4.42}$$

and by expanding the prescribed initial strain field $\varepsilon_{ij}^{(\mathrm{T})}$ into a Taylor series, the equivalency condition requires that F_{ij} and F_{ijkl} must satisfy the following system of linear equations (without summation on subscript α):

$$\begin{aligned}
&\Delta C_{\alpha\alpha 11} L_{11}(\mathbf{0}) + \Delta C_{\alpha\alpha 22} L_{22}(\mathbf{0}) - C^{\mathrm{s}}_{\alpha\alpha 11} F'_{11} - C^{\mathrm{s}}_{\alpha\alpha 22} F'_{22} = -C^{\mathrm{I}}_{\alpha\alpha 11} \varepsilon^{(\mathrm{T})}_{110} - C^{\mathrm{I}}_{\alpha\alpha 22} \varepsilon^{(\mathrm{T})}_{220} \\
&\frac{1}{2}\Delta C_{\alpha\alpha 11} \frac{\partial^2}{\partial x_1^2} L_{11}(\mathbf{0}) + \frac{1}{2}\Delta C_{\alpha\alpha 22} \frac{\partial^2}{\partial x_1^2} L_{22}(\mathbf{0}) - C^{\mathrm{s}}_{\alpha\alpha 11} F'_{1111} - C^{\mathrm{s}}_{\alpha\alpha 22} F'_{2211} \\
&\quad = -C^{\mathrm{I}}_{\alpha\alpha 11} \varepsilon^{(\mathrm{T})}_{1111} - C^{\mathrm{I}}_{\alpha\alpha 22} \varepsilon^{(\mathrm{T})}_{2211} \\
&\frac{1}{2}\Delta C_{\alpha\alpha 11} \frac{\partial^2}{\partial x_2^2} L_{11}(\mathbf{0}) + \frac{1}{2}\Delta C_{\alpha\alpha 22} \frac{\partial^2}{\partial x_2^2} L_{22}(\mathbf{0}) - C^{\mathrm{s}}_{\alpha\alpha 11} F'_{1122} - C^{\mathrm{s}}_{\alpha\alpha 22} F'_{2222} \\
&\quad = -C^{\mathrm{I}}_{\alpha\alpha 11} \varepsilon^{(\mathrm{T})}_{1122} - C^{\mathrm{I}}_{\alpha\alpha 22} \varepsilon^{(\mathrm{T})}_{2222} \\
&\Delta C_{1212} \frac{\partial^2}{\partial x_1 \partial x_2} L_{12}(\mathbf{0}) - C^{\mathrm{s}}_{1212} F'_{1212} = -C^{\mathrm{I}}_{1212} \varepsilon^{(\mathrm{T})}_{1212}
\end{aligned} \tag{4.43}$$

where

$$\begin{aligned}
\Delta C_{ijkl} &= C^{\mathrm{s}}_{ijkl} - C^{\mathrm{I}}_{ijkl} \\
L_{\alpha\beta}(\mathbf{x}) &= S_{\alpha\beta 11}(\mathbf{x}) F'_{11} + S_{\alpha\beta 22}(\mathbf{x}) F'_{22} + S_{\alpha\beta 1111}(\mathbf{x}) F'_{1111} + S_{\alpha\beta 1122}(\mathbf{x}) F'_{1122} \\
&\quad + S_{\alpha\beta 2211}(\mathbf{x}) F'_{2211} + S_{\alpha\beta 2222}(\mathbf{x}) F'_{2222} + S_{\alpha\beta 1212}(\mathbf{x}) F'_{1212} \\
F'_{ij} &= F_{ij} + \varepsilon^{(\mathrm{T})}_{ij0} \\
F'_{ijkl} &= F_{ijkl} + \varepsilon^{(\mathrm{T})}_{ijkl} \\
&(\alpha, \beta = 1, 2)
\end{aligned} \tag{4.44}$$

$\varepsilon_{ij0}^{(\mathrm{T})}$ and $\varepsilon_{ijkl}^{(\mathrm{T})}$ are the constant and the quadratic terms, respectively, in the Taylor series of $\varepsilon_{ij}^{(\mathrm{T})}$; and the rest have been previously defined in Section 4.2.1.

Once the coefficients F''s, thus F's and ε_{ij}^{*}, are determined, the elastic fields in the inhomogeneity problem can be obtained from the corresponding results of the equivalent inclusion problem as

$$\varepsilon_{ij}^{\mathrm{I}} = \varepsilon_{ij}^{\mathrm{H}} = S_{ijkl} F_{kl} + S_{ijklmn} F_{klmn} \tag{4.45}$$

$$\sigma_{ij}^{\mathrm{I}}(\mathbf{x}) = \begin{cases} C_{ijkl}^{\mathrm{s}}\left(\varepsilon_{kl}^{\mathrm{H}} - \varepsilon_{kl}^{*} - \varepsilon_{kl}^{(\mathrm{T})}\right) & \text{inside } \Omega \\ C_{ijkl}^{\mathrm{s}}\varepsilon_{kl}^{\mathrm{H}} & \text{outside } \Omega \end{cases} \tag{4.46}$$

The stresses in the skin and in the patch inside the reinforced region can then be determined from σ_{ij}^{I} as

$$\begin{aligned} \sigma_{ij}^{\mathrm{s}} &= C_{ijkl}^{\mathrm{s}}\left[\left(C_{klmn}^{\mathrm{I}}\right)^{-1}\sigma_{mn}^{\mathrm{I}} + \varepsilon_{kl}^{(\mathrm{T})}\right] \\ \sigma_{ij}^{\mathrm{p}} &= C_{ijkl}^{\mathrm{p}}\left[\left(C_{klmn}^{\mathrm{I}}\right)^{-1}\sigma_{mn}^{\mathrm{I}} + \varepsilon_{kl}^{(\mathrm{T})} - \varepsilon_{kl}^{(\mathrm{T})(\mathrm{p})}\right] \end{aligned} \tag{4.47}$$

while the stress in the skin outside Ω is equal to σ_{ij}^{I} as given before in Section 4.2.3. It is worthy to note that $\left(C_{klmn}^{\mathrm{I}}\right)^{-1}\sigma_{mn}^{\mathrm{I}} + \varepsilon_{kl}^{(\mathrm{T})}$ is equal to $\varepsilon_{kl}^{\mathrm{I}}$ via the first equation of (4.41), and Equation (4.47) is the same as Equation (4.39) if $\varepsilon_{kl}^{\mathrm{I}}$ is identified with $\varepsilon_{kl}^{\mathrm{f}}$.

4.3 Stage II: Fracture Analysis

In Section 4.2, the stresses in the repaired skin and patch due to mechanical and thermal loads are determined first as if the patch is bonded rigidly to an *uncracked* skin, by using the equivalent inclusion method. Among them, stresses at the prospective crack location are of interest since they will be used in the present fracture analysis. The stress intensity factor will be estimated in this section by using the displacement compatibility method for a sandwich plate with a part through and a debonding crack.

Consider a patched cracked sheet shown in Figure 4.5(a) subjected to a crack surface pressure $\sigma_0(\varsigma)$ which is the negative of the skin normal stress component σ_{yy} found in the stage I analysis (see Section 4.2). In the fracture model, both the skin and the patch

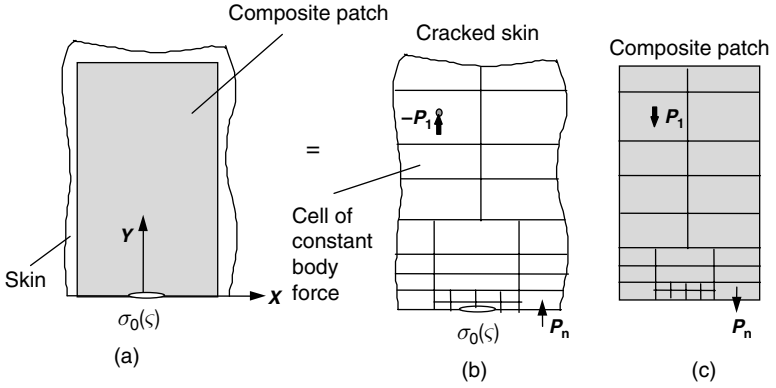

Fig. 4.5. Free body diagram of a patched cracked sheet under a crack surface pressure $\sigma_0(\varsigma)$. For illustration purpose, $P_1,\ P_2, \ldots P_n$ are the y-components of the transmitted shear body forces distributed uniformly over a discretized area (cell) of the bonded interface (Duong and Yu, 1997).

are infinite extent. The thicknesses of the cracked sheet and the composite patch are small relative to the other in-plane dimensions, so that each component can be considered to be under a generalized plane stress condition with the surface shears transmitted through the adhesive acting as body forces. These body forces are unknowns and only pertinent near the crack. The adhesive layer is treated as a two-dimensional shear spring. This problem is solved by the displacement compatibility method developed by Duong and Yu (1997), and Erdogan and Arin (1972). First, the bonded interfacial area between the patch and the cracked skin is divided into a number of small cells, as shown in Figure 4.5(b,c). The unknown shear body forces are then assumed to be constant in each cell. The shear body forces, therefore, have been approximated by a number of constant shear body forces. Due to the double symmetry of the problem considered, these constant shear body forces are symmetric with respect to the two coordinate axes. Even though the outer boundary of the patch is unbounded in stage II analysis, for numerical integration purposes, the bonded interfacial area assumes to be finite and equal to R, and R is chosen such that the stress intensity factor solution does not change appreciably for any larger area.

Let us denote the x- and y-components of the shear body force located at the ith cell that is centered at (x_i, y_i) as P_{1i} and P_{2i}. P_{1i} and P_{2i} have the same unit as stresses. The components of the constant shear body forces are then determined from the displacement compatibility requirement between the cracked sheet and the patch over the bonded interface. The patch–skin displacement compatibility equations in the y-direction are given by

$$\sum_{m=1}^{M}\left\{\sum_{\beta=1}^{2}\left[v_{\text{skin}}^{P_{\beta m}=1}(x_n, y_n; x_m, y_m) - v_{\text{patch}}^{P_{\beta m}=1}(x_n, y_n; x_m, y_m) - \frac{t_{\text{A}}}{G_{\text{A}} h_m d_m}\delta_{2\beta}\delta_{nm}\right]P_{\beta m}\right\}$$

$$= -v_{\text{skin}}^{\sigma_0(\zeta)}(x_n, y_n) \tag{4.48}$$

for $n = 1, 2, \ldots, M$. In the above equations, M is the number of cells making up the bonded interface; t_{A} and G_{A} are the thickness and shear modulus of the adhesive, respectively; P_{1m} and P_{2m} correspond to the x- and y-components of the constant shear body force applied to the mth cell which has a center at (x_m, y_m); h_m and d_m are the length and the width of the mth cell, respectively; $v^{P_{\beta m}=1}(x_n, y_n; x_m, y_m)$ is the y-displacement at the point (x_n, y_n) due to a unit β- (x or y) component of the shear body force acting over the mth cell with a center at (x_m, y_m); $v_{\text{skin}}^{\sigma_0(\zeta)}(x_n, y_n)$ is the displacement in the skin at (x_n, y_n) due to the crack surface pressure; δ_{ij} is defined similarly to the Kronecker delta which is equal to 0 when $i \neq j$, and 1 when $i = j$. The appropriate expressions for $v^{P_{\beta m}=1}(x_n, y_n; x_m, y_m)$ of the cracked skin and the patch, and $v_{\text{skin}}^{\sigma_0(\zeta)}(x_n, y_n)$ are given in Sections 4.3.1 and 4.3.2.

Similar equations for the displacement compatibility in the x-direction can also be derived. A total of $2M$ simultaneous equations will result for the determination of $P_{\beta m}$.

With the shear body forces known, the total stress intensity factors at each crack tip due to these constant shear body forces and due to the crack surface pressure $\sigma_0(\varsigma)$ can be calculated in a straightforward manner as illustrated in Section 4.3.3. In the

stage II–fracture analysis, the shear strain in the adhesive near the crack surface and the additional stresses in the patch due to the presence of the skin crack also need to be determined. The shear stresses in the adhesive are obviously equal to the obtained shear body forces. In contrast, the additional stresses in the patch due to the presence of the skin crack are computed using the complex variable approach outlined in Section 4.3.2 and then added to the results from the stage I analysis of Section 4.2 for the total patch stresses.

It should be noted that the method outlined in this section allows modeling the effects of the pre-existing disbond and the elastic-plastic behavior of the adhesive on the crack tip's stress intensity factor. To account for the former effect, the bonded interfacial area needs to be discretized in such a way that it will not include any pre-existing disbond region in its domain. For the latter effect, an iterative procedure must be employed in the analysis. For simplicity, the adhesive is modeled as an elastic-perfectly-plastic material. The shear body forces are first assumed to be unknown and the adhesive is assumed to behave linearly elastic. These unknown shear body forces are then determined by solving $2M$ simultaneous equations. If the shear body force in any cell exceeds the adhesive yield strength, its value will be set to the yield strength and that shear body force will no longer be a sought solution in the next iteration. The coefficient matrix and the right-hand side of the $2M$ simultaneous equations are then modified accordingly. In the next iteration, the relative displacement between the skin and the patch per unit adhesive thickness in cells with their shear body force being set to the adhesive yield strength must be checked to see if they are larger than the adhesive yield strain. If not, the prior settings of the values of the shear body forces in these cells to the adhesive yield strength are incorrect and therefore must be removed. Another iteration is then carried out, and the whole process is repeated until all prescribed requirements are met.

The solution procedure outlined in this section is general so that it can also be applied to the analysis of an infinite strip patch as well, where the effect of the finite patch width on the stress intensity factor can be properly accounted for. In that case, appropriate expressions for the displacements of an infinite strip patch must be used in Equation (4.48). The displacements of an infinite strip patch due to two symmetrical pairs of constant shear body forces are also given in Section 4.3.2.

As a final remark, an alternative approach to the above fracture analysis is by the crack-bridging model (Rose, 1987a; Cox and Rose, 1994). This latter approach can account for delamination in a self-consistent manner and yields explicit and accurate analytical estimate for the stress intensity factor. However, the approach presented here is more generic because additional effects such as the effects of stiffeners, asymmetric crack with respect to a patch, and cracks approaching to or growing out of the patching boundary can be included in the approach without much difficulty (Duong and Yu, 1997). With regard to the crack-bridging model, this model has been introduced in Chapter 3 and it will be discussed further in detail in Chapter 5 for the analysis of the un-supported one-sided patches.

4.3.1 Cracked sheet displacements and stresses

In the fracture problem, there are two types of loads applied to the cracked metallic sheet: the crack surface pressure $\sigma_0(\varsigma)$ and the constant shear body force with components of $P_x\ (x, y)$ and $P_y(x, y)$. Due to the double symmetry of the stage II problem, the shear body forces are symmetric with respect to the two coordinate axes. The constant shear body forces therefore always come into the analysis in double pairs as shown in Figure 4.6(a). The displacement solutions for the cracked skin due to these two types of loading will be given here briefly.

(a) Displacements due to an arbitrary crack surface pressure

Let $\sigma_0(\varsigma)$ be any arbitrary pressure acting on the crack surfaces; the displacements for this problem are given by (Tada et al., 1985)

$$u(x, y) = \int_{-a}^{a} u^*(x, y, \zeta) \cdot \sigma_0(\zeta) \mathrm{d}\zeta \tag{4.49}$$

$$v(x, y) = \int_{-a}^{a} v^*(x, y, \zeta) \cdot \sigma_0(\zeta) \mathrm{d}\zeta \tag{4.50}$$

$$u^*(x, y, \zeta) = \frac{1}{\pi E_s} \left\{ (1-\nu) \arg(\Xi) - (1+\nu) y \ \mathrm{Im} \left[\frac{\sqrt{a^2-\zeta^2}}{(z-\zeta)\sqrt{z^2-a^2}} \right] \right\}$$

$$v^*(x, y, \zeta) = \frac{1}{\pi E_s} \left\{ -2 \ln(\Xi) - (1+\nu_s) y \ \mathrm{Re} \left[\frac{\sqrt{a^2-\zeta^2}}{(z-\zeta)\sqrt{z^2-a^2}} \right] \right\} \tag{4.51}$$

$$\Xi = \frac{\mathrm{i}(\zeta z - a^2) + \sqrt{(a^2-\zeta^2)(z^2-a^2)}}{a(z-\zeta)}$$

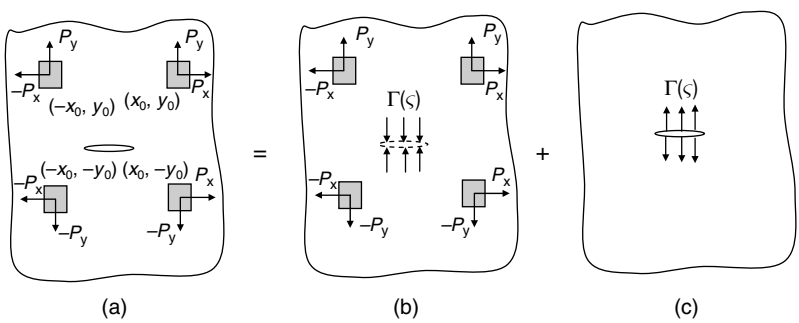

Fig. 4.6. A superposition method for analyzing an infinite cracked sheet under two symmetrical pairs of interfacial shear body forces: (a) the original problem; (b) an infinite sheet under shear body forces; and (c) an infinite cracked sheet under crack surface pressure caused by the shear body forces.

where a is the half crack length; u and v are displacements in the x- and y-directions, respectively; $\mathrm{i} = \sqrt{-1}$, is a imaginary number; $z = x + \mathrm{i}y$; Re and Im denote the real and the imaginary parts of a complex number, respectively, and arg indicates the argument of a complex number. It should be noted that the real and the imaginary parts of the complex function $\sin^{-1}\left[\frac{\zeta z - a^2}{a(z-\zeta)}\right]$ reported in the cited reference are given here explicitly in the above equation as $\arg(\Xi)$ and $\ln(\Xi)$, respectively, for FORTRAN coding purpose.

(b) Displacements and stresses due to two symmetrical pairs of constant shear body forces

The displacements due to two symmetrical pairs of constant shear body force are determined by the superposition of two parts as shown in Figures 4.6(b) and 4.6(c): (1) an uncracked sheet subjected to symmetrical pairs of constant shear body forces, and (2) a cracked sheet with tractions applied to the crack faces as caused by these constant shear body forces.

The displacements in an uncracked sheet due to the constant shear body forces are determined based on the complex stress function approach. For plane stress, the displacements in the body due to a single constant shear body force, distributed uniformly over a cell with an area h by d, are given in terms of the stress functions Ω's and ω's as

$$\begin{aligned} 2\mu_s u(x,y) &= \mathrm{Re}\left[\kappa_s \Omega_1(z,z_0) - z\overline{\Omega_1'}(z,z_0) - \overline{\omega}_1(z,z_0)\right] \\ 2\mu_s v(x,y) &= \mathrm{Im}\left[\kappa_s \Omega_2(z,z_0) - z\overline{\Omega_2'}(z,z_0) - \overline{\omega}_2(z,z_0)\right] \end{aligned} \tag{4.52}$$

$$\begin{aligned} \Omega_1 &= -\frac{P_x\varphi_1 + \mathrm{i}P_y\varphi_2}{2\pi(1+\kappa_\varepsilon)t_s} \\ \Omega_2 &= -\frac{P_x\varphi_2 + \mathrm{i}P_y\varphi_1}{2\pi(1+\kappa_\varepsilon)t_s} \\ \omega_1 &= \frac{\kappa_\varepsilon(P_x\varphi_1 - \mathrm{i}P_y\varphi_2)}{2\pi(1+\kappa_\varepsilon)t_s} + \frac{P_x\hat{\theta}_1 + \mathrm{i}P_y\hat{\theta}_2}{2\pi(1+\kappa_\varepsilon)t_s} \\ \omega_2 &= \frac{\kappa_\varepsilon(P_x\varphi_2 - \mathrm{i}P_y\varphi_1)}{2\pi(1+\kappa_\varepsilon)t_s} + \frac{P_x\hat{\theta}_2 + \mathrm{i}P_y\hat{\theta}_1}{2\pi(1+\kappa_\varepsilon)t_s} \end{aligned} \tag{4.53}$$

$$\kappa_\varepsilon = \frac{3-\nu_s}{1+\nu_s} \tag{4.54}$$

where P_x and P_y are the components of the constant shear body force in the x- and y- directions, respectively; t_s, ν_s, and μ_s are the thickness, Poisson's ratio, and shear modulus of the cracked sheet, respectively; i is the imaginary number, i.e., $\mathrm{i} = \sqrt{-1}$; $z_0 = x_0 + \mathrm{i}y_0$ is the center position of the cell in the complex plane over which the constant shear body acts; $z = x + \mathrm{i}y$ is the position of a point at which the displacements are evaluated in the complex plane; a bar indicates a complex conjugate, and

a prime indicates differentiation with respect to the complex variable z. $\varphi_j(z, z_0)$ and $\hat{\theta}_j(z, z_0)$, $j = 1, 2$, are defined by

Case 1: $\mathrm{Im}(z - z_0 - B_1) \cdot \mathrm{Im}(z - z_0 + B_1) > 0$,

$$\begin{aligned} \varphi_1(z, z_0) &= \varphi_{\mathrm{a}}(z, z_0) \\ \varphi_2(z, z_0) &= \varphi_{\mathrm{b}}(z, z_0) \\ \hat{\theta}_1(z, z_0) &= \hat{\theta}_{\mathrm{a}}(z, z_0) \\ \hat{\theta}_2(z, z_0) &= \hat{\theta}_{\mathrm{b}}(z, z_0) \end{aligned} \tag{4.55}$$

Case 2: $\mathrm{Im}(z - z_0 - B_1) \cdot \mathrm{Im}(z - z_0 + B_1) < 0$,

$$\begin{aligned} \varphi_2(z, z_0) &= \varphi_1(z, z_0) = \varphi_{\mathrm{b}}(z, z_0) \\ \hat{\theta}_2(z, z_0) &= \hat{\theta}_1(z, z_0) = \hat{\theta}_{\mathrm{b}}(z, z_0) \end{aligned} \tag{4.56}$$

where

$$\begin{aligned} \varphi_{\mathrm{a}}(z, z_0) = \frac{\mathrm{i}}{2} \big[& -(z - z_0 - B_1)^2 \log(z - z_0 - B_1) - (z - z_0 + B_1)^2 \log(z - z_0 + B_1) \\ & + (z - z_0 - \overline{B}_1)^2 \log(z - z_0 - \overline{B}_1) + (z - z_0 + \overline{B}_1)^2 \log(z - z_0 + \overline{B}_1) - 3\mathrm{i}hd \big] \\ \varphi_{\mathrm{b}}(z, z_0) = \frac{\mathrm{i}}{2} \Bigg\{ & (z - z_0)^2 \log \left[\frac{(z - z_0 - \overline{B}_1)(z - z_0 + \overline{B}_1)}{(z - z_0 - B_1)(z - z_0 + B_1)} \right] \\ & + \overline{B}_1^2 \log \big[(z - z_0 - \overline{B}_1)(z - z_0 + \overline{B}_1) \big] \\ & - B_1^2 \log \left[(z - z_0 - B_1)(z - z_0 + B_1) \right] + 2\overline{B}_1 (z - z_0) \log \left[\frac{z - z_0 + \overline{B}_1}{z - z_0 - \overline{B}_1} \right] \\ & - 2\, B_1 (z - z_0) \log \left[\frac{z - z_0 + B_1}{z - z_0 - B_1} \right] + 3\mathrm{i}hd \Bigg\} \\ \hat{\theta}_{\mathrm{a}}(z, z_0) = \mathrm{i} \big[& -(z - z_0 - B_1)(\overline{z}_0 + \overline{B}_1) \log(z - z_0 - B_1) \\ & - (z - z_0 + B_1)(\overline{z}_0 - \overline{B}_1) \log(z - z_0 + B_1) \\ & + (z - z_0 - \overline{B}_1)(\overline{z}_0 + B_1) \log(z - z_0 - \overline{B}_1) \\ & + (z - z_0 + \overline{B}_1)(\overline{z}_0 - B_1) \log(z - z_0 + \overline{B}_1) \big] \end{aligned} \tag{4.57}$$

$$\hat{\theta}_b(z, z_0) = \mathrm{i}\left\{(z-z_0)\bar{z}_0 \log\left[\frac{(z-z_0-\overline{B}_1)(z-z_0+\overline{B}_1)}{(z-z_0-B_1)(z-z_0+B_1)}\right]\right.$$
$$+\overline{B}_1(z-z_0)\log\left[\frac{z-z_0+B_1}{z-z_0-B_1}\right] - B_1\bar{z}_0\log\left[\frac{z-z_0+B_1}{z-z_0-B_1}\right]$$
$$-\overline{B}_1 B_1 \log\left[\frac{(z-z_0-\overline{B}_1)(z-z_0+\overline{B}_1)}{(z-z_0-B_1)(z-z_0+B_1)}\right]$$
$$\left.-B_1(z-z_0)\log\left[\frac{z-z_0+\overline{B}_1}{z-z_0-\overline{B}_1}\right] + \overline{B}_1\bar{z}_0\log\left[\frac{z-z_0+\overline{B}_1}{z-z_0-\overline{B}_1}\right]\right\}$$

and the complex number B_1 is defined by

$$B_1 = -(d/2 + \mathrm{i}h/2) \tag{4.58}$$

In these equations, the principal branch must be used in the evaluation of the logarithmic functions. It should be emphasized that the stress functions for these cases are much more complicated than those given for a point load, in which different branches of the multiple-valued stress functions must be chosen for the different combinations of $(z,\ z_0)$. For the constant shear body forces symmetric with respect to the two axes, $\varphi_j\,(z,\ z_0)$ and $\hat{\theta}_j\,(z,\ z_0)$, $j = 1, 2$, given by the above equations will yield displacements that satisfy the imposed symmetric conditions. In order to assure that the multiplicity of values of the stress functions is properly treated, a similar procedure is used to select the appropriate branches of the stress functions for an infinite orthotropic sheet under a constant shear body force, which results in displacements nearly identical to those obtained from Equation (4.52) for nearly isotropic materials. For two symmetrical pairs of shear body forces as shown in Figure 4.6(a), one must evaluate the above equations four times for the shear body forces with x- and y-components of (P_x, P_y), $(P_x, -P_y)$, $(-P_x, P_y)$, and $(-P_x, -P_y)$, which are applied respectively at (x_0, y_0), $(x_0, -y_0)$, $(-x_0, y_0)$, and $(-x_0, -y_0)$, and superimpose the results.

On the other hand, under plane stress condition, the stresses in an uncracked sheet due to a single constant shear body force are given in terms of the stress functions Ω' s and ω's as

$$\sigma_{yy}(x, y) = \mathrm{Re}\left[\Omega_3'(z, z_0) + \overline{\Omega_3'}(z, z_0) + z\overline{\Omega_3''}(z, z_0) + \overline{\omega_3'}(z, z_0)\right]$$
$$\tau_{xy}(x, y) = -\mathrm{Im}\left[\Omega_4'(z, z_0) + \overline{\Omega_4'}(z, z_0) + z\overline{\Omega_4''}(z, z_0) + \overline{\omega_4'}(z, z_0)\right] \tag{4.59}$$

where

$$\Omega_3 = -\frac{P_x\varphi_1 + iP_y\varphi_a}{2\pi(1+\kappa_\varepsilon)t_s}$$

$$\Omega_4 = -\frac{P_x\varphi_a + iP_y\varphi_1}{2\pi(1+\kappa_\varepsilon)t_s}$$

$$\omega_3 = \frac{\kappa_\varepsilon(P_x\varphi_1 - iP_y\varphi_a)}{2\pi(1+\kappa_\varepsilon)t_s} + \frac{P_x\hat{\theta}_1 + iP_y\hat{\theta}_a}{2\pi(1+\kappa_\varepsilon)t_s} \tag{4.60}$$

$$\omega_4 = \frac{\kappa_\varepsilon(P_x\varphi_a - iP_y\varphi_1)}{2\pi(1+\kappa_\varepsilon)t_s} + \frac{P_x\hat{\theta}_a + iP_y\hat{\theta}_1}{2\pi(1+\kappa_\varepsilon)t_s}$$

$\varphi_1, \varphi_a, \hat{\theta}_1, \hat{\theta}_a$, etc., have been defined previously, and the notations of prime and double primes again denote the differentiation of the complex function with respect to the complex variable z. The normal component $\Gamma(\zeta)$ of the traction along the prospective crack location of the uncracked sheet due to two symmetrical pairs of constant shear body forces, i.e., $\Gamma(\zeta) = -\sigma_{yy}(\zeta, 0), -a \le \zeta \le a$, is also of interest since it is needed in the second part of the displacement evaluation. Since $\sigma_{yy}(x, 0)$ due to a single shear body force can be determined from Equation (4.59), $\Gamma(\zeta)$ due to two symmetrical pairs of constant shear body forces can be obtained by superimposing the results of $-\sigma_{yy}(x, 0)$ due to individual shear body forces.

As shown in Figure 4.6, for a complete displacement solution, one must now consider the problem depicted in 4.6(c). For this problem, the stresses applied to the surfaces of the crack are determined from the uncracked solution described above. Due to the symmetry with respect to the x-axis, τ_{xy} is zero on the crack faces. The displacements for problem 4.6(c) clearly can be obtained by numerical integrations of Equations (4.49) and (4.50) with $\sigma_0(\varsigma)$, being replaced by $\Gamma(\zeta)$, where $\Gamma(\zeta)$ is equal to the negative of the skin normal stresses along the crack line of the problem shown in Figure 4.6(b).

4.3.2 Composite patch displacements and stresses

The displacements and stresses in the composite patch will be derived in this section for two different models: the infinite sheet patch and the infinite strip patch.

(a) Infinite sheet patch

The notation and development of the complex representation of the solution of plane stress problem for orthotropic elastic materials follow closely that of Lekhnitskii (1968). From Lekhnitskii (1968), the stress and displacement solutions of the orthotropic sheet in terms of the complex potentials $\tilde{\varphi}_1(z_1)$ and $\tilde{\varphi}_2(z_2)$ are given by

$$
\begin{aligned}
u(x,y) &= 2\ \mathrm{Re}\left[p_1\tilde{\varphi}_1(z_1) + p_2\tilde{\varphi}_2(z_2)\right] \\
v(x,y) &= 2\ \mathrm{Re}\left[q_1\tilde{\varphi}_1(z_1) + q_2\tilde{\varphi}_2(z_2)\right] \\
\sigma_{xx} &= 2\ \mathrm{Re}\left[s_1^2\tilde{\varphi}_1'(z_1) + s_2^2\tilde{\varphi}_2'(z_2)\right] \\
\sigma_{yy} &= 2\ \mathrm{Re}\left[\tilde{\varphi}_1'(z_1) + \tilde{\varphi}_2'(z_2)\right] \\
\tau_{xy} &= -2\ \mathrm{Re}\left[s_1\tilde{\varphi}_1'(z_1) + s_2\tilde{\varphi}_2'(z_2)\right]
\end{aligned}
\tag{4.61}
$$

where

$$
\begin{aligned}
z_k &= x + s_k y \\
p_k &= \frac{1}{E_x^y}\left(s_k^2 - \nu_{xy}^{\mathrm{p}}\right) \\
q_k &= \frac{1}{s_k E_y^{\mathrm{p}}}\left(1 - \nu_{yx}^{\mathrm{p}} s_k^2\right)
\end{aligned}
\tag{4.62}
$$

$k = 1, 2$; $E_x^{\mathrm{p}}, E_y^{\mathrm{p}}, \nu_{xy}^{\mathrm{p}}, \nu_{yx}^{\mathrm{p}}$, and μ^{p} are extensional moduli, Poisson's ratios, and shear modulus of the orthotropic patch, respectively, while s_1 and s_2 are the roots of

$$
s^4 + \left(\frac{E_x^{\mathrm{p}}}{\mu^{\mathrm{p}}} - 2\nu_{xy}^{\mathrm{p}}\right)s^2 + \frac{E_x^{\mathrm{p}}}{E_y^{\mathrm{p}}} = 0 \tag{4.63}
$$

for which $\mathrm{Im}(s_k) > 0$. In Equation (4.61), the prime denotes differentiation with respect to the complex variable z_1 or z_2.

For a concentrated load with its components of T_x and T_y acting at point (x_0, y_0) in an infinite patch sheet, $\tilde{\varphi}_1(z_1)$ and $\tilde{\varphi}_2(z_2)$ are given by (Erdogan and Arin 1972):

$$
\begin{aligned}
\tilde{\varphi}_1(z_1) &= \frac{\left(c_{11}T_x + c_{12}T_y\right)}{t_{\mathrm{p}}}\log\left(z_1 - z_{01}\right) \\
\tilde{\varphi}_2(z_2) &= \frac{\left(c_{21}T_x + c_{22}T_y\right)}{t_{\mathrm{p}}}\log\left(z_2 - z_{02}\right)
\end{aligned}
\tag{4.64}
$$

$$
z_{0k} = x_0 + s_k y_0 \quad (k = 1, 2) \tag{4.65}
$$

$$
c_{11} = \frac{\dfrac{1}{2\pi\mathrm{i}}\left(s_2 + \overline{s}_2 + \overline{s}_1 + \overline{s}_1 s_2 \overline{s}_2 \dfrac{\nu_{xy}^{\mathrm{p}} E_y^{\mathrm{p}}}{E_x^{\mathrm{p}}}\right)}{\left[\left(s_1 - s_2\right)\left(s_1 - \overline{s}_1\right)\left(1 - \dfrac{\overline{s}_2}{s_1}\right)\right]}
$$

$$
c_{12} = \frac{\dfrac{1}{2\pi\mathrm{i}}\left(s_2\overline{s}_2 + \overline{s}_1 s_2 + \overline{s}_1\overline{s}_2 + \nu_{xy}^{\mathrm{p}}\right)}{\left[\left(s_1 - s_2\right)\left(s_1 - \overline{s}_1\right)\left(1 - \dfrac{\overline{s}_2}{s_1}\right)\right]}
$$

$$c_{21} = \frac{\dfrac{1}{2\pi \mathrm{i}}\left(s_1 + \bar{s}_1 + \bar{s}_2 + \bar{s}_2 s_1 \bar{s}_1 \dfrac{\nu_{xy}^{\mathrm{p}} E_y^{\mathrm{p}}}{E_x^{\mathrm{p}}}\right)}{\left[(s_2 - s_1)(s_2 - \bar{s}_2)\left(1 - \dfrac{\bar{s}_1}{s_2}\right)\right]}$$

$$c_{22} = \frac{\dfrac{1}{2\pi \mathrm{i}}\left(s_1 \bar{s}_1 + \bar{s}_2 s_1 + \bar{s}_2 \bar{s}_1 + \nu_{xy}^{\mathrm{p}}\right)}{\left[(s_2 - s_1)(s_2 - \bar{s}_2)\left(1 - \dfrac{\bar{s}_1}{s_2}\right)\right]} \tag{4.66}$$

and t_{p} is the thickness of the composite patch.

The complex potentials for an interfacial shear body force with its components of P_x and P_y, distributed uniformly over a cell that has a center at (x_0, y_0) and an area of h by d, are obtained by integrating Equation (4.64) over the cell area. Because of the multiplicity of the values of the resulting expression for $\tilde{\varphi}_k(z_k),\ k = 1, 2$, in order to obtain the correct displacements under symmetric and anti-symmetric loads and also for very nearly isotropic materials, in this case, one must express the displacements in Equation (4.61) as follows:

$$\begin{aligned} u(x, y) &= 2\ \mathrm{Re}\left[p_1 \tilde{\varphi}_1^{(1)}(z_1) + p_2 \tilde{\varphi}_2^{(1)}(z_2)\right] \\ v(x, y) &= 2\ \mathrm{Re}\left[q_1 \tilde{\varphi}_1^{(2)}(z_1) + q_2 \tilde{\varphi}_2^{(2)}(z_2)\right] \end{aligned} \tag{4.67}$$

where $\tilde{\varphi}_k^{(1)}(z_k)$ and $\tilde{\varphi}_k^{(2)}(z_k)$ are defined by

For $\mathrm{Im}(z_k - z_{0k} - B_{k1}) \cdot \mathrm{Im}(z_k - z_{0k} + B_{k1}) > 0$:

$$\begin{aligned} \tilde{\varphi}_k^{(1)}(z_k) &= c_{k1} P_x \tilde{\varphi}_k^{\mathrm{a}}(z_k, z_{0k}) + c_{k2} P_y \tilde{\varphi}_k^{\mathrm{b}}(z_k, z_{0k}) \\ \tilde{\varphi}_k^{(2)}(z_k) &= c_{k1} P_x \tilde{\varphi}_k^{\mathrm{b}}(z_k, z_{0k}) + c_{k2} P_y \tilde{\varphi}_k^{\mathrm{a}}(z_k, z_{0k}) \end{aligned} \tag{4.68}$$

For $\mathrm{Im}(z_k - z_{0k} - B_{k1}) \cdot \mathrm{Im}(z_k - z_{0k} + B_{k1}) < 0$:

$$\tilde{\varphi}_k^{(2)}(z_k) = \tilde{\varphi}_k^{(1)}(z_k) = (c_{k1} P_x + c_{k2} P_y) \tilde{\varphi}_k^{\mathrm{b}}(z_k, z_{0k}) \tag{4.69}$$

$$\begin{aligned} \tilde{\varphi}_k^{\mathrm{a}}(z_k, z_{0k}) = \frac{1}{2 s_k t_{\mathrm{p}}} \big[& (z_k - z_{0k} - B_{k1})^2 \log (z_k - z_{0k} - B_{k1}) \\ & + (z_k - z_{0k} + B_{k1})^2 \log (z_k - z_{0k} + B_{k1}) \\ & - (z_k - z_{0k} - B_{k2})^2 \log (z_k - z_{0k} - B_{k2}) \\ & - (z_k - z_{0k} + B_{k2})^2 \log (z_k - z_{0k} + B_{k2}) - 3hds_k \big] \end{aligned}$$

$$\begin{aligned}\tilde{\varphi}_k^{\mathrm{b}}(z_k, z_{0k}) = \frac{1}{2s_k t_{\mathrm{p}}} \Bigg\{ & (z_k - z_{0k})^2 \log\left[\frac{(z_k - z_{0k} - B_{k1})(z_k - z_{0k} + B_{k1})}{(z_k - z_{0k} - B_{k2})(z_k - z_{0k} + B_{k2})}\right] \\ & + B_{k1}^2 \log\left[(z_k - z_{0k} - B_{k1})(z_k - z_{0k} + B_{k1})\right] \\ & - B_{k2}^2 \log\left[(z_k - z_{0k} - B_{k2})(z_k - z_{0k} + B_{k2})\right] \\ & + 2(z_k - z_{0k}) B_{k1} \log\left[\frac{(z_k - z_{0k} + B_{k1})}{(z_k - z_{0k} - B_{k1})}\right] \\ & - 2(z_k - z_{0k}) B_{k2} \log\left[\frac{(z_k - z_{0k} + B_{k2})}{(z_k - z_{0k} - B_{k2})}\right] - 3hds_k \Bigg\}\end{aligned} \tag{4.70}$$

$$\begin{aligned} B_{k1} &= \frac{d}{2} + s_k \frac{h}{2} \\ B_{k2} &= -\frac{d}{2} + s_k \frac{h}{2} \end{aligned} \tag{4.71}$$

Again, the principal branch of the logarithm function must be used in the evaluation of $\tilde{\varphi}_k^{\mathrm{a}}(z_k)$ and $\tilde{\varphi}_k^{\mathrm{b}}(z_k)$ and $k = 1, 2$. The displacement solution due to two symmetrical pairs of constant shear body forces is then obtained by superimposing the results due to individual shear body forces.

The stresses due to two symmetrical pairs of constant shear body forces can be obtained as follows, after resolving the multiple-valued problem of the derivatives of the stress functions. Similar to Equation (4.59), the stresses due to a single interfacial shear body force are given by

$$\begin{aligned} \sigma_{xx} &= 2\ \mathrm{Re}\left[s_1^2 \tilde{\varphi}_1'^{(3)}(z_1) + s_2^2 \tilde{\varphi}_2'^{(3)}(z_2)\right] \\ \sigma_{yy} &= 2\ \mathrm{Re}\left[\tilde{\varphi}_1'^{(3)}(z_1) + \tilde{\varphi}_2'^{(3)}(z_2)\right] \\ \tau_{xy} &= -2\ \mathrm{Re}\left[s_1 \tilde{\varphi}_1'^{(4)}(z_1) + s_2 \tilde{\varphi}_2'^{(4)}(z_2)\right] \end{aligned} \tag{4.72}$$

where $\tilde{\varphi}_k^{(3)}(z_k)$ and $\tilde{\varphi}_k^{(4)}(z_k)$ $(k = 1, 2)$ are defined by

For $\mathrm{Im}(z_k - z_{0k} - B_{k1}) \cdot \mathrm{Im}(z_k - z_{0k} + B_{k1}) > 0$:

$$\tilde{\varphi}_k^{(3)}(z_k) = \tilde{\varphi}_k^{(4)}(z_k) = \left(c_{k1} P_x + c_{k2} P_y\right) \tilde{\varphi}_k^{\mathrm{a}}(z_k, z_{0k}) \tag{4.73}$$

For $\mathrm{Im}(z_k - z_{0k} - B_{k1}) \cdot \mathrm{Im}(z_k - z_{0k} + B_{k1}) < 0$:

$$\begin{aligned} \tilde{\varphi}_k^{(3)}(z_k) &= \left[c_{k1} P_x \tilde{\varphi}_k^{\mathrm{b}}(z_k, z_{0k}) + c_{k2} P_y \tilde{\varphi}_k^{\mathrm{a}}(z_k, z_{0k})\right] \\ \tilde{\varphi}_k^{(4)}(z_k) &= \left[c_{k1} P_x \tilde{\varphi}_k^{\mathrm{a}}(z_k, z_{0k}) + c_{k2} P_y \tilde{\varphi}_k^{\mathrm{b}}(z_k, z_{0k})\right] \end{aligned} \tag{4.74}$$

$\tilde{\varphi}_k^{\mathrm{a}}$ and $\tilde{\varphi}_k^{\mathrm{b}}$ $(k = 1, 2)$ have been defined previously. The stresses due to two symmetrical pairs of shear body forces are again obtained by linear superposition of the individual contributions.

(b) Infinite strip patch

So far, only the solution for an infinite composite sheet has been given. For an infinite composite strip, one must superimpose another solution on the "infinite sheet" solution as indicated in Figure 4.7. The displacement solution of problem 4.7(c) is determined by using the Fourier integral transform method described below.

Referring to Figure 4.8, the displacement solution of a composite strip subjected to point loads can be obtained by the linear superposition of the infinite patch solution under point loads and the strip solution under tractions acting on the vertical boundaries. The former solutions can be easily obtained since that solution for a single point load with its components of T_x and T_y acting at (x_0, y_0) in an infinite sheet patch has been derived in part (a). The corresponding stresses σ_x and τ_{xy} along the lines $x = \pm W/2$ due to a single point load can also be evaluated by using Equations (4.61)–(4.66) in that part. These evaluations are straightforward since the derivatives of the stress functions for a single point load are single-valued. For the symmetrical loads shown in Figure 4.8, one must evaluate stresses σ_{xx} and τ_{xy} along the lines $x = \pm W/2$ four times due to point loads with x- and y-components of $\left(T_x, T_y\right)$, $\left(T_x, -T_y\right)$, $\left(-T_x, T_y\right)$, and $\left(-T_x, -T_y\right)$, which are applied respectively at (x_0, y_0), $(x_0, -y_0)$, $(-x_0, y_0)$, and $(-x_0, -y_0)$, and superimpose the results. For the present discussion, these stresses assume to be already calculated and denoted by $\sigma^v(y)$ and $\tau^v(y)$, respectively. The solutions of a composite strip subjected to vertical boundary tractions caused by four point loads symmetric with respect to two coordinate axes will be sought. As mentioned earlier, the displacement solutions of the latter problem are determined by using the Fourier integral transform method. The

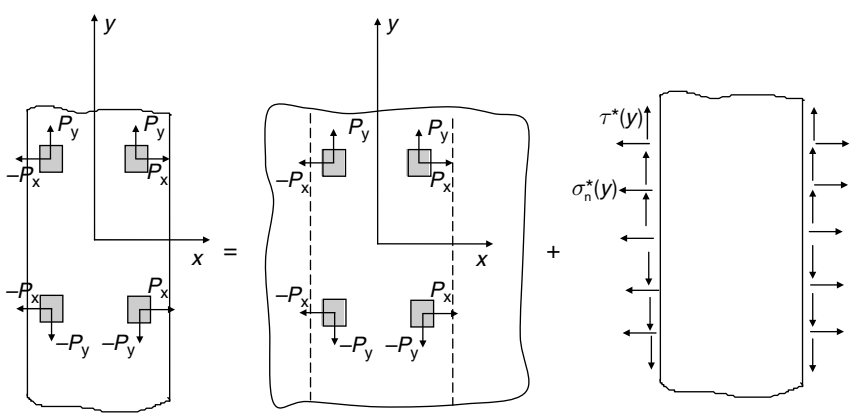

Fig. 4.7. A superposition method for analyzing an infinite strip patch under two symmetrical pairs of interfacial shear body forces.

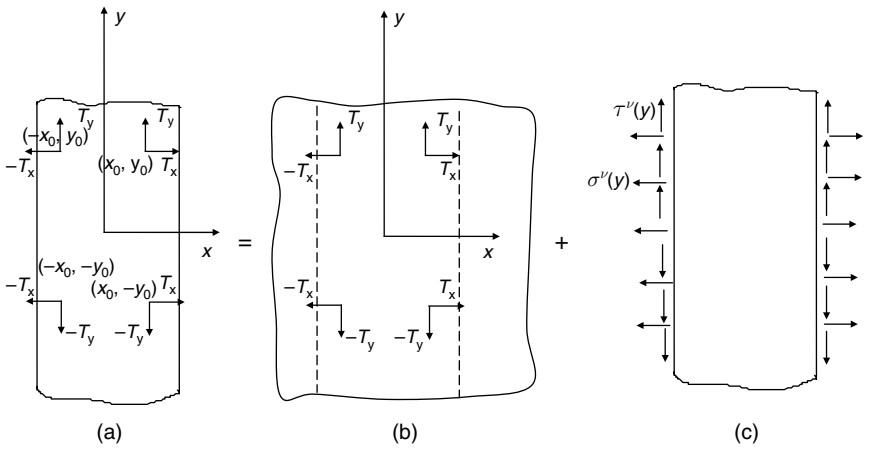

Fig. 4.8. A superposition for analyzing an infinite strip patch under two symmetrical pairs of point loads.

pertinent results from the general theory for an infinite orthotropic strip (Atluri, 1992) are summarized below. According to the Fourier transform theory, the displacement fields in an orthotropic strip patch can be expressed as

$$u(x, y) = \frac{2}{\pi} \int_0^{\infty} U(\lambda, x) \cos\, \lambda y \, \mathrm{d}\lambda$$
$$v(x, y) = \frac{2}{\pi} \int_0^{\infty} V(\lambda, x) \sin\, \lambda y \, \mathrm{d}\lambda \tag{4.75}$$

where $U(\lambda, x)$ and $V(\lambda, x)$ are the transformed displacements defined by

$$U(\lambda, x) = A_1(\lambda)\tilde{e}_1 \cosh\left(\hat{\beta}_1 x\right) + A_2(\lambda)\tilde{e}_2 \cosh\left(\hat{\beta}_2 x\right) + A_3(\lambda)\tilde{e}_1 \sinh\left(\hat{\beta}_1 x\right)$$
$$+ A_4(\lambda)\tilde{e}_2 \sinh\left(\hat{\beta}_2 x\right) \tag{4.76}$$

$$V(\lambda, x) = A_1(\lambda) \sinh\left(\hat{\beta}_1 x\right) + A_2(\lambda) \sinh\left(\hat{\beta}_2 x\right) + A_3(\lambda) \cosh\left(\hat{\beta}_1 x\right) + A_4(\lambda) \cosh\left(\hat{\beta}_2 x\right)$$

$$\tilde{e}_k = \frac{\mu^{\mathrm{p}} \hat{\beta}_k \left(1 - \nu_{xy}^{\mathrm{p}} \nu_{yx}^{\mathrm{p}}\right) - \lambda^2 E_y^{\mathrm{p}}}{\lambda \hat{\beta}_k \left[\nu_{xy}^{\mathrm{p}} E_y^{\mathrm{p}} + \mu^{\mathrm{p}} \left(1 - \nu_{xy}^{\mathrm{p}} \nu_{yx}^{\mathrm{p}}\right)\right]} \tag{4.77}$$

$\hat{\beta}_1$ and $\hat{\beta}_2$ are two roots (out of four) of the following characteristic equation, which have a positive real part:

$$\hat{\beta}^4 + \lambda^2 \left[2\nu_{yx}^{\mathrm{p}} - \frac{E_y^{\mathrm{p}}}{\mu^{\mathrm{p}}}\right] \hat{\beta}^2 + \frac{E_y^{\mathrm{p}}}{E_x^{\mathrm{p}}} \lambda^4 = 0 \tag{4.78}$$

A_1, A_2, A_3, and A_4 are constants, which depend only on λ and must be determined from the loading and the boundary conditions.

On the other hand, the transformed stress components $\overline{\sigma}_x(\lambda, x)$ and $\overline{\tau}_{xy}(\lambda, x)$ are given by

$$\begin{aligned}\overline{\sigma}_{xx}(\lambda, x) &= \left(\breve{M}_1\hat{\beta}_1\tilde{e}_1 + \breve{M}_2\lambda\right)\left[A_1\sinh\left(\hat{\beta}_1 x\right) + A_3\cosh\left(\hat{\beta}_1 x\right)\right] \\ &\quad + \left(\breve{M}_1\hat{\beta}_2\tilde{e}_2 + \breve{M}_2\lambda\right)\left[A_2\sinh\left(\hat{\beta}_2 x\right) + A_4\cosh\left(\hat{\beta}_2 x\right)\right] \\ \overline{\tau}_{xy}(\lambda, x) &= \mu^{\mathrm{p}}\left[\left(\hat{\beta}_1 - \tilde{e}_1\lambda\right)\left(A_1\cosh\left(\hat{\beta}_1 x\right) + A_3\sinh\left(\hat{\beta}_1 x\right)\right)\right. \\ &\quad \left. + \left(\hat{\beta}_2 - \tilde{e}_2\lambda\right)\left(A_2\cosh\left(\hat{\beta}_2 x\right) + A_4\sinh\left(\hat{\beta}_2 x\right)\right)\right]\end{aligned} \tag{4.79}$$

$$\begin{aligned}\breve{M}_1 &= \frac{E_x^{\mathrm{p}}}{1 - \nu_{xy}^{\mathrm{p}}\nu_{yx}^{\mathrm{p}}} \\ \breve{M}_2 &= \frac{E_y^{\mathrm{p}}\nu_{xy}^{\mathrm{p}}}{1 - \nu_{xy}^{\mathrm{p}}\nu_{yx}^{\mathrm{p}}}\end{aligned} \tag{4.80}$$

The constants A_1, A_2, A_3, and A_4 will be determined from the boundary conditions as follows. First, due to the symmetric condition with respect to the y-axis, $A_1 = A_2 = 0$. Secondly, defining $\hat{P}(\lambda)$ and $\hat{Q}(\lambda)$ as

$$\begin{aligned}\hat{P}(\lambda) &= \int_0^\infty \sigma^{\mathrm{v}}(y)\cos(\lambda y)\mathrm{d}y \\ \hat{Q}(\lambda) &= \int_0^\infty \tau^{\mathrm{v}}(y)\cos(\lambda y)\mathrm{d}y\end{aligned} \tag{4.81}$$

A_3 and A_4 are then determined from the boundary conditions at $x = W/2$, i.e.,

$$\begin{aligned}\overline{\sigma}_{xx}(\lambda,\ W/2) &= \left(\breve{M}_1\hat{\beta}_1\tilde{e}_1 + \breve{M}_2\lambda\right)A_3\cosh\left(\hat{\beta}_1 W/2\right) \\ &\quad + \left(\breve{M}_1\hat{\beta}_2\tilde{e}_2 + \breve{M}_2\lambda\right)A_4\cosh\left(\hat{\beta}_2 W/2\right) \\ &= -\hat{P}(\lambda) \\ \overline{\tau}_{xy}(\lambda,\ W/2) &= \mu^{\mathrm{p}}\left[\left(\hat{\beta}_1 - \tilde{e}_1\lambda\right)A_3\sinh\left(\hat{\beta}_1 W/2\right) + \left(\hat{\beta}_2 - \tilde{e}_2\lambda\right)A_4\sinh\left(\hat{\beta}_2 W/2\right)\right] \\ &= -\hat{Q}(\lambda)\end{aligned} \tag{4.82}$$

Thus, if $\hat{P}(\lambda)$ and $\hat{Q}(\lambda)$ are known, one can determine A_3 and A_4 from Equation (4.82).

Following the work of Atluri (1992) and Duong and Yu (1997), $\hat{P}(\lambda)$ and $\hat{Q}(\lambda)$ are found to be

$$\begin{aligned}\hat{P}(\lambda) = -\pi \sum_{j=1}^{4} \mathrm{Re}\Big(& s_1\left(c_{11}T_{xj} + c_{12}T_{yj}\right) \mathrm{i}\mathrm{e}^{\lambda\left\{-\left[\eta_1(W/2-x_{0j})-y_{0j}\right]\mathrm{i}+\rho_1\left(W/2-x_{0j}\right)\right\}} \\ & + s_2\left(c_{21}T_{xj} + c_{22}T_{yj}\right) \mathrm{i}\mathrm{e}^{\lambda\left\{-\left[\eta_2(W/2-x_{0j})-y_{0j}\right]\mathrm{i}+\rho_2\left(W/2-x_{0j}\right)\right\}}\Big) \\ \hat{Q}(\lambda) = \pi \sum_{j=1}^{4} \mathrm{Re}\Big(& \left(c_{11}T_{xj} + c_{12}T_{yj}\right) \mathrm{e}^{\lambda\left\{-\left[\eta_1(W/2-x_{0j})-y_{0j}\right]\mathrm{i}+\rho_1\left(W/2-x_{0j}\right)\right\}} \\ & + \left(c_{21}T_{xj} + c_{22}T_{yj}\right) \mathrm{e}^{\lambda\left\{-\left[\eta_2(W/2-x_{0j})-y_{0j}\right]\mathrm{i}+\rho_2\left(W/2-x_{0j}\right)\right\}}\Big)\end{aligned} \tag{4.83}$$

where η_k and ρ_k, $k = 1, 2$, are defined by $\eta_k + \mathrm{i}\rho_k = \frac{1}{s_k}$; T_{xj} and T_{yj}, $j = 1, 4$, are the x- and y-components of the jth concentrated load applied at (x_{0j}, y_{0j}) corresponding to loading configuration shown in Figure 4.8; and the rest are defined previously. Substituting Equation (4.76) into (4.75) and noting that $A_1 = A_2 = 0$ yield

$$\begin{aligned} u(x, y) &= \frac{2}{\pi} \int_0^{\infty} \left[A_3 \tilde{e}_1 \sinh\left(\hat{\beta}_1 x\right) + A_4 \tilde{e}_2 \sinh\left(\hat{\beta}_2 x\right)\right] \cos(\lambda y)\, \mathrm{d}\lambda \\ v(x, y) &= \frac{2}{\pi} \int_0^{\infty} \left[A_3 \cosh\left(\hat{\beta}_1 x\right) + A_4 \cosh\left(\hat{\beta}_2 x\right)\right] \sin(\lambda y)\, \mathrm{d}\lambda \end{aligned} \tag{4.84}$$

where A_3 and A_4 are determined by solving Equation (4.82) with $\hat{P}(\lambda)$ and $\hat{Q}(\lambda)$ given by (4.83). These Fourier integrals given by Equation (4.84) can be evaluated numerically by calling the appropriate subroutines of the mathematical package QUADPACK (Piessens and de Doncker, 1983), which is available free from the Internet.

So far the results have been derived for the point loads. For a similar loading configuration but with the constant shear body forces as shown in Figure 4.7, the same results still apply except for the formula of $\hat{P}(\lambda)$ and $\hat{Q}(\lambda)$. $\hat{P}(\lambda)$ and $\hat{Q}(\lambda)$ due to these constant shear body forces are obtained by integrating the corresponding "point load" formula over the cell area. In particular, $\hat{P}(\lambda)$ and $\hat{Q}(\lambda)$ for the shear body forces symmetric with respect to the two coordinate axes are derived as

$$\hat{P}(\lambda) = -\pi \sum_{j=1}^{4} \mathrm{Im}\left[\frac{s_1{}^2 \left(c_{11}P_{xj} + c_{12}P_{yj}\right)}{\lambda^2} \hat{E}_1(\lambda, x_{0j}, y_{0j}) \right.$$
$$\left. + \frac{s_2^2 \left(c_{21}P_{xj} + c_{22}P_{yj}\right)}{\lambda^2} \hat{E}_2(\lambda, x_{0j}, y_{0j}) \right]$$
$$\hat{Q}(\lambda) = -\pi \sum_{j=1}^{4} \mathrm{Re}\left[\frac{s_1 \left(c_{11}P_{xj} + c_{12}P_{yj}\right)}{\lambda^2} \hat{E}_1(\lambda, x_{0j}, y_{0j}) \right. \tag{4.85}$$
$$\left. + \frac{s_2 \left(c_{21}P_{xj} + c_{22}P_{yj}\right)}{\lambda^2} \hat{E}_2(\lambda, x_{0j}, y_{0j}) \right]$$

where

$$\hat{E}_k(\lambda, x_{0j}, y_{0j}) = \mathrm{e}^{\lambda\left\{-\left[\eta_k(W/2-x_{0j}-d_j/2)-y_{0j}-h_j/2\right]\mathrm{i}+\rho_k\left(W/2-x_{0j}-d_j/2\right)\right\}}$$
$$- \mathrm{e}^{\lambda\left\{-\left[\eta_k(W/2-x_{0j}-d_i/2)-y_{0j}+h_j/2\right]\mathrm{i}+\rho_k\left(W/2-x_{0j}-d_j/2\right)\right\}}$$
$$- \mathrm{e}^{\lambda\left\{-\left[\eta_k(W/2-x_{0j}+d_i/2)-y_{0j}-h_j/2\right]\mathrm{i}+\rho_k\left(W/2-x_{0j}+d_j/2\right)\right\}}$$
$$+ \mathrm{e}^{\lambda\left\{-\left[\eta_k(W/2-x_{0j}+d_i/2)-y_{0j}+h_j/2\right]\mathrm{i}+\rho_k\left(W/2-x_{0j}+d_j/2\right)\right\}} \tag{4.86}$$

$(k = 1,\ 2)$; P_{xj} and P_{yj}, $j = 1, 4$, are the x- and y-components of the jth shear body force acting over jth cell corresponding to the loading configuration shown in Figure 4.7; h_j and d_j are the length and width of the jth cell centered at (x_{0j}, y_{0j}), respectively.

4.3.3 Stress intensity factor evaluation

There are two types of loads applied to the cracked sheet: shear body forces and the crack surface pressure $\sigma_0(\varsigma)$. As mentioned in Section 4.3.1, the solution of a cracked sheet subjected to the interfacial shear forces can be determined from the linear superposition of the solution of an uncracked sheet under the prescribed loads with that of the cracked sheet under crack surface pressure caused by these loads (see Figure 4.6). It then becomes clear that only the latter solution will contribute to the stress intensity factor, and the crack surface pressure $\Gamma(\varsigma)$ caused by the interfacial shear loads can be determined from Equations (4.59)–(4.60) of Section 4.3.1. Thus, it remains here to derive the stress intensity factors for a cracked sheet under a pressure loading $\Gamma(\varsigma)$ and $\sigma_0(\varsigma)$ on the crack faces. The stress intensity factors at the two tips of a crack with a length of $2a$ due to the crack surface loading of $\Gamma(\varsigma)$ are given by (Tada et al., 1985)

$$K_I(\pm a) = \int_{-a}^{a} \frac{\Gamma(\zeta)}{\sqrt{\pi a}} \sqrt{\frac{a \pm \zeta}{a \mp \zeta}}\, \mathrm{d}\zeta \tag{4.87}$$

Using Chebyshev quadrature formula (Krylov, 1962), the above integral is evaluated numerically as

$$K_I(\pm a) = \frac{4\sqrt{\pi a}}{2n+1} \sum_{k=1}^{n} \sin^2\left(\frac{k\pi}{2n+1}\right) \Gamma\left(\pm a \cos\left(\frac{2k\pi}{2n+1}\right)\right) \tag{4.88}$$

where n is the number of quadrature points, and a is the half crack length. In the above numerical integration for K_I, n is determined by increasing its (integer) value until the change in the estimates of the integral from the two consecutive values for n are within a prescribed percentage tolerance of 0.01. Finally, the stress intensity factors due to the pressure loading $\sigma_0(\varsigma)$ obviously can be obtained by the same manner.

4.4 Numerical Illustrations

To illustrate the analytical methods described in this chapter and to assess the accuracy of those methods, two example problems are considered in this section. These examples are those taken out from the papers by Duong et al. (2001a) and Duong and Yu (2002a). In the first example, the stress field in an *uncracked* sheet reinforced with a composite patch as shown in Figure 4.9 is obtained and compared with results from the FE method. The length and width of the patch are 15.24 and 10.16 cm, respectively. The material properties and thickness of the skin and the patch as well as the far-field stresses are given below:

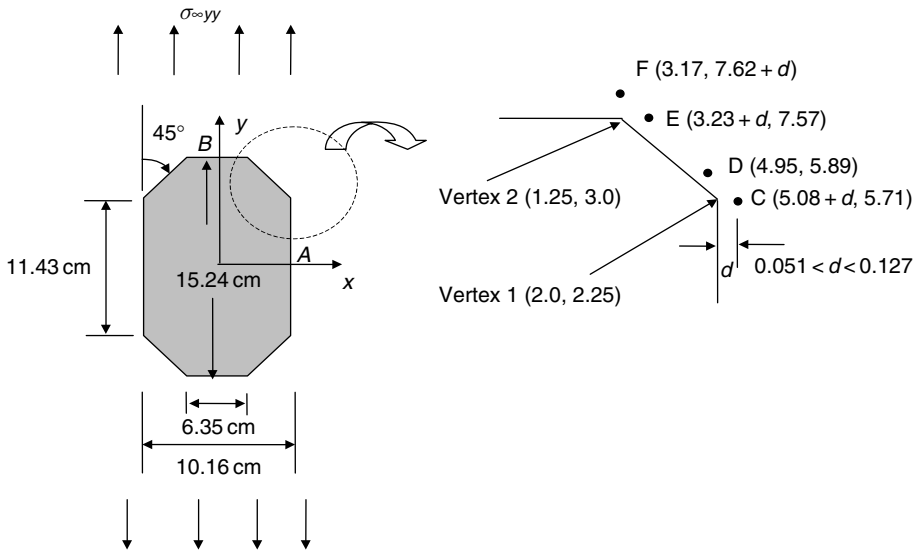

Fig. 4.9. Geometry of the first example problem. The coordinates of the points where the stresses are evaluated and compared are also listed.

Skin: Aluminum
$E = 72.4\,\text{GPa},\ \nu = 0.33,\ t_s = 1.6\,\text{mm}.$

Patch: Boron/Epoxy
$E_y = 193.6\,\text{GPa},\ E_x = 18.7\,\text{GPa},\ \nu_{yx} = 0.21,\ \mu = 5.5\,\text{GPa},\ t_p = 0.635\,\text{mm}$
$\sigma_{\infty x} = 0,\ \sigma_{\infty y} = 86.2\,\text{MPa}.$

This problem has been solved approximately by the analytical method outlined in Section 4.2.3 when eigenstrains are assumed to be polynomials of degree zero (constant) and polynomials of degree two (quadratic) in the global position coordinates (Duong et al., 2001a). The stresses along the line $y = 0$ are of special interest, since they are needed for stage II analysis of the Rose's approach. The normalized stress component σ_{yy} in the skin along the line $y = 0$ is plotted and compared with FE results in Figure 4.10. FE results are obtained by using FRANC2D/L code with eight-node isoparametric elements (Swenson and James, 1997). In the FE analysis, the adhesive is modeled as two-dimensional linear springs. Both typical and arbitrarily stiff adhesives are considered in the FE analysis. Typical values for shear modulus and thickness of an adhesive are 869.5 MPa and 0.127 mm, respectively. FE results for both cases of typical and stiff adhesives are presented in Figure 4.10, along with the analytical predictions. A small oscillation in FE results near the edge of the patch is probably due to the discontinuity in skin stresses at the patch edge and also due to severe straining in the adhesive. From Figure 4.10, analytical results are in excellent agreement with those from the FE method. In general, analytical results based on the higher-ordered eigenstrains are in better agreement with FE solutions. As the adhesive becomes stiffer, the difference in stresses between the analytical and the FE methods becomes smaller, as expected. For reference, the normalized stress $\sigma_{yy}/\sigma_{\infty yy}$ in the patch near the central region of Ω is also calculated and equals 2.3 and 2.1 according to constant and quadratic eigenstrain

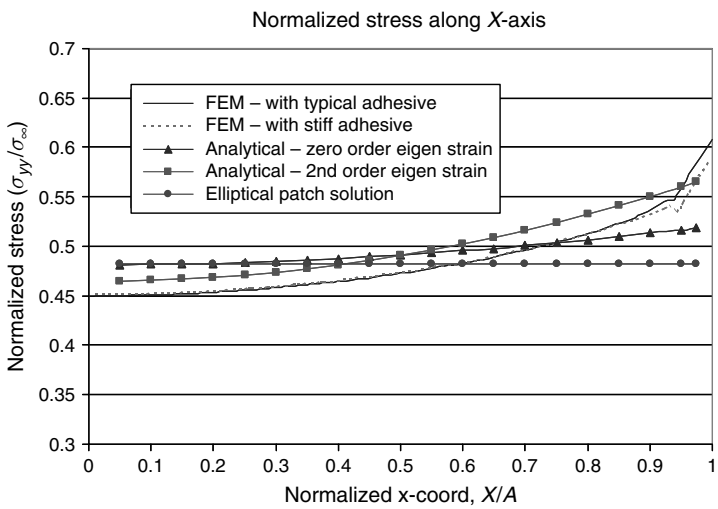

Fig. 4.10. Skin stress $\sigma_{yy}/\sigma_{\infty yy}$ underneath the patch and along the line $y = 0$.

Table 4.1. A comparison of the skin stress $\sigma_{yy}/\sigma_{\infty yy}$ at various locations just outside the patched region by different methods. The exact locations of these points are given in Figure 4.9. For points C, E, and F, the first number indicates the skin stress when $d = 1.27$ mm while the number given in parenthesis is for $d = 0.51$ mm.

Method	Point A	Point B	Point C	Point D	Point E	Point F
Analytical Zeroth ordered	0.662	1.303	0.690 (0.629)	0.961	1.304 (1.346)	1.415 (1.479)
Analytical Second ordered	0.644	1.278	0.680 (0.612)	0.998	1.330 (1.372)	1.435 (1.500)
FE based on stiff adhesive	0.620	1.240	0.804 (0.820)	0.922	1.278 (1.324)	1.376 (1.356)
FE based on typical adhesive	0.620	1.235	0.837 (0.850)	0.929	1.261 (1.288)	1.308 (1.322)

approximations, respectively, while the FE analysis using typical adhesive properties yields a result of 2.13.

The stresses in the skin just outside the patched area are also of practical interest due to possible high stress concentration or singularity there. These stresses are listed in Table 4.1 for various locations. The positions of these locations are defined in Figure 4.9. It was shown in Section 4.2.2 that the stresses at the vertices were weakly singular and of the logarithmic nature. Stress comparisons between analytical and FE results at the vertices are thus difficult unless a very fined mesh is employed in those local regions. To avoid this difficulty and just for a qualitative comparison, stresses at small distance away from the vertices are reported in Table 4.1 (see Figure 4.9 for positions of the reported points). The discrepancy between the analytical and the FE methods at points close to the vertices tends to be larger as their distance to the vertex decreases. It signifies the inability of the FE analysis in capturing the singularity with the presently employed mesh. For points adjacent to vertex 2, the agreement between two methods is fair for $d = 0.51$ mm (within 14%) and good for $d = 1.27$ mm (less than 10% difference). However, a much larger discrepancy is found for stresses at point C near vertex 1. It should be noted that the stress σ_{yy} is lower than the remote stress near vertex 1 but higher than the remote stress near vertex 2. As explained by Duong et al. (2001a), the amplitudes of the logarithmic singularity at vertices 1 and 2 obtained from the analytical method are in opposite signs as indicated in Table 4.2. The negative amplitude of the singularity near vertex 1 makes

Table 4.2. Amplitudes of the logarithmic singularity at vertices 1 and 2.

Method	Amplitude M_{xx} in $\sigma_{xx} \approx M_{xx} \log r$		Amplitude M_{yy} in $\sigma_{yy} \approx M_{yy} \log r$	
	Vertex 1	Vertex 2	Vertex 1	Vertex 2
Analytical Zeroth ordered	−123.2	123.2	−851.3	851.3
Analytical Second ordered	−152.1	139.6	−980.6	851.3

the stress field there very complicated, resulting in a rapid stress oscillation in FE results (which have not been shown here). This may attribute in part to the observed large discrepancy. Nevertheless, since stresses at point C near vertex 1 are not critical from the design viewpoint, this large discrepancy will not be resolved any further.

Finally, since the solution for an elliptical patch is relatively simple to obtain and available (Rose, 1981), it is therefore of practical interest to compare the present results with those for an elliptical patch of the same aspect ratio *A/B*. This comparison would provide a basis for assessing whether or not elliptical patch solution provides a sufficiently accurate estimate of the effect of patch aspect ratio for design purposes. The stress in the skin underneath an elliptical patch with the same aspect ratio *A/B* is uniform and also plotted in Figure 4.10 along with the FE and analytical results obtained previously for an octagonal patch. The elliptical patch solution is about 7% higher than FE result near the center. The normalized stresses in the skin at points A and B for the elliptical patch are found to be 0.55 and 1.39, respectively. The stress at point B in this case is approximately 12% higher than the corresponding FE result.

In the second example, a problem of a cracked repair with an octagonal patch under a uniform low operating temperature is considered. The repair configuration is shown in Figure 4.11. The effects of disbond and elastic-plastic adhesive (if any) will be ignored in the analysis. The material properties of the skin, patch, and adhesive as well as the temperature change used in the stage I and stage II analyses are given below:

Skin: Aluminum

$E = 72.4\,\text{GPa},\ \nu = 0.33,\ \alpha = 22.5\ \mu\,\text{per}\,^{\circ}\text{C},\ t_s = 1.6\,\text{mm}.$

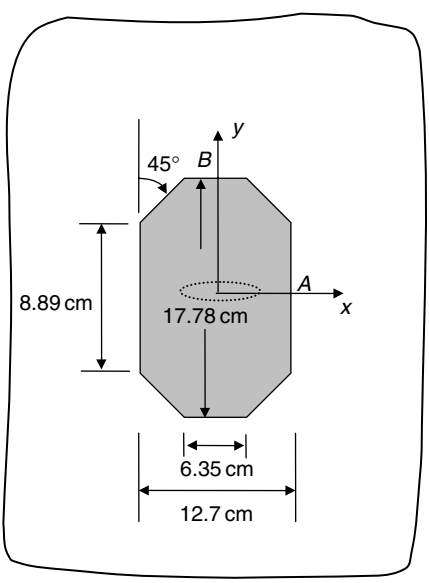

Fig. 4.11. Geometry of the second example problem.

Patch: Boron/Epoxy
$E_y = 193.6\,\text{GPa},\ E_x = 18.7\,\text{GPa},\ \nu_{yx} = 0.21,\ \mu = 5.5\,\text{GPa},\ t_\text{p} = 0.79\,\text{mm},$
$\alpha_y = 4.3\,\mu\,\text{per}\,^\circ\text{C},\ \alpha_x = 21.4\,\mu\,\text{per}\,^\circ\text{C}.$

Adhesive: FM-73
$G_\text{A} = 0.46\,\text{GPa},\ t_\text{A} = 0.127\,\text{mm}.$

Temperature change: $\Delta T = -75\,^\circ\text{C}.$

The sensitivity of the length of the repair cracks relative to the patch width is studied. Four crack lengths of 1.27, 2.54, 3.81, and 5.08 cm are considered in the analysis while the patch geometry is held constant. The thermal stress in the *uncracked* skin underneath the patch and along the line $y = 0$, resulting from stage I analysis, is plotted and compared with the FE solution in Figure 4.12. Stage I analysis is carried out using the method outlined in Section 4.2.4. FE results are obtained by using the commercial MSC/NASTRAN code (2001). The skin is modeled as a single layer of solid elements while the patch is modeled as six layers of solid elements, one for each ply. All elements are eight-node isoparametric solid elements. In the FE model, all nodes at the bottom of the skin surface are restrained from the out-of-plane displacement. The adhesive is modeled as one layer of anisotropic solids with very small extensional moduli. Stresses from FE analysis are those reported at the centroids of the solid elements and therefore are thickness-average stresses. From Figure 4.12, it appears that the analytical result is in general lower than the FE prediction, except near the edge of the patch, and they are in good agreement.

The crack-tip stress intensity factors are evaluated in stage II analysis using the method presented in Section 4.3. Their values are reported in Table 4.3 along with FE results.

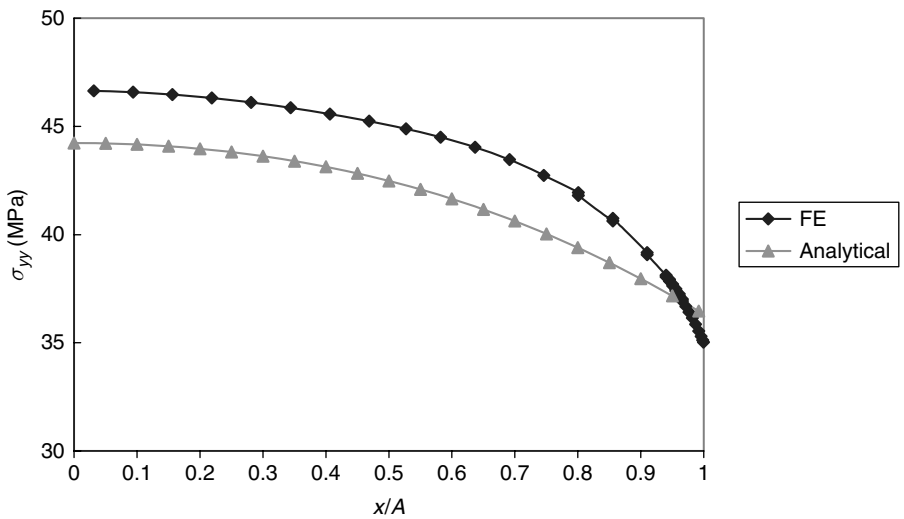

Fig. 4.12. Thermally induced skin stress σ_{yy} underneath the patch and along the line $y = 0$ for an uncracked patched skin subjected to a uniform temperature change of $-75\,^\circ\text{C}$.

Table 4.3. The stress intensity factors for a cracked skin repaired with an octagonal patch and being subjected to a uniform temperature change of −75 °C.

Half crack length, a (mm)	Analytical, K_I (MPa$\sqrt{m}$)	FE, K_I (MPa$\sqrt{m}$)
1.27	3.740	4.304
2.54	3.796	4.298
3.81	3.807	4.214
5.08	3.772	4.024

Typical telescopic grids used in the theoretical analysis are given in Figure 4.13. FE results are again obtained by using MSC/NASTRAN code (2001) with the crack actually being modeled. The skin, patch, and adhesive are modeled in a similar manner as for the case without a crack, but with a much finer mesh around the crack. A special 3-D crack-tip element is used in the MSC/NASTRAN analysis to compute the stress intensity factor. This crack-tip element is based on the hybrid assumed stress approach and is compatible with the regular displacement-based elements. Since the skin is modeled as a single layer of solid elements, the stress intensity factor obtained from the FE analysis is the mid-plane value. From Table 4.3, results from the two methods are in good agreement within 13%. However, the analytical results show a different trend when compared with the one predicted by the FE method. According to Duong and Yu (2002a), several factors might attribute to such discrepancy. First, the analytical method underestimates both the thermal stresses and their gradients in an uncracked skin (see Figure 4.12). Secondly, as shown in Section 3.3.4, the stress intensity factor for a patched cracked sheet with a uniform pressure acting on the crack surfaces will be nearly constant

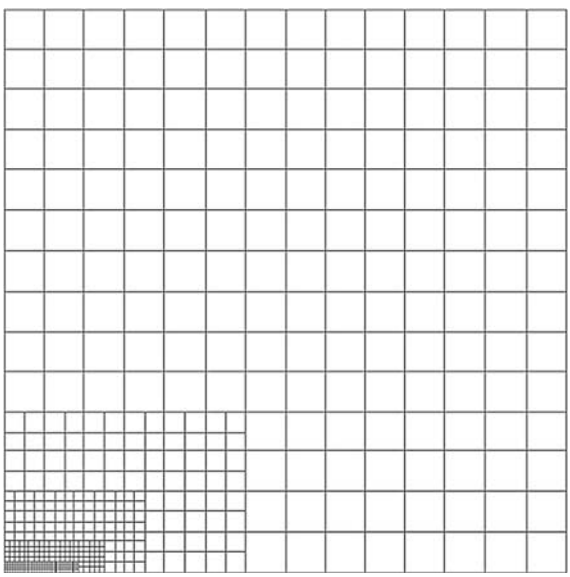

Fig. 4.13. Typical telescopic grids used in stage II analysis for evaluating the stress intensity factor.

and thus independent of the crack length when the crack exceeds a critical length Λ, provided that there is no edge boundary effect. Using Equation (3.27) for Λ together with appropriate material properties of the present skin, patch, and adhesive, this critical crack length is computed to be about 2.5 mm. Since all crack lengths considered in the present analyses exceed that critical length, the stress intensity factors are therefore expected to be nearly constant and probably (based on intuition) slightly higher for a longer crack in the uniform thermal stress field. This is what we observe from Table 4.3 for the crack length ratio $a/A < 0.4$. However, since the thermal stress field is a decreasing function of the x-coordinate which is more pronounced for $x/A > 0.4$, K_I may decrease with an increase in crack length for $a/A > 0.4$. Furthermore, since quite different meshes have been employed for different crack lengths in the FE analyses, this variation of meshes will definitely contribute partially to the mentioned discrepancy. For reference, the skin stress near the patch edge at $x = 0$ (point B of Figure 4.11) is found to be compressive with a value equal to -35.2 MPa from both analytical and FE methods.

To assess the effect of these thermal stresses on crack patching efficiency, the second example problem is reanalyzed for the case of far-field-mechanical loading only. The far-field stress is assumed to be 103.4 MPa, a typical fatigue stress range in transport aircraft fuselage. The stress in the *uncracked* skin along the line $y = 0$, resulting from stage I analysis, is plotted in Figure 4.14 for comparison with that from the case of thermal loading only. Figure 4.14 also includes parallel results from the FE method. The skin stress near the patch edge at point B is found to be tensile and close to 131 MPa from both methods. The crack-tip stress intensity factors for the latter loading case are reported in Table 4.4. From Tables 4.3 and 4.4, it appears that (a) analytical prediction for the mechanical loading case is more accurate than the former thermal loading, and (b) the thermal effect on the stress intensity factor can be very significant. For the same repair configuration, the thermal stress intensity factor can be more than 65% of that

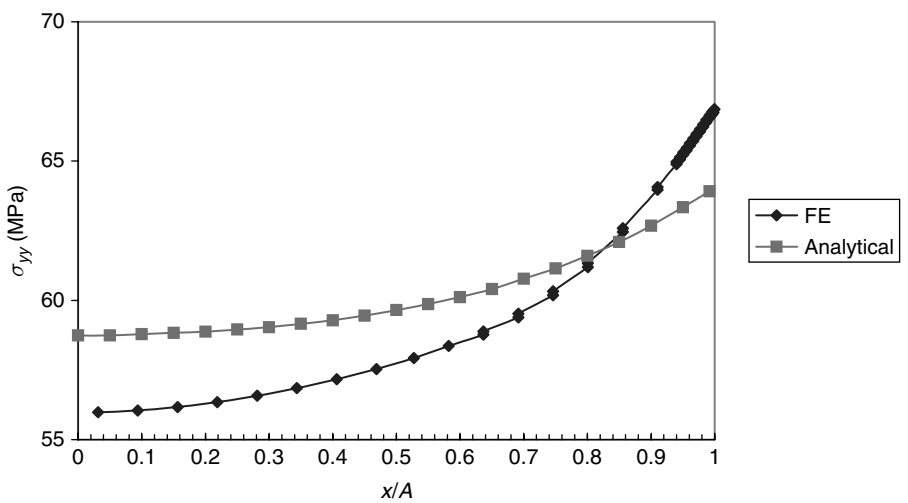

Fig. 4.14. Skin stress σ_{yy} underneath the patch and along the line $y = 0$ for an uncracked patched skin subjected to a far-field stress of 103.4 MPa.

Table 4.4. The stress intensity factors for a cracked skin repaired with an octagonal patch and being subjected to a far-field stress of 103.4 MPa.

Half crack length, a (mm)	Analytical, K_I (MPa$\sqrt{m}$)	FE, K_I (MPa$\sqrt{m}$)
1.27	4.973	5.154
2.54	5.211	5.260
3.81	5.522	5.403
5.08	5.952	5.655

resulting from the fatigue load. Thus, the effect of thermal stresses is to increase the crack-tip stress intensity factor while reducing the load attraction.

4.5 Thermal Constraints

In Section 4.2.4, for simplicity, the residual thermal stresses associated with curing of the adhesive have been obtained approximately by assuming that the skin is infinite and the steady state temperature distribution is a step function. However, in practice, structures to be reinforced may be finite in size or constrained by the surrounding structure. In addition, in reality the steady state temperature distribution is not represented by a step function. A method to quantify the effects of the structure's finite size and of the realistic temperature distribution on the thermal stresses is therefore given in this section, following the work of Wang et al. (2000).

Consider the configuration shown in Figure 4.15, in which an isotropic skin plate is reinforced by a circular patch of radius R_i. The coordinate system x_1–x_2 is chosen so

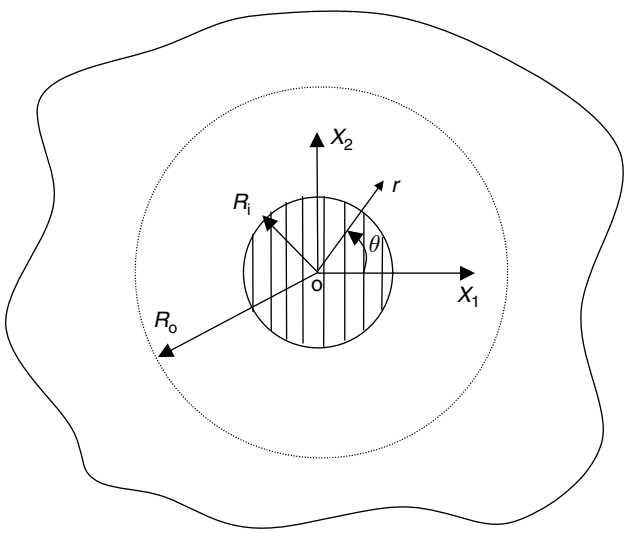

Fig. 4.15. Geometry of an infinite plate reinforced with a circular composite patch (Wang et al., 2000).

that the principal axes of the orthotropic patch are aligned and parallel to the x_1, x_2 axes. During the first step of bonding, suppose that the inner portion ($r < R_i$) is heated to a temperature T_i during the curing process, while the outer portion ($r \geq R_o$) is heated to T_o, with the usual convention that the ambient temperature is taken as the zero of temperature. The temperature field satisfies the Laplacian equation:

$$\nabla^2 T = 0 \tag{4.89}$$

which has the following solution:

$$T^{H}(r) = \begin{cases} T_i & r < R_i \\ T_o + (T_i - T_o)\frac{\ln(r/R_o)}{\ln(R_i/R_o)} & R_i < r < R_o \\ T_o & R_o < r \end{cases} \tag{4.90}$$

where the superscript H denotes the temperature change corresponding to the first step: heating. A schematic of the temperature distribution is shown in Figure 4.16. Due to this non-uniform temperature distribution, thermal stresses (equal biaxial) develop in the skin, which can be readily derived (Timoshenko and Goodier, 1970):

$$\sigma_{ij}^{s(H)} = -\frac{1}{2}\alpha_s E_s (T_i - T_o)\delta_{ij} \tag{4.91}$$

where α_s and E_s denote the thermal expansion coefficient and Young's modulus of the skin. Since $T_i - T_o > 0$ during heating, the above thermal initial stress is compressive, as expected. It should be noted that this thermal stress arises only in the case of localized heating of a large structure; for the case of a finite size specimen being uniformly heated to T_i, no thermal stress will develop. This stress distribution serves as the initial stress that will be added to the thermal stress induced by cooling the patched region down to the ambient temperature. On the other hand, it will be assumed that there is no shear stress in the adhesive layer during curing, so that the reinforcing patch expands freely without developing any stresses.

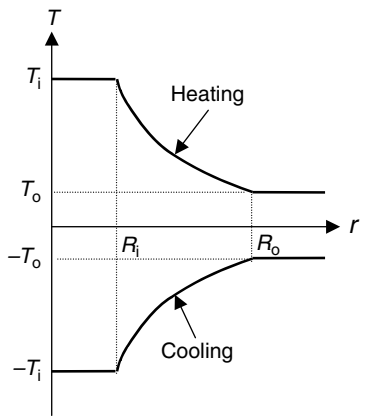

Fig. 4.16. Temperature distribution during heating and cooling (Wang et al., 2000).

After the adhesive is fully cured, the patched skin is cooled down to the ambient temperature. Thus, in the second step of adhesive bonding, the temperature change over the entire patched skin is subjected to the following temperature field, referring to Figure 4.16:

$$T^{\mathrm{C}}(r) = -T^{\mathrm{H}}(r) \tag{4.92}$$

where the superscript C denotes the temperature change corresponding to the second step: cooling. Now the problem is to determine the thermal stress $\sigma_{ij}^{\mathrm{s(C)}}$ on cooling to ambient temperature after curing. The final stress in the skin plate is thus equal to

$$\sigma_{ij}^{\mathrm{s}} = \sigma_{ij}^{\mathrm{s(H)}} + \sigma_{ij}^{\mathrm{s(C)}} \tag{4.93}$$

During this cooling process, it is assumed that the adhesive bond between the composite patch and the metal skin is absolutely rigid, so that the same strain-state prevails in both the patch and the skin directly beneath the patch. To quantify the finite size effect, Wang et al. used the model shown in Figure 4.17 to estimate thermal stresses in the skin and patch for various degree of constraints. The model shown in Figure 4.17 is an uncracked circular skin plate of radius R_0 reinforced with a concentric patch of radius R_i. The outer edge $r = R_{\mathrm{o}}$ is constrained by a continuous distribution of springs according to the following relation:

$$\sigma_{\mathrm{rr}}(r = R_{\mathrm{o}}) = -k_{\mathrm{s}} E_{\mathrm{s}} u_{\mathrm{r}}(r = R_{\mathrm{o}}) \tag{4.94}$$

For an infinite plate, k_{s} must set to

$$k_{\mathrm{s}} = \frac{1}{(1+\nu_{\mathrm{s}})R_{\mathrm{o}}} \tag{4.95}$$

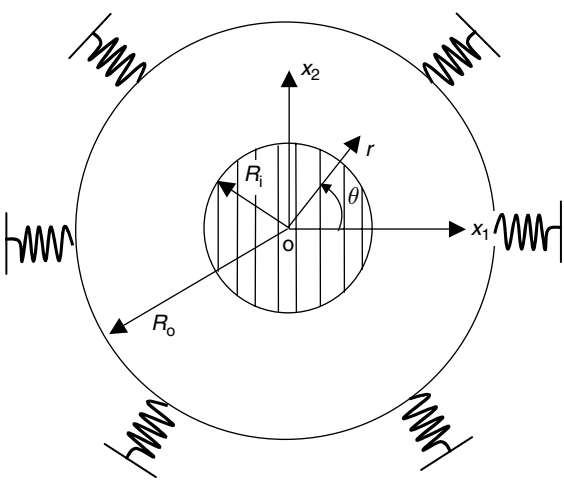

Fig. 4.17. Spring representation for simulating finite size effect (Wang et al., 2000).

On the other hand, the cases of free edge and a clamped edge at $r = R_o$ correspond to setting $k_s = 0$ and $k_s \to \infty$, respectively. To determine the thermal stresses developed in the patch and skin, the patched region is first cut out from the plate, and then surface tractions of equal magnitude but opposite in sign are applied, respectively, around the outer edge of the cut region and the hole of the skin plate. The unknown tractions are determined by closing the "gap" between the patch and the hole; in doing so, continuity in both the tractions and the displacement across the imaginary cut has to be satisfied simultaneously. Using that approach, Wang et al. (2000) derived explicitly the following stress results for the skin and patch during the cooling step:

$$\begin{Bmatrix} \sigma_{11}^{s(C)} \\ \sigma_{22}^{s(C)} \end{Bmatrix} = [C^s] \begin{Bmatrix} \varepsilon_{11}^{I} + \alpha_s T_i \\ \varepsilon_{22}^{I} + \alpha_s T_i \end{Bmatrix} \tag{4.96}$$

$$\begin{Bmatrix} \sigma_{11}^{p(C)} \\ \sigma_{22}^{p(C)} \end{Bmatrix} = [C^p] \begin{Bmatrix} \varepsilon_{11}^{I} + \alpha_{11}^{p} T_i \\ \varepsilon_{22}^{I} + \alpha_{22}^{p} T_i \end{Bmatrix} \tag{4.97}$$

where

$$\begin{Bmatrix} \varepsilon_{11}^{I} \\ \varepsilon_{22}^{I} \end{Bmatrix} = \left[C^I\right]^{-1} \begin{Bmatrix} l_1 \\ l_2 \end{Bmatrix} + \begin{Bmatrix} \alpha_{11}^{I} \\ \alpha_{22}^{I} \end{Bmatrix} (-T_i) \tag{4.98}$$

$$\begin{Bmatrix} \alpha_{11}^{I} \\ \alpha_{22}^{I} \end{Bmatrix} = \left[C^I\right]^{-1} [C^s] \begin{Bmatrix} \alpha_s \\ \alpha_s \end{Bmatrix} + \frac{t_p}{t_s} \left[C^I\right]^{-1} [C^p] \begin{Bmatrix} \alpha_{11}^{p} \\ \alpha_{22}^{p} \end{Bmatrix} \tag{4.99}$$

$$\begin{Bmatrix} l_1 \\ l_2 \end{Bmatrix} = \begin{Bmatrix} \frac{\left(\alpha_{11}^{I} - b_T\right) d_{22} - \left(\alpha_{22}^{I} - b_T\right) d_{12}}{d_{11} d_{22} - d_{12}^2} T_i \\ \frac{\left(\alpha_{22}^{I} - b_T\right) d_{11} - \left(\alpha_{11}^{I} - b_T\right) d_{21}}{d_{11} d_{22} - d_{12}^2} T_i \end{Bmatrix} \tag{4.100}$$

$$b_T = \frac{\alpha_s \chi_T}{1 - \chi_T R_i^2 / R_o^2} \left\{ \frac{T_o}{T_i} - \frac{R_i^2}{R_o^2} - \frac{(1 - R_i^2/R_o^2)(1 - T_o/T_i)}{2 \ln(R_i/R_o)} \right\} \tag{4.101}$$

$$\chi_T = \frac{1 - (1 + \nu_s) k_s R_o}{1 + (1 - \nu_s) k_s R_o} \tag{4.102}$$

$$\begin{aligned} d_{11} &= \frac{1}{E_{11}^{I}} + \frac{\gamma_1^T}{E_s} \\ d_{12} = d_{21} &= -\frac{\nu_{12}^{I}}{E_{11}^{I}} - \frac{\gamma_2^T}{E_s} \\ d_{22} &= \frac{1}{E_{22}^{I}} + \frac{\gamma_1^T}{E_s} \end{aligned} \tag{4.103}$$

$$\gamma_1^{\mathrm{T}} = \frac{(3-\nu_{\mathrm{s}})\,\eta_{\mathrm{T}} + (1+\nu_{\mathrm{s}})\,\lambda_{\mathrm{T}}}{2} \tag{4.104}$$

$$\gamma_2^{\mathrm{T}} = \frac{(3-\nu_{\mathrm{s}})\,\eta_{\mathrm{T}} - (1+\nu_{\mathrm{s}})\,\lambda_{\mathrm{T}}}{2}$$

$$\eta_{\mathrm{T}} = \frac{3-\nu_{\mathrm{s}} + (7+3\nu_{\mathrm{s}})\,R_i^2/R_0^2 + (1-3\nu_{\mathrm{s}})\,R_i^4/R_0^4 + (1+\nu_{\mathrm{s}})\,R_i^6/R_{\mathrm{o}}^6}{(3-\nu_{\mathrm{s}})\left(1-R_i^2/R_0^2\right)^3} \tag{4.105}$$

$$\lambda_{\mathrm{T}} = \frac{1+\nu_{\mathrm{s}} + \chi_{\mathrm{T}}\,(1-\nu_{\mathrm{s}})\,R_i^2/R_0^2}{(1+\nu_{\mathrm{s}})\left(1-\chi_{\mathrm{T}}R_i^2/R_0^2\right)} \tag{4.106}$$

$[C^{\mathrm{s}}]$, $[C^{\mathrm{p}}]$, and $\left[C^{\mathrm{I}}\right]$ are defined by Equations (4.31), and (4.32) of Section 4.2.3 and choosing $t_{\mathrm{I}} = t_{\mathrm{s}}$; $\left[C^{\mathrm{I}}\right]^{-1}$ is the inverse of $\left[C^{\mathrm{I}}\right]$; E_{11}^{I}, E_{22}^{I}, ν_{12}^{I} can be found from the following relation:

$$\begin{bmatrix} \dfrac{1}{E_{11}^{\mathrm{I}}} & -\dfrac{\nu_{12}^{\mathrm{I}}}{E_{11}^{\mathrm{I}}} & 0 \\ -\dfrac{\nu_{21}^{\mathrm{I}}}{E_{22}^{\mathrm{I}}} & \dfrac{1}{E_{22}^{\mathrm{I}}} & 0 \\ 0 & 0 & \dfrac{1}{G_{12}^{\mathrm{I}}} \end{bmatrix} = \left[C^{\mathrm{I}}\right]^{-1} \tag{4.107}$$

The results given by Equations (4.96)–(4.106) are not exact as pointed out by Wang et al. (2000), since the stresses in the patch and in the skin underneath the patch assume to be uniform in the derivation. In general, due to the finite size of the plate, these stresses are not constant. However, the error arising from this assumption will be small provided that the outer radius is reasonably greater than the inner radius. As a matter of fact, for $R_0/R_i \geq 3$, this error is anticipated to be less than 1%.

It is interesting to note that when the patch is isotropic, the thermal residual stresses $\sigma_{11}^{\mathrm{s(C)}}$ and $\sigma_{22}^{\mathrm{s(C)}}$ are given by the following simple expression, assuming that the thermal expansion coefficient, the Poisson's ratio, and the modulus of the patch are α_{p}, ν_{p}, and $\mathrm{E_p}$, respectively:

$$\sigma_{11}^{\mathrm{s(C)}} = \sigma_{22}^{\mathrm{s(C)}} = \sigma_0^{(\mathrm{C})} = \alpha_{\mathrm{s}}E_{\mathrm{s}}T_i\frac{(1-\nu_{\mathrm{s}})(1-b_{\mathrm{T}}/\alpha_{\mathrm{s}}) + (1-\alpha_{\mathrm{p}}/\alpha_{\mathrm{s}})(1+\nu_{\mathrm{s}})S\lambda_{\mathrm{T}}}{(1-\nu_{\mathrm{p}})(1+\lambda_{\mathrm{T}}+\lambda_{\mathrm{T}}\nu_{\mathrm{s}}-\nu_{\mathrm{s}}) + (1-\nu_{\mathrm{s}}^2)S\lambda_{\mathrm{T}}} \tag{4.108}$$

When the skin is also infinite, i.e., $k_s = 1/(1+\nu_{\mathrm{s}})R_0$, and $T_0 = 0$, Equation (4.108) is reduced to

$$\sigma_0^{(\mathrm{C})} = \alpha_{\mathrm{s}}E_{\mathrm{s}}T_i\frac{1-\nu_{\mathrm{p}} + (1-\alpha_{\mathrm{p}}/\alpha_{\mathrm{s}})(1+\nu_{\mathrm{s}})S}{2(1-\nu_{\mathrm{p}}) + (1-\nu_{\mathrm{s}}^2)S} \tag{4.109}$$

where S is the patch stiffness ratio, i.e., $S = \frac{E_{\mathrm{p}}t_{\mathrm{p}}}{E_{\mathrm{s}}t_{\mathrm{s}}}$.

The total thermal stress from heating and cooling phases of the curing cycle for this particular case of infinite skin and isotropic patch is finally given by

$$\sigma_s = -\frac{E_s S(1+\nu_s)}{2(1-\nu_p)+(1-\nu_s^2)S}\left[\alpha_p - \frac{\alpha_s(1+\nu_s)}{2}\right]T_i \tag{4.110}$$

for the skin under patch.

To validate the present theory and to examine the accuracy of the solution for finite size plate, a detailed FE analysis is carried out for both an isotropic patch and an orthotropic patch, simulating a cross-ply laminate composite patch. The properties and dimensions of the isotropic patch and the orthotropic patch are summarized in Tables 4.5 and 4.6, respectively. The ratios of the outer radius to inner radius, R_o/R_i, will be varied to investigate the size effect. Comparisons of the stresses in the skin plate as obtained using the FE method and the analytical solutions are shown in Figure 4.18 and 4.19. It is seen that the closed-form solution is in very good agreement with the FE results. More importantly the solution based on an equivalent isotropic reinforcement, which takes the major properties of the orthotropic reinforcement, provides a reasonably good correlation with the FE results. Thus, for an orthotropic patch, the maximum thermal residual stress in skin is well approximated by the solution for isotropic patch, which takes the major properties of the orthotropic patch.

It remains now to show how the curing model developed in Section 4.2.4 using a simplified (step) temperature distribution compares with the present results. A cursory example taken out from the paper by Duong and Yu (2002a) is, therefore, presented here. The thermal residual stresses are obtained and compared for one specific repair configuration using the simple curing model outlined in Section 4.2.4 and the present model. In these analyses, the patch is assumed to be circular and isotropic. The radius of the patch is 12.7 cm. The patch and skin properties are given below.

Table 4.5. Properties and dimensions of isotropic patch used in thermal stress analyses for a comparison between Wang and Rose's closed-form and FE solutions.

Material	Young's modulus (GPa)	Poisson's ratio	Thickness (mm)	Thermal coefficient
Skin	71	0.3	1.0	23×10^{-6}
Patch	156	0.3	0.5	6.24×10^{-6}

Table 4.6. Properties and dimensions of orthotropic patch used in thermal stress analyses for a comparison between Wang and Rose's closed-form and FE solutions.

Material	Young's modulus (GPa)	Poisson's ratio	Thickness (mm)	Thermal coefficient
Skin	71	0.3	3.0	23×10^{-6}
Patch	$E_1 = 156$ $E_2 = 29.7$	$\nu_{21} = 0.1097$ $\nu_{12} = 0.5762$	1.5	$\alpha_1 = 6.24 \times 10^{-6}$ $\alpha_2 = 16.96 \times 10^{-6}$

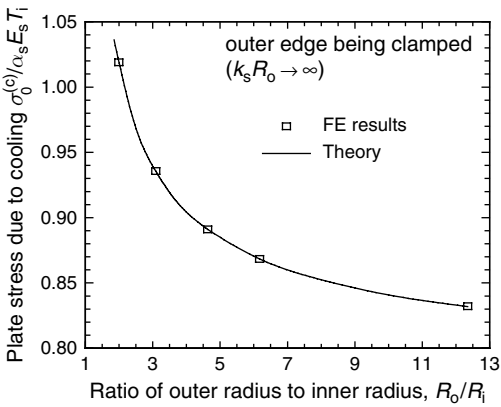

Fig. 4.18. Thermal residual stress resulting from cooling a circular isotropic patch over a concentric plate with outer edge being clamped.

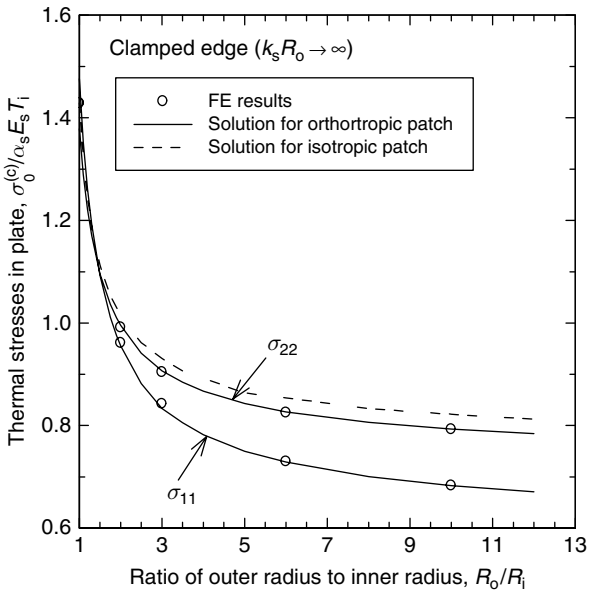

Fig. 4.19. Thermal residual stress resulting from cooling a circular orthotropic patch over a concentric plate with outer edge being clamped.

Skin: Aluminum
$E_s = 72.4\,\text{GPa},\ \nu_s = 0.33,\ \alpha_s = 22.5\,\mu$ per °C, $t_s = 1.6\,\text{mm}$.

Patch: Boron/Epoxy
$E_p = 193.6\,\text{GPa},\ \nu_p = 0.21,\ t_p = 0.79\,\text{mm},\ \alpha_p = 4.3\,\mu$ per °C

Temperature change: $\Delta T = -75\,°\text{C}$.

Table 4.7. A comparison of *y*-component thermal stresses between Wang and Rose's and Duong and Yu's curing models for a circular isotropic patch.

R_0/R_i	Wang and Rose's model		Duong and Yu's model	
	σ_s (MPa)	σ_p (MPa)	σ_s (MPa)	σ_p (MPa)
3	48.8	−140.5	–	–
4	46.4	−136.7	–	–
7	43.6	−131.1	–	–
Infinite plate	36.8	−111.8	36.8	−111.8

In order to use the curing model developed in Section 4.2.4, the shape of the heated region, but not its size, must be specified, since thermal stresses are only affected by shape of the heated region provided that this region is large enough to fully cover the patch. The heated region is thus specified to be circular as well.

To quantify the size effect, analyses using the present curing model are performed for different R_0 with a free edge condition as well as for the case of an infinite plate. Results from these analyses are then compared with the result from the simple curing model in Table 4.7 for $T_i - T_0 = -75\,°C$. From Table 4.7, it is clear that the previous model agree very well with the present model for an infinite plate.

It should be emphasized that while the previous curing model accounts for the effect of the patch shape, it does not account for the realistic temperature distribution and the structure finite size effect. Vice versa, the present model accounts for these latter effects but not the effect of the patch shape. However, through this cursory example, since two models give the same result for an infinite plate reinforced with a circular patch, one can improve the previous curing model via an engineering approach by introducing a "finite size" correction factor which is determined by performing the thermal stress analysis using the present curing model for a circular patch twice for a finite and infinite skin and computing the ratio of these two results.

4.6 Summary

This chapter presents an analytical method for analyzing a bonded repair with a polygon-shaped patch using Rose's two-stage analysis procedure. Different methods are employed for different stages of the analysis. The equivalent inclusion method by Eshelby combining with the computational algorithm for a polygonal inclusion are used for the stage I analysis. On the other hand, the stage II fracture analysis employs the displacement compatibility method. These methods are robust and versatile. In general, accurate results can be obtained from the developed analytical method without recourse to the FE method where it requires a substantial effort of modeling or meshing.

CHAPTER 5

Approximate Theory of Unsupported One-Sided Crack Patching

5.1 Introduction

In Chapter 4, the mathematical theory of either two-sided crack patching or supported one-sided patching was presented. When the structure is bonded symmetrically with one patch on each side, there is no secondary bending. Since most often only one face of a structure to be repaired is accessible and sometimes only one side of the structure is allowed to be patched for other reasons, one-sided repairs are often adopted in practical applications. In this case, if the structure is well supported against out-of-plane deflection, for example, by stiffeners attached to one side of the structure, then the analytical methods developed in Chapter 4 still can be used to assess the structural integrity of these one-sided repairs. Otherwise, new analytical models must be developed to address the effect of out-of-plane deflection associated with one-sided patching, and they will be presented in this chapter.

A two-stage analysis method similar to that considered in Chapter 4 will be employed in this chapter for solving a one-sided repair subjected to remote stresses and to a temperature excursion. In the first stage, a problem of an uncracked structure rigidly bonded with a patch is solved, as before. The stress distribution along the prospective crack path is determined. Due to the out-of-plane deflection, at any point in the plate, the stress varies through the plate thickness, resulting in membrane and bending components. In stage II, the problem of a crack pressurized by a combination of membrane force and bending moment is solved using a crack bridging model. In a geometrically linear analysis of a one-sided repair, both stage I and stage II will be performed within a geometrically linear analysis, and the mentioned two-stage procedure is merely a demonstration of the linear superposition method. On the other hand, in a geometrically nonlinear analysis of a repair, for simplicity, stage I will be solved within the framework of geometrically nonlinear elasticity while in stage II it is assumed the repaired region deforms geometrically linearly. This method is referred by Wang and Rose (1999) as the hybrid method. Wang and Rose (1999) had shown that the hybrid method will provide

reasonable results for the stress intensity factors when compared with those obtained from the full geometrically nonlinear FE analysis.

Before proceeding to the analyses of one-sided crack patching, the reader is reminded of the notations used in this chapter. As in Chapter 4 and throughout this book, within a topic of the equivalent inclusion method, C^{I}_{ijkl} denotes the moduli of the inhomogeneity and therefore of the inhomogeneous (patching) region Ω while σ^{I}_{ij} and $\varepsilon^{\mathrm{I}}_{ij}$ indicate the stress and strain fields in the inhomogeneity problem, respectively, and they describe stresses and strains of points both inside and outside Ω. In contrast, the superscript I when it is used within the context of a one-dimensional analysis will always denote the overlap or the patching region. Thus, within the context of a 1-D analysis, σ^{I}_{ij} and $\varepsilon^{\mathrm{I}}_{ij}$ will indicate the stress and the strain solutions in the overlap, respectively.

5.2 Stage I: Geometrically Linear Analysis

As in Chapter 4, stage I will be solved in this section by using the equivalent inclusion method. However, as shown later in Section 5.2.2, that method when extended to the problem of a bending plate will require a solution of an inclusion with a constant eigencurvature. The eigencurvature is defined here as the initial, thermal, or inelastic curvature which is prescribed in a finite subdomain Ω of an infinite plate and vanishes outside Ω, in the same spirit as the eigenstrain discussed in Chapter 4.

5.2.1 Inclusion with constant eigencurvature

Closed-form solution for an inclusion problem with a constant eigencurvature is presented in this section. While most existing works on inclusion problems are concerned with a plane or three-dimensional solid containing eigenstrains, only few deal with a plate containing eigencurvatures. Beom (1998) was the first one to derive the solution for the elastic fields in a plate containing an elliptical inclusion with a uniform eigencurvature. Beom's approach (1998) was later extended by Duong and Yu (2003a) to include analyses of polygonal inclusions. In Duong and Yu's approach, the curvature and the resultant moment are obtained by performing the integrations according to the algorithmic solution procedure given in Chapter 4 for a 2-D planar inclusion with eigenstrains.

(a) Polygonal inclusion

Consider a deformation of an infinite isotropic plate with moduli C^{s}_{ijkl} and thickness of t_{s}, containing a polygonal subregion Ω in which a uniform eigencurvature κ^{*}_{ij} is prescribed. Following Beom (1998), the curvature $\kappa_{ij}(\mathbf{x})$ and the eigencurvature κ^{*}_{ij} are related by an Eshelby-type tensor K_{ijkl} such that

$$\kappa_{ij}(\mathbf{x}) = K_{ijkl}(\mathbf{x})\,\kappa^{*}_{kl} \tag{5.1}$$

where

$$\kappa_{ij}(\mathbf{x}) = -\frac{\partial^2 w}{\partial x_i \partial x_j} \qquad (i,\ j,\ k,\ l = 1,\ 2) \tag{5.2}$$

$$K_{ijkl}(\mathbf{x}) = -\left[\int_{\Omega} \tilde{M}_{kl}(\mathbf{x}', \mathbf{x}) d\mathbf{x}'\right]_{,ij}$$

$$\tilde{M}_{kl}(\mathbf{x}', \mathbf{x}) = -\frac{1}{4\pi}\left[(1+\nu_s)\ln\rho\ \delta_{kl} + (1-\nu_s)\frac{(x_k' - x_k)(x_l' - x_l)}{\rho^2}\right] \tag{5.3}$$

$$\rho = |\mathbf{x}' - \mathbf{x}| = \sqrt{(x_1' - x_1)^2 + (x_2' - x_2)^2}$$

where w is the transverse displacement, $\mathrm{d}\mathbf{x}' = \mathrm{d}x_1' \cdot \mathrm{d}x_2'$, δ_{ij} is the Kronecker delta, ν_s is the Poisson's ratio, and the subscript comma denotes a partial differentiation with respect to the in-plane coordinates x_1 and x_2.

Introducing integrals $\hat{H}$ and $\hat{H}_{kl}$ defined, respectively, by

$$\hat{H}(\mathbf{x}) = \int_{\Omega} (\ln\rho)\mathrm{d}x_1'\mathrm{d}x_2'$$

$$\hat{H}_{kl}(\mathbf{x}) = \int_{\Omega} \frac{(x_k' - x_k)(x_l' - x_l)}{\rho^2}\mathrm{d}x_1'\mathrm{d}x_2' \tag{5.4}$$

then $K_{ijkl}(\mathbf{x})$ in the second equation of (5.2) can be rewritten as

$$K_{ijkl}(\mathbf{x}) = \frac{1}{4\pi}\left[(1+\nu_s)\hat{H}_{,ij}\delta_{kl} + (1-\nu_s)\hat{H}_{kl,ij}\right] \tag{5.5}$$

An algorithm to evaluate K_{ijkl} as prescribed by Equation (5.5) for an arbitrarily polygonal region will be outlined in the next part of this section. Once K_{ijkl} and κ_{ij} are determined, respectively, from Equations (5.5) and (5.1), the resultant moment is then computed from the curvature similar to the case of eigenstrain as

$$M_{ij} = \begin{cases} D^s_{ijkl}(\kappa_{kl} - \kappa^*_{kl}) & \text{inside } \Omega \\ D^s_{ijkl}\kappa_{kl} & \text{outside } \Omega \end{cases} \tag{5.6}$$

where D^s_{ijkl} is the bending stiffness tensor, i.e., $D^s_{ijkl} = \int_0^{t_s} C^s_{ijkl}(x_3 - h_0)^2\ \mathrm{d}x_3$ and h_0 is the x_3-coordinate of the reference plane of the skin plate.

Solution algorithm for Polygonal inclusion K_{ijkl} is evaluated by using the computational algorithm given in part (b) of Section 4.2.2. This algorithm will be briefly summarized here. The reader should refer to Section 4.2.2(b) for more details. This algorithm is implemented in three stages. First, the inclusion domain Ω is decomposed into a set of triangular elements in such a way that $\mathbf{x}$, the point where the solution is evaluated is a common vertex of all the elements (see Figure 4.3). Second, $\hat{H}(\mathbf{x})$, $\hat{H}_{kl}(\mathbf{x})$, and thus K_{ijkl} are calculated for each element in its element coordinate system and the components of K_{ijkl} transformed to global coordinates. Third, K_{ijkl} is assembled from the elemental contributions. The elemental tensor K_{ijkl} will be derived here for a simplex in its element coordinate system.

Referring to Figure 4.3 of Chapter 4, the element coordinate system can be described as follows. It has the origin at $\mathbf{x}$, basis vector ($\mathbf{n}$, $\mathbf{t}$), and the corresponding coordinates (η, ζ). In these coordinates, the positions of vertices are represented by the pairs (b, c^+) and (b, c^-). For a convex polygon, b is positive when $\mathbf{x}$ is an interior point of Ω and becomes negative for otherwise. For a simplex with one of the vertices defined by (b, c), $\hat{H}(\mathbf{x})$ and $\hat{H}_{kl}(\mathbf{x})$ in Equation (5.4) can be rewritten as

$$\begin{aligned}
\hat{H}(\mathbf{x}) &= \frac{1}{2}\int_0^b \int_0^{c\eta/b} \ln\left(\eta^2+\zeta^2\right)\mathrm{d}\zeta\,\mathrm{d}\eta \\
\hat{H}_{\zeta\zeta}(\mathbf{x}) &= \int_0^b \int_0^{c\eta/b} \frac{\zeta^2}{\eta^2+\zeta^2}\mathrm{d}\zeta\,\mathrm{d}\eta \\
\hat{H}_{\zeta\eta}(\mathbf{x}) &= H_{\eta\zeta}(\mathbf{x}) = \int_0^b \int_0^{c\eta/b} \frac{\zeta\eta}{\eta^2+\zeta^2}\mathrm{d}\zeta\,\mathrm{d}\eta \\
\hat{H}_{\eta\eta}(\mathbf{x}) &= \int_0^b \int_0^{c\eta/b} \frac{\eta^2}{\eta^2+\zeta^2}\mathrm{d}\zeta\,\mathrm{d}\eta
\end{aligned} \tag{5.7}$$

which, upon integration, will yield the following results:

$$\begin{aligned}
\hat{H}(b,c) &= -\frac{b}{4}\left[3c - 2b\tan^{-1}\left(\frac{c}{b}\right) - c\ln\left(b^2+c^2\right)\right] \\
\hat{H}_{\zeta\zeta}(b,c) &= \frac{b^2}{2}\left[\frac{c}{b} - \tan^{-1}\left(\frac{c}{b}\right)\right] \\
\hat{H}_{\zeta\eta}(b,c) &= H_{\eta\zeta}(b,c) = \frac{b^2}{4}\left[\ln\left(b^2+c^2\right) - \ln b^2\right] \\
\hat{H}_{\eta\eta}(b,c) &= \frac{b^2}{2}\tan^{-1}\left(\frac{c}{b}\right)
\end{aligned} \tag{5.8}$$

To obtain the tensor K_{ijkl} in the global coordinate system, $\hat{H}$ and $\hat{H}_{kl}$ must be differentiated with respect to $\mathbf{x}$ as indicated in (5.5). However, as mentioned in Section 4.2.3, it is more convenient to obtain K_{ijkl} in the element coordinate system since (i) $b = b(\mathbf{x})$, $c = c(\mathbf{x})$ and (ii) in the latter coordinates $\frac{\partial b}{\partial \eta} = \frac{\partial c}{\partial \zeta} = -1$ and $\frac{\partial b}{\partial \zeta} = \frac{\partial c}{\partial \eta} = 0$. It can be shown that K_{ijkl} in the element coordinate system, i.e., $\overline{K}_{ijkl}$, is represented by a 3×3 matrix as

$$
\begin{aligned}
\overline{K}_{\eta\eta\eta\eta} &= \frac{1}{4\pi}\left[2\hat{\alpha} - \frac{(2-\nu_s)}{2}\sin 2\hat{\alpha} + \frac{(1-\nu_s)}{8}\sin 4\hat{\alpha}\right] \\
\overline{K}_{\eta\eta\zeta\zeta} &= \frac{1}{4\pi}\left[2\nu_s\hat{\alpha} + \frac{(1-2\nu_s)}{2}\sin 2\hat{\alpha} - \frac{(1-\nu_s)}{8}\sin 4\hat{\alpha}\right] \\
\overline{K}_{\eta\eta\eta\zeta} &= \frac{(\nu_s-1)}{32\pi}\left[5 - 6\cos 2\hat{\alpha} + \cos 4\hat{\alpha} - 4\log\left(\sec^2\hat{\alpha}\right)\right] \\
\overline{K}_{\zeta\zeta\eta\eta} &= \frac{1}{16\pi}\left[2\nu_s - (1-\nu_s)\cos 2\hat{\alpha}\right]\sin 2\hat{\alpha} \\
\overline{K}_{\zeta\zeta\zeta\zeta} &= \frac{1}{16\pi}\left[2 + (1-\nu_s)\cos 2\hat{\alpha}\right]\sin 2\hat{\alpha} \\
\overline{K}_{\zeta\zeta\eta\zeta} &= \frac{1}{8\pi}\left[(1-\nu_s)\cos^2\hat{\alpha}\cos 2\hat{\alpha}\right] \\
\overline{K}_{\eta\zeta\eta\eta} &= \frac{1}{32\pi}\left[3\,(\nu_s-1) + 4\cos 2\hat{\alpha} - (1-\nu_s)\cos 4\hat{\alpha} + 2\,(1+\nu_s)\log\left(\sec^2\hat{\alpha}\right)\right] \\
\overline{K}_{\eta\zeta\zeta\zeta} &= \frac{1}{32\pi}\left[(1-\nu_s) + 4\nu_s\cos 2\hat{\alpha} + (1-\nu_s)\cos 4\hat{\alpha} + 2\,(1+\nu_s)\log\left(\sec^2\hat{\alpha}\right)\right] \\
\overline{K}_{\eta\zeta\eta\zeta} &= \frac{1}{4\pi}\left[(1-\nu_s)\cos\hat{\alpha}\sin^3\hat{\alpha}\right] \\
\hat{\alpha} &= \tan^{-1}\left(\frac{c}{b}\right)
\end{aligned}
\tag{5.9}
$$

Similar to the strain solution derived in Chapter 4 for a "planar" inclusion with a uniform eigenstrain, the present curvature solution has a logarithmic singularity near the vertex and it is not constant inside subregion Ω. This vertex singularity can be addressed in a similar manner as in Section 4.2.2. By assigning the subscripts 1 and 2 to the edges that form the vertex (see Figure 4.4) and denoting lengths of these edges by ℓ_1 and ℓ_2, from Figure 4.4, the following relations hold for a point $\mathbf{x}$ close to the vertex:

$$
\begin{aligned}
b_1 &= r\sin\beta^*{}_1, \quad c_1^+ = r\cos\beta^*{}_1, \quad c_1^- = -\ell_1 + r\cos\beta^*{}_1 \approx -\ell_1 \\
b_2 &= r\sin\beta^*{}_2, \quad c_2^+ = \ell_2 - r\cos\beta^*{}_2 \approx \ell_2, \quad c_2^- = -r\cos\beta^*{}_2
\end{aligned}
\tag{5.10}
$$

where r is the distance from $\mathbf{x}$ to the vertex and it approaches 0. By evaluating K_{ijkl} at $\mathbf{x}$ (via Equation 5.9) using the results given by Equation (5.10) for b and c, and discarding

all non-singular terms, K_{ijkl} in matrix form, i.e., $\mathbf{K}$, takes the following asymptotic form:

$$\mathbf{K} \approx \frac{1}{16\pi}\left(\hat{\mathbf{M}}_1 - \hat{\mathbf{M}}_2\right)\ln\frac{\ell}{r} \tag{5.11}$$

where ℓ is a representative edge length, tensors $\hat{\mathbf{M}}_1$ and $\hat{\mathbf{M}}_2$ are represented by the same matrix in the basis $(\mathbf{n}_1, \mathbf{t}_1)$ and $(\mathbf{n}_2, \mathbf{t}_2)$, and that matrix is defined by

$$\hat{\mathbf{M}} = \begin{bmatrix} 0 & 0 & 2(1-\nu_s) \\ 0 & 0 & 0 \\ 1+\nu_s & 1+\nu_s & 0 \end{bmatrix} \tag{5.12}$$

(b) Elliptical inclusion

For an elliptical inclusion, $\hat{H}(\mathbf{x})$ and $\hat{H}_{kl}(\mathbf{x})$ for $x \in \Omega$ can be evaluated from Equation (5.4) explicitly as

$$\begin{aligned} \hat{H}(\mathbf{x}) &= \frac{1}{2}H^*_{ij}x_i x_j \\ \hat{H}_{kl}(\mathbf{x}) &= \frac{1}{2}H^*_{klij}x_i x_j \end{aligned} \tag{5.13}$$

where

$$\begin{aligned} H^*_{12} &= H^*_{21} = 0 \\ H^*_{11} &= 2\pi\frac{a_2}{a_1+a_2} \\ H^*_{22} &= 2\pi\frac{a_1}{a_1+a_2} \end{aligned} \tag{5.14}$$

$$\begin{aligned} H^*_{1111} &= -H^*_{2211} = 2\pi\frac{a_2^2}{(a_1+a_2)^2} \\ H^*_{2222} &= -H^*_{1122} = 2\pi\frac{a_1^2}{(a_1+a_2)^2} \\ H^*_{1212} &= 2\pi\frac{a_1 a_2}{(a_1+a_2)^2} \end{aligned} \tag{5.15}$$

It then follows from Equation (5.5) that

$$K_{ijkl} = \frac{1}{4\pi}\left[(1+\nu_s)H^*_{ij}\delta_{kl} + (1-\nu_s)H^*_{ijkl}\right] \qquad \mathbf{x} \in \Omega \tag{5.16}$$

The formula for exterior points of the inclusion is different from Equation (5.16), and it is much more involved. The reader who is interested in that formula should refer to the work by Beom (1998).

(c) Illustrative examples

Numerical examples of the curvature given by Equation (5.1) are shown in this section. The curvatures κ_{ij} are computed for a family of regular polygons inscribed into a unit circle centered at the origin O of the coordinate system as shown in Figure 5.1. The Poisson's ratio of the plate is assumed to be 0.3 throughout the computation. The vertices of the polygon in polar coordinates are prescribed by

$$r_k = 1 \quad \text{and} \quad \theta_k = 2\pi\frac{(k-1)}{p}; \quad k = 1, 2, \ldots, p$$

where p is the number of sides of the polygon. Computational results of κ_{11} and κ_{22} along the x_1-axis for $\kappa^*_{ij} = (1,\ 0,\ 0)$ and for various values of p are plotted in Figures 5.2(a) and Figure 5.2(b), respectively. It should be noted that κ_{12} are equal to 0 in this case. The result from part (b) for a circular inclusion is also included in the figure for comparison. Similarly, the results of κ_{12} along the x_1-axis for $\kappa^*_{ij} = (0,\ 0,\ 1)$ are plotted in Figure 5.3 while κ_{11} and κ_{22} are determined to be zero. In Figures 5.2 and 5.3, κ_{11}, κ_{22}, and κ_{12} are evaluated along the x_1-axis using 20 points at equal spaces over the half polygonal domain and these points correspond to those chosen on the plots. From Figures 5.2 and 5.3, the curvature distributions are not uniform inside the inclusion but approach to the circular inclusion solutions with the increasing number of sides.

5.2.2 Geometrically linear analysis of polygonal patch

Consider an infinite, elastic, isotropic (skin) plate containing an orthotropic patch with a polygonal shape Ω (Figure 5.4). For simplicity, the patch is assumed to be orthotropic and rigidly bonded to the infinite plate. The bonded plate is subjected to a uniform temperature change ΔT and remote applied stresses $\sigma_{\infty ij}$. The thermal effect associated with curing, where structural constraint from the surrounding still cool structure must be accounted for, will be discussed separately in Section 5.5. The just stated problem then will be solved within the framework of geometrically linear analysis using the equivalent inclusion method. Since the patch is rigidly bonded to the plate, the reinforced region of

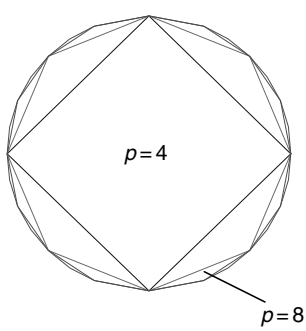

Fig. 5.1. Regular polygon-shaped inclusions.

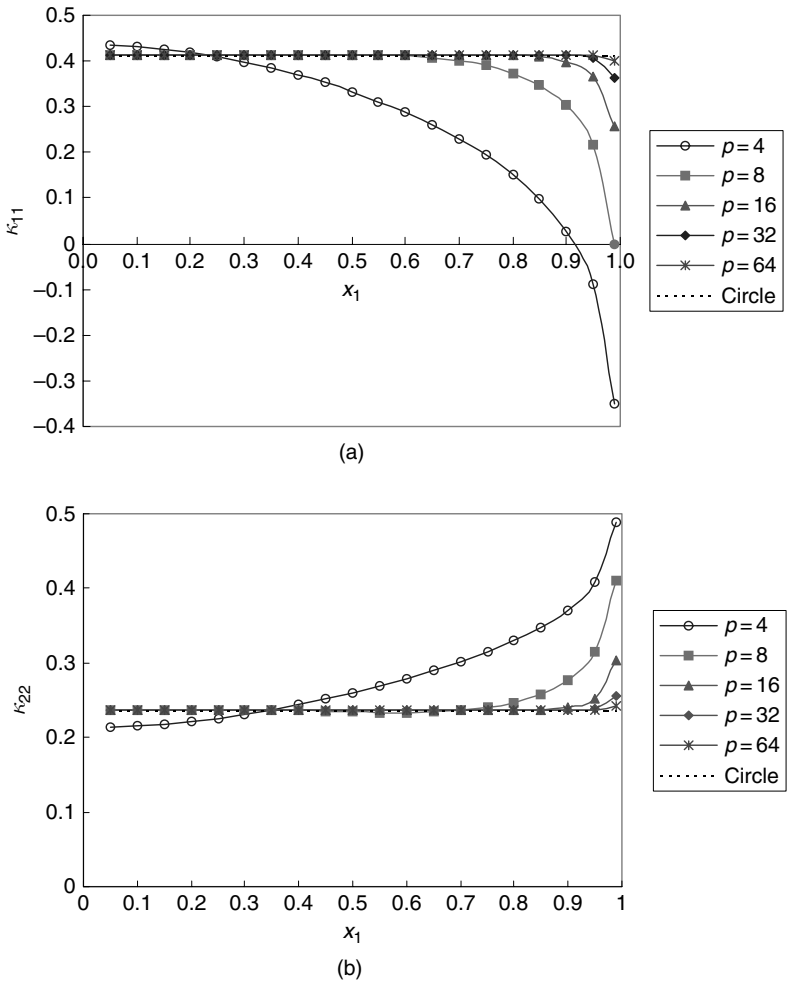

Fig. 5.2. Curvatures κ_{11} and κ_{22} in regular polygon-shaped inclusion along the x_1-axis for an eigencurvature $\kappa^*_{ij} = (1, 0, 0)$: (a) κ_{11}; (b) κ_{22}.

the plate is treated as an inhomogeneity. The constitutive relation of the inhomogeneity problem is given by

$$N^{\mathrm{I}}_{ij} = \begin{cases} A^{\mathrm{I}}_{ijkl}\bar{\varepsilon}^{\mathrm{I}}_{kl} + B^{\mathrm{I}}_{ijkl}\kappa^{\mathrm{I}}_{kl} - N^{(\mathrm{T})}_{ij} & \text{inside } \Omega \\ A^{\mathrm{s}}_{ijkl}\bar{\varepsilon}^{\mathrm{I}}_{kl} & \text{outside } \Omega \end{cases}$$

$$M^{\mathrm{I}}_{ij} = \begin{cases} B^{\mathrm{I}}_{ijkl}\bar{\varepsilon}^{\mathrm{I}}_{kl} + D^{\mathrm{I}}_{ijkl}\kappa^{\mathrm{I}}_{kl} - M^{(\mathrm{T})}_{ij} & \text{inside } \Omega \\ D^{\mathrm{s}}_{ijkl}\kappa^{\mathrm{I}}_{kl} & \text{outside } \Omega \end{cases} \tag{5.17}$$

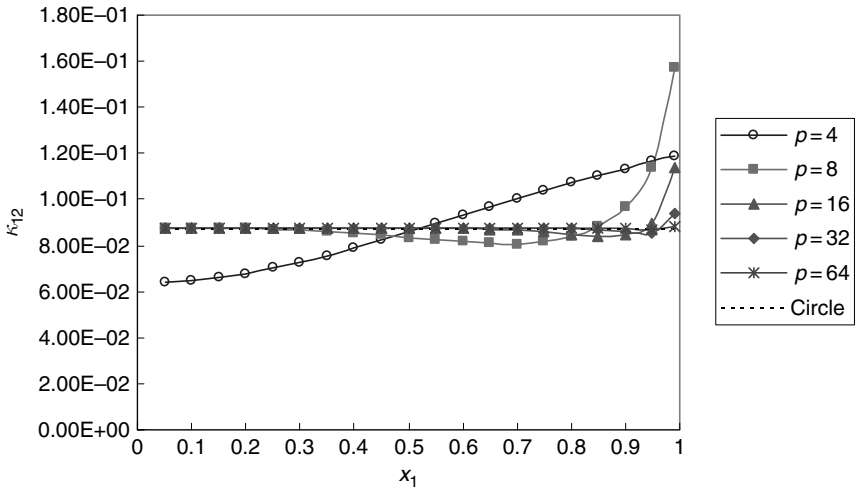

Fig. 5.3. Curvatures κ_{12} in regular polygon-shaped inclusion along the x_1-axis for an eigencurvature $\kappa^*_{ij} = (0, 0, 1)$.

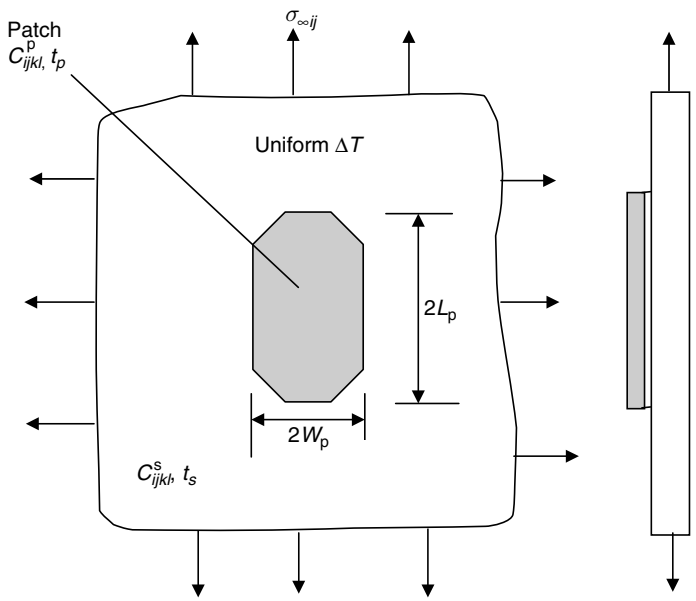

Fig. 5.4. Geometry of a repaired plate.

where A_{ijkl}, B_{ijkl}, and D_{ijkl} are the extensional, coupling, and bending stiffness tensors, respectively; N_{ij} and M_{ij} are the stress and moment resultants; $\bar{\varepsilon}_{ij}$ and κ_{ij} are the in-plane strain tensors measured at some reference plane and curvature, respectively. The superscripts I and s that appear in a quantity denote the inhomogeneity and the

isotropic skin plate, respectively. A_{ijkl}, B_{ijkl}, D_{ijkl}, N_{ij}, and M_{ij} in Equation (5.17), are defined by (Jones, 1975):

$$\begin{aligned} A_{ijkl} &= \int_0^t C_{ijkl}\mathrm{d}x_3; \quad B_{ijkl} = \int_0^t C_{ijkl}(x_3 - h_0)\mathrm{d}x_3; \quad D_{ijkl} = \int_0^t C_{ijkl}(x_3 - h_0)^2\mathrm{d}x_3 \\ N_{ij} &= \int_0^t C_{ijkl}\varepsilon_{kl}\mathrm{d}x_3; \quad M_{ij} = \int_0^t C_{ijkl}\varepsilon_{kl}\,(x_3 - h_0)\,\mathrm{d}x_3 \end{aligned} \tag{5.18}$$

where C_{ijkl} and t are the elasticity tensor and thickness, respectively, and h_0 is the x_3-coordinate of the reference plane. In particular, for the inhomogeneity,

$$\begin{aligned} A^{\mathrm{I}}_{ijkl} &= \int_0^{t_\mathrm{s}} C^{\mathrm{s}}_{ijkl}\mathrm{d}x_3 + \int_{t_\mathrm{s}}^{t_\mathrm{s}+t_\mathrm{p}} C^{\mathrm{p}}_{ijkl}\mathrm{d}x_3 \\ B^{\mathrm{I}}_{ijkl} &= \int_0^{t_\mathrm{s}} C^{\mathrm{s}}_{ijkl}\,(x_3 - h_0)\;\mathrm{d}x_3 + \int_{t_\mathrm{s}}^{t_\mathrm{s}+t_\mathrm{p}} C^{\mathrm{p}}_{ijkl}\,(x_3 - h_0)\,\mathrm{d}x_3 \\ D^{\mathrm{I}}_{ijkl} &= \int_0^{t_\mathrm{s}} C^{\mathrm{s}}_{ijkl}\,(x_3 - h_0)^2\,\mathrm{d}x_3 + \int_{t_\mathrm{s}}^{t_\mathrm{s}+t_\mathrm{p}} C^{\mathrm{p}}_{ijkl}\,(x_3 - h_0)^2\,\mathrm{d}x_3 \end{aligned} \tag{5.19}$$

In Equation (5.19), the subscript or superscript p signifies the patch. For convenience, the reference plane is chosen to be at the mid-plane of the skin in the evaluation of B_{ijkl}, D_{ijkl}, in-plane strains, and moment resultants of the skin and also of the inhomogeneity. It was shown in Section 4.2.4 of Chapter 4 that the problem of a bonded plate subjected to uniform cooling can be formulated as an initial strain problem in which the patch is prescribed with an initial strain given by

$$\varepsilon^{(\mathrm{T})(\mathrm{p})}_{ij} = \Delta\alpha_{ij}\cdot\Delta T \tag{5.20}$$

where $\Delta\alpha_{ij} = \alpha^{\mathrm{p}}_{ij} - \alpha_\mathrm{s}\delta_{ij}$. α^{p}_{ij}, α_s are the thermal expansion coefficient tensors; δ_{ij} is the Kronecker delta, and the superscript p again signifies the patch. It then follows from Jones (1975) and Duong and Yu (2003b) that $N^{(\mathrm{T})}_{ij}$ and $M^{(\mathrm{T})}_{ij}$ in Equation (5.17) are given by

$$\begin{aligned} N^{(\mathrm{T})}_{11} &= \left(\frac{E^{\mathrm{p}}_{11}\Delta\alpha_{11}}{1-\nu^{\mathrm{p}}_{12}\nu^{\mathrm{p}}_{21}} + \frac{\nu^{\mathrm{p}}_{12}E^{\mathrm{p}}_{22}\Delta\alpha_{22}}{1-\nu^{\mathrm{p}}_{12}\nu^{\mathrm{p}}_{21}}\right)\Delta T\cdot t_\mathrm{p} \\ N^{(\mathrm{T})}_{22} &= \left(\frac{\nu^{\mathrm{p}}_{21}E^{\mathrm{p}}_{11}\Delta\alpha_{11}}{1-\nu^{\mathrm{p}}_{12}\nu^{\mathrm{p}}_{21}} + \frac{E^{\mathrm{p}}_{22}\Delta\alpha_{22}}{1-\nu^{\mathrm{p}}_{12}\nu^{\mathrm{p}}_{21}}\right)\Delta T\cdot t_\mathrm{p} \\ N^{(\mathrm{T})}_{12} &= 0 \\ M^{(\mathrm{T})}_{ij} &= \frac{\left(t_\mathrm{s}+t_\mathrm{p}-h_0\right)^2 - \left(t_\mathrm{s}-h_0\right)^2}{2\cdot t_\mathrm{p}} N^{(\mathrm{T})}_{ij} \end{aligned} \tag{5.21}$$

where h_0 is defined earlier as the x_3-coordinate of the reference plane, and it equals to $\frac{t_\mathrm{s}}{2}$ in the present case. This inhomogeneity problem will be solved by the equivalent inclusion method outlined in the next part of this section.

(a) Equivalent inclusion method for a bending plate

In Chapter 4, the equivalent inclusion method by Eshelby was presented for a 2-D elasticity. This method was extended to the problem of an inhomogeneous plate with bending by Beom and Earmme (1999). In the extended form, the equivalent inclusion method can be stated as follows: The stress, reference strain, and curvature fields induced by the inhomogeneity-occupied region Ω will be the same as those induced by eigenstrain field ε^*_{ij} and eigencurvature κ^*_{ij} prescribed over the same region Ω in a homogeneous problem when ε^*_{ij} and κ^*_{ij} are selected appropriately (Figure 5.5). The constitutive relations of the latter homogeneous (inclusion) problem are given by

$$N^{\mathrm{H}}_{ij} = \begin{cases} A^{\mathrm{s}}_{ijkl}\left(\bar{\varepsilon}^{\mathrm{H}}_{kl} - \varepsilon^*_{kl}\right) & \text{for } \mathbf{x} \text{ inside } \Omega \\ A^{\mathrm{s}}_{ijkl}\bar{\varepsilon}^{\mathrm{H}}_{kl} & \text{for } \mathbf{x} \text{ outside } \Omega \end{cases} \tag{5.22}$$

$$M^{\mathrm{H}}_{ij} = \begin{cases} D^{\mathrm{s}}_{ijkl}\left(\kappa^{\mathrm{H}}_{kl} - \kappa^*_{kl}\right) & \text{for } \mathbf{x} \text{ inside } \Omega \\ D^{\mathrm{s}}_{ijkl}\kappa^{\mathrm{H}}_{kl} & \text{for } \mathbf{x} \text{ outside } \Omega \end{cases} \tag{5.23}$$

In the above equations, the superscript H denotes a homogeneous problem, A^{s}_{ijkl} and D^{s}_{ijkl} are previously defined. For a constant (or uniform) ε^*_{ij} and κ^*_{ij}, from Sections 4.2.2 and 5.2.1, the elastic solutions of the homogeneous problem can be expressed as

$$\begin{aligned} \bar{\varepsilon}^{\mathrm{H}}_{ij}(\mathbf{x}) &= S_{ijkl}(\mathbf{x})\varepsilon^*_{kl} + \varepsilon_{\infty ij} \\ \kappa^{\mathrm{H}}_{ij}(\mathbf{x}) &= K_{ijkl}(\mathbf{x})\kappa^*_{kl} \end{aligned} \tag{5.24}$$

where S_{ijkl} and K_{ijkl} are Eshelby and Eshelby-type tensors for eigenstrain and eigencurvature, respectively. Algorithms for evaluating these tensors are detailed in Section 4.2.2

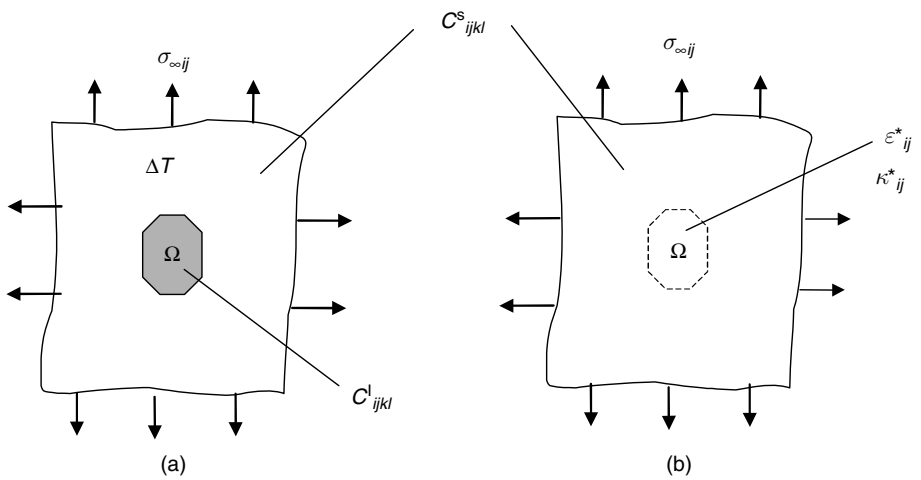

Fig. 5.5. An illustration of the equivalent inclusion method: (a) an inhomogeneity problem; and (b) an inclusion problem with a uniform eigenstrain ε^*_{ij} and a uniform eigencurvature κ^*_{ij}.

for S_{ijkl} and in Section 5.2.1 for K_{ijkl}. $\bar{\varepsilon}_{ij}^{\mathrm{H}}$ and κ_{ij}^{H} are in general not uniform inside Ω except for an elliptical region Ω. The equivalency condition between the inhomogeneity and the homogeneous problem requires that the strain (measured at the reference plane), curvature, stress, and moment resultant fields inside Ω of the two problems must be the same, i.e.,

$$\begin{aligned}
\bar{\varepsilon}_{ij}^{\mathrm{I}} &= \bar{\varepsilon}_{ij}^{\mathrm{H}} \\
\kappa_{ij}^{\mathrm{I}} &= \kappa_{ij}^{\mathrm{H}} \\
N_{ij}^{\mathrm{I}} &= N_{ij}^{\mathrm{H}} \\
M_{ij}^{\mathrm{I}} &= M_{ij}^{\mathrm{H}}
\end{aligned} \tag{5.25}$$

Since $\bar{\varepsilon}_{ij}^{\mathrm{H}}$ and κ_{ij}^{H} are in general not uniform inside Ω as mentioned above, the equivalency condition given by Equation (5.25) can only be satisfied approximately when ε_{ij}^{*} and κ_{ij}^{*} are approximated by a (unknown) constant tensor. By enforcing condition (5.25) at point (0, 0), i.e., the origin of the coordinate system, and by substituting results from Equations (5.17) and (5.22)–(5.24) into (5.25), one finally obtains the following linear algebraic equations for the unknown ε_{ij}^{*} and κ_{ij}^{*} (without summation on the subscript α):

$$\begin{aligned}
&\Delta A_{\alpha\alpha 11}\left(S_{1111}(\mathbf{0})\varepsilon_{11}^{*}+S_{1122}(\mathbf{0})\varepsilon_{22}^{*}\right)+\Delta A_{\alpha\alpha 22}\left(S_{2211}(\mathbf{0})\varepsilon_{11}^{*}+S_{2222}(\mathbf{0})\varepsilon_{22}^{*}\right) \\
&\quad+A_{\alpha\alpha 11}^{\mathrm{s}}\varepsilon_{11}^{*}+A_{\alpha\alpha 22}^{\mathrm{s}}\varepsilon_{22}^{*}+B_{\alpha\alpha 11}^{\mathrm{I}}\left(K_{1111}(\mathbf{0})\,\kappa_{11}^{*}+K_{1122}(\mathbf{0})\,\kappa_{22}^{*}\right) \\
&\quad+B_{\alpha\alpha 22}^{\mathrm{I}}\left(K_{2211}(\mathbf{0})\,\kappa_{11}^{*}+K_{2222}(\mathbf{0})\,\kappa_{22}^{*}\right)=N_{\alpha\alpha}^{(\mathrm{T})}+\Delta A_{\alpha\alpha 11}\varepsilon_{11}^{\infty}+\Delta A_{\alpha\alpha 22}\varepsilon_{22}^{\infty} \\
&B_{\alpha\alpha 11}^{\mathrm{I}}\left(S_{1111}(\mathbf{0})\,\varepsilon_{11}^{*}+S_{1122}(\mathbf{0})\,\varepsilon_{22}^{*}\right)+B_{\alpha\alpha 22}^{\mathrm{I}}\left(S_{2211}(\mathbf{0})\,\varepsilon_{11}^{*}+S_{2222}(\mathbf{0})\varepsilon_{22}^{*}\right) \\
&\quad+\Delta D_{\alpha\alpha 11}\left(K_{1111}(\mathbf{0})\,\kappa_{11}^{*}+K_{1122}(\mathbf{0})\,\kappa_{22}^{*}\right)+\Delta D_{\alpha\alpha 22}\left(K_{2211}(\mathbf{0})\,\kappa_{11}^{*}+K_{2222}(\mathbf{0})\kappa_{22}^{*}\right) \\
&\quad+D_{\alpha\alpha 11}^{\mathrm{s}}\kappa_{11}^{*}+D_{\alpha\alpha 22}^{\mathrm{s}}\kappa_{22}^{*}=M_{\alpha\alpha}^{(\mathrm{T})}+B_{\alpha\alpha 11}^{\mathrm{I}}\varepsilon_{11}^{\infty}+B_{\alpha\alpha 22}^{\mathrm{I}}\varepsilon_{22}^{\infty}
\end{aligned} \tag{5.26}$$

$$\begin{aligned}
\varepsilon_{\infty ij} &= C_{ijkl}^{\mathrm{s}-1}\sigma_{\infty kl} \\
\Delta A_{ijkl} &= A_{ijkl}^{\mathrm{I}}-A_{ijkl}^{\mathrm{s}} \\
\Delta D_{ijkl} &= D_{ijkl}^{\mathrm{I}}-D_{ijkl}^{\mathrm{s}} \\
&\text{for } \alpha=1,\,2
\end{aligned} \tag{5.27}$$

In deriving Equation (5.26), all in-plane shear components of the stress and moment resultant have been assumed to be zero. This assumption is appropriate for the present problem in the absence of the applied shear loads.

Once ε_{ij}^{*} and κ_{ij}^{*} are determined, the in-plane strain and curvature fields of the homogeneous problem can be calculated from Equations (5.24) while the stress and moment resultants are evaluated using Equations (5.22) and (5.23), respectively. The strain, curvature, stress and moment resultant fields of the inclusion problem are also those of the inhomogeneity problem via the equivalency condition given by Equation (5.25). Similar to those given in Chapter 4, the stress distribution in the skin and in the patch across their thickness inside Ω are finally given by

$$\begin{aligned}\sigma_{ij}^{\mathrm{s}} &= C_{ijkl}^{\mathrm{s}}\left[\bar{\varepsilon}_{kl}^{\mathrm{I}} + (x_3 - h_0)\ \kappa_{kl}^{\mathrm{I}}\right] \\ \sigma_{ij}^{\mathrm{p}} &= C_{ijkl}^{\mathrm{p}}\left[\bar{\varepsilon}_{kl}^{\mathrm{I}} - \varepsilon_{kl}^{(\mathrm{T})\,(\mathrm{p})} + (x_3 - h_0)\ \kappa_{kl}^{\mathrm{I}}\right]\end{aligned} \tag{5.28}$$

where from Equation (5.17) and noting $N_{ij}^{\mathrm{I}} = N_{ij}^{\mathrm{H}}$ and $M_{ij}^{\mathrm{I}} = M_{ij}^{\mathrm{H}}$ with N_{ij}^{H} and M_{ij}^{H} given respectively by (5.22) and (5.23),

$$\begin{Bmatrix}\bar{\varepsilon}_{ij}^{\mathrm{I}} \\ \kappa_{ij}^{\mathrm{I}}\end{Bmatrix} = \begin{bmatrix}A_{ijkl}^{\mathrm{I}} & B_{ijkl}^{\mathrm{I}} \\ B_{ijkl}^{\mathrm{I}} & D_{ijkl}^{\mathrm{I}}\end{bmatrix}^{-1} \left\{\begin{bmatrix}A_{klmn}^{\mathrm{s}} & 0 \\ 0 & D_{klmn}^{\mathrm{s}}\end{bmatrix}\begin{Bmatrix}\bar{\varepsilon}_{mn}^{\mathrm{H}} - \varepsilon_{mn}^{*} \\ \kappa_{mn}^{\mathrm{H}} - \kappa_{mn}^{*}\end{Bmatrix} + \begin{Bmatrix}N_{kl}^{(\mathrm{T})} \\ M_{kl}^{(\mathrm{T})}\end{Bmatrix}\right\} \tag{5.29}$$

while the stress distribution in the skin across its thickness outside Ω is equal to $C_{ijkl}^{\mathrm{s}}[\bar{\varepsilon}_{kl}^{\mathrm{H}} + (x_3 - h_0)\kappa_{kl}^{\mathrm{H}}]$.

(b) Illustrative examples

To illustrate the analytical method presented in this section, the thermal stresses in a bonded patched skin shown in Figure 5.6 are obtained and compared with the results from the FE analyses. The bonded plate is subjected to uniform temperature change of $-75\,^{\circ}\mathrm{C}$ from a stress-free temperature. The material properties of the skin and the patch are given below:

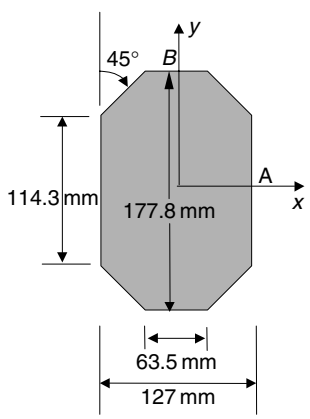

Fig. 5.6. Geometry of a bonded patched skin considered for thermal stresses.

Skin plate: isotropic

$E_s = 72.4\,\text{GPa},\ \nu_s = 0.33,\ \alpha_s = 22.5\text{E-}06\,\text{per}\,^\circ\text{C}.$

Patch: orthotropic

$E_x = 18.7\,\text{GPa},\ E_p = E_y = 193.1\,\text{GPa},\ \nu_{xy} = 0.21,$

$\mu = 5.5\,\text{GPa},\ \alpha_x = 21.4\text{E}-06\,\text{per}\,^\circ\text{C},\ \alpha_p = \alpha_y = 4.3\text{E}-06\,\text{per}\,^\circ\text{C}$

The thickness of the skin is kept constant at 1.6 mm while the thickness of the patch varies from four to eight plies with the thickness per ply equal to 0.132 mm. Since the thermal stresses in the patch are compressive and they will be negated under a far-field-tensile stress, we therefore concentrate our effort to the skin's thermal stresses.

The thermal stresses in the skin at the patch's center in the x_2-component are of special interest since they are needed for fracture analysis using Wang and Rose's crack-bridging model. These stresses are plotted in Figure 5.7 as a function of the patch stiffness ratio $\frac{E_p t_p}{E_s t_s}$, along with FE results. Stresses near the top and the bottom surfaces of the skin are presented in that figure to show the effect of the out-of-plane bending. FE results are obtained by using MSC/NASTRAN code (2001). In the FE analysis, the skin is modeled as three layers of solid elements while each ply of the patch is modeled individually as one layer of solid elements. All elements are eight-node (linear) solid elements. From Figure 5.7, it is found that the analytical results are in very good agreement with FE predictions.

So far only one particular octagonal shape has been considered. Examples of patches of rectangular shapes therefore will be presented next. In these examples, material properties of the skin and the patch will be the same as those given in the previous example. The thickness of the skin is again kept constant at 1.6 mm. The thickness and width of the patch are also kept constant at 0.66 and 25.4 mm, respectively. The uniform temperature change is $-75\,^\circ$C. As before, the thermal stresses in the skin at the patch's center in the x_2-component are of interest and they are presented in Figure 5.8 for rectangular patches with different patch length to patch width ratios (L_p/W_p). Corresponding 3-D FE results are also shown there for comparison. From Figure 5.8, the same good agreement is found between analytical predictions and FE results.

5.3 Geometrically Nonlinear Analysis of Stage I

An infinite isotropic skin plate with a finite patch made of a different material will develop thermal stresses during temperature excursions. When a plate is bonded unsymmetrically with a patch on one of its two sides, the thermal load will induce both in-plane deformations and the out-of-plane deflection in the plate. Moreover, the effect of large deflection is found to be significant on the thermally induced stresses. These nonlinear thermal stresses had been addressed by Duong and Yu (2003c) in a simplified approach for a composite repair under a uniform low operating temperature and/or curing. Even though their approach lacks the scientific rigor, it appears technically sound and provides quite good estimates of thermal stresses in all specific example problems considered by them. Their approach therefore will be reviewed in Section 5.3.1.

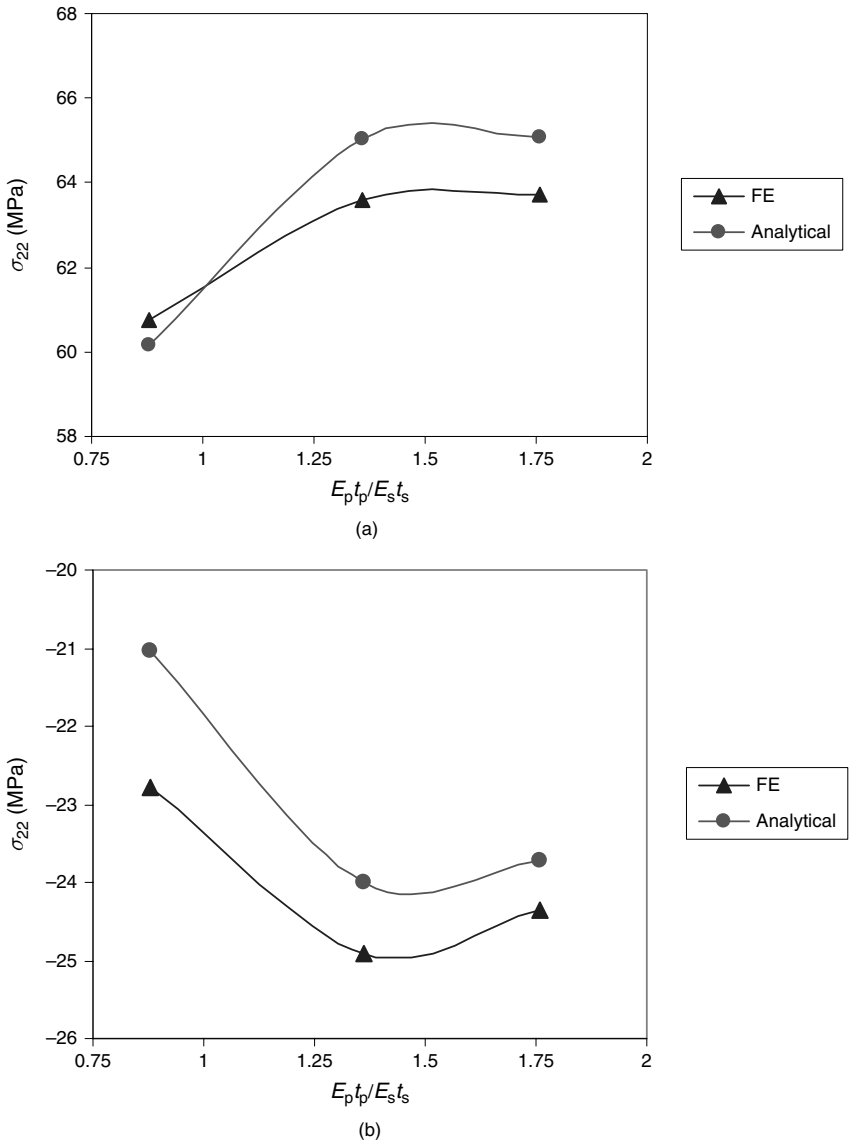

Fig. 5.7. x_2-component thermal stresses in the skin plate at the patch's center for different patch stiffness ratios $E_p t_p / E_s t_s$: (a) near the top surface; and (b) near the bottom surface.

A patched plate subjected to a purely tensile load will also experience an out-of-plane bending, even when the patch is made of the same material as the skin, mainly due to the load path eccentricity. However, the mechanically induced deflection opposes the thermally induced deflection mentioned earlier. As before, it is also necessarily to determine the mechanically induced stresses within a large deflection theory. However, analytical solutions for this mechanical problem have been limited to the analysis of

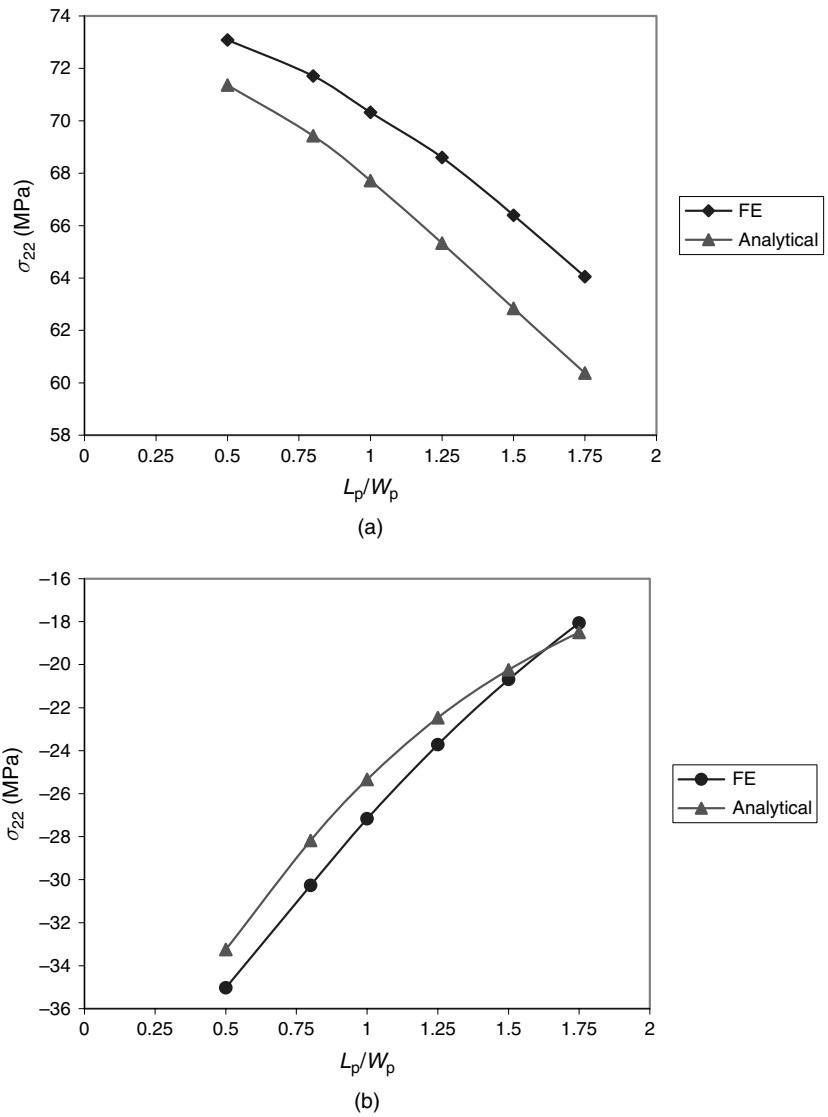

Fig. 5.8. x_2-component thermal stresses in the skin plate at the patch's center for different patch aspect ratios L_p/W_p: (a) near the top surface; and (b) near the bottom surface.

a patch that spans across the entire width of the plate. This analytical solution will be extended in Section 5.3.2 to include the "initial stress" effect (Duong, 2004) for latter use in the analysis of a repair under a combined thermo-mechanical loading.

An application of a tensile load will alleviate greatly the initial bending associated with curing of the adhesive and low operating temperature. However, in contrast to

a geometrically linear problem, the total stresses in a one-sided bonded repair under combined thermo-mechanical loading would not be simply a sum of the nonlinear thermal stresses associated with curing or low operating temperature and the nonlinear mechanical stresses associated with the mechanical loading as if these stresses are obtained separately. An approximated solution method proposed by Duong (2004) is therefore introduced in Section 5.3.3 to address the effect of the combined thermo-mechanical loading in a one-sided bonded repair. This solution method is based on an engineering approach, which combines methods developed in Sections 5.3.1 and 5.3.2, respectively, for a polygonal patch and for a patch spanning across the entire width of the plate in a one-sided repair under purely thermal loads and purely mechanical loads.

5.3.1 Thermal stresses in polygonal patch

(a) Preliminary analysis

Consider a patch that spans across the entire width of the skin plate, so that the stresses in the patch and the skin within the reinforced region are uniform along the skin's width as shown in Figure 5.9 and therefore they can be solved by a one-dimensional analysis. The patch and skin are assumed to be fused together with no relative sliding at the

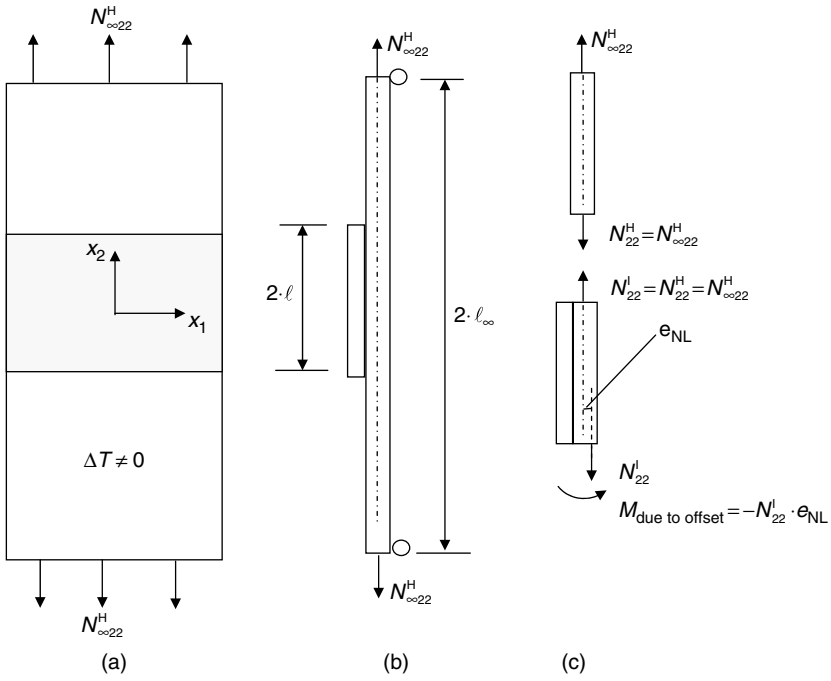

Fig. 5.9. Plate reinforced with a patch spanning across the entire width's plate: (a) plan view; (b) side view; (c) free body diagram used to explain the effects of shifting the reference plane's position. Note that for the case of purely thermal loading, $N^{H}_{\infty 22} = 0$.

interface. The whole patched skin is subjected to a uniform temperature excursion. This problem will be solved exactly within a large deflection theory. In the absence of the transverse load, the equilibrium equations based on the von Karman plate theory are given by (Timoshenko and Woinowsky-Krieger, 1959)

$$N_{22,2} = 0 \tag{5.30}$$

$$M_{22,22} + N_{22} w_{,22} = 0 \tag{5.31}$$

where N_{22} and M_{22} are the stress and moment resultants, respectively, and the comma indicates partial differentiation. It then follows from Equation (5.30) upon integration that

$$N_{22} = \text{constant} = \text{C} \tag{5.32}$$

On the other hand, the kinematics and constitutive relations for a laminated plate are given by (Sun and Chin, 1988)

$$\begin{aligned} \varepsilon_{22} &= \bar{\varepsilon}_{22} + \varepsilon_{22}^{\text{NL}} + \kappa_{22}\,(x_3 - h_0) \\ \bar{\varepsilon}_{22} &= v_{,2} \\ \varepsilon_{22}^{\text{NL}} &= \frac{1}{2} w_{,2}^2 \end{aligned} \tag{5.33}$$

$$\begin{aligned} N_{22} &= A_{22}\left(v_{,2} + \frac{1}{2} w_{,2}^2 - \alpha_{22}\Delta T\right) - B_{22} w_{,22} \\ M_{22} &= B_{22}\left(v_{,2} + \frac{1}{2} w_{,2}^2 - \alpha_{22}\Delta T\right) - D_{22} w_{,22} \end{aligned} \tag{5.34}$$

where A_{22}, B_{22}, and D_{22} are extensional, coupling, and bending stiffnesses, respectively (in Voight notation), defined previously by Equation (5.18); v and w are the longitudinal and transverse displacements, respectively; α_{22} is the thermal expansion coefficient; $\varepsilon_{22}^{\text{NL}}$ is the nonlinear strain; h_0 is the x_3-coordinate of the reference plane; and κ_{22} is the curvature. As before, the reference plane is chosen to be at the mid-plane of the skin plate, i.e., $h_0 = \frac{t_s}{2}$, for regions both inside and outside the overlap.

Applying Equations (5.31), (5.32), and (5.34) to the region outside the overlap (see Figure 5.9) and enforcing the boundary condition at infinity, i.e., $N_{\infty 22}^{\text{H}} = 0$, yield

$$\begin{aligned} N_{22}^{\text{H}} &= 0 \\ M_{22,22}^{\text{H}} &= 0 \end{aligned} \tag{5.35}$$

$$\begin{aligned} N_{22}^{\text{H}} &= A_{22}^{\text{s}}\left(v_{,2}^{\text{H}} + \frac{1}{2} w_{,2}^{\text{H2}} - \alpha_{\text{s}}\Delta T\right) = 0 \\ M_{22}^{\text{H}} &= -D_{22}^{\text{s}} w_{,22}^{\text{H}} \end{aligned} \tag{5.36}$$

where the superscript H denotes the homogeneous skin region outside the overlap, s indicates the skin, and B_{22}^{s} of the skin plate outside the overlap is equal to zero because the skin is a single layer of homogeneous material and thus symmetric with respect to the reference plane, resulting in no stretching-bending coupling stiffness. Substituting the second equation of (5.36) for M_{22}^{H} into the second equation of (5.35) gives

$$w_{,2222}^{H} = 0 \tag{5.37}$$

By integrating Equation (5.37) and enforcing the simply supported conditions at the ends, i.e., $M_{22}^{H}(l_\infty) = w^{H}(l_\infty) = V_{22}^{H}(l_\infty) = 0$, where V_{22}^{H} is the transverse shear force defined as $V_{22}^{H} = \frac{dM_{22}^{H}}{dx_2}$, the transverse displacement and curvature outside the overlap are then found to be

$$\begin{aligned} w^{H}(x_2) &= C_1(l_\infty - x_2) \\ w_{,22}^{H}(x_2) &= 0 \end{aligned} \tag{5.38}$$

where C_1 is an unknown constant which must be determined from the displacement, slope, and traction continuity at end of the overlap. For latter use, the first equation of (5.36) is also rewritten as

$$\left(v_{,2}^{H} + \frac{1}{2}w_{,2}^{H2}\right) = \alpha_s \Delta T \tag{5.39}$$

Similarly, the region inside the overlap also has $N_{22}^{I} = \text{constant} = 0$ from consideration of the force equilibrium. With that, applying Equations (5.31), (5.32), and (5.34) to the region inside the overlap yields

$$\begin{aligned} N_{22}^{I} &= 0 \\ M_{22,22}^{I} &= 0 \end{aligned} \tag{5.40}$$

$$\begin{aligned} N_{22}^{I} &= A_{22}^{I}\left(v_{,2}^{I} + \frac{1}{2}w_{,2}^{I2} - \alpha_{22}^{I}\Delta T\right) - B_{22}^{I}w_{,22}^{I} = 0 \\ M_{22}^{I} &= B_{22}^{I}\left(v_{,2}^{I} + \frac{1}{2}w_{,2}^{I2} - \alpha_{22}^{I}\Delta T\right) - D_{22}^{I}w_{,22}^{I} \end{aligned} \tag{5.41}$$

where the superscript I indicates the inhomogeneous region inside the overlap. Equation (5.41) can also be rewritten as

$$\begin{aligned} \left(v_{,2}^{I} + \frac{1}{2}w_{,2}^{I2}\right) &= \frac{B_{22}^{I}}{A_{22}^{I}}w_{,22}^{I} + \alpha_{22}^{I}\Delta T \\ M_{22}^{I} &= \left(\frac{B_{22}^{I\,2}}{A_{22}^{I}} - D_{22}^{I}\right)w_{,22}^{I} \end{aligned} \tag{5.42}$$

Substituting the second equation of (5.42) into the second equation of (5.40) gives:

$$w^{\mathrm{I}}_{,2222} = 0 \tag{5.43}$$

Upon integrating Equation (5.43) and enforcing the symmetry conditions at the center of the reinforced skin, one finally obtains

$$w^{\mathrm{I}}(x_2) = C_2 - \frac{\kappa}{2}x_2^2 \tag{5.44}$$

where C_2 and κ are new constants yet to be determined. From this

$$\begin{aligned} w^{\mathrm{I}}_{,2}(x_2) &= -\kappa \cdot x_2 \\ w^{\mathrm{I}}_{,22}(x_2) &= -\kappa = \text{constant} \end{aligned} \tag{5.45}$$

Thus, the constant κ is the curvature of the patched skin inside the overlap, i.e., $\kappa^{\mathrm{I}}_{22} = \kappa$. Substituting Equation (5.45) into the first equation of (5.42) yields

$$v^{\mathrm{I}}_{,2}(x_2) = -\frac{B^{\mathrm{I}}_{22}}{A^{\mathrm{I}}_{22}}\kappa + \alpha^{\mathrm{I}}_{22}\Delta T - \frac{\kappa^2}{2}x_2^2 \tag{5.46}$$

The fist two conditions for determining the three constants C_1, C_2, and κ in (5.38) and (5.44) are the displacement and slope continuity conditions at the end of the overlap, i.e.,

$$\begin{aligned} w^{\mathrm{H}}(\ell_\infty - \ell) &= w^{\mathrm{I}}(\ell) \\ w^{\mathrm{H}}_{,2}(\ell_\infty - \ell) &= w^{\mathrm{I}}_{,2}(\ell) \end{aligned} \tag{5.47}$$

The third condition is derived from the continuity of the normal stress resultant of the skin across the overlap interface, i.e.,

$$N^{\mathrm{I(s)}}_{22}(\ell) = A^{\mathrm{s}}_{22} \cdot \left(v^{\mathrm{I}}_{,2}(\ell) + \frac{1}{2}w^{\mathrm{I}2}_{,2}(\ell) - \alpha_{\mathrm{s}}\Delta T \right) = N^{\mathrm{H}}_{22}(\ell_\infty - \ell) = 0 \tag{5.48}$$

where $N^{\mathrm{I(s)}}_{22}(\ell)$ is the stress resultant in the skin of the patch–skin combination at the end of the overlap. $N^{\mathrm{I(s)}}_{22}$ in the above equation has been derived based on the condition that the strains of the skin and of the patch–skin combination are the same in the overlap and by using the first equation of (5.34) with $B_{22} = 0$. It is worthy to note that $N^{\mathrm{I(s)}}_{22}(\ell)$ is also equal to $N^{\mathrm{I}}_{22}(\ell)$ since the patch is stress-free at the end of the overlap. It then follows from Equation (5.48) that

$$v^{\mathrm{I}}_{,2}(\ell) = \alpha_{\mathrm{s}}\Delta T - \frac{\ell^2}{2} \cdot \kappa^2 \tag{5.49}$$

where the result $w^{\mathrm{I}}_{,2}(\ell) = -\kappa\ell$ from the first equation of (5.45) has been utilized in the derivation. However, $v^{\mathrm{I}}_{,2}(\ell)$ can also be obtained by evaluating equation of (5.46) at $x_2 = \ell$ as

$$v^{\mathrm{I}}_{,2}(\ell) = -\frac{B^{\mathrm{I}}_{22}}{A^{\mathrm{I}}_{22}}\kappa + \alpha^{\mathrm{I}}_{22}\Delta T - \frac{\ell^2}{2} \cdot \kappa^2 \tag{5.50}$$

Thus, the constant κ can be determined from Equations (5.49) and (5.50) as

$$\kappa = \frac{A_{22}^{\mathrm{I}}}{B_{22}^{\mathrm{I}}}\left(\alpha_{\mathrm{s}} - \alpha_{22}^{\mathrm{I}}\right)\Delta T \tag{5.51}$$

Once κ is found, then C_1 and C_2 can be determined from the conditions given by Equation (5.47). For future discussion, the average nonlinear strain inside the overlap, i.e., $-\ell \le x_2 \le \ell$ over the patch length, is also calculated to be

$$\bar{\varepsilon}_{22}^{\mathrm{NL}} = \frac{\int_{-\ell}^{\ell} \frac{1}{2} w_{,2}^{\mathrm{I}2}\, \mathrm{d}x_2}{2\cdot\ell} = \frac{\int_{-\ell}^{\ell} \frac{1}{2}\left(\kappa x_2\right)^2 \mathrm{d}x_2}{2\cdot\ell} = \frac{1}{6}\kappa^2\,\ell^2 \tag{5.52}$$

since $w_{,2}^{\mathrm{I}} = -\kappa x_2$ by virtue of Equation (5.45).

In summary, under purely thermal loading, this preliminary analysis predicts that the curvature of the patched skin is constant inside the overlap as indicated by Equation (5.45) and equals zero outside the overlap via second equation of (5.38). Furthermore, since the curvature of the plate is zero outside the overlap, the term $N_{22}w_{,22}$ associated with the large transverse deflection in the moment equilibrium Equation (5.31) also equals zero in that region.

For future discussion, it is also of interest to show an approximate geometrically nonlinear solution for the above thermal stress problem of a patched skin in the presence of an additionally small tensile load. When the patched skin is subjected additionally to the remote tensile stress, i.e., $N_{\infty 22}^{\mathrm{H}} > 0$, the curvatures of the patched skin inside and outside the overlap are not necessarily constant and zero, respectively. However, if $N_{\infty 22}^{\mathrm{H}}$ is sufficiently small, i.e., $N_{\infty 22}^{\mathrm{H}} \ll 1$, the previous results for the curvature and for the nonlinear term $N_{22}w_{,22}$ of the case of purely thermal loading may still hold approximately for this latter case. In particular, the curvature is still approximately constant and zero inside and outside the overlap while the nonlinear term $N_{22}w_{,22}$ can be assumed to be zero outside the overlap. Furthermore, the average nonlinear strain inside the overlap over the patch length is represented by the same equation as (5.52). In that case, the average moment inside the overlap over the patch length is derived from Equation (5.31) as follows:

$$\begin{aligned} M_{22,22}^{\mathrm{I}} - N_{\infty 22}^{\mathrm{H}}\kappa &= 0 \\ M_{22}^{\mathrm{I}} &= \frac{N_{\infty 22}^{\mathrm{H}}\kappa\cdot x_2^2}{2} \\ \overline{M}_{22}^{\mathrm{I}} &= \frac{\int_{-\ell}^{\ell} M_{22}^{\mathrm{I}}}{2\cdot\ell} = \frac{1}{6}\kappa\ell^2 N_{\infty 22}^{\mathrm{H}} \end{aligned} \tag{5.53}$$

since $N_{22}^{\mathrm{I}} = N_{22}^{\mathrm{H}} = N_{\infty 22}^{\mathrm{H}}$, and $w_{,22}^{\mathrm{I}}(x_2) \approx -\kappa$ via the second equation of (5.45).

In contrast, a geometrically linear analysis of the latter thermo-mechanical problem will significantly over-predict the bending stresses inside the overlap. This is because the geometrically linear analysis ignores the nonlinear term $N_{22}w_{,22}$ in the moment

equilibrium Equation (5.31) and the nonlinear strain term $\varepsilon_{ij}^{\mathrm{NL}}$ in the kinematics relation (5.33). However, if in the geometrically linear analysis the reference plane of the overlap is purportedly shifted from $x_3 = h_0 = \frac{t_s}{2}$ to $x_3 = h_0 - e_{\mathrm{NL}} = \frac{t_s}{2} - e_{\mathrm{NL}}$, where $e_{\mathrm{NL}} = \frac{1}{6}\kappa\ell^2$ and κ is the sought curvature, then the effect of the geometrically nonlinearity will be accounted for approximately in average sense as explained later in the paragraph below. In that case, the kinematics relation for regions inside and outside the overlap are given by

$$\begin{aligned} \varepsilon_{22} &= v_{,2} + \kappa_{22}\,(x_3 - h_0 + e_{\mathrm{NL}}) \qquad |x_2| \le \ell \\ \varepsilon_{22} &= v_{,2} + \kappa_{22}\,(x_3 - h_0) \qquad |x_2| > \ell \end{aligned} \tag{5.54}$$

It is worthy to note that in a geometrically linear analysis, both inside and outside regions of the overlap have the kinematics relations prescribed by the second equation of (5.54).

From Equation (5.54), it is clear that there is no explicitly nonlinear strain term $\varepsilon_{ij}^{\mathrm{NL}}$ in the kinematics relation (5.54) as that in (5.33). However, since the first equation of (5.54) contains the extra term $\kappa_{22}e_{\mathrm{NL}}$ that is equal to $\frac{\kappa^2\ell^2}{6}$ (when compared to the linear kinematics relation) and since the average over the patch length of the nonlinear strain $\overline{\varepsilon}_{ij}^{\mathrm{NL}}$ is also equal to $\frac{\kappa^2\ell^2}{6}$ as given by Equation (5.52), the effect of the shift of the reference plane's position inside the overlap is to raise the linear strains there by an amount equal to the average nonlinear strain predicted by the corresponding nonlinear analysis. In addition, from Figure 5.9 (c), this positional shift of the reference plane will also induce a constant moment of $N_{\infty 22}^{\mathrm{H}} e_{\mathrm{NL}} = \frac{1}{6}\kappa\ell^2 N_{\infty 22}^{\mathrm{H}}$ that in turn equals $\overline{M}_{22}^{\mathrm{I}}$, the average moment over the patch length from the nonlinear analysis, since $\overline{M}_{22}^{\mathrm{I}} = \frac{1}{6}\kappa\ell^2 N_{\infty 22}^{\mathrm{H}}$ by the third equation of (5.53). However, both the present geometrically linear analysis with the mentioned shift of the reference plane's position and the approximated geometrically nonlinear analysis (for the thermo-mechanical loading case with a small tensile load $N_{\infty 22}^{\mathrm{H}}$) described earlier before the preceding paragraph assume the nonlinear term $N_{22}w_{,22}$ to be equal to 0 for the region outside the overlap. Thus, the modified geometrically linear analysis in average sense seems to be equivalent to the approximate nonlinear analysis. In other words, it appears that any geometrically nonlinear thermo-mechanical problem can be solved approximately by the geometrically linear analysis but with the appropriate shift of the reference plane's position inside the overlap, providing that the stress resultant remains small at every point in the patched skin. Even though this "modified geometrically linear analysis" approach to the nonlinear problem may lack the scientific rigor, however, it appears technically sound from the engineering viewpoint. This simplified approach was used by Duong and Yu (2003c) in their analysis of thermal stresses of a repaired plate with a polygonal patch, and it will be presented in the next part of this section.

(b) Formulation for a polygonal patch

Consider an infinite isotropic skin plate bonded rigidly with a polygon-shaped patch Ω. The patch is either isotropic or orthotropic with its material principal axes parallel to the global coordinate axes. Let us also assume that the patch when it is orthotropic will have a larger mismatch in the thermal expansion coefficient with the skin along the

x_2-direction. The patched skin assumes to be subjected to a uniform temperature change ΔT as in Figure 5.4 but in the absence of the remote stresses. For simplicity, all shear components are also assumed to be zero. Since the patch is rigidly bonded to a skin, the patched region of the skin is treated as an inhomogeneity. An approximate solution based on the engineering approach similar to that outlined in part (a) will be presented here. However, the approach mentioned there will be extended to the 2-D analysis in this part with details shown below, and its results will be compared later with the FE solutions for a wide range of patch's configurations in part (d).

In contrast to the results of patching across the entire width of the skin, the stress resultants inside the skin reinforced with a polygonal patch due to a uniform temperature change will not necessarily be equal to zero even without remote applied stresses. It should be remembered that except at infinity only the average stress resultant across the skin width is required to equal zero, and therefore the stress resultant may not necessarily equal zero at every point in the patched skin. However, if these stress resultants are assumed to be small, then the thermal stresses in the latter problem can be solved approximately by a geometrically linear analysis with the reference plane of the patched region being shifted purportedly from $x_3 = h_0 = \frac{t_s}{2}$ to $x_3 = h_0 - e_{\mathrm{NL}} = \frac{t_s}{2} - e_{\mathrm{NL}}$ as mentioned in part (a) of this section. Thus, the considered patched skin is divided into two regions; each will be modeled using different kinematics and constitutive relations. The region outside the patch is a homogeneous infinite isotropic plate. On the other hand, the inhomogeneous region is a finite asymmetric laminated plate that is composed of two layers corresponding to the skin and the patch. The kinematics relations used to describe the inhomogeneity and the homogeneous region are summarized below, which are the 2-D generalization of Equation (5.54).

$$\varepsilon_{ij}^{\mathrm{I}} = \begin{cases} \bar{\varepsilon}_{ij}^{\mathrm{I}} + (x_3 - h_0 - e_{\mathrm{NL}})\,\kappa_{ij}^{\mathrm{I}} & \text{inside } \Omega \\ \bar{\varepsilon}_{ij}^{\mathrm{I}} + (x_3 - h_0)\,\kappa_{ij}^{\mathrm{I}} & \text{outside } \Omega \end{cases}$$
$$\bar{\varepsilon}_{ij}^{\mathrm{I}} = \frac{1}{2}\left(u_{i,j}^{\mathrm{I}} + u_{j,i}^{\mathrm{I}}\right) \tag{5.55}$$

$$e_{\mathrm{NL}} = \frac{1}{6}\kappa_0 \ell^2$$
$$\kappa_{ij}^{\mathrm{I}} = -\frac{\partial^2 w^{\mathrm{I}}}{\partial x_i \partial x_j} \tag{5.56}$$

where κ_0 is a representative curvature in the x_2 direction inside region Ω, ℓ is the longest half length of the polygonal patch measured from its center, $\varepsilon_{ij}^{\mathrm{I}}$ (or σ_{ij}^{I} as discussed later) is the strain (or stress) field of the inhomogeneity problem that describes strain (or stress) of both interior and exterior points of the inhomogeneous region Ω, and the rest are previously defined. The above conjecture will then be tested for its validity for a wide range of patch's configurations. As shown later in part (d), the above conjecture will yield sufficiently accurate results for stresses in the skin near the center of the patch and thus at the prospective crack location in the bonded repair when these results are compared with FE solutions.

Once the kinematics relations are established, the constitutive relations can be derived using the classical plate theory (Jones, 1975; Duong and Yu, 2003b) as

$$N_{ij}^{\mathrm{I}} = \begin{cases} A_{ijkl}^{\mathrm{I}} \bar{\varepsilon}_{kl}^{\mathrm{I}} + B_{ijkl}^{\mathrm{I}} \kappa_{kl}^{\mathrm{I}} - N_{ij}^{(\mathrm{T})} & \text{inside } \Omega \\ A_{ijkl}^{\mathrm{s}} \bar{\varepsilon}_{kl}^{\mathrm{I}} & \text{outside } \Omega \end{cases}$$
$$M_{ij}^{\mathrm{I}} = \begin{cases} B_{ijkl}^{\mathrm{I}} \bar{\varepsilon}_{kl}^{\mathrm{I}} + D_{ijkl}^{\mathrm{I}} \kappa_{kl}^{\mathrm{I}} - M_{ij}^{(\mathrm{T})} & \text{inside } \Omega \\ D_{ijkl}^{\mathrm{s}} \kappa_{kl}^{\mathrm{I}} & \text{outside } \Omega \end{cases} \tag{5.57}$$

where A_{ijkl}, B_{ijkl}, D_{ijkl}, $N_{ij}^{(\mathrm{T})}$, $M_{ij}^{(\mathrm{T})}$, etc are defined previously by Equations (5.19) and (5.21) in Section 5.2.2. Equation (5.57) seems to be exactly the same as Equation (5.17) of Section 5.2.2 for a geometrically linear analysis. However, since the x_3-position of the reference plane of the inhomogeneity has been shifted down to $(h_0 - e_{\mathrm{NL}})$ in the present formulation, A_{ijkl}^{I}, B_{ijkl}^{I}, A_{ijkl}^{I}, $M_{ij}^{(\mathrm{T})}$, etc must be evaluated with respect to this new position of the reference plane.

(c) Solution method

In part (b), a problem of an infinite isotropic plate with a polygon-shaped patch under uniform cooling was formulated as an inhomogeneity problem with the kinematics and constitutive relations prescribed by Equations (5.55) and (5.57), respectively. This inhomogeneity problem then will be solved by the equivalent inclusion method. When e_{NL} in Equation (5.56) is prescribed as a known constant, the solution of the present inhomogeneity problem can be obtained in an exact manner as in Section 5.2.2 since all governing equations will be the same, providing that A_{ijkl}^{I}, B_{ijkl}^{I}, A_{ijkl}^{I}, $M_{ij}^{(\mathrm{T})}$, etc must be evaluated with respect to the reference plane located at $x_3 = h_0 - e_{\mathrm{NL}}$. Like before in Section 5.2.2, one first solves for ε_{ij}^{*} and κ_{ij}^{*} via Equation (5.27), and then calculates the strain, curvature, stress and moment resultants from Equations (5.24), (5.22), and (5.23), respectively. Similar to Equations (5.28) and (5.29), the stresses in the skin plate and in the patch inside Ω are finally given by:

$$\sigma_{ij}^{\mathrm{s}} = C_{ijkl}^{\mathrm{s}} \left[\bar{\varepsilon}_{kl}^{\mathrm{I}} + (x_3 - h_0 + e_{\mathrm{NL}})\, \kappa_{kl}^{\mathrm{I}} \right]$$
$$\sigma_{ij}^{\mathrm{p}} = C_{ijkl}^{\mathrm{p}} \left[\bar{\varepsilon}_{kl}^{\mathrm{I}} - \varepsilon_{kl}^{(\mathrm{T})(\mathrm{p})} + (x_3 - h_0 + e_{\mathrm{NL}})\, \kappa_{kl}^{\mathrm{I}} \right] \tag{5.58}$$

$$\begin{Bmatrix} \bar{\varepsilon}_{ij}^{\mathrm{I}} \\ \kappa_{ij}^{\mathrm{I}} \end{Bmatrix} = \begin{bmatrix} A_{ijkl}^{\mathrm{I}} & B_{ijkl}^{\mathrm{I}} \\ B_{ijkl}^{\mathrm{I}} & D_{ijkl}^{\mathrm{I}} \end{bmatrix}^{-1} \left\{ \begin{bmatrix} A_{klmn}^{\mathrm{s}} & 0 \\ 0 & D_{klmn}^{\mathrm{s}} \end{bmatrix} \begin{Bmatrix} \bar{\varepsilon}_{mn}^{\mathrm{H}} - \varepsilon_{mn}^{*} \\ \kappa_{mn}^{\mathrm{H}} - \kappa_{mn}^{*} \end{Bmatrix} + \begin{Bmatrix} N_{kl}^{(\mathrm{T})} \\ M_{kl}^{(\mathrm{T})} \end{Bmatrix} \right\} \tag{5.59}$$

So far e_{NL} has been assumed to be known a priori. However, in reality, e_{NL} is also part of the sought solutions since it depends on the x_2-component of the curvature inside Ω as defined in Equation (5.56). Since the curvature field inside Ω in general is not uniform, the curvature at any point inside Ω can be used as κ_0 in the evaluation of e_{NL}.

However, it is found that the following definition of κ_0 will yield sufficiently accurate solutions for a skin plate repaired with patches of different shapes' aspect ratios:

$$\kappa_0 = \kappa_{22}^{\mathrm{I}}(0, \bar{y})$$
$$\bar{y} = \text{minimum } of \{\ell, W\} \tag{5.60}$$

In the above equation, the notation $\kappa_{22}^{\mathrm{I}}(0, \bar{y})$ means that κ_{22}^{I} is evaluated at a point $(0, \bar{y})$ on the x_2-axis, where $\bar{y}$ is either the half-length ℓ or the half-width W of the patch, whichever is smaller.

With the solution procedure for a fixed value of e_{NL} described and κ_0 defined, the solution of the geometrically nonlinear problem can be obtained by the following simple iterative procedure. First, κ_0 and thus e_{NL} are assumed to be zero, and the elastic solutions for stress, strain, and curvature field are obtained in a usual manner using the prescribed value of e_{NL}. Second, the newly obtained curvature field κ_{22}^{I} is evaluated at point $(0, \bar{y})$ and compared with the value of κ_0 assumed at the beginning of the iterative cycle. If their values are the same, then the just obtained solution has converged to the true solution of the problem. Otherwise, another value of κ_0, thus e_{NL}, will be assumed and the above steps are repeated until convergence. A new trial value for κ_0 will be calculated using the following recursive formula (Carnahan et al., 1969):

$$\kappa_0^{(i+1)} = (1 - k_{\mathrm{c}})\kappa_0^{(i-1)} + \mathrm{k_c}\kappa_{22}^{\mathrm{I}(i)}(0, \bar{y}) \tag{5.61}$$

where $\kappa_0^{(i+1)}$ and $\kappa_0^{(i-1)}$ are values of κ_0 in the next and previous iterative cycles, respectively; $\kappa_{ij}^{\mathrm{I}(i)}$ is the elastic solution for the curvature field obtained from current iterative cycle that is based on $e_{\mathrm{NL}} = \frac{1}{6}\kappa_0^{(i-1)}\ell^2$; and k_{c} is a scalar factor which takes values between 0 and 1. It should be noted that a normal direct substitution method corresponds to a case of $k_{\mathrm{c}} = 1$.

(d) Illustrative examples

To illustrate the method presented in this section for nonlinear thermal stresses in a skin repaired with polygonal patches, particular cases corresponding to typical repair configurations considered in the paper by Duong and Yu (2003c) are analyzed in this part. All computations in this section unless noted otherwise are carried out for a temperature excursion of $-75\,^{\circ}\mathrm{C}$, corresponding to a typical temperature change experienced by the aircraft during high altitude cruising. The first case is an infinite skin repaired with a square patch ($L_{\mathrm{p}}/W = 1$). A patch is bonded rigidly to a plate. The material properties and thickness of the skin and the patch are given below:

Skin: Aluminum

$E_{\mathrm{s}} = 72.4\,\mathrm{GPa},\ \nu_{\mathrm{s}} = 0.33,\ \alpha_{\mathrm{s}} = 22.5\text{E-}06\,\mathrm{per}\,^{\circ}\mathrm{C},\ t_{\mathrm{s}} = 1.6\,\mathrm{mm}.$

Patch: Boron/Epoxy

$E_x = 18.7\,\mathrm{GPa},\ E_{\mathrm{p}} = E_y = 193.6\,\mathrm{GPa},\ \nu_{yx} = 0.21,$

$\mu = 5.5\,\mathrm{GPa},\ \alpha_{\mathrm{x}} = 21.4\text{E-}06\,\mathrm{per}\,^{\circ}\mathrm{C},\ \alpha_{\mathrm{p}} = \alpha_{\mathrm{y}} = 4.3\text{E-}06\,\mathrm{per}\,^{\circ}\mathrm{C},\ t_{\mathrm{p}} = 0.66\,\mathrm{mm}.$

The patch stiffness ratio $E_p t_p / E_s t_s$ (S) is 1.1. The sensitivity of the length of the patch relative to the skin thickness is studied. Four patch lengths $(2 \cdot L_p)$ of 10.16, 20.32, 30.48, and 40.64 cm are considered in the analysis. Since the thermal stresses in the patch are compressive and they will be negated under far-field tensile as found in Chapter 4 and Section 5.2.2, only the skin's thermal stresses will be reported here.

Thermal stresses in the skin at a patch's center in the x_2-component are of special interest, as they are needed for fracture analysis using Wang–Rose's crack-bridging model. Since the stress distributions in the plate and patch are linear through their thickness, it will be more meaningful to report these stresses in terms of the mean and bending values. These values of thermal stresses are plotted in Figure 5.10 as the functions of the normalized

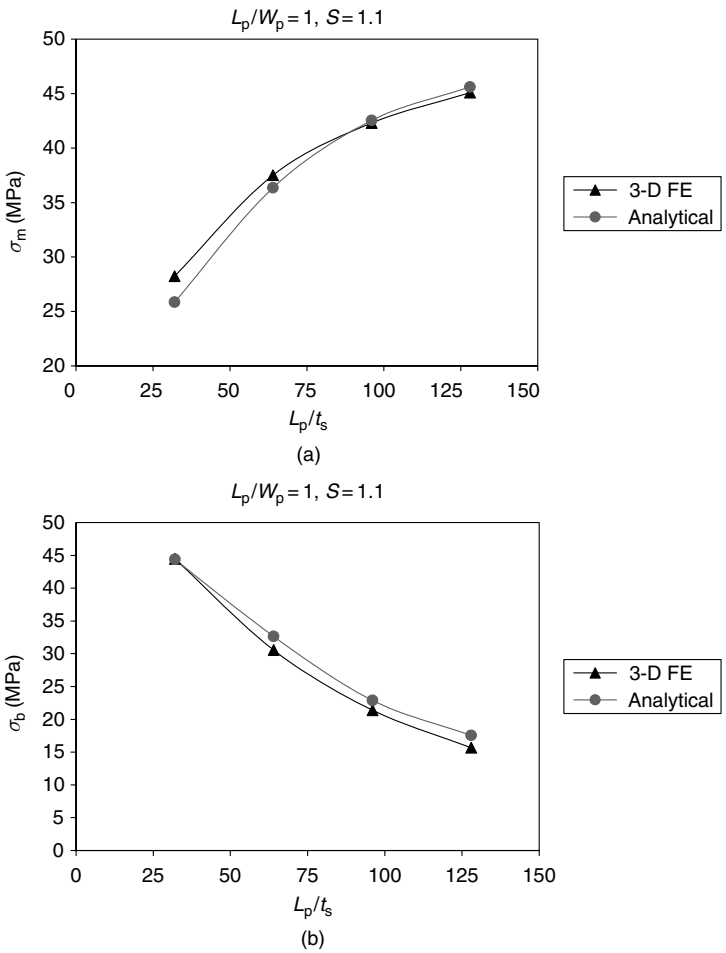

Fig. 5.10. Thermal stresses in the middle of a skin reinforced with a square patch for different normalized half patch lengths: (a) the mean stresses; and (b) the bending stresses.

half patch length L_p/t_s, where t_s is the skin thickness. The mean and bending stresses are defined as half of the sum and difference of stresses near the top and bottom surfaces of the skin. All analytical solutions are obtained using k_c in the recursive formula given in Equation (5.61) equal to 0.1, and they converge within about 30 iterations. To assess the accuracy of the analytical method, results from the FE analysis are also obtained and compared with the analytical predictions in Figure 5.10. FE analyses are carried out using ABAQUS (1997) with the skin and each ply of the patch modeled separately. The skin is modeled as three layers of 20-node solid elements while each ply of the patch by one layer of solid elements. To avoid the adverse effect of the small thickness-to-length ratio on the solution, stiffness matrices of all solid elements are evaluated using reduced integration. In the FE model, the skin was restrained from the out-of-plane deflection along its periphery. Similar results but for different patch's aspect ratios are presented in Figure 5.11 for $L_p/W_p = 2$ and in Figure 5.12 for $L_p/W_p = 1/2$. In contrast to the results from the plane-stress and linear bending analyses, from Figures 5.10–5.12, thermal stresses in the skin are affected by the patch size. For a same patch's aspect ratio, the mean components of the thermal stresses in the plate increase with patch sizes while the bending components show a reverse trend. These bending stresses will eventually vanish for large values of L_p/t_s as expected. In general, analytical predictions are in quite good agreement with the FE results (within 12%) for all aspect ratios L_p/W_p considered.

To show the effect of a patch's thickness on the thermal stresses, analyses of a few selective patch configurations above but with a thickness of 1.057 mm are performed and their results are summarized in Table 5.1. For reference, corresponding results previously presented in Figures 5.10–5.12 are repeated in the table. It follows from Table 5.1 that a thicker patch will induce higher thermal stresses in the skin as expected and a same good agreement is observed between the analytical and the FE results. Additional results, but not shown here, indicate that repaired skins with a same patch stiffness ratio $E_p t_p/E_s t_s$, same aspect ratio L_p/W_p, and same parameter L_p/t_s will have the same thermal stresses. Thus, for a given temperature change, the nonlinear thermal stresses can be characterized in terms of three non-dimensional parameters $E_p t_p/E_s t_s$, L_p/W_p, and L_p/t_s.

So far only patches of rectangular or square shapes have been considered. Another common shape of the patch is therefore selected for presentation. An octagonal patch sometimes is preferred to a rectangular patch because of its superior performance in preventing peeling near the corner of the patch. An analysis of an octagonal patch therefore will be demonstrated next. The geometry of the octagonal patch is the same as that shown in Figure 5.6. Material properties and thickness of the patch and the skin are identical to those given earlier in the beginning of this section. Analytical predictions as well as FE results for the thermal stresses in the skin are given below:

Analytical predictions, $\sigma_m = 32.1\,\text{MPa}$, $\sigma_b = 36.4\,\text{MPa}$.

FE results, $\sigma_m = 35.1\,\text{MPa}$, $\sigma_b = 34.7\,\text{MPa}$.

Again the analytical method predicts well the nonlinear thermal stresses.

As a final example, an infinite skin rigidly bonded with a square Boron/Epoxy patch ($L_p/W_p = 1$, $S = 1.1$, $L_p/t_s = 128$) under a wide range of temperature excursions is

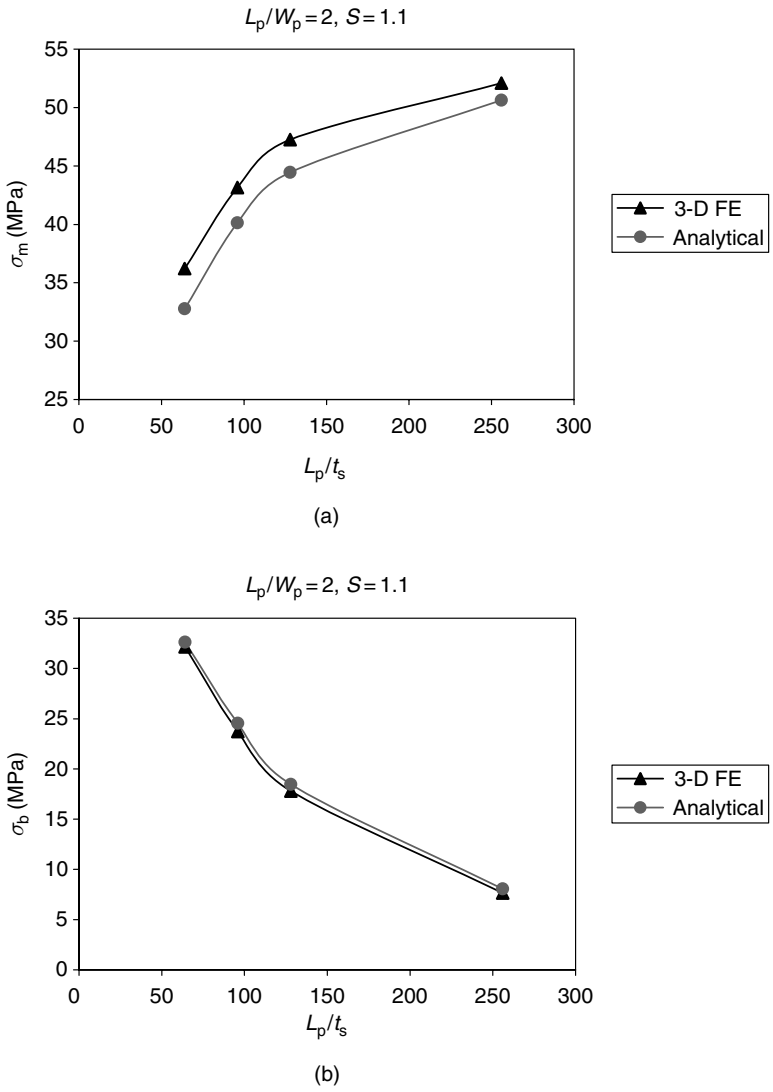

Fig. 5.11. Thermal stresses in the middle of a skin reinforced with a rectangular patch ($L_p/W_p = 2$) for different normalized half patch lengths: (a) the mean stresses; and (b) the bending stresses.

considered. The mean and bending components of the thermal stresses in a middle of the skin are plotted in Figures 5.13(a) and 5.13(b), respectively, for different cooling temperature ranges $|\Delta T|$. For a future discussion, the normalized bending stresses (σ_b/σ_m) are also plotted versus $|\Delta T|$ in Figure 5.14. From Figure 5.13, it seems that analytical predictions for the mean stresses are in excellent agreement with FE results for all $|\Delta T|$ while the analytical predictions for the bending stresses show a larger discrepancy with FE solutions. The deviation between analytical and FE results for the bending

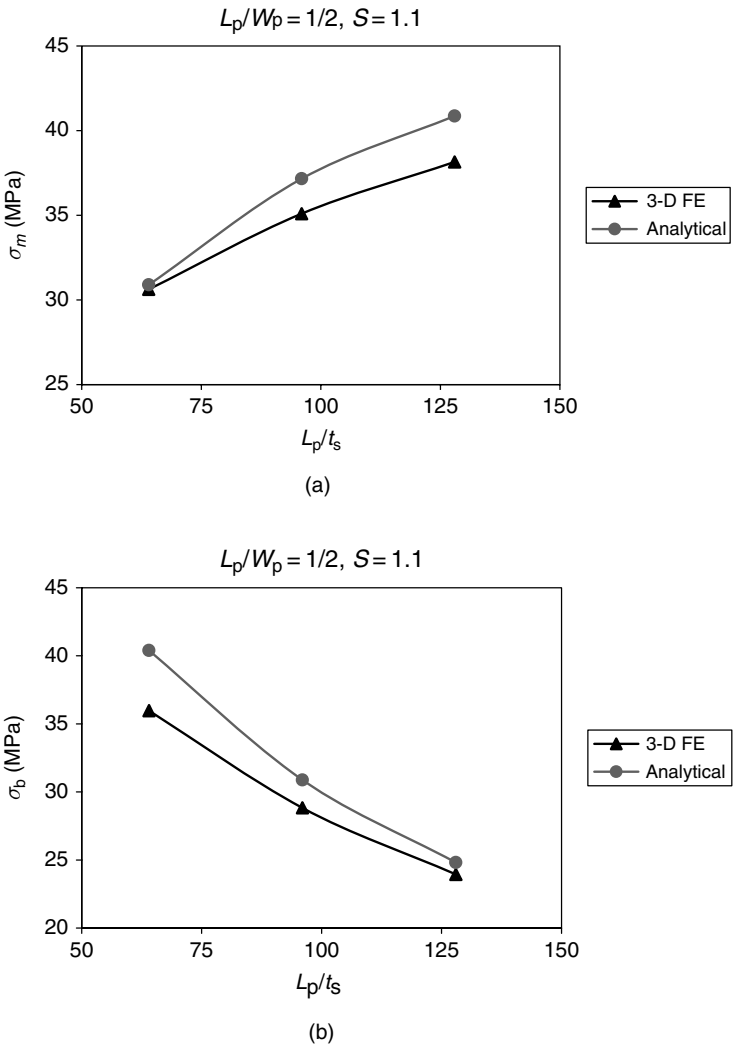

Fig. 5.12. Thermal stresses in the middle of a skin reinforced with a rectangular patch ($L_p/W_p = 1/2$) for different normalized half patch lengths: (a) the mean stresses; and (b) the bending stresses.

stresses may exceed 20% for $|\Delta T| > 100\,^{\circ}\text{C}$ and attains a largest value of 30% when $|\Delta T| = 138\,^{\circ}\text{C}$. However, since the contribution of the bending component to the total stress is significantly smaller for $|\Delta T| > 100\,^{\circ}\text{C}$ as illustrated in Figure 5.14 via σ_b/σ_m, this discrepancy may not be significant as it appears in Figure 5.13. For example, the analytical method predicts that the bending stress is 21% of the mean stresses when $|\Delta T| = 138\,^{\circ}\text{C}$ while the FE method yields a ratio of 28%. Thus, the agreement between two methods is considered to be satisfactory, in view of the approximate nature of the analytical model.

Table 5.1. Comparison of thermal stresses in the middle of a patched plate with different patch thicknesses.

L_p/t_s	L_p/W_p	t_p/t_s	Analytical method		FE method	
			σ_m^0 (MPa)	σ_b^0 (MPa)	σ_m^0 (MPa)	σ_b^0 (MPa)
128	1	0.416	45.6	17.6	45.1	15.7
128	1	0.666	49.8	20.1	49.3	18.5
128	2	0.416	44.4	18.4	47.3	17.8
128	2	0.666	49.9	20.2	53.0	20.0

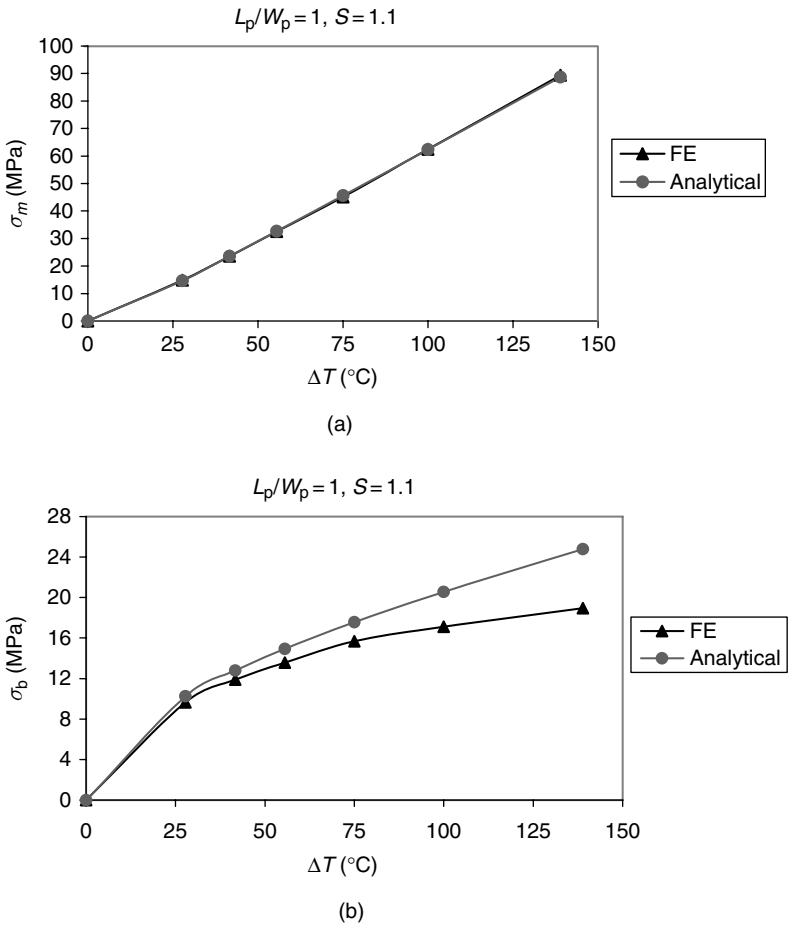

Fig. 5.13. Thermal stresses in the middle of a skin reinforced with a square patch for different temperature excursions: (a) the mean stresses; and (b) the bending stresses.

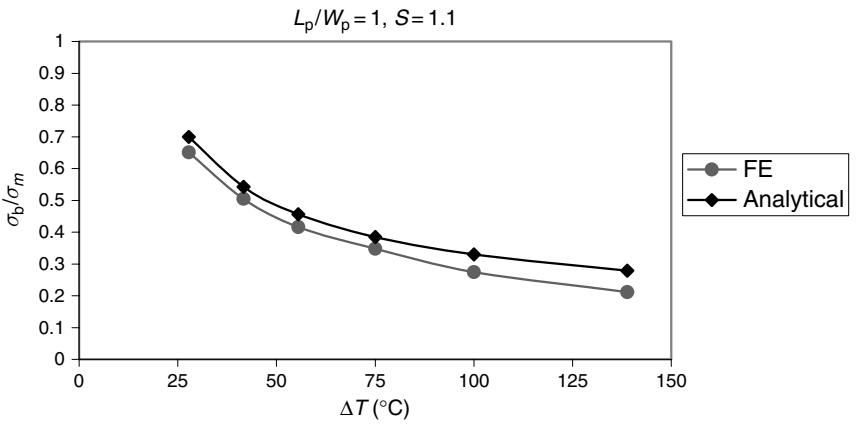

Fig. 5.14. Normalized bending stresses in the middle of a skin reinforced with a square patch for different temperature excursions.

5.3.2 Patch spanning across the entire plate's width under purely mechanical loading

The derivation presented here will be based on the approach given in Chapter 2 as employed by Rose (1988) and Hart-Smith (1999; Hart-Smith and Wilkins, 2000), which is different from the one considered earlier in part (a) of Section 5.3.1. The patched skin is initially flat before the external load per unit width P is applied (Figure 5.15). However, to make this solution generic for latter use in Section 5.3.3, the skin assumes to be pre-stressed with an initial stress of $\sigma_0^{(\text{init})}$ while the patch remains stress free. It should be emphasized that the initial load per unit width P_0 associated with $\sigma_0^{(\text{init})}$, i.e., $\sigma_0^{(\text{init})} t_s$, is different from the external load P. This problem may appear to be hypothetical; however, it will be shown to be relevant to the real physical problem of a bonded repair at the end of this section.

The development begins by writing the moment equilibrium equation for the region outside the overlap as

$$M_{22}^{\text{H}} = -D_{22}^{\text{s}} \frac{\mathrm{d}^2 w^{\text{H}}}{\mathrm{d}y^2} = -(P + P_0)\, w^{\text{H}} \quad \text{for} \quad 0 \le y \le l_\infty - \ell \tag{5.62}$$

or

$$\frac{\mathrm{d}^2 w^{\text{H}}}{\mathrm{d}y^2} - \frac{P + P_0}{D_{22}^{\text{s}}} w^{\text{H}} = 0 \tag{5.63}$$

The solution of Equation (5.63) is

$$w^{\text{H}} = W_1^{\text{H}} \cosh(\xi_{\text{H}} y) + W_2^{\text{H}} \sinh(\xi_{\text{H}} y) \tag{5.64}$$

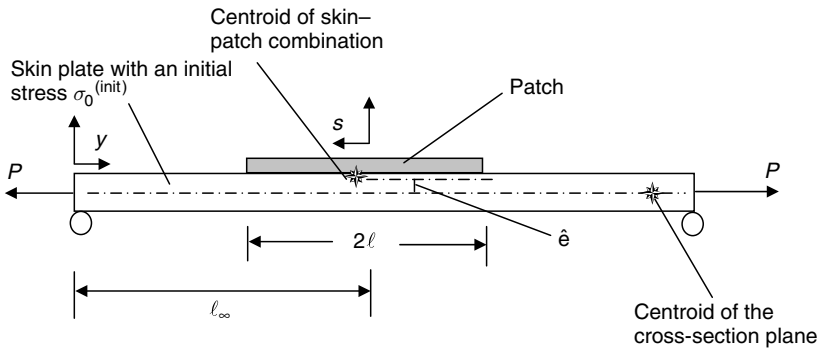

Fig. 5.15. Geometry for a one-dimensional analysis of a skin plate reinforced with a patch spanning across entire plate width under purely mechanical loading.

where

$$\xi_{\mathrm{H}} = \sqrt{\frac{P + P_0}{D_{22}^{\mathrm{s}}}} \tag{5.65}$$

The coefficient W_1^{H} must set equal to zero since there is no displacement at the support point $y = 0$. If the length of the skin plate is much longer than the overlap length, then Equation (5.64) together with $W_1^{\mathrm{H}} = 0$ will yield the following approximations for the displacement and slope at $y = l_\infty - \ell$:

$$\begin{aligned} w^{\mathrm{H}}\left(y = l_\infty - \ell\right) &\approx \frac{W_2^{\mathrm{H}}}{2} e^{\xi_{\mathrm{H}}(l_\infty - \ell)} \\ \frac{\mathrm{d}w^{\mathrm{H}}}{\mathrm{d}y}\left(y = l_\infty - \ell\right) &\approx \frac{W_2^{\mathrm{H}}}{2\zeta_{\mathrm{H}}} e^{\xi_{\mathrm{H}}(l_\infty - \ell)} \end{aligned} \tag{5.66}$$

Similarly, the moment equilibrium equation for the region inside the overlap can be expressed as

$$M_{22}^{\mathrm{I}} = -D_{22}^{\mathrm{I}} \frac{\mathrm{d}^2 w^{\mathrm{I}}}{\mathrm{d}s^2} = -P\left(w^{\mathrm{I}} - \hat{e}\right) - P_0 w^{\mathrm{I}} \quad \text{for} \quad 0 \le s \le \ell \tag{5.67}$$

where $\hat{e}$ is the eccentricity between the centroid of the skin and that of the skin–patch combination; D_{22}^{I} is the bending stiffness with respect to the centroid of the skin–patch combination.[1] The solution of this is

$$w^{\mathrm{I}} = W_1^{\mathrm{I}} \cosh\left(\xi_{\mathrm{I}} s\right) + W_2^{\mathrm{I}} \sinh\left(\xi_{\mathrm{I}} s\right) - \frac{P\hat{e}}{P + P_0} \tag{5.68}$$

[1] It is defined here differently from those given earlier in the previous sections. In the previous sections, D_{ijkl}^{I} was calculated with respect to the mid-plane of the skin.

where

$$\xi_{\mathrm{I}} = \sqrt{\frac{P + P_0}{D_{22}^{\mathrm{I}}}} \tag{5.69}$$

Enforcing the symmetry condition about the location $s = 0$ yields $W_2^{\mathrm{I}} = 0$, thus

$$w^{\mathrm{I}} = W_1^{\mathrm{I}} \cosh(\xi_{\mathrm{I}} s) - \frac{P\hat{e}}{P + P_0} \tag{5.70}$$

Completing the bending solution requires that the deflections and slopes match at the junction, $y = (l_\infty - \ell)$, $s = -\ell$. These conditions determine the unknown constants W_1^{I} and W_2^{H} as

$$\begin{aligned} W_1^{\mathrm{I}} &= \frac{P\hat{e}}{P + P_0} \left[\frac{1}{\cosh(\xi_{\mathrm{I}}\ell) + \dfrac{\xi_{\mathrm{I}}}{\xi_{\mathrm{H}}} \sinh(\xi_{\mathrm{I}}\ell)} \right] \\ W_2^{\mathrm{H}} &= -2\frac{\xi_{\mathrm{I}}}{\xi_{\mathrm{H}}} W_1^{\mathrm{I}} \sinh(\xi_{\mathrm{I}}\ell) \cdot e^{-\xi_{\mathrm{H}}(l_\infty - \ell)} \end{aligned} \tag{5.71}$$

recalling that $w^{\mathrm{H}}(y = l_\infty - \ell)$ and $\dfrac{\mathrm{d}w^{\mathrm{H}}}{\mathrm{d}y}(y = l_\infty - \ell)$ are given by Equation (5.66). Substituting Equation (5.70) for w^{I} and the first equation of (5.71) for W_1^{I} into (5.67) and evaluating the resulting expression of M_{22}^{I} at $s = 0$ yield the bending moment at the middle of the plate as

$$M_{22}^{\mathrm{I}}(0) = -\frac{P\hat{e}}{\cosh(\xi_{\mathrm{I}}\ell) + \dfrac{\xi_{\mathrm{I}}}{\xi_{\mathrm{H}}} \sinh(\xi_{\mathrm{I}}\ell)} \tag{5.72}$$

Once the bending moment is calculated, the bending stresses in the patch and skin at their middle can be determined by first obtaining the curvature via Equation (5.67), then the linear strain distribution across the thickness, and finally applying the constitutive relation, i.e.,

$$\begin{aligned} \kappa_{22}^{\mathrm{I}}(0) &= -\frac{\mathrm{d}^2 w^{\mathrm{I}}}{\mathrm{d}s^2} = \frac{M_{22}^{\mathrm{I}}(0)}{D_{22}^{\mathrm{I}}} \\ \varepsilon_{22}^{\mathrm{I}}(0,\ x_3) &= \left(x_3 - \breve{h}_0\right) \kappa_{22}^{\mathrm{I}}(0) \end{aligned} \tag{5.73}$$

$$\hat{\sigma}_{22}^{\mathrm{s}}(0) = -\frac{P\cdot\hat{e}\cdot t_{\mathrm{s}}\cdot E_{\mathrm{s}}'}{2\cdot\left[\cosh(\xi_{\mathrm{I}}\ell)+\dfrac{\xi_{\mathrm{I}}}{\xi_{\mathrm{H}}}\sinh(\xi_{\mathrm{I}}\ell)\right]D_{22}^{\mathrm{I}}}$$

$$\bar{\sigma}_{22}^{\mathrm{s}}(0) = \frac{P\cdot\hat{e}^2\cdot E_{\mathrm{s}}'}{\left[\cosh(\xi_{\mathrm{I}}\ell)+\dfrac{\xi_{\mathrm{I}}}{\xi_{\mathrm{H}}}\sinh(\xi_{\mathrm{I}}\ell)\right]D_{22}^{\mathrm{I}}}$$

$$\hat{\sigma}_{22}^{\mathrm{p}}(0) = -\frac{P\cdot\hat{e}\cdot t_{\mathrm{p}}\cdot E_{\mathrm{p}}'}{2\cdot\left[\cosh(\xi_{\mathrm{I}}\ell)+\dfrac{\xi_{\mathrm{I}}}{\xi_{\mathrm{H}}}\sinh(\xi_{\mathrm{I}}\ell)\right]D_{22}^{\mathrm{I}}} \tag{5.74}$$

$$\bar{\sigma}_{22}^{\mathrm{p}}(0) = \frac{P\cdot\hat{e}\cdot\left(\hat{e}-\frac{t_{\mathrm{p}}+t_{\mathrm{s}}}{2}\right)\cdot E_{\mathrm{p}}'}{\left[\cosh(\xi_{\mathrm{I}}\ell)+\dfrac{\xi_{\mathrm{I}}}{\xi_{\mathrm{H}}}\sinh(\xi_{\mathrm{I}}\ell)\right]D_{22}^{\mathrm{I}}}$$

where $\breve{h}_0$ is the x_3-coordinate of the neutral plane of the patch–plate combination, i.e., $\breve{h}_0 = \frac{t_{\mathrm{s}}}{2}+\hat{e}$; $E_{\mathrm{s}}' = \frac{E_{\mathrm{s}}}{1-\nu_{\mathrm{s}}^2}$; $E_{\mathrm{p}}' = \frac{E_{22}^{\mathrm{p}}}{1-\nu_{12}^{\mathrm{p}}\cdot\nu_{21}^{\mathrm{p}}}$; $\hat{\sigma}_{22}^{\mathrm{s}}, \bar{\sigma}_{22}^{\mathrm{s}}$, $\hat{\sigma}_{22}^{\mathrm{p}}$, and $\bar{\sigma}_{22}^{\mathrm{p}}$ are the bending and the mean components of the stresses in the skin and patch, respectively; the bending and mean stresses in a skin or patch are defined as half of the difference and sum of stresses near the top and the bottom surfaces of the skin or patch. It is interesting to note that the bending moment at the middle of the overlap also contribute to the mean stresses of the patch and skin since the centroids of the individual skin and patch are offset from the centroid of the patch–skin combination.

So far only the bending solution of the patched plate is considered. For the complete solution, one must add the axial solution due to the axial load to the previous bending solution. The axial solution for this problem due to load P without the prescribed "initial stress" is thus sought since the initial stress has no effect on the axial behavior and that initial stress can be simply added to the sought solution later. This axial stress solution is derived from the force equilibrium equation and the strain compatibility condition as follows. At any cross section, the net force must be equal to P. Thus, at the middle of the patched skin,

$$\begin{aligned}\sigma_{22}^{\mathrm{s}}t_{\mathrm{s}}+\sigma_{22}^{\mathrm{p}}t_{\mathrm{p}} &= P\\ \left(E_{\mathrm{s}}'t_{\mathrm{s}}+E_{\mathrm{p}}'t_{\mathrm{p}}\right)\,\varepsilon_{22}^{\mathrm{I}} &= P\end{aligned} \tag{5.75}$$

where the strain compatibility condition $\varepsilon_{22}^{\mathrm{s}} = \varepsilon_{22}^{\mathrm{p}} = \varepsilon_{22}^{\mathrm{I}}$ and the stress–strain relation of the skin and patch have been used in the derivation. It is then very easy to show from Equation (5.75) that the axial stresses in the skin and in the patch are given by

$$\begin{aligned}\sigma_{22}^{\mathrm{s}} &= \frac{P}{(1+S)\,t_{\mathrm{s}}}\\ \sigma_{22}^{\mathrm{p}} &= \frac{P\cdot S}{(1+S)\,t_{\mathrm{p}}}\end{aligned} \tag{5.76}$$

where

$$S = \frac{E'_{\mathrm{p}} t_{\mathrm{p}}}{E'_{\mathrm{s}} t_{\mathrm{s}}} \tag{5.77}$$

The total mean stresses in the skin or patch then can be derived by linear superposition of the initial stress, bending and axial solutions as

$$\begin{aligned}
\bar{\sigma}^{\mathrm{s}}_{22}(0) &= \sigma_0^{(\mathrm{init})} + \frac{P}{(1+S)\,t_{\mathrm{s}}} + \frac{P \cdot \hat{e}^2 \cdot E'_{\mathrm{s}}}{\left[\cosh(\xi_{\mathrm{I}}\ell) + \dfrac{\xi_{\mathrm{I}}}{\xi_{\mathrm{H}}}\sinh(\xi_{\mathrm{I}}\ell)\right] D^{\mathrm{I}}_{22}} \\
\bar{\sigma}^{\mathrm{p}}_{22}(0) &= \frac{P \cdot S}{(1+S)\,t_{\mathrm{p}}} + \frac{P \cdot \hat{e} \cdot E'_{\mathrm{p}} \left(\hat{e} - \dfrac{t_{\mathrm{p}} + t_{\mathrm{s}}}{2}\right)}{\left[\cosh(\xi_{\mathrm{I}}\ell) + \dfrac{\xi_{\mathrm{I}}}{\xi_{\mathrm{H}}}\sinh(\xi_{\mathrm{I}}\ell)\right] D^{\mathrm{I}}_{22}}
\end{aligned} \tag{5.78}$$

It is clear from Equations (5.74) and (5.78) that load P causes the following additional mean and bending stresses in the skin and the patch near their middle besides the prescribed initial stress $\sigma_0^{(\mathrm{init})}$:

$$\begin{aligned}
\Delta\bar{\sigma}^{\mathrm{s}}_{22}(0) &= \frac{P}{(1+S)\,t_{\mathrm{s}}} + \frac{P \cdot \hat{e}^2 \cdot E'_{\mathrm{s}}}{\left[\cosh(\xi_{\mathrm{I}}\ell) + \dfrac{\xi_{\mathrm{I}}}{\xi_{\mathrm{H}}}\sinh(\xi_{\mathrm{I}}\ell)\right] D^{\mathrm{I}}_{22}} \\
\Delta\hat{\sigma}^{\mathrm{s}}_{22}(0) &= -\frac{P \cdot \hat{e} \cdot t_{\mathrm{s}} \cdot E'_{\mathrm{s}}}{2 \cdot \left[\cosh(\xi_{\mathrm{I}}\ell) + \dfrac{\xi_{\mathrm{I}}}{\xi_{\mathrm{H}}}\sinh(\xi_{\mathrm{I}}\ell)\right] D^{\mathrm{I}}_{22}} \\
\Delta\bar{\sigma}^{\mathrm{p}}_{22}(0) &= \frac{P \cdot S}{(1+S)\,t_{\mathrm{p}}} + \frac{P \cdot \hat{e} \cdot \left(\hat{e} - \dfrac{t_{\mathrm{s}} + t_{\mathrm{p}}}{2}\right) \cdot E'_{\mathrm{p}}}{\left[\cosh(\xi_{\mathrm{I}}\ell) + \dfrac{\xi_{\mathrm{I}}}{\xi_{\mathrm{H}}}\sinh(\xi_{\mathrm{I}}\ell)\right] D^{\mathrm{I}}_{22}} \\
\Delta\hat{\sigma}^{\mathrm{p}}_{22}(0) &= -\frac{P \cdot \hat{e} \cdot t_{\mathrm{p}} \cdot E'_{\mathrm{p}}}{2 \cdot \left[\cosh(\xi_{\mathrm{I}}\ell) + \dfrac{\xi_{\mathrm{I}}}{\xi_{\mathrm{H}}}\sinh(\xi_{\mathrm{I}}\ell)\right] D^{\mathrm{I}}_{22}}
\end{aligned} \tag{5.79}$$

On the other hand, the corresponding increases in the mean and the bending stresses of the skin and the patch due to P based on the geometrically linear analysis[2] and plane stress analysis (without considering the out-of-plane deflection) are given, respectively, by

[2] It is easy to show that the only difference between the geometrically linear and nonlinear analyses is that the bending moment at the middle of the overlap in the former analysis is equal to $P\hat{e}$ instead of that given by Equation (5.72). In fact, the bending moment in the linear analysis is constant inside the overlap.

$$
\begin{aligned}
\Delta\bar{\sigma}_{22}{}^{\text{s-LN}}(0) &= \frac{P}{(1+S)\,t_{\text{s}}} + \frac{P\cdot\hat{e}^2\cdot E'_{\text{s}}}{D^{\text{I}}_{22}}\\
\Delta\hat{\sigma}_{22}{}^{\text{s-LN}}(0) &= -\frac{P\cdot\hat{e}\cdot t_{\text{s}}\cdot E'_{\text{s}}}{2\cdot D^{\text{I}}_{22}}\\
\Delta\bar{\sigma}_{22}{}^{\text{s-PLANE}}(0) &= \frac{P}{(1+S)\,t_{\text{s}}}\\
\Delta\hat{\sigma}_{22}{}^{\text{s-PLANE}}(0) &= 0\\
\Delta\bar{\sigma}^{\text{p-LN}}_{22}(0) &= \frac{P\cdot S}{(1+S)\,t_{\text{p}}} + \frac{P\cdot\hat{e}\left(\hat{e}-\dfrac{t_{\text{s}}+t_{\text{p}}}{2}\right)\cdot E'_{\text{p}}}{D^{\text{I}}_{22}}\\
\Delta\hat{\sigma}^{\text{p-LN}}_{22}(0) &= -\frac{P\cdot\hat{e}\cdot t_{\text{p}}\cdot E'_{\text{p}}}{2\cdot D^{\text{I}}_{22}}\\
\Delta\bar{\sigma}_{22}{}^{\text{p-PLANE}}(0) &= \frac{P\cdot S}{(1+S)\,t_{\text{p}}}\\
\Delta\hat{\sigma}_{22}{}^{\text{p-PLANE}}(0) &= 0
\end{aligned}
\tag{5.80}
$$

From Equations (5.79) and (5.80), and by noting that $\xi_{\text{I}} = \sqrt{\frac{P_0+P}{D^{\text{I}}_{22}}}$, it is clear that for low load levels of P and P_0, $\Delta\bar{\sigma}^{\text{s}}_{22}(0)$, $\Delta\hat{\sigma}^{\text{s}}_{22}(0)$, $\Delta\bar{\sigma}^{\text{p}}_{22}(0)$, and $\Delta\hat{\sigma}^{\text{p}}_{22}(0)$ are approximately equal to the geometrically linear solutions $\Delta\bar{\sigma}^{\text{s-LN}}_{22}(0)$, $\Delta\hat{\sigma}^{\text{s-LN}}_{22}(0)$, $\Delta\bar{\sigma}^{\text{p-LN}}_{22}(0)$, and $\Delta\hat{\sigma}^{\text{p-LN}}_{22}(0)$, respectively, and they approach the plane stress solutions $\Delta\bar{\sigma}^{\text{s-PLANE}}_{22}(0)$, $\Delta\hat{\sigma}^{\text{s-PLANE}}_{22}(0)$, $\Delta\bar{\sigma}^{\text{p-PLANE}}_{22}(0)$, and $\Delta\hat{\sigma}^{\text{p-PLANE}}_{22}(0)$ for a combination of long overlap and high load P since $\cosh(\xi_{\text{I}}\ell)\approx 1$, $\sinh(\xi_{\text{I}}\ell)\approx 0$ for $\xi_4 c \ll 1$, and $\cosh(\xi_4 c)\gg 1$, $\sinh(\xi_4 c)\gg 1$ for $\xi_{\text{I}}\ell \gg 1$. Physically, for a high load P, the skin/patch combination tries to deflect sufficiently to align its centroid with the line of action of the applied load. Moreover, since $\xi_{\text{I}} = \sqrt{\frac{P+P_0}{D^{\text{I}}_{22}}}$, the effect of the initial load P_0 is to make this alignment of the centroid to occur earlier at the lower load P for a given overlapped length. For future development, it is very easy to show from Equations (5.79) and (5.80) that $\Delta\bar{\sigma}^{\text{s}}_{22}(0)$, $\Delta\hat{\sigma}^{\text{s}}_{22}(0)$, $\Delta\bar{\sigma}^{\text{p}}_{22}(0)$, and $\Delta\hat{\sigma}^{\text{p}}_{22}(0)$ can be expressed in terms of $\Delta\bar{\sigma}^{\text{s-LN}}_{22}(0)$, $\Delta\hat{\sigma}^{\text{s-LN}}_{22}(0)$, $\Delta\bar{\sigma}^{\text{s-PLANE}}_{22}(0)$, $\Delta\hat{\sigma}^{\text{s-PLANE}}_{22}(0)$, $\Delta\bar{\sigma}^{\text{p-LN}}_{22}(0)$, $\Delta\hat{\sigma}^{\text{p-LN}}_{22}(0)$, $\Delta\bar{\sigma}^{\text{p-PLANE}}_{22}(0)$, and $\Delta\hat{\sigma}^{\text{p-PLANE}}_{22}(0)$ as

$$
\begin{aligned}
\Delta\bar{\sigma}^{\text{s}}_{ij}(0) &= \chi_{\text{b}}\cdot\chi^{\text{s}}_{m-1}\cdot\Delta\bar{\sigma}^{\text{s-LN}}_{ij}(0) + (1-\chi_{\text{b}})\cdot\chi^{\text{s}}_{m-2}\cdot\Delta\bar{\sigma}^{\text{s-PLANE}}_{ij}(0)\\
\Delta\hat{\sigma}^{\text{s}}_{ij}(0) &= \chi_{\text{b}}\cdot\Delta\hat{\sigma}^{\text{s-LN}}_{ij}(0)\\
\Delta\bar{\sigma}^{\text{p}}_{ij}(0) &= \chi_{\text{b}}\cdot\chi^{\text{p}}_{m-1}\cdot\Delta\bar{\sigma}^{\text{p-LN}}_{ij}(0) + (1-\chi_{\text{b}})\cdot\chi^{\text{p}}_{m-2}\cdot\Delta\bar{\sigma}^{\text{p-PLANE}}_{ij}(0)\\
\Delta\hat{\sigma}^{\text{p}}_{ij}(0) &= \chi_{\text{b}}\cdot\Delta\hat{\sigma}^{\text{p-LN}}_{ij}(0)
\end{aligned}
\tag{5.81}
$$

where χ^{s}_{m-1}, χ^{s}_{m-2}, χ^{p}_{m-1}, χ^{p}_{m-2}, and χ_b defined by

$$\chi^{s}_{m-1} = \frac{\Delta\bar{\sigma}^{s}_{22}(0)}{\Delta\bar{\sigma}^{s-LN}_{22}(0)} = \frac{\dfrac{1}{(1+S)\,t_s} + \dfrac{\hat{e}^2 \cdot E'_s}{\left[\cosh(\xi_I \ell) + \dfrac{\xi_I}{\xi_H}\sinh(\xi_I \ell)\right] D^{I}_{22}}}{\dfrac{1}{(1+S)\,t_s} + \dfrac{\hat{e}^2 \cdot E'_s}{D^{I}_{22}}}$$

$$\chi^{s}_{m-2} = \frac{\Delta\bar{\sigma}^{s}_{22}(0)}{\Delta\bar{\sigma}^{s-PLANE}_{22}(0)} = \frac{\dfrac{1}{(1+S)\,t_s} + \dfrac{\hat{e}^2 \cdot E'_s}{\left[\cosh(\xi_I \ell) + \dfrac{\xi_I}{\xi_H}\sinh(\xi_I \ell)\right] D^{I}_{22}}}{\dfrac{1}{(1+S)\,t_s}}$$

$$\chi_b = \frac{\Delta\hat{\sigma}^{s}_{22}(0)}{\Delta\hat{\sigma}^{s-LN}_{22}(0)} = \frac{\Delta\hat{\sigma}^{p}_{22}(0)}{\Delta\hat{\sigma}^{p-LN}_{22}(0)} = \frac{1}{\left[\cosh(\xi_I \ell) + \dfrac{\xi_I}{\xi_H}\sinh(\xi_I \ell)\right]} \tag{5.82}$$

$$\chi^{p}_{m-1} = \frac{\Delta\bar{\sigma}^{p}_{22}(0)}{\Delta\bar{\sigma}^{p-LN}_{22}(0)} = \frac{\dfrac{S}{(1+S)\,t_p} + \dfrac{\hat{e}\left(\hat{e} - \dfrac{t_s + t_p}{2}\right) \cdot E'_p}{\left[\cosh(\xi_I \ell) + \dfrac{\xi_I}{\xi_H}\sinh(\xi_I \ell)\right] D^{I}_{22}}}{\dfrac{S}{(1+S)\,t_p} + \dfrac{\hat{e}\left(\hat{e} - \dfrac{t_s + t_p}{2}\right) \cdot E'_p}{D^{I}_{22}}}$$

$$\chi^{p}_{m-2} = \frac{\Delta\bar{\sigma}^{p}_{22}(0)}{\Delta\bar{\sigma}^{p-PLANE}_{22}(0)} = \frac{\dfrac{S}{(1+S)\,t_p} + \dfrac{\hat{e}\left(\hat{e} - \dfrac{t_s + t_p}{2}\right) \cdot E'_p}{\left[\cosh(\xi_I \ell) + \dfrac{\xi_I}{\xi_H}\sinh(\xi_I \ell)\right] D^{I}_{22}}}{\dfrac{S}{(1+S)\,t_p}}$$

It remains now to show how the solution of the hypothetical problem posed above can be applied to the real physical problem of a repair. Consider a problem of a skin plate reinforced with a patch spanning across the entire width of the skin subjected to the temperature change of ΔT and the remote stress $\sigma_{\infty 22} = E'_s\left(\alpha^{p}_{22} - \alpha_s\right)\Delta T$. When one writes $\sigma_{\infty 22} = E'_s\left(\alpha^{p}_{22} - \alpha_s\right)\Delta T$, it only means that the magnitude of the remote stress $\sigma_{\infty 22}$ is specified to be equal to the numerical value of $E'_s\left(\alpha^{p}_{22} - \alpha_s\right)\Delta T$. The stress and strain solutions of this problem will be given by

$$\begin{aligned}
\varepsilon^{s}_{22} &= \varepsilon^{p}_{22} = \alpha^{p}_{22}\Delta T \\
\sigma^{s}_{22} &= E'_s\left(\varepsilon^{s}_{22} - \alpha_s \Delta T\right) = E'_s\left(\alpha^{p}_{22} - \alpha_s\right)\Delta T = \sigma_{\infty 22} \\
\sigma^{p}_{22} &= E'_p\left(\varepsilon^{p}_{22} - \alpha^{p}_{22}\Delta T\right) = E'_p\left(\alpha^{p}_{22}\Delta T - \alpha^{p}_{22}\Delta T\right) = 0
\end{aligned} \tag{5.83}$$

These above solutions for stresses and strains clearly satisfy the equilibrium equation, i.e., the net force per unit width at any cross section in the skin is equal to $\sigma_{\infty 22} t_s$, the strain compatibility condition between the plate and the patch inside the overlap, the traction continuity at the end of the overlap, and the constitutive relations. Since the strains in the skin and the patch are not only equal to each other but they are also uniformly distributed across their thickness, the repaired skin must be flat under the prescribed thermo-mechanical loads. Let us assume now that instead of applying the remote stress $\sigma_{\infty 22} = E'_s\left(\alpha^p_{22} - \alpha_s\right)\Delta T$, one applies the higher remote stress $\sigma'_{\infty 22} = E'_s\left(\alpha^p_{22} - \alpha_s\right)\Delta T + \Delta\sigma_{\infty 22}$, where $\Delta\sigma_{\infty 22} > 0$. It is then clear that the solution of the latter problem will be the same as that of the hypothetical problem posed in the beginning of this section if P and $\sigma_0^{(\text{init})}$ are defined as $P = \Delta\sigma_{\infty 22} t_s$ and $\sigma_0^{(\text{init})} = E'_s\left(\alpha^p_{22} - \alpha_s\right)\Delta T$, respectively. This is because the initial state of the hypothetical problem, i.e., a flat skin with an initial stress in the skin but a zero stress in the patch, is the same as the deformed state of the present thermo-mechanical problem at the remote stress level of $E'_s\left(\alpha^p_{22} - \alpha_s\right)\Delta T$. Thus, as the load increases from $\sigma_{\infty 22} = E'_s\left(\alpha^p_{22} - \alpha_s\right)\Delta T$ to $E'_s\left(\alpha^p_{22} - \alpha_s\right)\Delta T + \Delta\sigma_{\infty 22}$, the patched skin in the thermo-mechanical problem will behave the same as that of the hypothetical problem.

5.3.3 Polygonal patch under combined thermo-mechanical loading

Consider an infinite isotropic skin plate bonded rigidly with a polygon-shaped patch Ω as in Section 5.3.1. However, the repaired skin assumes to be subjected to uniform stresses at infinity in addition to the uniform temperature change ΔT (see Figure 5.4). For simplicity, all shear components are assumed to be zero. Again, the patched region of the skin is treated as an inhomogeneity.

It is rather unwieldy to solve the stated problem using a rigorous geometrically nonlinear analysis. An approximate solution based on an engineering approach developed by Duong (2004) therefore will be presented in this section. Since all materials involved are assumed to be linear elastic and no geometrically nonlinear instability is assumed to occur, the loading sequence of the thermal and mechanical loads will not affect the final results. Thus, in the solution procedure, the repaired skin assumes to be subjected to the thermal load first and subsequently to the mechanical load, instead of applying these two loads simultaneously. The solution procedure proposed by Duong (2004) for the thermo-mechanical problem of a polygonal patch involves three steps. Depending on the magnitudes of the far-field-applied stresses relative to the thermal stresses, as explained later, the solution of the thermo-mechanical problem may be achieved after only the first step, first two steps or all three steps of the procedure.

Step 1

In the first step of the solution procedure, the mechanical load is set equal to zero and the solution of the problem of nonlinear thermal stress is obtained by the method described in Section 5.3.1. The purpose of this step is to determine the purely thermal stresses in the repair and the nonlinear parameter e_{NL} (see Section 5.3.1). It should be emphasized that this step involves an iterative process. It is clear that when there is no mechanical load involved in the solving problem, the solution of this step will also be the final solution. On the other hand, when there is no thermal load involved in the

solving problem, the solution of this step is trivial, i.e., thermal stresses and e_{NL} are equal to zero.

Step 2

In the second step of the solution procedure, fictitious stresses σ_{ij}^{f} proportional to the prescribed remote stresses $\sigma_{\infty ij}$ are applied to the repaired skin in addition to the prescribed temperature change. Thus, stresses σ_{ij}^{f} are defined by $\sigma_{ij}^{\mathrm{f}} = \lambda \sigma_{\infty ij}$, where λ is a scalar number. The purpose of the second step is to determine the minimum fictitious applied stresses σ_{ij}^{f}, denoted by $\sigma_{ij}^{\mathrm{f}*}$, that will nullify the initial curvature caused by thermal loads. For $0 \leq \sigma_{ij}^{\mathrm{f}} \leq \sigma_{ij}^{\mathrm{f}*}$, the response of the repaired skin is dominated by the thermal loading. The stresses $\sigma_{ij}^{\mathrm{f}*}$ are in general determined by trial and error. Solutions of the thermo-mechanical problem for different trial values of σ_{ij}^{f} are obtained, and the bending stresses at the middle of the repaired skin are evaluated for these cases. The applied stress $\sigma_{ij}^{\mathrm{f}*}$ is then determined as the smallest of σ_{ij}^{f} among its trial values that results in zero bending stresses at the middle of the repaired skin for the very first time.

In order to determine $\sigma_{ij}^{\mathrm{f}*}$ mentioned above, the solution of the thermo-mechanical problem for a given σ_{ij}^{f} must be obtained. The solution method for this thermo-mechanical problem is therefore outlined next. Since the response of the repaired skin is dominated by the thermal loading for $0 \leq \sigma_{ij}^{\mathrm{f}} \leq \sigma_{ij}^{\mathrm{f}*}$, the incremental displacement field caused by σ_{ij}^{f} assumes to be a *linear* perturbation of the principal displacement field due to purely thermal loading. However, the reader is reminded that the principal displacement field due to purely thermal loading is geometrically nonlinear and corresponds to $\sigma_{ij}^{\mathrm{f}} = 0$. As shown in Section 5.3.1, since the geometrical nonlinearity enters into the formulation only through the parameter e_{NL}, the implication of the above assumption for the incremental displacement field caused by σ_{ij}^{f} is that for $0 \leq \sigma_{ij}^{\mathrm{f}} \leq \sigma_{ij}^{\mathrm{f}*}$ the thermo-mechanical can be solved using the solution approach developed earlier in Section 5.2 (for geometrically linear analysis) with the following changes similar to those given in Section 5.3.1: (i) stiffness tensors A_{ijkl}^{I}, B_{ijkl}^{I}, and D_{ijkl}^{I}, thermal stress and moment resultants $N_{ij}^{(\mathrm{T})}$ and $M_{ij}^{(\mathrm{T})}$ of the inhomogeneity are evaluated with respect to the reference plane $x_3 = h_0 - e_{\mathrm{NL}}$ while stiffness tensors A_{ijkl}^{s}, B_{ijkl}^{s}, and D_{ijkl}^{s} of the region outside the inhomogeneity or of the homogeneous problem are evaluated with respect to the reference plane $x_3 = h_0$, and (ii) h_0 in Equation (5.28) is replaced by $(h_0 - e_{\mathrm{NL}})$, where e_{NL} in (i) and (ii) is a known constant determined previously from step 1, which represents the effect of geometrical nonlinearity on the displacement field of the repaired skin under purely thermal loading.

Once stresses $\sigma_{ij}^{\mathrm{f}*}$ are determined, they will be compared with prescribed remote stresses $\sigma_{\infty ij}$. If $\sigma_{\infty ij} \leq \sigma_{ij}^{\mathrm{f}*}$, the response of the repaired skin under a combined far-field-applied stresses $\sigma_{\infty ij}$ and temperature excursion will be still dominated by the thermal loading. The solution of the thermo-mechanical problem posed originally at the beginning of this section, therefore, can be obtained by the process given in the preceding paragraph using the actual remote stresses $\sigma_{\infty ij}$ since $0 \leq \sigma_{\infty ij} \leq \sigma_{ij}^{\mathrm{f}*}$ in this case, and step 3 below will be omitted. On the other hand, when $\sigma_{\infty ij} > \sigma_{ij}^{\mathrm{f}*}$, it is necessary to divide the prescribed far-field-applied stresses $\sigma_{\infty ij}$ into two portions: $\sigma_{ij}^{\mathrm{f}*}$ and $(\sigma_{\infty ij} - \sigma_{ij}^{\mathrm{f}*})$. This is because as the applied stresses $\sigma_{\infty ij}$ increase from zero to their final values, the curvature of the repaired skin will first reduce from its initial value associated with the thermal bending to zero

and then will reverse in sign as the remote stresses $\sigma_{\infty ij}$ increase beyond the $\sigma_{ij}^{\mathrm{f}*}$ values. The response of the repaired skin due to the first portion of $\sigma_{\infty ij}$, i.e., $\sigma_{ij}^{\mathrm{f}*}$, is dominated by the thermal loading, and therefore it can be obtained by following the process described in the preceding paragraph with remote stresses equal to $\sigma_{ij}^{\mathrm{f}*}$. In contrast, the response of the repaired skin due to the second portion $(\sigma_{\infty ij} - \sigma_{ij}^{\mathrm{f}*})$ of the applied far-field stresses is dominated by the mechanical loading, which must be determined by a new solution method. This new solution method for the mechanically dominated regime is described in step 3 below. It should be noted that the response of the repaired skin is flat at $\sigma_{ij}^{\mathrm{f}*}$ so that there is no bending stresses in the repaired skin at that applied stress level. However, at the applied stress $\sigma_{ij}^{\mathrm{f}*}$, the skin will have high *mean* tensile stresses while the patch will be virtually stress-free. For the future development, these mean stresses in the skin at the center of the patch due to the combined thermal load and $\sigma_{ij}^{\mathrm{f}*}$ will be denoted by $\sigma_{ij}^{\mathrm{s-step2}}(\mathbf{0})$ while the patch stresses are approximately zero there. It is obvious that in the absence of the thermal load, $\sigma_{ij}^{\mathrm{f}*}$ and $\sigma_{ij}^{\mathrm{s-step2}}(\mathbf{0})$ are equal to zero so that step 2 can be omitted.

Step 3

In step 3, the response of a pre-stressed flat skin repaired with a polygonal patch and subjected to the far-field-applied stresses $(\sigma_{\infty ij} - \sigma_{ij}^{\mathrm{f}*})$ is determined. As mentioned in the preceding paragraph, even though the repaired skin becomes flat at $\sigma_{ij}^{\mathrm{f}*}$, however, the repaired skin is not stress-free. The repaired plate has a mean stress of $\sigma_{ij}^{\mathrm{s-step2}}(\mathbf{0})$ locked in the skin. Thus, stresses $\sigma_{ij}^{\mathrm{s-step2}}(\mathbf{0})$ are modeled as the "initial stresses" in this step. It should be emphasized that the thermal loads will not be considered in this step since their effect is already accounted for in the formulation indirectly through the initial stresses $\sigma_{ij}^{\mathrm{s-step2}}(\mathbf{0})$. The solution of the problem considered in this step is available for a patch spanning across the entire width of the skin, and it is given in Section 5.3.2. It should be noted that P and P_0 defined in that section are related to $(\sigma_{\infty ij} - \sigma_{ij}^{\mathrm{f}*})$ and $\sigma_{ij}^{\mathrm{s-step2}}(\mathbf{0})$ described here by $P = (\sigma_{\infty 22} - \sigma_{22}^{\mathrm{f}*}) \cdot t_{\mathrm{s}}$ and $P_0 = t_{\mathrm{s}} \cdot \sigma_{22}^{\mathrm{s-step2}}(\mathbf{0})$.

Similar to the analysis given in Section 5.3.2, the *final* mean and bending stresses in the skin and the patch at their middle of the thermo-mechanical problem with a polygonal patch will be expressed as

$$\begin{aligned}
\bar{\sigma}_{ij}^{\mathrm{s}}(\mathbf{0}) &= \sigma_{ij}^{\mathrm{s-step2}}(\mathbf{0}) + \Delta\bar{\sigma}_{ij}^{\mathrm{s}}(\mathbf{0}) \\
\hat{\sigma}_{ij}^{\mathrm{s}}(\mathbf{0}) &= \Delta\hat{\sigma}_{ij}^{\mathrm{s}}(\mathbf{0}) \\
\bar{\sigma}_{ij}^{\mathrm{p}}(\mathbf{0}) &= \Delta\bar{\sigma}_{ij}^{\mathrm{p}}(\mathbf{0}) \\
\hat{\sigma}_{ij}^{\mathrm{p}}(\mathbf{0}) &= \Delta\hat{\sigma}_{ij}^{\mathrm{p}}(\mathbf{0})
\end{aligned} \tag{5.84}$$

where $\Delta\bar{\sigma}_{ij}^{\mathrm{s}}$, $\Delta\hat{\sigma}_{ij}^{\mathrm{s}}$, $\Delta\bar{\sigma}_{ij}^{\mathrm{p}}$, and $\Delta\hat{\sigma}_{ij}^{\mathrm{p}}$ are the additional mean and bending stresses in the skin and the patch, respectively, due to the remote stresses $(\sigma_{\infty ij} - \sigma_{ij}^{\mathrm{f}*})$. It should be noted that the bending stresses in Equation (5.84) have no corresponding contributions from step 2 since the response of the repaired skin is flat at $\sigma_{ij}^{\mathrm{f}*}$. Also, the mean stress in the patch at its middle has only arisen from step 3. By generalizing the results given in Section 5.3.2 for a patch spanning across the skin width to the polygonal patch,

the geometrically nonlinear solutions $\Delta\bar{\sigma}_{ij}^{s}(\mathbf{0})$, $\Delta\hat{\sigma}_{ij}^{s}(\mathbf{0})$, $\Delta\bar{\sigma}_{ij}^{p}(\mathbf{0})$, and $\Delta\hat{\sigma}_{ij}^{p}(\mathbf{0})$ of the polygonal patch problem can be determined approximately as

$$\begin{aligned}
\Delta\bar{\sigma}_{ij}^{s}(\mathbf{0}) &= \chi_b \cdot \chi_{m-1}^{s} \cdot \Delta\bar{\sigma}_{ij}^{s-LN}(\mathbf{0}) + (1-\chi_b) \cdot \chi_{m-2}^{s} \cdot \Delta\bar{\sigma}_{ij}^{s-PLANE}(\mathbf{0}) \\
\Delta\hat{\sigma}_{ij}^{s}(\mathbf{0}) &= \chi_b \cdot \Delta\hat{\sigma}_{ij}^{s-LN}(\mathbf{0}) \\
\Delta\bar{\sigma}_{ij}^{p}(\mathbf{0}) &= \chi_b \cdot \chi_{m-1}^{p} \cdot \Delta\bar{\sigma}_{ij}^{p-LN}(\mathbf{0}) + (1-\chi_b) \cdot \chi_{m-2}^{p} \cdot \Delta\bar{\sigma}_{ij}^{p-PLANE}(\mathbf{0}) \\
\Delta\hat{\sigma}_{ij}^{p}(\mathbf{0}) &= \chi_b \cdot \Delta\hat{\sigma}_{ij}^{p-LN}(\mathbf{0})
\end{aligned} \tag{5.85}$$

where $\Delta\bar{\sigma}_{ij}^{s-LN}(\mathbf{0})$, $\Delta\hat{\sigma}_{ij}^{s-LN}(\mathbf{0})$, $\Delta\bar{\sigma}_{ij}^{p-LN}(\mathbf{0})$, and $\Delta\hat{\sigma}_{ij}^{p-LN}(\mathbf{0})$ are the corresponding solutions obtained from a *geometrically linear* analysis of a polygonal patch; $\Delta\bar{\sigma}_{ij}^{s-PLANE}(\mathbf{0})$ and $\Delta\bar{\sigma}_{ij}^{p-PLANE}(\mathbf{0})$ are the corresponding plane stress solutions (without considering the out-of-plane bending); χ_{m-1}^{s}, χ_{m-2}^{s}, χ_{m-1}^{p}, χ_{m-2}^{p}, and χ_b are defined in Equation (5.82) based on a one-dimensional analysis. $\Delta\bar{\sigma}_{ij}^{s-LN}(\mathbf{0})$, $\Delta\hat{\sigma}_{ij}^{s-LN}(\mathbf{0})$, $\Delta\bar{\sigma}_{ij}^{p-LN}(\mathbf{0})$, and $\Delta\hat{\sigma}_{ij}^{p-LN}(\mathbf{0})$ can be easily obtained by following the process given in Section 5.2.2 while the plane stress solutions $\Delta\bar{\sigma}_{ij}^{s-PLANE}(\mathbf{0})$ and $\Delta\bar{\sigma}_{ij}^{p-PLANE}(\mathbf{0})$ can be found by the method outlined in Chapter 4. Since there is no interaction effect between the initial stresses and the far-field-applied stresses in a geometrically linear analysis or plane stress analysis, $\Delta\bar{\sigma}_{ij}^{s-LN}(\mathbf{0})$, $\Delta\hat{\sigma}_{ij}^{s-LN}(\mathbf{0})$, $\Delta\bar{\sigma}_{ij}^{p-LN}(\mathbf{0})$, and $\Delta\hat{\sigma}_{ij}^{p-LN}(\mathbf{0})$ or $\Delta\bar{\sigma}_{ij}^{s-PLANE}(\mathbf{0})$ and $\Delta\bar{\sigma}_{ij}^{p-PLANE}(\mathbf{0})$ are determined from these analyses for a plate repaired with a polygonal patch subjected to remote stresses $(\sigma_{\infty ij} - \sigma_{ij}^{f*})$ alone without considering the "initial stresses" $\sigma_{ij}^{s-step2}(\mathbf{0})$. On the other hand, the nonlinear correction factors χ_{m-1}^{s}, χ_{m-2}^{s}, χ_{m-1}^{p}, χ_{m-2}^{p}, and χ_b are calculated by Equation (5.82), noting that P and P_0 appearing implicitly in that equation through ξ_H and ξ_I are defined by $P = (\sigma_{\infty 22} - \sigma_{22}^{f*}) \cdot t_0$ and $P_0 = t_s \cdot \sigma_{22}^{s-step2}(\mathbf{0})$ while the bending stiffness D_{22}^{I} defined there (in Section 5.3.2) must be evaluated with respect to the centroid of the patch–skin combination, not the mid-plane of the skin as done in Section 5.2 and the rest of Section 5.3 including this sub-Section 5.3.3.

Illustrative examples

To illustrate the analytical method presented in this section, a problem of an infinite skin repaired with a rigidly bonded square patch ($L_p/W_p = 1$) is considered. The length of the patch ($2 \cdot L_p$) is 10.16 cm while the material properties and thickness of the skin and patch are given below:

Skin plate: Aluminum, $E_s = 72.4\,\text{GPa}$, $\nu_s = 0.33$, $\alpha_s = 22.5\text{E-}06\,\text{per}\,^\circ\text{C}$, $t_s = 1.6\,\text{mm}$.

Patch: Boron/Epoxy, $E_x = 18.7\,\text{GPa}$, $E_p = E_y = 193.6\,\text{GPa}$, $\nu_{yx} = 0.21$,

$\mu = 5.5\,\text{GPa}$, $\alpha_x = 21.4\text{E-}06\,\text{per}\,^\circ\text{C}$, $\alpha_p = \alpha_y = 4.3\text{E-}06\,\text{per}\,^\circ\text{C}$, $t_p = 0.66\,\text{mm}$.

The analyses are performed for two loading cases. In the first loading case, the repaired skin is subjected to purely mechanical loading. A stress $\sigma_{\infty 22}$ is applied to the repaired skin, which increases monotonically from 0 to 137.9 MPa. On the other hand, the second

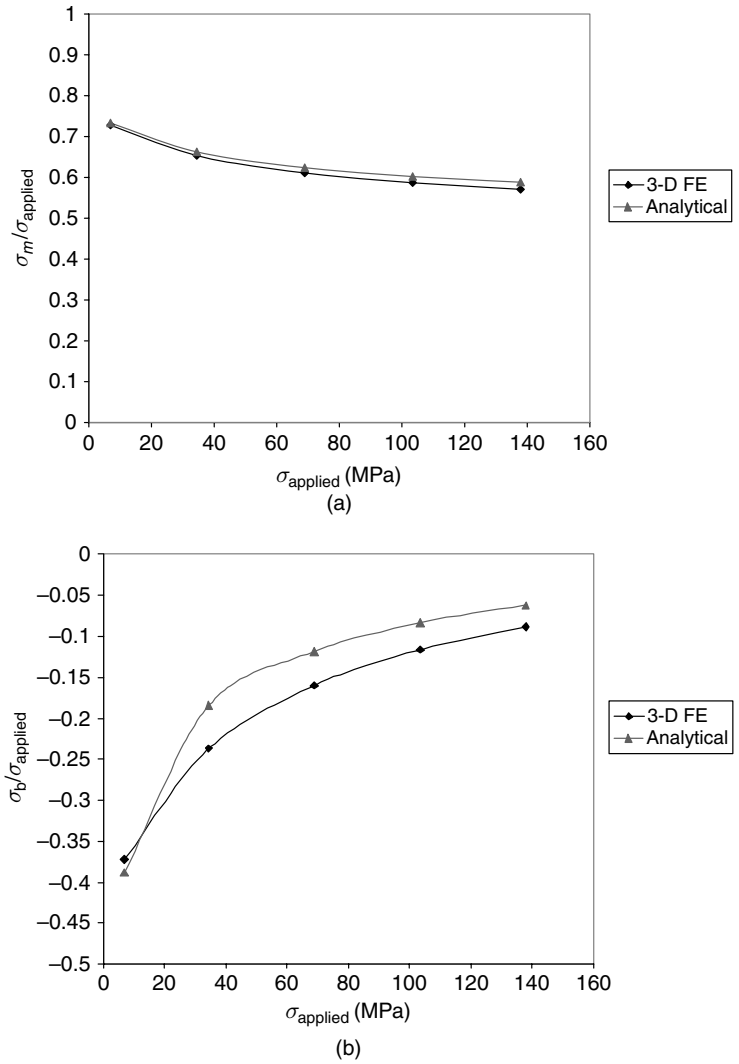

Fig. 5.16. Normalized stresses in the skin of a repair with a 10.16×10.16 cm square patch under purely mechanical loading: (a) normalized mean stress; and (b) normalized bending stresses.

loading case involves a uniform temperature excursion of $-75\,^{\circ}\text{C}$ in addition to the above mechanical load. As mentioned throughout this chapter, stresses in the skin at the patch's center in the x_2-component are of special interest since they are needed to determine the crack-tip stress intensity factor using Wang–Rose's crack-bridging model (1999). Since the stress distribution in the skin is linear through its thickness, both mean and bending value of the skin's stress component σ_{22} therefore will be presented here. These mean and bending stresses are plotted as the functions of the far-field-applied stress $\sigma_{\infty 22}$ in Figures 5.16(a) and 5.16(b) for purely mechanical loading and in Figures 5.17(a) and 5.17(b) for thermo-mechanical loading. In Figure 5.16, the bending and the mean

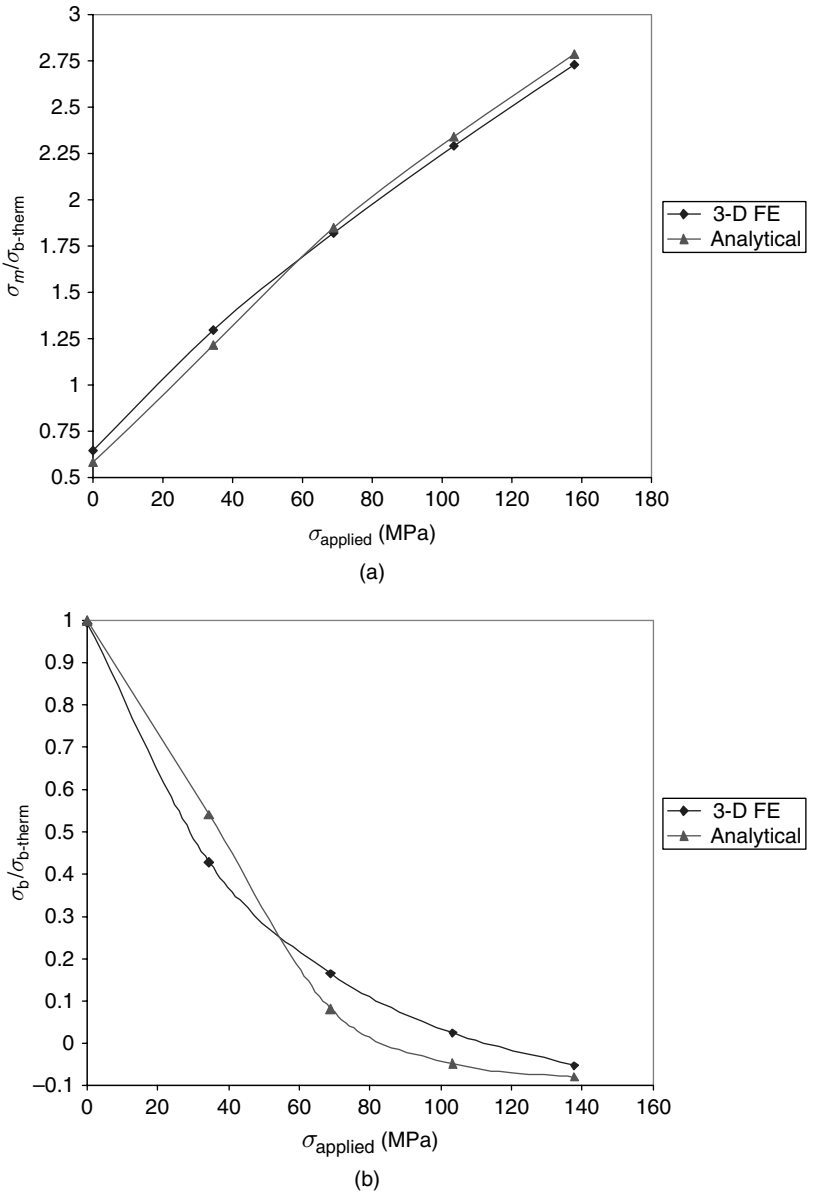

Fig. 5.17. Normalized stresses in the skin of a repair with a 10.16×10.16 cm square patch under thermo-mechanical loading: (a) normalized mean stress; and (b) normalized bending stresses.

stresses in the skin are normalized with respect to the far-field-applied stress while in Figure 5.17 these stresses are normalized with respect to the initially thermal bending stress that is found to be 44.44 MPa. For purely mechanical loading, analytical results are obtained directly from step 3 without going through the first two steps since the

thermal stresses, e_{NL}, $\sigma_{ij}^{\mathrm{f}*}$, and $\sigma_{ij}^{\mathrm{s-step2}}(\mathbf{0})$ are identical to zero. In contrast, the procedure for determining the stress in the skin under thermo-mechanical loading is much more involved. First, e_{NL} must be determined from step 1. Second, $\sigma_{22}^{\mathrm{f}*}$ and $\sigma_{22}^{\mathrm{s-step2}}(\mathbf{0})$ are determined from step 2 as 74.95 and 87.01 MPa, respectively. For $\sigma_{\infty 22} \leq 74.95$ MPa, the thermo-elastic stress in the skin is determined from step 2 with e_{NL} equal to a constant value found in step 1. Otherwise, step 3 must be performed and the result of $\sigma_{ij}^{\mathrm{s-step2}}(\mathbf{0})$ from step 2 is utilized.

To assess the accuracy of the analytical method, results from the FE analysis are also obtained and compared with the analytical predictions in Figures 5.16 and 5.17. The FE analysis is carried out using ABAQUS (1997) with the skin and each ply of the patch modeled separately. The skin is modeled as three layers of 20-node solid elements while each ply of the patch as one layer of solid elements. To avoid the adverse effect of the small thickness-to-length ratio on the solution, stiffness matrices of all solid elements are evaluated using reduced integration. In the FE model, the skin was restrained from the out-of-plane deflection along its periphery. From Figures 5.16 and 5.17, the bending stresses decrease with the applied stresses and they will eventually vanish for large values of applied stresses, as expected. In general, the analytical predictions agree reasonably well with the FE results.

To show the effect of a patch's size on the stresses, the above thermo-mechanical analysis is repeated for a patch length of 40.64 cm and its results are presented in Figure 5.18. Again, the mean and the bending stresses in Figure 5.18 are normalized with respect to the initially thermal bending stress that is found to be 17.57 MPa. The agreement between the analytical and the FE results is considered to be satisfactory. It follows from Figure 5.18 that a larger patch will result in lower bending stresses in the skin as expected.

5.4 Stage II: Fracture Analysis Using Crack-bridging Model

The purpose of stage II analysis is to estimate the crack-tip stress intensity factor, shear and peel stresses in the adhesive near the middle of the crack surfaces as well as the patch's stress there. It should be emphasized that in order to obtain the total stress in the patch, one needs to add the contribution determined from this stage II analysis to that from the stage I analysis as given in either Section 5.2 or 5.3. To retain the results obtained by Wang and Rose (1999) and to follow closely with their work, new and different positive sign conventions for the bending moment, moment–curvature relation, and transverse shear will be adopted in this section, as depicted in Figure 5.19.

In the previous sections, the stress distribution σ_{ij}^{s} along the prospective crack path in the uncracked skin (with patch) is determined. At any point in the skin, σ_{ij}^{s} varies through the skin thickness. σ_{ij}^{s} was also presented in terms of the mean and bending components $\bar{\sigma}_{ij}^{\mathrm{s}}$ and $\hat{\sigma}_{ij}^{\mathrm{s}}$. In the fracture analysis, for simplicity, $\bar{\sigma}_{ij}^{\mathrm{s}}$ and $\hat{\sigma}_{ij}^{\mathrm{s}}$ will be assumed to be constant along the crack line and equal to those values at the center of the skin plate. Let us denote these mean and bending stresses as σ_m^0 and σ_{b}^0, i.e., $\sigma_m^0 = \bar{\sigma}_{22}^{\mathrm{s}}(\mathbf{0})$ and

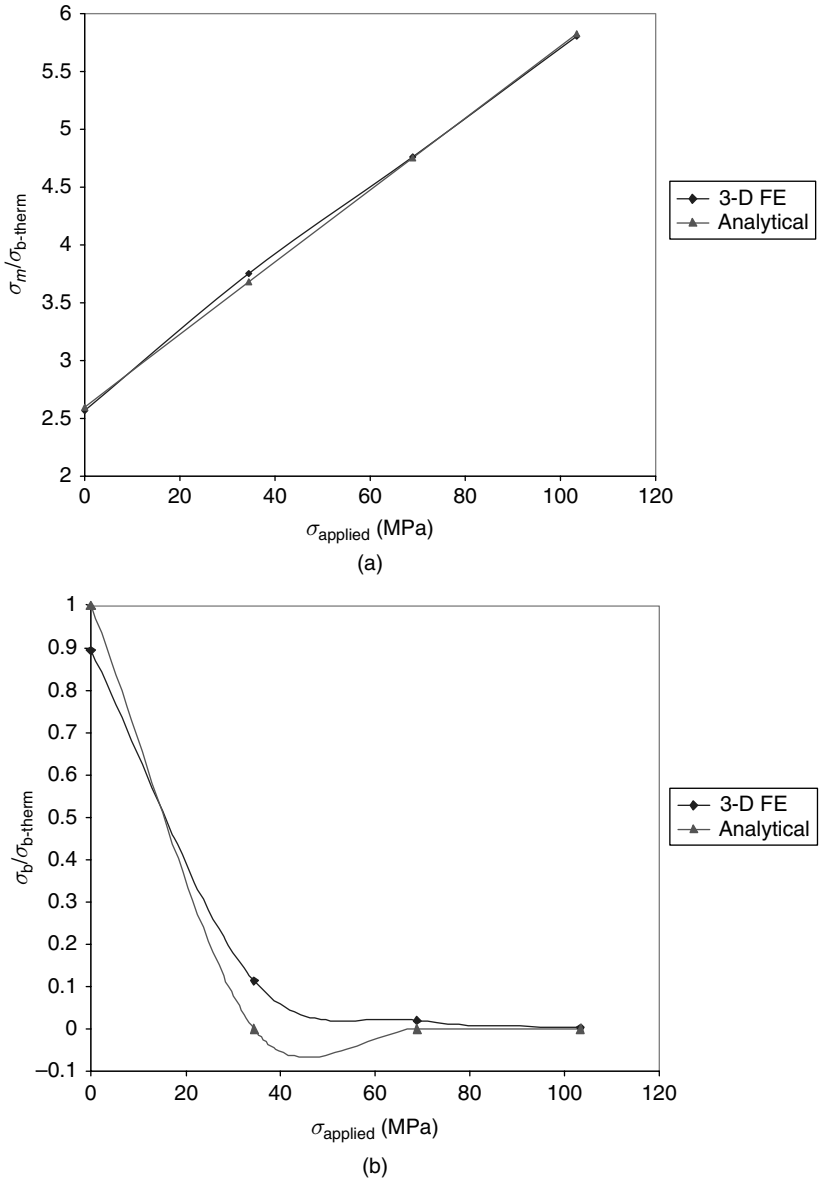

Fig. 5.18. Normalized stresses in the skin of a repair with a 40.64×40.64 cm square patch under thermo-mechanical loading: (a) normalized mean stress; and (b) normalized bending stresses.

$\sigma_b^0 = -\hat{\sigma}_{22}^s(\mathbf{0})$ (a negative sign is due to a different positive sign convention for the bending moment in this section). By treating the cracked skin and the patch as thin plates, the stress distribution on the crack faces can be considered as the superposition of a membrane force $-N_0$ and a bending moment $-M_0$, with the stress distribution being

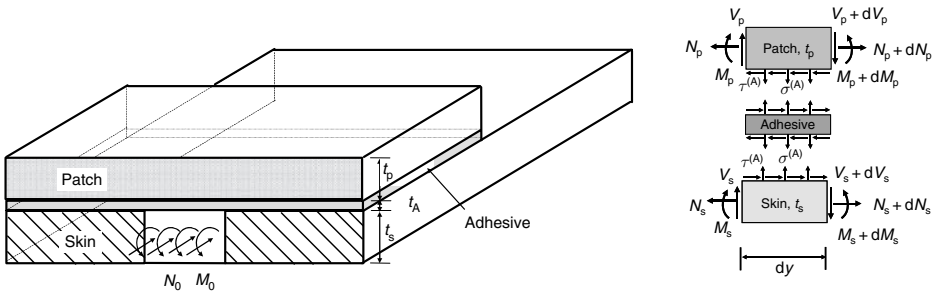

Fig. 5.19. Perturbation problem of a repaired cracked skin subjected to tension (Wang and Rose, 1999).

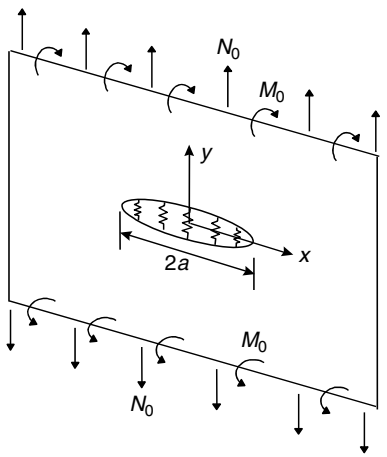

Fig. 5.20. A skin plate with a through crack reinforced with tension and bending springs (Wang and Rose, 1999).

given by $\sigma_{22}^{s}(x_1, x_2 = 0, x_3) = -(N_0/t_s - 12M_0x_3/t_s^3)$, for $|x_1| \leq a$, where $N_0 = \sigma_m^0 t_s$ and $M_0 = \frac{\sigma_b^0 t_s^2}{6}$, and a is the half crack length. In this section, the perturbation problem of a crack pressurized by a combination of membrane force and bending moment as shown in Figure 5.19 is solved using a crack-bridging model, within the framework of geometrically linear elasticity. The basic idea underlying the crack-bridging model to be described below is that (i) by representing the effect of the patch by an infinite number of tension and bending springs bridging the crack faces, and (ii) by deriving the spring constants of these springs from the analysis of a single-strap joint in plane strain, one can model the problem depicted in Figure 5.19 as a plate containing a through crack reinforced by distributed tension and bending springs (Figure 5.20). Thus a complicated three-dimensional problem is reduced to a two-dimensional problem of a

bridged crack, and a one-dimensional problem to determine the crack-bridging traction law. The resulting hyper-singular integral equations are then solved using the Galerkin method.

5.4.1 Determination of spring constants

In order to formulate a crack-bridging model, it is essential to determine first the spring constants. As depicted in Figure 5.21, let us denote the crack face displacement and rotation as v and θ, in relation to the mid-plane of the skin, caused by the application of a membrane force n_0 and bending moment m_0. The relationship between (n_0, m_0) and (v, θ) can be determined by analyzing the single-strap joint under plane strain conditions as follows.

The governing equations for the adhesive shear and peel strains, which are assumed to be constant throughout the adhesive thickness, are respectively (see Equations (2.155) and (2.149)),

$$\frac{\mathrm{d}^3\gamma^{(\mathrm{A})}}{\mathrm{d}y^3} - 4\beta_{\mathrm{A}}^2\frac{\mathrm{d}\gamma^{(\mathrm{A})}}{\mathrm{d}y} = 0 \tag{5.86}$$

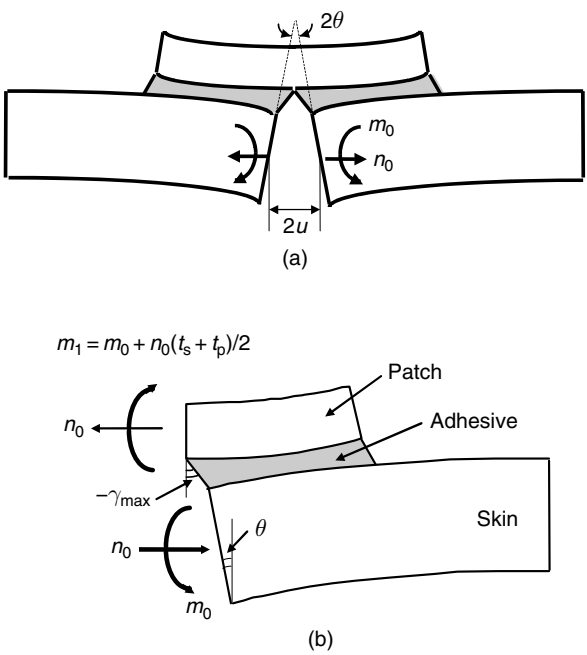

Fig. 5.21. (a) Single-strap joint representing one-sided repairs subjected to membrane tension and bending moment; and (b) notations and boundary conditions.

$$\frac{\mathrm{d}^4\varepsilon^{(\mathrm{A})}}{\mathrm{d}y^4} + 4\tilde{v}^4\varepsilon^{(\mathrm{A})} = 0 \tag{5.87}$$

where

$$\begin{aligned} \gamma^{(\mathrm{A})} &= \frac{\tau^{(\mathrm{A})}}{G_{\mathrm{A}}} \\ \beta_{\mathrm{A}}^2 &= \frac{G_{\mathrm{A}}}{t_{\mathrm{A}}}\left[\frac{1}{E'_{\mathrm{s}}t_{\mathrm{s}}} + \frac{1}{E'_{\mathrm{p}}t_{\mathrm{p}}}\right] \end{aligned} \tag{5.88}$$

$$\tilde{v}^4 = \frac{E'_{\mathrm{A}}}{4t_{\mathrm{A}}}\left[\frac{1}{D_{\mathrm{s}}} + \frac{1}{D_{\mathrm{p}}}\right] \tag{5.89}$$

G_{A} and t_{A} represent the shear modulus and the thickness of the adhesive layer, respectively; D_{s} and D_{p} refer to the bending stiffness of the skin plate and patch, $D_{\mathrm{s,p}} = E'_{\mathrm{s,p}}t^3_{\mathrm{s,p}}/12$; $E'_{\mathrm{s,p}} = \frac{E_{\mathrm{s,p}}}{1-\nu^2_{\mathrm{s,p}}}$; and $E'_{\mathrm{A}} = 2G_{\mathrm{A}}/(1-\nu_{\mathrm{A}})$ is the Young's modulus of the adhesive under plane strain condition. The differential Equation (5.86) has the following solution in the domain $y > 0$,

$$\gamma^{(\mathrm{A})} = \gamma^{(\mathrm{A})}_{\max} e^{-2\beta_{\mathrm{A}}y} \tag{5.90}$$

where $\gamma^{(\mathrm{A})}_{\max}$ represents the maximum shear strain at $y = 0$. Similarly the relevant solution for the adhesive peel stress in the case of semi-infinite overlap in the domain $y > 0$ is

$$\varepsilon^{(\mathrm{A})} = (A\cos\tilde{v}y + B\sin\tilde{v}y)\, e^{-\tilde{v}y} \tag{5.91}$$

The three unknowns $\gamma^{(\mathrm{A})}_{\max}$ and constants A and B need to be determined from the appropriate boundary conditions.

For future development, it should be noted from Figure 5.21(a) that the stress and the moment resultants in the skin and patch are given by

$$\begin{aligned} M^{\mathrm{s}}(y=0) &= -m_0 \\ M^{\mathrm{p}}(y=0) &= m_1 = m_0 + n_0\left(\frac{t_{\mathrm{s}}+t_{\mathrm{p}}}{2}\right) \\ N^{\mathrm{s}}(y=0) &= -n_0 \\ N^{\mathrm{p}}(y=0) &= n_0 \end{aligned} \tag{5.92}$$

It is also worthy to note the following relevant results from the theory of one-sided bonded doublers and joints developed in Chapter 2. First, similar to Equations (2.120)

and (2.121), and noting the different sign conventions for the shear and moment in this Section 5.4, the strain on each side of the bond line is given by

$$\begin{aligned}\varepsilon_{\mathrm{p}}\left(x_3 = t_{\mathrm{s}}/2 + t_{\mathrm{A}}, y = 0\right) &= \frac{\mathrm{d}v_{\mathrm{p}}\left(y=0\right)}{\mathrm{d}y} \\ &= \frac{N^{\mathrm{p}}\left(y=0\right)}{E'_{\mathrm{p}}t_{\mathrm{p}}} + \frac{t_{\mathrm{p}}M^{\mathrm{p}}\left(y=0\right)}{2D_{\mathrm{p}}} = \frac{n_0}{E'_{\mathrm{p}}t_{\mathrm{p}}} + \frac{m_1 \cdot t_{\mathrm{p}}}{2D_{\mathrm{p}}} \\ \varepsilon_{\mathrm{s}}\left(x_3 = t_{\mathrm{s}}/2, y = 0\right) &= \frac{\mathrm{d}v_{\mathrm{s}}\left(y=0\right)}{\mathrm{d}y} \\ &= \frac{N^{\mathrm{s}}\left(y=0\right)}{E'_{\mathrm{s}}t_{\mathrm{s}}} - \frac{t_{\mathrm{s}}M^{\mathrm{s}}\left(y=0\right)}{2D_{\mathrm{s}}} = -\frac{n_0}{E'_{\mathrm{s}}t_{\mathrm{s}}} + \frac{m_0 \cdot t_{\mathrm{s}}}{2D_{\mathrm{s}}}\end{aligned} \tag{5.93}$$

Secondly, from Equations (2.110) and (2.111) after accounting for the different sign conventions for moment, moment–curvature relation, and transverse shear,

$$\begin{aligned}\left.\frac{\mathrm{d}M^{\mathrm{p}}}{\mathrm{d}y}\right|_{y=0} &= D_{\mathrm{p}}\left.\frac{\mathrm{d}^3 w_{\mathrm{p}}}{\mathrm{d}y^3}\right|_{y=0} = \left.V_{\mathrm{p}} + \frac{\tau^{(\mathrm{A})}t_{\mathrm{p}}}{2}\right|_{y=0} = V_{\mathrm{p}}\left(y=0\right) + \frac{\gamma^{(\mathrm{A})}_{\max}G_{\mathrm{A}}t_{\mathrm{p}}}{2} \\ \left.\frac{\mathrm{d}M^{\mathrm{s}}}{\mathrm{d}y}\right|_{y=0} &= D_{\mathrm{s}}\left.\frac{\mathrm{d}^3 w_0}{\mathrm{d}y^3}\right|_{y=0} = \left.V_{\mathrm{s}} + \frac{\tau^{(\mathrm{A})}t_{\mathrm{s}}}{2}\right|_{y=0} = V_{\mathrm{s}}\left(y=0\right) + \frac{\gamma^{(\mathrm{A})}_{\max}G_{\mathrm{A}}t_{\mathrm{s}}}{2}\end{aligned} \tag{5.94}$$

With the results from Equations (5.92)–(5.94) in mind and noting $\gamma^{(\mathrm{A})} = \frac{v_{\mathrm{p}}(x_3 = t_{\mathrm{s}}/2 + t_{\mathrm{A}}) - v_{\mathrm{s}}(x_3 = t_{\mathrm{s}}/2)}{t_{\mathrm{A}}}$, the boundary condition for the shear strain is

$$\begin{aligned}\left.\frac{\mathrm{d}\gamma^{(\mathrm{A})}}{\mathrm{d}y}\right|_{y=0} &= \frac{\varepsilon_{\mathrm{p}}(x_3 = t_{\mathrm{s}}/2 + t_{\mathrm{A}}) - \varepsilon_{\mathrm{s}}(x_3 = t_{\mathrm{s}}/2)}{t_{\mathrm{A}}} \\ &= \frac{1}{t_{\mathrm{A}}}\left[\frac{1}{E'_{\mathrm{p}}t_{\mathrm{p}}} + \frac{1}{E'_{\mathrm{s}}t_{\mathrm{s}}} + \frac{3(t_{\mathrm{p}} + t_{\mathrm{s}})}{E'_{\mathrm{p}}t_{\mathrm{p}}^2}\right]n_0 + \frac{6}{t_{\mathrm{A}}}\left[\frac{1}{E'_{\mathrm{p}}t_{\mathrm{p}}^2} - \frac{1}{E'_{\mathrm{s}}t_{\mathrm{s}}^2}\right]m_0\end{aligned} \tag{5.95}$$

The relevant boundary conditions for the adhesive peel strain at $y = 0$ are

$$\begin{aligned}\left.\frac{\mathrm{d}^2\varepsilon^{(\mathrm{A})}}{\mathrm{d}y^2}\right|_{y=0} &= \frac{1}{t_{\mathrm{A}}}\frac{\mathrm{d}^2(w_{\mathrm{p}} - w_{\mathrm{s}})}{\mathrm{d}y^2} = \frac{1}{t_{\mathrm{A}}}\left[\frac{M^{\mathrm{p}}(y=0)}{D_{\mathrm{p}}} - \frac{M^{\mathrm{s}}(y=0)}{D_{\mathrm{s}}}\right] \\ &= \frac{1}{t_{\mathrm{A}}}\left(\frac{m_1}{D_{\mathrm{p}}} + \frac{m_0}{D_{\mathrm{s}}}\right) = \frac{1}{t_{\mathrm{A}}D_{\mathrm{p}}}\frac{t_{\mathrm{p}} + t_{\mathrm{s}}}{2}n_0 + \frac{1}{t_{\mathrm{A}}D_{\mathrm{p}}}\left(1 + \frac{D_{\mathrm{p}}}{D_{\mathrm{s}}}\right)m_0\end{aligned} \tag{5.96}$$

and

$$\begin{aligned}\left.\frac{\mathrm{d}^3\varepsilon^{(\mathrm{A})}}{\mathrm{d}y^3}\right|_{y=0} &= \frac{1}{t_{\mathrm{A}}}\frac{\mathrm{d}^3(w_{\mathrm{p}} - w_{\mathrm{s}})}{\mathrm{d}y^3} = \frac{1}{t_{\mathrm{A}}}\left(\frac{V_{\mathrm{p}} + \gamma^{(\mathrm{A})}_{\max}t_{\mathrm{p}}/2}{D_{\mathrm{p}}} - \frac{V_{\mathrm{s}} + \gamma^{(\mathrm{A})}_{\max}t_{\mathrm{s}}/2}{D_{\mathrm{s}}}\right) \\ &= \frac{G_{\mathrm{A}}}{2t_{\mathrm{A}}}\left(\frac{t_{\mathrm{p}}}{D_{\mathrm{p}}} - \frac{t_{\mathrm{s}}}{D_{\mathrm{s}}}\right)\gamma^{(\mathrm{A})}_{\max}\end{aligned} \tag{5.97}$$

where the conditions that the shear force V_s and V_p are both zero at $y = 0$ have been used. From condition (5.95) one obtains

$$\gamma_{\max}^{(A)} = -\frac{1}{2\beta_A t_A}\left[\frac{1}{E_p' t_p} + \frac{1}{E_s' t_s} + \frac{3(t_p + t_s)}{E_p' t_p^2}\right] n_0 - \frac{6}{2\beta_A t_A}\left[\frac{1}{E_p' t_p^2} - \frac{1}{E_s' t_s^2}\right] m_0 \tag{5.98}$$

and referring to Equations (5.96) and (5.97) one has

$$-2\tilde{v}^2 B = \frac{1}{t_A D_p}\frac{t_p + t_s}{2} n_0 + \frac{1}{t_A D_p}\left(1 + \frac{D_p}{D_s}\right) m_0 \tag{5.99}$$

$$2\tilde{v}^3 (A + B) = \frac{G_A}{2t_A}\left(\frac{t_p}{D_p} - \frac{t_s}{D_s}\right) \gamma_{\max}^{(A)} \tag{5.100}$$

thus

$$\tilde{v}(A - B) = \frac{G_A t_s}{4\tilde{v}^2 t_A}\left(\frac{t_p}{D_p} - \frac{t_s}{D_s}\right) \gamma_{\max}^{(A)} + \frac{t_p + t_s}{2\tilde{v} t_A D_p} n_0 + \frac{1}{\tilde{v} t_A D_p}\left(1 + \frac{D_p}{D_s}\right) m_0 \tag{5.101}$$

Denote the rotation of the skin at $y = 0$ as $\tilde{\theta}_0$, since $\partial w_p/\partial y|_{y=0} = 0$ because of symmetry, and $\varepsilon^{(A)} = (w_p - w_s)/t_A$, one has, by definition,

$$\begin{aligned}
\tilde{\theta}_0 &= \left.\frac{\partial w_s}{\partial y}\right|_{y=0} = \left.\frac{\partial\left(w_s - w_p\right)}{\partial y}\right|_{y=0} = -t_A \left.\frac{\partial \varepsilon^{(A)}}{\partial y}\right|_{y=0} = \tilde{v} t_A (A - B) \\
&= \left\{\frac{t_s + t_p}{2\tilde{v} D_p} - \frac{G_A}{8v^2 \beta_A t_A}\left(\frac{t_p}{D_p} - \frac{t_s}{D_s}\right)\left[\frac{1}{E_p' t_p} + \frac{1}{E_s' t_s} + \frac{t_p(t_p + t_s)}{4D_p}\right]\right\} n_0 \\
&\quad + \left[\frac{1}{\tilde{v} D_p}\left(1 + \frac{D_p}{D_s}\right) - \frac{G_A}{16\tilde{v}^2 \beta_A t_A}\left(\frac{t_p}{D_p} - \frac{t_s}{D_s}\right)^2\right] m_0
\end{aligned} \tag{5.102}$$

The opening displacement at the mid-surface of the skin is

$$\begin{aligned}
\tilde{v}_0 &= -\gamma_{\max}^{(A)} t_A + \tilde{\theta}_s t_s/2 \\
&= \left[\frac{t_s(t_p + t_s)}{4\tilde{v} D_p} + \left[\frac{1}{E_p' t_p} + \frac{1}{E_s' t_s} + \frac{t_p(t_p + t_s)}{4D_p}\right]\left[\frac{1}{2\beta_A} - \frac{G_A t_s}{16\tilde{v}^2 \beta_A t_A}\left(\frac{t_p}{D_p} - \frac{t_s}{D_s}\right)\right]\right] n_0 \\
&\quad + \left\{\frac{t_s}{2\tilde{v} D_p}\left(1 + \frac{D_p}{D_s}\right) + \left(\frac{t_p}{2D_p} - \frac{t_s}{2D_s}\right)\left[\frac{1}{2\beta_A} - \frac{G_A t_s}{16\tilde{v}^2 \beta_A t_A}\left(\frac{t_p}{D_p} - \frac{t_s}{D_s}\right)\right]\right\} m_0
\end{aligned} \tag{5.103}$$

It is now possible to express the crack opening displacement and crack face rotation in terms of the membrane force and the bending moment in a matrix form,

$$\begin{Bmatrix} \tilde{v}_0 \\ \tilde{\theta}_0 \end{Bmatrix} = \begin{bmatrix} c_{tt} & c_{tb} \\ c_{bt} & c_{bb} \end{bmatrix} \begin{Bmatrix} n_0 \\ m_0 \end{Bmatrix} \tag{5.104}$$

where

$$
\begin{aligned}
c_{\mathrm{tt}} &= \frac{t_{\mathrm{s}}(t_{\mathrm{s}}+t_{\mathrm{p}})}{4\tilde{\nu}D_{\mathrm{p}}} + \left[\frac{1}{E'_{\mathrm{p}}t_{\mathrm{p}}} + \frac{1}{E'_{\mathrm{s}}t_{\mathrm{s}}} + \frac{t_{\mathrm{p}}(t_{\mathrm{p}}+t_{\mathrm{s}})}{4D_{\mathrm{p}}}\right]\left[\frac{1}{2\beta_{\mathrm{s}}} - \frac{G_{\mathrm{A}}t_{\mathrm{s}}}{16\tilde{\nu}^2\beta_{\mathrm{A}}t_{\mathrm{A}}}\left(\frac{t_{\mathrm{p}}}{D_{\mathrm{p}}} - \frac{t_{\mathrm{s}}}{D_{\mathrm{s}}}\right)\right] \\
c_{\mathrm{tb}} &= \frac{t_{\mathrm{s}}}{2\tilde{\nu}D_{\mathrm{p}}}\left(1+\frac{D_{\mathrm{p}}}{D_{\mathrm{s}}}\right) + \left(\frac{t_{\mathrm{p}}}{2D_{\mathrm{p}}} - \frac{t_{\mathrm{s}}}{2D_{\mathrm{s}}}\right)\left[\frac{1}{2\beta_{\mathrm{A}}} - \frac{G_{\mathrm{A}}t_{\mathrm{s}}}{16\tilde{\nu}^2\beta_{\mathrm{A}}t_{\mathrm{A}}}\left(\frac{t_{\mathrm{p}}}{D_{\mathrm{p}}} - \frac{t_{\mathrm{s}}}{D_{\mathrm{s}}}\right)\right] \\
c_{\mathrm{bt}} &= \frac{t_{\mathrm{p}}+t_{\mathrm{s}}}{2\tilde{\nu}D_{\mathrm{p}}} - \frac{G_{\mathrm{A}}}{8\tilde{\nu}^2\beta_{\mathrm{A}}t_{\mathrm{A}}}\left(\frac{t_{\mathrm{p}}}{D_{\mathrm{p}}} - \frac{t_{\mathrm{s}}}{D_{\mathrm{s}}}\right)\left[\frac{1}{E'_{\mathrm{p}}t_{\mathrm{p}}} + \frac{1}{E'_{\mathrm{s}}t_{\mathrm{s}}} + \frac{t_{\mathrm{p}}(t_{\mathrm{s}}+t_{\mathrm{p}})}{4D_{\mathrm{p}}}\right] \\
c_{\mathrm{bb}} &= \frac{1}{\tilde{\nu}D_{\mathrm{p}}}\left(1+\frac{D_{\mathrm{p}}}{D_{\mathrm{s}}}\right) - \frac{G_{\mathrm{A}}}{16\tilde{\nu}^2\beta_{\mathrm{A}}t_{\mathrm{A}}}\left(\frac{t_{\mathrm{p}}}{D_{\mathrm{p}}} - \frac{t_{\mathrm{s}}}{D_{\mathrm{s}}}\right)^2
\end{aligned}
\tag{5.105}
$$

It is evident that the cross terms, c_{tb} and c_{bt}, are non-zero, indicative of the coupling between in-plane and out-of-plane deformation. According to the Maxwell's reciprocal relation, the matrix of spring compliance should be symmetric, i.e., $c_{\mathrm{tb}} = c_{\mathrm{bt}}$. However, due to the approximate nature of the plate theory, the resulting matrix is not exactly symmetric, but the deviation from symmetry is small. From Equation (5.104) one can obtain the stiffness matrix:

$$
\begin{Bmatrix} n_0 \\ m_0 \end{Bmatrix} = \begin{bmatrix} d_{\mathrm{tt}} & d_{\mathrm{tb}} \\ d_{\mathrm{bt}} & d_{\mathrm{bb}} \end{bmatrix} \begin{Bmatrix} \tilde{v}_0 \\ \tilde{\theta}_0 \end{Bmatrix} \tag{5.106}
$$

where

$$
\begin{aligned}
d_{\mathrm{tt}} &= c_{\mathrm{bb}}/\Delta, \quad d_{\mathrm{tb}} = -c_{\mathrm{tb}}/\Delta \\
d_{\mathrm{bt}} &= -c_{\mathrm{bt}}/\Delta, \quad d_{\mathrm{bb}} = c_{\mathrm{tt}}/\Delta \\
\Delta &= c_{\mathrm{tt}}c_{\mathrm{bb}} - c_{\mathrm{tb}}c_{\mathrm{bt}}
\end{aligned}
\tag{5.107}
$$

To facilitate the following analysis it is advantageous to express the spring traction law in terms of the generalized displacements corresponding to the membrane stress $\tilde{\sigma}^0_m (= n_0/t_{\mathrm{s}})$ and the maximum bending stress $\tilde{\sigma}^0_b$ $(= 6m_0/t_s^2)$. Since the total strain energy release rate per unit thickness is given by

$$
G = \tilde{\sigma}^0_m \tilde{v}_0 + \frac{1}{6}\tilde{\sigma}^0_{\mathrm{b}}\tilde{\theta}_0\, t_{\mathrm{s}} \tag{5.108}
$$

it is clear that the associated generalized placements are, respectively, $\tilde{v}_0$ and $\tilde{\theta}_0\ t_{\mathrm{s}}/6$. From Equation (5.106) we can express the relationship between $(\tilde{\sigma}^0_m,\ \tilde{\sigma}^0_b)$ and $(\tilde{v}_0,\ \tilde{\theta}_0 t_{\mathrm{s}}/6)$ as

$$
\begin{Bmatrix} \tilde{\sigma}^0_m \\ \tilde{\sigma}^0_{\mathrm{b}} \end{Bmatrix} = E_{\mathrm{s}} \begin{bmatrix} k_{\mathrm{tt}} & k_{\mathrm{tb}} \\ k_{\mathrm{bt}} & k_{\mathrm{bb}} \end{bmatrix} \begin{Bmatrix} \tilde{v}_0 \\ \frac{1}{6}\tilde{\theta}_0\, t_{\mathrm{s}} \end{Bmatrix} \tag{5.109}
$$

where k_{ij} represent spring constants which have a unit of $length^{-1}$:

$$k_{tt} = \frac{1}{E_s t_s} d_{tt} \equiv \frac{c_{bb}}{E_s t_s \Delta} \qquad k_{tb} = \frac{6}{E_s t_s^2} d_{tb} \equiv -\frac{6c_{tb}}{E_s t_s^2 \Delta} \tag{5.110}$$

$$k_{bt} = \frac{6}{E_s t_s^2} d_{bt} \equiv -\frac{6c_{bt}}{E_s t_s^2 \Delta} \qquad k_{bb} = \frac{36}{E_s t_s^3} d_{bb} \equiv \frac{36c_{tt}}{E_s t_s^3 \Delta} \tag{5.111}$$

According to elastic reciprocity we should have $k_{tb} = k_{bt}$. However, due to the approximate nature of the plate theory employed in the present work, the cross terms c_{tb} and c_{bt} are not exactly identical but the numerical difference is relatively small. It is also possible to symmetrize the spring stiffness matrix if required:

$$k^*_{tb} = k^*_{bt} = \frac{k_{tb} + k_{bt}}{2} \tag{5.112}$$

which is the only permissible symmetrization to ensure the equivalence in the total energy release rate.

5.4.2 Fracture analysis by crack-bridging model

The basic idea of crack-bridging model is to model the patching problem as a single plate with a through crack reinforced by distributed tension and bending springs sprung over the crack faces, where the spring constant matrix has already been obtained in Section 5.4.1. As mentioned in the introduction of Section 5.4, a crack pressurized by a combination of $-N_0$ and $-M_0$ is solved in the stage II analysis. Under the action of $-N_0$ and $-M_0$, the crack surfaces will open and rotate. However, the crack opening displacement and rotation will be restrained partially by the patch that is represented in the crack-bridging model by distributed springs. Thus, the internal forces and moments in these springs physically represent the force and moments exerted by the patch on the cracked skin. Since the crack opening displacement and rotation vary along the crack surfaces, the spring forces and moments also vary along the crack surfaces. However, the spring forces and moments at any point along the crack surface are still related to the crack opening displacements and rotation there by the same stiffnesses given by Equations (5.110) and (5.111). The boundary conditions of the present fracture problem along $y = 0$, therefore, can be expressed in terms of the yet unknown displacement and rotation as

$$\begin{aligned} N_{yy}(x, 0^+) &= -N_0 + d_{tt}\tilde{v}(x) + d_{tb}\tilde{\theta}(x) \\ M_{yy}(x, 0^+) &= -M_0 + d_{bt}\tilde{v}(x) + d_{bb}\tilde{\theta}(x) \end{aligned} \qquad -a < x < a \tag{5.113}$$

where a is a half crack length.

Making use of the solution of the in-plane displacement of a bridged crack under tension (see Joseph and Erdogan, 1987, 1989; Nemat-Nasser and Hori, 1987), the unknown crack face displacement (one half of the total crack opening displacement) can be expressed as,

$$\frac{E_s t_s}{2\pi} \int_{-a}^{a} \frac{\tilde{v}(\xi)}{(x-\xi)^2} \mathrm{d}\xi = N_{yy}(x,\ 0^+) \equiv -N_0 + d_{tt}\tilde{v}(x) + d_{tb}\tilde{\theta}(x) \tag{5.114}$$

The integral in the above equation is interpreted as a Hadamard finite part (Hadamard, 1952), which can be viewed as the derivative of a Cauchy principal value integral. Despite the higher order of singularity in the integrand, the present formulation has many advantages over that based on the derivative of the displacement, or dislocation density, mainly because the unknown displacement function is bounded unlike the density function which is singular near the crack tip. Numerical methods and convergence for this class of strongly singular integral equations have been investigated by a number of authors (Frenkel, 1983; Golberg, 1983, 1985; Joseph and Erdogan, 1987; Kaya and Erdogan, 1987; Ervin and Stephan, 1992) and it has been found that the hyper-singular integral equations can be efficiently solved by using either Galerkin's method or collocation methods.

Since the cross terms d_{tb} and d_{bt} are non-zero, the membrane resistance of the distributed springs is dependent on not only the crack face displacement but also the crack face rotation. Therefore the tensile stretching of the crack is coupled with the bending, and vice versa. To quantify the bending deformation of a plate, one needs to adopt a plate theory. In this regard, Kirchhoff–Poisson plate bending theory (Timoshenko and Woinowsky-Krieger, 1959) and Reissner's shear deformation theory (Reissner, 1947) are probably the most widely used plate theories. Both plate theories will be employed in the following analyses.

Due to the use of higher-order differential equations, the analysis based on Reissner's plate theory is considerably more complicated than that based on the classical plate theory. For a single plate containing a long through crack ($a/t_s \to \infty$), the expenses of using a much more complicated Reissner's plate theory may overweigh the gain of improved accuracy. This is because the classical plate theory would correctly predict the strain energy release rate in the long crack limit, identical to that obtained from Reissner's plate theory (Hui and Zehnder, 1993). Hence there exists a universal relationship between the stress intensity factor from Reissner's plate theory and that from the classical plate theory:

$$K_{\mathrm{b}}^{(\mathrm{R})} = \sqrt{\frac{1+\nu_{\mathrm{s}}}{3+\nu_{\mathrm{s}}}} K_{\mathrm{b}}^{(\mathrm{K})} \tag{5.115}$$

where $K_{\mathrm{b}}^{(\mathrm{R})}$ and $K_{\mathrm{b}}^{(\mathrm{K})}$ denote respectively the bending stress intensity factors determined from Reissner's plate theory and Kirchhoff–Poisson plate theory. However, it will be shown later in Section 5.4.5 that this same relationship will not hold for a cracked plate repaired on one side due to the coupling between the tensile and the bending springs sprung between crack faces. Thus, both plate theories will be employed in this section.

(a) Kirchhoff–Poisson plate bending theory

Referring to the second equation of (5.113) and making use of the solutions for a single plate with a through crack based on Kirchhoff–Poisson plate theory (Joseph and Erdogan, 1987), the following hyper-singular integral equation can be obtained:

$$\frac{3+\nu_{\mathrm{s}}}{1+\nu_{\mathrm{s}}} \frac{E_{\mathrm{s}} t_{\mathrm{s}}^3}{24\pi} \int_{-a}^{a} \frac{\tilde{\theta}(\varsigma)}{(x-\varsigma)^2} \mathrm{d}\varsigma = M_{\mathrm{yy}}(x, 0^+) \equiv -M_0 + d_{\mathrm{bt}} \tilde{v}(x) + d_{\mathrm{bb}} \tilde{\theta}(x)\,, \tag{5.116}$$

which, together with Equation (5.114), furnishes a set of coupled integral equations.

For the purpose of computation, the following non-dimensional variables are introduced:

$$\tilde{h}_1(x) = \tilde{v}(x)/a \tag{5.117}$$

$$\tilde{h}_2(x) = \frac{1}{6}\tilde{\theta}(x)\, t_s/a \tag{5.118}$$

The integral Equations (5.114) and (5.116) can thus be normalized to become

$$\begin{aligned} &-\frac{1}{2\pi}\int_{-1}^{1}\frac{\tilde{h}_1(\eta)}{(r-\eta)^2}\mathrm{d}\eta + (k_{tt}a)\tilde{h}_1(r) + (k_{tb}a)\tilde{h}_2(r) = \frac{\sigma_m^0}{E_s} \\ &-\frac{3+\nu_s}{1+\nu_s}\frac{3}{2\pi}\int_{-1}^{1}\frac{\tilde{h}_2(\eta)}{(r-\eta)^2}\mathrm{d}\eta + (k_{bt}a)\,\tilde{h}_1(r) + (k_{bb}a)\,\tilde{h}_2(r) = \frac{\sigma_b^0}{E_s} \end{aligned} \tag{5.119}$$

where $r = x/a,\ \eta = \varsigma/a,\ \sigma_m^0$ and σ_b^0 are again the mean and the bending stresses of the uncracked skin reinforced with a patch and measured at the center of the patch.

The coupled integral Equations (5.119) have no closed-form solutions. However, their solutions can be readily obtained numerically using the Galerkin method: expand the unknown functions in terms of Chebyshev polynomials and then determine the coefficients numerically, similar to the approach used by Nemat-Nasser and Hori (1987) for the case of tension springs only. Details will be shown in Section 5.4.3. It may be shown that the following functions are also bounded everywhere within $(-1, 1)$:

$$\bar{h}_{1,2}(r) = \frac{\tilde{h}_{1,2}(r)}{\sqrt{1-r^2}} \tag{5.120}$$

Furthermore, the left-hand sides in Equations (5.119) give the membrane and bending stresses outside the cut $(-1,\ 1)$, which are singular near $r \to 1^+$ or $r \to -1^-$. Using the following asymptotic behavior for $r \to 1^+$,

$$\lim_{r\to 1^+}\frac{1}{2\pi}\int_{-1}^{1}\frac{f(\eta)\sqrt{1-\eta^2}}{(r-\eta)^2}\mathrm{d}\eta = \lim_{r\to 1^+}\frac{f(1)}{2\sqrt{2(r-1)}} \tag{5.121}$$

where f denotes any bounded function within $(-1,\ 1)$. It is easily shown that the membrane stress intensity factor is given by

$$K_{\mathrm{mem}} = \lim_{r\to 1^+}\sqrt{2\pi a(r-1)}\,\sigma_{yy}(r,\ 0) = \frac{E_s\sqrt{\pi a}}{2}\bar{h}_1(1) \tag{5.122}$$

Similarly, the bending stress intensity factors based on Kirchhoff–Poisson plate theory (using stress definition) is

$$K_b^{(K)} = \frac{3+\nu_s}{1+\nu_s}\frac{3E_s\sqrt{\pi a}}{2}\bar{h}_2(1) \tag{5.123}$$

It should be noted that when the Kirchhoff–Poisson plate theory is employed, the displacement-based definition will lead to an answer different from Equation (5.123). However, since Kirchhoff–Poisson plate theory is a stress-based formulation, the stress definition of the bending stress intensity factor is perhaps the only valid definition.

(b) Reissner's plate theory

Similarly, the crack face rotation for a bridged crack subjected to bending is given by Joseph and Erdogan (1989):

$$\frac{E_s t_s^3}{24\pi}\int_{-a}^{a}\frac{\tilde{\theta}(\varsigma)}{(x-\varsigma)^2}d\varsigma+\frac{5}{1+\nu_s}\frac{E_s t_s}{24\pi}\int_{-a}^{a}\hat{L}(\tilde{s})\tilde{\theta}(\varsigma)d\varsigma=M_{yy}(x,\ 0^+) \tag{5.124}$$

where

$$\tilde{s}=\sqrt{10}\,|x-\varsigma|/t_s \tag{5.125}$$

$$\hat{L}(\tilde{s})=-\frac{48}{\tilde{s}^4}+\frac{4}{\tilde{s}^2}+4\left[\hat{K}_2(\tilde{s})-\hat{K}_0(\tilde{s})\right]+\frac{24}{\tilde{s}^2}\hat{K}_2(\tilde{s}) \tag{5.126}$$

and $\hat{K}_0$ and $\hat{K}_2$ are the modified Bessel functions of the second kind. It can be shown (Joseph and Erdogan, 1987) that $\hat{L}(\tilde{s})$ is a Fredholm kernel with only a logarithmic singularity near $\tilde{s}=0$ as proved in Wang and Rose (1999).

By adopting the normalization introduced earlier, the integral Equations (5.114) and (5.124) can be normalized to become

$$\begin{aligned}
&-\frac{1}{2\pi}\int_{-1}^{1}\frac{\tilde{h}_1(\eta)}{(r-\eta)^2}d\eta+(k_{tt}a)\tilde{h}_1(r)+(k_{tb}a)\tilde{h}_2(r)=\frac{\sigma_m^0}{E_s}\\
&-\frac{3}{2\pi}\int_{-1}^{1}\frac{\tilde{h}_2(\eta)}{(r-\eta)^2}d\eta-\frac{15}{(1+\nu_s)2\pi}\left(\frac{a}{t_s}\right)^2\int_{-1}^{1}\hat{L}\left(\sqrt{10}\frac{a}{t_s}|r-\eta|\right)\tilde{h}_2(\eta)d\eta\\
&+(k_{bt}a)\,\tilde{h}_1(r)+(k_{bb}a)\,\tilde{h}_2(r)=\frac{\sigma_b^0}{E_s}
\end{aligned} \tag{5.127}$$

While the membrane stress intensity factor is still given by Equation (5.122), the bending stress intensity factor can be derived using either stress-based definition or displacement-based definition (which will yield identical answer) as

$$K_b^{(R)}=\frac{3E_s\sqrt{\pi a}}{2}\bar{h}_2(1) \tag{5.128}$$

Since Reissner's plate theory yields the same angular distribution of the asymptotic stress state as given by elasticity theory, we can define a stress intensity factor at coordinate z through the skin thickness:

$$K_I(x_3)=K_{mem}-\frac{2x_3}{t_s}K_b \tag{5.129}$$

whereas this is not the case for Kirchhoff–Poisson plate theory.

5.4.3 Numerical solutions of integral equations

An effective way of solving the hyper-singular equations, numerically, is provided by expanding the unknowns using Chebyshev polynomials of the second kind, $\hat{U}_i$:

$$\tilde{h}_1(r) = \hat{W}(r)\bar{h}_1(r) \cong \hat{W}(r)\sum_{i=0}^{N}\hat{f}_i\hat{U}_i(r) \tag{5.130}$$

$$\tilde{h}_2(r) = \hat{W}(r)\bar{h}_2(r) \cong \hat{W}(r)\sum_{i=0}^{N}\hat{g}_i\hat{U}_i(r) \tag{5.131}$$

where $\hat{W}(r) = \sqrt{1-r^2}$, $\hat{U}_i(r) = \frac{\sin[(i+1)\cos^{-1}r]}{\sin(\cos^{-1}r)}$, $\hat{f}_i$ and $\hat{g}_i$ $(i = 0, 1, 2, \ldots, N)$ are coefficients yet to be determined. Here N is selected to be sufficiently large to ensure convergence within an acceptable accuracy. The method is effective because, with this expansion, the hyper-singular integral can be evaluated analytically, e.g.,

$$\int_{-1}^{1}\frac{\hat{W}(r)\hat{U}_i(r)\mathrm{d}r}{(x-r)^2} = -\pi(i+1)\hat{U}_i(x) \quad (-1 < x < 1) \tag{5.132}$$

One can now develop a Galerkin-type method to determine the unknown coefficients ($\hat{f}_i$ and $\hat{g}_i$).

(a) Classical plate theory

Making use of Equation (5.132), Equation (5.119) can be written as

$$\begin{aligned}
&\sum_{i=0}^{N}\frac{(i+1)}{2}\hat{f}_i\hat{U}_i(r) + \hat{W}(r)(k_{\mathrm{tt}}a)\sum_{i=0}^{N}\hat{f}_i\hat{U}_i(r) + \hat{W}(r)(k_{\mathrm{tb}}a)\sum_{i=0}^{N}\hat{g}_i\hat{U}_i(r) = \frac{\sigma_m^0}{E_{\mathrm{s}}}\\
&\frac{3(3+\nu_{\mathrm{s}})}{1+\nu_{\mathrm{s}}}\sum_{i=0}^{N}\frac{(i+1)}{2}\hat{g}_i\hat{U}_i(r) + \hat{W}(r)(k_{\mathrm{bt}}a)\sum_{i=0}^{N}\hat{f}_i\hat{U}_i(r) + \hat{W}(r)(k_{\mathrm{bb}}a)\sum_{i=0}^{N}\hat{g}_i\hat{U}_i(r) = \frac{\sigma_{\mathrm{b}}^0}{E_{\mathrm{s}}}
\end{aligned} \tag{5.133}$$

By exploiting the discrete orthogonality of Chebyshev polynomials of the second kind, this equation can be rewritten as, after multiplying Equation (5.133) with $\hat{W}(r)\hat{U}_j(r)$ then integrating from -1 to 1 (Wang and Rose, 1999),

$$\begin{cases}
\hat{A}_{ij}\hat{f}_j + \hat{B}_{ij}\hat{g}_j = \dfrac{\pi}{2}\dfrac{\sigma_m^0}{E_{\mathrm{s}}}\delta_{0j} & (i,\ j = 0, 1, 2, \ldots, N)\\
\hat{C}_{ij}\hat{f}_j + \hat{D}_{ij}\hat{g}_j = \dfrac{\pi}{2}\dfrac{\sigma_{\mathrm{b}}^0}{E_{\mathrm{s}}}\delta_{0j} & (i,\ j = 0, 1, 2, \ldots, N)
\end{cases} \tag{5.134}$$

where

$$\hat{A}_{ij} = \frac{1}{4}\pi(i+1)\delta_{ij} + (k_{tt}a)\Lambda_{ij}$$

$$\hat{B}_{ij} = (k_{\mathrm{tb}}a)\Lambda_{ij}$$

$$\hat{C}_{ij} = (k_{\mathrm{bt}}a)\Lambda_{ij}$$

$$\hat{D}_{ij} = \frac{3(3+\nu_{\mathrm{s}})\pi}{4(1+\nu_{\mathrm{s}})}(i+1)\delta_{ij} + (k_{\mathrm{bb}}a)\Lambda_{ij} \tag{5.135}$$

$$\Lambda_{ij} = \int_{-1}^{1} [\hat{W}(r)]^2 \hat{U}_i(r)\hat{U}_j(r)\mathrm{d}r$$

$$= \begin{cases} 0 & i+j \text{ is odd} \\ \dfrac{4(i+1)(j+1)}{(i+j+3)(i+j+1)(i-j+1)(j-i+1)} & i+j \text{ is even} \end{cases}$$

and δ_{ij} being the Kronecker delta.

(b) Reissner's plate theory

In a similar manner as described in part (a), the second equation of (5.127) can be expressed as

$$\begin{aligned} &\frac{3}{2}\sum_{i=0}^{N}(i+1)\hat{g}_i\hat{U}_i(r) - \frac{15}{(1+\nu_{\mathrm{s}})2\pi}\left(\frac{a}{t_{\mathrm{s}}}\right)^2\sum_{i=0}^{N}\hat{g}_i\bar{L}_i(r) \\ &\quad + \hat{W}(r)(k_{\mathrm{bt}}a)\sum_{i=0}^{N}\hat{f}_i\hat{U}_i(r) + \hat{W}(r)(k_{\mathrm{bb}}a)\sum_{i=0}^{N}\hat{g}_i\hat{U}_i(r) = \frac{\sigma_{\mathrm{b}}^0}{E_{\mathrm{s}}} \end{aligned} \tag{5.136}$$

where

$$\bar{L}_i(r) = \int_{-1}^{1}\hat{L}\left(\sqrt{10}\frac{a}{t_{\mathrm{s}}}|r-\eta|\right)\hat{W}(\eta))\hat{U}_i(\eta)\mathrm{d}\eta \tag{5.137}$$

Multiplying Equation (5.136) with $W(r)U_j(r)$ then integrating from -1 to 1, one obtains, noting that the tensile stretching equation is identical to the first of Equation (5.134),

$$\begin{cases} \hat{A}_{ij}\hat{f}_j + \hat{B}_{ij}\hat{g}_j = \dfrac{\pi}{2}\dfrac{\sigma_m^0}{E_{\mathrm{s}}}\delta_{0j} \quad (i,\ j = 0, 1, 2, \ldots, N) \\ \hat{C}_{ij}\hat{f}_j + \hat{F}_{ij}\hat{g}_j = \dfrac{\pi}{2}\dfrac{\sigma_{\mathrm{b}}^0}{E_{\mathrm{s}}}\delta_{0j} \quad (i,\ j = 0, 1, 2, \ldots, N) \end{cases} \tag{5.138}$$

where

$$\hat{F}_{ij} = \frac{3}{4}\pi(i+1)\delta_{ij} + (k_{bb}a)\Lambda_{ij} - \frac{15}{(1+\nu_s)2\pi}\left(\frac{a}{t_s}\right)^2 \tilde{L}_{ij} \tag{5.139}$$

$$\begin{aligned}\tilde{L}_{ij} &= \int_{-1}^{1} \bar{L}_i(r)\hat{W}(r)\hat{U}_j(r)\mathrm{d}r \\ &\equiv \int_{-1}^{1}\int_{-1}^{1} \hat{L}\left(\sqrt{10}\,|r-\eta|\,a/t_s\right)\hat{W}(\eta)\,\hat{W}(r)\,\hat{U}_i(\eta)\,\hat{U}_j(r)\,\mathrm{d}\eta\mathrm{d}r\end{aligned} \tag{5.140}$$

$\hat{A}_{ij}$, $\hat{B}_{ij}$, $\hat{C}_{ij}$, and Λ_{ij} are given by Equation (5.135). Since the kernel $\hat{L}(\tilde{s})$ has a logarithm singularity, the above double integration presents a major time-consuming operation for the numerical analysis. One way to attenuate this difficulty is to separate the logarithm singularity, which can be calculated in closed form (Joseph and Erdogan, 1987):

$$\begin{aligned}\tilde{L}_{ij} &= \int_{-1}^{1}\int_{-1}^{1}\left[\hat{L}\left(\sqrt{10}\,|r-\eta|\,a/t_s\right) - \ln|r-\eta| + \ln|r-\eta|\right]\hat{W}(\eta)\,\hat{W}(r)\,\hat{U}_i(\eta)\,\hat{U}_j(r)\,\mathrm{d}\eta\mathrm{d}r \\ &= \int_{-1}^{1}\int_{-1}^{1}\left[\hat{L}\left(\sqrt{10}\,|r-\eta|\,a/t_s\right) - \ln|r-\eta|\right]\hat{W}(\eta)\,\hat{W}(r)\,\hat{U}_i(\eta)\,\hat{U}_j(r)\,\mathrm{d}\eta\mathrm{d}r + \tilde{L}^{R}_{ij}\end{aligned} \tag{5.141}$$

where

$$\tilde{L}^{R}_{ij} = \begin{cases} -\dfrac{\pi^2}{16}[1+4\ln 2] & i=j=1 \\ -\dfrac{\pi^2}{8}\left(\frac{1}{j-1}+\frac{1}{j+1}\right) & i=j>1 \\ \dfrac{\pi^2}{8(j-1)} & j=i+2 \\ \dfrac{\pi^2}{8(j+1)} & j=i-2 \\ 0 & \text{otherwise} \end{cases} \tag{5.142}$$

The remaining integrand in Equation (5.141) is a smooth function everywhere within the integration interval, thus allowing the integral to be evaluated using simple quadrature rules.

The coupled linear set of Equations (5.134) or (5.138) can be readily solved for the unknown coefficients $\hat{f}_i$ and $\hat{g}_i$, from which the membrane and the bending stress intensity factors can then be determined via Equations (5.122), (5.123), and (5.128), noting

$$\bar{h}_1(1) = \sum_{i=0}^{N}(1+i)\hat{f}_i \tag{5.143}$$

$$\bar{h}_2(1) = \sum_{i=0}^{N}(1+i)\hat{g}_i \tag{5.144}$$

since $\hat{U}_i(1) = 1+i$.

Table 5.2. Convergence of solution using Kirchhoff–Poisson plate theory.

N	$K_m/\sigma_m^0\sqrt{\pi a}$	Difference (%)	$K_b^{(K)}/\sigma_b^0\sqrt{\pi a}$	Difference (%)
$(k_{tt}a = 1.0)$				
2	0.720183	3.096	1.6896	4.923
4	0.732071	1.497	1.65512	2.781
8	0.739196	0.538	1.62692	1.030
16	0.742024	0.157	1.61504	0.294
32	0.742885	0.042	1.61155	0.076
64	0.743123	0.0095	1.61061	0.017
128	0.743186	0.0011	1.61037	0.002
256	0.743194		1.61033	
$(k_{tt}a = 10)$				
2	0.301707	−16.542	0.831925	−5.417
4	0.329653	−8.8112	0.890410	1.2320
8	0.347698	−3.8196	0.906460	3.0567
16	0.356674	−1.3366	0.894024	1.6428
32	0.360270	−0.3419	0.883558	0.4529
64	0.361216	−0.0802	0.880411	0.0952
128	0.361472	−0.0094	0.879674	0.0114
256	0.361506	–	0.879574	–

Notes:

1. $k_{bt}/k_{tt} = -3.4744,\ k_{bb}/k_{tt} = 18.5263$.
2. The difference is measured relative to the value of $N = 256$ and is used as a measure of convergence of the series.

Table 5.2 illustrates the convergence of the solutions for intermediate and long crack cases, based on Kirchhoff–Poisson plate theory. The Reissner's plate theory formulation exhibits a similar convergence. In this table the reduction in the stress intensity factor as a result of repair is calculated for different numbers of leading terms in the expansion in terms of the Chebyshev polynomials. From Table 5.2 it can be seen that as the crack length increases more terms are required to achieve the same degree of accuracy. For instance, for $k_{tt}a = 1.0$, a total of 32 terms is sufficient to achieve an accuracy better than 0.1%, whereas 64 terms are needed to achieve the same accuracy for $k_{tt}a = 10.0$. The main reason for this is the boundary layer effect in the crack face opening displacement: as the stiffness of the bridging springs increases, the crack-opening displacement becomes essentially constant over the entire crack length, except in the vicinity of the crack tips, where the crack-opening displacement sharply decreases to zero (Rose, 1987a; Nemat-Nasser and Hori, 1987). However, as will be shown later, the stress intensity factors obtained for a normalized crack length of $k_{tt}a = 10.0$ is sufficiently close to the long crack limit, $k_{tt}a \to \infty$, so that no further calculations involving much higher order of expansion is necessary.

It remains now to determine the stresses in the patch and in the adhesive from the above normalized displacement and rotation solutions. Since these stresses are normally critical at the middle of crack, their values there will be derived here. As mentioned earlier, the internal forces and moments of the distributed tension and bending springs represent the forces and moments exerted by the patch on the cracked skin. Conversely, the cracked skin will exert the similar forces and moments on the patch. Since the sum

of the forces and moments acting on the cracked plate due to the patch and those acting on the patch due to the skin (about a common reference plane) must be equal to zero, the stress and the moment resultants in the patch about its neutral plane will be given by Equation (5.92) as

$$\begin{aligned} N_{22}^{\mathrm{p}}(y=0;\ x=0) &= n_0 = d_{\mathrm{tt}}\tilde{v}(x=0) + d_{\mathrm{tb}}\tilde{\theta}(x=0) \\ M_{22}^{\mathrm{p}}(y=0;\ x=0) &= m_0 + n_0\left(\frac{t_{\mathrm{p}}+t_{\mathrm{s}}}{2}\right) \\ &= d_{\mathrm{bt}}\tilde{v}(x=0) + d_{\mathrm{bb}}\tilde{\theta}(x=0) \\ &\quad + \left(\frac{t_{\mathrm{p}}+t_{\mathrm{s}}}{2}\right)\cdot\left[d_{\mathrm{tt}}\tilde{v}(x=0) + d_{\mathrm{tb}}\tilde{\theta}(x=0)\right] \end{aligned} \tag{5.145}$$

where the relation (5.106) has been utilized in the derivation. It should be remembered from Equations (5.117), (5.118), (5.130), and (5.131) that

$$\begin{aligned} \tilde{v}(x=0) &= a\cdot\tilde{h}_1(r=0) = a\cdot\sum_{i=0}^{N}\hat{f}_i\hat{U}_i(0) \\ \tilde{\theta}(x=0) &= \frac{6a}{t_{\mathrm{s}}}\cdot\tilde{h}_2(r=0) = \frac{6a}{t_{\mathrm{s}}}\cdot\sum_{i=0}^{N}\hat{g}_i\hat{U}_i(0) \end{aligned} \tag{5.146}$$

Since the stress distribution in the patch across its thickness is linear, the patch stress distribution at the middle of the crack surface can be derived from the stress and the moment resultants N_{22}^{p} and M_{22}^{p}, respectively, given by Equation (5.145) via a simple formula such as $\sigma_{22}^{\mathrm{p}} = \frac{N_{22}^{\mathrm{p}}}{t_{\mathrm{p}}} - \frac{M_{22}^{\mathrm{p}}}{D_{\mathrm{p}}}x_3$. On the other hand, the shear strain in the adhesive at the middle of the crack surface, i.e., $\gamma^{(\mathrm{A})}(x=0,\ y=0)$, can be determined from Equation (5.98) with n_0 and m_0 defined in Equation (5.145). Since the analysis in Section 5.4.1 is for a vertical strip along any line of constant x so that the result of $\gamma_{\max}^{(\mathrm{A})}$ given by Equation (5.98) is really $\gamma^{(\mathrm{A})}(y=0, x=\text{constant})$. Similarly, the peel strain in the adhesive can be found by first solving Equations (5.99) and (5.100) for the unknown constants B and A since n_0, m_0, and $\gamma_{\max}^{(\mathrm{A})}$ that appear in these equations are already determined, and noting that from Equation (5.91) $\varepsilon^{(\mathrm{A})} = A$ at $y=0$. Once the shear and peel strains are obtained, the corresponding stresses are found by multiplying strains with the appropriate moduli.

5.4.4 Illustrative examples

For illustration, the case of a repair with a patch spanning across the entire width of the skin under remote tension is considered. The dimensions and material properties of the cracked plate, patch, and the adhesive layer are summarized in Table 5.3, which represents a typical repair that has been extensively used in practical applications (Baker and Jones, 1988). Both geometrically linear and nonlinear analyses are performed.

Table 5.3. Physical dimensions and material properties of a typical repair.

Layer	Young's modulus (GPa)	Poisson's ratio	Thickness (mm)
Skin plate	71	0.3	3.0
Patch	207	0.3	1.0
Adhesive	1.89	0.33	0.2

However, the effect of geometrically nonlinear deformation will be analyzed using a hybrid method.

Case 1: Geometrically linear analysis

The plate is assumed to be subjected to a uniform tension, σ_∞, remotely. The prospective membrane and the maximum bending stresses acting on the crack faces are given by Equation (5.80), noting that the "initial" stress is zero in the present case. These stresses are given, respectively, by

$$\sigma_{\mathrm{m}}^{0} = \frac{P}{(1+S)\,t_{\mathrm{s}}} + \frac{P\cdot\hat{e}^{2}\cdot\dfrac{E_{\mathrm{s}}}{1-\nu_{\mathrm{s}}^{2}}}{D_{22}^{\mathrm{I}}}$$
$$\sigma_{\mathrm{b}}^{0} = +\frac{P\cdot\hat{e}\cdot t_{\mathrm{s}}\cdot\dfrac{E_{\mathrm{s}}}{1-\nu_{\mathrm{s}}^{2}}}{2\cdot D_{22}^{\mathrm{I}}} \tag{5.147}$$

noting a positive sign for σ_{b}^{0} since $\sigma_{\mathrm{b}}^{0} = -\hat{\sigma}_{22}^{\mathrm{s-LN}}(0)$ due to the difference in sign convention for the bending moment between this section and the previous sections.

With the material properties and dimensions given in Table 5.3, the coupled Equations (5.134) and (5.138), representing Kirchhoff–Poisson plate theory and Reissner's plate theory, are solved numerically. The results are plotted in Figure 5.22. It is clear that the formulation-based Kirchhoff-Poisson plate theory significantly over-predicts the bending stress intensity factor as compared to Reissner's plate theory, while the membrane stress intensity factor appears to be well predicted. Even when the Kirchhoff-Poisson bending stress intensity factor is converted to an equivalent Reissner bending stress intensity factor using Equation (5.115), Kirchhoff-Poisson plate theory prediction still remains considerably higher than that predicted using Reissner's plate theory. The breakdown of the relationship (5.115) is due to the coupling between the tensile and the bending springs sprung between crack faces, resulting in the inapplicability of the path-independent integral used in deriving (5.115). Therefore in the following analyses solutions based on Kirchhoff-Poisson plate theory will not be discussed further.

The numerical results obtained from the formulation based on Reissner's plate theory, i.e., Equation (5.138), are plotted in Figure 5.23, together with the results of a

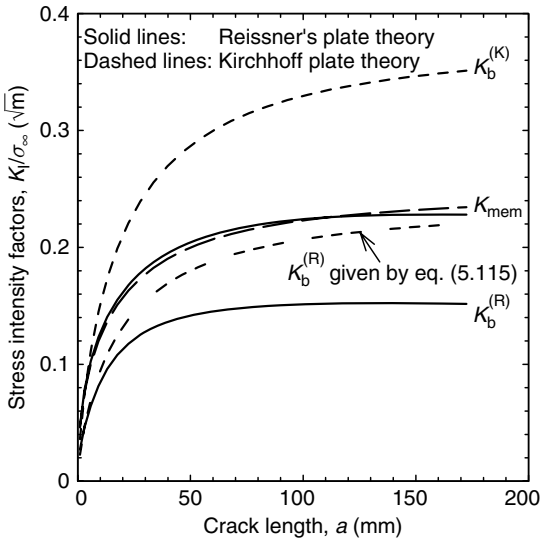

Fig. 5.22. Comparison of models based on Kirchoff–Poisson plate theory and the Reissner's plate theory.

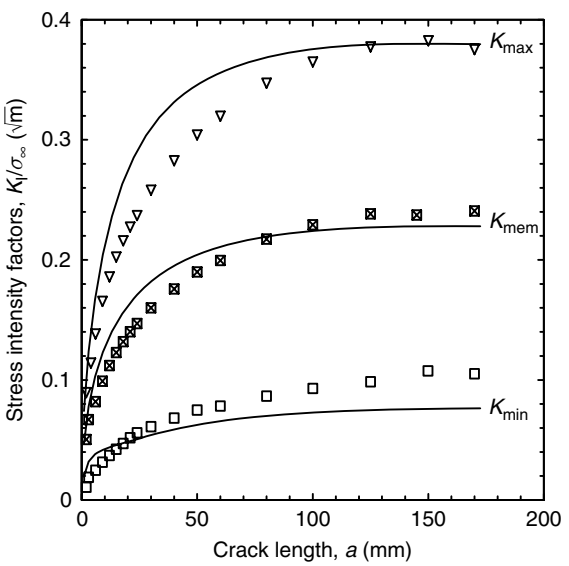

Fig. 5.23. Theoretical predictions and finite element results for a plate repaired with a patch spanning across the plate's full width assuming geometrically linear deformation.

three-dimensional FE analysis (Callinan et al, 1997b). Considering the approximate nature of the crack-bridging model and the FE method, the correlation between the predictions and the FE results is reasonably good, except for the discrepancies in the short crack regime.

Case 2: Geometrically nonlinear analysis

As mentioned earlier in the Introduction of Section 5.4, the geometrically nonlinear problem is solved approximately using the hybrid method, in which the prospective stress distribution is solved using geometrically nonlinear elasticity but the spring constants and the perturbed solution are derived from the linear analyses. The prospective membrane and maximum bending stresses are obtained from Equation (5.78) with $\sigma_0^{(\text{init})} = 0$. In this example, the overlap length is assumed to be long so that these stresses are given, respectively, by

$$\begin{aligned} \sigma_m^0 &= \frac{1}{1+S}\sigma^\infty \\ \sigma_\text{b}^0 &= 0 \end{aligned} \tag{5.148}$$

With this stress distribution, the coupled Equations (5.138) are then solved numerically and the results are plotted in Figure 5.24. When compared with the geometrically linear analysis, both the membrane and the bending stress intensity factors have reduced by almost a factor of 2, suggesting a strong influence of the geometrically non-linear deformation on the repair efficiency of one-sided repairs. Nevertheless, the results shown in Figure 5.24 also reveal that the repair efficiency of a one-sided repair is still much lower than the equivalent two-sided repairs, with the mean and the maximum stress intensity factors being about twice and four times those of equivalent two-sided repairs for the geometry being considered. It is interesting to note that although the prospective maximum bending stress is zero, there is still a significant bending stress intensity factor, resulting from the coupling between the tension and the bending springs.

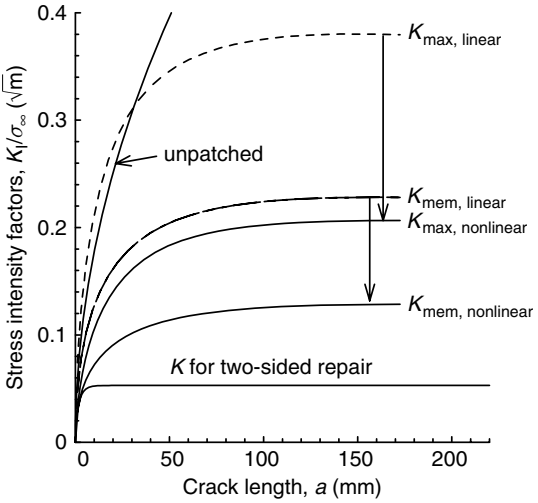

Fig. 5.24. Influence of geometrically nonlinear deformation on the repair efficiency.

5.5 Thermal Residual Stresses Resulting from Bonding

In Sections 5.2 and 5.3, only thermal stresses resulting from a uniform temperature change due to a low operating temperature were addressed. However, since curing of the adhesive in a bonded repair involves first heating the local area to be repaired above ambient temperature, and subsequently cooling the fully cured patch-adhesive system to the ambient temperature, the above uniform temperature model unless being modified cannot be used to predict the latter form of thermal stresses. This section is, therefore, devoted to address residual thermal stresses associated with curing of the adhesive. Three curing models with various degrees of complexity will be described here. Among them, Wang and Erjavec's model is most complicated.

5.5.1 Rose's or Barneveld–Fredell's curing model

In Rose's (1988) or Barneveld–Fredell's model (Barneveld, 1994; Fredell, 1994), the curing process of the adhesive can be simulated as a uniform cooling process of a whole bonded structure with the skin's thermal expansion coefficient being approximated by a (lower) "effective" value. For a circular heated region as depicted in Figure 4.15, Barneveld and Fredell derived the following effective thermal expansion coefficient for the skin, which can be used in the uniform temperature model to simulate residual thermal stresses due to curing:

$$\alpha_{\mathrm{s}}^{\mathrm{effective}} = \frac{\alpha_{\mathrm{s}}}{2}(1+\nu_{\mathrm{s}})\left\{1-\frac{T_{\mathrm{o}}}{T_i}+\frac{R_i}{R_{\mathrm{o}}}\left(\frac{T_{\mathrm{o}}}{T_i}-1\right)-\frac{1-\dfrac{T_{\mathrm{o}}}{T_i}}{2\ln\left(\dfrac{R_i}{R_{\mathrm{o}}}\right)}\left[\frac{R_i}{R_{\mathrm{o}}}-1-2\frac{R_i^2}{R_{\mathrm{o}}^2}\ln\left(\frac{R_i}{R_{\mathrm{o}}}\right)\right]\right\} \tag{5.149}$$

In deriving the above formula, they assumed that both the patch and the skin in the heat transfer model for calculating the temperature distribution are circular with respective radius of R_i and R_{o}, while the skin in the elasticity model for calculating thermal stresses is infinite. Furthermore, Barneveld–Fredell's model calculates the temperature at the edge of the skin using the theory of heat transfer through extended surface instead of setting this temperature equal to the ambient temperature. This model was originally developed for a two-sided bonded repair. However, since the effect of the local heating and the effect of elastic constraint due to the surrounding structure that is still at the ambient temperature enter into the analysis only through the effective thermal expansion of the skin, therefore, it will be deliberated here to assume that these effects can also be accounted for in the analysis of a one-sided repair by the same way, for both geometrically linear and nonlinear analyses.

5.5.2 Duong and Yu's curing model

In Section 4.2.4, the residual thermal stress problem associated with curing was formulated as an initial strain problem. The only difference between the curing problem and the uniform cooling problem found from Section 4.2.4 is that the initial strain prescribed

in the patch for the former problem is given by Equation (4.40) instead of (4.36). Thus, by employing this model, the thermal effect due to curing can be addressed within geometrically linear or nonlinear theory in a similar manner as that considered in Section 5.2 or 5.3 providing that the thermal force and moment defined by Equation (5.21) are computed based on the appropriate expression of $\varepsilon_{ij}^{(T)(p)}$ and used in the analysis (Duong, 2003a). It is worthy to note that the skin is assumed to be infinite in this model while the temperature distribution during the heating and cooling phases of the bonding process is represented by a step function.

5.5.3 Wang and Erjavec's curing model

Here the Wang et al's curing model (2000) developed in Section 4.5 is extended to characterize bending deformation. As in Section 4.5, this model considers only a circular patch, which has a radius R_i. The thermal stresses developed in the patched region are determined with the help of a set of imaginary cutting, straining, and welding operations, while continuities of extensional forces, bending moments, in-plane displacements, and out-of-plane displacements along the imaginary cut are maintained. The solutions are derived within a geometrically linear plate theory, i.e., Kirchhoff–Poisson plate theory (Wang and Erjavec, 2000).

During the first step of bonding, suppose that the inner portion ($r < R_i$) is heated to a temperature T_i during the curing process, while the outer portion ($r \geq R_o$) is heated to T_o, with the usual convention that the ambient temperature is taken as the zero of temperature. The temperature field and the thermal stresses developed in the skin due to this non-uniform temperature distribution are given respectively by Equations (4.90) and (4.91) while the patch remains stress-free. It should be noted that the patch is stress-free since during the heating step the adhesive is assumed to be very soft so that the patch can expand freely under the temperature change without any restraint from the skin. In contrast, thermal stress in the skin arises only in the case of localized heating of a large structure; for the case of a finite-sized specimen being uniformly heated to T_i, no thermal stress will develop. This stress distribution serves as the initial stress that will be added to the thermal stress induced by cooling the patched region down to the ambient temperature.

After the adhesive is fully cured, the patched skin is then cooled down to the ambient temperature. The temperature change over the entire patched skin during the cooling step is subjected to the temperature field which is opposite (in sign) to that of the heating step. During this cooling process, it is assumed that the adhesive bond between the composite patch and the metal skin is absolutely rigid, so that the patch–plate combination in the circular patched area is treated as an inhomogeneity. The thermal expansion coefficients, the bending stiffness, and the in-plane extensional stiffness of the equivalent inhomogeneity are established using the classical laminate theory as in Section 5.2.2. Since the thermal stresses resulting from a thermal loading may depend on the nature of the constraint imparted by the surrounding structures, to incorporate this size effect on the residual thermal stress, Wang and Erjavec (2000) used a model

of a circular patch on a concentric circular skin plate which is constrained at radius R_o by a continuous distribution of springs according to the following relation:

$$\sigma_{rr} = -k_s E_s u_r \qquad (r = R_o) \tag{5.150}$$

As mentioned in Section 4.5, by selecting appropriate spring stiffness k_s, various degrees of in-plane constraint imparted by the surrounding structure can be represented. For instance, the following spring stiffness will recover the case of an infinite skin:

$$k_s = \frac{1}{(1+\nu_s)R_o} \tag{5.151}$$

Free edge and clamped edge conditions at $r = R_o$ can be represented by $k_s = 0$ and $k_s \to \infty$, respectively. Provided the outer radius R_o is sufficiently large as compared to the patch size R_i, the precise value of k_s has no significant effect on the distribution of the thermal residual stresses. Due to the finite size of the skin, the strains and bending curvatures in the inclusion are not uniform. A rigorous analysis would involve the use of "stretched coordinate", rendering the analysis rather unwieldy, as the solutions need to be represented by infinite series. For simplicity, Wang and Erjavec (2000) assumed that the effect of finite size is entirely limited to the in-plane deformation. This simplification will not result in any significant error since the bending moment in the skin plate decreases at a rate proportional to the square of the radius so that the bending moment at the outer radius is approximately zero, provided that the ratio of outer radius to inner radius R_o/R_i is moderately greater than unity.

Following the work of Wang and Erjavec (2000), it can be shown that thermal stresses in the skin and the patch at their middle due to the cooling step are given by

$$\begin{Bmatrix} \sigma_{11}^{s(C)}(x_3) \\ \sigma_{22}^{s(C)}(x_3) \end{Bmatrix} = [C^s] \begin{Bmatrix} \bar{\varepsilon}_{11}^{I} - \kappa_{11}^{I}(x_3 - h_{01}) + \alpha_s T_i \\ \bar{\varepsilon}_{22}^{I} - \kappa_{22}^{I}(x_3 - h_{02}) + \alpha_s T_i \end{Bmatrix} \tag{5.152}$$

$$\begin{Bmatrix} \sigma_{11}^{p(C)}(x_3) \\ \sigma_{22}^{p(C)}(x_3) \end{Bmatrix} = [C^p] \begin{Bmatrix} \bar{\varepsilon}_{11}^{I} - \kappa_{11}^{I}(x_3 - h_{01}) + \alpha_{11}^{p} T_i \\ \bar{\varepsilon}_{22}^{I} - \kappa_{22}^{I}(x_3 - h_{02}) + \alpha_{22}^{p} T_i \end{Bmatrix} \tag{5.153}$$

$$h_{01} = \frac{S_x(t_s + t_p)}{2(1+S_x)}, \quad S_x = E_{11}^{p} t_p (1-\nu_s^2)/E_s t_s (1-\nu_{12}^{p}\nu_{21}^{p}) \tag{5.154}$$

$$h_{02} = \frac{S_y(t_s + t_p)}{2(1+S_y)}, \quad S_y = E_{22}^{p} t_p (1-\nu_s^2)/E_s t_s (1-\nu_{12}^{p}\nu_{21}^{p}) \tag{5.155}$$

where $\bar{\varepsilon}_{ij}^{I}$ denotes the mean strain in the overlap region at the neutral plane of the patch–plate combination as shown in Figure 5.25,[3] κ_{ij}^{I} is the curvature, and the superscript C

[3] Unlike Sections 5.2 and 5.3, $\bar{\varepsilon}_{ij}^{I}$ is measured at the neutral plane of the skin–patch combination while in Sections 5.2 and 5.3, except Section 5.3.2, $\bar{\varepsilon}_{ij}^{I}$ is measured at the mid-plane of the skin.

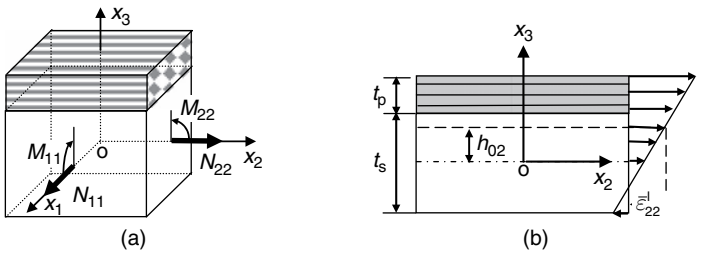

Fig. 5.25. Inclusion representation of a rigidly bonded patch and plate showing (a) stress and moment resultants and (b) strain distribution.

indicates the cooling step as used in Section 4.5. The parameters h_{01} and h_{02} denote the x_3-coordinates of the neutral axis in the x_1–x_3 plane and x_2–x_3 plane, respectively; $T_i > 0$; and the rest have been defined previously. The curvatures and mean strains can be calculated using the following explicit expressions:

$$\begin{Bmatrix} \bar{\varepsilon}^{\mathrm{I}}_{11} \\ \bar{\varepsilon}^{\mathrm{I}}_{22} \end{Bmatrix} = [L_3]^{-1}\{R_2\}(-T_i) - [L_3]^{-1}[L_4]\begin{Bmatrix} \kappa^{\mathrm{I}}_{11} \\ \kappa^{\mathrm{I}}_{22} \end{Bmatrix} \tag{5.156}$$

$$\begin{Bmatrix} \kappa^{\mathrm{I}}_{11} \\ \kappa^{\mathrm{I}}_{22} \end{Bmatrix} = \left([L_2] - [L_1][L_3]^{-1}[L_4]\right)^{-1}\left(\{R_1\} - [L_1][L_3]^{-1}\{R_2\}\right)(-T_i) \tag{5.157}$$

$$[L_1] = -\frac{t_{\mathrm{s}} + t_{\mathrm{p}}}{6D_{\mathrm{s}}(1-\nu_{\mathrm{s}})}[G_{\mathrm{T}}]\left(2[h_0]\left[C^{\mathrm{I}}\right] - 2\left[C^{\mathrm{I}}\right][h_0] + t_{\mathrm{p}}[C^{\mathrm{p}}]\right) \tag{5.158}$$

$$[L_2] = \begin{bmatrix} 1 & 1 \\ 1 & -1 \end{bmatrix} + \frac{1}{3D_{\mathrm{s}}(1-\nu_{\mathrm{s}})}[G_{\mathrm{T}}]\left(\left[D^{\mathrm{I}}\right] - [h_0][\delta_{\mathrm{T}}]\right) \tag{5.159}$$

$$\begin{aligned}\{R_1\} = &-\frac{t_{\mathrm{s}} + t_{\mathrm{p}}}{3D_{\mathrm{s}}(1-\nu_{\mathrm{s}})}[G_{\mathrm{T}}]\left([h_0]\left[C^{\mathrm{I}}\right] - \left[C^{\mathrm{I}}\right][h_0]\right)\begin{Bmatrix} \alpha^{\mathrm{I}}_{11} \\ \alpha^{\mathrm{I}}_{22} \end{Bmatrix} \\ &-\frac{(t_{\mathrm{s}} + t_{\mathrm{p}})t_{\mathrm{p}}}{6D_{\mathrm{s}}(1-\nu_{\mathrm{s}})}[G_{\mathrm{T}}]\,[C^{\mathrm{p}}]\begin{Bmatrix} \alpha^{\mathrm{p}}_{11} \\ \alpha^{\mathrm{p}}_{2} \end{Bmatrix}\end{aligned} \tag{5.160}$$

$$\begin{Bmatrix} \alpha^{\mathrm{I}}_{11} \\ \alpha^{\mathrm{I}}_{22} \end{Bmatrix} = \frac{t_{\mathrm{s}}}{t_{\mathrm{s}} + t_{\mathrm{p}}}\left[C^{\mathrm{I}}\right]^{-1}[C^{\mathrm{s}}]\begin{Bmatrix} \alpha_{\mathrm{s}} \\ \alpha_{\mathrm{s}} \end{Bmatrix} + \frac{t_{\mathrm{p}}}{t_{\mathrm{s}} + t_{\mathrm{p}}}\left[C^{\mathrm{I}}\right]^{-1}[C^{\mathrm{p}}]\begin{Bmatrix} \alpha^{\mathrm{p}}_{11} \\ \alpha^{\mathrm{p}}_{22} \end{Bmatrix} \tag{5.161}$$

$$[G_{\mathrm{T}}] = \begin{bmatrix} 3 & 3 \\ 1 & -1 \end{bmatrix} \tag{5.162}$$

$$[L_3] = \begin{bmatrix} 1 & 0 \\ 0 & 1 \end{bmatrix} + \frac{t_{\mathrm{s}} + t_{\mathrm{p}}}{E_{\mathrm{s}} t_{\mathrm{s}}}[H_{\mathrm{T}}]\left[C^{\mathrm{I}}\right] \tag{5.163}$$

$$[L_4] = [h_0] + \frac{1}{E_s t_s}[H_T][\delta_T] \tag{5.164}$$

$$\{R_2\} = \begin{Bmatrix} b_T \\ b_T \end{Bmatrix} + \frac{t_s + t_p}{E_s t_s}[H_T]\left[C^I\right]\begin{Bmatrix} \alpha^I_{11} \\ \alpha^I_{22} \end{Bmatrix} \tag{5.165}$$

$$[h_0] = \begin{bmatrix} h_{01} & 0 \\ 0 & h_{02} \end{bmatrix} \tag{5.166}$$

$$[\delta_T] = \frac{E_s t_s}{1-\nu_s^2}\begin{bmatrix} 0 & (\nu_s - \nu^p_{12})h_{02} \\ (\nu_s - \nu^p_{21})h_{01} & 0 \end{bmatrix} \tag{5.167}$$

$$[H_T] = \begin{bmatrix} \gamma_1^T & -\gamma_2^T \\ -\gamma_2^T & \gamma_1^T \end{bmatrix} \tag{5.168}$$

$$b_T = \frac{\alpha_s \chi_T}{1 - \chi_T R_i^2/R_o^2}\left\{T_o/T_i - R_i^2/R_o^2 - \frac{(1 - R_i^2/R_o^2)(1 - T_o/T_i)}{2\ln(R_i/R_o)}\right\} \tag{5.169}$$

$$\gamma_1^T = \frac{(3-\nu_s)\eta_T + (1+\nu_s)\lambda_T}{2} \tag{5.170}$$

$$\gamma_2^T = \frac{(3-\nu_s)\eta_T - (1+\nu_s)\lambda_T}{2} \tag{5.171}$$

$$\eta_T = \frac{3 - \nu_s + (7+3\nu_s)R_i^2/R_o^2 + (1-3\nu_s)R_i^4/R_o^4 + (1+\nu_s)R_i^6/R_o^6}{(3-\nu_s)(1 - R_i^2/R_o^2)^3} \tag{5.172}$$

$$\lambda_T = \frac{1 + \nu_s + (1-\nu_s)\chi_T R_i^2/R_o^2}{(1+\nu_s)(1 - \chi_T R_i^2/R_o^2)} \tag{5.173}$$

$$\chi_T = \frac{1 - (1+\nu_s)k_s R_o}{1 + (1-\nu_s)k_s R_o} \tag{5.174}$$

$$\begin{aligned}\left[D^I\right] = {} & \frac{t_s^3}{12}[C^s] + \frac{t_p^3}{12}[C^p] + t_s[C^s][h_0]^2 + \frac{t_p}{4}[C^p] \\ & \times \begin{bmatrix} (t_s + t_p - 2h_{01})^2 & 0 \\ 0 & (t_s + t_p - 2h_{02})^2 \end{bmatrix}\end{aligned} \tag{5.175}$$

where D_s is bending stiffness of the skin plate, i.e., $D_s = \frac{E_s t_s^3}{12(1-\nu_s^2)}$; $[C]$ is the elasticity matrix; $\left[C^I\right]$ is defined by Equations (4.31)–(4.33) but with the effective thickness of the inhomogeneity chosen to be $t_s + t_p$. It is worthy to note that b_T, γ_1^T, γ_2^T, λ_T, η_T, and χ_T have been defined previously in Section 4.5; however, their definitions are repeated here for convenience.

As a special case, the solutions pertaining to two-sided repairs can be recovered by equating the curvatures κ_{11}^{I} and κ_{22}^{I} in Equation (5.156) to zero, which yields

$$\begin{Bmatrix} \bar{\varepsilon}_{11}^{\mathrm{I}} \\ \bar{\varepsilon}_{22}^{\mathrm{I}} \end{Bmatrix} = [L_3]^{-1} \{R_2\} (-T_i) \tag{5.176}$$

It can be shown that this solution is identical to that given by Equation (4.98). It is worthy to note that even though this curing model accounts for the realistic temperature distribution and the effect of structure finite size, however, it only deals with one particular patch's shape, a circular patch. In contrast, the Duong and Yu's curing model is developed for a general shaped patch in an infinite structure size and under a simple temperature distribution. Thus, these two models certainly can be combined for better predictions of the geometrically linear thermal stresses in a one-sided bonded repair by using a "shape correction" factor approach as described in Section 4.5.

5.6 Characterization of Fatigue Crack Growth in One-Sided Patching

Due to the out-of-plane bending, the stress intensity factor varies across the plate thickness. As common practices, either the maximum value or the root mean square (rms) value of the stress intensity factor across the skin thickness is used to predict the fatigue crack growth. $K_{\max}$ and K_{rms} are defined, respectively, by

$$\begin{aligned} K_{\max} &= K_{\mathrm{mem}} + K_{\mathrm{b}} \\ K_{rms} &= \sqrt{K_{\mathrm{mem}}^2 + \frac{K_{\mathrm{b}}^2}{3}} \end{aligned} \tag{5.177}$$

where K_{mem} and K_{b} are the membrane and the bending components of the stress intensity factor, respectively. However, it was found by Duong (2003b) and Duong and Wang (2004) that the effective or equivalent stress intensity factor defined as

$$K_{\mathrm{eq}} = K_{\max} + \left(1 - \sqrt{3}\right) \frac{K_{\mathrm{b}}}{K_{\max}} K_{\mathrm{rms}} \tag{5.178}$$

will consistently yield best crack growth predictions when compared with the test data generated under the Composite Repair of Aircraft Structure (CRAS) program. The physical significance of K_{eq} will be discussed in Chapter 11.

5.7 Summary

An approximate method has been presented for analyzing the tensile stretching and bending of a cracked skin plate, which is repaired on one side, subjected to tension and thermal excursion. The method employs a hybrid approach, in which, the stage I analysis is performed within either geometrically linear or nonlinear theory while stage II analysis is always within geometrically linear analysis. In addition, stage I problem

has been solved approximately using the equivalent inclusion method that was extended to include analysis of the bending plates. Even though the method employed for the geometrically nonlinear analysis of stage I lacks scientific rigor, however, it predicts reasonably well the thermo-mechanical stresses in the skin for a wide range of repair configurations and thus provides practical way for analyzing a one-sided bonded repair. On the other hand, stage II problem has been solved using the crack-bridging model within both Kirchhoff–Poisson and Reissner plate theories. The repaired structure is modeled as a plate containing a through thickness crack, bridged by tension and bending springs, whose stiffness constants are determined from a one-dimensional analysis of a single-strap joint. The results from the crack-bridging model show that the Kirchhoff–Poisson plate theory would considerably overestimate the bending stress intensity factor, while the formulation-based on the Reissner's plate theory provides a reasonably good estimate of both the membrane and the bending stress intensity factors, when compared with results from a three-dimensional FE analysis. The results show that a one-sided repair is still much less efficient in reducing the stress intensity factor than an equivalent two-sided repair.

CHAPTER 6

Analytical Approach to Repairs of Corrosion Grind-Outs

6.1 Introduction

Corrosive damage on the outer surfaces of aircraft is generally removed by grinding during periodic, routine maintenance. Aircraft manufacturers provide maintenance specifications that allow a limited amount of material removal, but it is sometimes necessary to exceed these limits in order to completely remove the corrosion. In these cases, the structure must be replaced or repaired before further operation of the aircraft is permitted. Whenever a repair is sought, bonded composite doublers may be preferred due to high stiffness and high strength of the composite.

In the past, stress analysis of a bonded repair over a corrosion grind-out cavity was normally done using the FE method. The corrosion repairs are thought to be too complex to be analyzed by an analytical method. However, Duong et al. (2001b), and Duong and Yu (2002b, 2003b) in a series of papers presented a procedure for solving this repair problem analytically. This analytical procedure followed Rose's original approach (1981, 1982, 1988) for the analysis of crack patching, and it was used for analyzing elliptical and polygon-shaped patch over an elliptical cut-out or grind-out cavity with a uniform or spherical depth. It also accounted for the effects of thermal stresses due to curing and/or cruising and the effects of the filler stiffness. The procedure had been used successfully in estimating stresses and strains in a patch and skin analytically at various critical locations such as near the patch edge, around the damage edge, and at the bottom of a grind-out cavity. The analytical methods based on this procedure therefore will be presented in this chapter.

6.2 Fundamental Concepts

To illustrate the fundamental concepts behind the analytical methods employed by Duong et al. (2001b), and Duong and Yu (2002b, 2003b), the analysis of an isotropic skin with an

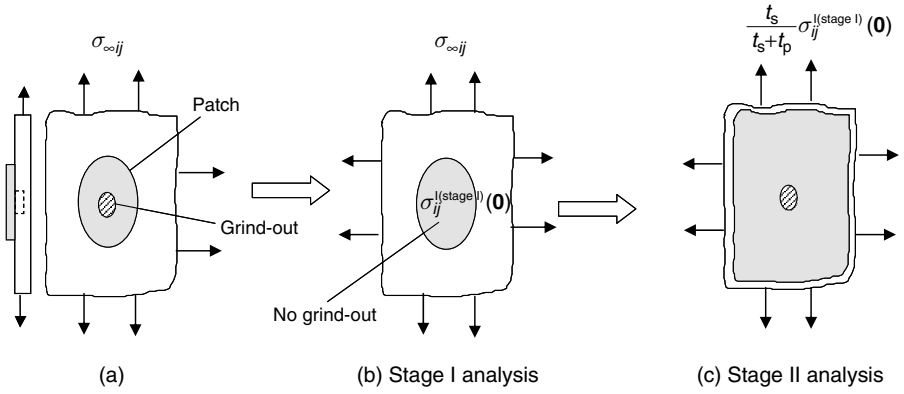

Fig. 6.1. Two-stage analytical solution procedure for a bonded repair problem.

internal elliptical corrosion grind-out, or cut-out repaired with an elliptical isotropic patch, is presented first in this section since it is mathematically simplest. For simplicity, the effect of thermal stresses is also ignored in the present discussion. Analyses including this effect together with other complexities such as polygon-shaped and orthotropic patches will be given in Section 6.3. As mentioned in the Introduction of this chapter, the analysis of a corrosion repair also follows the similar two-stage procedure originally proposed by Rose (1981, 1988) for a crack patching analysis (Figure 6.1). In the first stage, an infinite skin reinforced by an elliptical patch under prescribed far-field stresses $\sigma_{\infty ij}$ is analyzed using the inclusion analogy, without considering the grind-out or cut-out. The constant stresses inside the patched area denoted by $\sigma_{ij}^{\text{I(stage I)}}(\mathbf{0})$ are then calculated and later used as the far-field-boundary conditions for the second (stage II) problem. In the second stage, the patch is assumed to be infinite and an integral part of the skin. Stage II analysis then involves solving a problem of an infinite patched skin containing an elliptical grind-out or cut-out under far-field stresses $\sigma_{ij}^{\text{I(stage I)}}(\mathbf{0})$. The latter problem is also solved using the inclusion analogy. Because the patch in a typical design is much larger than the damaged area, the solutions of the first and the second problems are approximately the same as the solutions of the original problem inside and outside the patched area, respectively. In order to solve for these first- and the second-stage problems, the solutions of the elliptical inclusions and inhomogeneities are required. These solutions obviously can be obtained using the computational algorithm given in Sections 4.2.1 and 4.2.2 of Chapter 4 for a regular polygon with a large number of sides. However, explicit solutions for elliptical inclusions and inhomogeneities are available in literature through pioneered work by Eshelby, and therefore they are summarized in the next subsection.

6.2.1 Eshelby solution for elliptical inhomogeneities

For simplicity, all formulas presented in this section are obtained directly from a book by Mura (1998) for plane strain condition. These formulas can be modified for plane stress case by replacing the Young's modulus E with $E(1+2\nu)/(1+\nu)^2$ and the Poisson's ratio ν with $\nu/(1+\nu)$ while keeping the shear modulus μ unchanged. Consider an infinitely extended material with the elastic moduli C_{ijkl}^0 containing an elliptic cylindrical

domain Ω (minor and major axes are a_1 and a_2, respectively) with the elastic moduli C^{I}_{ijkl} and subjected to the applied stress $\sigma_{\infty ij}$ at infinity. The solution of this problem will be obtained by the equivalent inclusion method outlined in Section 4.2.1 of Chapter 4. According to this method, the stress disturbance in an applied stress due to the presence of an inhomogeneity can be simulated by the disturbance caused by an eigenstrain field (or an initial strain filed) ε^*_{ij} occurring in the same region Ω in an infinitely extended homogenous material with the moduli C^0_{ijkl}, where ε^*_{ij} is determined from the equivalency conditions as (see Equation 4.5):

$$\begin{aligned} &\Delta C_{ijkl}\, S_{klmn}\, \varepsilon^*_{mn} - C^0_{ijkl}\varepsilon^*_{kl} = -\Delta C_{ijkl}\varepsilon_{\infty kl} \\ &\qquad\qquad\qquad\qquad\qquad\qquad\qquad\qquad \text{in } \Omega \\ &\Delta C_{ijkl} = C^0_{ijkl} - C^{\mathrm{I}}_{ijkl} \end{aligned} \tag{6.1}$$

where S_{ijkl} is the Eshelby tensor. For an elliptical domain, if $\sigma_{\infty ij}$ is uniform, ε^*_{ij} as determined from Equation (6.1) is also found to be uniform in Ω since S_{ijkl}, as shown later, is a constant tensor which depends only on material constants and geometric dimensions of Ω but not the spatial coordinates. Explicit formula for S_{ijkl} for an elliptical domain is well known (Mura, 1998), and it will be given in the next paragraph. Thus, the only unknown in Equation (6.1) will be the eigenstrain ε^*_{ij}. Once the eigenstrain is determined from Equation (6.1), the stress and strain inside the inhomogeneity can be obtained from Equations (4.1)–(4.3) as

$$\begin{aligned} &\varepsilon^{\mathrm{I}}_{ij} = \varepsilon^{\mathrm{H}}_{ij} = S_{ijkl}\varepsilon^*_{kl} + \varepsilon_{\infty ij} \\ &\qquad\qquad\qquad\qquad\qquad\qquad\qquad\qquad \text{in } \Omega \\ &\sigma^{\mathrm{I}}_{ij} = \sigma^{\mathrm{H}}_{ij} = C^0_{ijkl}\,(\varepsilon^{\mathrm{H}}_{kl} - \varepsilon^*_{kl}) \end{aligned} \tag{6.2}$$

where $\varepsilon^{\mathrm{H}}_{ij}$ and σ^{H}_{ij} are defined in Chapter 4 as the strain and stress in the "equivalent" inclusion (homogeneous) problem. It should be emphasized that the stress and strain inside the inhomogeneity are uniform according to Equation (6.2) since both S_{ijkl} and ε^*_{ij} are constant tensors. Thus, by denoting the stress and strain at point (0, 0), i.e., the origin of the coordinate system, as $\sigma^{\mathrm{I}}_{ij}(\mathbf{0})$ and $\varepsilon^{\mathrm{I}}_{ij}(\mathbf{0})$, the stress and strain fields inside Ω must also equal $\sigma^{\mathrm{I}}_{ij}(\mathbf{0})$ and $\varepsilon^{\mathrm{I}}_{ij}(\mathbf{0})$, respectively. For point exterior to Ω, the elastic fields are not uniform. Even though the stress and the strain σ^{I}_{ij} and $\varepsilon^{\mathrm{I}}_{ij}$ for point exterior to Ω are still equal respectively to σ^{H}_{ij} and $\varepsilon^{\mathrm{H}}_{ij}$, where $\sigma^{\mathrm{H}}_{ij} = C^0_{ijkl}\varepsilon^{\mathrm{H}}_{kl}$ and $\varepsilon^{\mathrm{H}}_{ij} = S_{ijkl}\varepsilon^*_{kl} + \varepsilon_{\infty ij}$; however, another formula for S_{ijkl} different than that given in the paragraph below must be used since S_{ijkl} as given later by Equation (6.4) applies only to points inside Ω.[1] As pointed out by Mura (1998), the stress and strain fields outside Ω are more conveniently determined by using a method proposed by Tanaka and Mura, which is illustrated in Figure 6.2. In Figure 6.2, $\sigma^{\mathrm{I}}_{ij}(\mathbf{0})$ again denotes the stresses inside Ω. The Tanaka and Mura method will be described later.

For computations, it is more convenient to represent a tensor by a matrix using Voight's convention. By assuming that all materials involved are isotropic and invoking the

[1] The Eshelby tensor S_{ijkl} derived in Section 4.2.3, on the other hand, applies to both exterior and interior points of Ω.

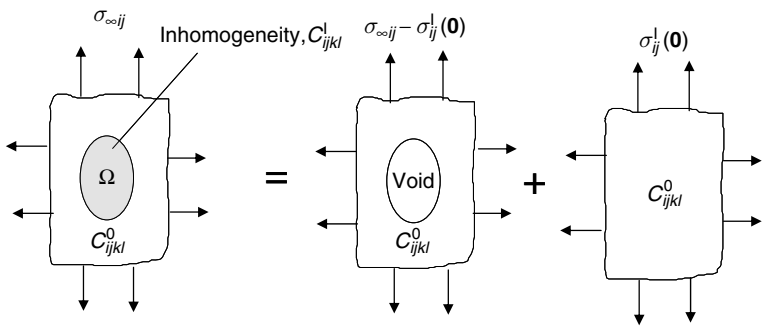

Fig. 6.2. Tanaka–Mura method for calculating the elastic field at a point outside Ω. $\sigma^{\mathrm{I}}_{ij}(\mathbf{0})$ is the stress in the inhomogeneity at its center inside Ω.

double symmetry conditions of the problem, all shear components become zero so that Equations (6.1) and (6.2) in matrix form are given by

$$\begin{aligned}
&\left([\Delta C][S] + \left[C^0\right] \right) \{\varepsilon^*\} = -[\Delta C]\ \{\varepsilon_\infty\} \\
&\left\{\varepsilon^{\mathrm{I}}\right\} = \left\{\varepsilon^{\mathrm{I}}(\mathbf{0})\right\} = [S]\{\varepsilon^*\} + \{\varepsilon_\infty\} \qquad \text{in } \Omega \\
&\left\{\sigma^{\mathrm{I}}\right\} = \left\{\sigma^{\mathrm{I}}(\mathbf{0})\right\} = \left[C^0\right]\left\{\varepsilon^{\mathrm{I}} - \varepsilon^*\right\}
\end{aligned} \tag{6.3}$$

where

$$\begin{aligned}
&[\Delta C] = \left[C^{\mathrm{I}}\right] - \left[C^0\right] \\
&\left[C^{\mathrm{I}}\right] = \frac{2\mu^{\mathrm{I}}}{1-2\nu^{\mathrm{I}}} \begin{bmatrix} (1-\nu^{\mathrm{I}}) & \nu^{\mathrm{I}} \\ \nu^{\mathrm{I}} & (1-\nu^{\mathrm{I}}) \end{bmatrix} \\
&\left[C^0\right] = \frac{2\mu}{1-2\nu} \begin{bmatrix} (1-\nu) & \nu \\ \nu & (1-\nu) \end{bmatrix} \\
&[S] = \frac{1}{2(1-\nu)} \begin{bmatrix} \dfrac{a_2^2 + 2a_1a_2}{(a_1+a_2)^2} + (1-2\nu)\dfrac{a_2}{a_1+a_2} & \dfrac{a_2^2}{(a_1+a_2)^2} - (1-2\nu)\dfrac{a_2}{a_1+a_2} \\ \dfrac{a_1^2}{(a_1+a_2)^2} - (1-2\nu)\dfrac{a_1}{a_1+a_2} & \dfrac{a_1^2 + 2a_1a_2}{(a_1+a_2)^2} + (1-2\nu)\dfrac{a_1}{a_1+a_2} \end{bmatrix} \\
&\{\varepsilon^*\} = \begin{Bmatrix} \varepsilon^*_{11} \\ \varepsilon^*_{22} \end{Bmatrix};\ \{\varepsilon_\infty\} = \begin{Bmatrix} \varepsilon_{\infty 11} \\ \varepsilon_{\infty 22} \end{Bmatrix} = \left[C^0\right]^{-1} \begin{Bmatrix} \sigma_{\infty 11} \\ \sigma_{\infty 22} \end{Bmatrix};\ \{\varepsilon\} = \begin{Bmatrix} \varepsilon_{11} \\ \varepsilon_{22} \end{Bmatrix};\ \{\sigma\} = \begin{Bmatrix} \sigma_{11} \\ \sigma_{22} \end{Bmatrix}
\end{aligned} \tag{6.4}$$

μ and ν are shear modulus and Poisson's ratio, the superscripts I and 0 of the elasticity tensor or elastic constants denote the inhomogeneity and the homogeneous material, respectively, and $\left[C^0\right]^{-1}$ is the inverse of C^0_{ijkl}. It should be emphasized that, as in Chapter 4, $\varepsilon^{\mathrm{I}}_{ij}$ and σ^{I}_{ij} throughout this book indicate the strain and stress fields of the inhomogeneity problem and they describe the strain and stress fields of points both inside and outside the inhomogeneous region.

On the other hand, using the Tanaka and Mura method (see Figure 6.2), the stresses outside Ω, at the ends of the minor and major axes of the elliptical inhomogeneity, are summarized below as they are of practical interest:

At $(\pm a_1^+, 0)$

$$\sigma_{11}^{\mathrm{I}}\left(\pm a_1^+, 0\right) = \sigma_{11}^{\mathrm{I}}(\mathbf{0}) \tag{6.5}$$

$$\sigma_{22}^{\mathrm{I}}\left(\pm a_1^+, 0\right) = -\left(\sigma_{22}^{\mathrm{I}}(\mathbf{0}) - \sigma_{\infty 22}\right)\left(1 + \frac{2a_1}{a_2}\right) + \left(\sigma_{11}^{\mathrm{I}}(\mathbf{0}) - \sigma_{\infty 11}\right) + \sigma_{22}^{\mathrm{I}}(\mathbf{0})$$

At $(0,\ \pm a_2^+)$

$$\sigma_{11}^{\mathrm{I}}\left(0,\ \pm a_2^+\right) = -\left(\sigma_{11}^{\mathrm{I}}(\mathbf{0}) - \sigma_{\infty 11}\right)\left(1 + \frac{2a_2}{a_1}\right) + \left(\sigma_{22}^{\mathrm{I}}(\mathbf{0}) - \sigma_{\infty 22}\right) + \sigma_{11}^{\mathrm{I}}(\mathbf{0}) \tag{6.6}$$

$$\sigma_{22}^{\mathrm{I}}\left(0,\ \pm a_2^+\right) = \sigma_{22}^{\mathrm{I}}(\mathbf{0})$$

where $(\pm a_1^+, 0)$ and $(0,\ \pm a_2^+)$ denote points outside Ω but infinitesimally close to points $(\pm a_1,\ 0)$ and $(0,\ \pm a_2)$ while $\sigma_{ij}^{\mathrm{I}}(\mathbf{0})$ are stresses inside Ω at its center which are uniform throughout Ω for an elliptical inhomogeneity as in the present problem.

6.2.2 Analytical solution of elliptical patches

Consider an isotropic skin with an internal elliptical cut-out or corrosion grind-out repaired with an elliptical isotropic patch and the skin is subjected to remote biaxial stresses as shown in Figure 6.1(a). The elastic moduli of the skin and patch are denoted respectively by C_{ijkl}^{s} and C_{ijkl}^{p}. Furthermore, the aspect ratio of the elliptical grind-out is b/a while the patch has an aspect ratio of B/A. The remaining skin thickness in the grind-out is denoted by t_{r}. Since the size of the patch is usually much larger than the size of the skin damaged area in typical repairs, it therefore assumes that being the case in the present analysis. Furthermore, by limiting the application of the present approach to the repair situation where the out-of-plane bending effect is insignificant, the problem considered in Figure 6.1(a) can be analyzed by a basic model with the following simplifying assumptions:

- All material behavior is linearly elastic and isotropic.
- All skin and patch materials are in a state of generalized plane stress.
- The presence of a grind-out will not disturb the stresses outside the patch.
- The patch is modeled as an integral part of the skin using inclusion analogy.
- The grind-out has a constant depth.

This basic model will bring out more clearly the essential features of the analytical approach presented in this chapter. It should be noted that the third assumption listed

above is a direct consequence of the underlying assumption that the size of the cut-out or grind-out is much smaller than that of the patch.

In the analysis of bonded repairs, two regions of shear load transfer must be distinguished. The first is the zone at the edge of the patch. Using 1-D bonded joint theory, it had been shown (Rose, 1981, 1988) that in typical repairs the size of this zone is small compared with overall patch dimensions to allow the modeling of a patch as an integral part of the skin. The second load transfer zone is around the edge of the skin damage. While the latter transfer zone definitely affects the stress distribution near the edge of the skin damage, it in general has little influence on the stress concentration in the middle of the damaged region. Since the stresses in the skin and in the patch are expected to be highest near the middle of the damaged region, one may be concerned only about these stresses in designing a patch. Thus, the analysis method developed in this section (to solve for the basic problem) can be used for the preliminary design purpose. As a matter of fact, explicit results obtained from this section will be used extensively in Chapter 10 when discussing the preliminary design approach for corrosion repairs.

Two-stage analytical solution

The analysis of a bonded repair over an elliptical cut-out or grind-out cavity is divided into two stages similar to that originally proposed by Rose for crack patching problem, as indicated in Figure 6.1.

Stage I analysis In the first stage, an infinite skin reinforced by an elliptical patch under a prescribed far-field stress is analyzed using the inclusion analogy, without considering the grind-out. The uniform stresses inside the patched area of the patch–skin combination are then calculated and later used as the far-field-boundary conditions for the second (stage II) problem. For clarity, the stresses of the skin–patch combination inside the patched area from the present stage I analysis will be referred to as $\sigma_{ij}^{\mathrm{I(stage\ I)}}(\mathbf{0})$. Since the patch is considered to be an integral part of the skin, the patched area is treated as an elliptical inhomogeneity with an aspect ratio of B/A. The material properties of this elliptical inhomogeneity, which are equivalent to those of the patched skin, are derived in a similar manner as in Section 4.2.3 of Chapter 4, but for plane strain condition[2] as

$$\begin{aligned}
\mu^{\mathrm{I}} &= \frac{\mu_{\mathrm{s}} t_{\mathrm{s}} + \mu_{\mathrm{p}} t_{\mathrm{p}}}{t_{\mathrm{I}}} \\
\nu^{\mathrm{I}} &= \frac{1}{\left(1 - \dfrac{1}{\frac{\mu^{\mathrm{I}} t_{\mathrm{I}}}{\lambda_\nu} - 1}\right)} \\
\lambda_\nu &= \frac{\mu_{\mathrm{s}} t_{\mathrm{s}} (1 - \nu_{\mathrm{s}})}{1 - 2\nu_{\mathrm{s}}} + \frac{\mu_{\mathrm{p}} t_{\mathrm{p}} (1 - \nu_{\mathrm{p}})}{1 - 2\nu_{\mathrm{p}}}
\end{aligned} \tag{6.7}$$

[2] For uniformity purpose, the formulations for stage I and II analyses are also given under plane strain conditions. For plane stress conditions, appropriate changes in the elastic constants E, ν and μ, similar to those described earlier in Section 6.2.1, must be made.

where μ and ν denote the shear modulus and Poisson's ratio, respectively, while the superscript or subscript I and subscripts s and p signify the inhomogeneity, skin, and patch, respectively. The inhomogeneity thickness t_{I} can be chosen arbitrarily; however, as in Section 4.2.3, t_{I} has been chosen to be the same as t_{s} in stage I for direct application of the results derived in Section 6.2.1. The uniform stresses $\sigma_{ij}^{\mathrm{I(stage\ I)}}(\mathbf{0})$ inside the patched region are calculated by first solving for the eigenstrain, then computing the strains and finally the stresses according to Equations (6.3) and (6.4), respectively. The stresses in the skin and in the patch inside the reinforced area then can be computed from the following equations, similar to those given at the end of Section 4.2.3:

$$\begin{aligned} \{\sigma^{\mathrm{s}}(\mathbf{0})\} &= [C^{\mathrm{s}}]\left[C^{\mathrm{I}}\right]^{-1}\left\{\sigma^{\mathrm{I(stage\ I)}}(\mathbf{0})\right\} \\ \{\sigma^{\mathrm{p}}(\mathbf{0})\} &= [C^{\mathrm{p}}]\left[C^{\mathrm{I}}\right]^{-1}\left\{\sigma^{\mathrm{I(stage\ I)}}(\mathbf{0})\right\} \end{aligned} \qquad \text{in } \Omega \tag{6.8}$$

which is based on a condition that the bond allows no relative displacement between the patch and the skin. In Equation (6.8), $[C]$ is again the elasticity matrix; the subscripts or superscripts p, s, and I have been previously defined. It is worthy to note that by using "composite" terminology, $\sigma_{ij}^{\mathrm{I(stage\ I)}}(\mathbf{0})$ will be the "laminate" stresses while stresses in the skin and patch are the "ply" stresses. On the other hand, the skin stresses and strains outside the reinforced region at the ends of the minor and major axes of the patch are determined from Equations (6.5) and (6.6). It is worthy to note that since the inhomogeneity's thickness was chosen to be t_{s} in stage I, $\sigma_{ij}^{\mathrm{I(stage\ I)}}(\mathbf{0})$ was therefore defined based on the reference thickness of t_{s}. In contrast, as discussed later, all stresses in the second-stage analysis will be defined based on the reference thickness of $(t_{\mathrm{s}}+t_{\mathrm{p}})$. Consequently, the stresses $\sigma_{ij}^{\mathrm{I(stage\ I)}}(\mathbf{0})$ obtained from the stage I analysis must be scaled by a factor $t_{\mathrm{s}}/(t_{\mathrm{s}}+t_{\mathrm{p}})$ before they can be used as the far-field-applied stresses for the second-stage problem.

Stage II analysis In the second stage, the patch is assumed to be infinite and an integral part of the skin. Stage II analysis then involves solving a problem of an infinite fully patched skin containing an elliptical cut-out or grind-out cavity with a uniform depth under far-field stresses $\sigma_{ij}^{\mathrm{I(stage\ I)}}(\mathbf{0}) \cdot \frac{t_{\mathrm{s}}}{t_{\mathrm{s}}+t_{\mathrm{p}}}$. This problem is also solved using the inclusion analogy. The equivalent elastic constants of the patched skin outside the elliptical cut-out or grind-out cavity can be evaluated by using Equation (6.7) with $t_{\mathrm{I}} = t_{\mathrm{s}} + t_{\mathrm{p}}$. Similar to stage I analysis, the damaged region is now treated as an elliptical soft inhomogeneity with an aspect ratio of b/a. The equivalent elastic constants for this soft inhomogeneity again can be obtained from Equation (6.7) with t_{s} appearing in the equation being replaced by t_{r} (t_{r} can be equal to zero as in the case of a cut-out), and with t_{I} chosen to be equal to $t_{\mathrm{s}} + t_{\mathrm{p}}$. Stresses inside the (soft) inhomogeneity and their contributions to the skin and patch can be determined by the same manner as in stage I analysis, i.e., via Equations (6.3), (6.4), and (6.8), respectively. The stresses outside the damaged area at the ends of its major and minor axes are still evaluated by Equations (6.5) and (6.6). However, since the region outside the damaged area is now made of a laminate of skin and patch materials, a further step is needed which calculates the skin and patch components of these stresses via equations similar to (6.8).

Illustrative example

The method outlined above will be illustrated via one example problem, which is taken out from the paper by Duong et al. (2001b). The stress solution of the repair over a circular damaged area shown in Figure 6.3 is obtained and compared with results from the FE method. The radius of the damaged area is 12.7 mm. For simplicity, the patch is also assumed to be circular with a radius of 38.1 mm. The material properties and thickness of the skin and the patch as well as the far-field stress are given below:

Skin

$\mu_s = 27.2\,\text{GPa}$, $\nu_s = 0.33$, full thickness $t_s = 2.0\,\text{mm}$, remaining thickness in the damaged area $t_r = 0.762\,\text{mm}$.

Patch

$\mu_p = 75.2\,\text{GPa}$, $\nu_s = 0.33$, thickness $t_p = 0.635\,\text{mm}$.

$\sigma_{\infty 1} = 0$, $\sigma_{\infty 2} = 68.95\,\text{MPa}$

All analyses are carried out under plane stress condition. Stress comparisons between analytical predictions and FE results at various locations are listed in Table 6.1. In Table 6.1, all stresses are normalized with respect to the far-field stress. For reference, the normalized stress in the skin near the middle of the damaged area of an un-patched skin is also calculated using the Eshelby solution given in Section 6.2.1 with the grind-out area modeled as an inhomogeneity, and it is found to be 1.7. FE results are obtained by using FRANC2D/L code (Swenson and James, 1997). In the FE analysis, the adhesive is modeled as two-dimensional linear shear springs. Both typical and arbitrarily stiff adhesives are considered in the FE analysis. Typical values for shear modulus and thickness of an adhesive are 0.66 GPa and 0.15 mm, respectively. The analytical predictions in general agree well with the FE results except at point "1" where they are overestimated. As explained by Duong et al. (2001b), this discrepancy is due to the effect of adhesive.

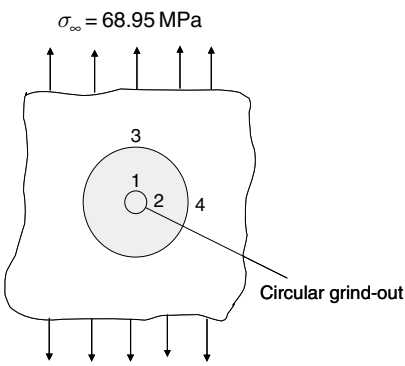

Fig. 6.3. Geometry of a circular grind-out problem repaired with a circular isotropic patch.

Table 6.1. Stress comparison between analytical predictions and FE results for an isotropic skin containing a 1.238 mm deep circular grind-out repaired with a circular isotropic patch of 0.636 mm thickness. All stresses are normalized with respect to far field stress.

	Center	Point 1	Point 2	Point 3	Point 4
Analytical					
Skin	0.818	0.544	0.818	1.184	0.631
Patch	2.260	1.502	2.260		
FEM (stiff adhesive)					
Skin	0.813	0.477	0.803	1.139	0.645
Patch	2.247	1.695	2.201		
FEM-(typical adhesive)					
Skin	0.808	0.408	0.843	1.127	0.696
Patch	2.203	1.854	2.076		

As the adhesive becomes stiffer, the difference in stresses between the two methods becomes smaller as expected, especially at point "1".

A good agreement between the two methods at point "3" but not at point "1" is also explained by Duong et al. as follows. Based on the 1-D bonded joint theory (see Chapter 2), using typical values for the adhesive parameters and the above material properties and thicknesses for the skin and patch, the length of the load transfer zone in this case is calculated to be about 4 mm. The stresses near the load transfer load zone could not be predicted with sufficient accuracy by the present analytical method unless the overall dimensions of the patch and the damage size are much larger than the length of the load transfer zone. With the dimension of the patch three times larger than the damage size, the stress prediction at point "3" is therefore expected to be more accurate than that at point "1". It remains now to explain the high stress results of the analytical method at point "1" in comparison with those from the FE method. The stiffness of the structure inside the damaged area in the analytical model is stiffer than its actual state since the damaged skin and patch are assumed to act as one piece. Thus, more loads are attracted to the damaged area than in reality, and the resulting stresses at point "1" higher than FE results. However, stresses near the middle of the damaged skin are only slightly higher than the corresponding FE results, which are apparently unaffected by the "edge" effect as expected.

6.2.3 Formulas for a special case of an elliptical isotropic patch with a Poisson's ratio same as skin

For elliptical patches with the Poisson's ratio same as that of the skin, simple formulas similar to those given by Hart-Smith and Duong (2005) can be deducted from the above solution procedure. It should be remembered that the formulas given in the cited reference were derived by a different method than the equivalent inclusion method. However, the latter method is quite cumbersome since it requires the displacement solution of a skin with an elliptical hole and that of an elliptical plate, and therefore it will not be discussed in this book.

Similar to the results derived in Chapter 3, the stresses $\sigma_{ij}^{\text{I(stage I)}}(\mathbf{0})$ in the inhomogeneity of the stage I problem and the corresponding skin stresses underneath the patch, i.e., $\sigma_{ij}^{\text{s(stage I)}}(\mathbf{0})$ (denoted by σ_{0x} and σ_0 for the 11- and 22-stress components, respectively), can be obtained from the equivalent inclusion method outlined in Section 6.2.1 as

$$\begin{aligned}
\sigma_{11}^{\text{I(stage I)}}(\mathbf{0}) &= \frac{\sigma_{\infty 22}(1+S)}{Z}\left\{S\left[1-\nu_s-2\nu_s\frac{A}{B}\right]\right. \\
&\quad \left.+\Sigma\left[(1+S)\left(3+2\frac{A}{B}\right)+1+\nu_s S+2\frac{B}{A}\right]\right\} \\
\sigma_{22}^{\text{I(stage I)}}(\mathbf{0}) &= \frac{\sigma_{\infty 22}(1+S)}{Z}\left\{(1+S)\left(3+2\frac{B}{A}\right)+1+\nu_s S+2\frac{A}{B}\right. \\
&\quad \left.+\Sigma\cdot S\left(1-\nu_s-2\nu_s\frac{B}{A}\right)\right\}
\end{aligned} \tag{6.9}$$

$$\begin{aligned}
\sigma_{0x} = \sigma_{11}^{\text{s(stage I)}}(\mathbf{0}) &= \frac{\sigma_{\infty 22}}{Z}\left\{S\left[1-\nu_s-2\nu_s\frac{A}{B}\right]\right. \\
&\quad \left.+\Sigma\left[(1+S)\left(3+2\frac{A}{B}\right)+1+\nu_s S+2\frac{B}{A}\right]\right\} \\
\sigma_0 = \sigma_{22}^{\text{s(stage I)}}(\mathbf{0}) &= \frac{\sigma_{\infty 22}}{Z}\left\{(1+S)\left(3+2\frac{B}{A}\right)+1+\nu_s S+2\frac{A}{B}\right. \\
&\quad \left.+\Sigma\cdot S\left(1-\nu_s-2\nu_s\frac{B}{A}\right)\right\}
\end{aligned} \tag{6.10}$$

where

$$\sigma_{ij}^{\text{I(stage I)}}(\mathbf{0}) = (1+S)\ \sigma_{ij}^{\text{s(stage I)}}(\mathbf{0}) \tag{6.11}$$

or

$$\begin{aligned}
\sigma_{11}^{\text{I(stage I)}}(\mathbf{0}) &= (1+S)\,\sigma_{0x} \\
\sigma_{22}^{\text{I(stage I)}}(\mathbf{0}) &= (1+S)\,\sigma_0
\end{aligned} \tag{6.12}$$

where

$$\begin{aligned}
Z &= 3\ (1+S)^2 \quad +2\ (1+S)\left(\frac{B}{A}+\frac{A}{B}+\nu_s S\right)+1-\nu_s^2 S^2 \\
\Sigma &= \frac{\sigma_{\infty 11}}{\sigma_{\infty 22}}
\end{aligned} \tag{6.13}$$

S is the patch stiffness to skin stiffness ratio, i.e., $S = \frac{E'_p t_p}{E'_s t_s} = \frac{E_p t_p}{E_s t_s}$; $E'_{s,p} = \frac{E_{s,p}}{1-\nu^2_{s,p}}$; ν is again the Poisson's ratio; A and B are minor and major axes of the elliptical patch; Σ is the biaxial stress ratio; and the subscript p or s again denote patch and skin, respectively.

Furthermore, the skin stress concentration factor near the tip of the patch's edge is found to be

$$K_t = \frac{\sigma_{22}^{s(\text{stage I})}(0,\ \pm B^+)}{\sigma_{\infty 22}} = (1+S)\frac{\sigma_0}{\sigma_{\infty 22}} \tag{6.14}$$

In contrast, the skin stresses near the bottom of a grind-out cavity and around the damage edge are obtained from a stage II analysis. Since stage II problem is itself also an inhomogeneity problem, one can use the above explicit results but with minor modifications for a stage II analysis by noting the similarities and differences between stage I and II problems as follows. First, as indicated in Figure 6.1(c), the far-field stress in the stage II problem is given by

$$\sigma_{\infty ij}^{(\text{stage II})} = \sigma_{ij}^{\text{I (stage I)}}(\mathbf{0}) \cdot \frac{t_s}{t_s + t_p} \tag{6.15}$$

which upon substitution of Equation (6.12) for $\sigma_{ij}^{\text{I(stage I)}}(\mathbf{0})$ results in

$$\begin{aligned} \sigma_{\infty 11}^{(\text{stage II})} &= (1+S)\,\sigma_{0x} \cdot \frac{t_s}{t_s + t_p} \\ \sigma_{\infty 22}^{(\text{stage II})} &= (1+S)\,\sigma_0 \cdot \frac{t_s}{t_s + t_p} \end{aligned} \tag{6.16}$$

Second, since S is defined in the first stage problem as

$$\begin{aligned} S &= \frac{E'_p t_p}{E'_s t_s} = \frac{E'_p t_p + E'_s t_s}{E'_s t_s} - 1 \\ &= \frac{\text{stiffness of inhomogeneity}}{\text{stiffness of base material or stiffness of material outside inhomogeneity}} - 1 \end{aligned} \tag{6.17}$$

a similar but new stiffness ratio for the stage II problem will be defined as

$$\begin{aligned} S_{\text{corro}} &= \frac{E'_s t_r + E'_p t_p}{E'_s t_s + E'_p t_p} - 1 = -\frac{E'_s (t_s - t_r)}{E'_s t_s + E'_p t_p} \\ &= -\frac{t_s - t_r}{(1+S)\,t_s} \end{aligned} \tag{6.18}$$

where t_r is the remaining or minimum skin thickness, $(t_s - t_r)$ is the depth of a grind-out. It is worthy to note from the above equation that S_{corro} has a negative value (Hart-Smith and Duong, 2005). Finally, the aspect ratio of the inhomogeneity in a stage II analysis is now the aspect ratio of a grind-out cavity, i.e., *b/a*.

With the above similarities and differences in mind, the stresses of the corroded skin–patch combination inside the grind-out cavity can be evaluated similarly using Equation (6.9) with $\sigma_{\infty ij}^{(\text{stage II})}$, S_{corro}, and *b/a* in place of $\sigma_{\infty ij}^{(\text{stage I})}$, *S*, and *B/A*. This evaluation leads to the following results:

$$\begin{aligned}\sigma_{11}^{\text{I(stage II)}}(\mathbf{0}) &= \frac{\sigma_{\infty 22}^{(\text{stage II})}(1+S_{\text{corro}})}{Z_{\text{corro}}}\left\{S_{\text{corro}}\left[1-\nu_{\text{s}}-2\nu_{\text{s}}\frac{a}{b}\right]\right.\\ &\left.+\Sigma_{\text{corro}}\left[(1+S_{\text{corro}})\left(3+2\frac{a}{b}\right)+1+\nu_{\text{s}}S_{\text{corro}}+2\frac{b}{a}\right]\right\}\\ \sigma_{22}^{\text{I(stage II)}}(\mathbf{0}) &= \frac{\sigma_{\infty 22}^{(\text{stage II})}(1+S_{\text{corro}})}{Z_{\text{corro}}}\left\{(1+S_{\text{corro}})\left(3+2\frac{b}{a}\right)+1+\nu_{\text{s}}S_{\text{corro}}\right.\\ &\left.+2\frac{a}{b}+\Sigma_{\text{corro}}\cdot S_{\text{corro}}\left(1-\nu_{\text{s}}-2\nu_{\text{s}}\frac{b}{a}\right)\right\}\end{aligned} \tag{6.19}$$

where

$$\begin{aligned}Z_{\text{corro}} &= 3\ (1+S_{\text{corro}})^2+2\ \ (1+S_{\text{corro}})\ \left(\frac{b}{a}+\frac{a}{b}+\nu_{\text{s}}S_{\text{corro}}\right)+1-\nu_{\text{s}}^2S_{\text{corro}}^2\\ \Sigma_{\text{corro}} &= \frac{\sigma_{\infty 11}^{(\text{stage II})}}{\sigma_{\infty 22}^{(\text{stage II})}}=\frac{\sigma_{0\text{x}}}{\sigma_0}\end{aligned} \tag{6.20}$$

Due to the rigid bond assumption, strains of the skin, patch, and skin–patch combination inside the grind-out cavity will be the same. The stresses $\sigma_{ij}^{\text{s(stage II)}}(\mathbf{0})$ in the skin inside the grind-out cavity then can be obtained as

$$\sigma_{ij}^{\text{s(stage II)}}(\mathbf{0}) = E_{\text{s}}'\cdot\varepsilon_{ij}^{\text{s}}(\mathbf{0}) = E_{\text{s}}'\cdot\varepsilon_{ij}^{\text{I(stage II)}}(\mathbf{0}) = E_{\text{s}}'\cdot\frac{\sigma_{ij}^{\text{I(stage II)}}(\mathbf{0})}{\left(E_{\text{s}}'t_{\text{r}}+E_{\text{p}}'t_{\text{p}}\right)/\left(t_{\text{s}}+t_{\text{p}}\right)} \tag{6.21}$$

where $(E_{\text{s}}'t_{\text{r}}+E_{\text{p}}'t_{\text{p}})/(t_{\text{s}}+t_{\text{p}})$ is the effective modulus of the corroded skin–patch combination inside a grind-out cavity. Substituting Equation (6.19) for $\sigma_{ij}^{\text{I(stage II)}}(\mathbf{0})$ into (6.21) and subsequently (6.16) for $\sigma_{\infty ij}^{(\text{stage II})}$ into the resulting equation and noting $1+S_{\text{corro}} = (E_{\text{s}}'t_{\text{r}}+E_{\text{p}}'t_{\text{p}})\big/(E_{\text{s}}'t_{\text{s}}+E_{\text{p}}'t_{\text{p}})$ and $1+S=(E_{\text{s}}'t_{\text{s}}+E_{\text{p}}'t_{\text{p}})\big/E_{\text{s}}'t_{\text{s}}$ yield

$$\begin{aligned}\sigma_{\text{cx}} = \sigma_{11}^{\text{s(stage II)}}(\mathbf{0}) &= \frac{\sigma_0}{Z_{\text{corro}}}\left\{\frac{\sigma_{0\text{x}}}{\sigma_0}\cdot\left[(1+S_{\text{corro}})\left(3+2\frac{a}{b}\right)+1+\nu_{\text{s}}S_{\text{corro}}+2\frac{b}{a}\right]\right.\\ &\left.+S_{\text{corro}}\left(1-\nu_{\text{s}}-2\nu_{\text{s}}\frac{b}{a}\right)\right\}\end{aligned} \tag{6.22}$$

$$\begin{aligned}\sigma_{\text{c}} = \sigma_{22}^{\text{s(stage II)}}(\mathbf{0}) &= \frac{\sigma_0}{Z_{\text{corro}}}\left\{(1+S_{\text{corro}})\left(3+2\frac{b}{a}\right)+1+\nu_{\text{s}}S_{\text{corro}}\right.\\ &\left.+2\frac{a}{b}+\frac{\sigma_{0\text{x}}}{\sigma_0}\cdot S_{\text{corro}}\left(1-\nu_{\text{s}}-2\nu_{\text{s}}\frac{b}{a}\right)\right\}\end{aligned} \tag{6.23}$$

The 22-component stress in the patch at its center then becomes

$$\sigma_{22}^{\mathrm{p}}(\mathbf{0}) = \sigma_{\mathrm{c}} \left(\frac{E'_{\mathrm{p}}}{E'_{\mathrm{s}}}\right) \tag{6.24}$$

where σ_{c} is given by Equation (6.23) above.

On the other hand, the stresses in the patch–skin combination near the damage edge are determined from Equations (6.5) and (6.6) with $\sigma_{\infty ij}^{(\text{stage II})}$ given by (6.16) as

$$\begin{aligned}
\sigma_{11}^{\text{I(stage II)}}\left(0,\ \pm b^{+}\right) &= \left(\sigma_{0\mathrm{x}}(1+S)\frac{t_{\mathrm{s}}}{t_{\mathrm{s}}+t_{\mathrm{p}}} - \sigma_{11}^{\text{I(stage II)}}(\mathbf{0})\right)\cdot\left(1+2\frac{b}{a}\right) + \sigma_{11}^{\text{I(stage II)}}(\mathbf{0}) \\
&\quad - \left(\sigma_{0}(1+S)\frac{t_{\mathrm{s}}}{t_{\mathrm{s}}+t_{\mathrm{p}}} - \sigma_{22}^{\text{I(stage II)}}(\mathbf{0})\right) \\
\sigma_{22}^{\text{I(stage II)}}\left(\pm a^{+},\ 0\right) &= \left(\sigma_{0}(1+S)\frac{t_{\mathrm{s}}}{t_{\mathrm{s}}+t_{\mathrm{p}}} - \sigma_{22}^{\text{I(stage II)}}(\mathbf{0})\right)\cdot\left(1+2\frac{a}{b}\right) + \sigma_{22}^{\text{I(stage II)}}(\mathbf{0}) \\
&\quad - \left(\sigma_{0\mathrm{x}}(1+S)\frac{t_{\mathrm{s}}}{t_{\mathrm{s}}+t_{\mathrm{p}}} - \sigma_{11}^{\text{I(stage II)}}(\mathbf{0})\right)
\end{aligned} \tag{6.25}$$

where only the 22-component stress at the left or right edge of the grind-out cavity and the 11-component stress at tip edge of the cavity are given since similar to the results of stress concentrations for a hole, they are the only stress components which may become critical at those locations. $\sigma_{ij}^{\text{I(stage II)}}(\mathbf{0})$ in Equation (6.25) can be expressed in terms of skin stresses at the bottom of a grind-out cavity by rearranging Equation (6.21) and noting $\sigma_{11}^{\text{s(stage II)}}(\mathbf{0}) \equiv \sigma_{\mathrm{cx}}$ and $\sigma_{22}^{\text{s(stage II)}}(\mathbf{0}) \equiv \sigma_{\mathrm{c}}$, i.e.,

$$\begin{aligned}
\sigma_{11}^{\text{I(stage II)}}(\mathbf{0}) &= \frac{\sigma_{\mathrm{cx}}}{E'_{\mathrm{s}}}\frac{\left(E'_{\mathrm{s}}t_{\mathrm{r}} + E'_{\mathrm{p}}t_{\mathrm{p}}\right)}{t_{\mathrm{s}}+t_{\mathrm{p}}} \\
\sigma_{22}^{\text{I(stage II)}}(\mathbf{0}) &= \frac{\sigma_{\mathrm{c}}}{E'_{\mathrm{s}}}\frac{\left(E'_{\mathrm{s}}t_{\mathrm{r}} + E'_{\mathrm{p}}t_{\mathrm{p}}\right)}{t_{\mathrm{s}}+t_{\mathrm{p}}}
\end{aligned} \tag{6.26}$$

The skin stresses near the damage edge are finally derived based on a rigid bond assumption between skin and patch outside the cavity region as

$$\begin{aligned}
\sigma_{11}^{\mathrm{s}}\left(0,\ \pm b^{+}\right) = E'_{\mathrm{s}}\cdot\varepsilon_{11}^{\mathrm{s}}\left(0,\ \pm b^{+}\right) &= E'_{\mathrm{s}}\cdot\varepsilon_{11}^{\text{I(stage II)}}\left(0,\ \pm b^{+}\right) \\
&= E'_{\mathrm{s}}\cdot\frac{\sigma_{11}^{\text{I(stage II)}}\left(0,\ \pm b^{+}\right)}{\left(E'_{\mathrm{s}}t_{\mathrm{s}} + E'_{\mathrm{p}}t_{\mathrm{p}}\right)/\left(t_{\mathrm{s}}+t_{\mathrm{p}}\right)} \\
\sigma_{22}^{\mathrm{s}}\left(\pm a^{+}, 0\right) = E'_{\mathrm{s}}\cdot\varepsilon_{22}^{\mathrm{s}}\left(\pm a^{+}, 0\right) &= E'_{\mathrm{s}}\cdot\varepsilon_{22}^{\text{I(stage II)}}\left(\pm a^{+},\ 0\right) \\
&= E'_{\mathrm{s}}\cdot\frac{\sigma_{22}^{\text{I(stage II)}}\left(\pm a^{+},\ 0\right)}{\left(E'_{\mathrm{s}}t_{\mathrm{s}} + E'_{\mathrm{p}}t_{\mathrm{p}}\right)/\left(t_{\mathrm{s}}+t_{\mathrm{p}}\right)}
\end{aligned} \tag{6.27}$$

which upon substitution of Equation (6.25) for $\sigma_{11}^{\text{I(stage II)}}(0,\ \pm b^{+})$ and $\sigma_{22}^{\text{I(stage II)}}(\pm a^{+},\ 0)$ and (6.26) for $\sigma_{ij}^{\text{I(stage II)}}(\mathbf{0})$ into the resulting Equation yield

$$\begin{aligned}
\sigma_{11}^{\text{s}}\left(0,\ \pm b^{+}\right) = &\left\{\left(\sigma_{0\text{x}}\left(1+S\right)\frac{t_{\text{s}}}{t_{\text{s}}+t_{\text{p}}} - \frac{\sigma_{\text{cx}}}{E_{\text{s}}'}\frac{\left(E_{\text{s}}'t_{\text{r}}+E_{\text{p}}'t_{\text{p}}\right)}{t_{\text{s}}+t_{\text{p}}}\right)\cdot\left(1+2\frac{b}{a}\right)\right.\\
&+\frac{\sigma_{\text{cx}}}{E_{\text{s}}'}\frac{\left(E_{\text{s}}'t_{\text{r}}+E_{\text{p}}'t_{\text{p}}\right)}{t_{\text{s}}+t_{\text{p}}}\\
&\left.-\left(\sigma_{0}\left(1+S\right)\frac{t_{\text{s}}}{t_{\text{s}}+t_{\text{p}}} - \frac{\sigma_{\text{c}}}{E_{\text{s}}'}\frac{\left(E_{\text{s}}'t_{\text{r}}+E_{\text{p}}'t_{\text{p}}\right)}{t_{\text{s}}+t_{\text{p}}}\right)\right\}\cdot\frac{E_{\text{s}}'\left(t_{\text{s}}+t_{\text{p}}\right)}{E_{\text{s}}'t_{\text{s}}+E_{\text{p}}'t_{\text{p}}}\\
\sigma_{22}^{\text{s}}\left(\pm a^{+},\ 0\right) = &\left\{\left(\sigma_{0}\left(1+S\right)\frac{t_{\text{s}}}{t_{\text{s}}+t_{\text{p}}} - \frac{\sigma_{\text{c}}}{E_{\text{s}}'}\frac{\left(E_{\text{s}}'t_{\text{r}}+E_{\text{p}}'t_{\text{p}}\right)}{t_{\text{s}}+t_{\text{p}}}\right)\cdot\left(1+2\frac{a}{b}\right)\right.\\
&+\frac{\sigma_{\text{c}}}{E_{\text{s}}'}\frac{\left(E_{\text{s}}'t_{\text{r}}+E_{\text{p}}'t_{\text{p}}\right)}{t_{\text{s}}+t_{\text{p}}}\\
&\left.-\left(\sigma_{0\text{x}}\left(1+S\right)\frac{t_{\text{s}}}{t_{\text{s}}+t_{\text{p}}} - \frac{\sigma_{\text{cx}}}{E_{\text{s}}'}\frac{\left(E_{\text{s}}'t_{\text{r}}+E_{\text{p}}'t_{\text{p}}\right)}{t_{\text{s}}+t_{\text{p}}}\right)\right\}\cdot\frac{E_{\text{s}}'\left(t_{\text{s}}+t_{\text{p}}\right)}{E_{\text{s}}'t_{\text{s}}+E_{\text{p}}'t_{\text{p}}}
\end{aligned} \tag{6.28}$$

6.3 General Solution of Polygon-Shaped Patches

In this section, the problem of an isotropic skin with an internal elliptical grind-out repaired with a polygonal orthotropic patch is analyzed. The analytical method described in Section 6.2 will be extended in this section to deal in particular with additional complexities such as polygonal patch, a grind-out cavity with a spherical depth, and the effects of thermal stresses due to curing and cruising. In addition, it was shown from the 3-D FE study (Duong and Yu, 2002b) that the use of the inclusion analogy in a stage II analysis as done in the solution procedure outlined in Section 6.2 may not yield sufficiently accurate results for a repair problem of a very deep grind-out cavity in a thick skin. It should be noted that the good agreement between analytical and FE results was observed in Section 6.2.2 since the skin in the example illustrated in that section is relatively thin (2 mm) while the grind-out cavity is only 50% deep. The solution procedure outlined in Section 6.2 is therefore modified here to improve the analyses of deep cavities in a thick skin. However, as in Section 6.2, for simplicity, the analysis will be conducted under plane stress assumption. As shown later in Section 6.3.2, the present analysis will require a solution of a polygonal inhomogeneity with variable stiffness. We therefore begin the development with the derivation of that solution.

6.3.1 Polygonal inhomogeneity with variable stiffness

Let us consider a problem of an infinite isotropic, linear elastic skin with the moduli C_{ijkl}^{0} containing a polygon-shaped inhomogeneity Ω with the elastic moduli C_{ijkl}^{1} and subjected

to an initial strain field $\varepsilon_{ij}^{(\mathrm{T})}$. The infinite isotropic skin may be composed of two layers of different isotropic materials. A strain field of $\varepsilon_{\infty ij}$ is applied to the skin at infinity. When uniform stresses are prescribed at infinity, one can simply convert them to strains using Hook's law. To make this problem more generic than those already considered in Chapter 4 (for the latter developments), both the skin and the inhomogeneity are also subjected to an additional initial strain field $\varepsilon_{ij}^{(\mathrm{init})}$. In contrast to $\varepsilon_{ij}^{(\mathrm{T})}$, the latter initial strain field is continuous across the inhomogeneity's interface. Furthermore, the present inhomogeneity is also (materially) inhomogeneous with its property varying as a second-degree polynomial of spatial coordinates, i.e., the stiffness of the inhomogeneity C_{ijkl}^{I} can be represented by

$$C_{ijkl}^{\mathrm{I}}(\mathbf{x}) = C_{ijkl}^{\mathrm{I(min)}} + C_{ijkl}^{\mathrm{I(prime)}}\left(x_1^2 + \frac{x_2^2}{\Theta^2}\right) \tag{6.29}$$

where $C_{ijkl}^{\mathrm{I(min)}}$ and $C_{ijkl}^{\mathrm{I(prime)}}$ are constant tensors, and Θ is a constant scalar. For a materially homogeneous inhomogeneity, i.e., an inhomogeneity with a spatially uniform material property, $C_{ijkl}^{\mathrm{I(prime)}} = 0$. The stresses in the inhomogeneity and in the region outside of the inhomogeneity are given respectively by

$$\sigma_{ij}^{\mathrm{I}}(\mathbf{x}) = \begin{cases} C_{ijkl}^{\mathrm{I}}\left(\varepsilon_{kl}^{\mathrm{I}} - \varepsilon_{kl}^{(\mathrm{T})} - \varepsilon_{kl}^{(\mathrm{init})}\right) & \text{inside} \quad \Omega \\ C_{ijkl}^{0}\left(\varepsilon_{kl}^{\mathrm{I}} - \varepsilon_{kl}^{(\mathrm{init})}\right) & \text{outside} \quad \Omega \end{cases} \tag{6.30}$$

where $\varepsilon_{kl}^{\mathrm{I}}$ is the strain field induced by the inhomogeneity and the far-field stresses, and it will be determined by the equivalent inclusion method. To simplify the development followed, the term $C_{ijkl}^{\mathrm{I}}(\varepsilon_{kl}^{(\mathrm{T})} + \varepsilon_{kl}^{(\mathrm{init})})$ in Equation (6.30) will be expressed alternatively as

$$C_{ijkl}^{\mathrm{I}}\left(\varepsilon_{kl}^{(\mathrm{T})} + \varepsilon_{kl}^{(\mathrm{init})}\right) = C_{ijkl}^{\mathrm{I(min)}}\left(\varepsilon_{kl}^{(\mathrm{T})(\mathrm{min})} + \varepsilon_{kl}^{(\mathrm{init})}\right) \tag{6.31}$$

where $\varepsilon_{ij}^{(\mathrm{T})(\mathrm{min})}$ is defined by

$$\varepsilon_{ij}^{(\mathrm{T})(\mathrm{min})} = C_{ijkl}^{\mathrm{I(min)}-1} C_{ijkl}^{\mathrm{I}}\left(\varepsilon_{kl}^{(\mathrm{T})} + \varepsilon_{kl}^{(\mathrm{init})}\right) - \varepsilon_{kl}^{(\mathrm{init})} \tag{6.32}$$

Substituting Equations (6.29) and (6.31) into Equation (6.30) yields

$$\sigma_{ij}^{\mathrm{I}}(\mathbf{x}) = \begin{cases} C_{ijkl}^{\mathrm{I(min)}}\left(\varepsilon_{kl}^{\mathrm{I}} - \varepsilon_{kl}^{\mathrm{T(min)}} - \varepsilon_{kl}^{(\mathrm{init})}\right) \\ \qquad + C_{ijkl}^{\mathrm{I(prime)}}\left(x_1^2 + \dfrac{x_2^2}{\Theta^2}\right)\varepsilon_{kl}^{\mathrm{I}} & \text{inside } \Omega \\ C_{ijkl}^{0}\left(\varepsilon_{kl}^{\mathrm{I}} - \varepsilon_{kl}^{(\mathrm{init})}\right) & \text{outside } \Omega \end{cases} \tag{6.33}$$

As before, the stress and strain fields induced by an inhomogeneity-occupied region Ω will be found from the solutions of an "equivalent" inclusion problem with a homogeneous material C_{ijkl}^{0} and under the eigenstrain field ε_{ij}^{*}. Following the procedure given in

Section 4.2.1 of Chapter 4 for a polygon-shaped inhomogeneity symmetric with respect to both coordinate axes, by approximating ε_{ij}^{*} as a second-ordered polynomial of the position coordinates with yet to be determined coefficients, i.e.,

$$\varepsilon_{ij}^{*} = F_{ij} + F_{ijkl} x_k x_l \tag{6.34}$$

and by expanding the prescribed initial strain fields $\varepsilon_{ij}^{(\mathrm{T})(\mathrm{min})}$ and $\varepsilon_{ij}^{(\mathrm{init})}$ into a Taylor series, the equivalency condition requires that F_{ij} and F_{ijkl} must satisfy the following system of linear equations (without summation on subscript α):

$$\begin{aligned}
&\Delta C_{\alpha\alpha 11} L_{11}(\mathbf{0}) + \Delta C_{\alpha\alpha 22} L_{22}(\mathbf{0}) - C^{0}_{\alpha\alpha 11} F'_{11} - C^{0}_{\alpha\alpha 22} F'_{22} = -\Delta C_{\alpha\alpha 11}\left(\varepsilon_{\infty 11} - \varepsilon_{110}^{(\mathrm{init})}\right) \\
&\quad - \Delta C_{\alpha\alpha 22}\left(\varepsilon_{\infty 22} - \varepsilon_{220}^{(\mathrm{init})}\right) - C_{\alpha\alpha 11}^{\mathrm{I}(\mathrm{min})} \varepsilon_{110}^{(\mathrm{T})(\mathrm{min})} - C_{\alpha\alpha 22}^{\mathrm{I}(\mathrm{min})} \varepsilon_{220}^{(\mathrm{T})(\mathrm{min})} \\
&\frac{1}{2}\Delta C_{\alpha\alpha 11} \frac{\partial^2}{\partial x_1^2} L_{11}(\mathbf{0}) + \frac{1}{2}\Delta C_{\alpha\alpha 22} \frac{\partial^2}{\partial x_1^2} L_{22}(\mathbf{0}) - C_{\alpha\alpha 11}^{\mathrm{I}(\mathrm{prime})} L_{11}(\mathbf{0}) - C_{\alpha\alpha 22}^{\mathrm{I}(\mathrm{prime})} L_{22}(\mathbf{0}) \\
&\quad - C^{0}_{\alpha\alpha 11} F'_{1111} - C^{0}_{\alpha\alpha 22} F'_{2211} = \Delta C_{\alpha\alpha 11} \varepsilon_{1111}^{(\mathrm{init})} + \Delta C_{\alpha\alpha 22} \varepsilon_{2211}^{(\mathrm{init})} - C_{\alpha\alpha 11}^{\mathrm{I}(\mathrm{min})} \varepsilon_{1111}^{(\mathrm{T})(\mathrm{min})} \\
&\quad - C_{\alpha\alpha 22}^{\mathrm{I}(\mathrm{min})} \varepsilon_{2211}^{(\mathrm{T})(\mathrm{min})} + C_{\alpha\alpha 11}^{(\mathrm{prime})} \varepsilon_{\infty 11} + C_{\alpha\alpha 22}^{(\mathrm{prime})} \varepsilon_{\infty 22} \qquad (6.35) \\
&\frac{1}{2}\Delta C_{\alpha\alpha 11} \frac{\partial^2}{\partial x_2^2} L_{11}(\mathbf{0}) + \frac{1}{2}\Delta C_{\alpha\alpha 22} \frac{\partial^2}{\partial x_2^2} L_{22}(\mathbf{0}) - \frac{1}{\Theta^2} C_{\alpha\alpha 11}^{\mathrm{I}(\mathrm{prime})} L_{11}(\mathbf{0}) - \frac{1}{\Theta^2} C_{\alpha\alpha 22}^{\mathrm{I}(\mathrm{prime})} L_{22}(\mathbf{0}) \\
&\quad - C^{0}_{\alpha\alpha 11} F'_{1122} - C^{0}_{\alpha\alpha 22} F'_{2222} = \Delta C_{\alpha\alpha 11} \varepsilon_{1122}^{(\mathrm{init})} + \Delta C_{\alpha\alpha 22} \varepsilon_{2222}^{(\mathrm{init})} - C_{\alpha\alpha 11}^{\mathrm{I}(\mathrm{min})} \varepsilon_{1122}^{(\mathrm{T})(\mathrm{min})} \\
&\quad - C_{\alpha\alpha 22}^{\mathrm{I}(\mathrm{min})} \varepsilon_{2222}^{(\mathrm{T})(\mathrm{min})} + \frac{1}{\Theta^2} C_{\alpha\alpha 11}^{(\mathrm{prime})} \varepsilon_{\infty 11} + \frac{1}{\Theta^2} C_{\alpha\alpha 22}^{(\mathrm{prime})} \varepsilon_{\infty 22} \\
&\Delta C_{1212} \frac{\partial^2}{\partial x_1 \partial x_2} L_{12}(\mathbf{0}) - C_{1212} F'_{1212} = -C_{1212}^{\mathrm{I}(\mathrm{min})} \varepsilon_{1212}^{(\mathrm{T})(\mathrm{min})}
\end{aligned}$$

where

$$\Delta C_{ijkl} = C^{0}_{ijkl} - C^{\mathrm{I}(\mathrm{min})}_{ijkl} \tag{6.36}$$

$$\begin{aligned}
L_{\alpha\beta}(\mathbf{x}) = {} & S_{\alpha\beta 11}(\mathbf{x}) F'_{11} + S_{\alpha\beta 22}(\mathbf{x}) F'_{22} + S_{\alpha\beta 1111}(\mathbf{x}) F'_{1111} + S_{\alpha\beta 1122}(\mathbf{x}) F'_{1122} \\
& + S_{\alpha\beta 2211}(\mathbf{x}) F'_{2211} + S_{\alpha\beta 2222}(\mathbf{x}) F'_{2222} + S_{\alpha\beta 1212}(\mathbf{x}) F'_{1212}
\end{aligned} \tag{6.37}$$

$$\begin{aligned}
F'_{ij} &= F_{ij} + \varepsilon_{ij0}^{(\mathrm{T})(\mathrm{min})} \\
F'_{ijkl} &= F_{ijkl} + \varepsilon_{ijkl}^{(\mathrm{T})(\mathrm{min})} \qquad (6.38) \\
(\alpha, \beta &= 1, 2)
\end{aligned}$$

$\varepsilon_{ij0}^{(\mathrm{T})(\min)}$ and $\varepsilon_{ijkl}^{(\mathrm{T})(\min)}$ are the constant and quadratic terms in the Taylor series of $\varepsilon_{ij}^{(\mathrm{T})(\min)}$, respectively; similarly, $\varepsilon_{ij0}^{(\mathrm{init})}$ and $\varepsilon_{ijkl}^{(\mathrm{init})}$ are the constant and quadratic terms in the Taylor series of $\varepsilon_{ij}^{(\mathrm{init})}$. In Equation (6.37), $S_{ijkl}(\mathbf{x})$ and $S_{ijklmn}(\mathbf{x})$ are again the Eshelby tensors which can be evaluated for any polygon-shaped inclusion by using the algorithmic approach outlined in Section 4.2.2, and all notations used in Section 4.2.1 are also retained here. It is worthy to note that Equations (6.35) and (6.37) are quite similar to Equations (4.10) and (4.11), and (4.43) and the second equation of (4.44).

Once the coefficients F''s, thus F's and ε_{ij}^{*}, are determined, the elastic fields in the inhomogeneity problem can be obtained as

$$\varepsilon_{ij}^{\mathrm{I}} = \varepsilon_{ij}^{\mathrm{H}} = S_{ijkl}F_{kl} + S_{ijklmn}F_{klmn} + \varepsilon_{\infty ij} \tag{6.39}$$

$$\sigma_{ij}^{\mathrm{I}}(\mathbf{x}) = \begin{cases} C_{ijkl}^{0}(\varepsilon_{kl}^{\mathrm{H}} - \varepsilon_{kl}^{*} - \varepsilon_{kl}^{\mathrm{T}} - \varepsilon_{kl}^{(\mathrm{init})}) & \text{inside } \Omega \\ C_{ijkl}^{0}\left(\varepsilon_{kl}^{\mathrm{H}} - \varepsilon_{kl}^{(\mathrm{init})}\right) & \text{outside } \Omega \end{cases} \tag{6.40}$$

which are similar to Equations (4.45) and (4.46) except for the additional terms $\varepsilon_{kl}^{(\mathrm{init})}$ and $\varepsilon_{\infty ij}$ appearing, respectively, in Equations (6.39) and (6.40) due to the presence of the far-field-applied strains and the continuous initial strain field as specified in the problem statement. It should be remembered that $\varepsilon_{kl}^{\mathrm{H}}$ is the strain solution of the homogeneous (inclusion) problem.

6.3.2 Repair over an elliptical grind-out

Consider an isotropic skin with an internal elliptical grind-out cavity of a spherical depth repaired with a polygonal composite patch. The skin is subjected to the remote stresses $\sigma_{\infty ij}$ as shown in Figure 6.4 with the dominated stress component being in the x_2-direction. The bonded skin also assumes to be subjected to a uniform temperature change ΔT and/or to a thermal cycle associated with curing of the adhesive. This problem will be analyzed under the same assumptions as in Section 6.2.2 except that the grind-out cavity now can have a spherical depth as in most realistic repairs and the patch is orthotropic. The rigid bond assumption is quite reasonable for stage I analysis of most common repair configurations; however, it may not be appropriate for stage II unless the cavity is filled with a very stiff or rigid material or for shallow cavities in a thin skin. For an unfilled cavity or a cavity being filled with a soft material in a relatively thick skin, this last assumption must be relaxed in the stage II analysis. It is worthy to note that the results from the present analytical method will be less accurate near structural discontinuities such as near the edge of the patch or grind-out cavity, where significant (out-of-plane) shear strains occur in the adhesive rather than none as in the rigid bond assumption.

Two-stage analysis procedure

As before, the analysis is divided into two stages as indicated in Figure 6.1. However, for use in the future development, the skin thickness profile in the grind-out cavity needs

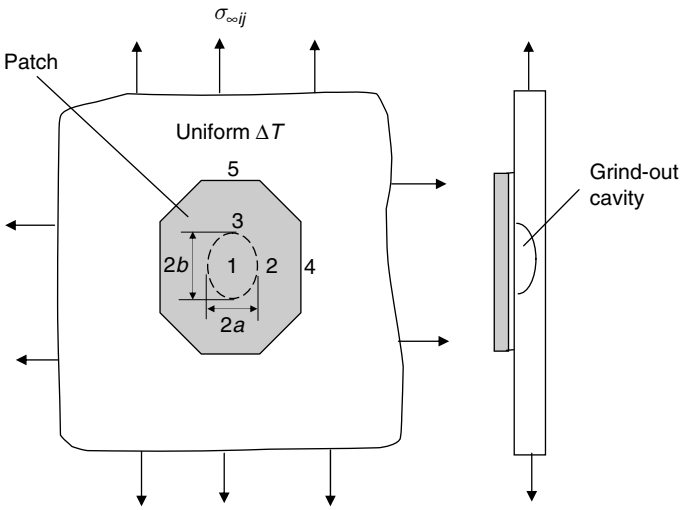

Fig. 6.4. Geometry of a bonded repair over an elliptical grind-out cavity. Numbers 1–5 indicate critical stress locations, which are of primary interest in the design.

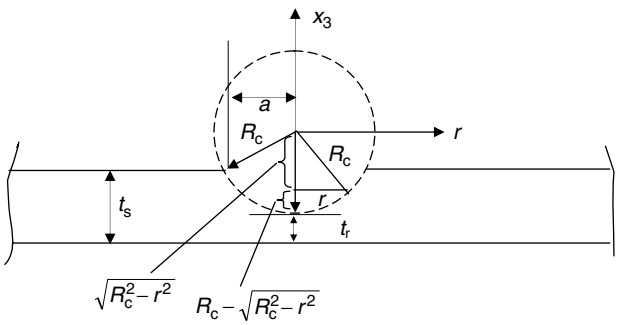

Fig. 6.5. Detailed geometry of a cross section of a skin containing a spherical deep grind-out cavity. In the figure, a is the minor axis of the ellipsoidal cavity as shown in Figure 6.4.

to be determined first from the geometry. An expression for a skin thickness profile in the grind-out cavity is thus derived here. Consider a cross section of a grind-out cavity as shown in Figure 6.5. It is clear from Figure 6.5 that a radius of curvature of the cavity and the skin thickness profile in the cavity as determined from the geometry are given by

$$R_c = \frac{(t_s - t_r)^2 + a^2}{2(t_s - t_r)} \tag{6.41}$$

$$t_{s\text{-inside}}(r) = t_r + R_c - \sqrt{R_c^2 - r^2} \qquad 0 \le r \le a \tag{6.42}$$

where t_s and t_r are the full and the minimum remaining thickness of the skin, a is a maximum (in-plane) radius of the grind-out as shown in the figure, and r is the radial distance from the center of a cavity. By expanding the expression given in Equation (6.42) into Taylor series, the skin thickness profile then can be approximated by the second-degree polynomial of r as

$$\begin{aligned} t_{\text{s-inside}}(r) &\approx t_{\text{s-inside}}(\mathbf{0}) + r \cdot \frac{\mathrm{d}t_{\text{s-inside}}}{\mathrm{d}r}(\mathbf{0}) + \frac{1}{2} r^2 \cdot \frac{\mathrm{d}^2 t_{\text{s-inside}}}{\mathrm{d}r^2}(\mathbf{0}) \\ t_{\text{s-inside}}(r) &= t_r + \frac{1}{2}\left(\frac{r^2}{R_c}\right) \end{aligned} \tag{6.43}$$

The skin thickness profile has been derived so far for a cross section. By assuming that the thickness profile for an ellipsoidal grind-out cavity is governed by the same relation as that given in (6.43), then

$$t_{\text{s-inside}}(x_1, x_2) = t_r + \frac{1}{2R_c}\left(x_1^2 + \frac{x_2^2}{\Theta^2}\right) \tag{6.44}$$

where Θ is an aspect ratio of an elliptical grind-out, i.e., $\Theta = b/a$. It should be noted that for a circular grind-out cavity ($\Theta = 1$), Equation (6.44) implies that the skin thickness profile in the cavity is axisymmetric. With the thickness profile of the skin inside the cavity having been determined, it is ready now to proceed with the first- and second-stage analyses.

Stage I analysis In a first stage, an infinite skin reinforced by a polygonal composite patch under a prescribed far-field stress and thermal field is analyzed using the inclusion analogy, without considering the grind-out cavity. Stresses around the patch and inside the patched area at the center of the prospective grind-out location are calculated. Since the patch is considered as an integral part of a skin in the analysis, a patched region is treated as a polygonal inhomogeneity. This problem had been solved in Section 4.2.3 under far-field stresses and in Section 4.2.4 under thermal loads. Thus, the solution of the present problem can be obtained by linear superposition of the individual contribution due to the far-field stress and due to the thermal load alone. However, it also can be obtained directly from the process outlined in Section 6.3.1 by noting the following relationships:

$$\begin{aligned} C_{ijkl}^{\mathrm{I}} &= C_{ijkl}^{\mathrm{I(min)}} \\ C_{ijkl}^{\mathrm{I(prime)}} &= 0 \\ \varepsilon_{ij}^{(\mathrm{T})} &= \varepsilon_{ij}^{(\mathrm{T})(\mathrm{min})} \\ \varepsilon_{ij}^{(\mathrm{init})} &= 0 \end{aligned} \tag{6.45}$$

where $C_{ijkl}^{\mathrm{I(min)}}$ and $\varepsilon_{ij}^{(\mathrm{T})(\mathrm{min})}$ are evaluated using the formulas given by Equations (4.31)–(4.33) and the second equation of (4.41) with the full skin thickness t_s. Moreover, $\varepsilon_{ij}^{\mathrm{T(p)}}$ appearing in a second equation of (4.41) is either defined by

Equation (4.36) or (4.40), depending on the type of thermal loading: due to a uniform operating temperature change or due to curing of the adhesive. Under these circumstances, Equation (6.35) in Section 6.3.1 will reduce identically to Equation (4.43) in Chapter 4 in the absence of the far-field-applied strains. It should be noted that as before the thickness of the inhomogeneity in the stage I analysis has been chosen arbitrarily the same as the full skin thickness t_s. Also, like before, for future discussion, stresses at the center of inhomogeneity determined from the present analysis will be denoted by $\sigma_{ij}^{\text{I(stage I)}}(\mathbf{0})$.

Stage II analysis As done in Section 6.2.2, in the second stage, a patch is assumed to be infinite and an integral part of a skin. Stage II analysis then involves solving a problem of an infinite fully patched skin containing an embedded elliptical grind-out cavity Ω as shown in the last picture of Figure 6.1. In addition, the patch layer of the skin–patch combination is also prescribed with an initial strain field $\varepsilon_{ij}^{(\mathrm{T})(\mathrm{p})}$. Explicit formulas for $\varepsilon_{ij}^{(\mathrm{T})(\mathrm{p})}$ associated with two common types of thermal loading are given before by Equations (4.36) and (4.40).

In Section 4.2.4, it was shown that due to the initial strain $\varepsilon_{ij}^{(\mathrm{T})(\mathrm{p})}$, using the second equation of (4.41), the bi-layer of patch–skin combination will be under an "effective" initial strain given by

$$\varepsilon_{ij}^{(\mathrm{T})} = \frac{t_\mathrm{p}}{t_\mathrm{I}} C_{ijkl}^{\mathrm{I}-1} C_{klmn}^{\mathrm{p}} \varepsilon_{mn}^{(\mathrm{T})(\mathrm{p})} \tag{6.46}$$

where C_{ijkl}^{I} and t_I are the elasticity tensor and the "effective" thickness of the patch–skin combination, C_{ijkl}^{p} is the elasticity tensor of the patch, and the superscript -1 denotes the inverse. C_{ijkl}^{I} of the patch–skin combination can be evaluated using Equations (4.31)–(4.33), which also can be rewritten in a compact notation as

$$C_{ijkl}^{\mathrm{I}} = \frac{t_\mathrm{s}}{t_\mathrm{I}} C_{ijkl}^{\mathrm{s}} + \frac{t_\mathrm{p}}{t_\mathrm{I}} C_{ijkl}^{\mathrm{p}} \tag{6.47}$$

Since regions both inside and outside the damaged area of the current stage II problem are bi-layers of patch–skin combination, due to $\varepsilon_{ij}^{(\mathrm{T})(\mathrm{p})}$ they also will be under similar "effective" initial strains. These "effective" initial strains will be derived below for the present analysis.

As detailed later, the fully patched skin of the stage II problem is divided into two separated regions: inside and outside the elliptical grind-out cavity Ω, and each region is itself a bi-layer of patch–skin combination which is described with different elastic moduli and different constitutive relation. The "effective" initial strains due to $\varepsilon_{ij}^{(\mathrm{T})(\mathrm{p})}$ in the patch layer for these two regions can be derived by using Equation (6.46) as

$$\varepsilon_{ij}^{(\mathrm{T})(\text{outside})} = \frac{t_\mathrm{p}}{t_\mathrm{p} + t_\mathrm{s}} C_{ijkl}^{0(\text{stage II})-1} C_{klmn}^{\mathrm{p}} \varepsilon_{mn}^{(\mathrm{T})(\mathrm{p})} \quad \text{outside } \Omega \tag{6.48}$$

$$\varepsilon_{ij}^{(\mathrm{T})(\text{inside})} = \frac{t_\mathrm{p}}{t_\mathrm{p} + t_\mathrm{s}} C_{ijkl}^{\mathrm{I(stage\ II)}-1} C_{klmn}^{\mathrm{p}} \varepsilon_{mn}^{(\mathrm{T})(\mathrm{p})} \quad \text{inside } \Omega \tag{6.49}$$

where $C_{ijkl}^{0(\text{stage II})}$ and $C_{ijkl}^{\text{I(stage II)}}$ denote the elasticity tensors of the regions outside and inside Ω, respectively. Expressions for $C_{ijkl}^{0(\text{stage II})}$ and $C_{ijkl}^{\text{I(stage II)}}$ will be defined in the paragraphs below. In deriving Equations (6.48) and (6.49), the "effective" thicknesses of the patch–skin combination, i.e., t_{I} in Equation (6.46), inside and outside of Ω have been chosen to be the same and equal to $t_{\text{p}} + t_{\text{s}}$. With the initial strains having been determined, the stage II problem is then fully described.

There are two different cases that will be considered for stage II analysis. In the first case, the cavity assumes to be filled with a rigid material so that the patched skin inside the grind-out-cavity region is again modeled as an (soft) inhomogeneity. The second case on the other hand deals with an unfilled cavity or a cavity being filled with a soft material. The analysis for the first case will be delineated first using an inclusion analogy.

Case 1: Cavity filled with rigid material

In order to use solutions developed in Section 6.3.1 for stage II, the patch material must now assume to be isotropic so that the fully patched skin region outside the grind-out cavity is isotropic as required by the formulation given in that section. The effect of neglecting patch orthotropy during stage II analysis is found to be small as illustrated later through the example problems. Using the same notation as in Section 6.3.1, from Equation (6.47), the elasticity tensor for the fully patched skin outside of the elliptical grind-out region is given by

$$C_{ijkl}^{0(\text{stage II})} = \frac{t_{\text{s}}}{t_{\text{s}} + t_{\text{p}}} C_{ijkl}^{\text{s}} + \frac{t_{\text{p}}}{t_{\text{s}} + t_{\text{p}}} C_{ijkl}^{\text{p}} \tag{6.50}$$

where the "effective" thickness of the patch–skin combination, i.e., t_{I} in Equation (6.47), outside Ω has been chosen to be equal to $t_{\text{p}} + t_{\text{s}}$, as in Section 6.2.2. It should be remembered that C_{ijkl}^{p} is calculated based on the assumption that the patch is isotropic with a modulus and Poisson's ratio equal to the principal modulus E_{22}^{p} and ν_{22}^{p}, respectively,[3] and the rest have been defined previously. Furthermore, the constitutive relation for the fully patched skin outside the grind-out region is given by

$$\sigma_{ij}^{\text{I(stage II)}} = C_{ijkl}^{0(\text{stage II})} \left(\varepsilon_{kl}^{\text{I(stage II)}} - \varepsilon_{kl}^{(\text{T})(\text{outside})} \right) \quad \text{outside } \Omega \tag{6.51}$$

where $\varepsilon_{kl}^{\text{I(stage II)}}$ is the strain field induced by the grind-out cavity and the far-field stresses, which is yet to be determined using method outlined in Section 6.3.1; $\varepsilon_{kl}^{(\text{T})(\text{outside})}$ and $C_{ijkl}^{0(\text{stage II})}$ have been previously defined by Equations (6.48) and (6.50). Next, the remote strain $\varepsilon_{\infty kl}^{(\text{stage II})}$ must be determined. $\varepsilon_{\infty kl}^{(\text{stage II})}$ is determined from the stresses $\sigma_{ij}^{\text{I(stage I)}}(\mathbf{0})$ obtained from stage I analysis as follows. As shown in Figure 6.1, the stresses $\frac{t_{\text{s}}}{t_{\text{s}}+t_{\text{p}}} \sigma_{ij}^{\text{I(stage I)}}(\mathbf{0})$ apply at infinity in stage II. Since the strain field $\varepsilon_{kl}^{\text{I(stage II)}}$

[3] Because of this assumption, C_{ijkl}^{p} in stage II in general will be different from that in stage I.

induced by the cavity and far-field stresses must approach the constant remote strain field $\varepsilon_{\infty kl}^{(\text{stage II})}$ at infinity, therefore, for points at infinity, Equation (6.51) should read

$$\sigma_{ij}^{\text{I(stage II)}}(\infty) = \frac{t_\text{s}}{t_\text{s}+t_\text{p}}\sigma_{ij}^{\text{I(stage I)}}(\mathbf{0}) = C_{ijkl}^{0(\text{stage II})}\left(\varepsilon_{\infty kl}^{(\text{stage II})} - \varepsilon_{kl}^{(\text{T})(\text{outside})}\right) \tag{6.52}$$

From this

$$\varepsilon_{\infty ij}^{(\text{stage II})} - \varepsilon_{ij}^{(\text{T})(\text{outside})} = \frac{t_\text{s}}{t_\text{s}+t_\text{p}}C_{ijkl}^{0(\text{stage II})-1}\sigma_{kl}^{\text{I(stage I)}}(\mathbf{0}) \tag{6.53}$$

It remains now to derive the elasticity tensor and stress–strain relation for a patched skin inside a grind-out cavity. Similar to the stage I analysis, this inside region will be modeled also as an elliptical inhomogeneity. By substituting Equation (6.44) for the skin thickness $t_{\text{s-inside}}$ inside Ω into Equation (6.47) and choosing the effective thickness of the patch–skin combination equal to $t_\text{p}+t_\text{s}$, the elasticity tensor for the elliptical inhomogeneity can be expressed as

$$C_{ijkl}^{\text{I(stage II)}} = C_{ijkl}^{\text{I(min)(stage II)}} + C_{ijkl}^{\text{I(prime)}}\left(x_1^2 + \frac{x_2^2}{\Theta^2}\right) \tag{6.54}$$

where

$$C_{ijkl}^{\text{I(min)(stage II)}} = \frac{t_\text{r}}{t_\text{s}+t_\text{p}}C_{ijkl}^{\text{s}} + \frac{t_\text{p}}{t_\text{s}+t_\text{p}}C_{ijkl}^{\text{p}} \tag{6.55}$$

$$C_{ijkl}^{\text{I(prime)}} = \frac{1}{2R_\text{c}\left(t_\text{s}+t_\text{p}\right)}C_{ijkl}^{\text{s}} \tag{6.56}$$

Similar to Equation (6.51), the constitutive relation for the inhomogeneity will take the following form:

$$\sigma_{ij}^{\text{I(stage II)}} = C_{ijkl}^{\text{I(stage II)}}\left(\varepsilon_{kl}^{\text{I(stage II)}} - \varepsilon_{kl}^{(\text{T})(\text{inside})}\right) \quad \text{inside } \Omega \tag{6.57}$$

where perhaps it needs to recall that $\varepsilon_{kl}^{(\text{T})(\text{inside})}$ is given by Equation (6.49). From Equation (6.49), it is clear that by defining $\varepsilon_{ij}^{(\text{T})(\text{inside}-\text{min})}$ as

$$\varepsilon_{ij}^{(\text{T})(\text{inside}-\text{min})} = \frac{t_\text{p}}{t_\text{s}+t_\text{p}}C_{ijkl}^{\text{I(min)(stage II)}-1}C_{klmn}^{\text{p}}\varepsilon_{mn}^{(\text{T})(\text{p})} \tag{6.58}$$

it follows that

$$C_{ijkl}^{\text{I(min)(stage II)}}\varepsilon_{kl}^{(\text{T})(\text{inside}-\text{min})} = C_{ijkl}^{\text{I(stage II)}}\varepsilon_{kl}^{(\text{T})(\text{inside})} \tag{6.59}$$

since they are both equal to $\frac{t_\text{p}}{t_\text{p}+t_\text{s}}C_{ijkl}^{\text{p}}\varepsilon_{kl}^{(\text{T})(\text{p})}$. Substituting Equations (6.54) and (6.59) into Equation (6.57) yields

$$\sigma_{ij}^{\text{I(stage II)}} = C_{ijkl}^{\text{I(min)(stage II)}}\left[\left(\varepsilon_{kl}^{\text{I(stage II)}} - \varepsilon_{kl}^{(\text{T})(\text{outside})}\right) - \left(\varepsilon_{kl}^{(\text{T})(\text{inside}-\text{min})} - \varepsilon_{kl}^{(\text{T})(\text{outside})}\right)\right]$$

$$+ C_{ijkl}^{\text{I(prime)}}\left(x_1^2 + \frac{x_2^2}{\Theta^2}\right)\varepsilon_{kl}^{\text{I(stage II)}} \quad \text{inside } \Omega \tag{6.60}$$

By comparing Equations (6.60) and (6.51) with Equation (6.33) in Section 6.3.1, it is clear that the present stage II problem can be solved by the method outlined in that section with all parameters used there being related to those derived here as follows:

$$\begin{aligned} C_{ijkl}^{0} &= C_{ijkl}^{0(\text{stage II})} \\ C_{ijkl}^{\text{I(min)}} &= C_{ijkl}^{\text{I(min)(stage II)}} \\ C_{ijkl}^{\text{I(prime)}} &= C_{ijkl}^{\text{I(prime)}} \\ \varepsilon_{\infty ij} &= \varepsilon_{\infty ij}^{(\text{stage II})} \\ \varepsilon_{ij}^{(\text{init})} &= \varepsilon_{ij}^{\text{(T)(outside)}} \\ \varepsilon_{ij}^{\text{(T)(min)}} &= \varepsilon_{ij}^{\text{(T)(inside}-\text{min)}} - \varepsilon_{ij}^{\text{(T)(outside)}} \end{aligned} \tag{6.61}$$

where each term in the right-hand side of these equations, except for the last equation then a first term, has been defined earlier throughout this section by Equations (6.50), (6.55), (6.56), (6.53), (6.48), and (6.58), respectively. With these, the strain field $\varepsilon_{ij}^{\text{I(stage II)}}$ induced by the inhomogeneity and thus the stress field $\sigma_{ij}^{\text{I(stage II)}}$ can be solved by the solution procedure outlined in Section 6.3.1. Similar to Equations (4.47), stresses in the skin are finally given by

$$\sigma_{ij}^{\text{s}} = \begin{cases} C_{ijkl}^{\text{s}} \left(C_{klmn}^{\text{I(stage II)}-1} \sigma_{mn}^{\text{I(stage II)}} + \varepsilon_{kl}^{\text{(T)(inside)}} \right) & \text{inside } \Omega \\ C_{ijkl}^{\text{s}} \left(C_{klmn}^{0(\text{stage II})-1} \sigma_{mn}^{\text{I(stage II)}} + \varepsilon_{kl}^{\text{T(outside)}} \right) & \text{outside } \Omega \end{cases} \tag{6.62}$$

while stresses in the patch are

$$\sigma_{ij}^{\text{p}} = \begin{cases} C_{ijkl}^{\text{p}} \left(C_{klmn}^{\text{I(stage II)}-1} \sigma_{mn}^{\text{I(stage II)}} + \varepsilon_{kl}^{\text{(T)(inside)}} - \varepsilon_{kl}^{\text{(T)(p)}} \right) & \text{inside } \Omega \\ C_{ijkl}^{\text{p}} \left(C_{klmn}^{0(\text{stage II})-1} \sigma_{mn}^{\text{I(stage II)}} + \varepsilon_{kl}^{\text{T(outside)}} - \varepsilon_{kl}^{\text{(T)(p)}} \right) & \text{outside } \Omega \end{cases} \tag{6.63}$$

Case 2: Unfilled cavity

Let us consider now the case of patching an unfilled cavity. It turns out that the patching analysis for an unfilled cavity can proceed in a similar manner as that for the first case. In the absence of any filler in the cavity, the skin and the patch expect to be strained differently inside the grind-out region. Furthermore, the stresses in the patch are also expected to be nearly constant inside the grind-out region and approximately equal to those just outside the cavity because no load transfer between the skin and the patch can take place inside the cavity. In order to use the inclusion analogy and thus the solution procedure outlined for case 1, one must assume that the patch is subjected to an additional unknown initial strain field $\left(\varepsilon_{ij}^{\text{(R)(p)}} \right)$ inside the grind-out region besides those mentioned in the first case. Physically $\varepsilon_{ij}^{\text{(R)(p)}}$ are components of the strain field in

the patch inside the grind-out region relative to that in the skin. When the skin and the patch are equally strained as previously assumed in the first case, components of $\varepsilon_{ij}^{(\mathrm{R})(\mathrm{p})}$ equal to zero. Since the present stage II problem involves very little in-plane shear, for simplicity, the component $\varepsilon_{12}^{(\mathrm{R})(\mathrm{p})}$ is assumed to be zero. The unknown strain components $\varepsilon_{11}^{(\mathrm{R})(\mathrm{p})}$ and $\varepsilon_{22}^{(\mathrm{R})(\mathrm{p})}$ for the present case are then determined by imposing the following stress continuity conditions on the patch:

$$\begin{aligned} \sigma_{11}^{\mathrm{p}}\big|_{\text{center}} &= \sigma_{11}^{\mathrm{p}}\big|_{\text{top edge}} \\ \sigma_{22}^{\mathrm{p}}\big|_{\text{center}} &= \sigma_{22}^{\mathrm{p}}\big|_{\text{right edge}} \end{aligned} \tag{6.64}$$

or

$$\begin{aligned} f &= \sigma_{11}^{\mathrm{p}}\big|_{\text{center}} - \sigma_{11}^{\mathrm{p}}\big|_{\text{top edge}} = 0 \\ g &= \sigma_{22}^{\mathrm{p}}\big|_{\text{center}} - \sigma_{22}^{\mathrm{p}}\big|_{\text{right edge}} = 0 \end{aligned} \tag{6.65}$$

These two conditions will be explained as follows. As mentioned earlier in beginning of this part, stresses in the patch inside the grind-out region are expected to be nearly constant and approximately the same as those just outside and near the edge of the cavity. At the top edge of the cavity (point 3 in Figure 6.4), the radial stress (or σ_{22} component in our x_1–x_2 coordinate system) in the skin varies significantly through the thickness since it must diminish near the top free surface where there is a hole but maintains high value near the bottom free surface. In addition, a significant out-of-plane shear also occurs there in the adhesive especially for the case the dominant load is in the x_2-direction as shown in Figure 6.4; $\gamma_{x_3-x_2}^{(\mathrm{A})}$ is therefore expected to be very high. On the other hand, the tangential stress (or σ_{11}) in the skin at that location is quite uniform through a thickness while $\gamma_{x_3-x_1}^{(\mathrm{A})}$ is low. The stress component σ_{11} in the patch at the center of the grind-out is therefore assumed to be the same as that at point 3. In contrast, at the right or left edge of the grind-out cavity (point 2 in Figure 6.4), the tangential stress (or σ_{22} component in our x_1–x_2 coordinate system) in the skin is more uniform through thickness while the out-of-plane shear component $\gamma_{x_3-x_2}^{(\mathrm{A})}$ in the adhesive there is low. Thus, stress component σ_{22} in the patch at the center of the grind-out is more accurately assumed to be the same as that at point 2.

It remains now to outline a procedure to determine the unknown initial strain components $\varepsilon_{11}^{(\mathrm{R})(\mathrm{p})}$ and $\varepsilon_{22}^{(\mathrm{R})(\mathrm{p})}$, which yield stresses in the patch satisfying Equation (6.65). It is clear that for a given $\varepsilon_{ij}^{(\mathrm{R})(\mathrm{p})}$, one can follow the solution method outlined above for case 1 to obtain stresses and strains in the skin and patch since everything will be the same as before except that the initial strain field prescribed in the patch inside the cavity region now is $\varepsilon_{ij}^{(\mathrm{R})(\mathrm{p})} + \varepsilon_{ij}^{(\mathrm{T})(\mathrm{p})}$ rather than $\varepsilon_{ij}^{(\mathrm{T})(\mathrm{p})}$ inside the grind-out region. In particular, the stage II problem with the additional initial strain $\varepsilon_{ij}^{(\mathrm{R})(\mathrm{p})}$ prescribed in the patch in the grind-out region can be solved by the method outlined in Section 6.3.1 with all parameters defined in Equation (6.61) remaining the same except for $\varepsilon_{ij}^{(\mathrm{T})(\mathrm{min})}$, which must be modified as

$$\varepsilon_{ij}^{(\mathrm{T})(\mathrm{min})} = \varepsilon_{ij}^{(\mathrm{T})(\mathrm{inside-min})} - \varepsilon_{ij}^{(\mathrm{T})(\mathrm{outside})} + \varepsilon_{ij}^{(\mathrm{R})(\mathrm{inside-min})} \tag{6.66}$$

where $\varepsilon_{ij}^{(\mathrm{R})(\mathrm{inside-min})}$ is given by a similar expression as (6.58) but with $\varepsilon_{ij}^{(\mathrm{T})(\mathrm{p})}$ being replaced by $\varepsilon_{ij}^{(\mathrm{R})(\mathrm{p})}$. In addition, the expression for the stresses in the patch inside the grind-out region given by the first equation of (6.63) also needs to be changed to

$$\sigma_{ij}^{\mathrm{p}} = C_{ijkl}^{\mathrm{p}} \left(C_{klmn}^{\mathrm{I(stage\ II)}-1} \sigma_{mn}^{\mathrm{I(stage\ II)}} + \varepsilon_{kl}^{(\mathrm{T})(\mathrm{inside})} - \varepsilon_{kl}^{(\mathrm{T})(\mathrm{p})} - \varepsilon_{kl}^{(\mathrm{R})(\mathrm{p})} \right) \quad \text{inside } \Omega \tag{6.67}$$

By linearizing Equation (6.65) as

$$\begin{aligned} f\left(\varepsilon_{11}^{(\mathrm{R})(\mathrm{p})}=0;\, \varepsilon_{22}^{(\mathrm{R})(\mathrm{p})}=0\right) + \left.\frac{\partial f}{\partial \varepsilon_{11}^{(\mathrm{R})(\mathrm{p})}}\right|_0 \varepsilon_{11}^{(\mathrm{R})(\mathrm{p})} + \left.\frac{\partial f}{\partial \varepsilon_{22}^{(\mathrm{R})(\mathrm{p})}}\right|_0 \varepsilon_{22}^{(\mathrm{R})(\mathrm{p})} = 0 \\ g\left(\varepsilon_{11}^{(\mathrm{R})(\mathrm{p})}=0;\, \varepsilon_{22}^{(\mathrm{R})(\mathrm{p})}=0\right) + \left.\frac{\partial g}{\partial \varepsilon_{11}^{(\mathrm{R})(\mathrm{p})}}\right|_0 \varepsilon_{11}^{(\mathrm{R})(\mathrm{p})} + \left.\frac{\partial g}{\partial \varepsilon_{22}^{(\mathrm{R})(\mathrm{p})}}\right|_0 \varepsilon_{22}^{(\mathrm{R})(\mathrm{p})} = 0 \end{aligned} \tag{6.68}$$

$$\begin{aligned} f &= \sigma_{11}^{\mathrm{p}}\big|_{\mathrm{center}} - \sigma_{11}^{\mathrm{p}}\big|_{\mathrm{top\ edge}} \\ g &= \sigma_{22}^{\mathrm{p}}\big|_{\mathrm{center}} - \sigma_{22}^{\mathrm{p}}\big|_{\mathrm{right\ edge}} \end{aligned} \tag{6.69}$$

where f and g are scalar functions of the parameters $\varepsilon_{11}^{(\mathrm{R})(\mathrm{p})}$ and $\varepsilon_{22}^{(\mathrm{R})(\mathrm{p})}$, and the notation $\left.\frac{\partial f}{\partial \varepsilon_{11}^{(\mathrm{R})(\mathrm{p})}}\right|_0$ means that the derivative $\frac{\partial f}{\partial \varepsilon_{11}^{(\mathrm{R})(\mathrm{p})}}$ is evaluated at $\left(\varepsilon_{11}^{(\mathrm{R})(\mathrm{p})}=0;\ \varepsilon_{11}^{(\mathrm{R})(\mathrm{p})}=0\right)$; the unknown initial strain components $\varepsilon_{11}^{(\mathrm{R})(\mathrm{p})}$ and $\varepsilon_{22}^{(\mathrm{R})(\mathrm{p})}$ can be solved by the following simple steps. First, stage II problem is solved as in case 1 by assuming that $\varepsilon_{ij}^{(\mathrm{R})(\mathrm{p})}=0$. Second, $f(0,\ 0)$ and $g(0,\ 0)$ are evaluated via Equation (6.69) with stresses in the patch inside and outside the cavity given, respectively, by Equation (6.67) and the second equation of (6.63) and based on the stress solution obtained from the previous step. In general, $f(0,\ 0)$ and $g(0,\ 0)$ will not equal zero as required by Equation (6.65). Next, all first derivatives of f and g are evaluated, numerically using the finite difference scheme. In doing that, $f(h_1,\ 0)$, $f(0,\ h_2)$, $g(h_1,\ 0)$, and $g(0,\ h_2)$ need to be evaluated where h_1 and h_2 are small spaces between grid points in the $\varepsilon_{11}^{(\mathrm{R})(\mathrm{p})}$–$\varepsilon_{22}^{(\mathrm{R})(\mathrm{p})}$ domain spaces of functions f and g. Computations for all example problems presented in this section are carried out with h_1 and h_2 chosen equal to

$$\begin{Bmatrix} h_1 \\ h_2 \end{Bmatrix} = \frac{1}{100} \begin{bmatrix} C_{11}^{\mathrm{p}} & C_{12}^{\mathrm{p}} \\ C_{21}^{\mathrm{p}} & C_{22}^{\mathrm{p}} \end{bmatrix}^{-1} \begin{Bmatrix} f(0,0) \\ g(0,0) \end{Bmatrix} \tag{6.70}$$

where C_{ij}^{p} is an element of the elasticity tensor of the patch in Voight (matrix) notation. Thus, this numerical differentiation step for the derivatives of f and g will involve solving stage II problem similar to the first case twice, first with $\left(\varepsilon_{11}^{(\mathrm{R})(\mathrm{p})}, \varepsilon_{22}^{(\mathrm{R})(\mathrm{p})}, \varepsilon_{12}^{(\mathrm{R})(\mathrm{p})}\right) = (h_1, 0, 0)$ and then with $\left(\varepsilon_{11}^{(\mathrm{R})(\mathrm{p})}, \varepsilon_{22}^{(\mathrm{R})(\mathrm{p})}, \varepsilon_{12}^{(\mathrm{R})(\mathrm{p})}\right) = (0, h_2, 0)$, where h_1 and h_2 are known since they can be determined from Equation (6.70), and performing the finite differences. With $f(0,\ 0)$, $g(0,\ 0)$, and all first derivatives of f and g known, the unknown initial

strain components $\varepsilon_{11}^{(R)(p)}$ and $\varepsilon_{22}^{(R)(p)}$ finally can be determined by solving the algebraic Equation (6.68). Once $\varepsilon_{11}^{(R)(p)}$ and $\varepsilon_{22}^{(R)(p)}$ are determined, the stress and strain solutions of stage II problem for the case of patching an unfilled cavity can be obtained in a straightforward manner as in the first case of rigid filling except with a different (known) initial strain field prescribed in the patch as mentioned in the beginning of this paragraph.

Illustrative examples

To illustrate the method presented in this section, three examples taken out from the paper by Duong and Yu (2002b) are considered here. Analytical predictions for these three examples will also be compared with results from the FE method. In the first example, a circular patch *rigidly* bonded over a circular grind-out cavity with a uniform depth as shown in Figure 6.6 is considered. This example is used to validate the analytical formulation. For that reason, the counterpart FE analysis for this example will also involve similar simplified assumptions as those in the analytical model, which may not realistically represent the actual repair. Realistic repairs will be discussed later in the next two examples. The radii of the patch and the grind-out cavity are 38.1 and 12.7 mm, respectively. The whole patched skin is subjected to a uniform temperature change of $-100\,^{\circ}$C. Only thermal loading is considered here because a similar problem under a purely mechanical loading had been presented in Section 6.2.2. The patch material is linear elastic and isotropic. The material properties and thickness of the skin and the patch are given below:

Skin:

$E_s = 72.4\,\text{GPa},\ \nu_s = 0.33,\ \alpha_s = 22.5\text{E-}6\ \text{per}\,^{\circ}\text{C}$ full skin thickness $t_s = 5.08\,\text{mm}$, remaining skin thickness $t_r = 2.54\,\text{mm}$.

Patch:

$E_p = 186.2\,\text{GPa},\ \nu_p = 0.21,\ \alpha_p = 4.3\text{E-}6\ \text{per}\,^{\circ}\text{C},\ t_p = 0.79\,\text{mm}$.

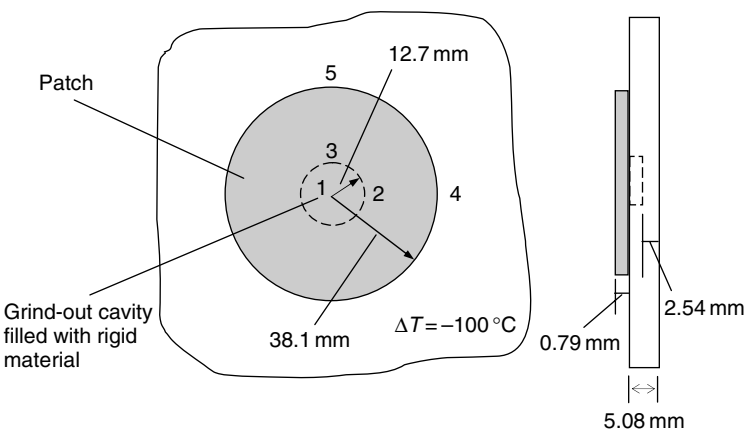

Fig. 6.6. Geometry of a repair problem with a circular isotropic patch under uniform temperature change.

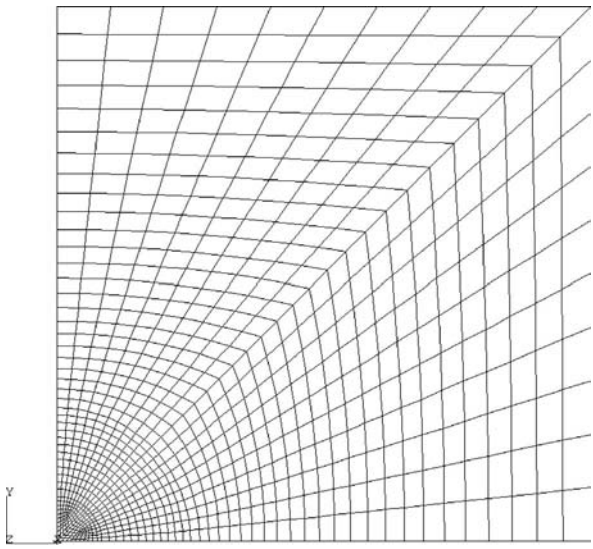

Fig. 6.7. A mesh of a damaged skin used in the FE analysis of the repair problem with a circular isotropic patch under uniform temperature change.

The FE analysis is carried out using MSC/NASTRAN code (2001) with the skin and the patch each being modeled as a separate layer of (2-D) plane stress elements (see Figure 6.7 for a typical mesh in a skin). Furthermore, the skin layer has different thickness for regions outside and inside of the damaged area. Because the skin and the patch are isotropic and also because of double symmetry of the repair, only stresses in the y-component are reported here in Table 6.2. Corresponding FE results are also given in the table for comparison. To ensure solution convergence, FE analyses had been performed using first linear and then quadratic elements for the mesh shown in Figure 6.7. From Table 6.2, analytical predictions agree very well with FE results as expected.

A second example involves a realistic bonded repair with an octagonal patch as illustrated in Figure 6.8. The dimensions of the patch are also given in that figure. The skin properties are the same as those in the first example. However, the grind-out cavity in

Table 6.2. Stress comparison between analytical predictions and FE results for an isotropic skin containing a 2.54 mm deep circular grind-out repaired with a circular orthotropic patch of 0.79 mm thickness. All stresses are in MPa.

Location	Analytical		FE (linear element)		FE (quadratic element)	
	Skin	Patch	Skin	Patch	Skin	Patch
1	53.2	−357.2	54.4	−354.4	54.5	−357.2
2	46.6	−372.3	48.2	−362.0	47.9	−369.6
3	34.1	−405.4	35.8	−399.2	35.0	−403.4
4	20.0	N/A	22.5	N/A	22.1	N/A
5	−20.1	N/A	−18.3	N/A	−20.0	N/A

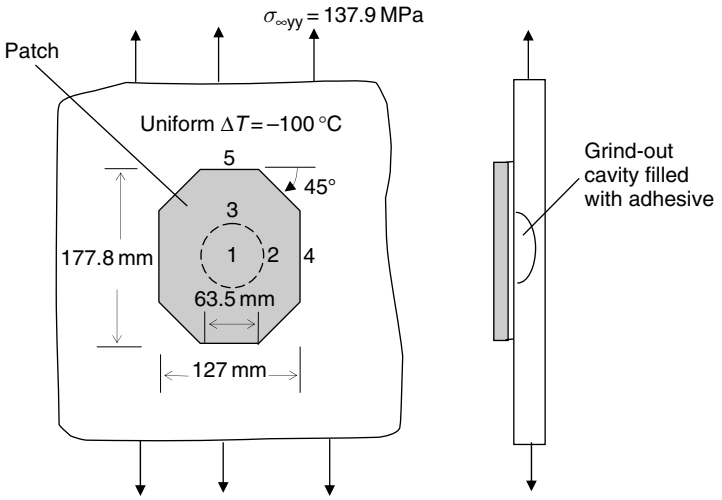

Fig. 6.8. Geometry of a repair problem with an orthotropic octagonal patch under thermo-mechanical loading.

the present example has a spherical depth with a minimum remaining skin thickness of 2.54 mm. The patch is assumed to be orthotropic with its material properties given below:

$$E_x = 18.7\,\text{GPa},\ E_y = 193.1\,\text{GPa},\ \nu_{yx} = 0.21,\ \mu = 5.5\,\text{GPa},$$
$$\alpha_x = 21.4\text{E-}06\ \text{per}\,^\circ\text{C},\ \alpha_y = 4.3\ \text{E-}06\ \text{per}\,^\circ\text{C},\ t_p = 0.79\,\text{mm}.$$

Two different loading conditions are considered in the second example. In the first loading condition, the repaired skin is subjected to a uniform temperature change of 100 °C as in the first example. On the other hand, a stress of 137.9 MPa is applied to the repaired skin at infinity in the second loading condition. Analytical predictions have been made assuming a cavity with either uniform or spherical depth and with or without filler. Analytical results for the second example are summarized in Table 6.3 along with those from the FE method. Table 6.3(a) shows results of the stress component σ_{22} in the skin and patch due to thermal loading at various critical locations while Table 6.3(b) is for mechanical loading. The letter (B) or (T) next to a numerical value listed in the "FE" column of Tables 6.3(a) and 6.3(b) indicates a bottom or top surface of the skin or patch where the reported stress value is approximately found. In the FE analysis, the skin, patch and adhesive are all modeled using 8-node hexahedral solid elements with a typical mesh given in Figure 6.9. Moreover, the cavity is also filled in with an adhesive as normally done in practice. The bottom of the skin is restrained from an out-of-plane (x_3-) deflection. Typical values for shear modulus (0.455 GPa) and thickness (0.127 mm) of the adhesive are used in the FE analysis. A very fine mesh is employed for regions inside and around a cavity to enable to model the spherical surface of the cavity with a great accuracy. Again FE analysis is carried out using MSC/NASTRAN (2001).

In contrast to the first example, stresses at critical locations from the FE method for the present example show a considerable thickness variation. In general, stresses in the

Table 6.3. Stress comparison between analytical predictions and FE results in x_2-normal-component for an isotropic skin containing a 2.54 mm deep grind-out cavity, repaired with an octagonal orthotropic patch, under individual thermal and mechanical loading. All stresses are in MPa.

(a) Due to uniform temperature change of −100 °C

Point	Uniform depth (rigidly filled)		Uniform depth (unfilled)		Spherical depth (rigidly filled)		Spherical depth (unfilled)		FE	
	Skin	Patch	Skin	Patch	Skin	Patch	Skin	Patch	Skin	Patch
1	38.6	−280.6	39.0	−283.5	39.6	−278.3	41.7	−294.6	(40.1) (B) (43.6) (T)	(−259.2) (T) (−268.9) (B)
2	36.8	−283.7	36.8	−283.5	31.4	−298.3	32.8	−294.6	(32.1) (T) (34.0) (B)	(−270.3) (T) (−272.3) (B)
3	24.7	−315.2	24.6	−315.8	27.0	−309.6	26.1	−312.1	(18.9) (T) (27.0) (B)	(−263.4) (B) (−285.4) (T)
4	19.4	N/A	19.4	N/A	19.4	N/A	19.4	N/A	(21.0) (T) (21.6) (B)	N/A
5	−15.2	N/A	−15.2	N/A	*multiplan1@ lN/A*		−15.2	N/A	(−1.72) (T) (−22.5) (B)	N/A

(b) Due to 137.9 MPa far field stress

Point	Uniform depth (rigidly filled)		Uniform depth (unfilled)		Spherical depth (rigidly Filled)		Spherical depth (unfilled)		FE	
	Skin	Patch	Skin	Patch	Skin	Patch	Skin	Patch	Skin	Patch
1	145.8	375.8	146.4	371.4	149.2	384.2	157.2	323.0	(151.0) (B) (164.8) (T)	(317.9) (T) (320.6) (B)
2	144.3	372.8	143.5	371.3	119.3	306.6	125.6	322.8	(121.3) (T) (126.2) (B)	(302.7) (T) (306.1) (B)
3	93.4	245.4	93.1	244.1	100.8	260.2	97.0	251.5	(67.5) (T) (100.5) (B)	(293.7) (B) (297.9) (T)
4	117.5	N/A	117.5	N/A	117.5	N/A	117.5	N/A	(115.6) (T) (115.6) (B)	N/A
5	153.6	N/A	153.6	N/A	153.6	N/A	153.6	N/A	(138.9) (T) (160.5) (B)	N/A

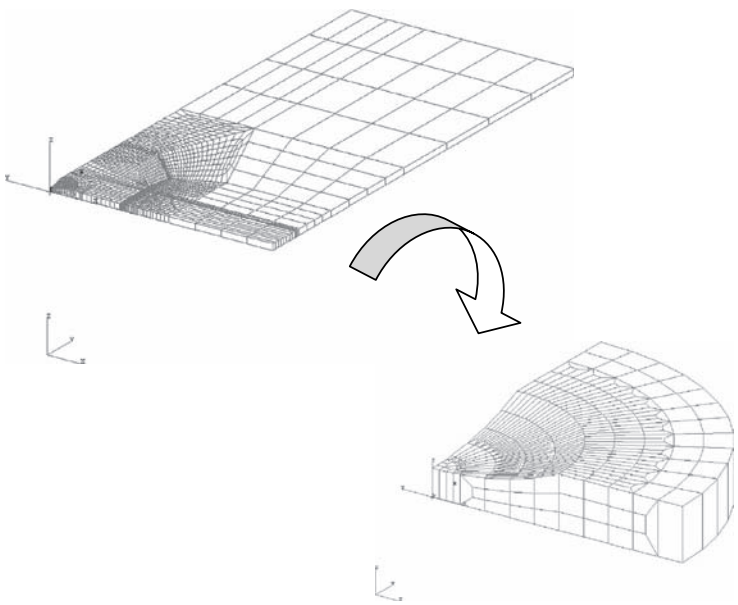

Fig. 6.9. A mesh of a damage skin used in FE analysis of a repair problem with an orthotropic octagonal patch.

skin and patch predicted by four different analytical models are in very good agreement with FE results at the center of the grind-out region for both loading conditions with the unfilled, spherically deep cavity model shown to be the most superior model. At point 2 location, a uniformly deep cavity model with or without filler appears to over-predict a skin's stress there. This is expected since the latter analytical model has more material being grinded out than that in the FE analysis so that more stress will diverge from point 3 to point 2. It should be noted that since stresses in the skin at points 4 and 5 are computed from stage I analysis which is common to four analytical models, these stresses are reported identically in Tables 6.3(a) and 6.3(b). Except for a patch's stress at location 3, the unfilled, spherically deep cavity model yields very accurate results in comparison with FE method. The patch's stress at point 3 for the second (purely mechanical) loading condition is grossly underestimated in all analytical models. This can be explained by the fact that the stress in the skin there varies significantly from 67.5 to 100.5 MPa through thickness while all analytical models predict an average stress of about 96 MPa. The skin at point 3 therefore carries more loads in analytical models than that in FE method, thus relieving some of the patch stress. Nevertheless, since the patch from the design viewpoint is not critical there, the method developed in this section is therefore considered to be good overall.

The last example is similar to a second example except for a much deeper grind-out cavity. The minimum remaining depth in the grind-out cavity is 1.016 mm. Results of the stress component σ_{22} in the skin and patch from the analytical method and from the FE analysis are presented in Tables 6.4(a) and 6.4(b) for the thermal and mechanical loading condition, respectively. From Tables 6.4(a) and 6.4(b), trends similar to those found in

Table 6.4. Stresses comparison between analytical predictions and FE results for an isotropic skin containing a 4.06 mm deep grind-out cavity, repaired with an octagonal orthotropic patch, under individual thermal and mechanical loading.

(a) Due to uniform temperature change of −100 °C

Point	Uniform depth (rigidly filled)		Uniform depth (unfilled)		Spherical depth (rigidly filled)		Spherical depth (unfilled)		FE	
	Skin	Patch	Skin	Patch	Skin	Patch	Skin	Patch	Skin	Patch
1	47.5	−258.8	48.4	−264.4	53.5	−244.4	62.5	−289.0	(62.1) (B) (65.8) (T)	(−247.5) (T) (−259.2) (B)
2	43.9	−264.8	43.9	−264.4	30.8	−300.1	35.0	−289.0	(35.6) (T) (38.5) (B)	(−264.1) (T) (−266.8) (B)
3	20.2	−326.7	19.7	−328.2	26.2	−311.9	23.1	−319.6	(12.8) (T) (22.4) (B)	(−251.7) (B) (−288.9) (T)
4	19.4	N/A	19.4	N/A	19.4	N/A	19.4	N/A	(21.1) (T) (21.6) (B)	N/A
5	−15.2	N/A	−15.2	N/A	−15.2	N/A	−15.2	N/A	(−1.72) (T) (−22.5) (B)	N/A

(b) Due to 137.9 MPa far field stress

Point	Uniform depth (rigidly filled)		Uniform depth (unfilled)		Spherical depth (rigidly Filled)		Spherical depth (unfilled)		FE	
	Skin	Patch	Skin	Patch	Skin	Patch	Skin	Patch	Skin	Patch
1	179.0	461.1	180.4	451.8	199.9	513.0	233.4	345.5	(236.5) (B) (251.7) (T)	(346.8) (T) (352.3) (B)
2	175.8	454.9	174.1	451.6	116.3	297.0	135.1	345.3	(133.8) (T) (142.7) (B)	(344.1) (T) (326.1) (B)
3	76.0	204.9	75.4	201.5	96.0	247.0	83.4	217.6	(43.5) (T) (86.9) (B)	(308.9) (B) (318.5) (T)
4	117.5	N/A	117.5	N/A	117.5	N/A	117.5	N/A	(115.8) (T) (115.8) (B)	N/A
5	153.6	N/A	153.6	N/A	153.6	N/A	153.6	N/A	(138.7) (T) (160.0) (B)	N/A

a second example are observed for stresses in the skin and in the patch at locations 1–5, and the unfilled, spherically deep cavity model again in general yields best results. For a deep grind-out cavity, two important results are found from this example. First, a stress in the skin at a center of a grind-out region could not be predicted with sufficient accuracy using a uniformly deep cavity. This is due to omitting the effect of a local curvature at the bottom of a cavity in that model and this effect becomes more pronounced for a deeper cavity. Within that context, it is important to note that approximating a spherically deep cavity by a uniformly deep cavity of the same volume will give erroneous results in the skin's stress at the center of the cavity. Using the constant volume approach, the cavity will be much shallow than the one reported in Tables 6.3 and 6.4, which in turn will reduce skin's stress further and cause even a larger discrepancy in comparison with the FE result. Secondly, the use of the original inclusion analogy without any modification in a stage II analysis will not yield sufficiently accurate results for a realistic repair over a very deep grind-out in a thick skin. In that case, the unfilled spherically deep cavity model developed in this section should be used.

6.4 Summary

Analytical methods for analyzing a bonded repair over an elliptical cut-out or corrosion grind-out cavity are presented in this chapter. These methods use eigenstrain theory and a global-local approach that is similar to Rose's two-stage analysis procedure for crack patching. In general, analytical predictions agree well with results obtained from the full 3-D FE analyses at most critical locations under both mechanical and thermal loading. However, for a relatively deep grind-out cavity, unless the rigid bond assumption is relaxed in the stage II analysis, the analytical methods may give inadequate stress results at the center of the grind-out region.

CHAPTER 7

Bond-Line Analysis at Patch Ends

7.1 Introduction

In Chapters 4 and 5, the peel and shear stresses in the adhesive of a bonded repair are only calculated near the crack surfaces. Since these stresses may be also critical near the end of the patch, an approximate method to estimate these stresses therefore will be introduced in this chapter. As shown later in Sections 7.4 and 7.5, this approximate method will utilize solutions delineated in Chapters 4 and 5 for two-dimensional (2-D) inclusions and inhomogeneities and also the one-dimensional (1-D) solutions for bonded joints and doublers. One-dimensional solutions for untapered joints and doublers had been considered in Chapter 2. However, since the adhesive stresses in bonded patches or doubler were normally peaked at the end of the overlap, which can cause failure of the adhesive and compromise the performance of the bonded patches or doublers, bonded patches or doublers are therefore usually tapered at their overlapped ends to reduce the severity of these peaks. Thus, 1-D solutions for tapered doublers or tapered patches are also of interest and they will be presented in Section 7.2. These 1-D solutions for tapered patch and doubler are extended in Section 7.3 to include the effects of thermal mismatch and adhesive plasticity. Finally, depending on whether the bonded patch is one-sided or two-sided, the approximate method for estimating the adhesive stresses near the patch edge will be described in details in Sections 7.4 and 7.5, respectively, for these two configurations, following the work of Duong (2003a).

7.2 One-Dimensional Analysis of Tapered Patches and Doublers

Due to the mathematical complexity, no closed-form solution is available in the literature for tapered patches or doublers. Numerical solutions are therefore sought for these tapered patches and doublers. In the numerical approach, a set of differential equations and boundary conditions is formulated with adherends modeled as classical beams, and the solutions of these differential equations are obtained by direct numerical integrations.

In a series of papers by Thomsen (1992), Thomsen et al. (1996), Mortensen and Thomsen (1997, 2002), a unified approach for analyzing the variety of bonded joints and doublers with and without tapered edges, and related problems using numerical integration method was given. This unified approach was also accounted for the effect of a (materially) nonlinear adhesive. However, it was limited to geometrically linear analyses of one-sided doublers or one-sided patches. Duong (2006) has extended this unified approach to include geometrically nonlinear analyses of the tapered joints and one-sided tapered doublers or patches, following the Goland–Reissner (1944) two-step solution method. Thus, the approach proposed by Duong for approximating the adhesive stresses in a bond line of a tapered bonded joint or doubler will be given in this section. For clarity, this approach will be demonstrated first for the case of a purely tensile load. Extension of the approach to account for the effects of thermal mismatch and adhesive plasticity will be described in Section 7.3.

7.2.1 Mathematical formulation and two-step solution method

Even though the approach presented here is so generic that it can be applied to a variety of tapered bonded joints and doublers, however, for the present purpose, only the formulation for a one-sided doubler and a two-sided doubler will be given here. The approach follows the Goland–Reissner solution method for a single-lap joint and involves a two-step procedure. The approach also allows for the analysis of tapered bonded doublers with non-identical adherends. The approach is first delineated for a tapered one-sided doubler as follows. In the first step of the procedure, the two adherends (skin and doubler) are assumed to be rigidly bonded, and the (geometrically) nonlinear moment distribution along the length of the joint is determined. Since the bending moment solution in this step is relatively simple, it will be derived in closed form using elementary functions. In the second step analysis, only the overlapped region of the joint is considered with the bending moments obtained from the first step at the end of the overlap prescribed as one of its boundary conditions. This latter problem is then solved by using multi-segment method of integration (Kalnins, 1964). However, in contrast to the original Goland–Reissner solution method, the second step analysis can be conducted within both geometrically linear and geometrically nonlinear deformation theory as detailed later.

For uniformity, the solution of a two-sided tapered doubler is also described within the framework of the above approach even though the latter solution does not require a geometrically nonlinear formulation nor step 1 of the above two-step solution procedure. This is because due to the symmetry of the doubler joint with respect to a mid-plane of a middle skin, the two-sided doubler configuration, within the one-dimensional beam theory, will not exhibit any out-of-plane bending deformation and therefore results in a trivially zero bending moment distribution along the joint.

7.2.2 Solution for nonlinear moment distribution along the joint

The equations governing the adhesive stresses require knowledge of the bending moment at the ends of the overlap as boundary conditions. Therefore, the analysis starts with

a solution for the nonlinear moment distribution along the joint. Consider a one-sided tapered doubler and a two-sided tapered doubler in Figures 7.1 and 7.2, respectively, under the in-plane tensile loads. The skin and doubler in each configuration are not necessarily identical (balanced) and they can be a general laminate with different ply materials, layups and thicknesses. The solution of a one-sided doubler will be delineated first. Due to symmetry, only (left) half of the doubler configuration will be considered. Figure 7.3 shows schematics of the analyzing model with separate coordinate system used for each segment of the doubler configuration. The length of each segment is denoted by ℓ_i.

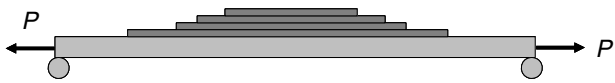

Fig. 7.1. Geometry of a tapered one-sided doubler under in-plane tensile load.

Fig. 7.2. Geometry of a tapered two-sided doubler under in-plane tensile load.

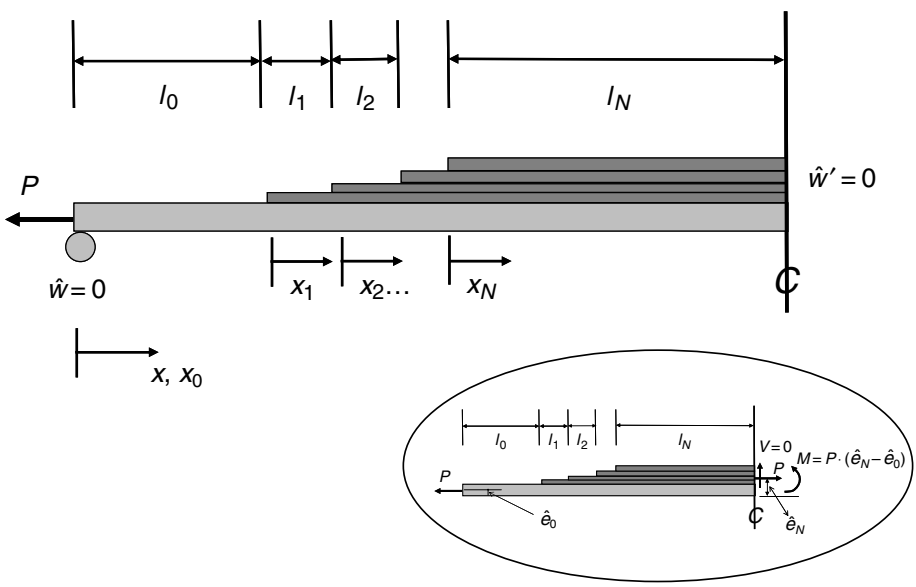

Fig. 7.3. Schematic representation of a tapered one-sided doubler for calculating the nonlinear bending moment distribution. In the linear analysis, the bending moment at a middle of the overlap can be determined just from the overall static equilibrium as shown in the inset figure.

From moment equilibrium consideration, the moment distribution in each segment along the joint is related to loads and displacements by

$$M_i = -P \cdot \hat{w}_i - P\left(\hat{e}_i - \hat{e}_0\right) \tag{7.1}$$

where $i = 0, \ldots, N$; N is the number of segments (steps) in the overlapped region; segment 0 (which corresponds to $i = 0$) is outside the overlap and consists of only the skin; M is the bending moment; P is the axial tensile load applied at the ends of the skin; $\hat{w}$ is the transverse deflection; $\hat{e}_i$ is the z-coordinate of the neutral axis of a beam cross section of the segment i measured from the bottom surface of the skin. Because of the rigid bond assumption, the skin and doubler in the overlapped region will be treated as a single composite beam in this analysis step. It is worthy to note that the first term in the right-hand side of Equation (7.1) represents the moment due to large deflections or "beam column" effect while the second term denotes the moment associated with a load path eccentricity due to the variation of the vertical position of the neutral axis along the length of a doubler. For a laminated segment i, $\hat{e}_i$ and M_i are given respectively by

$$\hat{e}_i = \frac{\frac{1}{2}\sum_{k=1}^{n_{\text{ply}}}\left(C_{11,k}\right)_i\left\{z_{k,i}^2 - z_{k-1,i}^2\right\}}{\sum_{k=1}^{n_{\text{ply}}}\left(C_{11,k}\right)_i\left\{z_{k,i} - z_{k-1,i}\right\}} \tag{7.2}$$

$$\begin{aligned} M_i &= -D_i \hat{w}_i''\left(x_i\right) \\ D_i &= \frac{1}{3}\sum_{k=1}^{n_{\text{ply}}}\left(C_{11,k}\right)_i\left\{\left(z_{k,i} - \hat{e}_i\right)^3 - \left(z_{k-1,i} - \hat{e}_i\right)^3\right\} \end{aligned} \tag{7.3}$$

where $\left(C_{11,k}\right)_i$ is the "(1,1) element" of the elasticity matrix of the kth ply of the ith beam segment, component (1,1) is along the length of beam, D is the flexural rigidity, z_k and z_{k-1} are z-coordinates of the top and bottom surface of the kth ply of the laminate, n_{ply} is the number of plies of the laminated segment i, and the prime denotes the differentiation with respect to the coordinate x. For a homogeneous and isotropic segment, $\hat{e}_i = \frac{t_i}{2}$ and $D_i = \frac{Et_i^3}{12}$, where t_i is the thickness of ith segment. It should be noted that contributions from both skin and doubler must be accounted for in the calculations of D and $\hat{e}$ for any segment inside the overlap.

Substituting Equation (7.3) into Equation (7.1) for M_i yields the following differential equations for each segment i:

$$\hat{w}_i'' - \frac{P}{D_i}\hat{w}_i = \frac{P\left(\hat{e}_i - \hat{e}_0\right)}{D_i} \tag{7.4}$$

The solution of Equation (7.4) is given by

$$\hat{w}_i\left(x_i\right) = W_{1i}\cosh\left(\xi_i x_i\right) + W_{2i}\sinh\left(\xi_i x_i\right) - \left(\hat{e}_i - \hat{e}_0\right) \tag{7.5}$$

where

$$\xi_i = \sqrt{\frac{P}{D_i}} \tag{7.6}$$

W_{1i} and W_{2i} are unknown constants which must be determined from the boundary conditions, and the first two terms in the right-hand side of Equation (7.5) represent the homogeneous solution while the last term is the particular solution. The displacement boundary condition at the right supported end and the symmetry condition at the middle of the doubler configuration require that

$$\hat{w} = 0 \quad \text{at} \quad x = 0 \qquad \text{or} \qquad \hat{w}_0 = 0 \quad \text{at} \quad x_0 = 0 \qquad \text{therefore } W_{10} = 0 \tag{7.7}$$

and the slope $\hat{w}' = 0$ at $x = \ell_0 + \ell_1 + \cdots + \ell_N$ or $\hat{w}'_N = 0$ at $x_N = \ell_N$, thus,

$$\xi_N W_{1N} \sinh(\xi_N \ell_N) + \xi_N W_{2N} \cosh(\xi_N \ell_N) = 0 \tag{7.8}$$

The displacement and slope continuity conditions at each segment junction also require that

$$\begin{aligned} &W_{1i} \cosh(\xi_i \ell_i) + W_{2i} \sinh(\xi_i \ell_i) - W_{1,i+1} = \hat{e}_i - \hat{e}_{i+1} \\ &\ell_i W_{1i} \sinh(\xi_i \ell_i) + \ell_i W_{2i} \cosh(\xi_i \ell_i) - \ell_{i+1} W_{2,i+1} = 0 \end{aligned} \tag{7.9}$$

Thus, Equations (7.7)–(7.9) provide a system of linear algebraic equations for determining the unknown constants W_{1i} and W_{2i} $(i = 0,\ 1, \ldots,\ N)$. Once these constants are determined, the nonlinear bending moment at the end of the overlap is found to be

$$M_L = M_0(x_0 = \ell_0) = -\xi_0^2 D_0 [W_{10} \cosh(\xi_0 \ell_0) + W_{20} \sinh(\xi_0 \ell_0)] \tag{7.10}$$

The first step analysis for a tapered bonded doubler will be concluded with the following remarks:

(a) First, in this analysis step, the bending moments M_i $(i = 0,\ 1, \ldots,\ N)$ and thus M_L are defined with respect to the neutral axis of the composite beam section, which varies along the joint due to the presence of the doubler and its multiple steps.

(b) Secondly, since the thin layer of adhesive will be modeled for in the second analysis step, which thickness may not be an order of magnitude smaller than the skin or doubler thickness, especially in a bonded composite repair, therefore, it will be necessary to account for the effect of the adhesive layer in the calculations of beam section properties such as $\hat{e}_i$ and D_i by including a small gap between the two adherends in the overlapped region in these calculations.

(c) Finally, since the lengths of the first $N-1$ steps of the doubler, i.e., $\ell_1, \ldots, \ell_{N-1}$, are normally small relative to ℓ_0 and ℓ_N, and the evaluations of hyperbolic functions in Equation (7.5) will result in a large exponential number for a certain large combinations of $\xi_0 \ell_0$ and $\xi_N \ell_N$, which will cause an ill condition when solving the system of the algebraic equations for the unknowns W_{1i} and W_{2i}, a special caution therefore must be taken in dealing with those cases. For instance, by using the transformed variables $W^*_{10} = W_{10} \cdot e^{-\xi_0 \ell_0}$ and $W^*_{20} = W_{20} \cdot e^{-\xi_0 \ell_0}$ for W_{10} and W_{20}, and expressing Equation (7.5) for the first segment in terms of these new variables, the mentioned ill condition can be eliminated.

In contrast to the one-sided doubler, the bending moment solution for a two-sided doubler considered in Figure 7.2 is trivially equal to zero. This is due to the symmetry condition of doubler configuration with respect to the mid-plane of skin so that within the 1-D beam theory the transverse displacement is zero along the length of the joint, i.e., $\hat{w}_i = 0$ $(i = 0, 1, \ldots, N)$.

7.2.3 Solutions for peel and shear stresses in the adhesive

The Goland–Reissner analysis for the adhesive peel and shear stresses in a bonded single-lap joint is based on the linear bending analysis of the overlap area of the joint, using their nonlinear estimate for the bending moments in the adherends just outside the bonded area from the first step rigid bond analysis as the key boundary conditions. This same analysis technique will be used here, but slightly modified to approximately account for the geometrical nonlinearity. As mentioned earlier in Section 7.2.1, due to mathematical complexity, this analysis portion will be carried out using the multi-segment method of integration. Again, the formulation and solution for a tapered one-sided doubler will be delineated first. With reference to Figure 7.4, the equilibrium equations are set up for the skin and doubler in each segment of the overlap area. These equilibrium equations for segment i $(i = 1, 2, \ldots, N)$ can be written as follows:

For the substrate or skin:

$$\begin{aligned} N'_{si} &= -\tau_{Ai} \\ V'_{si} &= -\sigma_{Ai} \\ M'_{si} &= V_{si} - \tau_{Ai}\left(\frac{t_s + t_A}{2}\right) - \underline{\underline{N_{si} \cdot \hat{w}'_i}} \end{aligned} \tag{7.11}$$

For the doubler or patch:

$$\begin{aligned} N'_{pi} &= \tau_{Ai} \\ V'_{pi} &= \sigma_{Ai} \\ M'_{pi} &= V_{pi} - \tau_{Ai}\left(\frac{t_{p1} + t_A}{2}\right) - \underline{\underline{N_{pi} \cdot \hat{w}'_i}} \end{aligned} \tag{7.12}$$

where N and V are normal stress resultant and vertical shear resultant, respectively; M again denotes the moment; τ_A and σ_A are the adhesive shear and peel stresses; t_s, t_{p1} and t_A are the *total* thickness of the skin, the *minimum* thickness of the doubler or patch at the tip edge, and the adhesive layer thickness, respectively; $\hat{w}_i$ is the transverse deflection of a segment i of the overlap area as if the skin and doubler act in unison; and the subscripts s and p denote skin and doubler, respectively. $\hat{w}_i$ is considered to be the overall transverse deflection of the overlap area and it is already obtained based on rigid bond assumption in Section 7.2.2 as part of the nonlinear bending moment solution. In Section 7.2.2, $\hat{w}_0$ $(i = 0)$ corresponds to the overall transverse displacement outside the overlap area

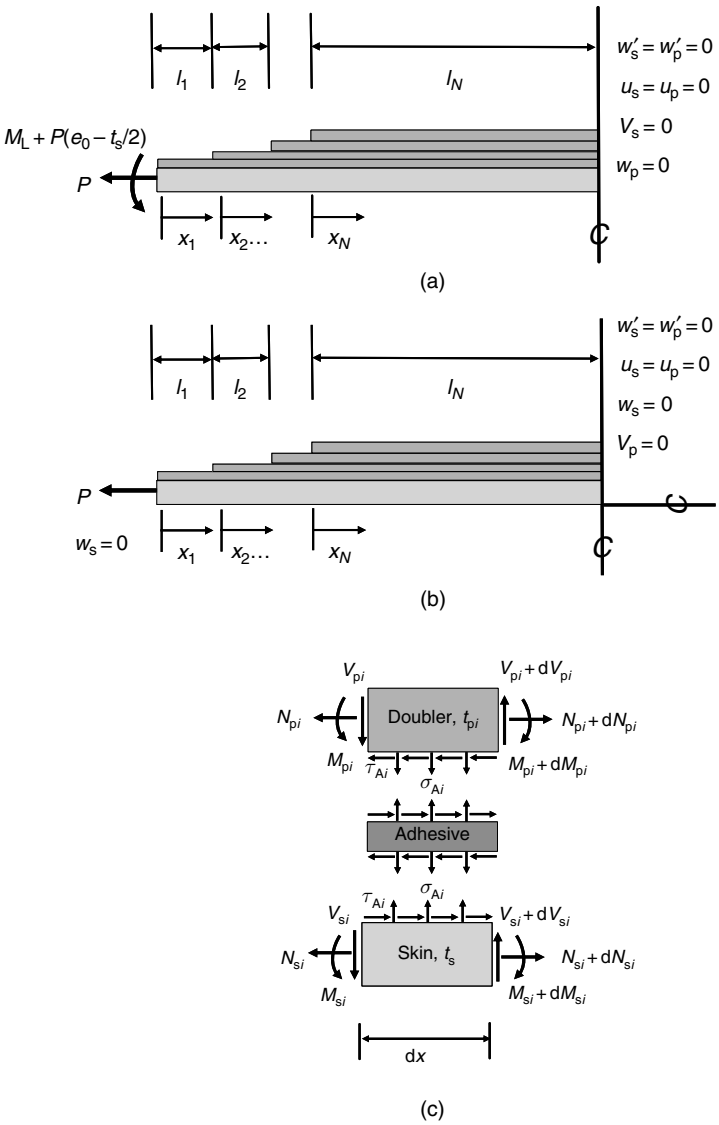

Fig. 7.4. Schematic diagrams for calculating adhesive peel and shear stresses: (a) an overlap of a tapered one-sided doubler; (b) an overlap of a tapered two-sided doubler; and (c) stress and moment resultants of a differential element in the overlap.

while $\hat{w}_i$ $(i = 1, 2, \ldots, N)$ is the deflection of the ith segment inside the overlap. At this point, it is important to point out the difference between the present formulation and that from Goland–Reissner analysis as well as any underlying assumptions for this second step analysis. First, the effect of the geometrical nonlinearity is accounted for in the present formulation by including the underlined terms in Equations (7.11) and (7.12). These terms represent approximately the additional moment in the skin

and doubler due to their large bending deflections. The otherwise geometrically linear analysis will totally omit them. Secondly, for simplification, the bending moment in the present analysis step is defined differently from the first step. The bending moment in the skin is now defined with respect to the mid-plane of the skin. In contrast, the bending moment in the doubler is always defined with respect to the mid-plane of the first segment of the doubler for all of its segments (steps). As detailed later, this definition of the doubler's bending moment is preferred because it will make the doubler moment and shear distributions to be continuous across the segment junctions. It should be emphasized that the effect of the geometrical nonlinearity has been accounted for in the present formulation approximately since only the "average" bending deflection of the overlap area obtained from Section 7.2.2 is used in Equations (7.11) and (7.12) as indicated by the underlined terms, rather than the individual bending deflections of the skin and doubler as it would be required in an *exact* nonlinear analysis. However, by using such approximation, Equations (7.11) and (7.12) will provide a system of linear differential equations that can be solved by an appropriate numerical method.

The equilibrium Equations (7.11) and (7.12) do not provide the complete equations for solving the adhesive peel and shear stresses. Additional equations that must be considered are the kinematics and constitutive relationships for the skin, doubler and adhesive, and they are given below:

For the *i*th segment of the skin:

$$
\begin{aligned}
u_{si} &= \bar{u}_{si} + z\tilde{\beta}_{si} \\
\tilde{\beta}_{si} &= -w'_{si} \\
\bar{u}'_{si} &= \frac{D_s}{D_s A_s - B_s^2} N_{si} - \frac{B_s}{D_s A_s - B_s^2} M_{si} \\
\tilde{\beta}'_{si} &= -\frac{B_s}{D_s A_s - B_s^2} N_{si} + \frac{A_s}{D_s A_s - B_s^2} M_{si}
\end{aligned}
\tag{7.13}
$$

For the *i*th segment of the doubler or patch:

$$
\begin{aligned}
u_{pi} &= \bar{u}_{pi} + z\tilde{\beta}_{pi} \\
\tilde{\beta}_{pi} &= -w'_{pi} \\
\bar{u}'_{pi} &= \frac{D_{pi}}{D_{pi} A_{pi} - B_{pi}^2} N_{pi} - \frac{B_{pi}}{D_{pi} A_{pi} - B_{pi}^2} M_{pi} \\
\tilde{\beta}'_{pi} &= -\frac{B_{pi}}{D_{pi} A_{pi} - B_{pi}^2} N_{pi} + \frac{A_{pi}}{D_{pi} A_{pi} - B_{pi}^2} M_{pi}
\end{aligned}
\tag{7.14}
$$

For the *i*th segment of the adhesive:

$$\sigma_{\mathrm{A}i} = \frac{E_{\mathrm{A}}}{t_{\mathrm{A}}}\left(w_{\mathrm{p}i} - w_{si}\right)$$
$$\tau_{\mathrm{A}i} = \frac{G_{\mathrm{A}}}{t_{\mathrm{A}}}\left(\bar{u}_{\mathrm{p}i} - \frac{t_{\mathrm{p1}}}{2}\beta_{\mathrm{p}i} - \bar{u}_{si} - \frac{t_{\mathrm{s}}}{2}\beta_{si}\right) \tag{7.15}$$

In Equations (7.13)–(7.15), u and $\bar{u}$ denote the extensional displacements measured at an arbitrary z plane and at a reference plane, respectively; $\tilde{\beta}$ is a rotation; A, B and D are the extensional, coupling and flexural rigidities and they are defined according to the classical laminate theory as

$$A = \sum_{k=1}^{n_{\mathrm{ply}}}\left(C_{11,k}\right)\left\{z_k - z_{k-1}\right\}$$
$$B = \frac{1}{2}\sum_{k=1}^{n_{\mathrm{ply}}}\left(C_{11,k}\right)\left\{\left(z_k - h_0\right)^2 - \left(z_{k-1} - h_0\right)^2\right\} \tag{7.16}$$
$$D = \frac{1}{3}\sum_{k=1}^{n_{\mathrm{ply}}}\left(C_{11,k}\right)\left\{\left(z_k - h_0\right)^3 - \left(z_{k-1} - h_0\right)^3\right\}$$

where h_0 is the z-coordinate of the reference plane; and the rest are previously defined. It is worthy to note that A_{s}, B_{s} and D_{s} are constant along the joint due to the uniformity of the skin plate so that the subscript i denoting the segment number has been dropped in these quantities for clarity. In contrast, $A_{\mathrm{p}i}$, $B_{\mathrm{p}i}$ and $D_{\mathrm{p}i}$ are expected to vary from segment to segment depending on the doubler thickness and its lay-up composition within each segment. For all segments of the skin and doubler, h_0 is always chosen to be equal to $\frac{t_{\mathrm{s}}}{2}$ for the skin and $\frac{t_{\mathrm{p1}}}{2}$ for the doubler to be consistent with the definition of bending moments stated earlier in this section for them.

By substituting Equation (7.15) for $\sigma_{\mathrm{A}i}$ and $\tau_{\mathrm{A}i}$ into Equations (7.11) and (7.12), the resulting equations together with (7.13) and (7.14) can be rewritten into a system of first-ordered differential equations as follows for each segment i:

$$\left\{\varphi_i'\right\} = \left[\Psi\right]_i\left\{\varphi_i\right\} = \begin{bmatrix}\left[\Psi_{11}\right]_i & \left[\Psi_{12}\right]_i \\ \left[\Psi_{21}\right]_i & \left[\Psi_{22}\right]_i\end{bmatrix}\left\{\varphi_i\right\} \tag{7.17}$$

where

$$\{\varphi_i\} = \begin{Bmatrix} \bar{u}_{si} \\ w_{si} \\ \tilde{\beta}_{si} \\ N_{si} \\ M_{si} \\ V_{si} \\ \bar{u}_{pi} \\ w_{pi} \\ \tilde{\beta}_{pi} \\ N_{pi} \\ M_{pi} \\ V_{pi} \end{Bmatrix}; [\Psi_{11}]_i = \begin{bmatrix} 0 & 0 & 0 & \frac{D_s}{D_s A_s - B_s^2} & \frac{-B_s}{D_s A_s - B_s^2} & 0 \\ 0 & 0 & -1 & 0 & 0 & 0 \\ 0 & 0 & 0 & \frac{-B_s}{D_s A_s - B_s^2} & \frac{A_s}{D_s A_s - B_s^2} & 0 \\ \frac{G_A}{t_A} & 0 & \frac{G_A}{t_A}\left(\frac{t_s}{2}\right) & 0 & 0 & 0 \\ \frac{G_A}{t_A}\left(\frac{t_s+t_A}{2}\right) & 0 & \frac{G_A t_s}{t_A}\left(\frac{t_s+t_A}{4}\right) & -\hat{w}_i' & 0 & 1 \\ 0 & \frac{E_A}{t_A} & 0 & 0 & 0 & 0 \end{bmatrix} \tag{7.18}$$

$$[\Psi_{12}]_i = \begin{bmatrix} 0 & 0 & 0 & 0 & 0 & 0 \\ 0 & 0 & 0 & 0 & 0 & 0 \\ 0 & 0 & 0 & 0 & 0 & 0 \\ -\frac{G_A}{t_A} & 0 & \frac{G_A}{t_A}\left(\frac{t_{p1}}{2}\right) & 0 & 0 & 0 \\ -\frac{G_A}{t_A}\left(\frac{t_s+t_A}{2}\right) & 0 & \frac{G_A t_{p1}}{t_A}\left(\frac{t_{p1}+t_A}{4}\right) & 0 & 0 & 0 \\ 0 & -\frac{E_A}{t_A} & 0 & 0 & 0 & 0 \end{bmatrix} \tag{7.19}$$

$$[\Psi_{21}]_i = \begin{bmatrix} 0 & 0 & 0 & 0 & 0 & 0 \\ 0 & 0 & 0 & 0 & 0 & 0 \\ 0 & 0 & 0 & 0 & 0 & 0 \\ -\frac{G_A}{t_A} & 0 & \frac{G_A}{t_A}\left(\frac{t_s}{2}\right) & 0 & 0 & 0 \\ \frac{G_A}{t_A}\left(\frac{t_{p1}+t_A}{2}\right) & 0 & \frac{G_A t_s}{t_A}\left(\frac{t_{p1}+t_A}{4}\right) & 0 & 0 & 0 \\ 0 & -\frac{E_A}{t_A} & 0 & 0 & 0 & 0 \end{bmatrix} \tag{7.20}$$

$$[\Psi_{22}]_i = \begin{bmatrix} 0 & 0 & 0 & \frac{D_{pi}}{D_{pi}A_{pi} - B_{pi}^2} & \frac{-B_{pi}}{D_{pi}A_{pi} - B_{pi}^2} & 0 \\ 0 & 0 & -1 & 0 & 0 & 0 \\ 0 & 0 & 0 & \frac{-B_{pi}}{D_{pi}A_{pi} - B_{pi}^2} & \frac{A_{pi}}{D_{pi}A_{pi} - B_{pi}^2} & 0 \\ \frac{G_A}{t_A} & 0 & -\frac{G_A}{t_A}\left(\frac{t_{p1}}{2}\right) & 0 & 0 & 0 \\ -\frac{G_A}{t_A}\left(\frac{t_{p1}+t_A}{2}\right) & 0 & \frac{G_A t_p}{t_A}\left(\frac{t_{p1}+t_A}{4}\right) & -\hat{w}_i' & 0 & 1 \\ 0 & \frac{E_A}{t_A} & 0 & 0 & 0 & 0 \end{bmatrix} \tag{7.21}$$

Equation (7.17), for $i = 1,\ 2, \ldots,\ N$, provides a system of $12 \times N$ first-order linear differential equations for N unknown vectors $\{\varphi_i\}$, which is subjected to the following boundary conditions:

(a) At the left end of the overlap area, with reference to Figure 7.4(a) the doubler is stress- and moment-free, thus $N_{p1}(0) = M_{p1}(0) = V_{p1}(0) = 0$, noting $i = 1$.

(b) In contrast, the stress, moment and shear resultants in the skin at the left overlap end are given respectively by $N_{s1}(0) = P$, $M_{s1}(0) = M_L + P\left(\hat{e}_0 - \frac{t_s}{2}\right)$ and $V_{s1}(0) = 0$, where M_L is obtained previously from the first step analysis in Section 7.2.2 and given by Equation (7.10). The fact that $M_{s1}(0) \neq M_L$ is because different reference planes have been used in the first and second step analyses in defining the bending moment of the skin. The reader is reminded that in the first step analysis, the bending moment M_L is defined with respect to the neutral axis (or neutral plane) of the skin while M_{s1} in the present analysis is defined with respect to the mid-plane of the skin. Unless the skin is a symmetric laminate or isotropic, in general, $\hat{e}_0 \neq \frac{t_s}{2}$ and thus $M_{s1}(0) \neq M_L$.

(c) In addition, since the reference plane for the computation of bending moment is selected to be the same throughout the overlap area for each adherend, the extensional and transverse deflections, the slope, and the normal stress, shear and moment resultants in the doubler and in the skin must be continuous across the segment junction. Thus,

$$\{\varphi(\ell_i)\}_i = \{\varphi(0)\}_{i+1} \tag{7.22}$$

(d) Finally, the (vertical) symmetry conditions at the middle of the overlap area require

$$\begin{aligned} \bar{u}_{sN}(\ell_N) &= \bar{u}_{pN}(\ell_N) = 0 \\ \tilde{\beta}_{sN}(\ell_N) &= \tilde{\beta}_{pN}(\ell_N) = 0 \\ V_{sN}(\ell_N) &= w_{pN}(\ell_N) = 0 \end{aligned} \tag{7.23}$$

It is worthy to note that the condition $w_{pN}(\ell_N) = 0$ is specified in lieu of $V_{pN}(\ell_N) = 0$ so that the unknown integration constant resulting from numerical integration of the transverse deflection can be uniquely determined. With these boundary conditions stated, the problem of determining adhesive peel and shear stresses in a doubler is completely formulated. Since the formulation of the two-sided doubler problem will be similar to that of a one-sided doubler, it will be presented here first before proceeding to the solution of Equation (7.17) with the boundary conditions listed in (a)–(d).

The governing equation for a one-sided doubler is still given by Equation (7.17) because of the similarity between the two configurations in the overlap area. However, there will be some difference in their boundary conditions. The boundary conditions listed as (a), (c) and (d) remain applicable to the double-sided doubler problem. However, the condition (b) needs to be changed as follows (see Figure 7.4(b)):

(b′) At the left overlap end,

$$N_{s1}(0) = P, \quad M_{s1}(0) = 0, \quad \text{and } w_{s1}(0) = 0 \tag{7.24}$$

It remains now to outline a numerical method for solving a set of differential equations given by Equation (7.17) along with boundary conditions listed either in (a)–(d) for a

one-sided doubler or in (a), (b′), (c) and (d) for a two-sided configuration. It was found in the earlier study by Thomsen (1992) and Thomsen et al. (1996) that the differential equation set (7.17) is most effectively solved by the so-called multi-segment method of integration, which is described in the following section.

Multi-segment method of integration

The differential equation set given by Equation (7.17) for $i = 1,\ 2, \ldots,\ N$, together with the boundary conditions listed in (a)–(d) or (a), (b′), and (c)–(d) constitute a multiple-point boundary value problem which can be expressed in the following general form:

$$\underset{12\cdot N\times 1}{\{\Phi'(x)\}} = \underset{12\cdot N\times 12\cdot N}{[\Lambda(x)]} \cdot \underset{12\cdot N\times 1}{\{\Phi(x)\}} \tag{7.25}$$

$$\underset{12\cdot N\times 12\cdot N}{[T_1]} \cdot \underset{12\cdot N\times 1}{\{\Theta_1\}} + \underset{12\cdot N\times 12\cdot N}{[T_2]} \cdot \underset{12\cdot N\times 1}{\{\Theta_2\}} = \underset{12\cdot N\times 1}{[G]} \tag{7.26}$$

where

$$\{\Phi\} = \begin{Bmatrix} \{\varphi_1\} \\ \{\varphi_2\} \\ \vdots \\ \{\varphi_N\} \end{Bmatrix}; \quad [\Lambda] = \begin{bmatrix} [\Psi]_1 & & & \\ & [\Psi]_2 & & \\ & & \ddots & \\ & & & [\Psi]_N \end{bmatrix} \tag{7.27}$$

$$\{\Theta_1\} = \begin{Bmatrix} \{\varphi_1(0)\} \\ \{\varphi_2(0)\} \\ \vdots \\ \{\varphi_N(0)\} \end{Bmatrix}; \quad \{\Theta_2\} = \begin{Bmatrix} \{\varphi_1(\ell_1)\} \\ \{\varphi_2(\ell_2)\} \\ \vdots \\ \{\varphi_N(\ell_N)\} \end{Bmatrix} \tag{7.28}$$

$[T_1]$, $[T_2]$ and $[G]$ are constant matrices known from the statements of the boundary conditions. It should be emphasized that the elements of matrices $\{\Theta_1\}$ and $\{\Theta_2\}$ are elements of $\{\Phi\}$ evaluated respectively at the beginning and end points of each segment i.

In the multi-segment method of integration, the boundary-value problem will be reduced to a series of initial-value problems as follows (Kalnins, 1964). Assuming that the solution of (7.25) can be written as

$$\underset{12\cdot N\times 1}{\{\Phi(x)\}} = \underset{12\cdot N\times 12\cdot N}{[\Omega(x)]} \cdot \underset{12\cdot N\times 1}{\{L\}} \tag{7.29}$$

where vector $\{L\}$ represents $12 \cdot N$ arbitrary constants, and $[\Omega(x)]$ is defined as the homogeneous solution of Equation (7.25) in the form

$$\underset{12\cdot N\times 12\cdot N}{[\Omega'(x)]} = \underset{12\cdot N\times 12\cdot N}{[\Lambda(x)]}\ \underset{12\cdot N\times 12\cdot N}{[\Omega(x)]} \tag{7.30}$$

The initial conditions for determining $[\Omega(x)]$ is

$$[\Omega(0)] = [I] \tag{7.31}$$

where $[I]$ is the identity matrix. A numerical integration scheme for obtaining this homogeneous solution will be detailed later. However, for the present discussion purpose, let us assume that the initial-value problem has been solved with its homogeneous solution denoted symbolically as $[\Omega(x)]$.

Evaluation of Equation (7.29) at $x = 0$ leads to $\{\Phi(0)\} = [\Omega(0)]\{L\}$, which upon substitution of Equation (7.31) for $[\Omega(0)]$ and noting from the first equations of (7.27) and (7.28) that $\{\Phi(0)\} = \{\Theta_1\}$, yields

$$\{\Theta_1\} = \{L\} \tag{7.32}$$

Thus, Equation (7.29) can be expressed as

$$\{\Phi(x)\} = [\Omega(x)]\{\Theta_1\} \tag{7.33}$$

The next step is to relate $\{\Theta_2\}$ to $\{\Theta_1\}$. Since elements of matrix $\{\Theta_2\}$ are elements of $\{\Phi\}$ evaluated at the end point of each segment i, an evaluation of Equation (7.33) at these end points will give the desired relationship between $\{\Theta_2\}$ and $\{\Theta_1\}$, i.e.,

$$\{\Theta_2\} = \{\Phi(x)\}|_{x=\text{segment endpoint}} = [\Omega(x)]|_{x=\text{segment endpoint}}\{\Theta_1\} \tag{7.34}$$

Equation (7.34) together with Equation (7.26) provides a system of algebraic equations for solving $\{\Theta_1\}$ and $\{\Theta_2\}$. Once $\{\Theta_1\}$ and $\{\Theta_2\}$ are solved, the solution at any value of x is obtained from Equation (7.33). In summary, the solution of the multiple-point boundary-value problem can be obtained by the following steps: (i) solving the initial-value problem with the governing differential equations given by Equation (7.30) and the initial conditions by Equation (7.31) for $[\Omega(x)]$, then (ii) solving the system of algebraic equations for $\{\Theta_1\}$ and $\{\Theta_2\}$ using Equations (7.34) and (7.26), and finally (iii) evaluating Equation (7.33) at any point of interest for its solution.

So far the homogeneous solution of the initial-value problem has been assumed to be already solved and denoted symbolically as $[\Omega(x)]$ in the preceding paragraphs. Thus, a brief description of a suitable numerical method for obtaining $[\Omega(x)]$ will be given here. Differential Equation (7.30) and initial condition (7.31) are compact forms of the following set of differential equations and initial condition:

$$\frac{\mathrm{d}}{\mathrm{d}x}\underset{12\cdot N\times 1}{\{\Omega_j\}} = \underset{12\cdot N\times 12\cdot N}{[\Lambda]}\ \underset{12\cdot N\times 1}{\{\Omega_j\}} \quad (j = 1, \ldots, 12\cdot N) \tag{7.35}$$

$$\{\Omega_j(0)\} = \{\delta_j\} \tag{7.36}$$

where $\{\Omega_j\}$ is a vector corresponding to a jth column of matrix $[\Omega(x)]$, and $\{\delta_j\}$ is a vector with all of its components null except for the jth component where it has a value of 1. Differential Equation (7.30) in its standard form of Equation (7.35) can be solved by means of any method of direct numerical integration. In the present analysis the direct integration was performed using adaptive step-size fourth- and fifth-order Runge–Kutta–Fehlberg method. A Fortran subroutine of this integration method is available in the Internet and was used by Duong in the above-cited reference (2006).

Throughout this section the number of segments for solving the adhesive peel and shear stresses has been chosen to be identical to that number of steps in the doubler overlap length as shown in Figure 7.4, i.e., $i = 1,\ 2, \ldots,\ N$. However, as discussed by Kalnins (1964), the solution obtained by the multi-segment method of integration may suffer a complete loss of accuracy at some critical length of the interval. Thus, if the length of the segment in the analysis exceeds this critical length, the obtained solution will be inaccurate. Nevertheless, the loss of accuracy of the solution can be avoided by subdividing the length of each segment into many sub-segments. Since these sub-segments can be treated identically as the original segments, the formulation in that case for adhesive peel and shear stresses will remain very much the same as before. For example, let assume that due to these segment's subdivisions the total number of segments increases from N to $N+m$ ($m > 0$), the formulation outlined in Section 7.2.3 will remain the same for this latter case except that (a) N is changed to $N+m$ in all related equations, and (b) $A_{\mathrm{p}i}$, $B_{\mathrm{p}i}$ and $D_{\mathrm{p}i}$ do not always vary from segment to segment and ℓ_i is now the sub-segment length.

7.2.4 Numerical examples

The present approach will be demonstrated first with numerical examples of untapered doublers with identical adherends. This is because closed-form solutions for these configurations are available in Chapter 2 for direct comparison with the results obtained from the present approach. In the first example, a one-sided doubler with two identical isotropic adherends is considered. The geometry and material properties of the skin, doubler and adhesive as well as the applied load per unit width P are given below:

- Skin and doubler, isotropic, $E_{\mathrm{s}} = E_{\mathrm{p}} = 68.95\,\mathrm{GPa}$, $\nu_{\mathrm{s}} = \nu_{\mathrm{p}} = 0.3$, $t_{\mathrm{s}} = t_{\mathrm{p}}$ (full patch thickness, i.e., $t_{\mathrm{p}N}$) $= 1.27\,\mathrm{mm}$, where the subscripts s and p denote skin and doubler, respectively.
- Adhesive: isotropic, $E_{\mathrm{A}} = 1.793\,\mathrm{GPa}$, $G_{\mathrm{A}} = 0.6895\,\mathrm{GPa}$, $t_{\mathrm{A}} = 0.127\,\mathrm{mm}$.
- Geometry: $\ell_0 = 25.4\,\mathrm{cm}$, overlap length is 6.35 cm.
- Tensile load: $P/t_{\mathrm{s}} = 137.9\,\mathrm{MPa}$.

Analytical solutions for this example problem using geometrically linear and nonlinear formulations in step 2 of the present approach are presented in Figures 7.5 and 7.6 for the adhesive peel and shear stresses, respectively, and these solutions for brevity will be simply referred to as linear and nonlinear solutions in all the following discussions. For comparison purpose, the corresponding Hart-Smith solutions presented in Section 2.3 of Chapter 2 are also shown in these figures along with the newly obtained solutions. It is found from Figures 7.5 and 7.6 that the present linear solution for the peak adhesive peel stress is in better agreement with the corresponding Hart-Smith solution than the nonlinear solution. However, an opposite trend is observed for the peak adhesive shear stress, in which a nonlinear solution is preferred to the linear solution. This abnormality can be explained as follows.

From Chapter 2, the Hart-Smith solution (2005b) for the adhesive peel utilizes the moment boundary condition at the end of the overlap and the condition of no net

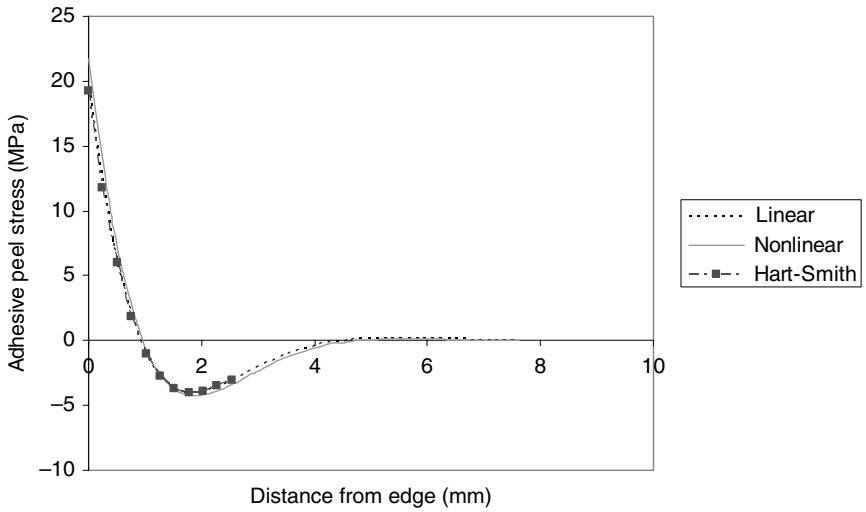

Fig. 7.5. Distribution of adhesive peel stress in an untapered one-sided doubler with $t_s = t_p =$ 1.27 mm.

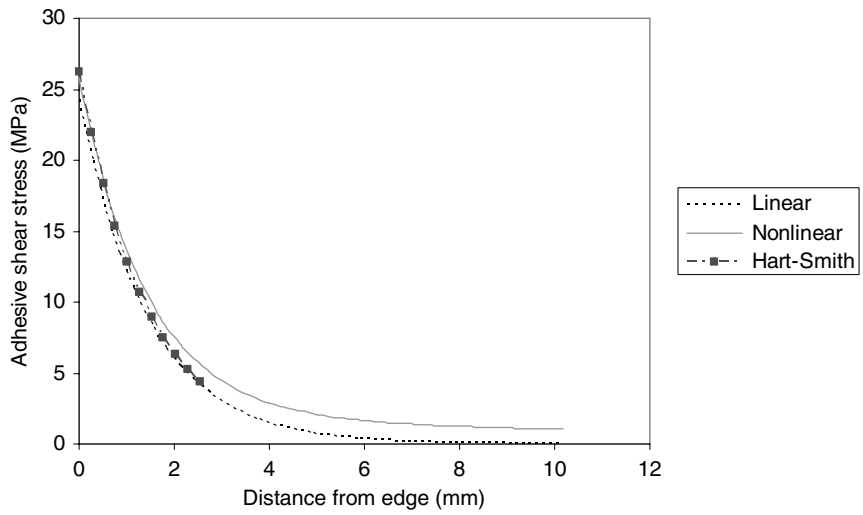

Fig. 7.6. Distribution of adhesive shear stress in an untapered one-sided doubler with $t_s = t_p =$ 1.27 mm.

resulting peel force across the interface for determining its unknown constants. The second boundary condition is equivalent to the condition that the vertical shear is zero at the overlap end. Since the adhesive stress analysis in the Hart-Smith second step is geometrically linear with all boundary conditions equivalently imposed at the end of the overlap, his peel stress solution therefore should be similar to the present linear result.

On the other hand, the adhesive shear stress solution has been derived using the same moment boundary condition at the overlap end as well as the implicitly zero bending moment condition at the middle of the doubler. This zero moment condition at the middle of the doubler is obtained from the first step geometrically nonlinear analysis for a doubler configuration with a long overlap length. It recalls that one of the boundary conditions for the adhesive shear stress in Section 2.3.3 is given by Equation (2.166) where it has been derived from the boundary condition (2.164) with the stress resultant $N_p(0)$ of the patch evaluated based on the zero moment condition at the middle of the doubler configuration. When the bending moment at the middle of the overlap is equal to zero, the stresses in the skin and doubler will be uniform across their thickness, and for a balanced doubler they are the same and equal to one half of the far-field stress. Even though the bending analysis in the second step for computing adhesive shear is considered to be a geometrically linear analysis, however, as explained later, the use of the second boundary condition at the middle of the overlap based on results of the first step nonlinear analysis will make Hart-Smith's analysis inconsistent. In other words, a truly linear analysis of Hart-Smith second step will require rather a different boundary condition at the middle of the doubler than the one specified in his analysis.

The second step analysis of the present approach for a doubler configuration always utilized the moment boundary conditions at the overlap end and the symmetric condition at the middle of the joint, regardless of the analysis type, i.e., linear or nonlinear analysis. However, upon solving the governing differential equations, this same symmetry condition will yield different solution for the normal stress and moment resultants at the middle of the doubler, depending on the type of the analysis, as demonstrated in Figures 7.7 and 7.8. This can be seen further by considering an example of a long doubler configuration under a high applied load. For a very long overlap length and for a high

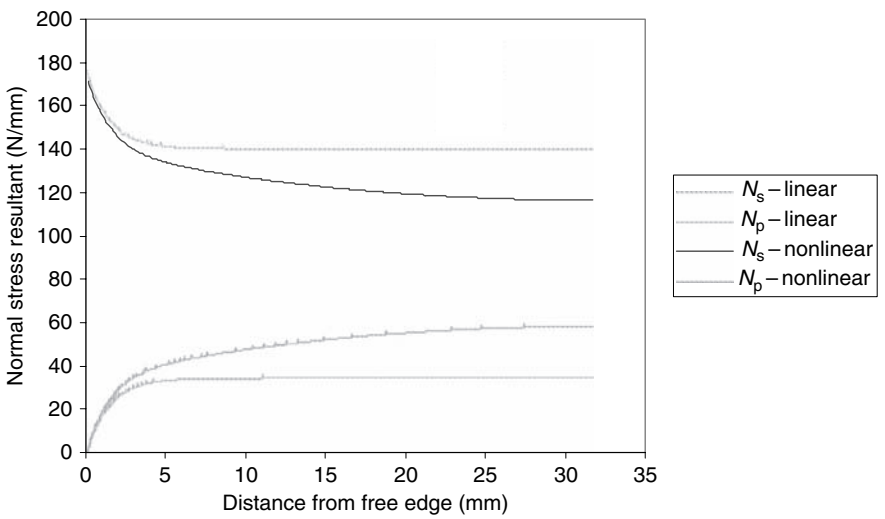

Fig. 7.7. Distribution of normal stress resultant in an untapered one-sided doubler with $t_s = t_p =$ 1.27 mm.

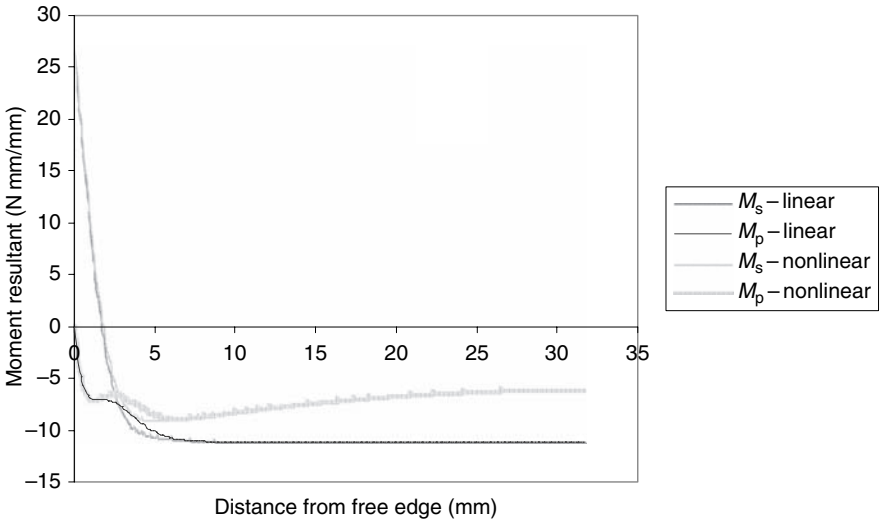

Fig. 7.8. Distribution of moment resultant in an untapered one-sided doubler with $t_s = t_p = 1.27\,\text{mm}$.

applied load, adhesive peel and shear stresses will be decayed to zero near the middle area of the overlap, and the skin and doubler will act as if they are rigidly bonded there. The bending moment at the middle of the overlap, therefore, as predicted by the first step nonlinear analysis, will be zero. If the second step is performed within a linear theory, the present approach will not necessarily yield the same zero bending moment condition there even for this extreme case of a very long overlap length and with high applied load. This is because the condition at the middle of the joint can be determined solely from considering the static moment equilibrium of the overlap area without explicitly solving the differential equations. From static moment equilibrium, there is always a bending moment at the middle of the overlap which from the inset of Figure 7.3 is equal to $P(\hat{e}_N - \hat{e}_0)$, noting transverse shear $V = 0$ there due to vertical symmetry. On the other hand, a second step analysis performed within a geometrically nonlinear theory will predict the zero bending moment condition at the joint middle as expected, since (a) the underlined nonlinear terms in the governing Equations (7.11) and (7.12) make the overlap area statically indeterminate so that the static moment equilibrium condition alone can not be used to determine the bending moment there, and (b) through inclusion of these nonlinear terms, the effect of the alignment of the neutral plane of the middle area of the overlap with the line of load on the bending moment distribution is correctly accounted for. In light of the above discussion, the Hart-Smith second step analysis for the adhesive shear stress will not be truly a linear analysis since it has used implicitly but inconsistently the zero bending moment at the joint middle. Such inconsistency is believed to make his adhesive shear stress solution being in a closer agreement with the present nonlinear result.

To validate the above claim, the above analysis for the one-sided configuration is repeated with a much thinner skin and doubler $\left(t_s = t_p = 0.254\,\text{mm}\right)$ where the effect of geometrical nonlinearity is more pronounced. It is worthy to note that the chosen

thicknesses of the skin and doubler in the current analysis are unrealistically small for typical joints used in practice; however, they are only used here to demonstrate the extreme difference between linear and nonlinear solutions of the adhesive stresses. Adhesive stress results from the new analysis are presented and compared with Hart-Smith solutions in Figures 7.9 and 7.10. Again, these new results follow the same trend

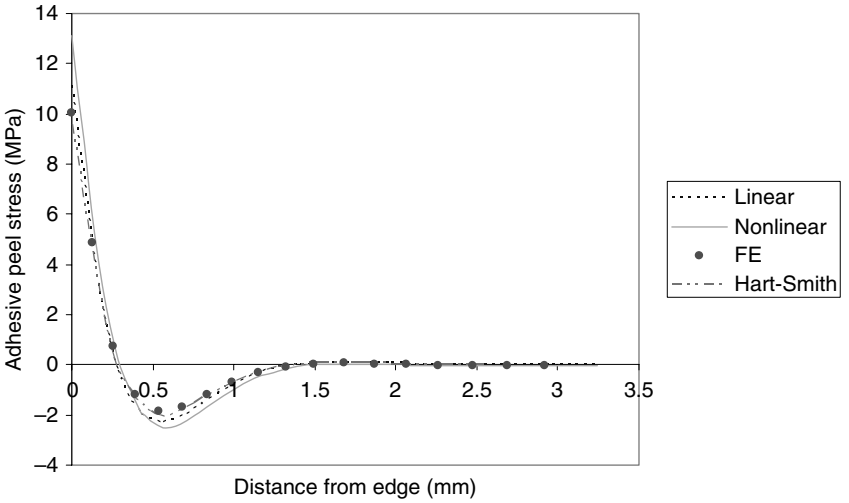

Fig. 7.9. Distribution of adhesive peel stress in an untapered one-sided doubler with $t_s = t_p =$ 0.254 mm.

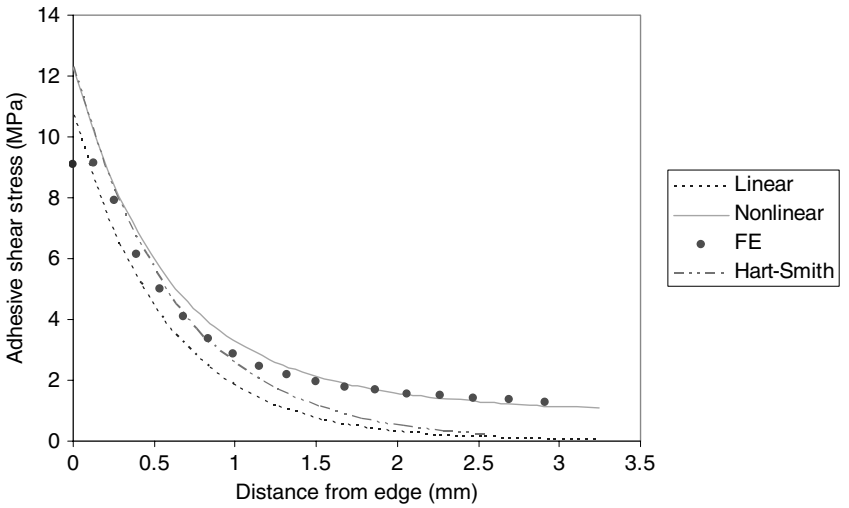

Fig. 7.10. Distribution of adhesive shear stress in an untapered one-sided doubler with $t_s = t_p =$ 0.254 mm.

Table 7.1. Normal stress and moment resultants in the skin and doubler at their middle.

Analysis	Normal stress resultant in a skin (N/mm)	Normal stress resultant in a doubler (N/mm)	Moment resultant in a skin (N mm/mm)	Moment resultant in a doubler (N mm/mm)
Nonlinear	17.72	17.30	−0.0086	−0.0086
Linear	28.93	6.09	−0.48	−0.48

when compared with Hart-Smith solutions for this extreme case. For reference, the normal stress and moment resultants in the skin and in a doubler at their middle are also reported in Table 7.1. It is clear from Table 7.1 that the nonlinear solution indicates a nearly zero bending moment at the middle of the overlap as expected, but not the linear solution.

So far the solutions of the present approach have been compared with the existing close-form solutions. It is also of interest to compare the new solution with the FE result. The previous solutions for the case of extremely thin skin and doubler $\left(t_s = t_p = 0.254\,\text{mm}\right)$ are compared with the FE results in Figures 7.9 and 7.10. In the FE analysis, the bottom adherend, the doubler or upper adherend and the adhesive are modeled by 2-D isoparametric elements. Due to symmetry, only half of the doubler joint configuration is modeled in the FE analysis with one end being simply supported and the other end at the vertical center line being imposed with symmetric condition (fixed longitudinal displacement and zero transverse force). The FE analyses were carried out by using MSC/NASTRAN code (2001) with geometrically nonlinear solution (Solution 106) and under plane stress condition. In Figures 7.9 and 7.10, the peel and shear stresses from the FE analyses are computed at the mid-plane of the adhesive layer, which are roughly equal to the average stresses across the adhesive thickness.

It has been shown in Chapter 2 that the adhesive stresses in the joint at the corner of its overlap ends are singular. The adhesive stresses therefore become mesh dependent there. In that regard, a comparison between the present solution and the FE result needs some physical interpretation. It also has been suggested in Chapter 2 that the failure in the adhesive can be predicted by using a stress intensity parameter of that corner singularity. Similar to the conventional linear elastic fracture mechanics approach, the corner stress intensity factor approach assumes that the adhesive will fail if its corner stress intensity factor reaches a critical value determined from the test (Groth, 1988; Reedy and Guess, 1997; Wang and Rose, 2000). Through a boundary layer type analysis and using a FE method, Wang and Rose (2000) further showed that these stress intensity factors can be estimated from the outer boundary layer adhesive peel and shear stresses via Equation (2.182). The outer boundary layer adhesive peel and shear stresses are those obtained from closed-form methods. Thus, within the corner singularity context, the present solutions for the peak adhesive peel and shear stresses probably should be compared with the corresponding FE results near the overlap end but outside the corner singularity–dominant region where the mesh dependency poses an interpretation problem.

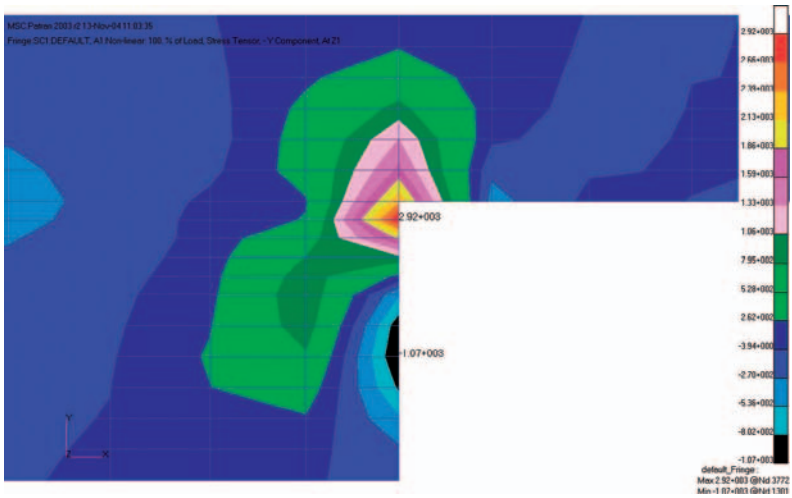

Fig. 7.11. Two dimensional distribution of adhesive peel stress in an untapered one-sided doubler with $t_s = t_p = 0.254$ mm.

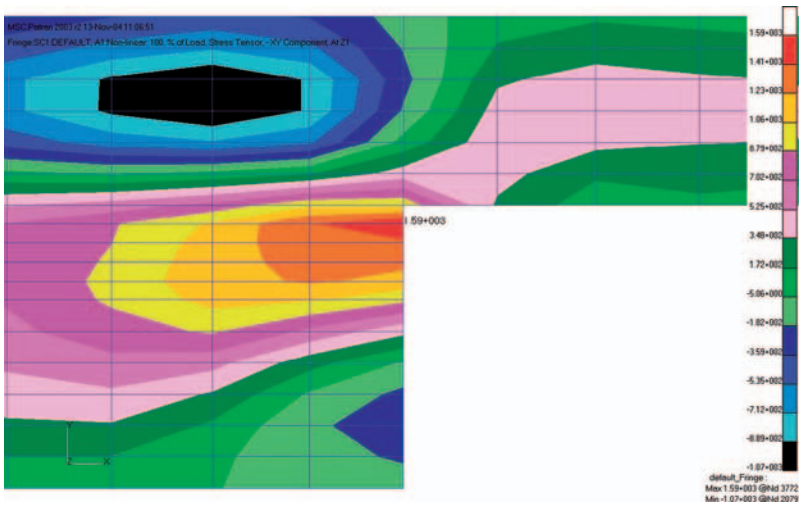

Fig. 7.12. Two dimensional distribution of adhesive shear stress in an untapered one-sided doubler with $t_s = t_p = 0.254$ mm.

The two dimensional stress distributions in the adhesive near an end of the overlap for the case of an extremely thin skin and doubler are plotted in Figures 7.11 and 7.12. Stresses in these fringe plots have been scaled by a factor roughly equal to 145, i.e., a stress value of 1000 in these fringe plots corresponds to 6.89 MPa. From Figure 7.12, the adhesive shear stress at the corner appears to attain the same high value over a

quite large zone. This corner shear stress value is therefore considered as the outer boundary layer type of stress to be compared with the analytical solution. This stress is found to be around 11 MPa for a thin doubler configuration. In contrast, the plot of the adhesive peel stresses from Figure 7.11 shows a much steeper stress gradient near the corner. However, by considering the peel stress at a distance of roughly one half adhesive thickness[1] away from the free edge as the outer boundary layer stress for comparison with analytical predictions, this peel stress is found to be 12.8 MPa and is very close to the analytical prediction. Another way to compare the two-dimensional FE results with the analytical predictions is to use the averaged adhesive peel and shear stresses across the thickness of the adhesive in the comparison as had been done in Figures 7.9 and 7.10. It is also interesting to note that the linear prediction of the peak adhesive shear stress is in better agreement with FE results than the nonlinear prediction (see Figure 7.10). In contrast, the nonlinear predictions tend to agree better with the FE results on the adhesive shear distribution over entire overlap length as shown in Figure 7.10.

Intuitively, the former observation appears to contradict with a normal expectation in which the nonlinear solution for the peak adhesive shear stress that assumes to be more accurate does not provide a better agreement with the FE results. However, as found in Oplinger (1994) and Tsai and Morton (1994), the bending moment distribution along the joint in the Goland–Reissner approach (1944) for a single-lap joint is inconsistent and may be inaccurate when compared with the FE results for some joint configurations. In contrast, the Goland–Reissner solutions for the adhesive stresses based on a second step linear bending analysis are very adequate. Thus, any error accrued from the first step analysis seems to be negated by the error introduced in the second step. Based on these findings, an improvement of the second step analysis alone without the first by including the nonlinear terms in the formulation may not lead to an overall improvement of adhesive stresses since any error accrued from the first step will remain through the rest of the analysis, assuming that the second step analysis is exact.

Having verified the present solutions for non-tapered joints and doublers with FE results and with Hart-Smith closed-form solutions in the preceding paragraphs, it remains now to demonstrate the solutions of a tapered doubler. Corresponding solutions to the previous first example problem but with a tapered edge doubler (Figure 7.13) are presented in Figures 7.14 and 7.15 for the adhesive peel and shear stresses, respectively. In the latter analysis, the doubler is tapered at its edge by a slope of 1:10 with the minimum thickness t_{p1} of 0.127 mm at the tip as shown in Figure 7.13. From Figures 7.14 and 7.15, it is clear that the effect of edge tapering is to reduce the peak adhesive stresses, as expected. However, except at the edge, the adhesive shear stresses are not peaked at the beginning of each step of the multiple-step tapered region as predicted by the classical non-bending solutions.

[1] Since the element size in that meshing area is about one adhesive thickness, adhesive peel stresses to be compared with analytical predictions are calculated close to the centroid of a most critical element at the free edge.

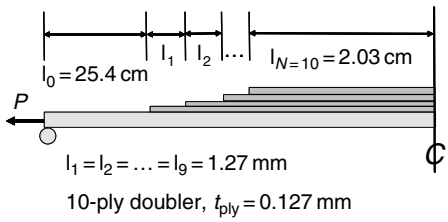

Fig. 7.13. Geometry of a balanced one-sided doubler with a taper ratio of 10:1 and $t_s = 1.27$ mm.

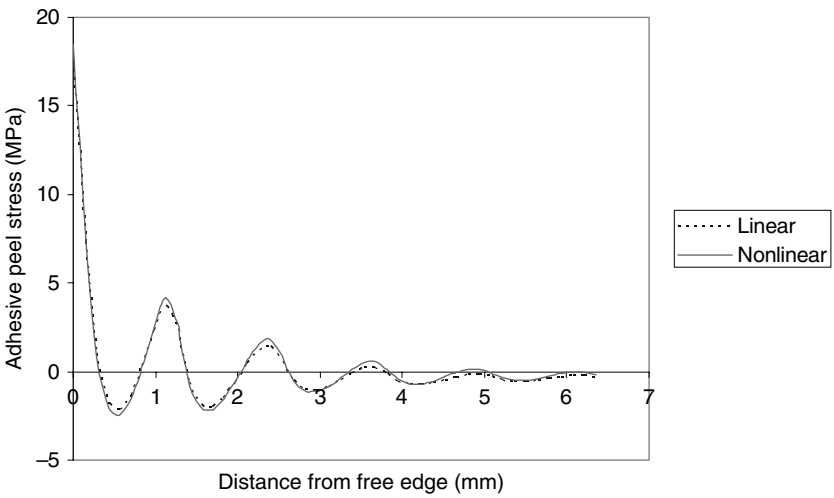

Fig. 7.14. Distribution of adhesive peel stress in a balanced one-sided doubler with a taper ratio of 10:1 and $t_s = 1.27$ mm.

To examine the effect of different doubler thickness on the adhesive stresses, the above analysis is repeated for full patch thickness $t_p = 2.54$ mm. Results from that analysis for an unbalanced doubler are presented in Figures 7.16 and 7.17. Compared to the previous results for $t_p = 1.27$ mm, the adhesive stresses are worst for a thicker doubler, especially in a shear component, as expected.

It remains now to demonstrate a solution of a tapered two-sided doubler example. A problem similar to example 1 but with two symmetrical doublers is analyzed. For a direct comparison with the one-sided doubler result, the thickness of the skin and the load of the two-sided doubler configuration will be twice of those considered in example 1 so that the ratio of the (total two) doubler stiffness to the skin stiffness and the total load of the two problems remain the same. The adhesive peel and shear stresses along the overlap length of a two-sided configuration are plotted in Figures 7.18 and 7.19, respectively.

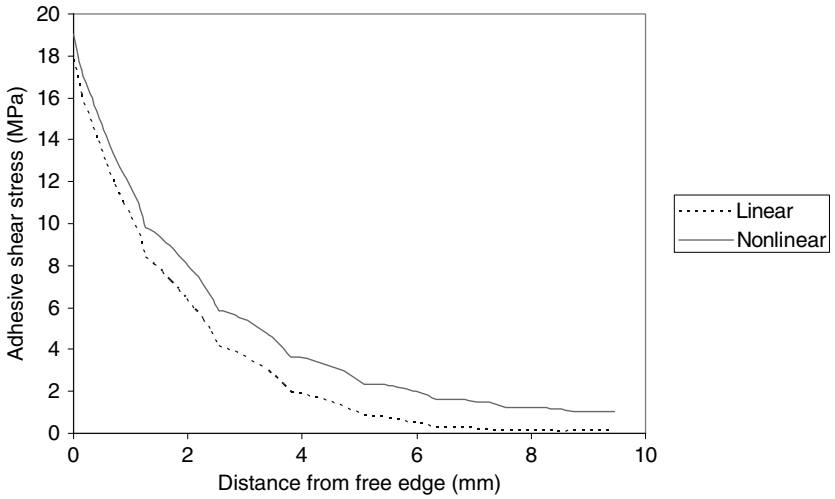

Fig. 7.15. Distribution of adhesive shear stress in a balanced one-sided doubler with a taper ratio of 10:1 and $t_s = 1.27\,\text{mm}$.

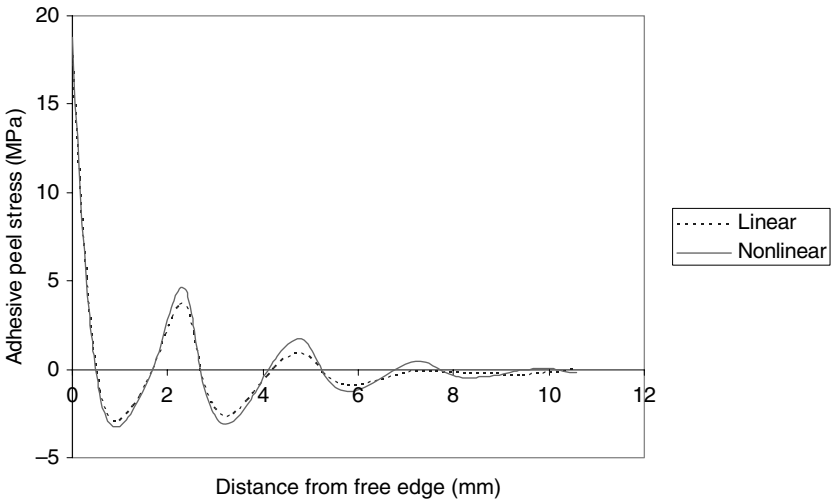

Fig. 7.16. Distribution of adhesive peel stress in a stiff one-sided doubler with a taper ratio of 10:1, $t_s = 1.27\,\text{mm}$, and full thickness $t_p = 2.54\,\text{mm}$.

7.3 One-Dimensional Analysis of Tapered Patches and Doublers Including Effects of Thermal Mismatch and Adhesive Plasticity

For clarity, the solution approach delineated in Section 7.2 did not account for the effect of the thermal mismatch nor the effect of adhesive plasticity. The purpose of this section therefore is to extend that approach to include these latter effects.

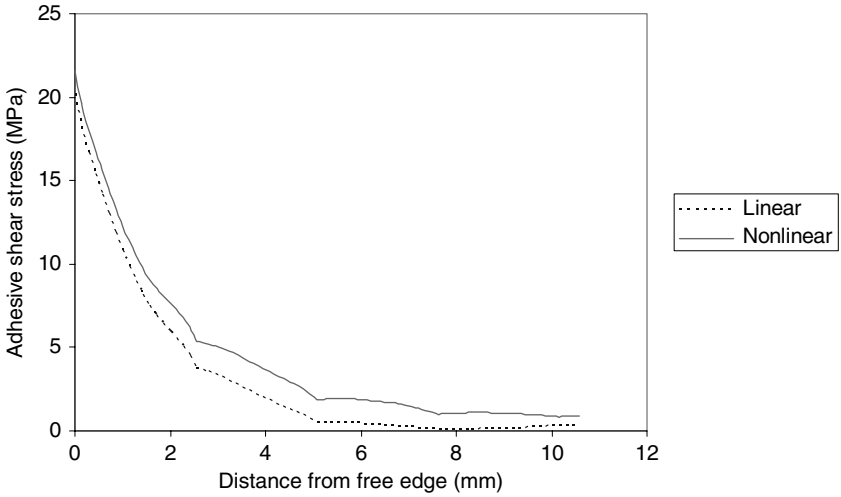

Fig. 7.17. Distribution of adhesive shear stress in a stiff one-sided doubler with a taper ratio of 10:1, $t_s = 1.27$ mm, and full thickness $t_p = 2.54$ mm.

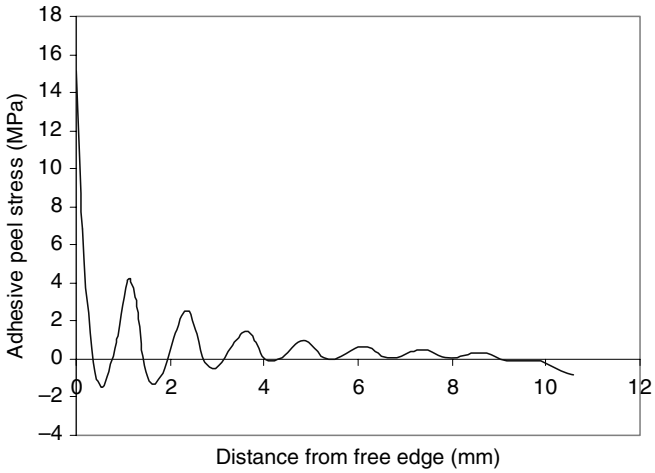

Fig. 7.18. Distribution of adhesive peel stress in a balanced two-sided doubler with a taper ratio of 10:1, $t_s = 2.54$ mm and a full thickness of each doubler equal to 1.27 mm.

7.3.1 Extension to include the effect of thermal mismatch

Following the similar procedure as in Section 7.2.2, the moment distribution in each segment along the joint is given by

$$M_i = -P \cdot \hat{w}_i - P\,(\hat{e}_i - \hat{e}_0) + M_i^{(\text{therm})} \tag{7.37}$$

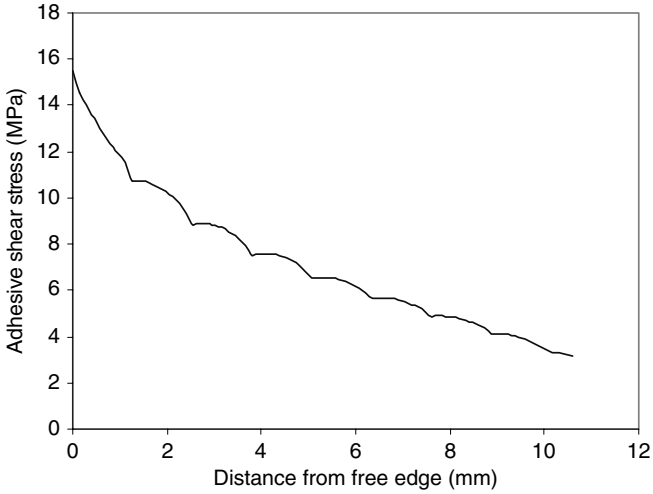

Fig. 7.19. Distribution of adhesive shear stress in a balanced two-sided doubler with a taper ratio of 10:1, $t_s = 2.54$ mm, and a full thickness of each doubler equal to 1.27 mm.

where

$$M_i^{(\text{therm})} = \frac{\left\{\sum_{k=1}^{n_{\text{ply}}} \left(C_{11,k}\right)_i \left(\left(\alpha_{11,k}\right)_i \left(Z_{k,i} - Z_{k-1,i}\right) \Delta T\right)\right\} \cdot \left\{\sum_{k=1}^{n_{\text{ply}}} \left(C_{11,k}\right)_i \left\{\left(z_{k,i} - \hat{e}_i\right)^2 - \left(z_{k-1,i} - \hat{e}_i\right)^2\right\}\right\}}{2\sum_{k=1}^{n_{\text{ply}}} \left(C_{11,k}\right)_i \left(Z_{k,i} - Z_{k-1,i}\right)}$$

$$- \frac{1}{2}\sum_{k=1}^{n_{\text{ply}}} \left(C_{11,k}\right)_i \left\{\left(z_{k,i} - \hat{e}_i\right)^2 - \left(z_{k-1,i} - \hat{e}_i\right)^2\right\} \alpha_{k,i} \Delta T \tag{7.38}$$

$\left(\alpha_{11,k}\right)_i$ is the (1,1) element of the thermal expansion coefficient tensor of the kth ply of the ith segment, n_{ply} indicates a number of plies in the segment, and the rest has been previously defined. For any segment outside the overlap, n_{ply} is the total number of plies in the skin laminate. In contrast, it will be the total number of plies of the skin–patch combination for any segment inside the overlap. It is worthy to note that $M_i^{(\text{therm})}$ defined in Equation (7.38) was derived from the following condition and definitions:

$$\begin{aligned} N_i^{(\text{therm})} &= \int_0^{t_i} C_{11,i} \left(\hat{\varepsilon}_i^{(\text{therm})} - \alpha_{11,i} \Delta T\right) \, \mathrm{d}z = 0 \\ M_i^{(\text{therm})} &= \int_0^{t_i} C_{11,i} \left(\hat{\varepsilon}_i^{(\text{therm})} - \alpha_{11,i} \Delta T\right) (z - \hat{e}_i) \, \mathrm{d}z \end{aligned} \tag{7.39}$$

where $\alpha_{11,i} \equiv \alpha_{11,i}(z)$, $C_{11,i} \equiv C_{11,i}(z)$, while $\hat{\varepsilon}_i^{(\text{therm})}$, $\hat{e}_i$, and ΔT are independent of coordinate z; $\hat{\varepsilon}_i^{(\text{therm})}$ is the total strain due to the thermal mismatch and yet to be determined from first equation of (7.39); t_i is the thickness of segment i, e.g., $t_i \equiv t_s$ for $i = 0$, and $t_i \equiv t_s + t_p$ for $i = N$. The first equation of (7.39) is deducted from the condition that the thermally induced stress resultant must be equal to zero. It is

worthy to note that $N_i^{(\text{therm})}$ and $M_i^{(\text{therm})}$ defined in Equations (7.38) and (7.39) have been derived for the case of a uniform temperature change. Thus, strictly speaking, the present analysis can only be used to address the effect of the thermal mismatch due to a low operating temperature. However, by adopting the Rose's or Barnevel-Freddel's curing model mentioned in Section 5.5.1 of Chapter 5, the effect of thermal mismatch due to curing of the adhesive can also be addressed approximately within the context of the present analysis by using an effective thermal expansion coefficient for the skin, rather than its real thermal expansion coefficient.

With that, the governing differential equations for bending moment distribution for each segment i then become

$$\hat{w}_i'' - \frac{P}{D_i}\hat{w}_i = \frac{P\,(\hat{e}_i - \hat{e}_0)}{D_i} - \frac{M_i^{(\text{therm})}}{D_i} \tag{7.40}$$

with the corresponding solutions given by

$$\hat{w}_i\,(x_i) = W_{1i}\cosh\,(\xi_i x_i) + W_{2i}\sinh\,(\xi_i x_i) - (\hat{e}_i - \hat{e}_0) + \frac{M_i^{(\text{therm})}}{P} \tag{7.41}$$

The unknown constants of integration W_{1i} and W_{2i} are still determined from the boundary conditions (7.7)–(7.9), except that the first equation of (7.9) must be modified to include the thermal moment terms as indicated below:

$$W_{1i}\cosh\,(\xi_i \ell_i) + W_{2i}\sinh\,(\xi_i \ell_i) - W_{1,i+1} = \hat{e}_i - \hat{e}_{i+1} + \frac{M_{i+1}^{(\text{therm})}}{P} - \frac{M_i^{(\text{therm})}}{P} \tag{7.42}$$

Once the moment distribution along is determined, the adhesive peel and shear stresses will be formulated and evaluated using the similar procedure as in Section 7.2.3. In the presence of a uniform thermal loading, the governing differential equations for the adhesive stresses are given similarly to Equation (7.17) as

$$\{\varphi_i'\} = [\Psi]_i\,\{\varphi_i\} + \{f_i\} = \begin{bmatrix} [\Psi_{11}]_i & [\Psi_{12}]_i \\ [\Psi_{21}]_i & [\Psi_{22}]_i \end{bmatrix}\{\varphi_i\} + \{f_i\} \tag{7.43}$$

where

$$\{f_i\} = \begin{Bmatrix} \varepsilon_{\text{s}}^{(\text{therm})} \cdot x_i \\ 0 \\ \kappa_{\text{s}}^{(\text{therm})} \cdot x_i \\ 0 \\ 0 \\ 0 \\ \varepsilon_{\text{p}i}^{(\text{therm})} \cdot x_i \\ 0 \\ \kappa_{\text{p}i}^{(\text{therm})} \cdot x_i \\ 0 \\ 0 \\ 0 \end{Bmatrix}; \quad \begin{Bmatrix} \varepsilon^{(\text{therm})} \\ \kappa^{(\text{therm})} \end{Bmatrix} = \begin{bmatrix} \dfrac{D}{DA - B^2} & \dfrac{-B}{DA - B^2} \\ \dfrac{-B}{DA - B^2} & \dfrac{-A}{DA - B^2} \end{bmatrix} \begin{Bmatrix} N^{(\text{T})} \\ M^{(\text{T})} \end{Bmatrix}$$

$$N^{(\text{T})} = \sum_{k=1}^{n_{\text{ply}}} C_{11,k}\;\alpha_{11,k}\;\Delta T\,\{z_k - z_{k-1}\}$$

$$M^{(\text{T})} = \frac{1}{2}\sum_{k=1}^{n_{\text{ply}}} C_{11,k}\;\alpha_{11,k}\;\Delta T\left\{(z_k - h_o)^2 - (z_{k-1} - h_0)^2\right\} \tag{7.44}$$

A, B and D are again the A, B and D matrices of the appropriate laminated segment of the doubler or skin; $\{\varphi_i\}$, $[\Psi_{11}]_i$, $[\Psi_{12}]_i$, $[\Psi_{21}]_i$, $[\Psi_{22}]_i$ are defined respectively by Equations (7.18)–(7.21), respectively, in Section 7.2.3. Since $\varepsilon^{(\text{therm})}$, $\kappa^{(\text{therm})}$, $N^{(\text{T})}$ and $M^{(\text{T})}$ for the ith segment of the doubler or skin are defined in a very similar manner, therefore, for simplicity, they have been specified in a general form by a set of equations given in the right column of (7.44) without a subscript s or p and i. It is worthy to note that $N^{(\text{T})}$ and $M^{(\text{T})}$ are thermal force and thermal moment (Jones, 1975), and $M^{(\text{T})}$ is different from $M^{(\text{therm})}$ defined earlier. Also, the term $\{f_i\}$ in Equation (7.43) arises from the constitutive relations which relate the displacement and curvature of the ith laminated segment of the doubler or skin to their corresponding stress and moment resultants, i.e.,

$$\begin{aligned}
\bar{u}'_{si} &= \frac{D_s}{D_s A_s - B_s^2} N_{si} - \frac{B_s}{D_s A_s - B_s^2} M_{si} + \varepsilon_s^{(\text{therm})} \\
\tilde{\beta}'_{si} &= -\frac{B_s}{D_s A_s - B_s^2} N_{1i} + \frac{A_s}{D_s A_s - B_s^2} M_{si} + \kappa_s^{(\text{therm})}
\end{aligned} \tag{7.45}$$

$$\begin{aligned}
\bar{u}'_{pi} &= \frac{D_{pi}}{D_{pi} A_{pi} - B_{pi}^2} N_{pi} - \frac{B_{pi}}{D_{pi} A_{pi} - B_{pi}^2} M_{pi} + \varepsilon_{pi}^{(\text{therm})} \\
\tilde{\beta}'_{pi} &= -\frac{B_{pi}}{D_{pi} A_{pi} - B_{pi}^2} N_{pi} + \frac{A_{pi}}{D_{pi} A_{pi} - B_{pi}^2} M_{pi} + \kappa_{pi}^{(\text{therm})}
\end{aligned} \tag{7.46}$$

The boundary conditions for the differential Equations (7.43) are exactly the same as those considered in Section 7.2.3. For example, the boundary conditions for a one-sided doubler are given by conditions (a)–(d) in that section while the conditions (a), (b′), (c) and (d) are the corresponding conditions for a two-sided doubler. The differential Equations (7.43) are again effectively solved by the multi-segment integration method.

The differential equation set given by Equation (7.43) for $i = 1, 2, \ldots, N$, together with its boundary conditions, constitutes a multiple-point boundary value problem which can be expressed in the following general form:

$$\underset{12\cdot N\times 1}{\{\Phi'(x)\}} = \underset{12\cdot N\times 12\cdot N}{[\Lambda(x)]} \cdot \underset{12\cdot Nx1}{\{\Phi(x)\}} + \underset{12\cdot Nx1}{\{F\}} \tag{7.47}$$

$$\underset{12\cdot N\times 12\cdot N}{[T_1]} \cdot \underset{12\cdot N\times 1}{\{\Theta_1\}} + \underset{12\cdot N\times 12\cdot N}{[T_2]} \cdot \underset{12\cdot N\times 1}{\{\Theta_2\}} = \underset{12\cdot N\times 1}{[G]} \tag{7.48}$$

where

$$\{F\} = \begin{Bmatrix} \{f_1\} \\ \{f_2\} \\ \vdots \\ \{f_N\} \end{Bmatrix} \tag{7.49}$$

Like before, the elements of matrices $\{\Theta_1\}$ and $\{\Theta_2\}$ are elements of $\{\Phi\}$ evaluated respectively at the beginning and end points of each segment i while $[T_1]$, $[T_2]$ and $[G]$ are constant matrices known from the statements of the boundary conditions.

Assuming that the solution of (7.47) can be written as

$$\underset{12\cdot N\times 1}{\{\Phi(x)\}} = \underset{12\cdot N\times 12\cdot N}{[\Omega(x)]}\cdot \underset{12\cdot N\times 1}{\{L\}} + \underset{12\cdot N\times 1}{\{\Phi_{\mathrm{p}}(x)\}} \tag{7.50}$$

where vector $\{L\}$ represents $12\cdot N$ arbitrary constants, $[\Omega(x)]$ and $\{\Phi_{\mathrm{p}}(x)\}$ are the homogeneous and particular solutions of Equation (7.47), respectively. In particular, $[\Omega(x)]$ is the solution of the following differential equations:

$$\underset{12\cdot N\times 12\cdot N}{[\Omega'(x)]} = \underset{12\cdot N\times 12\cdot N}{[\Lambda(x)]}\ \underset{12\cdot N\times 12\cdot N}{[\Omega(x)]} \tag{7.51}$$

with the initial conditions given by

$$[\Omega(0)] = [I] \tag{7.52}$$

where $[I]$ is the identity matrix. In contrast, the differential equations for the particular solution $\{\Phi_{\mathrm{p}}(x)\}$ are in the form

$$\underset{12\cdot N\times 1}{\{\Phi_{\mathrm{p}}'(x)\}} = \underset{12\cdot N\times 12\cdot N}{[\Lambda(x)]}\cdot \underset{12\cdot N\times 1}{\{\Phi_{\mathrm{p}}(x)\}} + \underset{12\cdot N\times 1}{\{F\}} \tag{7.53}$$

and they are subjected to the null initial conditions

$$\{\Phi_{\mathrm{p}}(0)\} = \{0\} \tag{7.54}$$

As outlined in Section 7.2.3, the homogeneous solution $[\Omega(x)]$ can be obtained by direct numerical integration of differential Equations (7.51) using adaptive step-size fourth- and fifth-order Runge–Kutta–Fehlberg method. Similarly, the particular solution $\{\Phi_{\mathrm{p}}(x)\}$ can be obtained from Equation (7.53) using the same adaptive integration method.

It remains now to determine the vector $\{L\}$ of the arbitrary constants of integration. Evaluation of Equation (7.50) at $x = 0$ and noting that $\{\Theta_1\} = \{\Phi(0)\} = [\Omega(0)]\{L\} + \{\Phi_{\mathrm{p}}(0)\} = [I]\{L\} + \{0\} = \{L\}$ lead to

$$\{\Phi(x)\} = [\Omega(x)]\cdot\{\Theta_1\} + \{\Phi_{\mathrm{p}}(x)\} \tag{7.55}$$

Furthermore, since elements of matrix $\{\Theta_2\}$ are elements of $\{\Phi\}$ evaluated at the end point of each segment i, $\{\Theta_2\}$ is related to $\{\Theta_1\}$ by

$$\begin{aligned}\{\Theta_2\} &= \{\Phi(x)\}|_{x=\text{segment endpoint}} \\ &= [\Omega(x)]|_{x=\text{segment endpoint}}\{\Theta_1\} + \{\Phi_p(x)\}|_{x=\text{segment endpoint}}\end{aligned} \tag{7.56}$$

Equation (7.56), together with Equation (7.48), provides a system of algebraic equations for solving $\{\Theta_1\}$ and $\{\Theta_2\}$. Once $\{\Theta_1\}$ and $\{\Theta_2\}$ are determined, the solution at any value of x is obtained from Equation (7.55).

7.3.2 Extension to include the effect of adhesive plasticity

Most adhesives will deform plastically even at a relatively low level of external loading. Unless the extent of the adhesive plastic deformation is small (small-scale yielding), the assumption of linear elasticity of the adhesive may not be realistic and the use of the corner singularity in predicting the bond-line strength may not be valid (see Sections 2.4.2 and 2.5 of Chapter 2). In that case, the effect of nonlinear adhesive must be accounted for. For simplicity, the adhesive will assume to behave nonlinearly only in shear while its peel behavior remains elastically through all ranges of adhesive normal stresses. In contrast to Chapter 2, the adhesive considered in this section is not necessarily limited to elastic-perfectly-plastic material. A general nonlinear shear-stress–shear-strain curve for the adhesive such as that shown in Figure 2.3 of Chapter 2 can be modeled in the present analysis.

The effect of nonlinear shear properties (plasticity) of the adhesive can be included in the formulation presented in Sections 7.2.3 and 7.3.1 by employing the secant modulus approach as frequently used in elasto-plastic analyses. According to the secant modulus approach, the solution procedure for determining the stress distribution in the adhesive layer can be described by the following steps (Thomsen, 1992; Mortensen and Thomsen, 1997):

(a) Calculate the adhesive shear strain and shear stress for a number of points in the adhesive layer at some predetermined locations along the overlap length, say x_k, $k = 1, 2, \ldots, M$, using the linear elastic solution procedure outlined in section 7.2 or 7.3.1 and assuming a uniform elastic shear modulus $G_A^{(1)}$ for adhesive, i.e., $G_A^{(1)}(x) \equiv G_A^{(ELAS)}$, where $G_A^{(ELAS)}$ is the initial elastic shear modulus of the adhesive (or the slope of the adhesive shear-stress–shear-strain curve below the proportional elastic limit). These shear strains and shear stresses are denoted by $\gamma_A(x_k)$ and $\tau_A(x_k)$, respectively.

(b) If the calculated adhesive shear stress $\tau_A(x_k)$ at any point in the adhesive layer exceeds the proportional elastic limit of the adhesive material, determine the adhesive shear stresses for each point x_k of the adhesive layer from the nonlinear shear-stress–shear-strain curve according to the adhesive shear strains and denote them by $\tau_A^*(x_k)$.

(c) Calculate the difference $\Delta\tau_A(x_k) = \tau_A(x_k) - \tau_A^*(x_k)$, and determine the secant shear modulus $G_A^{(2)}(x_k)$ defined by

$$G_A^{(2)}(x_k) = G_A^{(1)}(x_k)\left\{1 - \chi\left[\frac{\tau_A(x_k) - \tau_A^*(x_k)}{\tau_A^*(x_k)}\right]\right\} \tag{7.57}$$

where χ is a non-negative weight factor specified by the user which determines the change of modulus in each iteration.

(d) Rerun the procedure (steps (a) and (b)) with $G_A^{(1)}$ for each adhesive point modified as per step (c), i.e., $G_A^{(1)}(x) = G_A^{(2)}(x)$, where $G_A^{(2)}(x)$ is approximated by a multiple-linear curve defined by discrete points $\left(x_k, G_A^{(2)}(x_k)\right)$, $k = 1, 2, \ldots, M$ along the overlap length. Since the adhesive shear stresses at points x_k, $k = 1, 2, \ldots, M$,

may exceed the proportional elastic limit so that the adhesive shear modulus at these points must be modified as per step (c), the shear modulus of the adhesive is no longer uniform along the overlap length nor equal to the initial elastic shear modulus G_{A}^{ELAS}. It is worthy to note that the formulations in Sections 7.2 and 7.3.1 can be applied to both cases of uniform or non-uniform adhesive shear modulus along the overlap length. This is because the governing differential equations are solved by direct numerical integration. During direct numerical integration, it may require to evaluate G_{A}^{2} at some arbitrary location x which may be different from the predetermined points $x_k,\ k = 1, 2, \ldots, M$. In that case, $G_{\mathrm{A}}^{2}(x)$ at the required point x can be evaluated by linear interpolation or extrapolation from the known values of G_{A}^{2} at the predetermined location $x_k,\ k = 1, 2, \ldots, M$.

(e) Compare the calculated adhesive shear stresses $\tau_{(\mathrm{A})}(x_k)$ for each adhesive point with the values $\tau_{\mathrm{A}}^{*}(x_k)$ obtained from the adhesive shear-stress–strain-curve.

(f) Repeat steps (d) and (e) until the difference between $\tau_{\mathrm{A}}^{*}(x_k)$ and $\tau_{(\mathrm{A})}(x_k)$ at each point $x_k,\ k = 1, 2, \ldots, M$, drops below a specified tolerance.

7.4 Approximate Method for Adhesive Stresses at Patch End in a One-Sided Repair

Analyses for the adhesive peel and shear stresses at the end of the patch will be conducted within one-dimensional theory of bonded doublers, accounting for the geometrically nonlinear out-of-plane deflection. For the case of a tapered patch under purely mechanical loading, these adhesive stresses are determined approximately by (Duong, 2003a) (i) first obtaining the skin stress or load attraction at the end of the patch from a 2-D plane stress analysis of an untapered (polygonal) patch rigidly bonded to the skin using an inclusion analogy as outlined in Chapter 4, and (ii) performing a 1-D bond-line analysis with the skin stress determined from step (i) applying at far field, using the solution procedure outlined in Section 7.2 for a tapered one-sided doubler. In doing so, the effects of the two-dimensional (polygonal) patch and the geometrical nonlinearity can be accounted for approximately in an engineering sense. It is worthy to note that if step (i) is performed within one-dimensional inclusion analogy (the same as assuming the patch spans across the skin width), the skin stress at the patch end will equal the far-field-applied stress, thus resulting in no load attraction. Therefore, the applied load in step (ii) for the bond-line analysis in effect has been scaled up using the ratio of skin stresses at the patch end from 1-D and 2-D inclusion analogies to account for the load attraction in a real repair.

The approach mentioned above poses some difficulty when it applies to the analysis of a tapered patch under a combined thermo-mechanical loading. This is because the adhesive stresses due to the contribution of a thermal load alone can not include effect of the two-dimensional (polygonal) patch by simply multiplying the thermal load in the bond-line analysis by a same factor as that used for a mechanical load or by scaling

it in a similar manner as in step (ii). The thermal stresses in the skin at the patch end from 1-D (patch spanning across the skin width) and 2-D (a finite polygonal patch) inclusion analogies are equal to zero and a negative value, respectively, so that the ratio of the thermal stress there from the latter analysis to that of the former analysis becomes infinite. However, since the thermal loading and the mechanical loading have opposite effect on the skin load attraction and the adhesive stresses, and since the thermal effect predicted by a 1-D inclusion analogy is less significant than that by a corresponding 2-D inclusion analogy (thus, causing a less reduction in the skin load attraction and less alleviation of adhesive stresses that are due to the mechanical load alone), analytical predictions for the adhesive stresses at the patch end will be conservative if the bond-line analysis is carried out with the mechanical load of the 1-D analytical model presented in Section 7.3 being scaled up per step (ii) while keeping the thermal load the same as that defined in Section 7.3.

7.5 Approximate Method for Adhesive Stresses at Patch End in a Two-Sided Repair

Because of the symmetrical configuration of the two-sided repair with respect to the mid-plane of the skin, there will be no out-of-plane deflection in the repair. Unless the adhesive is stressed beyond its elastic limit, the adhesive stresses due to a combined thermo-mechanical loading can be obtained by linear superposition of the individual contribution from the mechanical and thermal loads. As in Section 7.4, the analyses of the adhesive stresses are conducted within one-dimensional theory of bonded doublers as follows, which accounts for the effect of the two-dimensional patch or load attraction in a real repair (Duong, 2003a):

(i) Determine the skin stress at the patch end due to the far-field load alone, using the 2-D inclusion analogy (a rigidly bonded polygonal patch) and denote that skin stress by $\sigma_{\text{tip}}^{\text{s(mech)}}$.

(ii) Determine skin thermal stresses at the patch center, also using 2-D inclusion analogy and denote it as $\sigma_{\text{c}}^{\text{s(therm)}}$.

(iii) Obtain the adhesive stresses and strains at the patch end due to the mechanical load alone with the far-field load per unit width based on the skin stress determined in step (i), i.e., $P = t_{\text{s}} \cdot \sigma_{\text{tip}}^{\text{s(mech)}}$, using the solution procedure outlined in Section 7.2 for a one-dimensional bond-line analysis of a tapered two-sided doubler. The effect of the two-dimensional (polygonal) patch is accounted for approximately in this case by scaling up the far-field load in the bond-line analysis from its actual value of $t_{\text{s}} \cdot \sigma_{\infty}$ to $t_{\text{s}} \cdot \sigma_{\text{tip}}^{\text{s(mech)}}$.

(iv) Obtain the adhesive stresses and strains due to thermal loads alone using a theory developed in Section 7.3.1 for a one-dimensional bond-line analysis of a tapered two-sided doubler. Since the skin thermal stresses at the patch center are different from 1-D (assuming patch spanning across the skin width) and 2-D (a finite polygonal patch) analyses using inclusion analogies, the effect of the

two-dimensional patch on the adhesive stresses and strains due to the thermal loads is accounted for via a correction factor given by

$$C.F. = \frac{\sigma_c^{s(\text{therm})}}{\dfrac{\left(\alpha_p - \alpha_s\right) E_s' \Delta T}{1 + \dfrac{E_s' t_s}{E_p' t_p}}}$$

where the denominator represents the skin thermal stress at the patch center from the 1-D inclusion analogy.

(v) The final (total) adhesive stresses and strains are then equal to the sum of the corresponding contribution from steps (iii) and (iv).

For an elastic-plastic adhesive, depending on the level of the far-field load, the above procedure may need to be modified. For a low level of the far-field load, the adhesive remains elastic so that the above procedure can be applied directly to determine the adhesive stresses and strains. In contrast, for a high far-field-applied load, the adhesive will yield. In that case the above procedure must be modified because the linear superposition principle is no longer valid. The analysis procedure then involves the following steps:

(i) Determine the skin stress at the patch end due to the far-field-mechanical load alone, using 2-D inclusion analogy.

(ii) Obtain the adhesive stresses and strains again using the solution procedure outlined in Section 7.3 for a one-dimensional bond-line analysis of a tapered two-sided doubler. However, as before, in the bond-line analysis, the far-field-mechanical load per unit width of the 1-D analytical model presented in Section 7.3 must be scaled up to $P = t_s \cdot \sigma_{tip}^{s(\text{mech})}$ to account for the load attraction, while the thermal load if there is any will be kept the same as that defined in Section 7.3. It is then clear that only the contribution due to the mechanical load has been accounted for the effect of the two-dimensional (polygonal) patch.

7.6 Summary

A unified approach for approximating the adhesive stresses in a bond line of a one-sided and two-sided tapered doubler is presented within a one-dimensional analysis. This approach is found to be versatile and robust for assessing bonded doublers in the daily design and analysis environment. To account for the effect of a two-dimensional patch or load attraction in a real repair, an approximate method for evaluating the adhesive stresses at the patch ends is also proposed, which utilizes solutions delineated in Chapters 4 and 5 for two-dimensional inclusions and inhomogeneities, combining with the present one-dimensional (1-D) solutions for tapered doublers.

CHAPTER 8

Fatigue Crack Growth Analysis of Repaired Structures

8.1 Introduction

The effectiveness of bonded repairs in terms of reducing the crack-tip stress intensity factor has been demonstrated in Chapters 3–5. Even though a reduction of the stress intensity factor will ultimately increase the residual strength and decrease fatigue crack growth rate, however, it is unclear that the prediction of the growth rate of patched cracks can be made using the crack growth data obtained from un-patched specimens, especially under spectrum loading. For un-patched cracks, it is now possible to obtain satisfactory predictions of the effects of stress ratio and variable amplitude loading on fatigue crack growth rate using crack-closure models (Newman, 1992). The aim of this chapter is therefore to establish a correspondence principle between patched cracks and un-patched cracks, with particular emphasis on the crack-closure behaviour under steady-state (constant amplitude loading) and transient conditions (spectrum loading). The effect of thermal residual stress resulting from the mismatch between the coefficients of thermal expansion for the composite patch and the parent metallic material will also be considered.

A repaired crack can be viewed as being bridged by a series of distributed springs sprang between the crack faces as modeled in Chapters 3 and 5. Under fatigue loading, these springs restrain the opening of the crack, and thus reducing the stress intensity factor. To analyze the effect of this bridging mechanism on the residual plastic wake behind the crack tip, the crack-bridging theory presented in Chapters 3 and 5 is employed together with a crack-closure model (Budiansky and Hutchinson, 1978) to analyze the steady-state closure of patched cracks subjected to constant amplitude loading. The analytical consideration proves that under small-scale yielding condition (the applied stress is far smaller than the material's yield stress), the steady-state crack closure level depends only on the applied stress ratio and is almost identical to that corresponding to un-repaired cracks subjected to the same applied stress ratio. This finding has been verified by a FE analysis. Furthermore, the transient crack closure behaviour following an overload,

which is the main mechanism responsible for crack growth retardation, has also been investigated by the FE method. The results reveal that patched cracks exhibit the same transient decrease/increase in the crack-closure stress as un-patched cracks. Based on these findings, a correspondence principle relating the transient crack-closure behaviour of patched cracks to that of un-patched cracks is proposed. It is finally shown that predictions based on this method are in good agreement with the experimental results obtained using two aircraft loading spectra.

8.2 Crack-Closure Analysis of Repaired Cracks

We begin with a crack-closure analysis of repaired cracks under a small-scale yielding assumption. It is then followed by the development for a general case of large-scale yielding.

8.2.1 Crack closure of repaired cracks under small-scale yielding

A schematic of a patch repair is shown in Figure 8.1, where it is assumed for simplicity that the cracked skin is restrained from out-of-plane deflection. The problem to be considered is a cracked skin plate repaired by a patch adhesively bonded on one side of the cracked skin. The skin, which has a thickness of t_s, contains a through crack of length $2a$. The thickness of the patch and the adhesive layer are respectively t_p and t_A. The front view in the xy plane and the cross-section in the yz plane are depicted in Figures 8.1(a) and (b). The Young's modulus and the Poisson's ratio of each individual layer are denoted as E and ν; here and in the following, subscripts s, p and A will

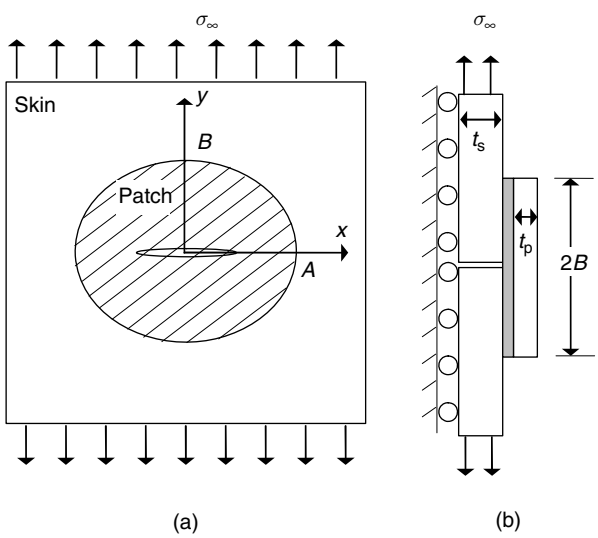

Fig. 8.1. Repair configuration: (a) plan view; and (b) cross-section along centre line.

be used to distinguish properties pertaining respectively to the skin, the patch and the adhesive layer.

The above elastic problem has been analyzed in Chapter 3 using a crack-bridging model and an integral equation method. For isotropic reinforcement having the same Poisson's ratio as the cracked plate, the stress intensity factor range can be expressed as, assuming that the adhesive remains elastic

$$\Delta K = \Delta\sigma_0\sqrt{\pi a}F(\pi\Lambda a) \tag{8.1}$$

where the parameter $\Delta\sigma_0$ denotes the stress range which would prevail at the prospective location of the crack for a patched but un-cracked plate, which can be related to the remotely applied stress $\Delta\sigma_\infty$ by

$$\Delta\sigma_0 = \phi\ \Delta\sigma_\infty \tag{8.2}$$

where the factor ϕ is given by Equation (3.18) for an elliptical patch having the same Poisson's ratio as the skin. The parameters Λ and S denote respectively the spring stiffness and patch stiffness ratio:

$$\Lambda = \frac{\beta_A\ S}{(1-\nu_s^2)(1+S)} \tag{8.3}$$

where $\beta_{\mathrm{A}} = \left[G_{\mathrm{A}}/t_{\mathrm{A}}(1/E'_{\mathrm{s}}t_{\mathrm{s}} + 1/E'_{\mathrm{p}}t_{\mathrm{p}})\right]^{1/2}$, $S = E'_{\mathrm{p}}t_{\mathrm{p}}/E'_{\mathrm{s}}t_{\mathrm{s}}$ and $E'_{\mathrm{s,p}} = E_{\mathrm{s,p}}/(1-\nu^2_{\mathrm{s,p}})$. The function F can be well approximated (within an error less than 0.5%) by

$$F(\pi\Lambda a) = \left[\frac{1}{\pi\Lambda a}\tanh\frac{\pi\Lambda a}{1+\hbar\pi\Lambda a}\right]^{1/2} \tag{8.4}$$

where the parameter $\hbar$ has been obtained by curve-fitting the numerical solution of integral equation representing patch repairs, e.g., $\hbar = 0.3$ for balanced repairs ($S = 1$) and $\hbar = 0.1$ for very stiff patch ($S \to \infty$).

In the long crack limit ($\pi\Lambda a \gg 1$), the stress intensity factor of patched cracks (see Equations (8.1) and (8.4)) asymptotes to the following upper limit, in the absence of disbonding and plastic deformation in the adhesive layer:

$$\Delta K = \frac{\Delta\sigma_0}{\sqrt{\Lambda}} \quad (\pi\Lambda a \gg 1) \tag{8.5}$$

This near constant stress intensity factor suggests that under constant amplitude loading, a patched crack would grow at an approximately constant rate, indicating a steady-state condition. In this case, it is reasonable to postulate that patched cracks ought to experience the same crack-closure as un-patched cracks subjected to the same stress ratio (as the amplitude of the stress intensity factor does not affect crack closure, provided small-scale yielding prevails at the crack tip). In this case the plastic zone size and

the crack-tip opening displacement are given by the following well-known relationship (Broek, 1987),

$$\omega_{\mathrm{K}} = \frac{\pi}{8}\left(\frac{K_{\mathrm{I}}}{\sigma_{\mathrm{Y}}}\right)^2 \tag{8.6}$$

$$CTOD_{\mathrm{K}} = \frac{K_{\mathrm{I}}^2}{E_{\mathrm{s}}\sigma_{\mathrm{Y}}} = \frac{8\sigma_{\mathrm{Y}}}{\pi E_{\mathrm{s}}}\omega_{\mathrm{K}} \tag{8.7}$$

where ω_{K} and $CTOD_{\mathrm{K}}$ denote the plastic zone size and the crack-tip opening displacement estimated based on stress intensity factor K_{I}, σ_{Y} is the yield strength of the skin plate.

The fatigue crack growth rate can be correlated using the effective stress intensity factor:

$$\Delta K_{\mathrm{eff}} = \frac{\Delta K}{1-R}\left(1-\frac{\sigma_{\mathrm{op}}}{\sigma_{\mathrm{max}}}\right) \tag{8.8}$$

where R denotes the applied stress ratio ($=\sigma_{\mathrm{min}}/\sigma_{\mathrm{max}}$), which is strongly influenced by the thermal residual stresses present in the skin plate induced by curing; further discussion will be presented later in Section 8.4. The crack-opening stress σ_{op} can be obtained by simplifying the expressions constructed by Newman (1984):

$$\frac{\sigma_{\mathrm{op}}}{\sigma_{\mathrm{max}}} = \begin{cases} A_0 & R<0 \\ A_0 + A_2R^2 + A_3R^3 & R>0 \end{cases} \tag{8.9}$$

where the constants $A_0,\ A_2,\ A_3$ are

$$\begin{aligned} A_0 &= 0.825 - 0.34\vartheta + 0.05\vartheta^2 \\ A_2 &= 2 - 3A_0 \\ A_3 &= 2A_0 - 1 \end{aligned} \tag{8.10}$$

The plastic constraint factor ϑ depends parametrically on only one non-dimensional parameter: the ratio of plastic zone size ω[1] to plate thickness t_{s} (Guo et al., 1998):

$$\vartheta = \frac{1+0.64[(\omega/t_{\mathrm{s}})^{1/2}+2(\omega/t_{\mathrm{s}})^2]}{1-2\nu_{\mathrm{s}}+0.54[(\omega/t_{\mathrm{s}})^{1/2}+2(\omega/t_{\mathrm{s}})^2]} \tag{8.11}$$

which is illustrated in Figure 8.2 together with the FE results obtained by Newman et al. (1995).

[1] The plastic zone size is denoted here as ω, rather than ω_{K}, since in Equation (8.11) the plastic zone size can be taken from either small- or large-scale yielding, and therefore it may not be necessarily equal to the estimate value given by Equation (8.6) based on the stress intensity factor.

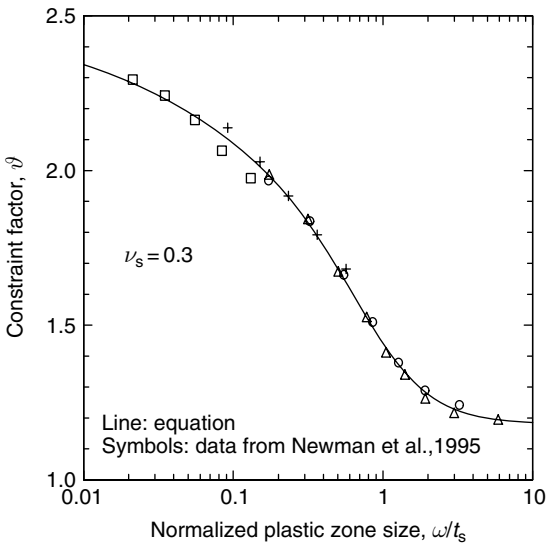

Fig. 8.2. Constraint factor versus normalized plastic zone size.

8.2.2 Crack closure of repaired cracks under large-scale yielding

The above method is valid in the limiting case of small-scale yielding, i.e., the applied stress is far smaller than the material's yield stress, the plastic zone size is far smaller than the crack size and the plate thickness. In practice, however, such conditions are not always met, especially when repairs are applied to fatigue cracks in high stress regions. To evaluate the range of the validity of the method presented in the previous section, the influences of large-scale yielding on the crack-tip plastic deformation and plasticity-induced crack closure will now be addressed. To this end, a model for patched cracks will be presented, which extends the complex function method of Budiansky and Hutchinson (1978) to include crack-bridging effect.

For simplicity, let us consider the long crack limit, i.e., $\pi\Lambda a \geq 1$, so that the stress intensity factor under maximum load can be considered as approximately constant. Since the CTOD is proportional to the square of the stress intensity factor, the residual plastic stretch attached to the crack faces would be approximately constant in thickness. A simple schematic of the deformed profile of a bridged crack at maximum stress is shown in Figure 8.3(a), while the boundary conditions upon unloading to the minimum stress are shown in Figure 8.3(b). Here the difference between a patched crack and an un-repaired crack is that the crack faces of a patched crack are bridged by a series of distributed springs. As will be seen later, this bridging mechanism will affect the plastic deformation ahead of the crack tip.

Following the Budiansky and Hutchinson's approach (1978), the crack closure analysis of repaired cracks under large-scale yielding will proceed by obtaining the crack-tip

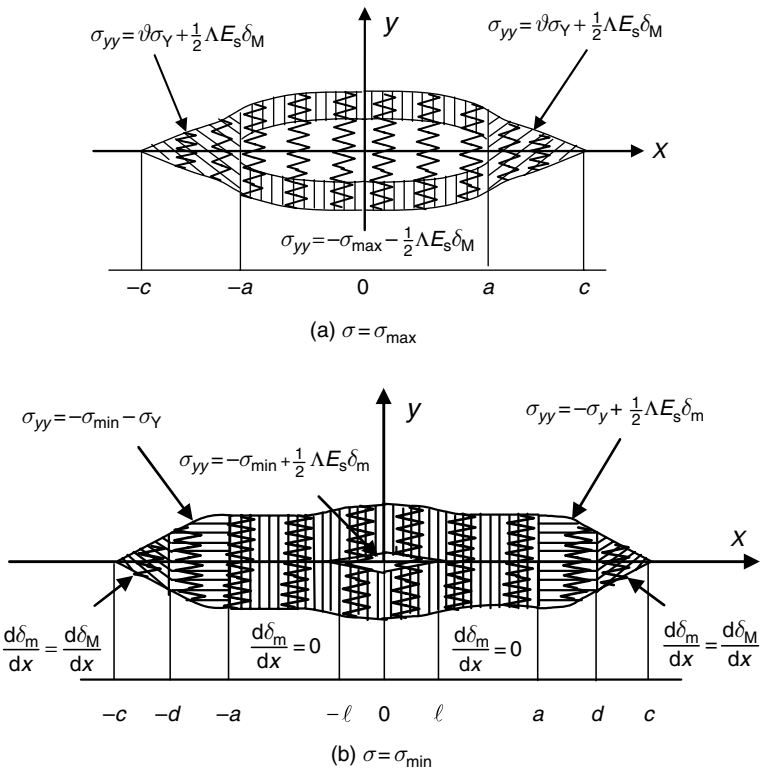

Fig. 8.3. Crack-closure model for short cracks.

plastic deformation and crack opening displacement at the maximum and minimum applied stresses.

(a) Large-scale yielding solution at the maximum applied stress

Adopting the Dugdale model (Dugdale, 1960), plastic deformation ahead of the crack tip is assumed to occur within the region $a < |x| < c$, where $c = a + \omega$. Here ω denotes the plastic zone size. The problem depicted in Figure 8.3(a) can be mathematically expressed as (see Equation (3.40))

$$-\frac{E_s}{2\pi}\int_{-c}^{c}\frac{u(t)}{(x-t)^2}\mathrm{d}t+\Lambda E_s u(x)=\begin{cases}\sigma_0 & |x|<a\\ \sigma_0-\vartheta\sigma_Y & a<|x|<c\end{cases} \tag{8.12}$$

where u denotes the crack face displacement, σ_Y the material's yield stress, and ϑ the plastic constraint factor discussed in Section 8.2.1. The first term in the left-hand side of Equation (8.12) represents the resistance of material to crack opening and the second term represents the resistance of springs.

The above hyper-singular integral equation can be solved using a Galerkin method: the unknown crack-face displacement u is expanded in terms of Chebyshev polynomials (Wang and Rose, 1999). The plastic zone size ω is determined so that the stress just outside the plastic zone $x = c^+$ is non-singular, i.e.,

$$K_I = \lim_{x \to c^+} \frac{E_s \sqrt{\pi a}}{2} \frac{u(x)}{\sqrt{c^2 - x^2}} \equiv 0 \tag{8.13}$$

which furnishes the necessary condition for determining the plastic zone for a given applied stress. Solution of ω can be determined by iteration: Equation (8.12) is first solved for a trial ω, then it is checked whether Equation (8.13) is satisfied. If this is the case, then convergence is achieved. The numerical results are presented in Figure 8.4. It is evident that provided the prospective stress is less than 40% of the material's yield stress, the plastic zone size is approximately equal to the estimate by the stress intensity factor (and thus by Equation (8.6)). At high stress levels, the prospective stress has a significant effect on the plastic zone size. As shown in Figure 8.4(a), the ratio of the plastic zone size for large-scale yielding to the estimate value by Equation (8.6) based on K_I solution can be well approximated by the following expression,

$$\frac{\omega}{\omega_K} = 1 + A \cdot \left[\sec\left(\frac{\pi}{2} \frac{\sigma_0}{\sigma_Y} \right) - 1 \right] \tag{8.14}$$

where the coefficient A is determined by a least square method, $A = 0.4272$. By contrast, the CTOD remains the same as that estimated based on the stress intensity factor (thus, by Equation (8.7)), for prospective stress up to 70% of the yield stress. Furthermore, it is interesting to note that the normalized plastic stretch variation ahead of the crack tip, as shown in Figure 8.4(b), seems to be reasonably insensitive to the level of applied stress. Therefore the plastic stretch variation is approximately given by a universal relation identical to that pertaining to un-patched cracks under small-scale yielding conditions. This universal relation is best illustrated by the ratio of the crack opening displacement to the maximum opening at the crack tip:

$$\frac{\delta(x)}{CTOD_K} = g(x/\omega) \tag{8.15}$$

where the function g is given in reference (Budiansky and Hutchinson, 1978) as

$$g(x/\omega) = \sqrt{1 - x/\omega} - \frac{x}{2\omega} \ln \left| \frac{1 + \sqrt{1 - x/\omega}}{1 - \sqrt{1 - x/\omega}} \right| \tag{8.16}$$

This important result provides a basis to extend existing crack closure model for un-patched cracks to analyze patched cracks.

(b) Plasticity-induced crack closure under large-scale yielding solutions

Having now determined the crack-tip plastic deformation at the maximum applied stress, it is now possible to characterize the plasticity-induced crack closure. Denote the crack opening at the maximum stress at δ_M and crack opening at the minimum stress at δ_m.

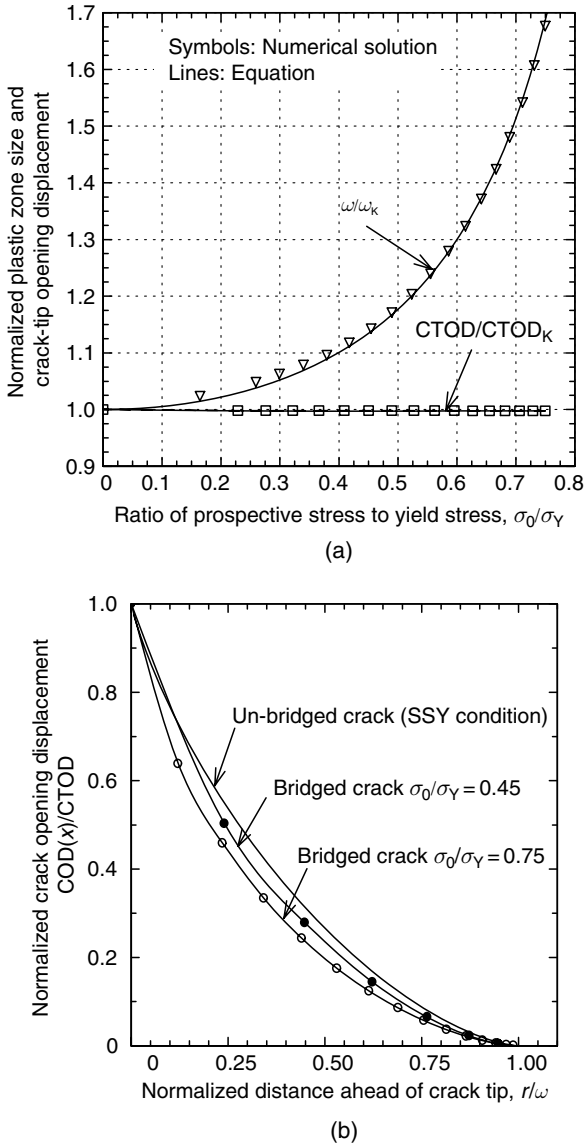

Fig. 8.4. Influence of applied stress on: (a) plastic zone size; and (b) crack-tip opening displacement.

Referring to Figure 8.3(b), upon unloading to the minimum stress, crack-surface contact is assumed to occur within the interval $\ell < |x| < a$, where ℓ denotes the as-yet-unknown size of the contact-free region. In the contact zone, the upper and lower crack surfaces are attached with a layer of plastically stretched material of as-yet-unknown size $\delta_R/2$. There is also a region ahead of the crack tip, of unknown length $d - a$, that has gone into reverse plastic flow, leading to a total crack-tip residual stretch equal to δ_R. Here d

denotes the coordinate of reversed plastic zone. Between $x = d$ and $x = c$ the plastic stretch is equal to the plastic stretch that existed at the maximum stress and remained unchanged. It is worthy to note from Budiansky and Hutchinson's work (1978) that the crack-tip deformation of a stationary crack under cyclic loading will be different from that of a growing fatigue crack. As the crack grows, it leaves in its wake plastic stretched material which is modeled here as an extra layer of material attaching to the surface of the growing crack. Since the thickness of this extra layer of material just behind the crack tip must be equal to the plastic stretch just ahead of the tip at the minimum load, the crack opening displacement δ_{m} for $a \le |x| \le d$ must satisfy the conditions that $\delta_{\mathrm{m}}(x) \le \delta_{\mathrm{R}}$ and $\delta_{\mathrm{m}}(|x| = a) = \delta_{\mathrm{R}}$. In addition, it was also found from the cited reference that δ_{R} must be smaller than the CTOD of a corresponding stationary crack at the minimum load. Thus, $\delta_{\mathrm{m}} \le \delta_{\mathrm{R}} \le CTOD$ for $a \le |x| \le d$.

The boundary-value problem depicted in Figure 8.3(b) can be analyzed using the complex function method (Budiansky and Hutchinson, 1978; Tanaka and Nakai, 1983; Rose and Wang, 2001). In particular, the boundary conditions can be expressed as

$$\left.\begin{array}{ll}
\sigma_{yy} = -\sigma_{\min} + \dfrac{1}{2}\Lambda E_{\mathrm{s}}\delta_{\mathrm{m}}(x) & |x| < \ell \\
\dfrac{\mathrm{d}\delta_{\mathrm{m}}}{\mathrm{d}x} = 0 \quad \text{or} \quad \delta_{\mathrm{m}} = \delta_{\mathrm{R}} & \ell < |x| < a \\
\sigma_{yy} = -\sigma_{\min} - \sigma_{\mathrm{Y}}\left(1 - \dfrac{\Lambda E_{\mathrm{s}}\delta_{\mathrm{m}}}{2\sigma_{\mathrm{Y}}}\right) & a < |x| < d \\
\dfrac{\mathrm{d}\delta_{\mathrm{m}}}{\mathrm{d}x} = \dfrac{\mathrm{d}\delta_{\mathrm{M}}}{\mathrm{d}x} \quad \text{or} \quad \delta_{\mathrm{m}} = \delta_{\mathrm{M}} & d < |x| < c \\
\dfrac{\mathrm{d}\delta_{\mathrm{m}}}{\mathrm{d}x} = 0 & |x| > c
\end{array}\right\} \tag{8.17}$$

Due to the presence of $\delta_{\mathrm{m}}(x)$ in the right-hand side of Equation (8.17), the solution of the present problem is more complicated than for the case of un-repaired crack ($\Lambda = 0$, also see (Rose and Wang, 2001)). One way of solving this equation is to adopt an iterative approach, by using the un-bridged crack solution of Rose and Wang (2001) as the first-order solution. By inserting the first-order solution into the right-hand side of Equation (8.17), second-order correction can be obtained. Higher-order solutions then can be obtained successively.

For low prospective stress, by noting $\delta_{\mathrm{m}} \le \delta_{\mathrm{R}} \le \mathrm{CTOD}$, $\Lambda = \frac{\sigma_0^2}{K_{\mathrm{I}}^2}$ by Equation (8.5), and $\mathrm{CTOD} = \frac{K_{\mathrm{I}}^2}{E_{\mathrm{s}}\sigma_{\mathrm{Y}}}$ by Equation (8.7), we have

$$\frac{\Lambda E_{\mathrm{s}}\delta_{\mathrm{m}}}{2\sigma_{\mathrm{Y}}} \le \frac{\Lambda E_{\mathrm{s}} \cdot \mathrm{CTOD}}{2\sigma_{\mathrm{Y}}} = \frac{1}{2}\left(\frac{\sigma_0}{\sigma_{\mathrm{Y}}}\right)^2 \le 0.125 \quad (\sigma_0 \le 0.5\sigma_{\mathrm{Y}}) \tag{8.18}$$

Therefore the term $\Lambda E\delta_{\mathrm{m}}/2\sigma_{\mathrm{Y}}$ in (8.17) can be neglected without appreciable loss of accuracy. Numerical results show that the higher-order correction is only a small fraction of the first-order solution, and thus can be ignored. This is primarily due to that the non-contact region ℓ is generally much smaller than the crack size a; neglecting the term $\Lambda E\delta_{\mathrm{m}}/2$ in the first expression of (8.17) would reduce the present problem to that pertinent to un-repaired crack ($\Lambda = 0$).

8.3 Overload Effect and Validation Using Finite Element Method

To verify the above analytical solutions, a FE analysis was performed. The FE model will also be employed to investigate the transient crack-closure behaviour of patched and un-patched cracks subjected to variable amplitude loading. The fatigue crack opening and closure stresses were obtained using a spring element release method, which involves introducing two sets of bi-linear spring elements along the crack plane, as illustrated in Figure 8.5(a). One set of spring elements, which are attached to all the nodes, are used to simulate the patch in restraining the opening of the crack as well as to maintain the zero displacement condition under compression. This series of spring elements have a force–displacement relationship to give the spring constant given by Equation (8.3), and an almost infinite compressive stiffness, as illustrated in Figure 8.5(b). For an element of width h, The force–displacement of this bi-linear spring attached its corner node is

$$P = (\Lambda \cdot h \cdot E_s)u \tag{8.19}$$

where P and u are the force and displacement pertaining to the spring element, respectively, and E_s is the Young's modulus of the skin material. In addition, a series of tension-only spring elements are also attached to each node ahead of the crack tip to maintain the zero displacement condition ahead of the crack tip under tension (Figure 8.5(c)). Crack-growth was simulated by releasing, at the maximum load, one tension-only spring-element every two cycles. The emphasis here is to determine the stabilized crack-closure stress, assuming that the crack will take many cycles to grow one element distance.

The FE model was developed using a general-purpose FE code, ABAQUS (1997). A quarter model of centre-crack panel is modeled using plane-stress quadrilateral elements. The material is assumed to have Young's modulus of 72 GPa, a Poisson's ratio of 0.3 and a yield stress of 400 MPa, typifying an aluminium alloy. The initial crack length, a_i, was 5 mm and the half panel width was 101 mm. For the patched crack, the spring elements are chosen to simulate a spring constant of $\Lambda = 120\,\mathrm{m}^{-1}$, and the applied stress is repeated tension with a maximum value of 150 MPa. For the un-patched centre-crack, the applied stress is also repeated tension but with a maximum value of 100 MPa

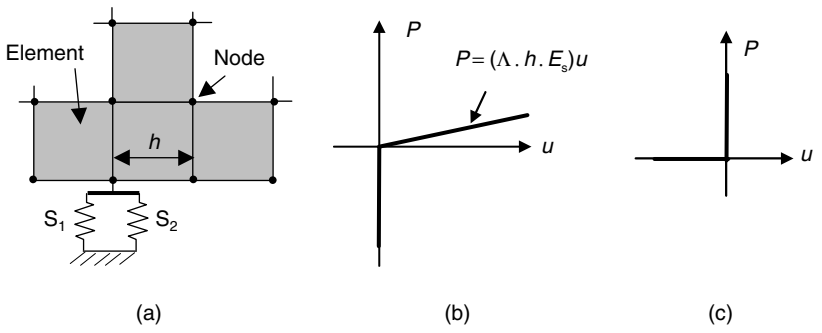

Fig. 8.5. Spring elements: (a) attached to one node, constitutive relations for; (b) bi-linear spring S_1; and (c) tension-only spring S_2.

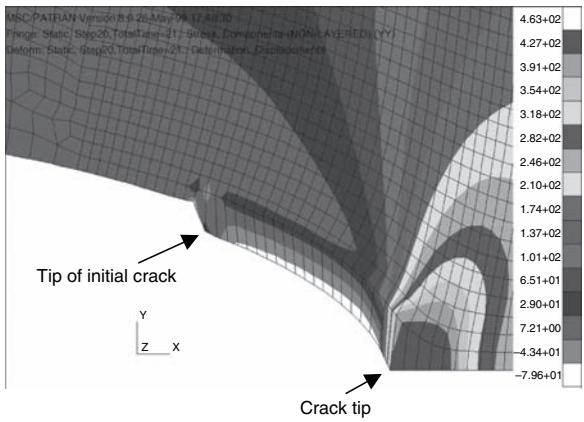

(a)

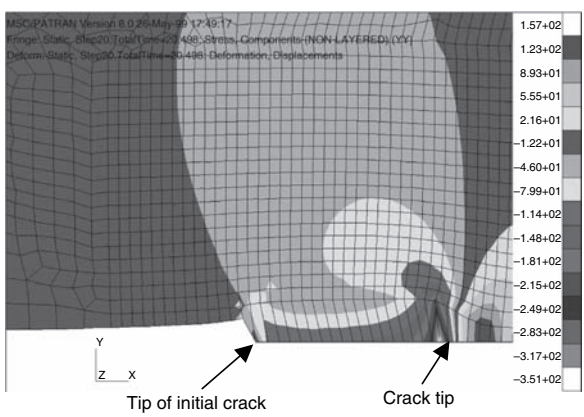

(b)

Fig. 8.6. Finite element solution of a patched crack growing under constant amplitude loading with $R = 0$: (a) at the maximum stress showing the residual plastic stretch; (b) at minimum stress showing crack surface closure.

to ensure the patched crack and the un-patched crack are subjected to approximately the same stress intensity factor. Shown in Figure 8.6 are the contours of the y-stress plotted on the deformed geometry of the patched crack after the crack has grown 0.8 mm under constant amplitude loading. As it can be seen in the figure, the residual plastic stretch at the crack tip caused the crack surface to close before the minimum stress is reached, similar to that observed in un-repaired cracks. In fact, the crack-closure stresses corresponding to the patched crack and the un-patched crack agree well with each other, and are in close correlation with the theoretical solution (Budiansky and Hutchinson, 1978) of un-repaired cracks subjected to the same stress ratio. Therefore, under constant amplitude loading, the crack-closure stress of patched cracks can be determined from the

known results of un-repaired cracks. It is also noted that under steady-state condition, the crack-closure stress depends solely on the applied stress ratio, and is independent of the level of the applied stress intensity factor. As discussed later, this is in sharp contrast with the transient crack closure under variable amplitude loading.

The same FE model has been used to further investigate the transient crack closure behaviour of patched cracks subjected to variable amplitude loading, with a view to identifying an equivalence between patched cracks and un-patched cracks. A simple overload sequence as shown in Figure 8.7 is applied to both an un-repaired crack and a patched crack. The maximum stress of the overload is about 30% higher than that of the background constant loading (150 MPa for patched crack and 100 MPa for un-patched crack). The patched crack experienced the same stress-intensity factor history as the un-repaired crack. Figure 8.8 shows the plastic wake created by the overload for an un-patched crack and a patched crack. It is evident that there is no discernible difference between the patched crack and the un-patched crack. A fundamental difference between the crack closure behaviour under steady-state condition (see Figure 8.6) and variable amplitude loading is that the crack-closure stress is independent of the magnitude of the residual plastic stretch under steady-state condition. By contrast, the transient crack-closure behaviour after an overload is dictated by the residual stretch created by the overload relative to that induced by prior constant amplitude loading. A schematic of the residual plastic wake associated with a single overload is shown in Figure 8.9. The ratios of the crack-closure stress (and crack-opening stress) to the maximum stress are calculated from the FE results and shown in Figure 8.10, for both the patched and the un-patched cracks. The crack advance is normalized by the distance between the plastic zone boundaries for the overload and the constant amplitude loading. Two important observations can be made from the results shown in Figure 8.10. First, following the overload, an initial sharp drop occurred in the crack-closure and crack-opening stresses for both the patched and un-patched cracks. After the initial drop, the crack-closure stress attained a higher value and it was only after considerable crack growth did the crack-closure stress return to the same level as prior to the overload. The fact that the higher (than steady-state value) crack-closure stress occurred over a crack advance greater than that over which the lower crack-closure stress occurred is a clear indication of net retardation in fatigue crack growth rates. Secondly, and more importantly, there is little difference between the transient evolution of the crack-closure stress for the patched crack and the un-patched crack. This implies that the crack closure behaviour of patched crack can be well approximated by that corresponding to an un-patched crack subjected to the same stress intensity factor. Therefore, the crack-closure behaviour of a patched crack can be obtained by analyzing an un-patched, centre crack subjected

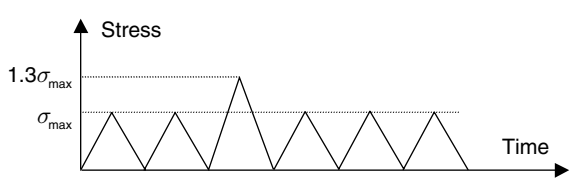

Fig. 8.7. A single overload superimposed on a constant amplitude loading sequence.

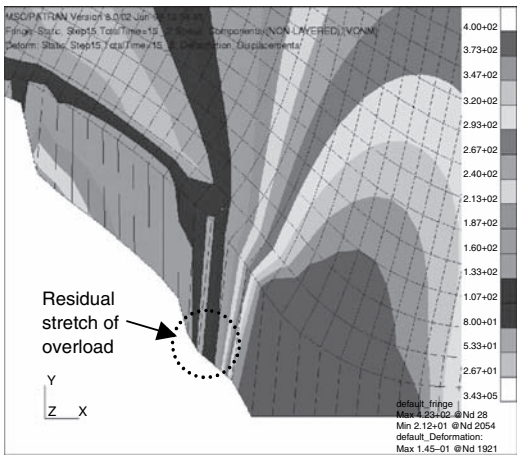

(a)

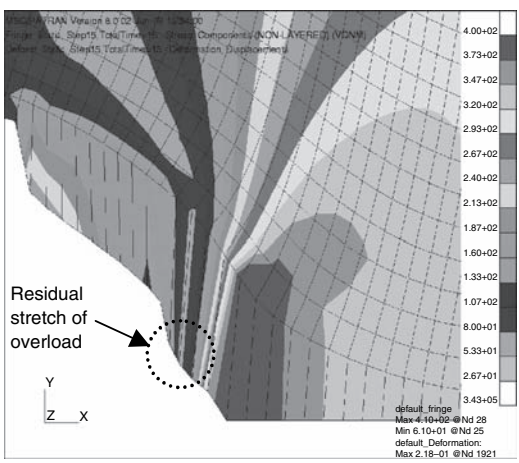

(b)

Fig. 8.8. Plastic wake induced by an overload for: (a) an un-patched crack; and (b) a patched crack subjected to approximately the same stress-intensity factor history.

to the same stress-intensity factor history as the patched crack, or the equivalent crack method (Wang et al., 1998c). In this regard, it is worth noting that the under-prediction of the fatigue crack growth rates of patched crack as reported in Wang et al. (1998c) is due to the ignorance of the thermal residual stress in the earlier analysis, an issue to be discussed in more detail in the next section.

8.4 Comparison with Experimental Results

Since composite patches generally have a lower thermal expansion coefficient than the metallic component to be repaired, thermal residual stresses would occur upon cooling the

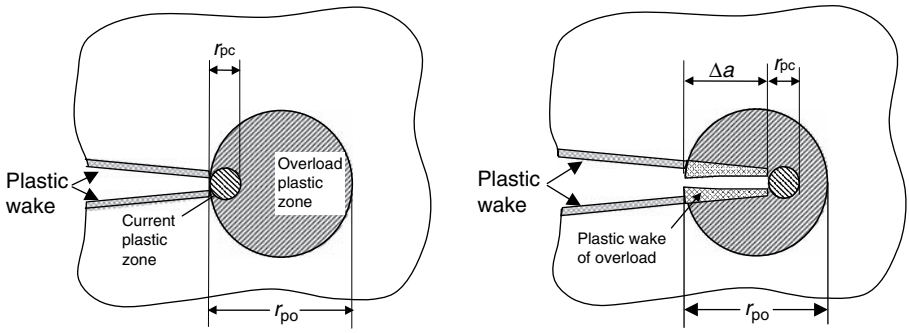

Fig. 8.9. Schematic of transient crack closure for a single overload.

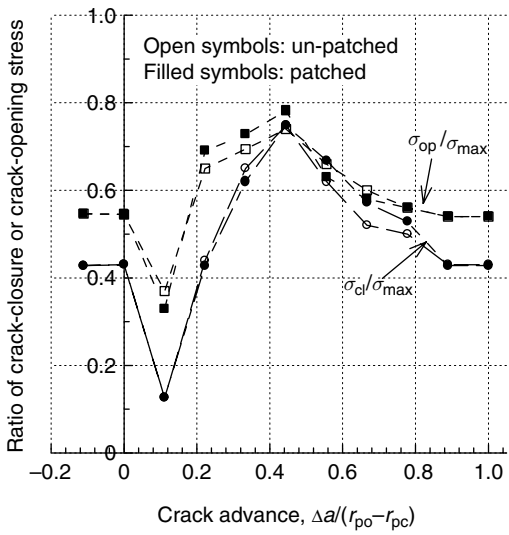

Fig. 8.10. Effect of overload on the crack-closure stress of patched and un-patched cracks.

fully cured repair from elevated temperature (typically around 80–120 °C for structural adhesives) to either the ambient temperature or the operating temperature. In particular, the residual stress in the metallic plate is generally positive, which may enhance fatigue crack growth rate due to increased stress ratio. Other complicating factors affecting fatigue crack propagation include possible changes in the patching efficiency resulting from adhesive plastic yielding and debonding (see Chapters 3 and 4 for details). In the following, we will focus our attention on the influence of thermal residual stress only.

For an orthotropic composite patch bonded to an isotropic skin, the resulting thermal residual stresses can be determined using the method developed in Chapter 4. By treating

the patch as isotropic, approximate and explicit solutions of the thermal stress in the skin for different thermal loading have been derived in Chapters 3 and 4 as follows:

Curing in a uniform temperature field, e.g., an oven (see Equation (3.72) and the remark at the end of Section 3.5)

$$\sigma_0^{\mathrm{T}} = -\alpha_{\mathrm{s}} E_{\mathrm{s}} \Delta T \frac{\left(1-\alpha_{\mathrm{p}}/\alpha_{\mathrm{s}}\right)\ S}{2\left(1-\nu_{\mathrm{p}}\right)+\left(1-\nu_{\mathrm{s}}^2\right)\ S}\left[\frac{\left(1-\nu_{\mathrm{p}}\right)\left(1+\nu_{\mathrm{s}}\right)+\left(1-\nu_{\mathrm{s}}^2\right)\ S}{\left(1-\nu_{\mathrm{p}}^2\right)+\left(1-\nu_{\mathrm{s}}^2\right)\ S}\right] \tag{8.20}$$

Curing by localized heating of the repair then followed by cooling to the room temperature (see Equation (4.110))

$$\sigma_0^{\mathrm{T}} = -\frac{E_{\mathrm{s}} S\left(1+\nu_{\mathrm{s}}\right)}{2\left(1-\nu_{\mathrm{p}}\right)+\left(1-\nu_{\mathrm{s}}^2\right)\ S}\left[\alpha_{\mathrm{p}} - \frac{\alpha_{\mathrm{s}}\left(1+\nu_{\mathrm{s}}\right)}{2}\right]\Delta T \tag{8.21}$$

where $\Delta T = T_{\mathrm{curing}} - T_{\mathrm{room}}$, $S = E_{\mathrm{p}} t_{\mathrm{p}} / E_{\mathrm{s}} t_{\mathrm{s}}$, α_{s} and α_{p} are the thermal expansion coefficients of the skin and patch, respectively, and the rest are previously defined. It is worthy to note that σ_0^{T} is generally a tensile stress for Boron patches with a coefficient of thermal expansion being far smaller than that of the metallic material, $\alpha_{\mathrm{p}} \ll \alpha_{\mathrm{s}}$.

For a constant amplitude loading, the presence of the residual thermal stress implies that the patched crack experiences a stress intensity factor R_{tip} different from the applied stress ratio:

$$R_{\mathrm{tip}} = \frac{K_{\min}}{K_{\max}} = \frac{\phi\sigma_{\infty,\min} + \sigma_0^{\mathrm{T}}}{\phi\sigma_{\infty,\max} + \sigma_0^{\mathrm{T}}} = R + \frac{1-R}{1+\phi\sigma_{\infty,\max}/\sigma_0^{\mathrm{T}}} \tag{8.22}$$

where R denotes the ratio of the applied stress, $R = \sigma_{\infty,\min}/\sigma_{\infty,\max}$. Since $\sigma_0^T \geq 0$, the actual stress intensity factor ratio is higher than the applied stress ratio. This difference needs to be considered when comparing the fatigue crack growth rates of patched and un-patched cracks. In this regard, a rational approach would be to adopt the effective stress intensity factor as the correlating parameter for fatigue crack growth. Take the example of aluminium alloy 2024-T3, the fatigue crack-growth rates obtained using an un-patched, edge cracked panel are plotted in Figure 8.11(a) against the applied stress-intensity factor range. It is evident that the stress ratio has a considerable effect on the crack-growth rates for a given applied stress-intensity factor range. By re-plotting the crack growth rates against the effective stress-intensity factor range determined using Equation (8.8), as shown in Figure 8.11(b), the crack-growth rate data corresponding to three different stress ratios fall within a narrow band (±100%), consistent with the crack growth rates independently obtained for the same material (Edwards and Newman, 1990). The plastic constraint factor ϑ employed in the analysis is equal to 1.8. The following expression provides the best fit to all the experimental data:

$$\frac{\mathrm{d}a}{\mathrm{d}N} = C(\Delta K_{\mathrm{eff}})^{\mathrm{m}} \tag{8.23}$$

where $C = 2.234 \times 10^{-10}$ and $m = 3.135$, in SI unit.

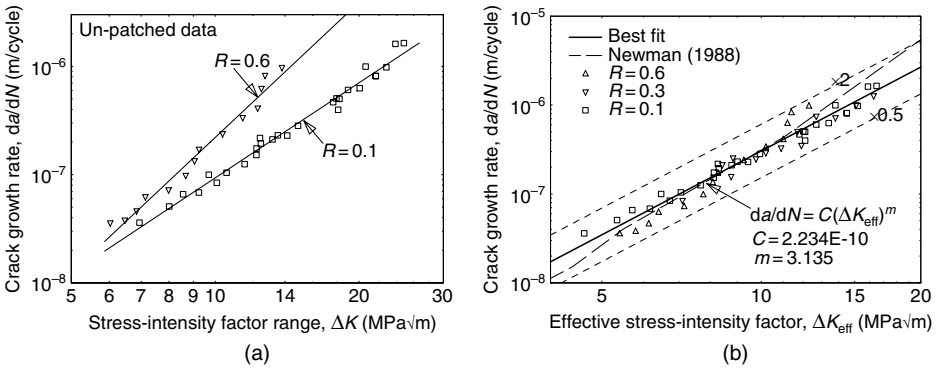

Fig. 8.11. Fatigue crack-growth rates in 2024-T3 Aluminium alloy (un-repaired) plotted against: (a) the applied stress-intensity factor range ΔK; and (b) the effective stress-intensity factor range ΔK_{eff}.

In light of the above success in correlating the crack-growth rates of the un-patched cracks, the experimental results of patched cracks reported in Baker (1996) are re-analyzed, taking into account the residual thermal stress. The results are shown in Figure 8.12. It can be seen that the experimental results of patched cracks also fall within the same band as the un-patched cracks. Here the stress intensity factors for the patched cracks are calculated using Equation (8.1), assuming that the adhesive remains elastic. With the actual stress ratio being determined from Equation (8.22), the crack-opening stress is evaluated by Equation (8.9), and the effective stress-intensity factor range is calculated via Equation (8.8). The good correlation between the patched and un-patched cracks as observed in Figure 8.12 confirms that growth rates of patched cracks and un-patched cracks are uniquely characterized by the effective stress-intensity

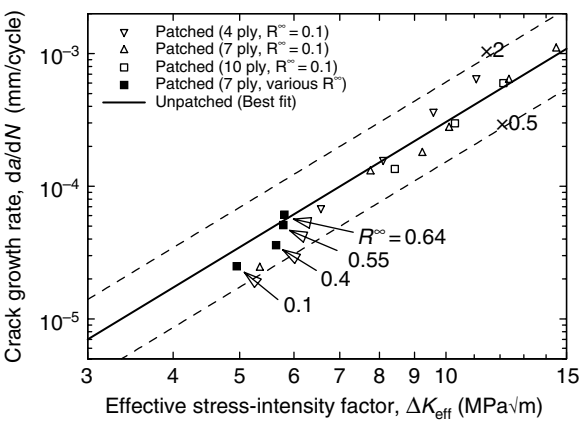

Fig. 8.12. Growth rates of patched and un-patched cracks under constant amplitude loading with various stress ratios. R^{∞} is the far field applied stress ratio.

factor range. Therefore, the growth behaviour of patched cracks and un-patched cracks, under constant amplitude loading, can be successfully rationalized by the concept of fatigue crack closure. This enables the crack growth rates of patched cracks to be predicted using the growth rates of un-patched cracks.

Under variable amplitude or spectrum loading, it is important to analyze the transient crack closure, especially the retardation effects associated with overloads. As already discussed in the previous section, after the application of an overload, a patched crack experiences nearly the same transient crack closure behaviour as un-patched crack subjected to the same stress intensity factor. Therefore the crack closure of patched cracks can be determined by analyzing the crack closure of a centre-cracked panel subjected to a reference stress, as illustrated in Figure 8.13. The reference that the centre-cracked panel is subjected to is determined to ensure that the stress intensity factor is the same as the patched crack, viz,

$$\sigma^*(t)\sqrt{\pi a} = [\phi\sigma_\infty(t) + \sigma_0^{\mathrm{T}}]\sqrt{\pi a}F(\pi\Lambda a) \tag{8.24}$$

which leads to

$$\sigma^*(t) = [\phi\sigma_\infty(t) + \sigma_0^{\mathrm{T}}]F(\pi\Lambda a) \tag{8.25}$$

Since the factor F decreases as the crack size increases, the equivalent stress $\sigma^*(t)$ would become a progressively smaller fraction of the applied stress, to ensure that the cyclic plastic deformation at the tip of the equivalent crack remain the same as that for the patched crack.

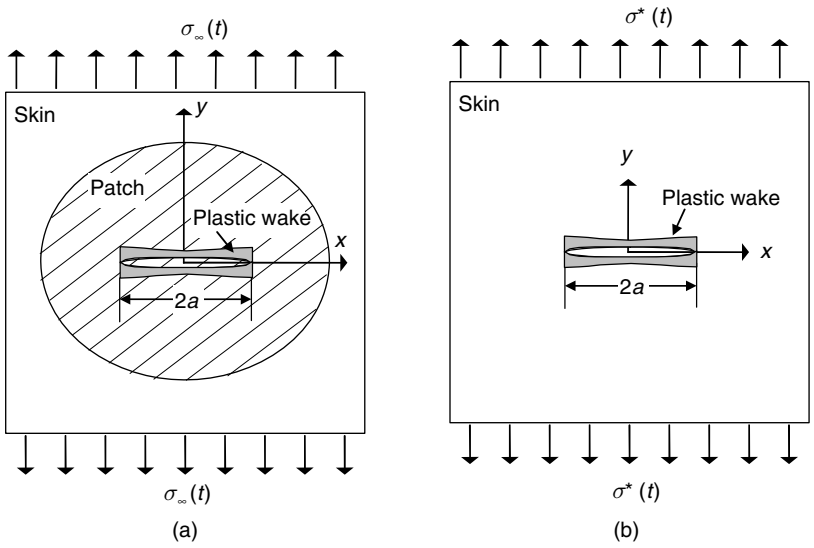

Fig. 8.13. Correspondence between a patched crack and an un-patched crack subject to an equivalent stress.

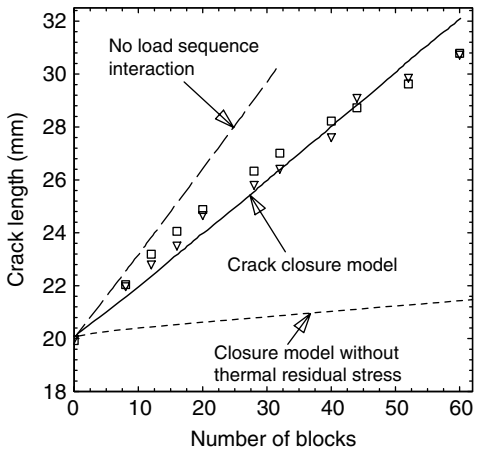

Fig. 8.14. Comparison between experimental and predicted growth behaviour of patched cracks under F-111 spectrum. Symbols denote experimental data.

A comparison with some experimental results (Boykett and Walker, 1996) is shown in Figure 8.14. The test specimens, which were made of 2024-T851 aluminium alloy panels having a thickness of 3.7 mm, were repaired with a boron composite patch after being pre-cracked to give a half crack size equal to 20 mm. Patches were made from Boron/Epoxy pre-preg fibre composites to form a 14-ply laminate; the lay-up is $[0_5, \pm 45]_s$. The patched specimens were subjected to a load spectrum (to be denoted as F-111) consisting of 36, 273 turning points per block, with the ratio of the minimum to the maximum equal to -0.278. The maximum applied stress, as listed in Table 8.1, was equal to 217 MPa, giving rise to a maximum plate stress (in a block) of about 112 MPa. The geometry and material properties of the patched specimen (denoted as F111) are summarized in Tables 8.1 and 8.2. The patches were bonded to the plate using an FM-73 adhesive and cured at 80 °C, resulting in a thermal residual stress of

Table 8.1. Geometry and material properties of specimens.

Specimen	E_s (GPa)	t_s (mm)	E_p (GPa)	t_p (mm)	G_A (GPa)	t_A (mm)	ϕ	Λ (1/m)	$\sigma_{\infty,\max}$ (MPa)
F-111	72	3.7	156	1.82	0.57	0.25	0.52	58.0	217
FALSTAFF	72	3.14	200	0.91	0.54	0.2	0.55	65.5	248

Table 8.2. Thermal properties and temperature change.

Specimen	α_s (plate)	α_p (patch)	ΔT (°C)	σ_0^T (MPa)
F-111	2.40*E*-05	4.00*E*-06	60	67.35
FALSTAFF	2.40*E*-05	4.00*E*-06	100	70.67

67.35 MPa. The base-line fatigue crack-growth data for the material were taken from the literature (DTDH, 1972), which were then converted to obtain the crack-growth rate against effective stress-intensity factor range relationship. This allows the experimental results from various stress-ratio tests to be collapsed within a single scatter band. The converted data can be well correlated using the standard Paris relationship, giving rise to the following constants $C = 7.4 \times 10^{-10}$ and $m = 2.93$. As seen in Figure 8.14, the predictions based on the equivalent crack method are in good agreement with the experimental results. It is also interesting to note that, due to the increased mean stress resulting from the thermal residual stress, simple predictions based on simply integrating the crack growth equation on a cycle-by-cycle basis, using the steady-state crack opening stress given by Equation (8.9), are slightly conservative. This implies that the retardation effect of the loading spectrum is also not very significant due to the high mean stress. Also shown in Figure 8.14 are the predictions based on the crack closure model, without considering the thermal residual stress. It is evident that the calculated crack growth rate is far lower than the experimental results, demonstrating the importance of the thermal residual stress in enhancing the fatigue crack-growth rates. This also highlights the need to minimize the thermal residual stress.

The experimental results of another series of tests involving FALSTAFF spectrum (Raizenne et al., 1988) are plotted in Figure 8.15, together with predictions made using equivalent crack method. The test specimens, which were made from 3.2 mm thick 2024-T3 aluminium sheets, were first fatigue pre-cracked under constant amplitude loading to two prescribed crack lengths: 5 mm and 25 mm. The test panels were then repaired with boron/epoxy using three different adhesive systems. Two edge-cracked face-sheets were bonded to an aluminium honeycomb core to form a sandwich panel to avoid out-of-plane bending. A total of six such panels were tested. The thermal residual stress, as listed in Table 8.2, was estimated based on Equation (8.20) to be approximately

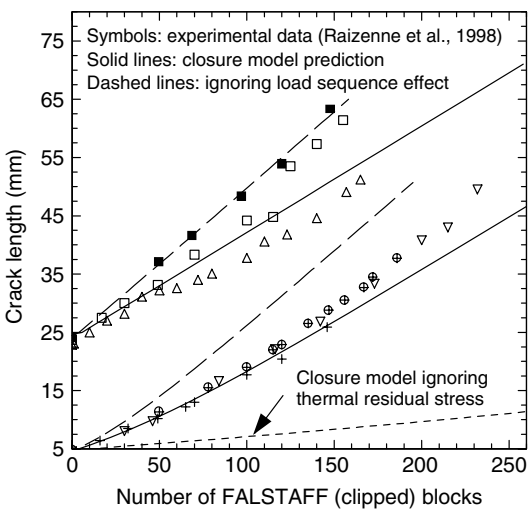

Fig. 8.15. Comparison between experimental and predicted growth behaviour of patched cracks under FALSTAFF spectrum.

70.67 MPa. This thermal residual stress is significant as the maximum skin stress $\phi\sigma_\infty$ is about 136 MPa. The spectrum used was a "clipped" FALSTAFF spectrum, in which the negative loading has been removed. As seen in the figure, the predictions based on the crack closure model, when thermal residual stress is taken into account, are in good correlation with the experimental data. As indicated by the dashed lines in Figure 8.15, predictions made by integrating the crack growth rate equation, with the crack-opening stress for each reversal being taken to be the steady-state value, are slightly on the conservative side. Similar to the results shown in Figure 8.14, this behaviour indicates that, due to the high thermal residual stress, the spectrum loading does not have a strong retardation effect. Also plotted in Figure 8.15 are the predictions made by neglecting the thermal residual stress. Again, much slower crack-growth rates are predicted. This confirms the observations made earlier regarding the importance of the thermal residual stresses and the need to minimize residual stresses in order to achieve lower crack-growth rates. It should be noted that the effects of disbond and adhesive plasticity have not been considered in this section, since the main objective here is to demonstrate the equivalence principle between patched and un-patched cracks.

8.5 Summary

It has been shown that under constant amplitude loading with the prospective stress much lower than the material yield stress, the closure behaviour of repaired cracks is nearly identical to that corresponding to un-patched cracks subjected to steady-state loading. Under variable amplitude loading, the crack closure behaviour of a patched crack has also been shown to be identical to that corresponding to an un-patched crack subjected to the same stress-intensity factor history.

An equivalent crack method has been developed, which enables the fatigue crack closure of patched cracks to be determined by analyzing a centre-cracked panel subjected to an equivalent stress given by

$$\sigma^*(t) = [\phi\sigma_\infty(t) + \sigma_0^{\mathrm{T}}]F(\pi\Lambda a)$$

Predictions based on this method have been found to correlate well the experimental results obtained under two aircraft loading spectra. It has also been found that the ignorance of the thermal residual stress would lead to significant under-predication of the crack growth rate.

CHAPTER 9

A Preliminary Design Approach for Crack Patching

9.1 Introduction

This chapter describes an approach to a patch design for a crack repair, based largely on the analyses developed in Chapters 2 and 3 and also by Duong (2003a) under the Composite Repair of Aircraft Structures (CRAS) program. The design process from this approach follows the guidelines given in the Composite Repair to Metallic Structure (CRMS) Guidelines (1998), RAAF Engineering Standard C5033 (Davis, 1995), and those recently developed by The Boeing Company under the CRAS program (Duong, 2003a,b; Duong et al., 2003). This approach does not include the effect of the out-of-plane bending and assumes that the repaired structural component is subjected to biaxial loading at the far field. The initially designed patch that is output from the process will be a unidirectional patch with the 0^0 plies aligned normal to the line of crack. For a general far-field loading (including a shear load), the principal stresses and principal directions of the far-field-applied stresses must be determined and the patch will then be designed with respect to the principal axes of the far-field stresses with its principal moduli and the crack orientation assuming to be parallel to those axes. Since a design of a patch in a cracked component under a primary compressive load can be accomplished in a similar manner to the case of a primary tensile load, for clarity, the design approach delineated in this chapter is specifically for a cracked structure subjected to the biaxial loading with a primary tensile load. However, as illustrated through examples in Chapter 4 and also shown later in Section 9.2.2, the effect of the compression loads and thermal loads are additive for the patch's stresses and for the skin stress concentration at the end of the patch while they are subtractive in the case of a tensile load. Thus, the criteria specified in Section 9.3 must be modified slightly for the case of a compressive load to reflect such difference and the appropriate material allowables for compression must be used in these criteria. In addition, the design approach in the latter case also does not address the global buckling of the structure nor local instability at the end of the patch as observed in some tests.

The design process for composite patching of cracks consists of establishment of design criteria, selection of the patch and adhesive materials, development of the initial design and refinement/validation by detailed analyses and/or test. The first three tasks of this process will be reviewed in this chapter while the last task has been covered in Chapters 2–8 and will be discussed in Chapter 11. For clarity, the basic analysis methods described in Chapters 2 and 3, which will be used in the preliminary design approach, will be reviewed first in Section 9.2 along with the extensional work developed under the CRAS program on the equivalency between a thermal and a mechanical problem (Duong, 2003a). The design criteria are established in Section 9.3 and they are followed by the guidelines for the selection of the patch and adhesive materials in Section 9.4. Finally, the initial design process is developed in Section 9.5.

9.2 Basic Analysis Methods Used in the Preliminary Design Approach

In this section, a brief summary of the basic analysis methods used in the preliminary design approach is presented. The quantities of practical interest in the design are stresses in the skin and patch, shear strain in the adhesive, and the stress intensity factor for residual strength and fatigue crack growth predictions. The Rose two-stage analysis procedure described in Chapter 3 for estimating these quantities will be reviewed here first and it will then be extended to include the thermal effects. As in Chapter 3, for simplicity, the analysis method is developed for an elliptical isotropic patch with the same Poisson's ratio as that of the skin. It was shown in Chapter 3 that the effect of the material orthotropy of the patch is insignificant on the sought quantities. The effect of tapering of the patch's edge as commonly done in practice is also ignored in the analysis. It should be emphasized that the thermo-mechanical analysis outlined in Section 9.2.1 below has been developed by Duong (2003a) and it is presented here for the first time in this book.

9.2.1 Analysis method for a repair subjected only to mechanical loads

In the first stage analysis of the Rose solution procedure, a patch is assumed to bond rigidly to an *uncracked* skin. Stresses in the skin near the edge of the patch and underneath the patch are determined in Chapter 3 and also Chapter 6 using an elliptical inclusion analogy. These skin stresses in the y-component derived from these chapters are given below.

Skin stress underneath the patch

$$\sigma_0^* = \frac{\sigma_\infty}{D}\left\{(1+S)\left[3+2\frac{B}{A}\right]+1+\nu_s S+2\frac{A}{B}+\Sigma\cdot S\left[1-\nu_s-2\nu_s\frac{B}{A}\right]\right\}$$
$$Z = 3(1+S)^2+2(1+S)\left[\frac{B}{A}+\frac{A}{B}+\nu_s S\right]+1-\nu_s^2 S^2 \tag{9.1}$$

Skin stress near the tip of the patch's edge

$$\sigma_{tip}^* = (1+S)\,\sigma_0^* \tag{9.2}$$

where S is the patch stiffness to skin stiffness ratio, i.e. $S = \frac{E'_p t_p}{E'_s t_s} = \frac{E_p t_p}{E_s t_s}$ for an isotropic patch with a Poisson's ratio same as skin, A and B are the axes of the ellipse with the dimension B parallel to the primary loading direction, ν_s is the skin's Poisson's ratio, Σ is the biaxial stress ratio, and the subscripts p or s denote the patch and skin, respectively. As found in Chapters 3 and 6, the skin stress underneath an elliptical patch is uniform, independent of the spatial coordinates and the patch's size. Furthermore, since the reinforced skin is stiffer than the remote skin, it can be shown from Equations (9.2) and (9.1) that σ^*_{tip} is always larger than the remote skin stress σ_∞. In other words, there is a stress concentration in the skin near the tip of the patch's edge. Since it is more convenient to use the skin stress concentration factor at the patch tip as a design parameter than σ^*_{tip}, Equation (9.2) therefore has been rewritten as:

$$K^*_t = \frac{\sigma^*_{tip}}{\sigma_\infty} = (1+S)\,\frac{\sigma^*_0}{\sigma_\infty} \tag{9.3}$$

Similar to the skin, the y-component stress in the patch is also uniform and found to be:

$$\sigma_p^{stageI} = \sigma^*_0 \frac{E'_p}{E'_s} = \sigma^*_0 \frac{E_p}{E_s} \tag{9.4}$$

In the second stage analysis of the Rose solution procedure, a patch is assumed to be of infinite extent and adhesively bonded to the skin. The skin now contains a crack with a pressure load of σ^*_0 acting on its surfaces and without any remote applied stresses. The purpose of the second stage analysis is to estimate the crack-tip stress intensity factor K_I, the maximum adhesive shear strain, and the additional stresses in the patch near the crack surfaces due to the loss of load carrying capability of the skin in the vicinity of the crack. For simplicity, the skin crack is assumed to be semi-infinite. As shown in Chapter 3, the stress intensity factor when it is estimated based on this semi-infinite crack model will have an upper bound value and will be denoted by $K_{I\infty}$. By considering the change in the potential energy of the patched cracked skin due to a virtual crack extension and using results from the 1D bonded joint theory, $K_{I\infty}$ had been derived in Chapter 3 as:

$$K_{I\infty} = \frac{\sigma^*_0}{\sqrt{\Lambda}} \tag{9.5}$$

where

$$\Lambda = \frac{\beta_A S}{(1+S)\,(1-\nu_s^2)} \tag{9.6}$$

$1/\beta_A$ as in Chapters 2 and 3 is the shear load transfer length with β_A defined by:

$$\beta_A = \sqrt{\frac{G_A}{t_A}\left(\frac{1}{E'_s t_s} + \frac{1}{E'_p t_p}\right)} \tag{9.7}$$

G_A and t_A are the shear modulus and thickness of the adhesive layer, respectively, S again is the patch stiffness to skin stiffness ratio, $E'_{s,p} = \frac{E_{s,p}}{1-\nu^2_{s,p}}$. As mentioned earlier, since $K_{I\infty}$ is the upper bound value for the stress intensity factor of a patched crack,

$K_{I\infty}$ given by Equation (9.5) is a constant and independent of the actual crack length. Furthermore, $K_{I\infty}$ must also be less than or equal to the corresponding stress intensity factor of an un-patched crack, i.e., $K_{I\infty} \leq \sigma_0^* \sqrt{\pi a}$ where $\sigma_0^* \sqrt{\pi a}$ is the well-known result for the stress intensity factor of a central crack of length $2a$ in an infinite sheet.

In contrast, the adhesive shear strain in the adhesive and the additional stress in the patch due to the presence of the skin crack are estimated using one-dimensional theory of a double-strap joint described in Chapter 2. The shear strain in the adhesive in general is highest near the patch's edge and near the crack surfaces. Since most of the repaired patches have a tapered edge that tends to reduce shear load transfer there, the maximum shear strain in the adhesive therefore normally occurs near the crack surfaces. When the shear load transfer length $1/\beta_A$ is small relative to the patch size, the adhesive's shear strain near the crack surfaces that results from the local load transfer between the cracked skin and the patch decays rapidly to zero for a small distance away from the crack. The maximum shear strain in the adhesive in this case is obtained from the displacements of the skin and patch given in Chapter 2 at the skin interruption end as:

$$\gamma_A^{max} = \frac{u_s(x=0) - u_p(x=0)}{t_A} = \frac{\sigma_0^* t_s \beta_A}{G_A} \tag{9.8}$$

where $u_s(0)$ has been evaluated using Equation (2.25) while $u_p(0) = 0$ due to symmetry. Similarly, the additional stress in the patch due to the presence of the skin crack is determined from the one-dimensional analysis as:

$$\sigma_p^{stageII} = \frac{\sigma_0^* t_s}{t_p} \tag{9.9}$$

The total stress in the patch is then equal to the sum of the individual contributions from the first and second stage analyses as given by Equations (9.4) and (9.9), respectively.

So far, all results have been obtained by assuming that the adhesive remains elastic for a given applied load. However, in many instances, the adhesive is loaded beyond its elastic shear stress limit. When the adhesive is modeled as an elastic-perfectly-plastic material as shown in Figure 2.3, from Chapters 2 and 3, the formulas for the maximum shear strain in the adhesive and $K_{I\infty}$ need to be changed to the following while the rest of the equations remain the same.

$$\gamma_A^{max} = \begin{cases} \dfrac{\sigma_0^* t_s \beta_A}{G_A} & \text{for } \sigma_0^* t_s \beta_A < \tau_Y^{(A)} \\ \dfrac{\tau_Y^{(A)}}{2G_A}\left\{1 + \left(\dfrac{\sigma_0^*}{\sigma_{0Y}}\right)^2\right\} & \text{otherwise} \end{cases} \tag{9.10}$$

$$K_{I\infty} = \begin{cases} \dfrac{\sigma_0^*}{\sqrt{\Lambda}} & \text{for } \sigma_0^* t_s \beta_A < \tau_Y^{(A)} \\ \dfrac{\sigma_0^*}{\sqrt{\Lambda}}\left[\dfrac{\left(\dfrac{\sigma_0^*}{\sigma_{0Y}}\right)^3 + 3\left(\dfrac{\sigma_0^*}{\sigma_{0Y}}\right) - 1}{3\left(\dfrac{\sigma_0^*}{\sigma_{0Y}}\right)^2}\right]^{1/2} & \text{otherwise} \end{cases} \tag{9.11}$$

where σ_{0Y} is defined by Equation (3.32) as $\sigma_{0Y} \equiv \frac{\tau_Y^{(A)}}{\beta_A t_s}$, $\gamma_Y^{(A)}$ is the elastic shear limit of the adhesive as defined in Figure 2.3, Λ is given by Equation (9.6), and the rest are previously defined. It is worthy to note that the second equation of (9.10) has been derived in a similar manner as that for the case of an elastic adhesive given above, except that the displacement of the skin at the interruption end is now given by Equation (2.62). In addition, the second equation of (9.11) is identical to Equation (3.35).

9.2.2 Analysis method for a repair subjected to thermo-mechanical loads

As before, the analysis of the thermo-mechanical problem is also divided into two stages. In the first stage, the skin's stresses underneath the patch, the patch's stresses and the skin stress concentration near the tip of a patch's edge are calculated using an inclusion analogy. For clarity, the analytical method for stage I analysis of a repair under purely thermal loads is delineated first.

Consider a problem of a patched skin that is cooled uniformly from a stress-free (ambient) temperature to a low operating temperature as experienced by the aircraft during high altitude cruising. Follow the procedure outlined in Section 4.2.4; the analysis of this problem proceeds in two steps. In the first step, the skin is cooled first to a low operating temperature while the patch is still at a stress-free (ambient) temperature. Furthermore, the patch is also subjected simultaneously to a fictitious uniform strain field of $\alpha_s \Delta T \delta_{ij}$ where α_s is the thermal expansion coefficient of the skin, and $\Delta T = \left(T_{\text{operating}} - T_{\text{ambient}}\right)$. Since the patch is subjected to a uniform strain field of $\alpha_s \Delta T \delta_{ij}$ that is compatible with the thermal strain of the skin, the skin will contract freely during this cooling phase without experiencing any exerted forces from the patch, resulting in a stress-free skin. Thus, the strain field in the skin and patch at the end of the first step of cooling will be given by:

$$\varepsilon_{ij}^{s(\text{step1})}(\mathbf{x}) = \varepsilon_{ij}^{p(\text{step1})}(\mathbf{x}) = \alpha_s \Delta T \delta_{ij} \tag{9.12}$$

In the second step of cooling, the patch is allowed to cool to a low operating temperature and also to relax simultaneously the fictitious strain field $\alpha_s \Delta T \delta_{ij}$ imposed previously on it. The problem of a second step cooling is then a problem of a patched skin with the following strain prescribed in the patch:[1]

$$\varepsilon_{ij}^{(T)(p)} = \left(\alpha_{ij}^p \Delta T - \alpha_s \Delta T \delta_{ij}\right) = \Delta \alpha_{ij} \cdot \Delta T \tag{9.13}$$

where α_{ij}^p is the thermal expansion coefficient tensor of the patch in the principal material directions, and δ_{ij} is the Kronecker delta. While the solution of this problem will be given in detail in the next paragraphs, let us assume for now that this solution is already obtained with the strain solutions for the skin and patch denoted as:

$$\varepsilon_{ij}^{s(\text{step2})}(\mathbf{x}) = \varepsilon_{ij}^{p(\text{step2})}(\mathbf{x}) = \varepsilon_{ij}^{**}(\mathbf{x}) \tag{9.14}$$

[1] See footnote 1 of Chapter 4.

The total strains in the skin and patch at the end of the cooling process are then equal to the sum of individual contributions from the first and second steps of cooling, and these strains are given by:

$$\varepsilon_{ij}^{\mathrm{s}}(\mathbf{x}) = \varepsilon_{ij}^{\mathrm{p}}(\mathbf{x}) = \varepsilon_{ij}^{**}(\mathbf{x}) + \alpha_{\mathrm{s}}\Delta T\delta_{ij} \tag{9.15}$$

On the other hand, the thermal stresses in the skin and patch after cooling are determined from the thermo-elastic constitutive relation, Equations (9.15) and (9.13) as:

$$\begin{aligned}
\sigma_{ij}^{\mathrm{s}}(\mathbf{x}) &= C_{ijkl}^{\mathrm{s}}\left[\varepsilon_{kl}^{\mathrm{s}}(\mathbf{x}) - \alpha_{\mathrm{s}}\Delta T\delta_{kl}\right] = C_{ijkl}^{\mathrm{s}}\varepsilon_{kl}^{**}(\mathbf{x}) \\
\sigma_{ij}^{\mathrm{p}}(\mathbf{x}) &= C_{ijkl}^{\mathrm{p}}\left[\varepsilon_{kl}^{\mathrm{p}}(\mathbf{x}) - \alpha_{kl}^{\mathrm{p}}\Delta T\right] = C_{ijkl}^{\mathrm{s}}\left[\varepsilon_{kl}^{**}(\mathbf{x}) - \left(\alpha_{kl}^{\mathrm{p}}\Delta T - \alpha_{\mathrm{s}}\Delta T\delta_{kl}\right)\right] \\
&= C_{ijkl}^{\mathrm{p}}\left[\varepsilon_{kl}^{**}(\mathbf{x}) - \Delta\alpha_{kl}\Delta T\right] \\
&= C_{ijkl}^{\mathrm{p}}\left[\varepsilon_{kl}^{**}(\mathbf{x}) - \varepsilon_{kl}^{(\mathrm{T})(\mathrm{p})}\right]
\end{aligned} \tag{9.16}$$

It remains now to outline a solution method for determining $\varepsilon_{ij}^{**}(\mathbf{x})$. It is more convenient to solve $\varepsilon_{ij}^{**}(\mathbf{x})$ using a mechanical problem analogue, because the solution of the thermal stress problem then can be easily combined with that of the purely mechanical problem for use in the patch design process. We begin the development by showing that problem of a patched skin under purely mechanical loads can be formulated as a type of the problem considered earlier in the second step of cooling, and consequently it can be made equivalent to the thermal problem. That equivalency is proven below.

Let us consider the problem of a patch bonded to a large skin that is subjected to the far field applied stresses $-\sigma_{11}^{\mathrm{T}}$ and $-\sigma_{22}^{\mathrm{T}}$, or equivalently to the far field applied strains $-\varepsilon_{11}^{\mathrm{T}}$ and $-\varepsilon_{22}^{\mathrm{T}}$ as depicted in Figure 9.1 where σ_{ij}^{T} and $\varepsilon_{ij}^{\mathrm{T}}$ are related by $\sigma_{ij}^{\mathrm{T}} = C_{ijkl}^{\mathrm{s}}\varepsilon_{kl}^{\mathrm{T}}$. This problem can be broken in two sub-problems as illustrated in the same figure. In the first sub-problem, the patch is assumed to be applied by fictitious uniform strain fields $-\varepsilon_{11}^{\mathrm{T}}$ and $-\varepsilon_{22}^{\mathrm{T}}$, while the skin is subjected to the given far-field stresses or strains. The patch in the first sub-problem will not exert any forces on the skin since its strains are compatible with those of the remote skin. The solution of the first sub-problem is therefore trivial since the skin and patch in this case have uniform strains that are the same as the far-field-applied strains. The stress components in the skin are thus also uniform and equal to $-\sigma_{11}^{\mathrm{T}}$ and $-\sigma_{22}^{\mathrm{T}}$. However, since the patch in reality is not subjected to such fictitious strain fields, these fictitious strain fields therefore must relieve to zero. The second sub-problem is therefore a problem of a large skin without any remote applied stresses nor applied strains but containing a patch prescribed with a uniform strain fields $\varepsilon_{ij}^{\mathrm{T}}$ as shown in Figure 9.1(c). Consequently, the problem shown in Figure 9.1(c) is equal to the difference between the mechanical problem shown in Figure 9.1(a) and the trivial problem shown in Figure 9.1(b), as illustrated in Figure 9.2. It should be noted that the far-field-applied stresses or strains and the prescribed strains in the patch of the problem shown in Figure 9.2(c) have opposite signs with those shown in Figure 9.1(b). Also, the strain components in the skin and patch of the problem shown in Figure 9.2(c) are equal to $\varepsilon_{11}^{\mathrm{T}}$ and $\varepsilon_{22}^{\mathrm{T}}$. Moreover, stresses in the skin and patch of all problems considered in Figures 9.1 and 9.2 are related to their corresponding strains by the isothermal constitutive relations, i.e. $\sigma_{ij}(\mathbf{x}) = C_{ijkl}\varepsilon_{kl}(\mathbf{x})$.

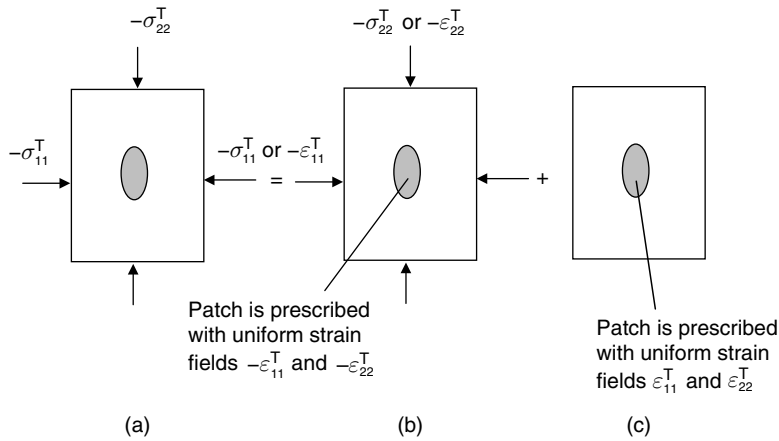

Fig. 9.1. A decomposition of a mechanical problem into two sub-problems: (a) the original mechanical problem; (b) a mechanical problem with uniform strains prescribed in the patch; and (c) the initial strain type problem. It should be noted that the solution of the problem shown in Figure 9.3(b) is trivial. Also, $\sigma_{ij}^{T} = C_{ijkl}^{s}\varepsilon_{kl}^{T}$.

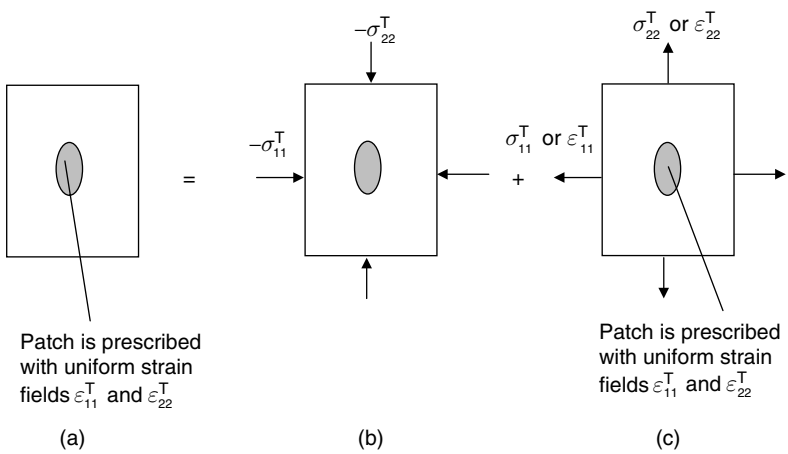

Fig. 9.2. A superposition method for analyzing a patched plate with a uniform strain field prescribed in the patch, noting $\sigma_{ij}^{T} = C_{ijkl}^{s}\varepsilon_{kl}^{T}$. If ε_{ij}^{T} is selected to be equal to $\varepsilon_{ij}^{(T)(p)}$, strain solution ε_{ij}^{**} will prevail in both patch and skin. Also, the solution of problem 9.2(c) is trivial, i.e. patch and skin are under uniform strain ε_{ij}^{T}.

According to the preceding paragraph, the solution of any problem of the type illustrated in Figure 9.2(a) can be obtained by superimposing the solutions of two problems shown respectively in Figures 9.2(b) and 9.2(c). The reader is reminded that a problem of a second step cooling of the original thermal stress problem also falls into that category.

Thus, by identifying $\varepsilon_{11}^{\mathrm{T}}$ and $\varepsilon_{22}^{\mathrm{T}}$ of the problem shown in Figure 9.2(a) as $\varepsilon_{ij}^{\mathrm{T}} = \varepsilon_{ij}^{(\mathrm{T})(\mathrm{p})} = \Delta\alpha_{ij}\Delta T$, noting $\varepsilon_{ij}^{(\mathrm{T})(\mathrm{p})}$ is given by Equation (9.13), the sought solution $\varepsilon_{ij}^{**}(\mathbf{x})$ of the original thermal stress problem can be easily found by the procedure shown in Figure 9.2 with σ_{11}^{T} and σ_{22}^{T} given by:

$$\begin{aligned}
\sigma_{11}^{\mathrm{T}} &= \frac{E_{\mathrm{s}}}{1-\nu_{\mathrm{s}}^2}\left(\varepsilon_{11}^{\mathrm{T}} + \nu_{\mathrm{s}}\varepsilon_{22}^{\mathrm{T}}\right) = \frac{E_{\mathrm{s}}}{1-\nu_{\mathrm{s}}^2}\left(\varepsilon_{11}^{(\mathrm{T})(\mathrm{p})} + \nu_{\mathrm{s}}\varepsilon_{22}^{(\mathrm{T})(\mathrm{p})}\right) \\
\sigma_{22}^{\mathrm{T}} &= \frac{E_{\mathrm{s}}}{1-\nu_{\mathrm{s}}^2}\left(\nu_{\mathrm{s}}\varepsilon_{11}^{\mathrm{T}} + \varepsilon_{22}^{\mathrm{T}}\right) = \frac{E_{\mathrm{s}}}{1-\nu_{\mathrm{s}}^2}\left(\nu_{\mathrm{s}}\varepsilon_{11}^{(\mathrm{T})(\mathrm{p})} + \varepsilon_{22}^{(\mathrm{T})(\mathrm{p})}\right)
\end{aligned} \tag{9.17}$$

Once $\varepsilon_{ij}^{**}(\mathbf{x})$ is obtained, the thermal stresses in the skin and patch are determined by Equation (9.16).

The above procedure for determining thermal stresses involves two separate steps: first determining $\varepsilon_{ij}^{**}(\mathbf{x})$ using the procedure illustrated in Figure 9.2 and then the thermal stresses via Equation (9.16). However, these two steps can be combined so that the thermal stresses can be obtained directly in a single step as follows.

From Equation (9.16), the thermal stresses in the skin and patch are equal to the product of their elasticity tensor and ε_{ij}^{**} or $\left(\varepsilon_{ij}^{**} - \varepsilon_{ij}^{(\mathrm{T})(\mathrm{p})}\right)$ where ε_{ij}^{**} is obtained from linear superposition of solutions of problems shown in Figures 9.2(b) and 9.2(c) with $\varepsilon_{ij}^{\mathrm{T}} = \varepsilon_{ij}^{(\mathrm{T})(\mathrm{p})}$, as mentioned above. From Figure 9.2, it is clear that strains in the skin and patch from this linear superposition are given by

$$\begin{aligned}
&\varepsilon_{ij}^{\mathrm{s(a)}} = \varepsilon_{ij}^{**} = \varepsilon_{ij}^{\mathrm{s(b)}} + \varepsilon_{ij}^{\mathrm{s(c)}} = \varepsilon_{ij}^{\mathrm{s(b)}} + \varepsilon_{ij}^{\mathrm{T}} \quad \text{and} \\
&\varepsilon_{ij}^{\mathrm{p(a)}} = \varepsilon_{ij}^{**} = \varepsilon_{ij}^{\mathrm{p(b)}} + \varepsilon_{ij}^{\mathrm{p(c)}} = \varepsilon_{ij}^{\mathrm{p(b)}} + \varepsilon_{ij}^{\mathrm{T}} \quad \text{or} \quad \varepsilon_{ij}^{\mathrm{p(b)}} = \varepsilon_{ij}^{**} - \varepsilon_{ij}^{\mathrm{p(c)}} = \varepsilon_{ij}^{**} - \varepsilon_{ij}^{\mathrm{T}}
\end{aligned} \tag{9.18}$$

where the superscripts a, b, and c denote respectively the problems shown in Figures 9.2(a)–9.2(c), and the strains in the skin and patch of the problem 9.2(c) are trivially equal to $\varepsilon_{ij}^{\mathrm{T}}$.

Let us consider now the linear superposition of problems shown in Figures 9.3(b) and 9.3(c). From Figures 9.3(b) and 9.3(c) and by noting that (i) Figure 9.3(b) is the same as Figure 9.2(b) so that strains in the skin and patch due to the contribution from Figure 9.3(b) will be $\varepsilon_{ij}^{\mathrm{s(b)}}$ and $\varepsilon_{ij}^{\mathrm{p(b)}}$, respectively, and (ii) strains in the skin of the problem shown in Figure 9.3(c) are equal to $\varepsilon_{ij}^{\mathrm{T}}$, the strains in the skin and patch from linear superposition of the results of problems shown in Figures 9.3(b) and 9.3(c) therefore are given by:

$$\begin{aligned}
\varepsilon_{ij}^{\mathrm{s}} &= \varepsilon_{ij}^{\mathrm{s(b)}} + \varepsilon_{ij}^{\mathrm{T}} \\
\varepsilon_{ij}^{\mathrm{p}} &= \varepsilon_{ij}^{\mathrm{p(b)}}
\end{aligned} \tag{9.19}$$

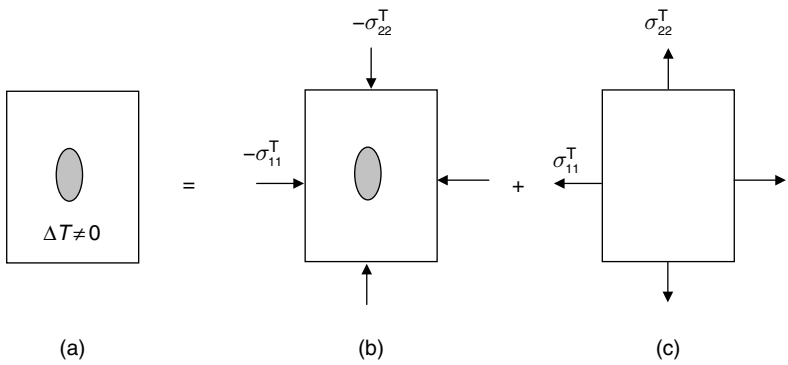

Fig. 9.3. A superposition method for determining thermal stresses in a patched plate.

However, since $\varepsilon_{ij}^{s(b)} + \varepsilon_{ij}^{T} = \varepsilon_{ij}^{**}$ and $\varepsilon_{ij}^{p(b)} = \varepsilon_{ij}^{**} - \varepsilon_{ij}^{T}$ by Equation (9.18), the strains in the skin and patch given by (9.19) can also be rewritten as

$$\begin{aligned} \varepsilon_{ij}^{s} &= \varepsilon_{ij}^{s(b)} + \varepsilon_{ij}^{T} = \varepsilon_{ij}^{**} \\ \varepsilon_{ij}^{p} &= \varepsilon_{ij}^{p(b)} = \varepsilon_{ij}^{**} - \varepsilon_{ij}^{T} \end{aligned} \tag{9.20}$$

while the corresponding stresses are given by

$$\begin{aligned} \sigma_{ij}^{s} &= C_{ijkl}^{s}\varepsilon_{kl}^{s} = C_{ijkl}^{s}\varepsilon_{kl}^{**} \\ \sigma_{ij}^{p} &= C_{ijkl}^{p}\varepsilon_{kl}^{p} = C_{ijkl}^{p}\left(\varepsilon_{kl}^{**} - \varepsilon_{kl}^{T}\right) \end{aligned} \tag{9.21}$$

Since the stresses in the skin and patch of the original thermal stress problem are also given by the same expression as (9.21) via Equation (9.16) and noting $\varepsilon_{ij}^{T} = \varepsilon_{ij}^{(T)(p)}$, the linear superposition of problems shown in Figures 9.3(b) and 9.3(c) will render the original thermal stress problem as indicated in Figure 9.3(a).

So far only thermal stresses of the problem associated with uniform cooling is considered. However, it can be shown in a similar manner that the thermal stress solutions of the problem associated with curing of the adhesive can be obtained by the same procedure as given in Figure 9.3, except for a new and different expression for $\varepsilon_{ij}^{(T)(p)}$. For a curing process using a circular heater blanket, this new expression for $\varepsilon_{ij}^{(T)(p)}$ can be derived as follows. As presented in Section 4.2.4, $\varepsilon_{ij}^{(T)(p)}$ associated with the curing of the adhesive is found from Equation (4.40) as

$$\varepsilon_{ij}^{(T)(p)} = -\alpha_{ij}^{p}\Delta T_{\text{heating}} + \varepsilon_{ij}^{s(\text{heating})} \tag{9.22}$$

where $\Delta T_{\text{heating}} = T_{\text{curing}} - T_{\text{ambient}}$, and $\varepsilon_{ij}^{s(\text{heating})}$ is the total strain of the skin inside the inclusion region Ω of a thermal inclusion problem with eigenstrain given by $\varepsilon_{ij}^{*} = \alpha_{s}\Delta T_{\text{heating}}\delta_{ij}$. For a curing process using a circular heater blanket, region Ω of this

thermal inclusion problem is also circular. Based on the results given in Section 6.2.1 for a circular inclusion, the strain in the skin inside Ω can be obtained from the Eshelby solution as:

$$\varepsilon_{ij}^{\mathrm{s(heating)}} = S_{ijkl}\varepsilon_{kl}^{*} \tag{9.23}$$

where S_{ijkl} is defined by Equation (6.4), and $\varepsilon_{ij}^{*} = \alpha_{\mathrm{s}}\Delta T_{\mathrm{heating}}\delta_{ij}$. Substituting Equation (9.23) into (9.22) for $\varepsilon_{ij}^{\mathrm{s(heating)}}$, noting $\varepsilon_{ij}^{*} = \alpha_{\mathrm{s}}\Delta T_{\mathrm{heating}}\delta_{ij}$, and evaluating S_{ijkl} by Equation (6.4) for a circular region Ω yield:

$$\begin{aligned}
\varepsilon_{11}^{(\mathrm{T})(\mathrm{p})} &= \left[-\left(\frac{\nu_{\mathrm{s}}}{2}+\frac{1}{2}\right)\alpha_{\mathrm{s}}+\alpha_{11}^{\mathrm{p}}\right]\left(T_{\mathrm{curing}}-T_{\mathrm{ambient}}\right)\\
\varepsilon_{22}^{(\mathrm{T})(\mathrm{p})} &= \left[-\left(\frac{\nu_{\mathrm{s}}}{2}+\frac{1}{2}\right)\alpha_{\mathrm{s}}+\alpha_{22}^{\mathrm{p}}\right]\left(T_{\mathrm{curing}}-T_{\mathrm{ambient}}\right)
\end{aligned} \tag{9.24}$$

With $\varepsilon_{ij}^{(\mathrm{T})(\mathrm{p})}$ associated with the curing process being determined, σ_{11}^{T} and σ_{22}^{T} of the equivalent mechanical problem shown in Figure 9.3 can be evaluated by the same equation as (9.17) but with $\varepsilon_{ij}^{(\mathrm{T})(\mathrm{p})}$ now defined by Equation (9.24).

The above equivalency between a thermal and a mechanical problem has many significant implications in the design of the repaired patch and has been verified independently by means of the FE method. First, all results derived in Section 9.2.1 still hold for the thermal problem with only minor changes since they are solutions of the problem shown in Figure 9.3(b), while the solution of the problem shown in Figure 9.3(c) is trivial. Second, using the above equivalency, a thermo-mechanical problem can be analyzed by the method illustrated in Figure 9.4. Third, the equivalency holds for any patch's geometry (octagonal, rectangular, etc.) even though it has been demonstrated in this section only through an example of an elliptical patch. Using the above equivalency and

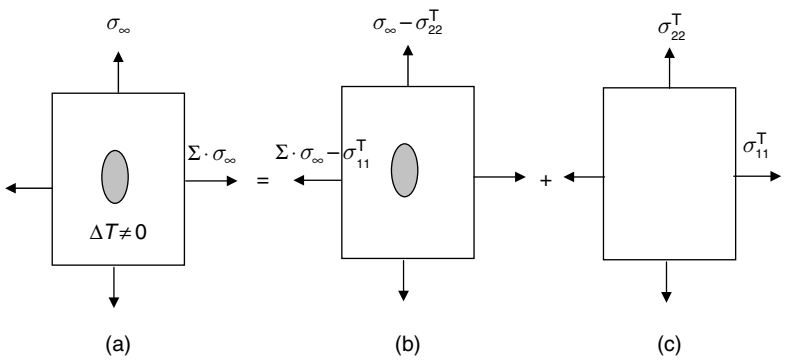

Fig. 9.4. A linear superposition method for analyzing the thermo-mechanical problem.

from Figure 9.4, it is quite easy to show that for a repair with thermo-mechanical loads, the counterparts of Equations (9.1)–(9.4) of the first stage analysis are given by:

$$\sigma_0 = \frac{\sigma_0^*}{\sigma_\infty}\left(\sigma_\infty - \sigma_{22}^{\mathrm{T}}\right) + \sigma_{22}^{\mathrm{T}}$$
$$\sigma_{\mathrm{tip}} = \frac{\sigma_{\mathrm{tip}}^*}{\sigma_\infty}\left(\sigma_\infty - \sigma_{22}^{\mathrm{T}}\right) + \sigma_{22}^{\mathrm{T}} \tag{9.25}$$

or

$$\frac{\sigma_0}{\sigma_\infty} = \frac{\sigma_0^*}{\sigma_\infty} + \frac{\sigma_{22}^{\mathrm{T}}}{\sigma_\infty}\left(1 - \frac{\sigma_0^*}{\sigma_\infty}\right) \tag{9.26}$$

$$K_{\mathrm{t}} = K_{\mathrm{t}}^* - \frac{\sigma_{22}^{\mathrm{T}}}{\sigma_\infty}\left(K_{\mathrm{t}}^* - 1\right) \tag{9.27}$$

and

$$\sigma_{\mathrm{p}}^{\mathrm{stageI}} = \left(\sigma_0 - \sigma_{22}^{\mathrm{T}}\right)\frac{E_{\mathrm{p}}}{E_{\mathrm{s}}} \tag{9.28}$$

where σ_0^*, σ_{tip}^*, and K_{t}^* are stresses in the skin underneath the patch, near the edge of the patch, and the stress concentration, respectively, due to the applied stress σ_∞ alone, and they are given by Equations (9.1)–(9.3), respectively.

The second stage analysis of Rose's approach for the present case of thermo-mechanical loading will be identical to that given in Section 9.1.1 except for a new value of the pressure load acting on the crack surfaces. Thus, the counterparts of Equations (9.5), (9.6), and (9.8)–(9.11) for a repair under thermo-mechanical loading are exactly the same except that σ_0^* is now replaced by σ_0 given by Equation (9.25). The reader is reminded that σ_{11}^{T} and σ_{22}^{T} are defined by Equation (9.17) where $\varepsilon_{11}^{(\mathrm{T})(\mathrm{p})}$ and $\varepsilon_{22}^{(\mathrm{T})(\mathrm{p})}$ for two typical thermal loading conditions (low operating temperature and curing of the adhesive) are given respectively by Equations (9.13) and (9.24).

It is interesting to note from Equations (9.26) and (9.27) that the effects of uniform cooling and curing increase the skin's stress underneath the patch ($\sigma_0/\sigma_\infty > \sigma_0^*/\sigma_\infty$) while at the same time reduce the stress concentration in the skin near the tip of the patch's edge ($K_{\mathrm{t}} < K_{\mathrm{t}}^*$), since $\frac{\sigma_0^*}{\sigma_\infty} < 1$, $\frac{\sigma_{22}^{\mathrm{T}}}{\sigma_\infty} > 0$, and $K_{\mathrm{t}}^* \geq 1$.

9.3 Design Criteria

The design of an effective patch requires that the patch will carry an appreciable percent of the applied load without any premature failure or disbond. To develop such a design, the patch, adhesive, and cracked skin after the repair must possess sufficient static strength and fatigue resistance. Criteria and guidelines to assure the structural integrity of the repair have been established in the CRMS Guidelines (1998) and in

the RAAF Engineering Standard C5033 (Davis, 1995). Additional guidelines have also been established by engineers performing repairs at Warnin-Robin Air Logistic Center (WR-ALC) (see CRAS Design Manual, 2003). Further improvements to enhance these criteria and guidelines have been developed under the CRAS program (Duong, 2003a; CRAS Design Manual, 2003). Basic criteria, described in this section, define acceptable patch stress, adhesive strain, skin stress, crack growth behavior and patch size based on load transfer and crack length.

9.3.1 Design criteria for cracked skin

Failure-inducing forces, acting on the repaired skin, are those at the crack and those at the edge of the patch. Failure at the crack typically results from fatigue crack growth, governed by the stress intensity factor. Any repair locally stiffens a structure and attracts load into the repaired area. The stress concentration at the edge of a patch can result in failure (cracking) at that location due to overstressing of the skin material. Design criteria are established for skin stress at the edge of the patch and the stress intensity factor at the crack tip.

Any patch draws load into the repaired area. A patch needs to be just stiff enough to repair the damage but not too stiff or it will result in high stress concentration at the edge of the patch and may induce cracking near that edge. The first criterion, identified by WR-ALC, is that the value of stress in the substrate at the patch edge, in the tensile load direction, should be limited to about 115 to 130% of the far field applied stress. This stress concentration at the edge should minimize peel stresses that develop at the adhesive edge and allay the concern that high fatigue loads at the end of the patch may induce cracking. Consistent with the WR-ALC key performance criterion, the skin stress concentration factor near the patch's edge tip due to the design ultimate load (DUL) is limited to values below 1.3 when the ratio of the material ultimate strength to the far-field stress at DUL exceeds 1.3, i.e., $\frac{F_{tu}}{\sigma_{\infty}\text{ at DUL}} > 1.3$, or below $\frac{F_{tu}}{\sigma_{\infty}\text{ at DUL}}$ when otherwise. The latter case corresponds to a case when the applied stress at DUL is so high that even though the skin stress concentration at the patch tip is below 1.3, the skin stress there still exceeds the material ultimate strength.

The stress intensity factor measures how strong the crack driving forces are. Plane stress and plane strain fracture toughness, K_C and K_{IC}, provide a measure of the resistance to crack propagation under static loads. In contrast, the fatigue crack growth is governed by the difference in stress intensity factors at the maximum and minimum loads of a fatigue cycle, i.e., ΔK_I. Repairs should be designed to reduce K_I so that no unstable crack growth will occur at the design static load and that the fatigue crack growth is slowed or stopped. In other words, the repaired stress intensity factor K_I due to a design static load should be limited to a value considerably less than the fracture toughness of the skin material and the repaired ΔK_I is below the fatigue threshold. The second and third criteria for the cracked skin therefore require that the crack-tip stress intensity factor must be equal to or less than 80% of the skin fracture toughness at the design ultimate load (DUL), and ΔK_I must be below the fatigue threshold at the design fatigue load (DFL). This second criterion is the same as having a margin of safety factor equal to 0.25 for skin fracture. To take advantage of stable crack growth in thin ductile materials,

the "apparent" plane stress skin fracture toughness K_C (Broek, 1987) will be used in the second criterion. However, it was found under CRAS program (Duong, 2003a,c; Duong et al., 2003) that the third criterion for fatigue crack growth is too restrictive and it can lead to overly stiff patch designs. Thus, the last skin criterion has been modified by allowing the crack to grow at the design fatigue load but at a slow enough rate such that the final crack length after the specified number of cycles of the fatigue load is still contained by the patch within 80% of the patch's width.

9.3.2 Design criteria for patch

In the repair practice, the stiffness ratio S is defined as the ratio of the stiffness after the repair has been installed to the stiffness of the original structure prior to the occurrence of damage. For a structure with cracks through the thickness, it is assumed that the after-repair stiffness is that of the patch alone and $S = E'_p t_p / E'_s t_s$. Since the intent of the repair is to return the stiffness to its original state, values of S should always be greater than 1.0. The CRMS Guidelines (1998) recommends a maximum value of 1.5 for the stiffness ratio. In a joint effort, Warner Robin Air Logistic Center and the Southwest Research Institute tested patches with values of S from 1.1 to 1.6 and they recommend that range as reasonable (Spigel et al., 1998). However, those references do not include the effect of residual thermal stress in their recommendations. An upper bound value of 2.0 is used under the CRAS program (Duong, 2003a; CRAS Design Manual, 2003). The stiffness requirement for the patch therefore is that $1 \leq S \leq 2$.

Minimum patch dimensions are established to assure an adequate and realistic design. Design criteria establish the minimum patch length based on load transfer through the adhesive, patch width to encompass the defect, and edge length for tapered octagonal patches to assure a reasonable shape. Minimum patch length is established by studying the adhesive shear stress developed in a bond (see Chapter 2). The durability of a repair is predicated on a bonded area large enough to resist the effects of stress on the bond line over time, or creep. An elastic anchor of very low shear stress in the adhesive will prevent creep. This region of low shear stress is defined as a function of the load transfer length $1/\beta_A$, mentioned in Chapter 2, and the minimum patch length criterion is based on this parameter.

The load transfer length $1/\beta_A$ is defined as the length over which the adhesive shear stress decreases from $\tau_{max}^{(A)}$ or $\tau_Y^{(A)}$ to nearly zero. The adhesive shear stress between the edge of the patch and the defect consists of two plastic zones at the ends and the elastic zone where the stress decreases from the adhesive shear yield strength value $\tau_Y^{(A)}$ to a low value, approaching zero (see Figure 2.4). As mentioned above, in order to assure that the overlap is long enough to develop a central area of very low adhesive shear stress which anchors the bond to resist creep, the elastic zone is determined to be $5/\beta_A$. The total length of the two plastic zones is designated ℓ_Y and the length of the elastic zone ℓ_E. The overlap length – that length required to develop a central region of low adhesive stress – is the distance between the edge of the patch and the defect and is equal to $\ell_E + \ell_Y$. The minimum patch length is equal to twice the overlap length plus the size of the defect and the tapered portion. The tapered portion of the patch is denoted by $2\ell_T$. For a crack, patch length is defined normal to the crack and the defect size in

the patch length direction is essentially zero. The minimum patch length is, therefore, equal to twice the overlap length plus the tapered portion or $2\,(\ell_E + \ell_Y + \ell_T)$, i.e.,

$$\begin{aligned}
\ell_E &= \frac{5}{\beta_A} \\
\ell_Y &= \frac{\sigma_0 t_s}{\tau_Y^{(A)}} \\
\ell_T &= \left(n_{ply} - 1\right) \cdot d \cdot t_{ply} \\
L_p &\geq \frac{10}{\beta_A} + \frac{2\sigma_0 t_s}{\tau_Y^{(A)}} + 2 \cdot \left(n_{ply} - 1\right) \cdot d \cdot t_{ply}
\end{aligned} \tag{9.29}$$

where n_{ply} is the number of plies, t_{ply} is the thickness per ply, d is the step-off rate and the rest have been previously defined. It is worthy to note that the minimum patch's length given by Equation (9.29) is different from that recommended by the CRMS Guidelines or the RAAF Engineering Standard C5033 (Davis, 1995), in which ℓ_E is specified in (9.29) to be $5/\beta_A$, not as $6/\beta_A$ as required in the two cited references. This new value of $\ell_E\,(5/\beta_A)$ was proposed recently by Hart-Smith (2001a) resulting from a revised analysis of his original work (1973) upon which the Engineering Standard and CRMS Guidelines were based. Furthermore, occasionally ℓ_E also has been recommended to be equal to $12/\beta_A$.

On the other hand, the minimum width, according to CRMS Guidelines, should overlap the initial crack length, prior to patching, by at least 25.4 mm and be at least twice that of the initial crack length. In contrast, CRAS bases the required minimum patch width on growth of the crack after patching (Duong, 2003a). CRAS computes crack growth for a specified number of fatigue cycles and requires that the patch width exceed the predicted crack length by 20% and also exceed an established minimum width of 2 $(a + \sqrt{a_o})$, where a is half the crack length after the designed number of cycles and a_o is half the original crack length before installation of the repair. Therefore, the minimum patch width will be specified in the present design process as (Duong, 2003a):

$$W_p \geq 2\left(a + \sqrt{a_0}\right) \quad \text{or} \quad W_p \geq 1.2a \tag{9.30}$$

Finally, the remaining criteria for the patch consider its strengths at the design ultimate load and at the design fatigue load. The maximum stress in the patch at DUL must be less than 83% of the material tensile ultimate strength of the patch. This corresponds to a margin of safety of 0.2 or higher for the patch strength. The margin safety factor is used to accommodate for any variation or degradation of the composite material properties. In contrast, the maximum stress in the patch at DFL must be less than 40% of the patch material strength allowable to assure the durability of the patch.

9.3.3 Design criteria for adhesive

The forces acting on a bond must be understood for a good patch design to be developed. The CRMS Manual summarizes failure modes related to those forces. An adhesive bond

is subjected to shear forces parallel to the bond surface and normal forces perpendicular to that surface. Load is transferred from the damaged structure to the patch through adhesive shear as shown in Figure 2.4. Shear stress is highest at the crack and at the edge of the patch. Tensile load perpendicular to the crack length tends to open the crack. The patch restrains such opening and adhesive shear stress is high at the discontinuity between the crack and the patch. The overlap length of the patch is increased to reduce the average shear stress in the bond line. Static strength of an adhesive bond is not what determines its overlap length. The overlap must be long enough to develop a central area of very low adhesive shear stress. This area anchors the bond to resist creep.

The offset of the neutral axis in a single-sided patch induces bending moments at the edge of the patch, resulting in peel forces. Peel forces are only addressed in the present design approach by incorporating patch taper, which can reduce those forces. Another important factor in the efficiency of a bond is the thickness of the adhesive. Thicker bond lines rely on the bulk cohesive properties of the adhesive, while thinner bonds take greater advantage of the interfacial adhesive forces.

Adhesive shear stress–strain properties are idealized with an elastic-perfectly-plastic stress strain curve, comprised of linear segments, as shown in Figure 2.3. The idealization is based on equal areas below the curves. Design parameters for the adhesive are: (a) elastic shear strain limit, (b) plastic shear strain, (c) shear strain at failure, (d) shear stress at linear limit, and (e) elastic shear modulus, G_A. These values are provided for various adhesives in Section 9.4.2.

The adhesive design criteria are based on allowable strains defined in that stress–strain curve and recommended in RAAF Engineering Standards C5033 (Davis, 1998) and CRMS Guidelines (1995). These criteria are (i) the maximum shear strain in the adhesive at DUL must be at or below 80% of the maximum allowable strain and (ii) the maximum shear strain in the adhesive at DFL must be equal to or less than twice the elastic shear strain limit.

9.4 Material Selection

The second step in designing a patch for crack or corrosion repair is to select materials, for the patch and the adhesive, on which to base the design. Sections 9.4.1 and 9.4.2 provide data to aid in this endeavor.

9.4.1 Patch materials

The CRMS Guidelines (1998) indicates that considerations in selection of a patch material include stiffness, strength, thickness, conformability, service temperature, and product form. Repair materials may be conventional metals, fiber metal laminates, or composites. Factors that may dictate patch material selection include thickness, weight, stiffness, thermal expansion coefficient, ability to inspect the damage through the patch, and operating temperature requirements. Thinner patches can be designed with higher modulus material. Composite materials have higher stiffness to weight ratio. Metals and

fiber metal laminates have CTE more compatible with the metal structure being repaired and are more capable of enduring elevated temperatures.

General guidelines for bonded patches are provided in RAAF Engineering Standard C5033 (Davis, 1998) as follows:

- The patch should not have an elastic modulus less than the material being patched.
- Bonded patches should match the surface profile to which they are bonded such that the adhesive film conforms within a tolerance of $+/-0.0508$ mm on the nominal adhesive thickness, during application of normal bonding pressure.
- Composite patches should have a balanced lay-up about the mid plane, with each layer of a particular orientation above the mid plane corresponding in orientation with an equivalent layer below the mid plane.
- Composite patches are to maximize strength by use of fiber-dominated lay-ups. Lay-up configurations in which the laminate strength is limited by the strength of the resin system are not desirable.

A summary of metallic and composite repair material characteristics is provided in Fredell (1994). That summary is the basis for Table 9.1, which provides those characteristics. Properties in this table are for unidirectional composite prepreg configurations with 60% fiber volume content, except for Aramid/Epoxy properties which are based on 50% fiber volume content. Specific tensile modulus is the tensile modulus divided by density and is used to provide an indication of the inherent stiffness to weight ratio of the material. The units of specific tensile modulus are, therefore, MPa divided by MPa/m and the values in the table are in units of millions of meters.

Table 9.2 is a list of composite material tensile properties from the CRAS Design Manual (2003). Boron/epoxy properties are those published by Textron Specialty Materials (Belason and Buccolo, 1995). Table 9.3 provides fiber metal laminate properties used in the USAF CalcuRep code (2001).

The material most commonly used for doubler design is Boron/epoxy (B/ep) which is selected for its high stiffness and strength (approximately three times that of aluminum in the zero degree ply direction), fatigue resistance, immunity to corrosion (since it is galvanically inert with aluminum, steel and titanium), and low electrical conductivity so that simple eddy current procedures can be used to monitor cracks under the patch. Typically, B/ep 5505 patches are pre-cured, since their 177 °C cure temperature is too high for aluminum structure. Consequently, only autoclave-cured data are presented for 5505. B/ep 5521 patches are cured at 121 °C and can be pre-cured or co-cured. Limited data are presented for both autoclave-cured and vacuum bag-cured 5521.

9.4.2 Adhesive materials

The CRMS Guidelines (1998) indicate that considerations in selection of an adhesive for patch bonding include service temperature, mechanical properties, cure temperature and

Table 9.1. Characteristics of repair materials.

Patch material	Specific tensile modulus* ($\times 10^6$ m)	Coefficient of thermal expansion ($\times 10^{-5}$/°C)	Approximate relative material cost	Characteristics
2024-T3 Aluminum (clad, polished)	2.667	2.3004	1	• Most widely used repair • Low cost • Ease of use • Wide availability • Bonding uncommon
S-Glass/Epoxy	2.032	0.6102	1	• Economical and widely available • High strain-to-failure (5%) • Stiffness lower than Al
Aramid/Epoxy	4.318	–	2	• Moderate cost • 1.6 times stiffness of Al • Sensitive to moisture (harmful to adhesive) • High residual thermal stress when bonded to aluminum
GLARE 2 (3/2)	2.667	1.9998	5	• Moderate cost • Same stiffness as Al • Exceptional resistance to fatigue and impact • Outer layer of aluminum acts as environmental barrier • Can be plastically deformed
HM 35 Carbon/Epoxy	12.319	–	16	• High cost • High stiffness • Susceptible to corrosion (large galvanic couple with Aluminum)
FT700 Carbon/Epoxy	19.812	–	24	

Table 9.1. (Continued)

Patch material	Specific tensile modulus* ($\times 10^6$ m)	Coefficient of thermal expansion ($\times 10^{-5}$/°C)	Approximate relative material cost	Characteristics
Boron/Epoxy	10.541	0.45	40	• High cost • High stiffness • Corrosion resistant • Stiff, prepreg makes forming and working difficult

* Measure of stiffness to weight ratio of material.

pressure, product forms, cure time, and prepreg compatibility. The cure temperature of adhesives is an especially significant parameter. Room temperature adhesives typically do not have adequate strength and durability at elevated operating temperatures.

Adhesives cured at temperatures above 121 °C tend to be brittle and have lower peel strength. Use of adhesives that require temperatures around 121 °C may potentially induce thermal damage to the structure due to mismatch of the coefficients of thermal expansion of the repair material and the structure to be repaired. High residual thermal stresses which develop during cooling, following application of elevated cure or bonding temperature, induce tensile loading in the metal and increase the stress intensity factor at the crack tip. Adhesives that cure between 93 and 121 °C have good strength and stiffness and adequate moisture resistance and are, therefore, most desirable for composite patching. Consequently, based on the cure temperature data of Table 9.4, FM-73 adhesive appears to be the best choice. Other considerations may impact the choice of adhesive. Adhesive shear stress–shear strain properties are generally idealized with an elastic-perfectly-plastic stress–strain curve, comprised of linear segments, as shown in Figure 2.3. The idealization is based on equal areas below the curves.

Selection criteria for the adhesive must consider operational loads, temperature, and humidity. Adhesive properties are shown in Table 9.4 for various cure temperatures. Except for the 80 °C cure FM-73 properties, which are from the CRMS Guidelines (1998), all properties are from the CRAS Design Manual (2003). Values from Table 9.4 are G_A, $\tau_Y^{(A)}$, and $\gamma_p^{(A)}$. There are several other factors that the designer must consider even though definitive design criteria are not established in this section. These factors, some of which are addressed in the previous chapters, include peel stress, disbonds, and operational temperatures.

Peel Stress: When a one-sided patch is applied, the neutral axis of the repair is shifted from the centerline of the skin towards the patch. Load application is therefore offset from the skin centerline and out-of-plane bending moments are induced at the patch edges and over the crack. Peel forces normal to the surface are counteracted by the overlap length and by patch taper.

Table 9.2. Composite patch material properties (tensile).

Laminate material	Temp. (°C)	E_1 (GPa)	E_2 (GPa)	Poisson's ratio	G_{12} (GPa)	F_{tu} (GPa)	CTE_1 (in/in/°C)	CTE_2 (in/in/°C)	Nominal ply thickness (mm)
Boron/Epoxy									
Boron/Epoxy 5505 Tape (177°C Autoclave)	−55	224.1	24.8	0.21	7.58	1.39	1.69E-05	4.50E-06	0.127
	RT	219.9	21.4	0.21	6.89	1.32	2.36E-05	4.50E-06	
	93	219.9	15.2	0.21	6.27	1.18	2.92E-05	4.50E-06	
	149	215.1	9.7	0.21	4.83	1.12	3.38E-05	4.50E-06	
	177	211.0	8.3	0.21	3.03	1.08	3.60E-05	4.50E-06	
Boron/Epoxy 5521 Tape (121°C Autoclave)	RT	195.1	19.4	0.21	5.52	1.56	2.41E-05	4.50E-06	0.127
	82	192.4	13.1	0.21	4.96	1.52	3.08E-05	4.50E-06	
Boron/Epoxy 5521 Tape (Vacuum bag 121°C, 711 mm Hg)	−59	173.1	20.7	0.21	5.38	1.41	2.27E-05	4.50E-06	0.127
	RT	181.3	15.9	0.21	5.10	1.31	2.79E-05	4.50E-06	
Boron/Epoxy 5521 Tape (Vacuum bag 121°C, 381 mm Hg)	RT	187.5	16.5	0.21	5.24	1.30	2.14E-05	4.32E-06	0.127
Carbon/Epoxy Tape (Generic)	−55	121.3	15.9	0.3	6.89				0.132
	RT	121.3	13.1	0.3	5.86	1.85			
	93	121.3	12.4	0.3	4.69				
C/E Cloth (Generic)	RT	75.8	72.4	0.06	6.89				0.356
AS/3501	RT	137.9	9.0	0.3	7.10	1.45	−3.06E-07	2.81E-05	0.132
AS/3501-6	RT	142.0	10.3	0.27	7.17	2.28	−9.00E-07	2.70E-05	0.132
AS4/977-3 Tape	−54	133.1	10.1	0.3	6.00				0.132
	RT	133.1	8.8	0.3	5.03				
	88	133.1	7.2	0.3	3.79				
	104	133.1	6.8	0.3	3.38				
	121	133.1	6.3	0.3	2.90				

AS4/977-3 Cloth	−54	71.0	71.0	0.05	5.79				0.356
	RT	71.0	71.0	0.05	4.96				
	88	71.0	71.0	0.05	3.72				
	104	71.0	71.0	0.05	3.31				
	121	71.0	71.0	0.05	2.83				
AS4/3501-6 Tape (DMS 2224)	RT	124.1	11.0	0.34	5.52	1.81	−9.00E-07	2.70E-05	0.132
AS4/3501-6 Cloth (DMS 2224)	RT	67.6	67.6	0.056	3.45	0.74	1.80E-05	1.80E-05	0.356
AS4/5250-4 (177 °C W)	RT	125.5	5.8	0.32	3.24	1.63	−1.80E-07	2.70E-05	0.132
AS4/APC2 PEEK	RT	131.7	8.8	0.28	5.03	2.06	−1.80E-06	2.39E-05	0.127
IM6/Epoxy	RT	203.1	11.2	0.27	8.41	3.50	−3.60E-07	3.01E-05	0.127
IM6/SC1081	RT	177.2	10.8	0.27	3.93	2.85	−3.60E-07	3.01E-05	0.127
IM7/977-3 Tape	−54	162.0	10.3	0.3	6.07				0.127
	RT	162.0	9.0	0.15	5.17	0.89	−1.98E-07	3.06E-05	
	88	162.0	7.3	0.3	3.86				
	104	162.0	6.9	0.3	3.45				
	121	162.0	6.4	0.3	2.96				
IM7/8851-7A Tape	RT	157.2	8.9	0.15	5.45	2.76	−1.80E-07	3.06E-05	0.127
T300/F934	RT	148.1	9.7	0.3	4.55	1.32	1.80E-08	2.25E-05	0.127
T300/5208	RT	181.3	10.3	0.28	7.24	1.50	1.80E-08	2.25E-05	0.127
E-Glass/Epoxy	RT	39.3	8.5	0.28	3.72	1.08	7.02E-06	2.11E-05	0.127
S-Glass/Epoxy	RT	43.4	8.9	0.27	4.55	1.28	5.04E-06	2.59E-05	0.127
7781/5245C	RT	29.7	29.7	0.17	5.31	0.37	1.01E-05	1.01E-05	0.127
Scotchply 1002	RT	38.6	8.3	0.34	4.14	0.97	7.20E-06	2.16E-05	3.810
Kevlar-49/epoxy	RT	86.9	5.5	0.34	2.14	1.28	−1.98E-06	5.94E-05	0.127

Values computed from data in reference; not measured test data.

Table 9.3. Fiber metal laminate properties.

Fiber metal laminate	Max thickness (mm)	E_1 (GPa)	E_2 (GPa)	Poisson's ratio	Shear modulus (GPa)
Glare-2-3/2-0.2	1.100	68.9	53.8	0.33	15.2
Glare-2-3/2-0.3	1.400	64.8	50.3	0.33	17.2
Glare-2-4/3-0.2	1.549	63.4	42.1	0.33	12.4
Glare-2-4/3-0.25	1.750	64.8	45.5	0.30	14.5
Glare-2-4/3-0.3	1.951	64.1	48.3	0.33	16.5
Glare-2-5/4-0.25	2.250	64.1	44.1	0.31	13.8
Glare-2-5/4-0.3	2.499	64.8	46.9	0.31	15.2
Glare (generic)	0.000	71.0	71.0	0.30	34.5

Fiber metal laminate	Tensile yld strength 1 (MPa)	Tensile yld strength 2 (MPa)	Tensile ult strength 1 (MPa)	Tensile ult strength 2 (MPa)	CTE1 (E-5/°C)	CTE2 (E-5/°C)
Glare-2-3/2-0.2	383.3	242.0	1187.3	313.7	1.638	2.448
Glare-2-3/2-0.3	359.9	228.2	1074.2	317.2	1.782	2.412
Glare-2-4/3-0.2	324.7	217.2	1490.0	217.2	1.476	2.448
Glare-2-4/3-0.25	328.9	233.0	1371.4	239.9	1.566	2.412
Glare-2-4/3-0.3	364.0	222.0	1157.6	289.6	1.728	2.412
Glare-2-5/4-0.25	328.2	228.2	1406.5	233.0	1.53	2.412
Glare-2-5/4-0.3	330.9	241.3	1310.0	252.3	1.602	2.358

Adhesive Disbonds: Voids in the adhesive or areas of bond line discontinuity generally result from poor surface preparation. However, disbonds along the crack can result from motion due either to operational cycling or crack growth itself. These may be tolerated if the crack growth rate is acceptable. Edge disbonds may permit moisture penetration and conditions that promote growth of the disbond itself. No criteria have been established for acceptable disbonds at the edge of a patch.

Operating Temperatures: Adhesive properties change over a range of operating temperatures as shown in Table 9.4. For example, shear yield stress for FM-73 adhesive, cured at 121 °C for two hours, varies from 15.9 MPa at 104 °C to 46.2 MPa at −41 °C. The adhesive must be capable of handling high and low operational temperatures and the change in material properties over the range of temperatures. Typically, adhesives become stiffer and more brittle at low temperature and are, therefore, more susceptible to disbonding. Adhesives become softer and more ductile at high temperature, adversely affecting the function of the repair.

9.5 Preliminary Design Procedure

The design procedure is an iterative process that requires adjustments of several variables or parameters until a satisfactory design that meets the established criteria is attained. Patch design variables are the patch stiffness ratio *S*, patch aspect ratio *B/A*, and the

Table 9.4. Adhesive material properties.

Adhesive type	Cure temp. (°C) and time of cure	One ply thickness [cured] (mm)	Environment	Shear modulus, G_A (MPa)	Shear yield stress, $\tau_Y^{(A)}$ (MPa)	Max. shear strain, $\gamma_{max}^{(A)}$	Elastic shear strain, $\gamma_Y^{(A)}$	Plastic shear strain, $\gamma_p^{(A)}$
FM-73	80 (8 h)	–	−40 °C/dry	737.7	52.7	0.192	0.071	0.121
			RT/dry	468.8	38.8	0.577	0.083	0.494
			80 °C/sat.	32.4	20.4	0.863	0.630	0.233
FM-73	121 (2 h)	1.143	−41 °C/dry	482.6	46.2	0.15	0.096	0.054
			−41 °C/sat.	455.1	42.7	0.15	0.094	0.056
			RT/dry	355.1	35.5	0.6	0.100	0.500
			RT/wet	326.7	33.4	0.756	0.102	0.654
			85 °C/dry	133.1	22.1	1.0	0.166	0.834
			85 °C/sat.	56.8	11.1	1.0	0.195	0.805
			104 °C/dry	17.2	15.9	1.0	0.920	0.080
FM-300	149 (4 h)	0.279	−54 °C/dry	606.7	46.5	0.19	0.077	0.113
			−54 °C/sat.	606.7	46.2	0.18	0.076	0.104
			RT/dry	459.7	31.0	0.275	0.067	0.208
			RT/sat.	459.7	26.2	0.26	0.057	0.203
			104 °C/dry	344.7	19.3	0.33	0.056	0.274
			104 °C/sat.	268.9	14.8	0.38	0.055	0.325
FM-300	177 (1 h)	0.152	RT/dry	393.0	35.2	0.33	0.089	0.241
			85 °C/dry	204.3	27.6	0.535	0.135	0.400
			85 °C/sat.	162.0	17.2	0.76	0.106	0.654
			104 °C/dry	170.1	25.5	0.6	0.150	0.450
			104 °C/sat.	124.1	15.9	0.85	0.128	0.722
FM300K	116 (1h) & 177 (2 h)	0.152	RT/dry	517.1	45.5	0.295	0.099	0.196
			RT/wet	427.5	39.3	0.38	0.108	0.272
			93 °C/dry	122.4	30.3	0.705	0.248	0.457
			93 °C/wet	65.5	27.9	1.035	0.426	0.609

(*Continued*)

Table 9.4. (Continued)

Adhesive type	Cure temp. (°C) and time of cure	One ply thickness [cured] (mm)	Environment	Shear modulus, G_A (MPa)	Shear yield stress, $\tau_Y^{(A)}$ (MPa)	Max. shear strain, $\gamma_{max}^{(A)}$	Elastic shear strain, $\gamma_Y^{(A)}$	Plastic shear strain, $\gamma_p^{(A)}$
FM-300-2K	121 (1.5–2 h) or 177 (1.5 h)	0.152	−54 °C/dry	841.2	42.1	0.11	0.050	0.060
			RT/dry	465.4	38.6	0.3	0.083	0.217
			82 °C/dry	280.6	24.1	0.68	0.086	0.594
			82 °C/wet	222.0	19.3	0.66	0.087	0.573
			104 °C/dry	226.8	17.2	0.8	0.076	0.724
			104 °C/wet	147.5	12.4	0.75	0.084	0.666
FM400	177 (1–2 h)	0.152	RT/dry	1082.5	60.7	0.169	0.056	0.113
			RT/wet	706.7	31.4	0.187	0.044	0.143
			93 °C/dry	861.8	46.2	0.187	0.054	0.133
			93 °C/wet	371.3	22.7	0.152	0.061	0.091
FM36	177 (2 h) & 316 (2 h)	0.152	−54 °C/dry	941.1	31.0	0.036	0.033	0.003
			RT/dry	672.2	26.9	0.06	0.040	0.020
			204 °C/dry	266.1	18.6	0.25	0.070	0.180
			204 °C/wet	257.2	17.9	0.18	0.070	0.110
			288 °C/dry	53.3	4.6	0.45	0.085	0.365
			288 °C/wet	34.5	4.6	0.4	0.132	0.268
EA9321	RT (2 h) & 88 (1h)	0.4572	RT/dry	551.6	25.5	0.0463	0.046	0.000
			104 °C/dry	20.0	2.0	0.11	0.100	0.010
			104 °C/sat.	12.0	1.2	0.11	0.100	0.010

Note: One ply thickness values are not measured data, but analytically derived values

patch length or width. However, it is more convenient to use other parameters than those just mentioned as the variables in the iterative process for the following reasons. In Section 9.3, all design criteria for the repairs of cracks are specified. Quantities required for the evaluations of these criteria are either given explicitly in Section 9.3 or estimated by the formula presented in Section 9.2. Since most of these quantities are commonly expressed in terms of the parameter σ_0 or σ_0^*, this common parameter will be used as a design variable in the present preliminary design procedure. By varying σ_0 or σ_0^* within a certain appropriate range, one can effectively control the crack-tip stress intensity, the maximum adhesive shear strain, etc., within their required range. Furthermore, since the skin stress concentration near the tip of the patch's edge is inevitably, present due to the high stiffness of the reinforced region relative to the surrounding materials, K_t or K_t^* will be selected as a second design variable. For clarity, we first delineate the design procedure for a repair subjected only to mechanical loads.

9.5.1 Design procedure for a repair subjected only to mechanical loads

There is no unique patch design that meets the criteria listed in Section 9.3. In a design process, one iteratively searches for a *first* design that meets the criteria. Thus, the design that results from the process will be different depending on what route the search has taken, and it may not necessarily always be the desired (optimal) design. A good logic for the design procedure with σ_0^* and K_t^* as the variables is therefore proposed here. It is expected that to meet the criteria a smaller patch in general will be thicker while a thinner patch will be larger in size. Thus, in the design logic, one starts to search for a design within a certain preset upper patch's size limit. If none of the design is found satisfactory, the preset upper patch's size limit is increased and the search is repeated with a new upper limit. In the design algorithm, this step corresponds to an outermost iterative loop.

In Chapter 3, Equations (9.1) and (9.3) were plotted in the special chart form as illustrated in Figure 3.6 to show how the design variables σ_0^* and K_t^* relate to the patch stiffness ratio S and aspect ratio B/A in a graphically useful way. Acceptable ranges for σ_0^* and K_t^* for a reasonably good patch design are indicated by the heavy lines in Figure 3.6. Any patch design that falls into that region will have a reasonable geometry, i.e. $\frac{1}{5} \leq \frac{B}{A} \leq 7$, and an acceptable stiffness ratio, i.e. $1 \leq S \leq 2$. In that region, values of $\frac{\sigma_0^*}{\sigma_\infty}$ are bounded between 0.8 and 0.33 while the range of K_t^* is between 2.0 and 1.05. The range of $\left.\frac{\sigma_0^*}{\sigma_\infty}\right|_{\text{at DUL}}$ in the iterative design process therefore will also be limited to values between 0.33 and 0.8. $\left.\frac{\sigma_0^*}{\sigma_\infty}\right|_{\text{at DUL}}$ was limited to 0.33 to avoid an unwanted overly stiff patch design ($S \leq 2$). The value of 0.33 for $\frac{\sigma_0^*}{\sigma_\infty}$ was determined from Figure 3.6 with $K_t^* = 1.05$ and $S = 2$. This particular choice of range for $\left.\frac{\sigma_0^*}{\sigma_\infty}\right|_{\text{at DUL}}$ has yielded reasonable patch designs in all considered benchmark test cases and these designs are quite similar to those obtained by other design tools such as the one mentioned in Spigel et al. (1998).

Referring to Figure 3.6, a higher value of σ_0^* will result in a smaller stiffness ratio and therefore a thinner patch for the same patch aspect ratio B/A. Thus, for a given preset upper patch's size limit, one can search for an acceptable design with a smallest

thickness within that limit by using a second inner iterative loop based on σ_0^* starting with a high value for σ_0^* of 0.8 and decreasing from that value by small decrements to 0.33. However, from Equations (9.1) and (9.3) or Figure 3.6, since S and B/A are only uniquely determined when σ_0^* and K_t^* are both specified and since K_t^* has not been specified in the outer and inner iterative loop mentioned above, an innermost iterative loop based on K_t^* must be used. For this innermost loop, to avoid obtaining an extremely wide and/or overly stiff patch design, $1.05 \leq K_t^* \leq 2$. While the upper limit for K_t^* can be as high as 2 as indicated in Figure 3.6 for all reasonable patch geometries, the patch criteria specified in Section 9.3 for it would require a smaller value to avoid potential cracking in the skin near the patch end. Thus, K_t^* will take values starting from 1.05 to an upper limit value set forth by the criteria specified in Section 9.3.

In summary, the design algorithm will have three nested loops with the outermost loop for the maximum allowable patch size, the next inner loop for σ_0^*, and the innermost loop for K_t^*. This algorithm with all the principal steps is briefly described below.

(i) Specify a maximum possible size for a patch, start with $A_{max} = a_0 + \sqrt{a_0}$ (or 25.4 mm if $a_0 = 0$, as in a preventive repair) and increase A_{max} incrementally to a value of $20a_0$ or 0.508 m, whichever has a larger value. The latter maximum size of 0.508 m is specified to include the case of preventive repairs, i.e. $a_0 = 0$.

(ii) Specify a value for $\left.\frac{\sigma_0^*}{\sigma_\infty}\right|_{\text{at DUL}}$, start with $\left.\frac{\sigma_0^*}{\sigma_\infty}\right|_{\text{at DUL}} = 0.8$ and decrease by small decrements to 0.33.

(iii) Specify a value for K_t^*, start with $K_t^* = 1.05$ and increase incrementally to 1.3 or $\frac{F_{tu}}{\sigma_{\infty(\text{at DUL})}}$, whichever is smaller in value.

(iv) Solve Equations (9.1) and (9.3) simultaneously for S and B/A with σ_0^* and K_t^* specified from steps (ii) and (iii).

(v) Calculate stresses in the patch and strains in the adhesive at the DUL and DFL using formula given in Section 9.1 with S, B/A, and σ_0^* obtained from previous steps. It should be noted that since the patch and skin are modeled as elastic materials and bonded together rigidly (i.e. no adhesive), $\left.\frac{\sigma_0^*}{\sigma_\infty}\right|_{\text{at DUL}} = \left.\frac{\sigma_0^*}{\sigma_\infty}\right|_{\text{at peak of DFL}} = \left.\frac{\sigma_0^*}{\sigma_\infty}\right|_{\text{at valley of DFL}}$. An appropriate value of σ_0^* at DUL and the peak of the DFL must be used in these formulas. The obtained stresses and strains in the patch and adhesive are then compared with their allowable according to the criteria established in Section 9.3.

(vi) Calculate the crack-tip stress intensity factor K_I at DUL, and at the peak and valley of the (cyclic) DFL using S and σ_0^*. Again, an appropriate value of σ_0^* at DUL and at the peak and valley of the DFL must be used in the formula. The obtained K_I at DUL is then compared with the skin material fracture toughness. The amount of crack growth at DFL is also calculated based on the computed ΔK, i.e. $\Delta K = K_I|_{\text{peak of DFL}} - K_I|_{\text{valley of DFL}}$, a specified number of loading cycles, and existing da/dN test data for the (unpatched) skin material.

(vii) Calculate the final crack length a, the required minimum patch length and width. Determine the length and width of the patch based on B/A found in step (iv) and the required minimum patch length or minimum patch width.

(viii) If a satisfactory design is found then the process is complete. Otherwise, one needs to return to step (iii) or (ii) or (i) depending on whether or not K_t^* and $\left.\frac{\sigma_0^*}{\sigma_\infty}\right|_{\text{at DUL}}$ have reached their upper limit specified in these steps.

So far the discussion has been limited to a design procedure for a repair subjected only to mechanical loads. It remains now to extend the procedure just described to a case of general thermo-mechanical loading, which is the subject of the next section.

9.5.2 Design procedure for a repair subjected to thermo-mechanical loads

There is no plot such as Figure 3.6 for a repair with thermo-mechanical loads. We will therefore try to make use of the results from Figure 3.6 and the above design logic as much as possible for the case of thermo-mechanical loading. The present design variables are the total skin stress underneath the patch σ_0 and the total skin stress concentration at the patch tip K_t. In Section 9.5.1, in the absence of thermal load, $\left.\frac{\sigma_0^*}{\sigma_\infty}\right|_{\text{at DUL}} = \left.\frac{\sigma_0^*}{\sigma_\infty}\right|_{\text{at DFL}}$ and $K_t^*|_{\text{DUL}} = K_t^*|_{\text{DFL}}$ since the design fatigue load and the design ultimate load assume to be proportional. However, for the combined thermo-mechanical loading, $\left.\frac{\sigma_0}{\sigma_\infty}\right|_{\text{at DUL}} \neq \left.\frac{\sigma_0}{\sigma_\infty}\right|_{\text{at DFL}}$ and $K_t|_{\text{DUL}} \neq K_t|_{\text{DFL}}$ even when the design fatigue load is proportional to the design ultimate load. This is because the thermal contributions to the total stress σ_0 and to the stress concentration K_t at the patch tip are constant, not proportional to the applied mechanical loads. Thus, σ_0 and K_t at the DUL are specifically chosen as the design variables for the case of thermo-mechanical loading. Throughout this section, σ_0, $\frac{\sigma_0}{\sigma_\infty}$, and K_t whenever they are mentioned will denote the total skin stress, the normalized skin stress, and the skin stress concentration at the patch tip, respectively, with the understanding that they are evaluated at the DUL.

In Section 9.5.1, it had been shown that the thermal effects increase the skin stress underneath the patch but reduce the skin stress concentration near the tip of a patch's edge. By rewriting Equations (9.26) and (9.27) as:

$$\frac{\sigma_0}{\sigma_\infty} = \left(1 - \frac{\sigma_{22}^T}{\sigma_\infty}\right)\frac{\sigma_0^*}{\sigma_\infty} + \frac{\sigma_{22}^T}{\sigma_\infty} \tag{9.31}$$

$$K_t = \left(1 - \frac{\sigma_{22}^T}{\sigma_\infty}\right)K_t^* + \frac{\sigma_{22}^T}{\sigma_\infty} \tag{9.32}$$

and plotting the resulting equations into diagrams as shown in Figures 9.5 and 9.6, it is clear that there are two distinct curves corresponding to two cases, i.e. $\frac{\sigma_{22}^T}{\sigma_\infty} \leq 1$ and $\frac{\sigma_{22}^T}{\sigma_\infty} > 1$. We therefore need to determine first the range of $\frac{\sigma_0}{\sigma_\infty}$ and K_t in the iterative loops of the design process for each case of $\frac{\sigma_{22}^T}{\sigma_\infty}$. It is interesting to note from Figure 9.5 that

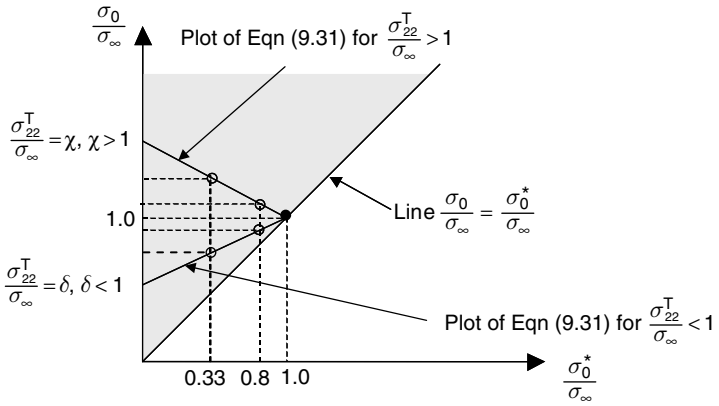

Fig. 9.5. A $\frac{\sigma_0}{\sigma_\infty}$ vs $\frac{\sigma_0^*}{\sigma_\infty}$ diagram for determining the appropriate range of $\frac{\sigma_0}{\sigma_\infty}$ in the iterative loop. As mentioned in the main text, $\frac{\sigma_0}{\sigma_\infty} \geq \frac{\sigma_0^*}{\sigma_\infty}$ which corresponds to the shaded region of the diagram. The open circles shown on the plotting curves of Equation (9.31) for two cases of $\frac{\sigma_{22}^T}{\sigma_\infty} > 1$ and $\frac{\sigma_{22}^T}{\sigma_\infty} < 1$ indicate upper and lower bounds of $\frac{\sigma_0}{\sigma_\infty}$ on the respective curve, which correspond to $\frac{\sigma_0^*}{\sigma_\infty} = 0.33$ and $\frac{\sigma_0^*}{\sigma_\infty} = 0.8$.

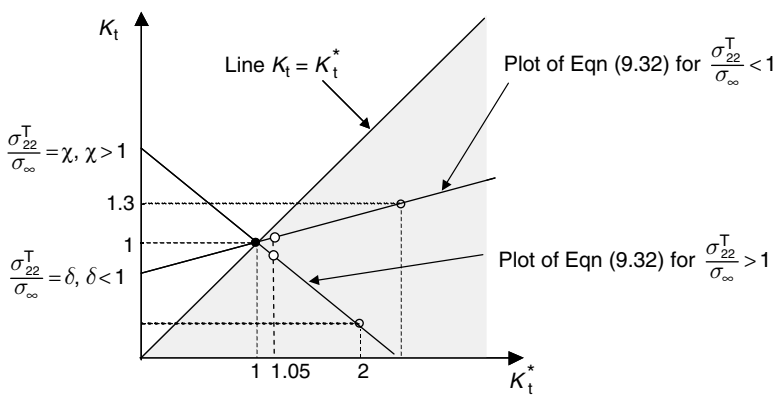

Fig. 9.6. A K_t vs K_t^* diagram for determining the appropriate range of K_t in the iterative loop. As mentioned in the main text, $K_t \leq K_t^*$ which corresponds to the shaded region of the diagram. The open circles shown on the plotting curves of Equation (9.32) for two cases of $\frac{\sigma_{22}^T}{\sigma_\infty} > 1$ and $\frac{\sigma_{22}^T}{\sigma_\infty} < 1$ indicate upper and lower bounds of K_t on the respective curve.

the plotted curves based on Equation (9.31) for two cases of $\frac{\sigma_{22}^T}{\sigma_\infty}$ are linear with the end points located at $(0, \sigma_{22}^T/\sigma_\infty)$ and (1,1). It should be reminded that in Equations (9.31) and (9.32), σ_0^* and K_t^* are skin stress and skin stress concentration due to the applied stress σ_∞ alone. Also, $\sigma_0 > \sigma_0^*$, $K_t < K_t^*$, and $\sigma_0^*/\sigma_\infty \leq 1.0$.

The patch can help to arrest the crack in two different ways, first by reducing the skin stress underneath the patch in stage I of Rose's procedure and second by bridging the crack in stage II. Because of this crack-bridging phenomenon, the stress intensity factor $K_{I\infty}$ of a patched crack is usually much less than that of an un-patched crack. From Figure 9.4, the (y-component) stress in the skin underneath the patch (σ_0) will be equal to or higher than σ_{22}^{T} when $\frac{\sigma_{22}^{T}}{\sigma_\infty} \leq 1$, and less than that value when $\frac{\sigma_{22}^{T}}{\sigma_\infty} > 1$. This is because the far-field-applied stresses of the problem shown in the Figure 9.4(b) corresponding to these two cases are tension and compression, respectively. The same results can also be seen from Figure 9.5. Because σ_{11}^{T} and σ_{22}^{T} are independent of the patch's geometry as seen from Equations (9.17), (9.13), and (9.24), and since their values are fixed for a given thermal loading condition, the only way to reduce σ_0 is by either reducing the tensile stress (when $\frac{\sigma_{22}^{T}}{\sigma_\infty} < 1$) or increasing the compressive stress (when $\frac{\sigma_{22}^{T}}{\sigma_\infty} > 1$) in the skin underneath the patch of the problem shown in Figure 9.4(b). It is interesting to note that when $\frac{\sigma_{22}^{T}}{\sigma_\infty} = 1$, from Figure 9.4 and also from Figure 9.5, σ_0 is independent of the patch's geometry and equal to σ_{22}^{T}. For that case, the patch aspect ratio ceases to be a design factor while the patch stiffness ratio still is because the latter parameter affects the bridging capability of a patch in stage II analysis.

Since $\frac{\sigma_0^*}{\sigma_\infty}$ and K_t^* in Equations (9.31) and (9.32) are the respective contributions to $\frac{\sigma_0}{\sigma_\infty}$ and K_t due to the remote applied stress alone, and they are related to the patch stiffness ratio S and the patch aspect ratio B/A via Equations (9.1) and (9.3) or alternatively through the design chart shown in Figure 3.6, the range of $\frac{\sigma_0}{\sigma_\infty}$ and K_t in the iterative loops of the design process will be determined based on the range of $\frac{\sigma_0^*}{\sigma_\infty}$ and K_t^*. From Figure 3.6, it appears that all possibly acceptable patch designs are confined to a region marked by the heavy line as indicated in the same figure. Any patch design that falls into that region will have a reasonable geometry, i.e. $\frac{1}{5} \leq \frac{B}{A} \leq 7$, and an acceptable stiffness ratio, i.e. $1 \leq S \leq 2$. In that region, values of $\frac{\sigma_0^*}{\sigma_\infty}$ are bounded between 0.8 and 0.33 as specified in the previous design logic while the range of K_t^* is larger with a lower and upper limit of 1.05 and 2.0, respectively (as opposed to 1.05 and 1.3 or $\frac{F_{tu}}{\sigma_{\infty(\text{at DUL})}}$). These particular ranges are the widest ranges of all possible ranges for $\frac{\sigma_0^*}{\sigma_\infty}$ and K_t^*, which will lead to reasonable patch designs. Since thermal effects reduce the skin stress concentration due to the applied stress σ_∞, K_t^* is allowed to exceed 1.3 or $\frac{F_{tu}}{\sigma_{\infty(\text{at DUL})}}$. If the thermal effects could not reduce the skin stress concentration due to the applied stress alone at its current maximum allowable value of 2.0 to a value below the design requirement, a smaller upper bound value for K_t^* will be used. With these in mind, we are now ready to discuss in detail the ranges of the normalized total skin stress $\frac{\sigma_0}{\sigma_\infty}$ and the total skin stress concentration K_t for the two particular cases of $\frac{\sigma_{22}^{T}}{\sigma_\infty} \leq 1$ and $\frac{\sigma_{22}^{T}}{\sigma_\infty} > 1$.

(a) Ranges of $\frac{\sigma_0}{\sigma_\infty}$ *and* K_t *for* $\frac{\sigma_{22}^{T}}{\sigma_\infty} \leq 1$

As mentioned in the preceding paragraph, we limit values of $\frac{\sigma_0^*}{\sigma_\infty}$, i.e. the contribution to the normalized total stress $\frac{\sigma_0}{\sigma_\infty}$ due to the far-field-applied stress alone, between 0.8 and 0.3 in the design process. The effect of limiting the values of $\frac{\sigma_0^*}{\sigma_\infty}$ within that range on the patch design will be examined in detail here. When σ_{22}^{T} is smaller than the applied stress

σ_∞, the only way to reduce σ_0 is to reduce the tensile stress in the skin underneath the patch of the problem shown in Figure 9.4(b) with a far-field stress in tension. Since the skin stress underneath the patch of the problem shown in Figure 9.4(b) when normalized by its far-field stress $(\sigma_\infty - \sigma_{22}^{\mathrm{T}})$ is equal to $\frac{\sigma_0^*}{\sigma_\infty}$, limiting the value of $\left.\frac{\sigma_0^*}{\sigma_\infty}\right|_{\text{at DUL}}$, i.e. a part of $\left.\frac{\sigma_0}{\sigma_\infty}\right|_{\text{at DUL}}$ due to the far-field stress alone, between values of 0.33 and 0.8 will have the same effect as limiting the normalized skin stress of the problem shown in Figure 9.4(b) within the same range. In general, a larger reduction in the normalized skin (tensile) stress underneath the patch of the problem shown in Figure 9.4(b) will require a higher patch stiffness ratio and a lower patch aspect ratio B/A which in turn produces a smaller value for $\frac{1}{\sqrt{\Lambda}}$, thus the crack-tip stress intensity factor, and overall a better crack growth retardation (via Equations (9.5) and (9.11)). It therefore appears that a lower bound value for $\frac{\sigma_0^*}{\sigma_\infty}$ in the iterative loop may be preferably smaller than 0.33. However, as mentioned before, since any further reduction in value of $\frac{\sigma_0^*}{\sigma_\infty}$ below 0.33 would result in an overly stiff patch design, the lower bound of $\frac{\sigma_0^*}{\sigma_\infty}$ is therefore maintained at 0.33. Substituting values of 0.8 or 0.33 for $\frac{\sigma_0^*}{\sigma_\infty}$ into Equation (9.31) yields respectively:

$$\frac{\sigma_0}{\sigma_\infty} = 0.8 + 0.2\frac{\sigma_{22}^{\mathrm{T}}}{\sigma_\infty} \tag{9.33}$$

$$\frac{\sigma_0}{\sigma_\infty} = 0.33 + 0.67\frac{\sigma_{22}^{\mathrm{T}}}{\sigma_\infty} \tag{9.34}$$

Thus, $\left.\frac{\sigma_0}{\sigma_\infty}\right|_{\text{at DUL}}$ is limited to values between $0.33 + 0.67\frac{\sigma_{22}^{\mathrm{T}}}{\sigma_\infty}$ and $0.8 + 0.2\frac{\sigma_{22}^{\mathrm{T}}}{\sigma_\infty}$. From the lower curve in Figure 9.5, it should also be noted that as $\frac{\sigma_0}{\sigma_\infty}$ decreases from $0.8 + 0.2\frac{\sigma_{22}^{\mathrm{T}}}{\sigma_\infty}$ to $0.33 + 0.67\frac{\sigma_{22}^{\mathrm{T}}}{\sigma_\infty}$ along that curve, $\frac{\sigma_0^*}{\sigma_\infty}$ will decrease from 0.8 to 0.33 accordingly, and also $\frac{\sigma_0}{\sigma_\infty}$ in this case could be higher than 0.8 but never exceed 1.

We next turn our attention to the skin stress concentration near the patch's edge. From the upper curve in Figure 9.6, since K_{t} is always greater than 1 and it can be potentially higher than 1.3 or $\frac{F_{\mathrm{tu}}}{\sigma_{\infty(\text{at DUL})}}$, its value is therefore limited to values below 1.3 or $\frac{F_{\mathrm{tu}}}{\sigma_{\infty(\text{at DUL})}}$, whichever is smaller in value, as before for a repair without thermal effects. In the present case, K_{t}^* may exceed 1.3 or $\frac{F_{\mathrm{tu}}}{\sigma_{\infty(\text{at DUL})}}$, but it is however still acceptable since thermal effects will reduce the skin stress concentration due to far-field-applied stresses to values below 1.3 or $\frac{F_{\mathrm{tu}}}{\sigma_{\infty(\text{at DUL})}}$ and thus will allow K_{t} to satisfy the required design criteria. In order to avoid obtaining a patch design with an extremely high aspect ratio, we added the further restriction that K_{t}^* as determined from K_{t} satisfies the condition $1.05 \le K_{\mathrm{t}}^* \le 2$ as recommended in the beginning of this section. This restriction requires that the minimum value of K_{t} is set equal to $1.05 - 0.05\left.\frac{\sigma_{22}^{\mathrm{T}}}{\sigma_\infty}\right|_{\text{at DUL}}$ while the maximum value of K_{t} is equal to the minimum of the three values of 1.3, $\frac{F_{\mathrm{tu}}}{\sigma_{\infty(\text{at DUL})}}$, and $2 - \left.\frac{\sigma_{22}^{\mathrm{T}}}{\sigma_\infty}\right|_{\text{at DUL}}$. K_{t} values of $1.05 - 0.05\left.\frac{\sigma_{22}^{\mathrm{T}}}{\sigma_\infty}\right|_{\text{at DUL}}$ and $2 - \left.\frac{\sigma_{22}^{\mathrm{T}}}{\sigma_\infty}\right|_{\text{at DUL}}$ have been derived by substituting respectively $K_{\mathrm{t}}^* = 1.05$ and $K_{\mathrm{t}}^* = 2$ into Equation (9.32).

(b) Ranges of $\frac{\sigma_0}{\sigma_\infty}$ and K_t for $\frac{\sigma_{22}^T}{\sigma_\infty} > 1$

As before, we limit values of $\frac{\sigma_0^*}{\sigma_\infty}$, i.e. the contribution to the normalized total stress $\frac{\sigma_0}{\sigma_\infty}$ due to the far-field-applied stress alone, between 0.8 and 0.3 in the design process. The effect of limiting the values of $\frac{\sigma_0^*}{\sigma_\infty}$ within that range on the patch design again will be examined. When σ_{22}^T is larger than σ_∞, the only way to reduce σ_0 is to increase the compressive stress in the skin underneath the patch of the problem shown in Figure 9.4(b) with a far-field stress in compression. Similar to the case for $\frac{\sigma_{22}^T}{\sigma_\infty} < 1$, limiting the value of $\left.\frac{\sigma_0^*}{\sigma_\infty}\right|_{\text{at DUL}}$ between values of 0.33 and 0.8 has the same effect as limiting the normalized (compressive) skin stress of the problem shown in Figure 9.4(b) within the same range. Since, in the present case, we want to maximize the normalized compressive skin stress underneath the patch of problem shown in Figure 9.4(b) in order to minimize the total skin stress $\frac{\sigma_0}{\sigma_\infty}$, it appears that the upper bound value for $\frac{\sigma_0^*}{\sigma_\infty}$ in the iterative loop may be preferably larger than 0.8. However, since an increase in that normalized compressive stress would require a thinner and slender patch and since a lower patch stiffness ratio will result in a larger value for $\frac{1}{\sqrt{\Lambda}}$ as indicated in Equation (9.6), any beneficial gain by the reduction in the total skin stress $\frac{\sigma_0}{\sigma_\infty}$ therefore will be offset by an increase in $\frac{1}{\sqrt{\Lambda}}$. An increase in $\frac{1}{\sqrt{\Lambda}}$ would lead to a higher stress intensity factor at the crack tip. Thus, the maximum value of $\frac{\sigma_0^*}{\sigma_\infty}$ has been maintained at a value of 0.8 for this case. $\left.\frac{\sigma_0}{\sigma_\infty}\right|_{\text{at DUL}}$ is, therefore, limited to values between $0.8 + 0.2\frac{\sigma_{22}^T}{\sigma_\infty}$ and $0.33 + 0.67\frac{\sigma_{22}^T}{\sigma_\infty}$. These limiting values of $\left.\frac{\sigma_0}{\sigma_\infty}\right|_{\text{at DUL}}$ are given by Equations (9.33) and (9.34) as in part (a), which correspond to $\frac{\sigma_0^*}{\sigma_\infty} = 0.8$ and 0.33, respectively. It is worthwhile to observe from the upper curve in Figure 9.5 that as $\frac{\sigma_0}{\sigma_\infty}$ increases from $0.8 + 0.2\frac{\sigma_{22}^T}{\sigma_\infty}$ to $0.33 + 0.67\frac{\sigma_{22}^T}{\sigma_\infty}$ along that curve, $\frac{\sigma_0^*}{\sigma_\infty}$ decreases from 0.8 to 0.33.

For the skin stress concentration near the tip of the patch's edge, since K_t is always less than 1 as shown by the lower curve in Figure 9.6, K_t may not be a critical design factor, unless it becomes negative and smaller than $-\frac{F_{cu}}{\sigma_{\infty(\text{at DUL})}}$ where F_{cu} is the *magnitude* of the compressive strength of the skin material. For ductile metals, it is customary to assume that F_{cu} equals to F_{tu}. In the absence of any specific restriction on K_t, the range of K_t will be derived from the range of K_t^* using the guideline given in the beginning of this section. According to that guideline, for an acceptable patch's geometry, $1.05 \le K_t^* \le 2$. It then follows from Equation (9.32) that $2 - \left.\frac{\sigma_{22}^T}{\sigma_\infty}\right|_{\text{at DUL}} \le K_t \le 1.05 - 0.05\left.\frac{\sigma_{22}^T}{\sigma_\infty}\right|_{\text{at DUL}}$. However, when $2 - \left.\frac{\sigma_{22}^T}{\sigma_\infty}\right|_{\text{at DUL}} < -\frac{F_{cu}}{\sigma_{\infty(\text{at DUL})}}$, then $-\frac{F_{cu}}{\sigma_{\infty(\text{at DUL})}} \le K_t \le 1.05 - 0.05\left.\frac{\sigma_{22}^T}{\sigma_\infty}\right|_{\text{at DUL}}$. It should be noted that as K_t^* increases, K_t decreases as seen from the lower curve in Figure 9.6.

(c) Design procedure

With the range of $\frac{\sigma_0}{\sigma_\infty}$ and K_t in the iterative loops of the design process having been determined in parts (a) and (b), the logic of the design procedure for a repair with

thermal effects now can be described. Similar to the previous design logic for a repair without thermal effects, the present design procedure involves the following steps:

(i) Start with $A_{\max} = a_0 + \sqrt{a_0}$ (or 25.4 mm if $a_0 = 0$) and increase $A_{\max}$ incrementally to a value of $20a_0$ or 0.508 m, whichever is higher in value.

(ii) Start with $\left.\frac{\sigma_0}{\sigma_\infty}\right|_{\text{at DUL}} = 0.8 + 0.2\frac{\sigma_{22}^{\text{T}}}{\sigma_\infty}$ and decrease by small decrements (when $\frac{\sigma_{22}^{\text{T}}}{\sigma_\infty} \le 1$) or increase incrementally (when $\frac{\sigma_{22}^{\text{T}}}{\sigma_\infty} > 1$) to $0.33 + 0.67\frac{\sigma_{22}^{\text{T}}}{\sigma_\infty}$.

(iii) Start with $K_{\text{t}} = 1.05 - 0.05\left.\frac{\sigma_{22}^{\text{T}}}{\sigma_\infty}\right|_{\text{at DUL}}$ and increase incrementally to 1.3, $\frac{F_{\text{tu}}}{\sigma_{\infty(\text{at DUL})}}$ or $2 - \left.\frac{\sigma_{22}^{\text{T}}}{\sigma_\infty}\right|_{\text{at DUL}}$, whichever is smaller in value, when $\frac{\sigma_{22}^{\text{T}}}{\sigma_\infty} \le 1$, or decrease by small decrements to $2 - \left.\frac{\sigma_{22}^{\text{T}}}{\sigma_\infty}\right|_{\text{at DUL}}$ or $-\frac{F_{\text{cu}}}{\sigma_{\infty(\text{at DUL})}}$, whichever is higher in value, when $\frac{\sigma_{22}^{\text{T}}}{\sigma_\infty} > 1$.

(iv) Calculate $\frac{\sigma_0^*}{\sigma_\infty}$ and K_{t}^* using Equations (9.31) and (9.32), with $\frac{\sigma_0}{\sigma_\infty}$ and K_{t} given from steps (ii) and (iii).

(v) Solve Equations (9.1) and (9.3) simultaneously for S and B/A with $\frac{\sigma_0^*}{\sigma_\infty}$ and K_{t}^* obtained from step (iv).

(vi) Calculate stresses in the patch, strains in the adhesive, the crack-tip stress intensity factor, etc., at DUL and DFL, and check the criteria.

(vii) Determine the patch width and length.

(viii) If a satisfactory design is found then the process is complete. Otherwise, one needs to return to step (iii) or (ii) or (i) depending on whether or not K_{t} and $\left.\frac{\sigma_0}{\sigma_\infty}\right|_{\text{at DUL}}$ have reached their upper limit specified in these steps.

Steps (vi) and (vii) have been described very briefly because they are very similar to those given earlier in the previous design logic. It is also important to note that the crack-tip stress intensity factor evaluated at the DUL and the peak of the DFL will include the effect of thermal stresses induced by the curing of the adhesive and the uniform temperature change due to the low operating temperature. However, the evaluation of the stress intensity factor at the valley of the DFL may include only the thermal effect associated with the curing of the adhesive as in the case of repairs of fuselage structures subjected to cabin pressurization cycles.

All the above design procedures compute the geometry of an elliptical patch based on simple formulas. Since boron/epoxy elliptical patches are impractical for manufacturing, an octagonal or rectangular shape can be approximately derived from the above elliptical design. A rectangular patch design assumes to have the same aspect ratio, length, width, and stiffness output from the previous design process for an elliptical shape. For an octagonal patch design, Hart-Smith (2001b) has developed a method to convert an elliptical patch to an octagonal shape. According to this method, the area of the octagonal patch should be the same as that of the elliptical one, and the edge length and width of the octagonal patch are 34.5% of the corresponding centered (full) dimensions as illustrated in Figure 9.7. The method was originally developed for an untapered patch but has been

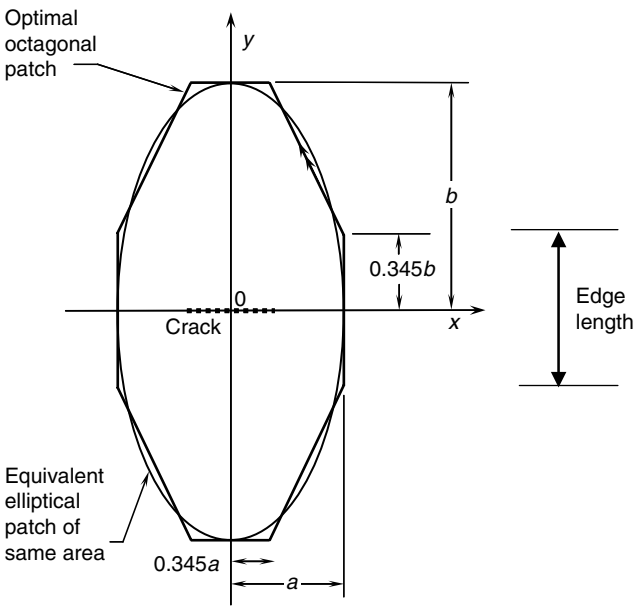

Fig. 9.7. An equivalent octagonal patch obtained from conversion of an elliptical design.

used in the CRAS program (Duong et al., 2002, 2003) for both tapered and untapered patches. This conversion method may yield geometric anomalies for short patches with long taper if the edge length of the octagonal patch design is smaller than twice the required taper length as shown in Figure 9.8. A minimum clearance between opposing taper regions is, therefore, specified arbitrarily as 1.27 cm. If the edge length is less than twice the taper length plus 1.27 cm, an alternate conversion method is employed. In that case, the patch's geometry will be modified as follows while still maintaining the outer

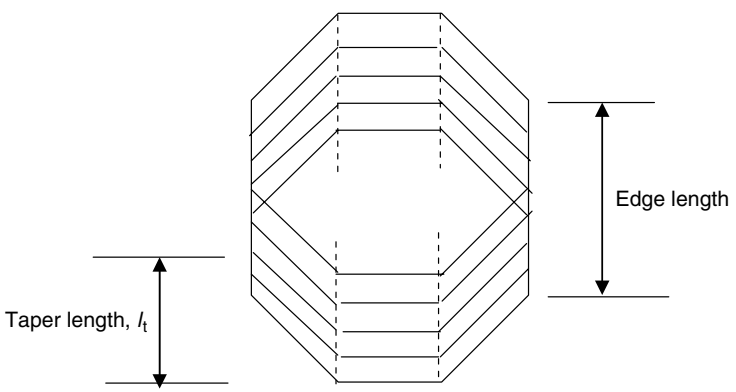

Fig. 9.8. An example of a bad patch's geometry, where the edge length is smaller than the required taper length.

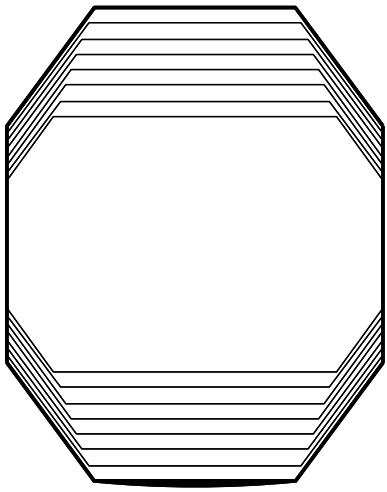

Fig. 9.9. An alternate conversion of elliptical patch to octagonal patch scheme to avoid taper overlap at the edge length.

length and width dimensions and therefore the aspect ratio of the originally elliptical design. The dimensions of each ply are determined independently. Corners are cut at 45 degrees. The amount trimmed from each side at a corner is equal to 25% of the shortest side of the ply, either the width or length dimension, whichever is smaller in value. This tapering technique results in tapered patch of the form shown in Figure 9.9. As the ply length decreases, less of the corner is cut-off.

9.6 An Illustrative Example Using Design Process

The CRMS Guidelines (1998) presents several case studies where bonded repairs are used. One of these is repair of multiple small cracks in the upper (crown) section of the C-5A fuselage. Two bonded repairs were implemented, in 1995, at fuselage stations 1700 and 1784 by a team of Wright Laboratory, SA-ALC, and USAF Academy personnel. Their designs and analyses were performed using the analytical code CalcuRep (2001) and the finite element code FRANC2D/L (Swenson and James, 1997). A summary of the applied Glare patch design and analyses is presented in the cited reference.

The example of this section sizes a Glare rectangular patch to repair cracks similar to those that developed in the C-5A fuselage. The 22 mm crack at station 1784 is the subject of this example, which follows the process outlined in Section 9.5. This example is very simplified compared to the actual C-5A damage and USAF repair. The fuselage cracks grew from rivet holes. Per reference, the situation was not one of ordinary fatigue cracking. The stress intensity factor computations used here are derived for central cracks in skin panels and therefore may be too simple for the actual repair condition. Both the rivets and the complicated substructure obscure the exact stress field around the crack. Also, room temperature dry material properties are used for the patch and adhesive

during the design process, even though the C-5A operational temperature is typically −51 °C corresponding to a low temperature experienced during high altitude cruising. Thermal stress effects are, however, included in the design and analysis. To facilitate the design process outlined in Section 9.5, its design algorithm was implemented into a computer code as part of the CRAS program. The patch design for this example was computed by this computer code (CRAS Software User Manual, 2003).

9.6.1 Loading conditions

The C-5A crown section is subjected to significant longitudinal tensile bending in addition to biaxial tension. For simplicity in this example, the crack is assumed to be oriented normal to that principal longitudinal tensile load. The applied far-field stresses are 212.4 MPa limit (318.5 MPa ultimate) and a fatigue stress of 113.1 MPa, the "typical" load. The fatigue loading is defined as the typical load that occurs 500 times per 1000 flight hours or 15,000 times during the 30,000-hour life of the C-5A. The number of times that stress is exceeded during 1000 hours of flight is shown in Figure 9.10. For this example, the number of fatigue cycles N, to be designed for, is 30,000 or twice the expected occurrence of the 113.1 MPa typical fatigue stress. The biaxial stress ratio is equal to 0.36. In contrast, the fatigue stress (R) ratio is 0.05.

9.6.2 Design parameters

Input parameters for the initial design process relate to the damaged structure, the loading conditions, and the selected patch and adhesive materials. For illustration purposes and

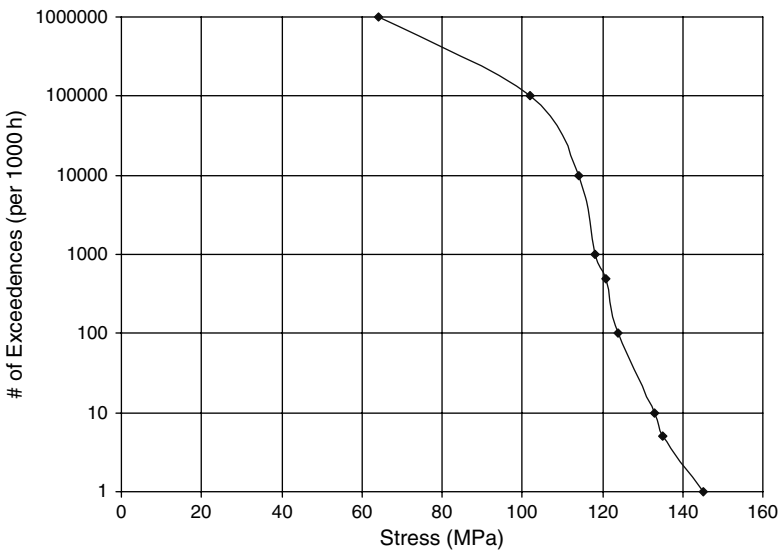

Fig. 9.10. Exceedance data for C-5A fuselage station 1784.

to simplify the example, room temperature dry properties are used for the initial design. In an actual design situation, properties at the operating temperature extremes would be utilized.

In the design process, the following information is provided:

- *Skin material properties*: Properties for the actual aluminum skin material, 7079-T6, are not available since 7079 has been deleted from MIL-HDBK-5. It is assumed that another aluminum alloy can be substituted without significantly impacting the design. 2024-T3 Clad properties from MIL-HDBK-5 are used here.
  - Young's modulus, $E_s = 72.4\,\text{GPa}$
  - Tensile ultimate strength, $F_{tus} = 420.6\,\text{MPa}$ (B Basis)
  - Tensile yield strength, $F_{tys} = 310.3\,\text{MPa}$ (B Basis)
  - Poisson's ratio, $\nu = 0.33$
  - Fracture toughness, $K_C = 102\,\text{MPa} \cdot \sqrt{\text{m}}$
  - Coefficient of thermal expansion, $\text{CTE}_s = 2.25\text{E-}05$ per °C
- Skin thickness, $t_s = 1.27\,\text{mm}$
- Crack length, $2a_o = 22\,\text{mm}$
- Loading conditions
  - Ultimate tensile stress normal to crack, $\sigma_{ult} = 318.5\,\text{MPa}$
  - Typical peak fatigue stress, $\sigma_{fat} = 113.1\,\text{MPa}$
  - Stress ratio (valley to peak), $R_{fat} = 0.05$
  - Number of fatigue cycles, $N = 30{,}000$
- Thermal conditions
  - Ambient temperature, $T_{amb} = 21\,°\text{C}$
  - Adhesive effective glass transition temperature, $T_{g\text{-}eff} = 82\,°\text{C}$
  - Low operating temperature, $T_{op} = -51\,°\text{C}$
- Patch material properties are based on a design of a Glare 2 4/3-0.2 patch with room temperature properties from Table 9.3. Glare consists of alternating layers of aluminum and glass/epoxy. Glare 2 indicates each glass/epoxy layer of the Glare material actually formed by two unidirectional (0^0) plies of glass/epoxy of 0.125 mm thick per ply. 4/3 indicates 4 layers of aluminum and 3 layers of glass/epoxy while 0.2 denotes the thickness of each aluminum layer in mm. The total thickness of one ply of Glare 2 4/3-0.2 is therefore 1.55 mm thick.
  - Elastic modulus (1 is fiber direction and normal to the principal tensile load) $E_1 = 63\,\text{GPa}$, $E_2 = 42\,\text{GPa}$
  - Ply thickness, $t_{ply} = 1.55\,\text{mm}$
  - Tensile ultimate strength $F_{tu_1} = 324.7\,\text{MPa}$

  - Coefficient of thermal expansion in 1 (fiber) direction, $CTE_{p\text{-}1} = 14.86\text{E-}06$ per °C
  - Coefficient of thermal expansion, in 2 (transverse) direction, $CTE_{p\text{-}2} = 24.50\text{E-}06$ per °C
- Adhesive material properties are based on use of FM-73 adhesive, cured at 121 °C for 2 hours. Room temperature, dry properties, from Table 9.4, are used for initial design.
  - Shear modulus, $G_A = 355.1$ MPa
  - Thickness, $t_A = 0.114$ mm
  - Shear yield stress, $\tau_Y^{(A)} = 35.5$ MPa
  - Maximum elastic shear strain, $\gamma_Y^{(A)} = 0.1$
  - Maximum plastic shear strain, $\gamma_p^{(A)} = 0.5$
  - Maximum shear strain, $\gamma_{max}^{(A)} = \gamma_Y^{(A)} + \gamma_p^{(A)} = 0.6$

The patch design from the present process will be a 1-ply patch (1.55 mm thick) which is 60.2 mm long by 59.4 mm wide. For reference, the previous design performed by a team of Wright Laboratory, SA-ALC, and USAF Academy personnel is also a 1-ply patch but with larger dimensions (100 mm by 89.9 mm).

9.7 Summary

This chapter presents a design algorithm for bonded repairs of metallic structures. The design algorithm uses simple closed-form solutions for an elliptical patch and analytical results from a 1D bonded joint theory, and it accounts for thermal stresses. To facilitate the design logic, the design chart presented in Chapter 3 has been used as a visual aid. A novel approach for analyzing a repair under a combined thermo-mechanical loading is also described, in which the thermal problem is shown to be equivalent to a mechanical problem.

CHAPTER 10

A Preliminary Design Approach for Corrosion Repairs

10.1 Introduction

In Chapter 9, a preliminary design approach for crack patching was presented. A similar approach but for a corrosion repair will be delineated in this chapter. The present design approach is based mainly on the work of Duong (2003a) and follows closely with his development. As in Chapter 9, the present design approach for a corrosion repair will be presented here for the case that the repaired structural component is subjected to a biaxial loading with a primary load being tensile. The cases of a general far field loading (including a shear load) and biaxial loading with a primary compressive load will be treated in a similar manner as in Chapter 9 and they will not be discussed any further in this chapter. The designed patch that is output from this approach will be a cross-ply patch with the 0° and 90° plies dispersed throughout the patch thickness and with the 0° plies aligned parallel to the primary loading direction. The ratio of the number of 90° plies to the number of 0° plies will be approximately the same as the applied biaxial stress ratio. To make use of the algorithm developed in Chapter 9 for a unidirectional patch design as much as possible and to account for stiffness of the 90° plies in the design process, the cross-ply patch will be treated as a unidirectional patch in all calculation below with the "effective" modulus, effective thermal expansion coefficient, and effective thickness given by $E_{\mathrm{p}} = E_{\mathrm{f}} + \Sigma \cdot E_m$, $\alpha_{\mathrm{p}} = \frac{E_{\mathrm{f}}\alpha_{\mathrm{f}} + \Sigma \cdot E_m \alpha_m}{E_{\mathrm{f}} + \Sigma \cdot E_m}$, and $t_{\mathrm{p}} = n^0_{\mathrm{ply}} \cdot t_{\mathrm{ply}}$, where E is the modulus, α_{p} is the patch thermal expansion coefficient, t_{p} is total thickness of all 0° plies of the patch, n^0_{ply} is the number of 0° plies, t_{ply} is the thickness of one ply of the composite patch, Σ is the biaxial stress ratio, and the subscript p, f, and m denote respectively the patch, the fiber and matrix directions of a lamina. After the "equivalent" unidirectional patch is computed from the design process, this unidirectional patch can be converted into a cross-ply patch design by adding the 90° plies to the former design accordingly based on the biaxial stress ratio. In addition, the patch of a corrosion repair may also need to be tapered in both length and width direction since the patch stiffness in the width direction may be no longer negligible when compared to the skin stiffness due to a possible presence of 90° plies.

10.2 Basic Analysis Methods Used in the Preliminary Design Approach

In this section, a brief summary of the basic analysis methods used in the preliminary design approach is presented. The quantities of practical interest in the design are stresses in the skin and patch, and shear strain in the adhesive. A two-stage analysis procedure for estimating these quantities as presented in Section 6.2 of Chapter 6 without considering thermal effects will be reviewed here first. The procedure is then expanded to include the thermal effects. The analysis methods are developed for an elliptical patch and under plane stress condition. For simplicity, the patch is also assumed to be isotropic with the same Poisson ratio as that of the skin in the analysis. As shown in Chapter 3, the effect of the material orthotropy of the patch appears to be insignificant for the sought quantities. The effect of tapering of the patch's edge as commonly done in practice is also ignored in the analysis.

10.2.1 Analysis method for a repair subjected only to mechanical loads

In the first stage analysis of the solution procedure (Figure 10.1(b)), a patch assumes to be rigidly bonded to an *undamaged* skin. For reference, Figure 6.1 has been reshown in Figure 10.1 with a minor change as noted in the caption of Figure 10.1. Stresses in the skin near the edge of the patch and underneath the patch are determined from the stage I analysis using an elliptical inclusion analogy. These skin stresses were determined from Section 6.2.3 of Chapter 6 as:

Skin stress underneath the patch

$$\begin{aligned}\sigma_0^* &= \frac{\sigma_\infty}{Z}\left\{(1+S)\left[3+2\frac{B}{A}\right]+1+\nu_s S+2\frac{A}{B}+\Sigma\cdot S\left[1-\nu_s-2\nu_s\frac{B}{A}\right]\right\}\\ \sigma_{0x}^* &= \frac{\sigma_\infty}{Z}\left\{S\left[1-\nu_s-2\nu_s\frac{A}{B}\right]+\Sigma\left[(1+S)\left(3+2\frac{A}{B}\right)+1+\nu_s S+2\frac{B}{A}\right]\right\}\end{aligned} \tag{10.1}$$

$$Z = 3(1+S)^2+2(1+S)\left[\frac{B}{A}+\frac{A}{B}+\nu_s S\right]+1-\nu_s^2 S^2 \tag{10.2}$$

Skin stress concentration factor near the tip of the patch's edge

$$K_t^* = \frac{\sigma_{tip}^*}{\sigma_\infty} = (1+S)\frac{\sigma_0^*}{\sigma_\infty} \tag{10.3}$$

where S is the patch stiffness to skin stiffness ratio, i.e., $S = \frac{E'_p t_p}{E'_s t_s} = \frac{E_p t_p}{E_s t_s}$, $E' = E/1-\nu^2$, A and B are minor and major axis of the elliptical patch, ν is the Poisson's ratio, Σ is the biaxial stress ratio, and the subscript p or s denote patch and skin, respectively.

In the second stage analysis of the solution procedure, a patch is assumed to be infinite extent and again rigidly bonded to the skin (see Figure 10.1(c)). The patched skin now

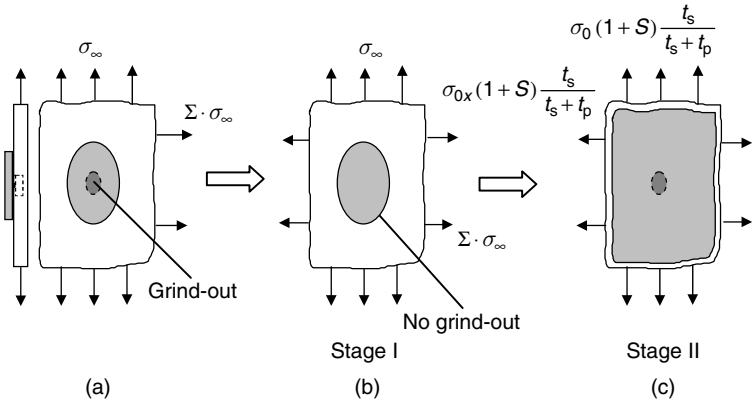

Fig. 10.1. An illustration of the two-stage analysis procedure. σ_0 and σ_{0x} are components of the skin stress underneath the patch of a problem shown in Figure 10.1(b). It is worthy to note that Figure 10.1(c) becomes identical to Figure 6.1(c) when its far field stresses are expressed in term of $\sigma_{ij}^{\text{I(stage I)}}(\mathbf{0})$ instead of σ_0 and σ_{0x} as illustrated here. $\sigma_{ij}^{\text{I(stage I)}}(\mathbf{0})$ are related to σ_0 and σ_{0x} by Equation (6.12).

contains an elliptical grind-out cavity with stresses $\sigma_0^* \frac{(1+S)t_s}{t_s+t_p}$ and $\sigma_{0x}^* \frac{(1+S)t_s}{t_s+t_p}$ applied at infinity where σ_0^* and σ_{0x}^* are obtained earlier from stage I analysis (see Section 6.2.3 of Chapter 6 and particularly Equation (6.16)). The purpose of the second stage analysis is to estimate the stresses in the skin near the bottom and near the edge of the grind-out cavity, and the maximum stress in the patch that usually occurs at the center of the patch. The stage II problem is again solved using the elliptical inclusion analogy as shown in Figure 10.1(c). It should be noted that Figure 10.1(c) depicts a problem of an infinite skin reinforced with an infinite patch and containing an elliptical inhomogeneity with the same aspect ratio as that of the grind-out cavity, which composes of a reduced thickness skin and a patch. The skin stresses near the bottom of the cavity are given by Equations (6.23) and (6.22) as

$$\sigma_{\text{c}}^* = \frac{\sigma_0^*}{Z_{\text{corro}}}\left[(1+S_{\text{corro}})\left(3+2\frac{b}{a}\right)+1+\nu_{\text{s}}S_{\text{corro}} + 2\frac{a}{b}+\frac{\sigma_{0x}^*}{\sigma_0^*}\cdot S_{\text{corro}}\left(1-\nu_{\text{s}}-2\nu_{\text{s}}\frac{b}{a}\right)\right] \tag{10.4}$$

$$\sigma_{\text{c}x}^* = \frac{\sigma_0^*}{Z_{\text{corro}}}\left\{\frac{\sigma_{0x}^*}{\sigma_0^*}\cdot\left[(1+S_{\text{corro}})\left(3+2\frac{a}{b}\right)+1+\nu_{\text{s}}S_{\text{corro}}+2\frac{b}{a}\right] + S_{\text{corro}}\left(1-\nu_{\text{s}}-2\nu_{\text{s}}\frac{a}{b}\right)\right\}$$

while the y-component patch's stress is given by (6.24):

$$\sigma_{\text{p}} = \sigma_{\text{c}}^*\left(\frac{E_{\text{p}}'}{E_{\text{s}}'}\right) \tag{10.5}$$

where from (6.20) and (6.18),

$$Z_{\text{corro}} = 3\,(1+S_{\text{corro}})^2 + 2\,(1+S_{\text{corro}})\left(\frac{b}{a}+\frac{a}{b}+\nu_{\text{s}}\,S_{\text{corro}}\right)+1-\nu_{\text{s}}^2\,S_{\text{corro}}^2$$
$$S_{\text{corro}} = -\frac{t_{\text{s}}-t_{\text{r}}}{(1+S)\,t_{\text{s}}} \tag{10.6}$$

b/a is the aspect ratio of the elliptical cavity, $(t_{\text{s}}-t_{\text{r}})$ is the depth of a grind-out, and the rest are previously defined. It should be noted from Equation (10.6) that S_{corro} is negative.

On the other hand, similar to the results of stress concentration for a hole, the y-component skin stress at the left or right edge of the cavity and the x-component skin stress at the tip edge of the cavity are of interest, especially for a very deep grind-out cavity. These stress components are determined from Section 6.2.3 as (see Equation (6.28)):

$$\sigma_{yy}^*(\pm a^+,0) = \left\{\left[\sigma_0^*(1+S)\frac{t_{\text{s}}}{t_{\text{s}}+t_{\text{p}}}-\frac{\sigma_{\text{c}}^*}{E_{\text{s}}'}\frac{(E_{\text{s}}'t_{\text{r}}+E_{\text{p}}'t_{\text{p}})}{t_{\text{s}}+t_{\text{p}}}\right]\cdot\left(1+2\frac{a}{b}\right)+\frac{\sigma_{\text{c}}^*}{E_{\text{s}}'}\frac{(E_{\text{s}}'t_{\text{r}}+E_{\text{p}}'t_{\text{p}})}{t_{\text{s}}+t_{\text{p}}}\right.$$
$$\left.-\left[\sigma_{0x}^*(1+S)\frac{t_{\text{s}}}{t_{\text{s}}+t_{\text{p}}}-\frac{\sigma_{cx}^*}{E_{\text{s}}'}\frac{(E_{\text{s}}'t_{\text{r}}+E_{\text{p}}'t_{\text{p}})}{t_{\text{s}}+t_{\text{p}}}\right]\right\}\cdot\frac{E_{\text{s}}'(t_{\text{s}}+t_{\text{p}})}{E_{\text{s}}'t_{\text{s}}+E_{\text{p}}'t_{\text{p}}} \tag{10.7}$$

$$\sigma_{xx}^*(0,\ \pm b^+) = \left\{\left[\sigma_{0x}^*(1+S)\frac{t_{\text{s}}}{t_{\text{s}}+t_{\text{p}}}-\frac{\sigma_{cx}^*}{E_{\text{s}}'}\frac{(E_{\text{s}}'t_{\text{r}}+E_{\text{p}}'t_{\text{p}})}{t_{\text{s}}+t_{\text{p}}}\right]\cdot\left[1+2\frac{b}{a}\right]+\frac{\sigma_{cx}^*}{E_{\text{s}}'}\frac{(E_{\text{s}}'t_{\text{r}}+E_{\text{p}}'t_{\text{p}})}{t_{\text{s}}+t_{\text{p}}}\right.$$
$$\left.-\left[\sigma_0^*(1+S)\frac{t_{\text{s}}}{t_{\text{s}}+t_{\text{p}}}-\frac{\sigma_{\text{c}}^*}{E_{\text{s}}'}\frac{(E_{\text{s}}'t_{\text{r}}+E_{\text{p}}'t_{\text{p}})}{t_{\text{s}}+t_{\text{p}}}\right]\right\}\cdot\frac{E_{\text{s}}'(t_{\text{s}}+t_{\text{p}})}{E_{\text{s}}'t_{\text{s}}+E_{\text{p}}'t_{\text{p}}}$$

In contrast to the case of crack patching, the present second stage analysis assumes a rigid bond between the damaged skin and the patch. The maximum strain in the adhesive therefore cannot be determined from the present solution procedure. However, since a crack-like damage appears to result in a larger maximum shear strain in the adhesive near an edge of the damage than that induced by a corrosion cavity, the maximum strain in the adhesive of a corrosion repair will be predicted conservatively as if it is estimated by using formula given in Chapter 9 for crack patching. The maximum shear strain in the adhesive near the corrosion cavity is therefore estimated by (see Equation (9.10) of Chapter 9):

$$\gamma_{\text{A}}^{\max} = \begin{cases} \dfrac{\sigma_0^* t_{\text{s}}\beta_{\text{A}}}{G_{\text{A}}} & \text{for } \sigma_0^* t_{\text{s}}\beta_{\text{A}} < \tau_{\text{Y}}^{(\text{A})} \\ \dfrac{\tau_{\text{Y}}^{(\text{A})}}{2G_{\text{A}}}\left[1+\left(\dfrac{\sigma_0^*}{\sigma_{0\text{Y}}}\right)^2\right] & \text{otherwise} \end{cases} \tag{10.8}$$

where $1/\beta_A$ as in previous chapters is the shear load transfer length with β_A defined by:

$$\beta_A = \sqrt{\frac{G_A}{t_A}\left(\frac{1}{E'_s t_s} + \frac{1}{E'_p t_p}\right)} \tag{10.9}$$

G_A and t_A are the shear modulus and thickness of the adhesive layer, respectively, σ_{0Y} is defined by Equation (3.32) as $\sigma_{0Y} \equiv \frac{\tau_Y^{(A)}}{\beta_A t_s}$, $\gamma_Y^{(A)}$ is the elastic shear limit of the adhesive as defined in Figure 2.3, and the rest are previously defined.

10.2.2 Analysis method for a repair subjected to thermo-mechanical loads

It had been shown in Chapter 9 that a thermo-mechanical problem could be made equivalent to a purely mechanical problem. For the problem of an *undamaged* skin reinforced with a bonded patch, this equivalency is illustrated in Figure 9.4 of Chapter 9 where σ_{11}^T and σ_{22}^T are given by:

$$\begin{aligned}\sigma_{11}^T &= \frac{E_s}{1-\nu_s^2}\left(\varepsilon_{11}^{(T)(p)} + \nu_s \varepsilon_{22}^{(T)(p)}\right)\\ \sigma_{22}^T &= \frac{E_s}{1-\nu_s^2}\left(\nu_s \varepsilon_{11}^{(T)(p)} + \varepsilon_{22}^{(T)(p)}\right)\end{aligned} \tag{10.10}$$

while $\varepsilon_{11}^{(T)(p)}$ and $\varepsilon_{22}^{(T)(p)}$ are defined from Chapter 9 as follows for two typical thermal loading conditions:

1. Due to a uniform operating temperature

$$\begin{aligned}\varepsilon_{11}^{(T)(p)} &= \left(\alpha_{11}^p - \alpha_s\right)\left(T_{operating} - T_{ambient}\right)\\ \varepsilon_{22}^{(T)(p)} &= \left(\alpha_{22}^p - \alpha_s\right)\left(T_{operating} - T_{ambient}\right)\end{aligned} \tag{10.11}$$

2. Due to curing of the adhesive using a circular heater blanket

$$\begin{aligned}\varepsilon_{11}^{(T)(p)} &= \left[-\left(\frac{\nu_s}{2} + \frac{1}{2}\right)\alpha_s + \alpha_{11}^p\right]\left(T_{curing} - T_{ambient}\right)\\ \varepsilon_{22}^{(T)(p)} &= \left[-\left(\frac{\nu_s}{2} + \frac{1}{2}\right)\alpha_s + \alpha_{22}^p\right]\left(T_{curing} - T_{ambient}\right)\end{aligned} \tag{10.12}$$

In Equations (10.11) and (10.12), α_{11}^p and α_{22}^p are thermal expansion coefficients of the patch in principal material directions, and α_s is the skin's thermal expansion coefficient.

Using the equivalency (see Figure 9.4), the stresses in the skin underneath the patch and near the patch tip of a stage I analysis were determined in Chapter 9 as (see Equations (9.25)–(9.27)):

$$\sigma_0 = \frac{\sigma_0^*}{\sigma_\infty}\left(\sigma_\infty - \sigma_{22}^{\mathrm{T}}\right) + \sigma_{22}^{\mathrm{T}}$$
$$\sigma_{\mathrm{tip}} = \frac{\sigma_{\mathrm{tip}}^*}{\sigma_\infty}\left(\sigma_\infty - \sigma_{22}^{\mathrm{T}}\right) + \sigma_{22}^{\mathrm{T}} \tag{10.13}$$

or

$$\frac{\sigma_0}{\sigma_\infty} = \frac{\sigma_0^*}{\sigma_\infty} + \frac{\sigma_{22}^{\mathrm{T}}}{\sigma_\infty}\left(1 - \frac{\sigma_0^*}{\sigma_\infty}\right) \tag{10.14}$$

$$K_{\mathrm{t}} = K_{\mathrm{t}}^* - \frac{\sigma_{22}^{\mathrm{T}}}{\sigma_\infty}\left(K_{\mathrm{t}}^* - 1\right) \tag{10.15}$$

where σ_0^*, σ_{tip}^* and K_{t}^* are stresses in the skin underneath the patch and near the edge of the patch, and the skin stress concentration at the patch tip, respectively, due to the mechanical loads alone, i.e., when $\sigma_{11}^{\mathrm{T}} = \sigma_{22}^{\mathrm{T}} = 0$, and they are given by Equations (10.1)–(10.3). When the damage is introduced into the skin, the skin stress σ_0 underneath the patch will change because of the load redistribution around the damage while the skin stress at the end of the patch assumes to remain the same. However, since σ_0, i.e., the skin stress underneath the patch of an undamaged skin, will be used as one of the design variables in Section 10.4 and also for evaluating the adhesive shear strain as discussed at the end of this section, a formula for σ_0 was therefore given.

In order to determine stresses in the skin near the bottom and near the edge of the cavity, and the maximum stress in the patch, the equivalency needs to cast in a slightly different form so that it can be extended easily to the case of a repair of a corroded skin (Duong, 2003a). From Chapter 9, a purely thermal stress problem can also be solved by (i) first determining the strain solution of the problem of a patched skin with a strain field $\varepsilon_{\mathrm{ij}}^{(\mathrm{T})(\mathrm{p})}$ prescribed in the patch as shown in Figure 10.2(a), using the linear superposition procedure shown in Figures 10.2(b) and 10.2(c), and (ii) then computing the thermal stresses accordingly to the formula given below:

$$\sigma_{ij}^{\mathrm{s}}(\mathbf{x}) = C_{ijkl}^{\mathrm{s}}\varepsilon_{kl}^{**}(\mathbf{x})$$
$$\sigma_{ij}^{\mathrm{p}}(\mathbf{x}) = C_{ijkl}^{\mathrm{p}}\left(\varepsilon_{kl}^{**}(\mathbf{x}) - \varepsilon_{kl}^{(\mathrm{T})(\mathrm{p})}\right) \tag{10.16}$$

where $\varepsilon_{ij}^{**}(\mathbf{x})$ denotes the strain solution obtained in step (i), and $\varepsilon_{ij}^{(\mathrm{T})(\mathrm{p})}$ is defined previously. Since the skin stress $\sigma_{ij}^{\mathrm{s}}(\mathbf{x})$ of the problem shown in Figure 10.2(a) is also equal to $C_{ijkl}^{\mathrm{s}}\varepsilon_{kl}^{**}(\mathbf{x})$ as that of the thermal stress problem, the skin thermal stress therefore can be obtained directly by superimposing the solutions of two problems shown in Figures 10.2(b) and 10.2(c). In contrast, the thermal stress in the patch still needs to be evaluated using Equation (10.16) since the patch stress of the problem shown in

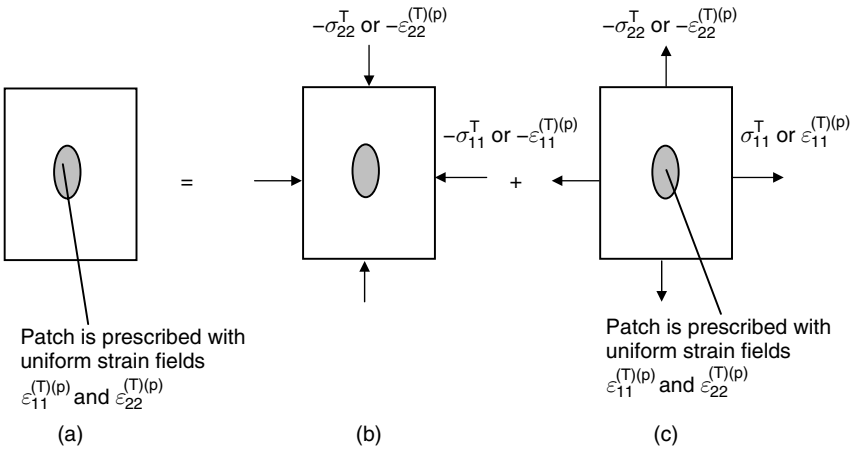

Fig. 10.2. A superposition method for analyzing a patched skin with the uniform strain field $\varepsilon_{ij}^{(T)(p)}$ prescribed in the patch. Note that $\sigma_{ij}^{T} = C_{ijkl}^{s}\varepsilon_{kl}^{(T)(p)}$.

Figure 10.2(a) is equal to $C_{ijkl}^{p}\varepsilon_{kl}^{**}(\mathbf{x})$, not $C_{ijkl}^{p}[\varepsilon_{kl}^{**}(\mathbf{x}) - \varepsilon_{\mathbf{kl}}^{(T)(p)}]$ as required by (10.16). From Equation (10.16), the patch thermal stress can be expressed alternatively in terms of the skin thermal stress as

$$\sigma_{ij}^{p}(\mathbf{x}) = C_{ijkl}^{p}\left(C_{klmn}^{s-1}\sigma_{mn}^{s}(\mathbf{x}) - \varepsilon_{kl}^{(T)(p)}\right) \tag{10.17}$$

Thus, while the skin stresses of the thermal stress problem can be determined according to the superposition procedure shown in Figures 10.2(b) and 10.2(c), the patch thermal stresses are rather obtained by Equation (10.17).

By using linear superposition, a problem of an undamaged skin reinforced with a patch under thermo-mechanical loading can be solved in a similar manner, in which the skin stress is first determined according to the approach given in Figure 10.3 while the patch stress is computed using Equation (10.17). It should be emphasized that the solutions of problems shown in Figures 10.2(c) and 10.3(c) are trivial since the resulting strains in the patch and skin in those problems are uniform and equal to the remote applied strains.

With the above approach and discussion in mind, we are now ready to present the solution approach for determining skin stresses near the bottom and near the edge of the grind-out cavity, and the maximum patch stress of the corrosion repair problem under a combined thermo-mechanical loading. With the equivalency between the thermo-mechanical and mechanical problems established and demonstrated in Figure 10.3, the problem of a corrosion repair subjected to thermo-mechanical loads can be analyzed by a method illustrated in Figure 10.4.

Problems shown in Figures 10.4(a)–10.4(c) are very similar to those shown in Figures 10.3(a)–10.3(c), except that the former problems include a corrosive damage.

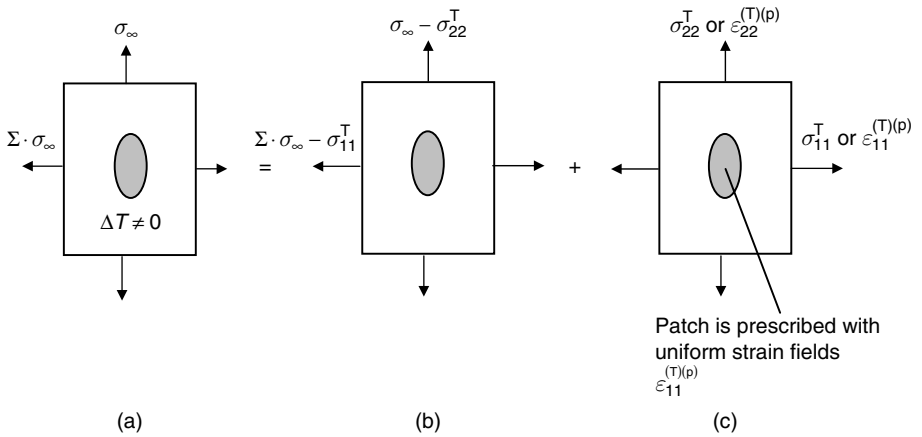

Fig. 10.3. Another form of the superposition method for analyzing an undamaged skin reinforced with a patch under thermo-mechanical loading that can be extended to the repair analysis of a corroded skin.

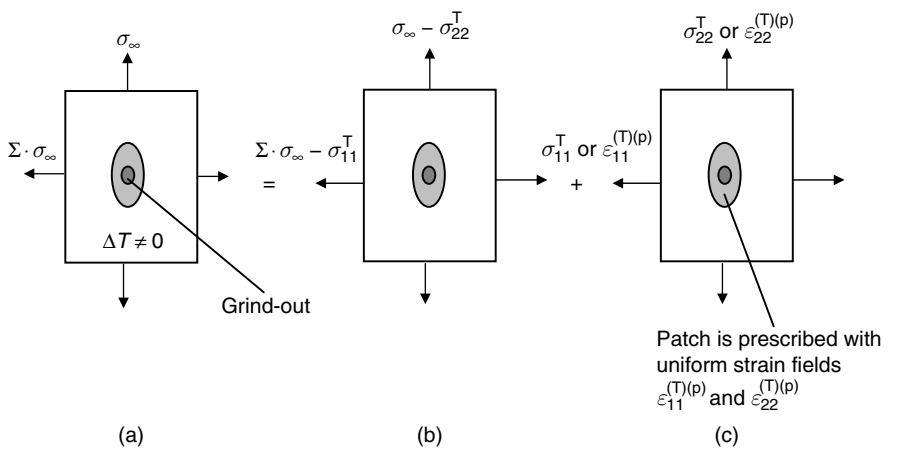

Fig. 10.4. A linear superposition method for analyzing the problem of a corrosion repair under thermo-mechanical loading.

The local skin stresses near the cavity of the problem depicted in Figure 10.4(b) can be obtained using the two-stage analysis procedure outlined in Section 10.1.1 since it is the same as the problem shown in Figure 10.1(a) except for the different far field applied stresses. The far field stress of the problem shown in Figure 10.4(b) is $\left(\sigma_{\infty ij} - \sigma_{ij}^T\right)$ rather than $\sigma_{\infty ij}$. The problem depicted in Figure 10.4(c) also can be solved using the mentioned two-stage analysis procedure. A two-stage analysis procedure for solving this problem 10.4(c) is illustrated in Figure 10.5. Since the problem shown in Figure 10.5(b) is a trivial problem with the resulting strains in the patch and skin being uniform and equal to the remote applied strains as noted in the preceding paragraph, stresses in the skin

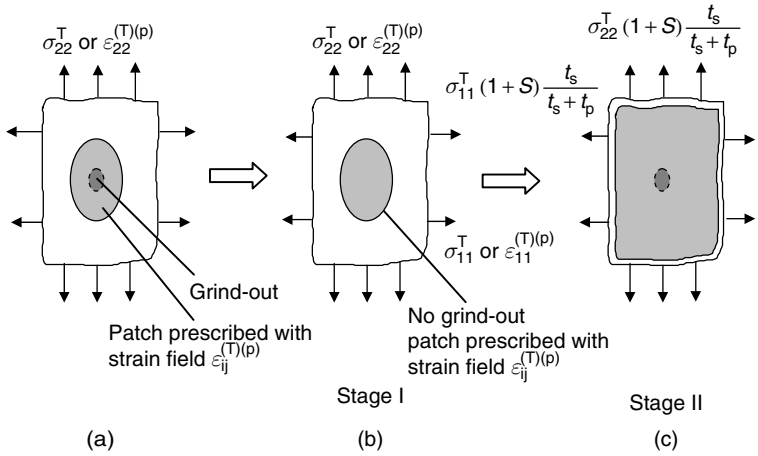

Fig. 10.5. A two-stage analysis procedure for solving problem shown in Figure 10.4(c). It should be noted that the solution of the problem shown in Figure 10.5(b) is trivial; the skin stress is uniform and equal to σ_{ij}^{T}.

of that problem will also be uniform and equal to σ_{ij}^{T}. Thus, the skin stress underneath the patch of the problem shown in Figure 10.5(b) is σ_{ij}^{T}. It was shown in Section 10.2.1 that when the skin stress components underneath the patch from stage I analysis was σ_0^* and σ_{0x}^*, the far field applied stress of the stage II problem would be $\sigma_0^* \frac{(1+S)t_s}{t_s+t_p}$ and $\sigma_{0x}^* \frac{(1+S)t_s}{t_s+t_p}$. In the similar manner, the far field applied stress of the problem shown in Figure 10.5(c) will be $\sigma_{ij}^{T} \frac{(1+S)t_s}{t_s+t_p}$, since problems shown in Figures 10.5(b) and 10.5(c) correspond respectively to the stage I and II problems of the problem depicted in Figure 10.4(c) and the skin stress underneath the patch from the stage I analysis is σ_{ij}^{T}.

Specifically, stresses in the skin near the cavity and the maximum patch stress can be evaluated using the following steps:

(i) Calculate σ_0^*, σ_{0x}^*, σ_c^*, σ_{cx}^*, $\sigma_{yy}^*(\pm a^+, 0)$ and $\sigma_{xx}^*(0, \pm b^+)$ for the problem shown in Figure 10.4(b) using formula given in Section 10.2.1, and denote them as $\sigma_0^{*(\text{part1})}$, $\sigma_{0x}^{*(\text{part1})}$, $\sigma_c^{*(\text{part1})}$, $\sigma_{cx}^{*(\text{part1})y}$, $\sigma_{yy}^{*(\text{part1})}(\pm a^+, 0)$ and $\sigma_{xx}^{*(\text{part1})}(0, \pm b^+)$.

(ii) Calculate σ_c^*, σ_{cx}^*, $\sigma_{yy}^*(\pm a^+, 0)$ and $\sigma_{xx}^*(0, \pm b^+)$ again using formula in Section 10.2.1, assuming $\sigma_0^* = \sigma_{22}^{T}$ and $\sigma_{0x}^* = \sigma_{11}^{T}$, and denote them as $\sigma_c^{*(\text{part2})}$, $\sigma_{cx}^{*(\text{part2})}$, $\sigma_{yy}^{*(\text{part2})}(\pm a^+, 0)$ and $\sigma_{xx}^{*(\text{part2})}(0, \pm b^+)$. Step (ii) basically corresponds to solving the problem shown in Figure 10.4(c) directly through stage II analysis, skipping the trivial stage I analysis.

(iii) The local skin stresses near the cavity of the thermo-mechanical problem are equal to the sum of individual contributions from steps (i) and (ii), i.e., $\sigma_c = \sigma_c^{*(\text{part1})} + \sigma_c^{*(\text{part2})}$, $\sigma_{yy}(\pm a^+, 0) = \sigma_{yy}^{*(\text{part1})}(\pm a^+, 0) + \sigma_{yy}^{*(\text{part2})}(\pm a^+, 0)$, etc.

(iv) Calculate the maximum patch stress via Equation (10.17) using skin stresses σ_c and σ_{cx} obtained in step (iii).

Finally, as before, the maximum shear strain in the adhesive is also of interest. The maximum shear strain in the adhesive again can be estimated (conservatively) using Equation (10.8) but with σ_0^* now being replaced by σ_0 as in Chapter 9, where σ_0 is given by Equation (10.13). It should be reminded that σ_0^* in Equation (10.13) is the skin stress under the patch due to the far field applied stress $\sigma_{\infty ij}$ alone and as if the skin contains no corrosive damage.

10.3 Design Criteria

The design of an effective patch requires that the patch will carry an appreciable percent of the applied load without any premature failure or disbond. To develop such a design, the patch, adhesive, and corroded skin after the repair must possess sufficient static strength. Criteria and guidelines to assure the structural integrity of the repair have been established in the CRMS Guidelines (1998) and in the RAAF Engineering Standard C5033 (Davis, 1995). This section will summarize these design criteria and guidelines. Most of these criteria and guidelines will be used in the present preliminary design approach with minor modifications for improvement whenever necessary. Basic criteria, described in this section, define acceptable patch stress, adhesive strain, skin stress and patch size, and they are described in the following sections.

10.3.1 Design criteria for corroded skin or substrate

Two design criteria are considered here for the corroded skin or substrate. First, at the design limit load (DLL), the stresses in the skin around and at the bottom of the grind-out cavity must be equal to or less than the skin yield strength. This criterion is to assure that the corroded skin after the repair will restore its original load-carrying capability. Second, the skin stress concentration factor near the patch's edge tip is limited to values below 1.3 when the ratio of the material ultimate strength to the far field stress at the design ultimate load (DUL) exceeds 1.3, i.e., $\frac{F_{\text{tu}}}{\sigma_{\infty(\text{at DUL})}} > 1.3$, or below $\frac{F_{\text{tu}}}{\sigma_{\infty(\text{at DUL})}}$ when otherwise. It is worthwhile to note that when $\frac{F_{\text{tu}}}{\sigma_{\infty(\text{at DUL})}} > 1.3$, K_{t} is still limited to values below 1.3 to prevent potential fatigue cracking in the skin near the patch's edge.

10.3.2 Design criteria for patch

Four design criteria are considered here for the repaired patch. First, the patch stiffness must be equal to or greater than the stiffness of the removal skin material. Second, the maximum stress in the patch at DUL must be less than 83% of the material tensile ultimate strength of the patch. This corresponds to a margin of safety of 0.2 or higher for the patch strength. The margin safety factor is used to accommodate for any variation or degradation of the composite material properties. Third, the length of the patch must be greater than or equal to the following value:

$$L_{\text{p}} \geq \frac{10}{\beta_{\text{A}}} + \frac{2\sigma_0 t_{\text{s}}}{\tau_{\text{Y}}^{(\text{A})}} + 2 \cdot \left(n_{\text{ply}} - 1\right) \cdot d \cdot t_{\text{ply}} + 2 \cdot b \tag{10.18}$$

where n_{ply} is the number of plies, t_{ply} is the thickness per ply, d is the step-off rate, b is the half length of an elliptical grind-out cavity, and the rest have been previously defined. As mentioned in Chapter 9, occasionally a value of $12/\beta_A$ is specified in Equation (10.18) in place of $10/\beta_A$. The purpose of this requirement is to assure that the overlap is long enough to develop a central area of very low adhesive shear stress, which anchors the bond to resist creep. The final patch criterion is a minimum width requirement which specifies

$$W_p \geq 2\left(a + \sqrt{a}\right) \tag{10.19}$$

where a is the half width of a grind-out cavity.

10.3.3 Design criteria for adhesive

In order to assure the structural integrity of the bond, the maximum shear strain in the adhesive at DUL is required to be at or below 80% of the maximum allowable strain.

10.4 Preliminary Design Procedure

The design procedure is an iterative process that requires adjustments of several variables or parameters until a satisfactory design that meets the established criteria is attained. Patch design variables are the patch stiffness ratio S, patch aspect ratio B/A, and the patch length or width. However, as shown in Chapter 9, it is more convenient to use σ_0 and K_t as the design variables in the iterative process since most of quantities used in the evaluation of criteria are commonly expressed in terms of these two parameters. By varying σ_0 and K_t within a certain appropriate range, one can effectively control the skin stress at the bottom of a grind-out cavity, the maximum adhesive shear strain, etc., within their required range.

There is no unique patch design that meets the criteria listed in Section 10.3. In a design process, one iteratively searches for a *first* design that meets the criteria. Thus, the design which results from the process will be different depending on what route the search has taken, and it may not necessarily always be the desired (optimal) design. A design procedure which is similar to that proposed in Chapter 9 for crack patching will be employed here. The design algorithm will involve three nested loops with the outermost loop for the maximum allowable patch size, the next inner loop for σ_0 and the innermost loop for K_t. In order to avoid obtaining any patch design with an extremely high aspect ratio or stiffness ratio, acceptable ranges of values for these design variables had been determined in Chapter 9. It was shown in Chapter 9 that the maximum allowable patch size ranges from $a + \sqrt{a}$ to $20 \cdot a$ or 0.508 m whichever is higher in value. On the other hand, the ranges for σ_0 and K_t are given by the following expression depending on the ratio of $\frac{\sigma_{22}^T}{\sigma_\infty}$

For $\dfrac{\sigma_{22}^{T}}{\sigma_{\infty}} \le 1$

$$0.33+0.67\frac{\sigma_{22}^{T}}{\sigma_{\infty}} < \frac{\sigma_0}{\sigma_{\infty}} < 0.8+0.2\frac{\sigma_{22}^{T}}{\sigma_{\infty}};\ 1.05-0.05\left.\frac{\sigma_{22}^{T}}{\sigma_{\infty}}\right|_{\text{at DUL}} \le K_t \le 1.3,\ \frac{F_{tu}}{\sigma_{\infty(\text{at DUL})}},$$

or $\left. 2-\dfrac{\sigma_{22}^{T}}{\sigma_{\infty}}\right|_{\text{at DUL}}$, whichever is smaller in value.

For $\dfrac{\sigma_{22}^{T}}{\sigma_{\infty}} > 1$,

$$0.8+0.2\frac{\sigma_{22}^{T}}{\sigma_{\infty}} < \frac{\sigma_0}{\sigma_{\infty}} < 0.33+0.67\frac{\sigma_{22}^{T}}{\sigma_{\infty}};\ \left. 2-\frac{\sigma_{22}^{T}}{\sigma_{\infty}}\right|_{\text{at DUL}} \le K_t \le 1.05-0.05\left.\frac{\sigma_{22}^{T}}{\sigma_{\infty}}\right|_{\text{at DUL}}$$

or $-\dfrac{F_{cu}}{\sigma_{\infty}\text{ at DUL}} \le K_t \le 1.05-0.05\left.\dfrac{\sigma_{22}^{T}}{\sigma_{\infty}}\right|_{\text{at DUL}}$ if $\left. 2-\dfrac{\sigma_{22}^{T}}{\sigma_{\infty}}\right|_{\text{at DUL}} < -\dfrac{F_{cu}}{\sigma_{\infty(\text{at DUL})}}$

where F_{tu} and F_{cu} are the *magnitudes* of the tensile and compressive strengths of the skin material. For detailed discussion on how these ranges were determined, a reader should refer to Chapter 9. With the range of σ_0 and K_t having been determined, the design algorithm can now be described. The design algorithm involves the following principal steps:

(i) Start with $A_{max} = a + \sqrt{a}$ and increase A_{max} incrementally to a maximum value of $20a$ or 0.508 m whichever is higher in value.

(ii) Start with $\left.\dfrac{\sigma_0}{\sigma_{\infty}}\right|_{\text{at DUL}} = 0.8+0.2\dfrac{\sigma_{22}^{T}}{\sigma_{\infty}}$ and decrease by small decrements (when $\dfrac{\sigma_{22}^{T}}{\sigma_{\infty}} \le 1$) or increase incrementally (when $\dfrac{\sigma_{22}^{T}}{\sigma_{\infty}} > 1$) to $0.33+0.67\dfrac{\sigma_{22}^{T}}{\sigma_{\infty}}$.

(iii) Start with $K_t = 1.05-0.05\left.\dfrac{\sigma_{22}^{T}}{\sigma_{\infty}}\right|_{\text{at DUL}}$ and increase incrementally to 1.3, $\dfrac{F_{tu}}{\sigma_{\infty(\text{at DUL})}}$ or $\left. 2-\dfrac{\sigma_{22}^{T}}{\sigma_{\infty}}\right|_{\text{at DUL}}$, whichever is smaller in value, when $\dfrac{\sigma_{22}^{T}}{\sigma_{\infty}} \le 1$, or decrease by small decrements to $\left. 2-\dfrac{\sigma_{22}^{T}}{\sigma_{\infty}}\right|_{\text{at DUL}}$ or $-\dfrac{F_{cu}}{\sigma_{\infty(\text{at DUL})}}$, whichever is higher in value, when $\dfrac{\sigma_{22}^{T}}{\sigma_{\infty}} > 1$.

(iv) Calculate $\dfrac{\sigma_0^{*}}{\sigma_{\infty}}$ and K_t^{*} by the first equation of (10.13) and a second equation of (10.14) with $\dfrac{\sigma_0}{\sigma_{\infty}}$ and K_t given from steps (ii) and (iii).

(v) Solve the first equation of (10.1) and Equation (10.3) simultaneously for S and B/A with $\dfrac{\sigma_0^{*}}{\sigma_{\infty}}$ and K_t^{*} obtained from step (iv). It is important to note that since S and t_p are the stiffness ratio and the thickness of an equivalent unidirectional patch (with effective moduli accounting for the cross plies), respectively, the

number of piles determined from S will be n_{ply}^0, as mentioned in the Introduction of this chapter.

(vi) Calculate stresses in the patch and strains in the adhesive at DUL, and the skin stresses around and at the bottom of the grind-out cavity at DLL using the formula and/or the analysis procedure given in Section 10.1 and check the criteria specified in Section 10.2.

(vii) Determine the patch width and length, noting n_{ply} in Equation (10.18) for the minimum patch length given by $n_{\text{ply}} = n_{\text{ply}}^0 + \sum \cdot n_{\text{ply}}^0$.

(viii) If a satisfactory design is found then the process has completed. Otherwise, one needs to return to step (iii) or (ii) or (i) depending on whether or not K_t and $\left.\frac{\sigma_0}{\sigma_\infty}\right|_{\text{at DUL}}$ have reached their upper limit specified in these steps.

As in Chapter 9, the design procedure computes the geometry of an elliptical patch based on simple formulas. Since elliptical patches are impractical for manufacturing, an octagonal or rectangular shape can be approximately derived from the elliptical design using the process similar to that outlined in Chapter 9. A rectangular patch design assumes to have the same aspect ratio, length and width output from the previous design process for an elliptical shape. In contrast, the above elliptical patch design can be converted to an octagonal patch design using the Hart-Smith equivalent volume concept.

10.5 Summary

This chapter presents a design algorithm for bonded repairs of corroded metallic structures. The design algorithm uses simple closed-form solutions for an elliptical patch and analytical result from a 1-D bonded joint theory and accounts for thermal stresses. The algorithm is robust and versatile, which can greatly reduce the patch design cycle time in practice.

CHAPTER 11

Experimental Verifications of Analytical Methods

11.1 Introduction

In Chapters 3–5, analytical methods for predicting the stress distribution and crack-tip stress intensity factor in a skin with a supported or unsupported one-sided and two-sided repair are presented. Even though the results from these analytical methods were always compared with the FE solutions in the previous chapters, such comparisons with experimental data have not been made. These analytical and FE results will be verified experimentally in this chapter.

There are four main individual effects, which are important for the design of a bonded repair.

1. Residual thermal stresses
2. Patch aspect ratio (load attraction)
3. Tapering ratio
4. Out-of-plane bending.

Several analytical models have been developed in Chapters 3–5 to address these individual effects. As part of the Composite Repair Aircraft Structures (CRAS) study effort performed by the Boeing Company and funded by the United States Air Force Research Laboratory (AFRL), a comprehensive experimental program was conducted to provide data for validating these analytical models (Duong, 2003b; Duong and Wang, 2004; Duong et al., 2006). Since these analytical models employ a different set of simplifying assumptions, which yield results with a different level of accuracy, a building block approach is employed in the test. According to this testing approach, first, each of these effects will be assessed individually through a basic test and compared with the analytical predictions. After this, these individual effects will be tested in different combinations and again compared with analytical results.

To determine the effectiveness of the bonded repair, two important quantities of interest are as follows:

1. The crack-tip stress intensity factor, which is linked directly to the crack growth rates underneath the patch;
2. The stress concentration (load attraction) in the skin near the edge of the patch, which is important for assessment of damage initiation in the skin adjacent to the patch.

Since each of these two quantities requires a different set of testing techniques and loading for its determination, two different sets of tests are conducted. In the first set, specimens are loaded in fatigue and crack growth data is collected and directly compared with analytical predictions. In the second set, in order to collect load attraction data, specimens are coated with a photo-elastic coating on one side and with strain gauges on the other side, which are subjected to a static load. Specimen configurations corresponding to these two sets of tests will be described in detail in Sections 11.2 and 11.3. All specimens were fabricated and tested at the United States Air Force Academy (USAFA) according to the designs and instructions provided by The Boeing Company.

11.2 Fatigue Crack Growth Tests and Method Validation

11.2.1 Fatigue crack growth tests

Relatively wide geometrical and material configurations of patches and cracked plates are tested for fatigue crack growths. The details of these specimen configurations for a two-sided repair type are listed below. All two-sided repair test specimens have a sandwich configuration where two one-sided, patched, cracked plates are bonded back to back onto a honeycomb core, in order to eliminate the out-of-plane bending at the crack (Figure 11.1). The plates in the sandwich configuration are 3.175 mm thick. Similarly, the descriptions of the test specimens corresponding to one-sided repairs are summarized in Table 11.1. The cracked plates in both configurations are made of Aluminum 7075-T6 bare with dimensions of 22.9 cm × 61 cm unless noted otherwise. The plates have a starter crack of 25 mm and a final crack length of 60 mm. All patches are rectangular. The pre-crack stress level range is 60-3 MPa, and the fatigue test was conducted at a range of 120-6 MPa. The adhesive is FM-73M from Cytec. The details of the test procedure and test results are documented in Duong (2003b). In contrast, detailed descriptions of the tested sandwich configurations are as follows:

- Configurations F1 and F2: Each side of the honeycomb core is a cracked plate bonded with a 10-ply boron/epoxy patch (the nominal thickness of each ply is 0.127 mm, and the patch stiffness ratio S, i.e., $E_p t_p / E_s t_s$, equals 1.11). The patch dimensions are 76.2 mm × 177.8 mm. The patch is unidirectional with the zero-degree ply oriented normally to the crack. Configurations F1 and F2 are nearly identical, except that the patch in the latter configuration is tapered with a tapering ratio of 30:1 (1 mm rise for every 30 mm edge length).
- Configurations F3 and F4: Configurations F3 and F4 are similar to F1 and F2, respectively, except for the patch material, thickness and edge's tapering ratio.

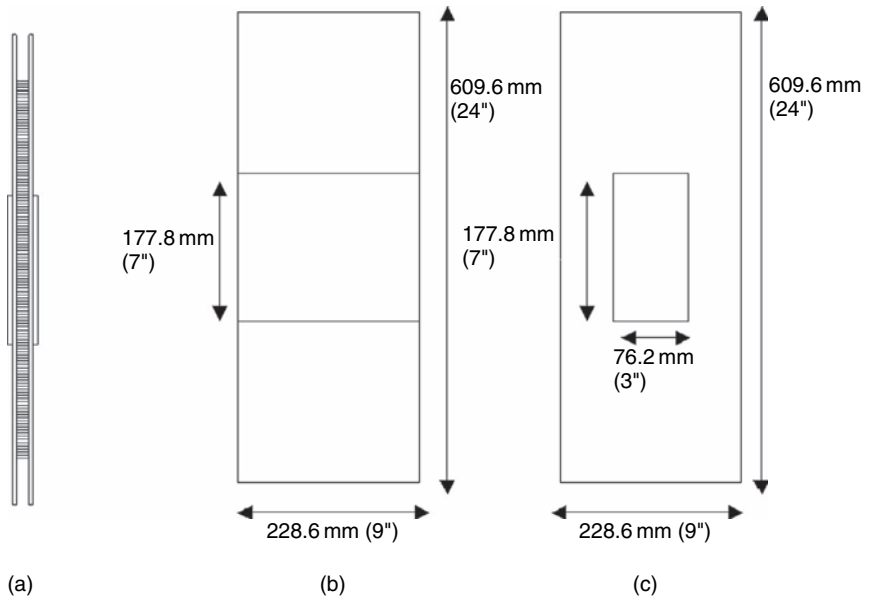

Fig. 11.1. A sandwich configuration of fatigue crack growth specimens: (a) side view; (b) plan view of a specimen with a patch spanning across the full plate's width; and (c) plan view of a specimen with a finite-size rectangular patch.

The patches in configurations F3 and F4 are also aluminum like the cracked plates, thus there will be no residual thermal stresses associated with curing of the adhesive in these configurations. Furthermore, in order to keep the patch stiffness ratio of configurations F3 and F4 approximately the same as those of F1 and F2, the thickness of the patches in the former configurations is equal to 3.683 mm ($S = 1.16$). In addition, the tapering ratio in configuration F4 is only 10:1. This is because the tapering ratio is recommended in practice to be equal to ten times the patch modulus ratio E_p/E_s (Davis, 1995; CRMS Report, 1998).

- Configurations F5 and F6: Each side of the honeycomb core is a cracked plate bonded with a 10-ply boron/epoxy patch (S equals 1.11). The patch spans across the full plate's width with a length of 177.8 mm. Configuration F6 differs from configuration F5 by the tapered edge of the patch with a tapering ratio of 30:1.

11.2.2 Characterization of fatigue crack growth in one-sided and two-sided repairs

Analytical predictions for the growth rates of patched cracks are based on a correspondence principle between the patched cracks and the un-patched cracks. This principle has been proven theoretically and demonstrated in Chapter 8 for a flight spectrum loading. According to this principle, patched and un-patched cracks under a constant amplitude cyclic load will have the same crack growth behavior if their tips experience the

Table 11.1. Detailed description of patched specimen configurations used for validating the analytical and FE models. In the table, S is defined as ratio of patch stiffness to the plate stiffness, and the nominal thickness of a boron-epoxy ply is 0.127 mm.

Specimen configuration	Plate thickness and material	Patch thickness and material	Patch geometry
S1	3.175 mm thick Al 7075-T6 bare	10-ply boron-epoxy ($S = 1.11$)	76.2 mm wide, 177.8 mm long
S2	1.27 mm thick Al 7075-T6 bare	4-ply boron-epoxy ($S = 1.11$)	76.2 mm × 177.8 mm
S3	3.175 mm thick Al 7075-T6 bare	3.683 mm thick Aluminum ($S = 1.16$)	76.2 mm × 177.8 mm
S4	1.27 mm thick Al 7075-T6 bare	1.524 mm thick Aluminum ($S = 1.2$)	76.2 mm × 177.8 mm
S5	1.175 mm thick Al 7075-T6 bare	18-ply boron-epoxy ($S = 2$)	76.2 mm × 177.8 mm
S6	3.175 mm thick Al 2024-T3 bare	10-ply boron-epoxy ($S = 1.16$)	76.2 mm × 177.8 mm
S7	3.175 mm thick Al 7075-T6 bare	10-ply boron-epoxy ($S = 1.16$)	Patch spans the plate's full width with a length of 177.8 mm
S8	3.175 mm thick Al 7075-T6 bare	3.683 mm thick Aluminum ($S = 1.16$)	Patch spans the plate's full width with a length of 177.8 mm
S9	1.27 mm thick Al 7075-T6 bare	1.524 mm thick Aluminum ($S = 1.2$)	Patch spans the plate's full width with a length of 71.12 mm

same history of $\Delta K (= K_{\max-\text{load}} - K_{\min-\text{load}})$ and R-ratio $\left(= \dfrac{K_{\min-\text{load}}}{K_{\max-\text{load}}}\right)$ where K is the stress intensity factor and the subscripts min-load and max-load denote the valley and the peak of the cyclic load, respectively. Thus, the growth rate of patched cracks can be predicted using the crack growth data obtained from the un-patched specimens. The crack growth $\mathrm{d}a/\mathrm{d}N$ data obtained from these un-patched specimens when it is expressed in terms of ΔK and R-ratio will be a material property that is independent of specimen geometries (coupon or structural component, patched or un-patched crack) and applied loads. Typical $\mathrm{d}a/\mathrm{d}N$ data for a given material depends on the testing environment (lab air, relative humidity [RH]) and specimen thickness.

The un-patched specimens used to determine $\mathrm{d}a/\mathrm{d}N$ data of a given material are usually tested under in-plane tensile loading so that the specimens do not exhibit any out-of-plane deflection and therefore the crack-tip stress intensity factor is uniform across the plate thickness. Similarly, two-sided bonded composite repairs also have no secondary bending due to the symmetric lay-up of the patch-plate combination. Thus, fatigue crack growths in these two configurations are clearly characterized by the constant through-thickness stress intensity factors evaluated at the maximum and the minimum loads of the loading cycle. The stress intensity factor at the crack tip of a two-sided repair can

be evaluated by the analytical methods given in Chapter 4, which follows the two-stage analysis procedure and accounts for various effects such as residual thermal stresses, the local disbond around the crack surfaces, and the materially nonlinear behavior of the adhesive.

In contrast to symmetric repairs, predicting crack growth in a plate with a one-sided repair poses a real challenge. This is because the stress intensity factor at the crack tip of a plate with a one-sided repair will vary across the plate thickness as shown in Figure 11.2 due to the out-of-plane deflection induced by the load path eccentricity, and it is therefore unclear which through-thickness value of the stress intensity factor governs the observed fatigue crack growth. Even though the maximum, mean and root mean square (rms) values of the thickness-varying stress intensity factors were commonly suggested for use in practice for predicting fatigue crack growth in a plate with a one-sided repair, there is no comprehensive experimental study of their validity to date since the work of Ratwani (1980). However, as found later by Rose (1988) and Arendt and Sun (1994), Klug and Sun (1998) and Sun et al. (1966), the effect of the out-of-plane bending was not correctly accounted for in the Ratwani's work. The good agreement between crack growth predictions using the maximum-thickness values of the stress intensity factors and test results in that work therefore may be a coincidence.

As mentioned earlier, due to the out-of-plane bending induced by load-path eccentricity, the crack-tip stress intensity factor will vary across the plate thickness. Various values of the stress intensity factor can be evaluated for the plate with a one-sided repair using the analytical model described in Chapter 5 that accounts for the effects of geometric nonlinearity and thermal stresses. For future discussion, values of the thickness-varying stress intensity factor that are commonly used in practice for predicting fatigue crack

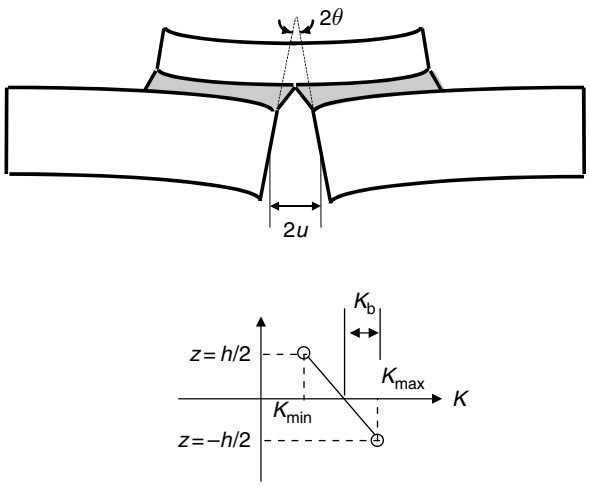

Fig. 11.2. Variation of the stress intensity factor through the plate thickness.

growth of a general bending crack are defined below, in terms of the membrane and bending values (Wang et al., 1998).

$$K_{\max} = K_{\text{mem}} + K_{\text{b}}$$

$$K_{\text{mean}} = \frac{K_{\max} + K_{\min}}{2} = K_{\text{mem}} \tag{11.1}$$

$$K_{\text{rms}} = \sqrt{K_{\text{mem}}^2 + \frac{K_{\text{b}}^2}{3}}$$

In Equation (11.1), the subscripts max, min, b, membrane, mean and rms denote respectively the maximum, minimum, bending, membrane, mean and root mean square values of the stress intensity factor. Generally, the K_{rms} value is only slightly higher than the K_{mean} value. However, as shown by Duong (2003) and also later in the next subsection, the predictions using $K_{\max}$ in many instances will yield unrealistically high crack growth rates when compared with the test results. On the other hand, the predictions using K_{rms} or K_{mean} in other instances will grossly underestimate the crack growth rates of the plates with a one-sided repair. Thus, a new effective K accounting for the thickness variation of the stress intensity factor in a plate with a one-sided repair as proposed by Duong (2003b) and later refined by Duong and Wang (2004) will be used to characterize the fatigue crack growth in one-sided patched specimens.

Duong (2003b) has postulated that a bending crack would probably grow according to $K_{\max}$ at low values of K_{b} but by K_{rms} at high values of K_{b}. This is particularly true for the two extreme cases of without bending and with pure bending. An equivalent (effective) stress intensity factor denoted by K_{eq} is therefore proposed for crack growth prediction of a patched bending crack that conforms with the above postulate as follows:

$$K_{\text{eq}} = \max\left[K_{\text{rms}}, K_{\text{mean}} + \lambda K_{\text{b}}\right] \tag{11.2}$$

where λ will be derived semi-empirically later using a one-sided strap joint theory, and it is less than or equal to 1. λ is assumed to equal 1 for a low bending case and 0 for a high bending case. According to Equation (11.2), K_{eq} equals either K_{rms} or $K_{\text{mean}} + \lambda K_{\text{b}}$, whichever has a larger numerical value.

According to the one-sided strap joint theory described in Chapter 2, if the overlap joint is sufficiently long, there will be no interaction between the skin interruption end and the patch end. The amount of load transferred from the skin to the patch at the patch end is equal to $\frac{P \cdot S}{S+1}$, where P and S are the applied load per unit width and patch stiffness ratio, respectively. Thus, the skin will carry a load of $P\left[1 - \frac{S}{S+1}\right]$ at the middle of the *half* overlap length between the skin interruption end and the patch end. This remaining load in the skin must be transferred to the patch at the skin interruption end. This latter load transfer is the source for local bending at the skin interruption end. It is worthy to note that the overall bending at the skin interruption end will be governed solely by this local bending since the global bending of the patch/skin combination is negligible for a long overlap strap joint according to the geometrically nonlinear deformation theory.

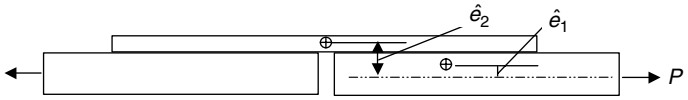

Fig. 11.3. Schematic of a one-sided strap joint.

The local bending at the skin interruption end depends on the remaining load in the skin after the first load transfer at the patch end and the eccentricity between the centroid of the patch/skin combination and the centroid of the region directly over the interruption end (Figure 11.3). The centroids $\hat{e}_1$ and $\hat{e}_2$ shown in Figure 11.3 are found respectively from the second equation of (2.81) in Chapter 2 and the geometry as

$$\begin{aligned} \hat{e}_1 &= \frac{S}{1+S}\left[\frac{t_s+t_p}{2}\right] \\ \hat{e}_2 &= \frac{t_s+t_p}{2} \\ \frac{\hat{e}_2}{\hat{e}_1} &= \frac{S+1}{S} \end{aligned} \tag{11.3}$$

where S is defined previously as the patch stiffness ratio, and noting $\hat{e}_1$ was denoted as $\hat{e}$ in Section 2.3.1. It was shown in Section 2.3.1 of Chapter 2 that the bending moments of the patch and skin at the interruption end in the one-sided strap joint are approximately equal to the followings for a sufficient long overlap (see Equation (2.109), assuming $\ell \gg 1$ and $M^{\text{therm}} = 0$ in that equation)

$$\begin{aligned} M_p &= -P \cdot \left[\frac{t_p+t_s}{2} - \hat{e}_1\right] \\ &= -P \cdot \frac{t_p+t_s}{2} \cdot \left[1 - \frac{S}{S+1}\right] \\ M_s &= 0 \end{aligned} \tag{11.4}$$

The bending moment in the patch at the skin interruption end also can be expressed in a normalized form as

$$m_p = \frac{M_p}{-P \cdot \dfrac{t_p+t_s}{2}} = 1 - \frac{S}{S+1} \tag{11.5}$$

From Equation (11.5), m_p is approximately 0 for $S \gg 1$, and 1 for $S \ll 1$. For a very stiff strap, i.e., $S \gg 1$, most of the remote load in the skin will be transferred at the patch end, leaving only a small remaining load in the skin needed to be transferred at the skin interruption end, and the eccentricity in the load path near the skin interruption end will also be small as dictated by the last equation of (11.3), i.e., $\hat{e}_2 \approx \hat{e}_1$ so that

$\hat{e}_2 - \hat{e}_1 \approx 0$. As a result, there is only small local bending near the skin interruption end, thus small m_p. In contrast, for a very soft patch, only a small portion of the remote load in the skin will be transferred at the patch end, leaving a large remaining load in the skin after the first load transfer, which together with a high eccentricity in the load path near the skin interruption end causes the high local bending there. Thus, m_p is a good parameter for quantifying the effect of the local bending near the crack surface of a one-sided bonded repair. Furthermore, $m_p = 0$ for a small local bending at the crack surfaces, and $m_p = 1$ for a high local bending there. Since the sought coefficient λ of Equation (11.2) is assumed to be equal to 1 for a small bending case and 0 for a high bending case, it is then clear that $\lambda \propto (1 - m_p) \propto \frac{S}{S+1}$. A general expression for λ has been derived empirically by correlating crack growth predictions by analytical methods for single-sided repairs with all available test data generated under the CRAS project. Through these analysis correlations with various fatigue crack growth data, the following definition of λ yields crack growth predictions that are consistently in good agreement with the test data (Duong, 2003b):

$$\lambda = \begin{cases} \dfrac{S}{S+1} & S > 1 \\ \dfrac{S}{S+1} \cdot S & S \leq 1 \end{cases} \tag{11.6}$$

It is worthy to note that λ defined by Equation (11.6) will be continuous at $S = 1$ and ranges between 1 and 0, as required.

While the use of K_{eq} defined by Equations (11.5) and (11.6) to characterize the fatigue crack growth in a one-sided repair produces encouraging prediction results, there are two drawbacks with that approach. First, the use of the non-dimensional parameter $S/(S+1)$ implies that the proposed approach is limited to cracks in patched plates. Secondly, since the only similitude parameter for fracture and fatigue crack growth is the stress intensity factor at the crack tip, it is therefore preferred to express K_{eq} solely in terms of K_{rms}, K_{max}, and K_b rather than a mixture of these stress intensity factors with $S/(S+1)$ as indicated by Equations (11.6) and (11.2).

To generalize the above concept, Duong and Wang (2004) have suggested an alternative form of the above equivalent (effective) stress intensity factor in terms of K_{rms}, K_{max} and K_b for a balanced or stiff patch repair ($S \geq 1$). Similar to the previous approach, the equivalent stress intensity factor for characterizing the fatigue crack growth in a one-sided repair is postulated to be given by

$$K_{eq} = K_{max} + \alpha \frac{K_b}{K_{max}} K_{rms} \tag{11.7}$$

where α is determined from the two conditions given below:

$$\begin{aligned} K_{eq} &= K_{max} \quad \text{for } \frac{K_b}{K_{max}} = 0 \quad \text{(pure tension)} \\ K_{eq} &= K_{rms} \quad \text{for } \frac{K_b}{K_{max}} = 1 \quad \text{(pure bending, } K_{mem} = 0) \end{aligned} \tag{11.8}$$

For the second condition of Equation (11.8), $K_{max} = K_b$ and $K_{max} = K_b = \sqrt{3} \cdot \frac{K_b}{\sqrt{3}} = \sqrt{3} \cdot K_{rms}$ by the last equation of (11.1) and noting $K_{mem} = 0$ in the case of pure bending. Thus, evaluation of Equation (11.7) for this condition yields $\alpha = 1 - \sqrt{3}$. Consequently, Equation (11.7) becomes

$$K_{eq} = K_{max} + \left(1 - \sqrt{3}\right) \frac{K_b}{K_{max}} K_{rms} \tag{11.9}$$

or

$$K_{eq} = K_{mem} + K_b + \left(1 - \sqrt{3}\right) \frac{K_b}{K_{mem} + K_b} \sqrt{K_{mem} + \frac{K_b^2}{3}} \tag{11.10}$$

According to Equation (11.9), K_{eq} for any value K_b/K_{max} between 0 and 1 is determined by linear interpolation of the results of the two extreme cases: $K_b/K_{max} = 0$ (pure tension) and $K_b/K_{max} = 1$ (pure bending). It is interesting to note that for all one-sided repair configurations considered in this chapter as well as those additional configurations reported in Duong (2003b) with patch stiffness ratio greater than 1, the values of K_{eq} given by Equation (11.9) are nearly the same (within 6% deviation) as those given by Equations (11.2) and (11.6). This observation can be generalized to all one-sided repair configurations since the repair configurations considered in this chapter and in the report by Duong (2003b) cover quite a wide range of different combinations of K_b/K_{max} and K_{rms} or K_{mean}. Thus, the latter definition of K_{eq} will be employed in the subsequent correlations of analytical predictions of fatigue crack growths of specimens described in Table 11.1 with the test results.

As mentioned earlier in the beginning of this section, in order to be able to compare the analytical and FEM predictions to the test results for the crack growth, it is necessary to have da/dN versus ΔK curves for each R-ratio that will be predicted by the analysis. Since the analysis will probably predict many different R-ratios at the crack tip due to the thermally induced residual stress, this will mean that one would have to create these curves for all these different R-ratios. However, by using the principle of the effective stress intensity factor ΔK_{eff}, all different $da/dN - \Delta K$ for each possible R-ratio will fall on top of each other or collapse into a single curve, i.e., da/dN will only depend on ΔK_{eff}, independent of R. The equation that transforms ΔK and R into ΔK_{eff} is only valid within certain R-range and also for a certain material. For Al 7075-T6 and for $R > 0$, De Koning (1980) showed that the effect of the R-ratio could be incorporated into a single da/dN versus ΔK_{eff} curve with the latter parameter given by

$$\Delta K_{eff} = \Delta K \ (0.55 + 0.35R + 0.5R^2 - 0.4R^3) \tag{11.11}$$

where $\Delta K = K_{max-load} - K_{min-load}$ and $R = K_{min-load}/K_{max-load}$, and the subscripts "max-load" and "min-load" denotes, respectively, the peak and valley of the cyclic load.

Several un-patched Al 7075 specimens that came from the same batch of material as the one used for all the patched specimens were tested. These tests had been done over a specific ΔK_{eff} range for two Al 7075 plate thicknesses, i.e., 1.27 mm thick and 3.175 mm thick. Since the crack growth may be affected by the RH, da/dN data are also generated for both low and high RH. Figures 11.4 and 11.5 show da/dN versus ΔK_{eff} on linear scale for two Al 7075 plate thicknesses. These raw data are then fitted by a fourth degree polynomial. Equations of these fourth degree polynomial fits are given in Table 11.2

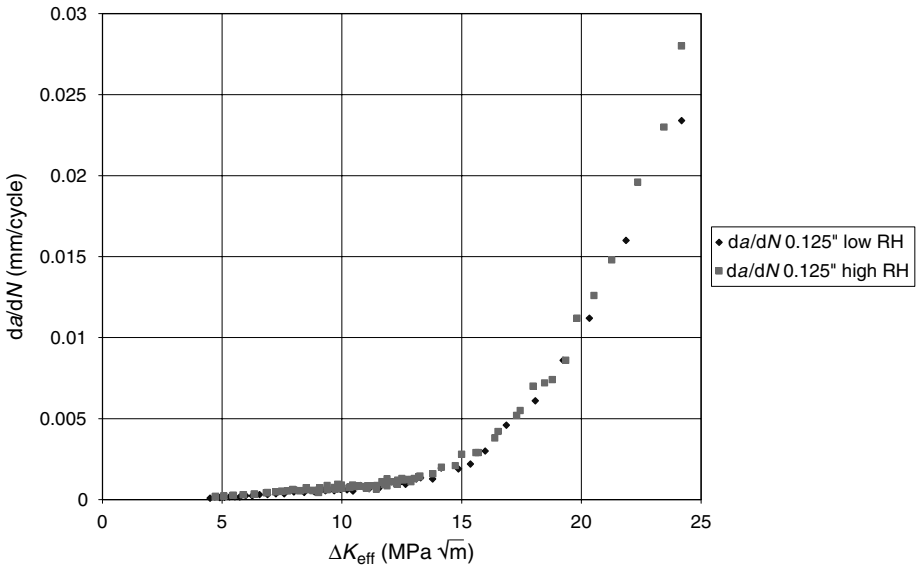

Fig. 11.4. da/dN versus ΔK_{eff} for Al 7075-T6 3.175 mm thick sheet.

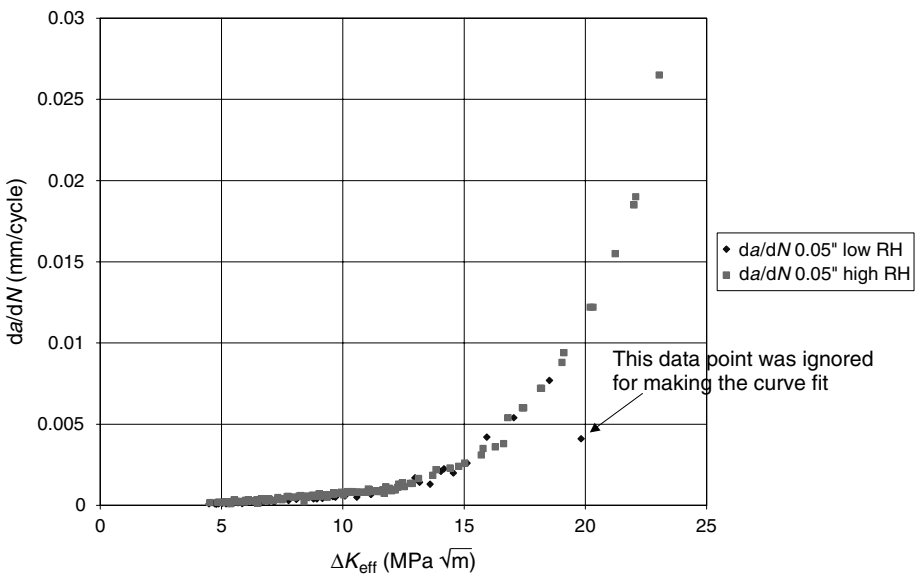

Fig. 11.5. da/dN versus ΔK_{eff} for Al 7075-T6 1.27 mm thick sheet.

Table 11.2. Coefficients of the fourth degree polynomial fits to da/dN–ΔK_{eff} data for Al 7075-T6 bare material. The polynomial fit takes the form of $y = a + bx + cx^2 + dx^3 + ex^4$, where y and x stand for da/dN and ΔK_{eff}, with a unit of mm/cycle and MPa$\sqrt{m}$, respectively.

Plate thickness (mm)	Relative humidity (%)	Applicable range	a	b	c	d	e
1.27	4–8	$4.485 < \Delta K_{eff} < 18.517$	−8.166536E-6	−8.4353778E-5	4.147869E-5	−5.061604E-6	2.326616E-7
1.27	14–23	$4.532 < \Delta K_{eff} < 23.045$	1.1444186E-4	−2.6661175E-4	9.1705431E-5	9.2909308E-6	3.4035549E-7
3.175	6–12	$4.494 < \Delta K_{eff} < 24.185$	−2.201150E-4	2.3847794E-4	−3.207314E-5	7.0813134E-7	7.9250803E-8
3.175	21–23	$4.716 < \Delta K_{eff} < 24.176$	−1.655046E-4	1.0414462E-4	1.0676499E-5	−3.153469E-6	1.867254E-7

with both the applicable range of ΔK_{eff} and the associated level of RH indicated. In many patched specimen configurations, the values of the predicted ΔK_{eff} may be outside the valid domains of these equations. In that case, the following linear equations are suggested to use instead:

High RH, 3.175 mm and 1.27 mm thick plate
$y = 0.0001x - 0.0004$

Low RH, 3.175 mm thick plate
$y = 1.E\text{-}4x - 0.0003$

Low RH, 1.27 mm thick plate
$y = 0.8E\text{-}4x - 0.0003.$

The latter linear-fit equations are plotted against the collapsed un-patched crack growth data in Figures 11.6 and 11.7 for $\Delta K_{\text{eff}} < 10$, on linear scale. For all ranges of ΔK_{eff}, the equations that are closest to the actual test conditions of the patched specimens will be used in the correlations. It remains now to outline a procedure for predicting crack growth in a plate with a bonded repair. That topic is therefore presented in the next subsection.

11.2.3 Fatigue crack growth analysis

The analytical predictions of the crack growth versus number of loading cycles for the patched specimens described above involve the following steps (Duong, 2003b; Duong and Wang, 2004):

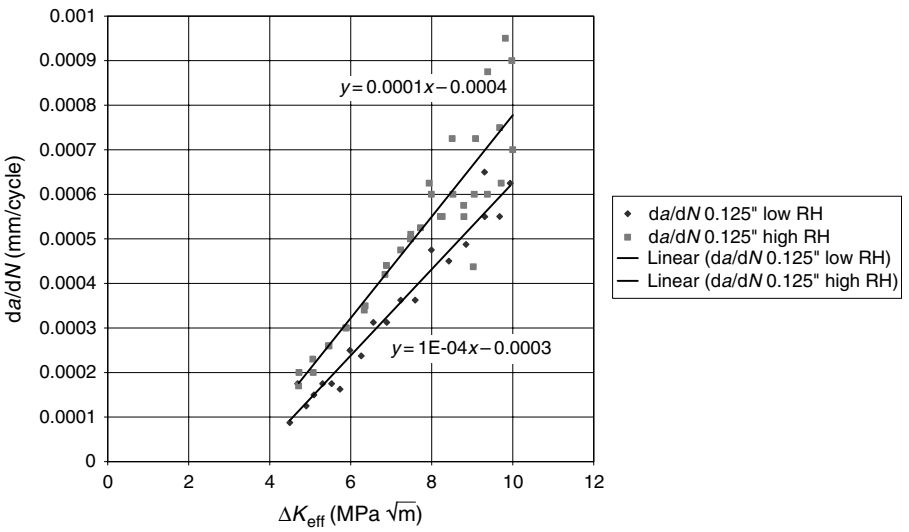

Fig. 11.6. A linear fit of $\mathrm{d}a/\mathrm{d}N$ versus ΔK_{eff} for Al 7075-T6 3.175 mm thick plate at low ΔK_{eff} range.

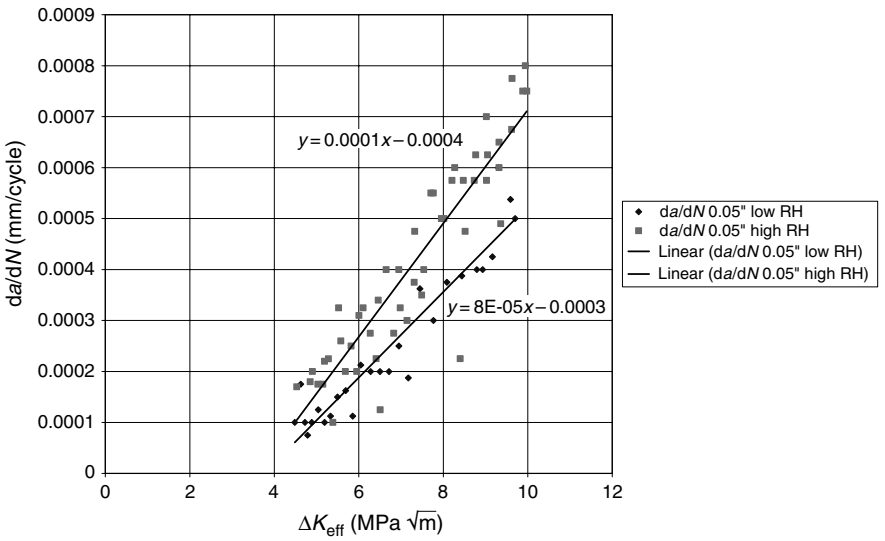

Fig. 11.7. A linear fit of da/dN versus ΔK_{eff} for Al 7075-T6 1.27 mm thick plate at low ΔK_{eff} range.

(a) Calculate the stress intensity factors of the *repaired* crack in a patched specimen at the maximum ($K_{\max-\text{load}}$) and minimum loads ($K_{\min-\text{load}}$) of the fatigue cycle for a given crack length using the analysis methods described in Chapter 4 or 5, accounting for any thermally induced residual stresses associated with curing. Due to crack patching, the values of these stress intensity factors will be low compared to those unrepaired values. The ΔK values will be low as well.

(b) Calculate ΔK and R-ratio. It should be noted that due to the thermally induced residual stresses, the R-ratio is generally different from the applied stress ratio, i.e., $R = K_{\min-\text{load}}/K_{\max-\text{load}} \neq \sigma_{\infty\,\min-\text{load}}/\sigma_{\infty\,\max-\text{load}}$

(c) Calculate da/dN using the available un-patched crack growth data with values of ΔK and R-ratio obtained from step (b). The un-patched crack growth data for Al 7075-T6 bare material were also generated using the same batch materials as those used in patched specimens and they are represented in terms of fourth power fit empirical equations, as mentioned in the last paragraph of the previous subsection. These empirical equations account for the R-ratio effect as well as the effects of RH and thickness of the cracked plate. In contrast, the un-patched crack growth data for Al 2024-T3 are available in table form from the Boeing in-house material database for various R-ratios.

(d) Calculate the amount of crack growth for a specific number of cycles, say for every 1000 cycles.

(e) Calculate the total number of cycles that have passed since the start of fatigue loading and also the total crack length after that total number of cycles.

(f) Repeat steps (a)–(e) for the new (growing) crack length.

For one-sided patched specimens, since various values of K, i.e., K_{max}, K_{rms}, or K_{eq}, can be used for crack growth predictions, the stress intensity factors referred to in steps (a)–(b) obviously can be identified with any of the mentioned values. To facilitate the crack growth predictions, the above procedure was implemented into a Fortran code. To simplify the crack growth analysis, $K_{max-load}$ and $K_{min-load}$ of a given patched specimen are first computed for a range of crack lengths starting from 11.43 mm to 36.83 mm using the analytical methods described in Chapter 4 or 5. A table of crack lengths versus these stress intensity factors is then input to the Fortran code. Step (a) of the above procedure is performed in the Fortran code for a given crack length by linear interpolation of the stress intensity factor data listed in the mentioned input table.

11.2.4 Comparison between analytical predictions and test results

(a) Sandwich Configurations

In this subsection, crack growth predictions for specimens F1–F6 are made and compared with test results (Duong, 2003b; Duong et al., 2005).

Since the boron patch has a lower thermal expansion coefficient than the cracked aluminum plate, residual thermal stresses will occur upon cooling the fully cured repair from elevated curing temperature to the ambient temperature. Even though the curing temperature of the FM-73 adhesive in the test is specified to be 93.3 °C, the adhesive may only harden at a much lower temperature which is denoted here as T_g. Thermal stresses are only built up after the adhesive is solidified since the boron patch and the aluminum cracked plate are freely expanded or contracted at temperatures above T_g. Since T_g is generally unknown, it must be determined indirectly from the test by measuring the residual thermal stresses in the patch and skin through strain gauges of one of the patched specimens and correlating with the analytical predictions using various assumed values of T_g until the analytical predictions and test results of these thermal stresses are in close agreement. Once the value of T_g is determined, it will be used in the predictions of the rest specimens.

In the present test-analysis correlations, T_g is determined from strain gauge measurements of specimen F1 since this specimen has no tapering effect, which can be predicted accurately by the analytical model. To limit the search for a value of T_g, it was found before in another CRAS study (Duong, 2003b) as well as in an independent report (Spigel et al., 1998) that an assumed value T_g of 82.2 °C for FM-73 will yield thermal strain predictions consistent with the strain gauge measurements. To confirm this previous finding, the same value of T_g will be assumed here in the theoretical analysis of thermal stresses of specimen F1 (also assuming $T_{ambient} = 21.1$ °C), and these analytical predictions will be compared with the gauge measurements at locations 13, 14, 7, and 8 (Figure 11.8 for actual gauge locations). Strains are measured at these locations right after curing and before test, and they are summarized in Table 11.3. Due to symmetric configuration of specimen F1 with respect to the mid-plane of the honeycomb core, one would expect the strain gauge reading at locations 13 and 14 to be the same. Similarly, the readings at locations 7 and 8 are expected to be the same. However, from Table 11.3, these readings are not the same, especially when comparing the readings of gauge

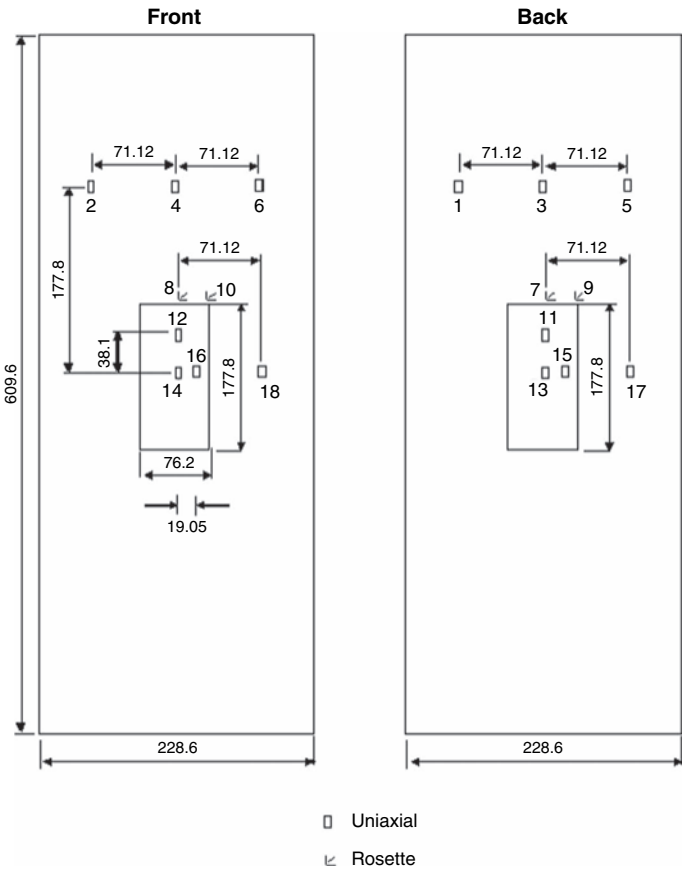

Fig. 11.8. Gauge locations for measuring thermally residual strains in specimen F1.

Table 11.3. Gauge measurements of residual thermal strains in specimen configuration F1.

Gauge location	Vertical reading (micro)	Horizontal reading (micro)
7	34	−182
8	−157	−22
13	−638	–
14	−468	–

7 with gauge 8. Since the readings at gauges 13 and 14 are considered close in light of the experimental scatter, the average value of these two readings therefore will be used to compare with the analytical prediction. In contrast, only the reading at gauge 8 will be used in the correlation since the reading at gauge 7 gives positive strain instead of a negative value in the skin at the end of the curing process, which therefore appears to be wrong. These strain readings were converted to stresses and compared with analytical

predictions in Table 11.4. The material properties of Al 7075, boron/epoxy, and FM-73 (for future reference) used in the present and subsequent analyses are listed in Table 11.5. A good agreement is found between the two. Thus, the effect of curing will be simulated in the subsequent analyses of boron patches as a uniform cooling process of the whole specimen from 82.2 °C to 21.1 °C.

The stress intensity factors at the peak and the valley of the constant amplitude load for specimen F1 are computed by the analytical method for different crack lengths, and they are summarized in Table 11.6. For comparison, the results from the 3-D FE analyses for selective crack lengths are also shown in the table. Since the analytical model developed in Chapter 4 ignores the effect of patch's tapered edge on the stress intensity factor solution, the analytical predictions for configurations F1 and F2 will be the same. In contrast, the FE results reported in Table 11.6 are obtained specifically

Table 11.4. Comparison of analytical predictions and test results for residual thermal stresses in specimen configuration F1.

Gauge location	Stress in loading direction (MPa)	
	Test	Analytical prediction
8	−30.3	−22.1
13&14	−106.9	−94.5

Table 11.5. Material properties of Al 7075, Boron/Epoxy, and FM-73.

Al 7075-T6	Boron/Epoxy	Adhesive FM-73
$E = 71\,\text{GPa}$	$E_1 = 193\,\text{GPa}$	$G = 0.69\,\text{GPa}$
$\nu = 0.33$	$E_2 = 18.7\,\text{GPa}$	$t = 0.127\,\text{mm}$
$t = 3.175\,\text{mm}$ or $1.27\,\text{mm}$	$\nu_{12} = 0.21$	
	$G_{12} = 5.5\,\text{GPa}$	
	$t = 0.137\,\text{mm}$ per ply	
	$\alpha_1 = 4.3\,\mu$ per °C	
$\alpha = 22.5\,\mu/°\text{C}$	$\alpha_2 = 21.4\,\mu$ per °C	

Table 11.6. Stress intensity factor solutions for configurations F1 and F2 by the analytical and FE methods.

a (mm)	Analytical Method		FE Method	
	K_{max} (MPa-$\sqrt{}$m)	K_{min} (MPa-$\sqrt{}$m)	K_{max} (MPa-$\sqrt{}$m)	K_{min} (MPa-$\sqrt{}$m)
11.43	10.127	2.895	11.007	3.576
16.51	10.326	2.886	–	–
21.59	10.474	2.885	11.528	3.588
26.67	10.592	2.794	–	–
31.75	10.737	2.718	11.708	3.412
36.83	11.035	2.661	–	–

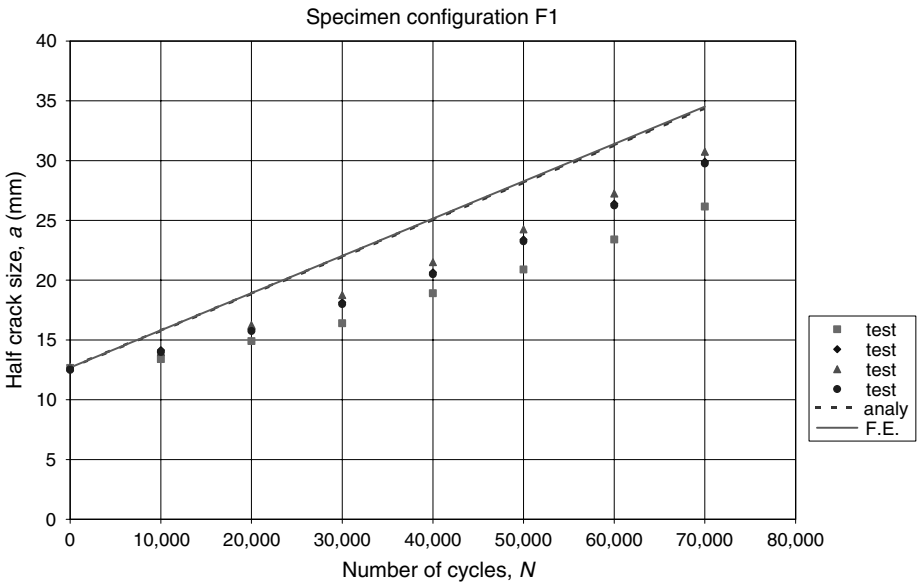

Fig. 11.9. Crack growth predictions and test results for specimen configuration F1.

for configuration F1. The crack growth predictions vs number of cycles are plotted in Figures 11.9 and 11.10 for specimen configurations F1 and F2, respectively. From Figure 11.9, analytical and FE predictions are in excellent agreement. However, crack growths predicted by the analytical and FE methods are faster than the actual test results for both specimens. Theoretical predictions are thus conservative. Since fatigue crack growth data is widely known for its scattering nature, the above correlations are considered to be good.

Similarly, crack growth predictions for the rest specimens F3–F6 are presented in Figures 11.11–11.14. From these figures, analytical predictions and test results are in excellent agreement. It is worthy to note that specimen configurations F3 and F4 have no residual thermal stresses.

(b) One-sided patched specimens

Crack growth predictions for specimen configurations S1 and S2 using various values of the stress intensity factors (i.e, $K_{\max}$, K_{rms} and K_{eq}) are presented and compared with test results in Figures 11.15 and 11.16, respectively, with the stress intensity factor solutions for various crack lengths reported in Tables 11.7 and 11.8 (Duong, 2003b; Duong and Wang, 2004). The material properties of the aluminum cracked plate, boron-epoxy patch, and FM-73 adhesive used in the computations of the stress intensity factors are the same as in the Part (a) 'sandwich configuration' as given in Table 11.5. Like before for a boron-epoxy patch, thermally induced residual stresses in a patched specimen are simulated as a uniform cooling process of the whole specimen with a differential temperature of $-61\,^{\circ}\text{C}$. For comparison, the stress intensity factors from 3-D FE analyses

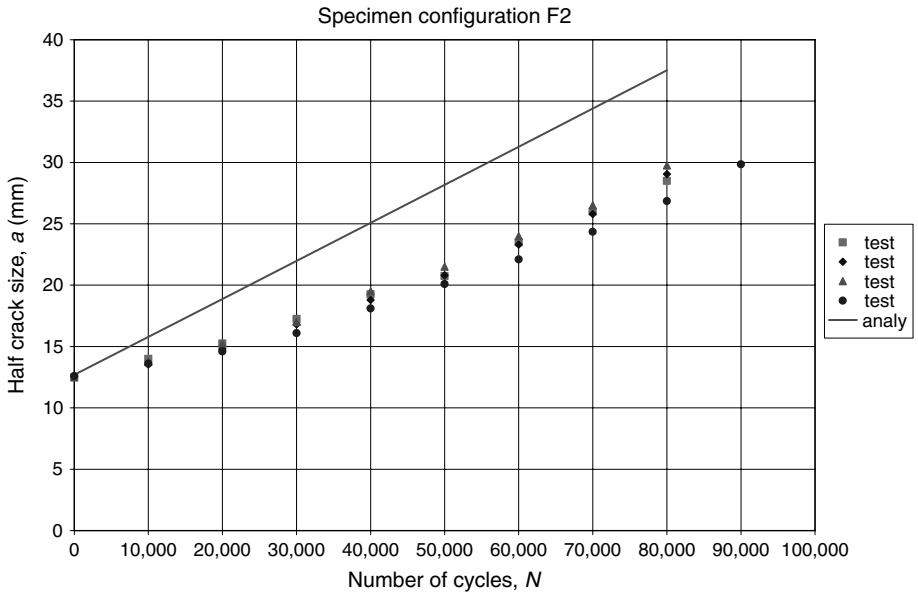

Fig. 11.10. Crack growth predictions and test results for specimen configuration F2.

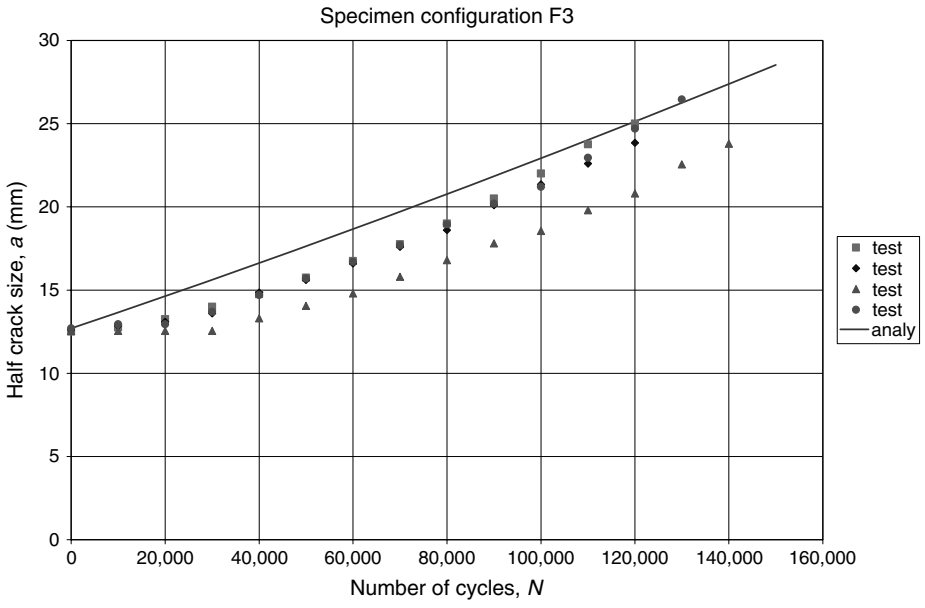

Fig. 11.11. Crack growth predictions and test results for specimen configuration F3.

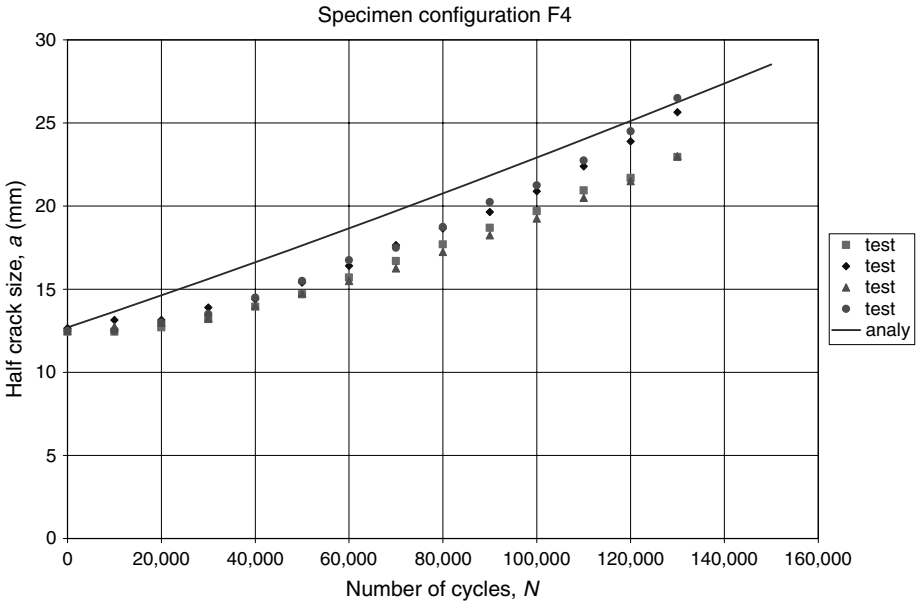

Fig. 11.12. Crack growth predictions and test results for specimen configuration F4.

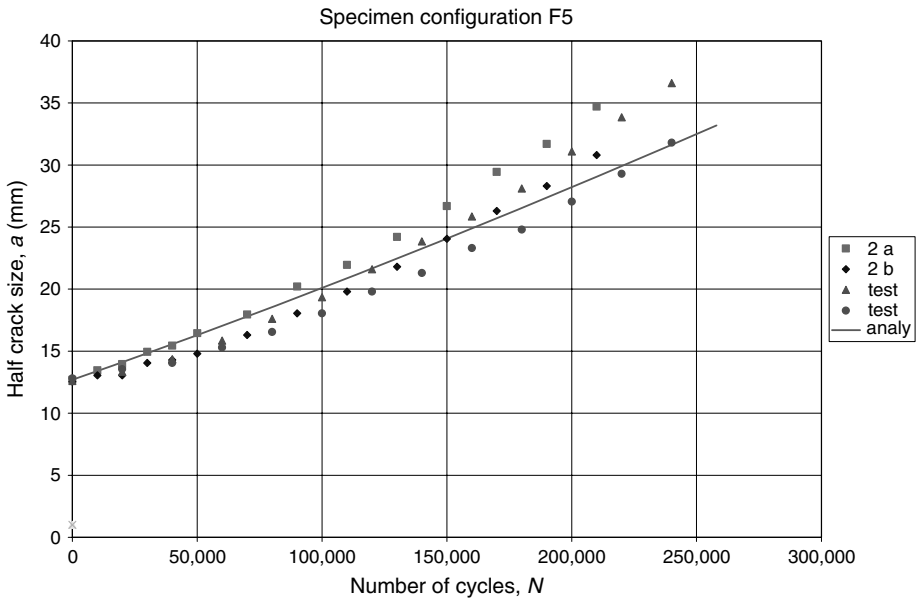

Fig. 11.13. Crack growth predictions and test results for specimen configuration F5.

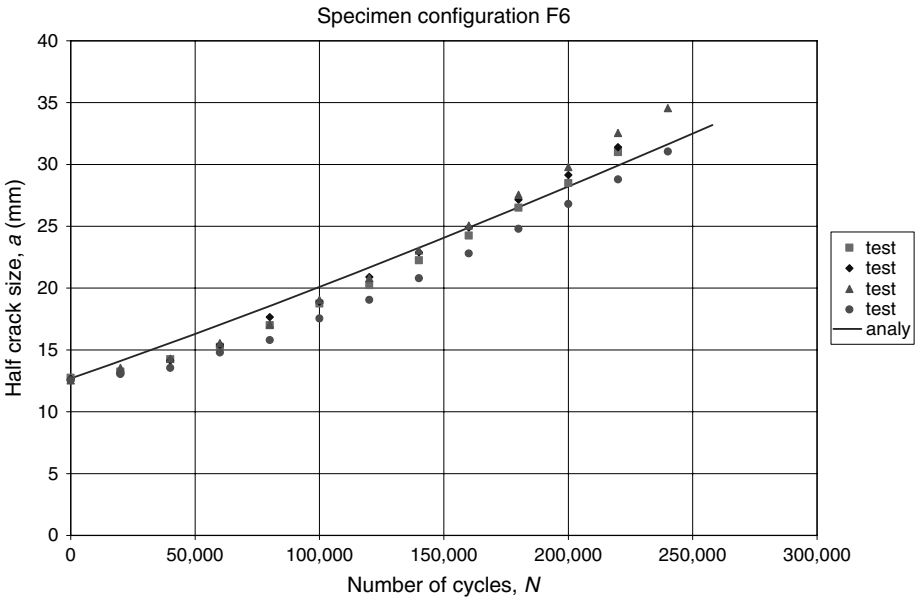

Fig. 11.14. Crack growth predictions and test results for specimen configuration F6.

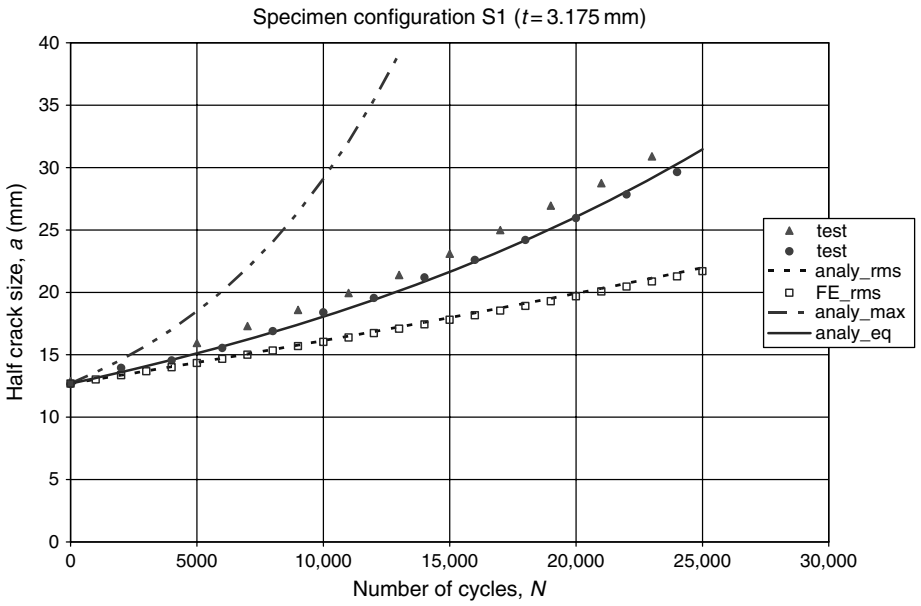

Fig. 11.15. Analytical predictions versus test results of crack growth in specimen configuration S1.

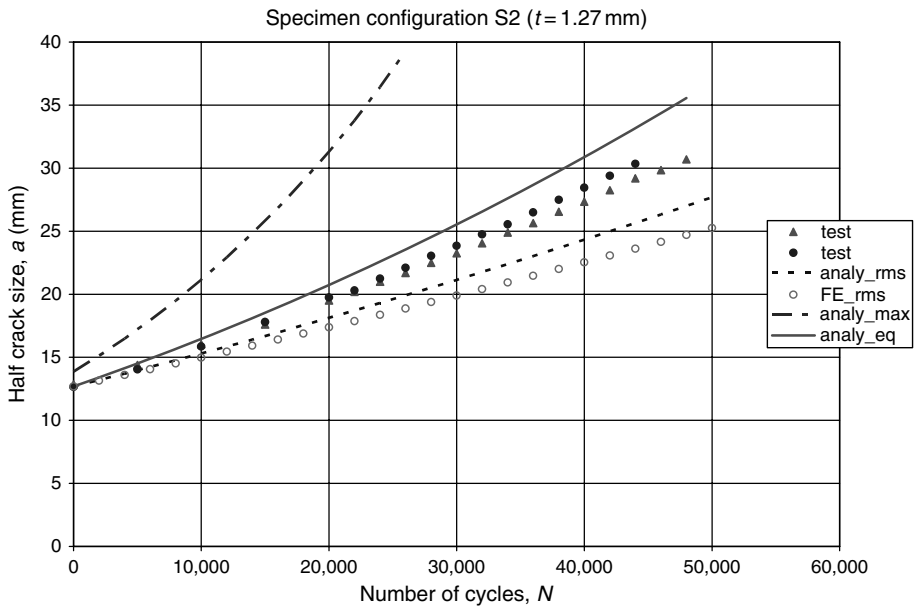

Fig. 11.16. Analytical predictions versus test results of crack growth in specimen configuration S2.

for selective crack lengths and the corresponding crack growth predictions using these FE results are also presented respectively in Tables 11.7 and 11.8, and Figures 11.15 and 11.16. From Figures 11.15 and 11.16, it is clear that predictions using K_{max} will yield unrealistically high crack growth rate for specimen configurations S1 and S2. In contrast, predictions using K_{rms} will grossly underestimate the actual crack growth of specimen configuration S1. However, crack growth predictions using K_{eq} are in excellent agreement with the test data. To show the importance of including the effect of stress intensity factor due to bending, crack growth prediction for configuration S1 without considering the effect of bending was also made but not shown there. The number of cycles to reach the same final crack length for the non-bending case was found to be 60,000 cycles, as opposed to 25,000 cycles from the present predictions using K_{eq}, as indicated in Figure 11.15.

Similar crack growth predictions for specimen configurations S3 and S4 are presented, respectively, in Figures 11.17 and 11.18, along with the test data. Again, the analytical predictions using K_{eq} yield best agreement with test results when compared with those using K_{max} or K_{rms}. It is interesting to note that configurations S3 and S4 involve no thermally induced residual stress since the patch is aluminum and that the predictions using K_{max} will not grossly overestimate the actual crack growth rate like before, since the bending components K_b of these two configurations are small relative to those of configurations S1 and S2. Comparisons between analytical predictions and test results for crack growth of the rest of the configurations (S5–S9) are shown respectively in Figures 11.19–11.23. Since crack growth predictions using K_{max} were shown to be too high in the last five configurations, these predictions are therefore not included in

Table 11.7. Stress intensity factor solutions for specimen configuration S1.

a (mm)	Analytical method (MPa-$\sqrt{m}$)						FE method (MPa-$\sqrt{m}$)					
	Peak			Valley			Peak			Valley		
	K_{mem}	K_b	K_{rms}	K_{mem}	K_b	K_{rms}	K_{mem}	K_b	K_{rms}	K_{mem}	K_b	K_{rms}
11.43	15.231	6.922	15.745	2.650	−0.15	2.653	14.839	6.708	15.335	2.918	−0.63	2.940
16.51	16.945	8.357	17.619	2.916	0.	2.916	–	–	–	–	–	–
21.59	18.144	9.393	18.937	3.102	0.204	3.104	18.111	9.136	18.864	3.427	−0.15	3.428
26.67	19.034	10.177	19.921	3.238	0.323	3.244	–	–	–	–	–	–
31.75	19.724	10.792	20.685	3.343	0.416	3.351	20.035	10.826	20.988	3.642	0.245	3.644
36.83	20.275	11.285	21.297	3.427	0.493	3.438	–	–	–	–	–	–

Table 11.8. Stress intensity factor solutions for specimen configuration S2.

a (mm)	Analytical method (MPa-$\sqrt{m}$)						FE method (MPa-$\sqrt{m}$)					
	Peak			Valley			Peak			Valley		
	K_{mem}	K_b	K_{rms}	K_{mem}	K_b	K_{rms}	K_{mem}	K_b	K_{rms}	K_{mem}	K_b	K_{rms}
11.43	13.210	6.473	13.729	3.304	0.725	3.331	12.890	5.268	13.244	3.792	0.648	3.810
16.51	14.362	7.461	14.994	3.576	0.955	3.617	–	–	–	–	–	–
21.59	15.137	8.146	15.850	3.756	1.115	3.811	14.353	5.850	14.744	4.260	0.976	4.296
26.67	15.731	8.683	16.511	3.893	1.242	3.958	–	–	–	–	–	–
31.75	16.249	9.161	17.088	4.011	1.355	4.085	14.851	6.327	15.293	4.284	1.279	4.348
36.83	16.756	9.640	17.656	4.124	1.466	4.210	–	–	–	–	–	–

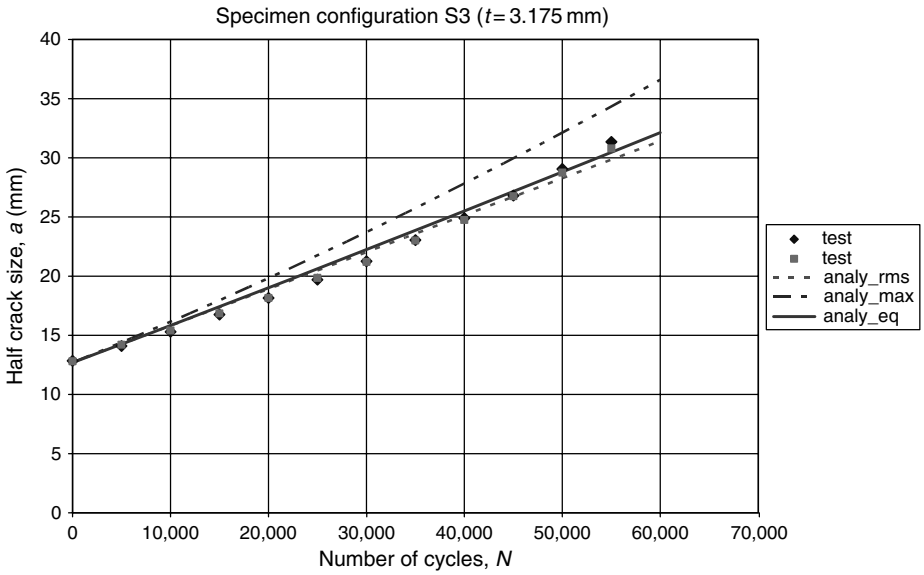

Fig. 11.17. Analytical predictions versus test results of crack growth in specimen configuration S3.

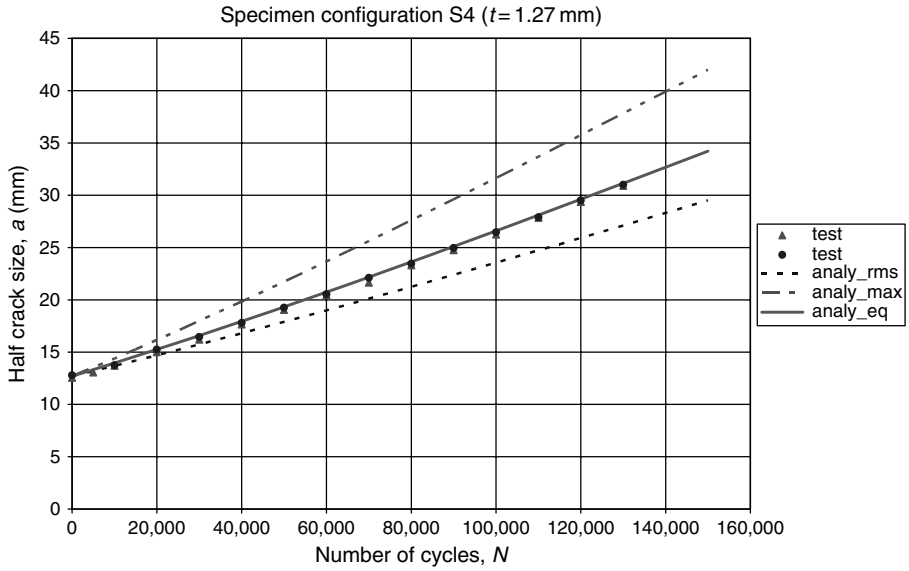

Fig. 11.18. Analytical predictions versus test results of crack growth in specimen configuration S4.

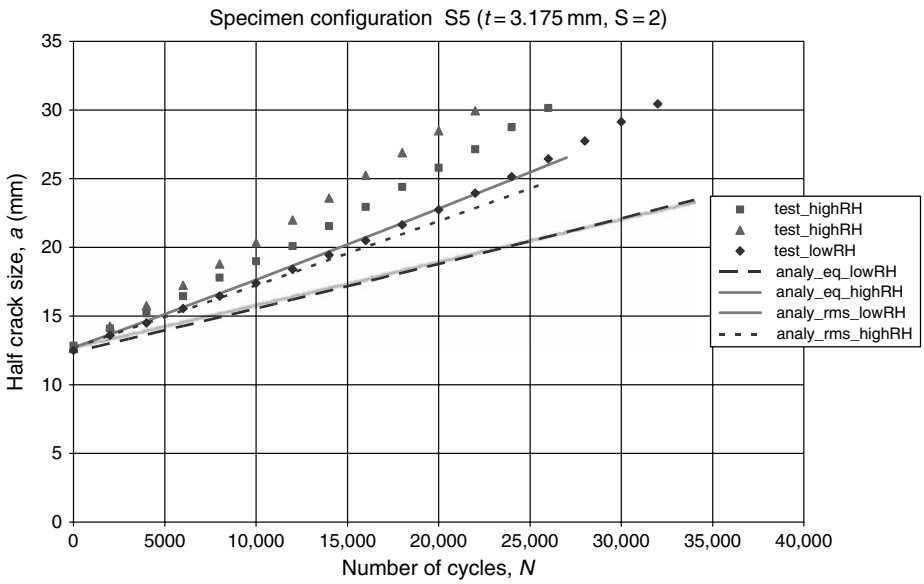

Fig. 11.19. Analytical predictions versus test results of crack growth in specimen configuration S5. Since the RH condition in this particular test varies quite significantly from one specimen to another, RH condition of the specimen is also indicated in the figure's legend with "low" and "high" meaning low and high values of RH.

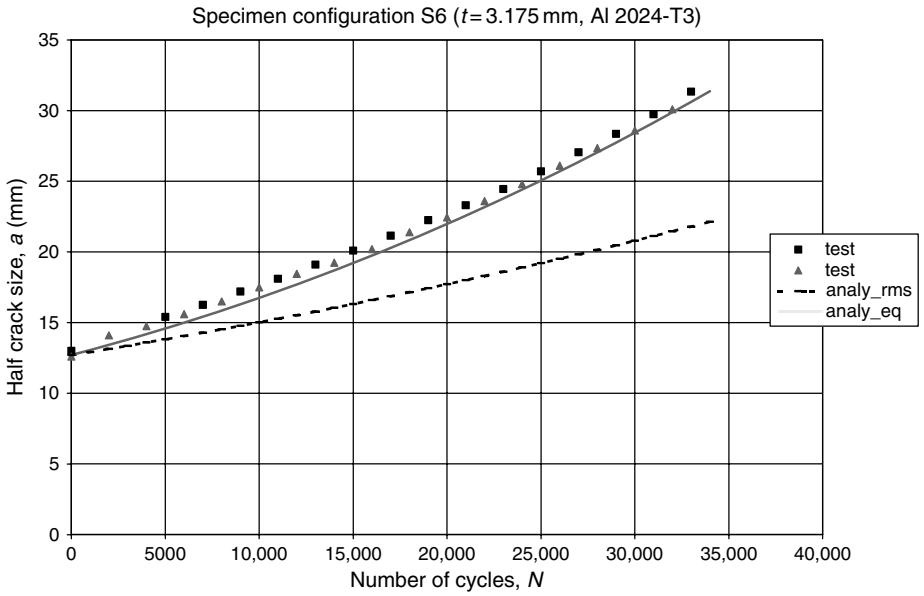

Fig. 11.20. Analytical predictions versus test results of crack growth in specimen configuration S6.

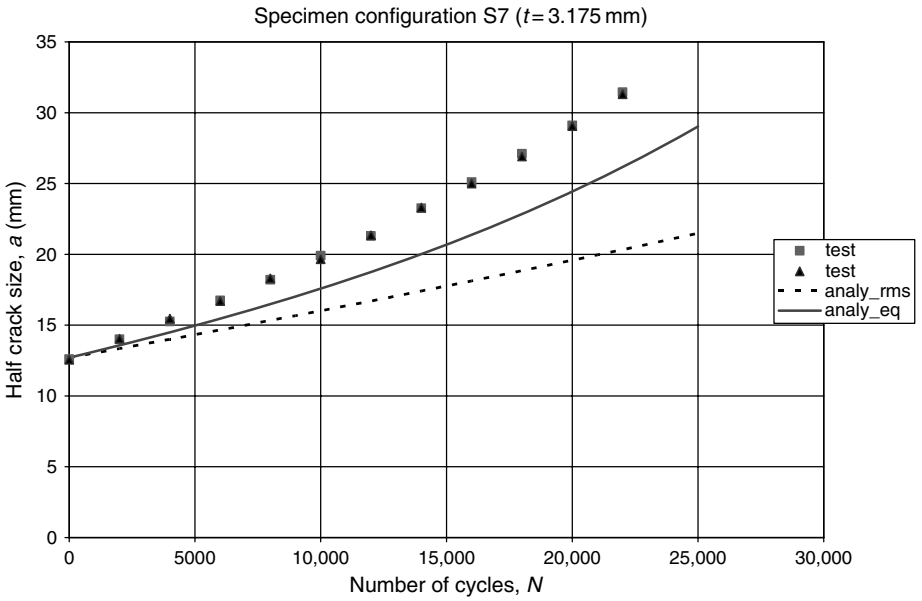

Fig. 11.21. Analytical predictions versus test results of crack growth in specimen configuration S7.

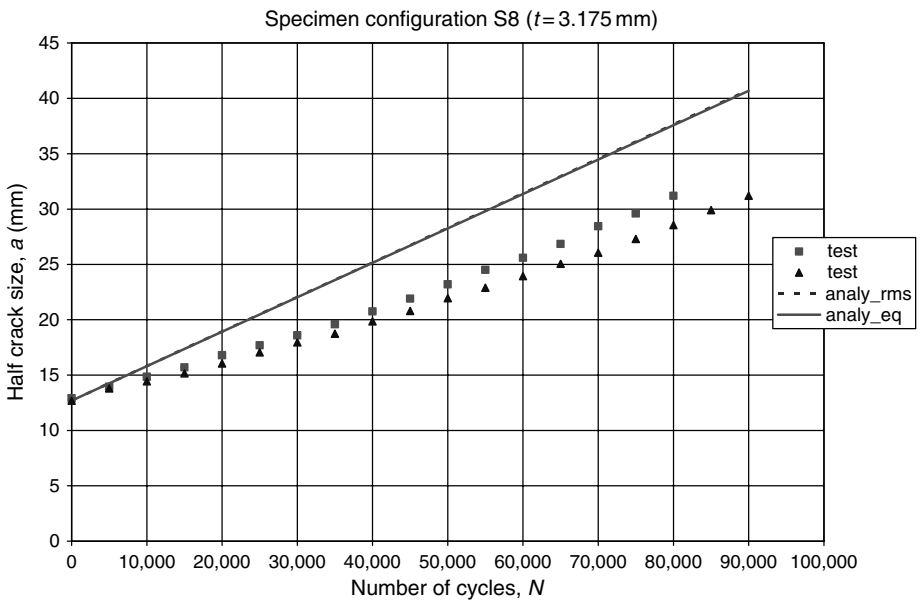

Fig. 11.22. Analytical predictions versus test results of crack growth in specimen configuration S8.

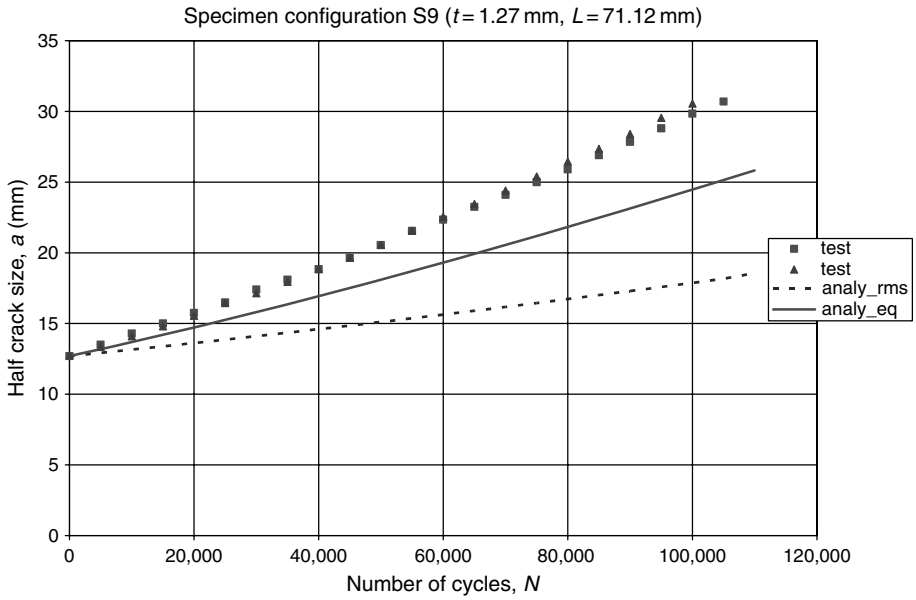

Fig. 11.23. Analytical predictions versus test results of crack growth in specimen configuration S9.

Figures 11.19–11.23. Like before, a good agreement is observed between the analytical predictions using K_{eq} and experimental results, considering the inherent scatter in the crack growth data. For example, the agreement seems to be worst for specimen configuration S8 as shown in Figure 11.22. However, if the analytical prediction for this specimen configuration is compared with test result in terms of crack growth rate, it seems that the analytical model is still doing a decent job. The analytical prediction of the crack growth rate in this case is approximately constant and equal to 3.12E-4 mm/cycle while the measured rates ranging from 2.06E-4 to 2.29E-4 mm/cycle. The predicted crack growth rate is therefore 50% higher than the measured rate, which is normally considered to be good in fatigue crack growth prediction due to the inherent scatter in typical crack growth test data. It should be emphasized that the good agreement between analytical predictions and test results observed in this study was found for a variety of patched specimen configurations involving different patch materials (boron-epoxy, aluminum), plate thicknesses (1.27 and 3.175 mm), plate materials (7075-T6, 2024-T3), patch stiffness ratios (1.11 and 2), patch geometries (finite rectangle and full width), and patch lengths (177.8 and 71.12 mm).

11.3 Load Attraction Tests and Method Validation

11.3.1 Load attraction tests

A second set of tests to measure the strain and stress distributions around the patch and inside the patched region of a reinforced uncracked plate is also conducted. The purpose of

the load attraction tests is to validate the "polygon-shaped" inclusion model developed in Chapter 4 for stage I analysis of the two-stage analytical procedure (Duong 2003b; Duong et al., 2005). The following four sandwich configurations will be analyzed in this section:

1. L1: Rectangular boron patch ($S = 1.11$)
2. L2: Octagonal boron patch ($S = 1.11$)
3. L3: Rectangular aluminum patch ($S = 1.16$)
4. L4: Octagonal aluminum patch ($S = 1.16$)

The geometries of these sandwich configurations are similar to those used in the fatigue crack growth test. A plate is 3.175 mm thick, 22.9 cm wide, and 61 cm long. A rectangular patch has dimensions of 76.2 mm × 177.8 mm. An octagonal patch has the same dimensions but edges cut off equally at the corner by a length of 25.4 mm (thus, the corner cut-off angle is 45°) as shown in Figure 11.24. For direct comparison, all patches have no tapered edge as assumed by the analytical model. All specimens are coated with photo-elastic material on one side and instrumented with strain gauges on the other side. The side with photo-elastic material coating will provide the difference in principal stresses at the critical locations while the gauges on the other side measure the various components of strains at these locations.

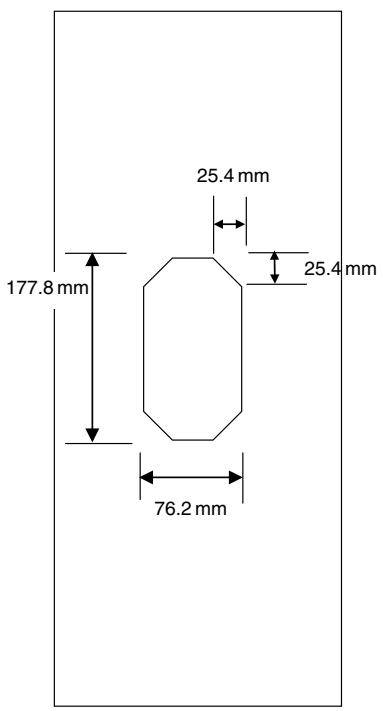

Fig. 11.24. Geometry of the load attraction specimen with an octagonal patch.

11.3.2 Comparison between analytical prediction and test results

Strain gauge locations for specimens with rectangular and octagonal patches are illustrated, respectively, in Figures 11.25 and 11.26. Similarly, the photo-elastic locations for these two configurations are given in Figures 11.27 and 11.28, respectively. The photo-elastic locations are as close as possible to the locations of the strain gauge for comparison purpose.

Analytical predictions for strains at locations 1–4 of specimen configuration L1 are compared with test results in Table 11.9. In contrast, a comparison between analytical predictions and photo-elastic results for the difference of principal stresses at locations 1–4 for the same specimen is reported in Table 11.10. Similar strain and stress comparisons with respective strain gauge and photo-elastic results are presented in Tables 11.11 and 11.12, respectively, for configuration L2. In general, strain predictions are in excellent agreement with the strain gauge readings for a rectangular patch (configuration L1) and they are considered to be satisfactory for an octagonal patch (configuration L2). However, a reverse trend is observed when comparing the stress predictions with the photo-elastic results.

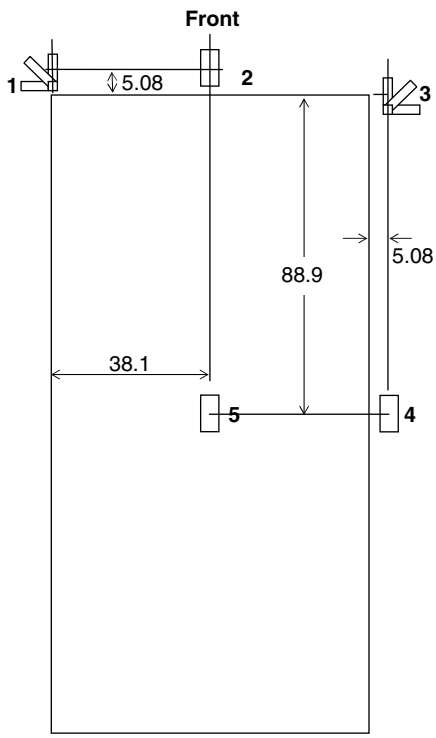

Fig. 11.25. Strain gauge locations for a sandwich plate with rectangular patches.

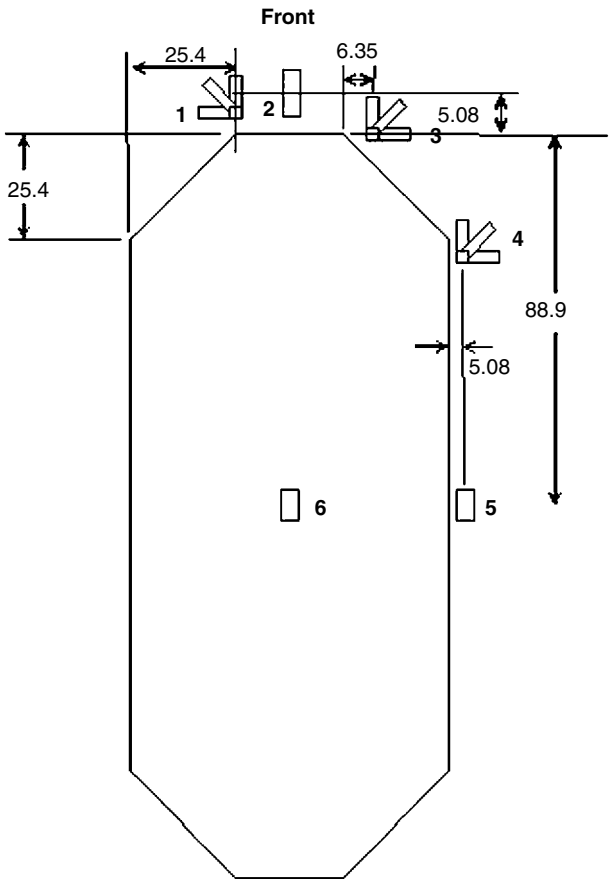

Fig. 11.26. Strain gauge locations for a sandwich plate with octagonal patches.

Specimen configurations L3 and L4 are identical to configurations L1 and L2, respectively, except for the aluminum patches. There is no residual thermal stress in configurations L3 and L4. Strain and stress predictions for configurations L3 are compared, respectively, with the strain gauge readings and photo-elastic results in Tables 11.13 and 11.14. Similar comparisons for configuration L4 are reported in Tables 11.15 and 11.16. As before, the strain predictions are generally more accurate for the rectangular patch.

11.4 Summary

Based on a comprehensive experimental study of load attraction and fatigue crack growth in two-sided and one-sided bonded repairs performed under the CRAS program, existing analytical methods for analyzing two-sided bonded repairs are shown to be capable of predicting the fatigue crack growths and load attraction in these repairs. However, for a

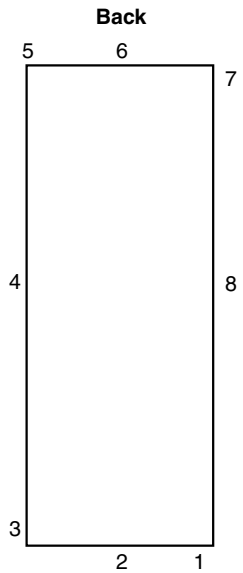

Fig. 11.27. Photo-elastic locations for a sandwich plate with rectangular patches.

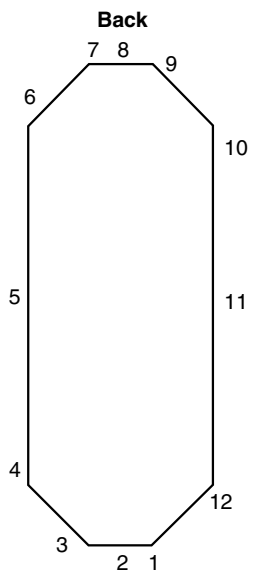

Fig. 11.28. Photo-elastic locations for a sandwich plate with octagonal patches.

Table 11.9. A strain comparison between analytical predictions and strain gauge readings for configuration L1.

Gauge location	Analytical predictions (μ mm/mm)	Gauge reading (μ mm/mm)
1V	1724	1760
1C	718	674
1H	−529	−577
3V	1627	1678
3C	609	895
3H	−530	−607
2	1791	1834
4	1525	1575

Table 11.10. A stress comparison between analytical predictions and photo-elastic results for configuration L1.

Photo-elastic location	Analytical predictions (MPa)	Photo-elastic results (MPa)
1	135.1	121.4
2	140.8	105.7
3	113.4	85.9
4	89.1	62.1

Table 11.11. A strain comparison between analytical predictions and strain gauge readings for configuration L2.

Gauge location	Analytical predictions (μ mm/mm)	Gauge reading (μ mm/mm)
1V	1834	1658
1C	677	538
1H	−558	−528
3V	1800	1620
3C	647	430
3H	−573	−606
4V	1588	1622
4C	511	487
4H	−566	−619
2	1818	1625
5	1521	1605

Table 11.12. A stress comparison between analytical predictions and photo-elastic results for configuration L2.

Photo-elastic location	Analytical predictions (MPa)	Photo-elastic results (MPa)
1	152.9	145.1
2	144.9	148.5
3	148.6	129.6
4	112.9	106.2
5	88.2	86.6

Table 11.13. A strain comparison between analytical predictions and strain gauge readings for configuration L3.

Gauge location	Analytical predictions (μ mm/mm)	Gauge reading (μ mm/mm)
1V	1889	1769
1C	1059	749
1H	−528	−428
3V	1573	1531
3C	789	684
3H	−458	−563
2	2046	2024
4	1225	1086

Table 11.14. A stress comparison between analytical predictions and photo-elastic results for configuration L3.

Photo-elastic location	Analytical predictions (MPa)	Photo-elastic results (MPa)
1	137.9	125.8
2	143.2	129.9
3	113.4	102.4
4	87.2	79.7

Table 11.15. A strain comparison between analytical predictions and strain gauge readings for configuration L4.

Gauge location	Analytical predictions (μ mm/mm)	Gauge reading (μ mm/mm)
1V	2157	1942
1C	888	844
1H	−628	−639
3V	2061	1846
3C	839	621
3H	−645	−733
4V	1443	1690
4C	736	452
4H	−560	−53
2	2108	1681
5	1216	1118

Table 11.16. A stress comparison between analytical predictions and photo-elastic results for configuration L4.

Photo-elastic location	Analytical predictions (MPa)	Photo-elastic results (MPa)
1	152.2	129.6
2	144.2	128.9
3	148.0	117.2
4	113.7	95.2
5	86.6	73.2

one-sided repair, an equivalent or effective stress intensity factor, i.e., K_{eq}, must be used for characterizing its fatigue crack growth. This concept of using K_{eq} for characterizing fatigue crack growth with out-of-plane bending has been verified experimentally for a wide variety of repair geometries and cracked plate materials and it appears to be promising and versatile. Even though the proposed approach, in theory, can also be applied to the case of a general bending crack, it needs further study and evaluation before it can be used in the general case. Moreover, when there is a relatively large discrepancy between the two methods, analytical predictions for the fatigue crack growth and critical stress or strain concentration appear to be conservative.

CHAPTER 12

Repair of Sonic Fatigue

12.1 Introduction

Sonic or acoustic fatigue is induced by predominately resonant response of structural components to radiated sound excitations, typically associated with engines and aerodynamic boundary layers impinging on the structure. The primary source of excitation is the varying sound pressure level over the structure. While good detail designs (ESDU, 1986) are now available to reduce a structure's susceptibility to sonic fatigue, structural failures resulting from sonic fatigue remains a significant issue for some fighter aircraft (Brewer, 1994; Callinan et al., 1997a), where overall sound pressure levels of the order of 170 dB have been found to exist on the lower external surface of the inlet nacelle skin (Brewer, 1994). Repairs designed in accordance with the standard methods of repairs (RAAF, 2006), which are, strictly speaking, applicable to structures subjected to in-plane loading, have been found to be ineffective (Callinan et al., 1998). It was reported that although the composite patch did to some extent reduce in the crack growth driving force, the original crack continued to grow unabated, eventually emerging from the edge of the repair.

Since large portions of many aircraft structures, including fuselage, wings, and control surfaces, are constructed from thin panels reinforced by rectangular or near rectangular array of stiffeners, acoustically induced fatigue cracks normally occur near where the panel is attached to the stiffeners. This is because the bending stresses resulting from the out-of-plane vibrations are highest at these clamped boundaries. Figure 12.1 shows a structural model of a skin panel clamped at all edges. The vibrational response of such a panel excited by broad frequency band random forces can be treated as the summation of responses in relatively large number of modes. Such an approach is too complicated to be used in design. A very much simplified theory (Miles, 1954; Clarkson, 1968) has been developed, derived on the assumptions that (i) the response is dominated by the contribution of one mode, and (ii) the acoustic pressures are exactly in-phase over the whole panel. In this case, the root-mean-square level of the plate displacement,

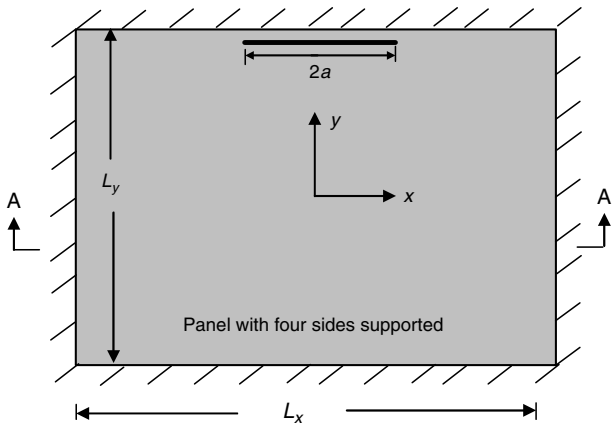

Fig. 12.1. Geometry and notations for a rectangular plate containing an edge crack.

$w_{\text{rms}}(x, y)$, can be expressed in term of the displacement response of the plate to a uniform static pressure of unit magnitude, $w_{\text{s}}(x, y)$. This can be written as

$$w_{\text{rms}}(x, y) = p_{\text{rms}} w_{\text{s}}(x, y) \sqrt{\frac{\pi f_0}{2\eta_0}} \tag{12.1}$$

where f_0 and η_0 denote, respectively, the resonant frequency and the structural loss factor at the dominating resonant mode, and the parameter p_{rms} denotes the root mean square value of the fluctuating pressure described in the next section. It is important to note that both p_{rms} and η_0 may depend on frequency.

For a rectangular plate with four sides being fully fixed, the maximum static displacement response, which occurs at the centre of the plate, to a unit pressure is

$$w_{\text{s}} = \frac{L_x^4}{12D} \alpha_1 (L_x/L_y) \tag{12.2}$$

where L_x and L_y denote the edge lengths, D the bending stiffness. The values of α_1 are available in Roark and Young (1989). As shown in Figure 12.2, the numerical values can be well approximated by

$$\alpha_1 = 0.0284 \mathrm{e}^{-0.754(L_x/L_y)^{3.79}} \tag{12.3}$$

Similarly, the fundamental resonant frequency of a fully fixed rectangular plate is

$$f_0 = \frac{22.4}{2\pi} \sqrt{\frac{D}{m L_x^4}} \alpha_2 (L_x/L_y) \tag{12.4}$$

where m denotes the unit mass of the plate material, and the factor α_2 given by Roark and Young (1989) can be approximated by

$$\alpha_2 = \mathrm{e}^{0.477(L_x/L_y)^{2.3}} \tag{12.5}$$

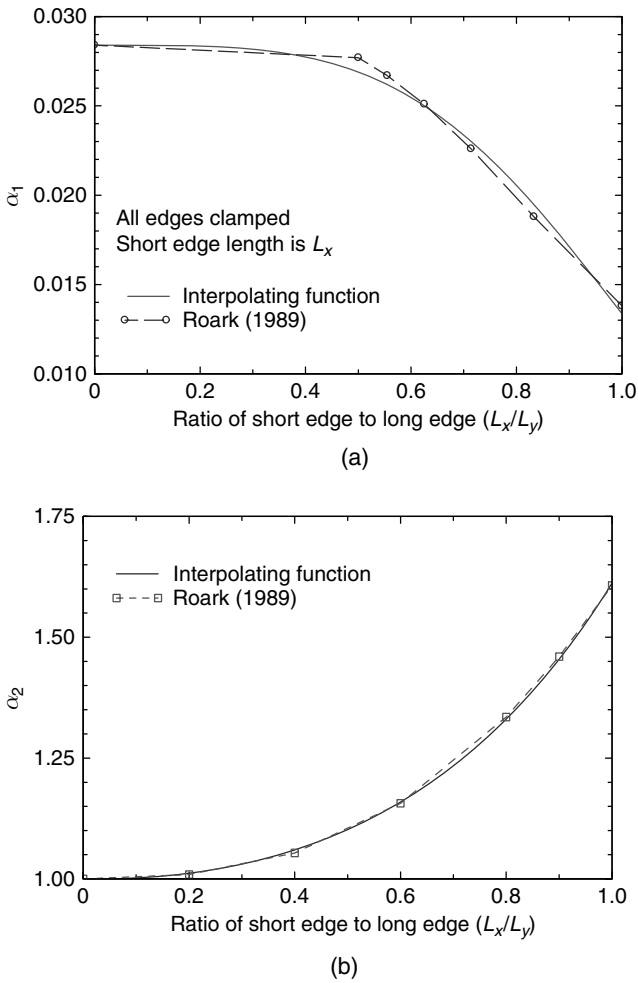

Fig. 12.2. Shape factors for: (a) displacement; and (b) resonant frequency.

Previous studies (Clarkson, 1968) confirmed that the theoretical solution (12.1) is in good agreement with experimental values for fully clamped plates as well as integrally stiffened panels.

For a broad band excitation, the root-mean-square pressure p_{rms} is approximately constant at the dominating resonant mode. In this case, the Miles solution suggests that it is important to increase the structural damping to at least offset the detrimental effect of increased resonant frequency resulting from the increased stiffness after repair. Therefore, it is essential to incorporate an efficient damping mechanism into repairs to achieve the required reduction in fatigue crack growth rates. As compared to conventional bonded patch repairs, damped repairs to acoustic fatigue employ a damping layer between the patch and the skin, as illustrated in Figure 12.3.

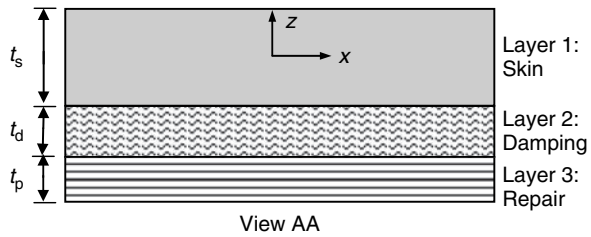

Fig. 12.3. Notations for highly damped repairs.

The application of highly damped repairs to acoustically damaged panels has been reported by Rogers et al. (1997). As part of a test program (Liguore et al., 1999), a highly damped repair was applied to the vertical fin of the F-15 aircraft. A series of repairs have been designed and tested in progressive wave tunnel (Gordon et al., 2001; Liguore et al., 2001). To measure the acoustic vibrations of aircaft panels during high speed subsonic flight, Boeing developed a small autonomous device called Dosimeter, which has been employed to monitor the performance of damped repairs (Ikegami et al., 2001). The Defence Science and Technology Organisation (DSTO) of Australia undertook a comprehensive investigation into the design and application of highly damped repairs (Callinan et al., 1999, 2005), culminating into a flight trial of a damped repair on F/A-18 aircraft (Callinan et al., 2005). This chapter focuses on the fundamental mechanics of damped repairs; readers are recommended to consult the aforementioned reports for details of experimental validation.

Under acoustic excitation, the damping layer undergoes intense shear deformation, as illustrated in Figure 12.4, which turns the mechanical energy into heat, thus reducing the amplitude of vibration. For a panel with fully clamped edges, the centre regions of the clamped edges are the most highly stressed locations. As a result, the design of

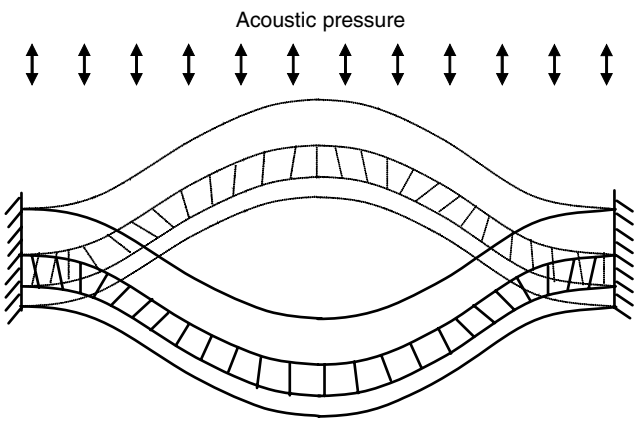

Fig. 12.4. Deflection under acoustic pressure showing the shear deformation of the damping layer.

damped repairs to this type of sonic fatigue damage requires optimizing the geometrical parameters as well as the selection of appropriate damping materials. In this chapter, the basic solutions for the stresses in a skin reinforced by highly damped repairs are first derived, which provide the basis for optimizing repair designs.

12.2 Structural Response to Acoustic Loading

Structural loadings from sonic excitations are often given in terms of sound pressure levels (SPL) in decibels, which relate the root mean square values of the fluctuating pressure (p_{rms}) relative to a reference pressure of $p_{\text{ref}} = 20\,\mu\text{Pa}$. The relationship between the fluctuating pressure and the spectrum SPL is given by (ESDU, 1996)

$$p_{\text{rms}} = p_{\text{ref}} 10^{\text{SPL}/20} \tag{12.6}$$

The power spectral density of the acoustic pressure at any given frequency is defined as

$$\wp = p_{\text{rms}}^2 \tag{12.7}$$

The severity of a particular acoustic excitation is characterized by the area under the normalized power spectral density $(p_{\text{rms}}/p_{\text{ref}})^2$. This area is often denoted as the overall sound pressure level (OASPL) as defined by

$$\text{OASPL} = 10 \log \int_1^\infty 10^{\text{SPL}/10} \text{d}f \tag{12.8}$$

In general, sound pressure levels are dependent on frequency. As an example, the relative sound pressure levels (RSPL = SPL – OASPL) measured on the external surface of an F/A-18 inlet nacelle are shown in Figure 12.5. The RSPL was derived from in-flight one-third octave band SPL measurements (Brewer, 1994). OASPLs of 172 dB have been

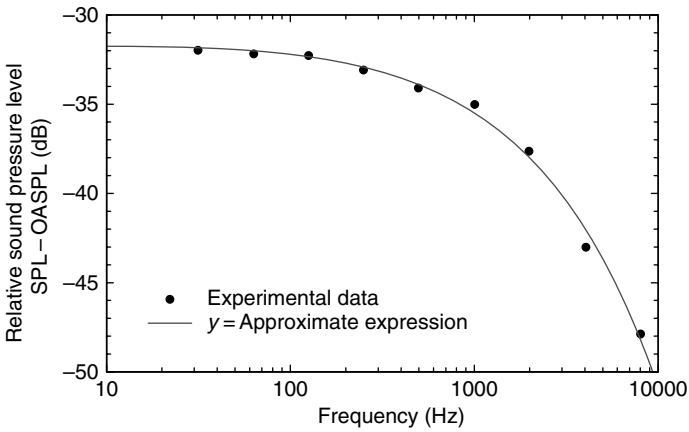

Fig. 12.5. Relative sound pressure levels (RSPL) over an external nacelle inlet.

measured on the inlet nacelle. The experimental data shown in Figure 12.5 can be well approximated by the following expression:

$$\mathrm{SPL} = \mathrm{OASPL} - 31.8415 \times 10^{(\log f)^5/5000} \tag{12.9}$$

It can be verified that the above expression automatically satisfies the definition of overall sound pressure level. This approximate expression can be utilized to estimate the sound pressure level at any given overall sound pressure level and frequency.

12.3 Analysis of Damped Repairs

For a given structural panel to be repaired, the major design consideration is to choose a damping material (shear modulus, loss factor, and thickness) and a patch (elastic modulus and thickness) to achieve the maximum reduction in the stress or the stress intensity factor of an existing crack. Similar to the case of statically loaded structures, the two-stage approach will be employed, in which the prospective stresses in the skin panel, in the absence of the crack, are first determined, then the crack bridging theory is utilized to calculate the stress intensity factors. Due to the presence of a low-stiffness damping layer, the repaired region (the skin, the damping layer, and the patch) can no longer be treated as rigidly bonded, since stress transfer is not restricted to the edges only. Instead, a distributed shear stress exists along the entire length of the repair, as illustrated in Figure 12.4. Consequently a layered-beam or layered-plate analysis, which is detailed in the following section, is required to solve the stresses in the skin and the patch, and the overall structural damping.

12.3.1 Dynamic analysis of layered beams

Consider a three-layer structure shown in Figure 12.3, which presents the cross-section AA indicated in Figure 12.1. Through the change of variables, the solutions for the layered beam can be extended to the case of two-dimensional panel. So only the pertinent solutions for a three-layer beam structure are presented in the following. Assume that the three-layer beam lies along the x-axis and is subjected to a space–time-dependent acoustic pressure $p(x,\ \tau)$. In the following the subscripts s, p, and d are employed to signify quantifies pertinent to the skin, the patch, and the damping layer, respectively. Since the three layers are adhesively bonded, they have identical displacement in the z direction, *i.e.*, $w_\mathrm{s} = w_\mathrm{p} = w_\mathrm{d} = w$. However, each layer has a different in-plane displacement. Denoting the in-plane displacements of the skin and the patch as u_s and u_p, respectively, the following equality holds since the sum of in-plane forces is equal to zero

$$E_\mathrm{s} t_\mathrm{s} \frac{\partial u_\mathrm{s}}{\partial x} + E_\mathrm{p} t_\mathrm{p} \frac{\partial u_\mathrm{p}}{\partial x} = 0 \tag{12.10}$$

where E and t denote the Young's modulus and thickness of a layer, respectively. The governing equations for the displacements w and u_s are given by (Mead and Markus, 1970)

$$D_t \frac{\partial^6 w}{\partial x^6} - gD_t(1+Y)\frac{\partial^4 w}{\partial x^4} + m_t\left[\frac{\partial^4 w}{\partial x^2 \partial \tau^2} - g\frac{\partial^2 w}{\partial \tau^2}\right] = \frac{\partial^2 p(x,\tau)}{\partial x^2} - g\ p(x,\tau) \tag{12.11}$$

$$\frac{\partial^2 u_s}{\partial x^2} - gu_s = -\frac{G_d d}{E_s t_s t_d}\frac{\partial w}{\partial x} \tag{12.12}$$

where

$$m_t = \rho_s t_s + \rho_d t_d + \rho_p t_p \tag{12.13}$$

$$D_t = E_s t_s^3/12 + E_p t_p^3/12 \tag{12.14}$$

$$Y = \frac{d^2}{D_t}\frac{E_s t_s E_p t_p}{E_s t_s + E_p t_p} \tag{12.15}$$

$$g = \frac{G_d}{t_d}\left[\frac{1}{E_s t_s} + \frac{1}{E_p t_p}\right] \tag{12.16}$$

$$d = t_d + (t_s + t_p)/2 \tag{12.17}$$

The shear modulus of the damping layer is G_d.

Inserting $w_m = e^{ik_m x}e^{i\omega_m \tau}$ and $p = 0$ into Equation (12.11), the mth resonant frequency ω_m can be expressed in terms of the wave number k_m:

$$\omega_m^2 = \frac{D_t k_m^4}{m_t}\left[1 + \frac{gY}{k_m^2 + g}\right] \tag{12.18}$$

The effect of damping will be considered in the following section.

12.3.2 Influence of structural damping

Assume that the skin, the damping layer, and the patch can all be described as linearly viscoelastic, and their complex moduli are given by

$$E_s^* = E_s(1 + i\eta_s) \tag{12.19}$$

$$G_d^* = G_d(1 + i\eta_d) \tag{12.20}$$

$$E_p^* = E_p(1 + i\eta_p) \tag{12.21}$$

Here the parameters η_s, η_d, and η_p denote the loss factors of the skin, the damping layer, and the patch, respectively. Inserting these complex moduli expressions into the shear parameter yields

$$g^* = \frac{G_d(1+i\eta_d)}{t_d}\left[\frac{1}{E_s t_s(1+i\eta_s)} + \frac{1}{E_p t_p(1+i\eta_p)}\right] = (1+i\eta_g)\, g' \tag{12.22}$$

where

$$g' = \frac{G_d}{t_d}\left[\frac{1+\eta_s\eta_d}{E_s t_s(1+\eta_s^2)} + \frac{1+\eta_d\eta_p}{E_p t_p(1+\eta_p^2)}\right] \tag{12.23}$$

$$\eta_g = \frac{E_s t_s(\eta_d-\eta_p)(1+\eta_s^2)+E_p t_p(\eta_d-\eta_s)(1+\eta_p^2)}{E_s t_s(1+\eta_d\eta_p)(1+\eta_s^2)+E_p t_p(1+\eta_s\eta_d)(1+\eta_p^2)} \tag{12.24}$$

It is clear that the above expression recovers the special solution of $\eta_g = \eta_d$ when $\eta_s = \eta_p = 0$.

Similarly, the total bending stiffness of the repaired structure is, noting $I = Et^3/12$,

$$D_t^* = E_s^* I_s + E_p^* I_p = E_s(1+i\eta_s)I_s + E_p(1+i\eta_p)I_p = D_t(1+i\eta_t) \tag{12.25}$$

with

$$\eta_t = \frac{E_s I_s \eta_s + E_p I_p \eta_p}{E_s I_s + E_p I_p} \tag{12.26}$$

It is advantageous to define a non-dimensional shear parameter g_m:

$$g_m = \frac{g'}{k_m^2} \tag{12.27}$$

where k_m denotes the wave number of the layered beam.

Inserting expressions (12.22), (12.25), and (12.27) into Equation (12.18) yields the following expression for the resonant frequency and the model loss factor pertinent to the mth mode

$$(\omega_m^*)^2 \equiv \omega_m^2(1+i\eta_m) = \frac{D_t(1+i\eta_t)k_m^4}{m_t}\left[1+\frac{g_m(1+i\eta_g)Y}{1+g_m(1+i\eta_g)}\right] \tag{12.28}$$

Clearly the resonant frequency ω_m is the real part on the right-hand side of expression (12.28), while the model loss factor η_m is equal to the ratio between the imaginary part and the real part. After algebraic manipulation, the following expressions are obtained:

$$\omega_m = \Omega_m\sqrt{\frac{D_t}{m_t}}k_m^2 \tag{12.29}$$

$$\eta_m = \frac{\eta_t+\eta_0}{1-\eta_t\eta_0} \tag{12.30}$$

with

$$\Omega_m = \sqrt{1+Yg_m\frac{1+g_m(1+\eta_g^2)}{1+2g_m+g_m^2(1+\eta_g^2)}} \tag{12.31}$$

$$\eta_0 = \frac{g_m\eta_g Y}{1+g_m(2+Y)+g_m^2(1+\eta_g^2)(1+Y)} \tag{12.32}$$

Expression (12.29) is a very important result, i.e., the resonant frequency of a damped repair is equal to the resonant frequency of a layered-structure with zero-stiffness core (as given by Equation (12.18) with $G_d = 0$ or $g = 0$) multiplied by the non-dimensional frequency ratio Ω_m.

In the case of a two-dimensional panel, the wave number k_m in Equations (12.27) and (12.29) should be replaced by $\sqrt{k_{mx}^2 + k_{my}^2}$, where k_{mx} and k_{my} denote respectively the wave numbers in the x and y directions. The wave numbers of the fundamental mode of a fully clamped plate are $k_{0x} = 2\pi/L_x$, $k_{0y} = 2\pi/L_y$, yielding

$$k_0 = 2\pi\sqrt{\frac{1}{L_x^2} + \frac{1}{L_y^2}} \tag{12.33}$$

12.3.3 Static and dynamic responses of damped repair

It can be shown that the Miles solution, Equation (12.1), can be readily extended to the problem of a damped repair. Denoting the displacement response to a unit static pressure, the resonant frequency, and the loss factor as $w_r(x, y)$, f_r, and η_r, respectively, the root-mean-square value of the dynamic response to random acoustic loading can be written as

$$w_{rms}(x, y) = p_{rms} w_r(x, y)\sqrt{\frac{\pi f_r}{2\eta_r}} \tag{12.34}$$

The loss factor of a damped repair η_r is given by Equation (12.30). Explicit expressions for $w_r(x, y)$ and f_r can be derived from the solutions presented in Sections 12.1 and 12.3.2, and are summarized in the following.

The resonant frequency and maximum static displacement of a three-layer structure with a zero-stiffness core, with all four edges being fully fixed, can be derived by substituting the bending stiffness and mass in Equations (12.4) and (12.2) by the total bending stiffness and total mass, respectively:

$$f_0 = \frac{22.4}{2\pi}\sqrt{\frac{D_t}{m_t L_x^4}}\alpha_2(L_x/L_y) \tag{12.35}$$

$$w_0 = \frac{L_x^4}{12D_t}\alpha_1(L_x/L_y) \tag{12.36}$$

The effects of finite-stiffness and damping of the core can be accounted for by using the non-dimensional frequency factor, recalling Equation (12.29) and its remark. The fundamental resonant frequency of a damped repair, f_r, is given by

$$f_r = \Omega_0 \frac{22.4}{2\pi}\sqrt{\frac{D_t}{m_t L_x^4}}\alpha_2(L_x/L_y) \tag{12.37}$$

Among the various shape functions that can approximately describe the shape of the fundamental mode of a rectangular plate (all edges are fixed), the static plate type has

been shown to produce good curvature (or strain) estimates (Byrne, 1977). Consequently the static plate mode shape will be adopted here. The static displacement $w_r(x, y)$ becomes

$$w_{\mathrm{r}}(x, y) = \left[1 - 4\left(\frac{x}{L_x}\right)^2\right]^2 \left[1 - 4\left(\frac{y}{L_y}\right)^2\right]^2 w_{\max} \tag{12.38}$$

with

$$w_{\max} = A\, w_0 \tag{12.39}$$

where A is an unknown coefficient to be determined. Here $w_{\max}$ is essentially the maximum displacement response of a damped repair to a unit static pressure, and hence the coefficient A denotes the ratio between the maximum static displacements of damped repair with the core having finite and zero stiffness.

The coefficient A can be derived by utilizing the approximate theory by Jones (1975), which contends that the maximum deflection of plates with arbitrary boundary conditions is inversely proportional to the square of the resonant frequency. This implies that the coefficient A is

$$A = \frac{1}{\Omega_0^2} \tag{12.40}$$

Here Ω_0 is given by Equation (12.31), in which g_0 and k_0 are given, respectively, by (12.27) and (12.33). Having obtained the solutions for the model loss factor and the resonant frequency, the remaining task is to determine the stresses in the repaired structure under acoustic loading.

12.3.4 Stresses and stress intensity factors in the repaired skin

With the displacement being given by Equation (12.34), the bending strains in the x and y directions are given by

$$\varepsilon_{\mathrm{b},xx}^{\mathrm{rms}} = -\frac{\partial^2 w_{\mathrm{rms}}}{\partial x^2}\frac{t_{\mathrm{s}}}{2} \tag{12.41}$$

$$\varepsilon_{\mathrm{b},yy}^{\mathrm{rms}} = -\frac{\partial^2 w_{\mathrm{rms}}}{\partial y^2}\frac{t_{\mathrm{s}}}{2} \tag{12.42}$$

The in-plane displacement components of the skin, $u_{\mathrm{s}}(x, y)$ and $v_{\mathrm{s}}(x, y)$, can be determined by inserting Equation (12.34) into Equation (12.12) and its equivalence for v_{s}, subjected to the zero-displacement boundary conditions pertinent to the fixed edges. The membrane strains in the x and y directions are given by

$$\varepsilon_{\mathrm{m},xx}^{\mathrm{rms}} = \frac{\partial u_{\mathrm{s}}}{\partial x} \tag{12.43}$$

$$\varepsilon_{\mathrm{m},yy}^{\mathrm{rms}} = \frac{\partial v_{\mathrm{s}}}{\partial y} \tag{12.44}$$

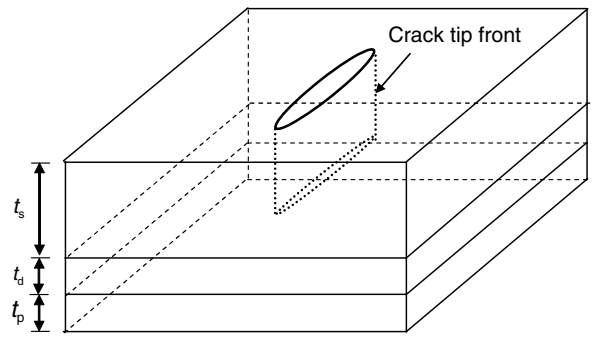

Fig. 12.6. Structural model of a cracked plate reinforced by a bonded patch.

The prospective stress components that are normal to the crack faces can be determined in accordance with the Hooke's law.

Consider the damped repair to a cracked skin as depicted in Figure 12.6. In the absence of the crack, the in-plane stress varies linearly through the skin thickness, as illustrated in Figure 12.7. For an edge crack lying between $(-a,\ L_y/2)$ and $(a,\ L_y/2)$, the prospective membrane stress σ_m and the prospective bending stress σ_b both vary with coordinate x (see Section 12.6). The crack bridging problem, viz, the integral Equation (5.119) of Chapter 5, can be solved numerically using a Galerkin method: expand the unknown functions in terms of Chebyshev polynomials and then determine the coefficients numerically. Because the prospective stresses vary with the position along the crack path, the matrix Equations (5.134) become

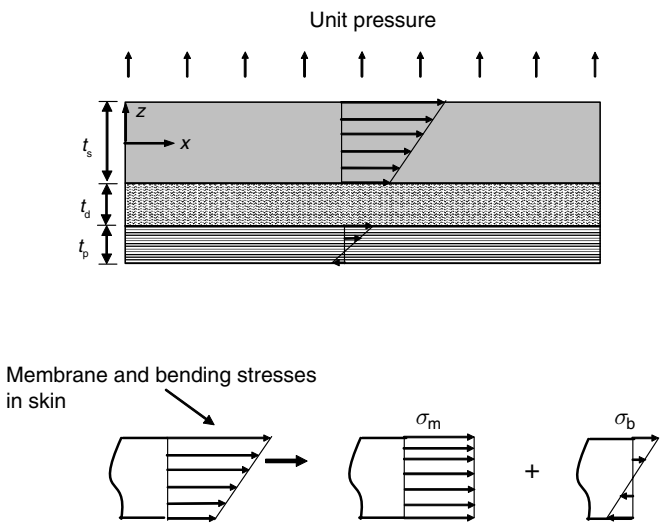

Fig. 12.7. Stress distributions in a layered structure subjected to out-of-plane loading.

$$\hat{A}_{ij}\hat{f}_j + \hat{B}_{ij}\hat{g}_j = \frac{1}{E_s}\int_{-1}^{1}\sqrt{1-r^2}U_j(r)\sigma_m(r)\mathrm{d}r \quad (i,\ j=0,\ 1,\ 2,\ldots,N)$$
$$\hat{C}_{ij}\hat{f}_j + \hat{D}_{ij}\hat{g}_j = \frac{1}{E_s}\int_{-1}^{1}\sqrt{1-r^2}U_j(r)\sigma_b(r)\mathrm{d}r \quad (i,\ j=0,\ 1,\ 2,\ldots,N) \tag{12.45}$$

where U_j denotes the Chebyshev polynomials of the second kind, and $r = x/a$.

It should be noted that the crack bridging solution is, strictly speaking, applicable to cracks remote from any boundary constraints. For the case of a crack being along a fully fixed edge, as illustrated in Figure 12.1, a geometry correction factor is required to account for the influence of the edge. For instance, the bending stress intensity factor of an unrepaired crack close an edge is given by

$$K = \gamma\sigma_b\sqrt{\pi a} \tag{12.46}$$

where σ_b is the bending stress existent along the prospective crack path. Experimental measurements (Byrne, 1977) indicated $\gamma = 0.8$. A detailed FE analysis (Callinan, et al., 2006) yielded $\gamma = 0.7$. This correction factor is also applicable to repaired cracks.

12.4 Fatigue Crack Growth Analysis

One important feature of acoustic fatigue is the high frequency at which structural panels vibrate. Since the addition of a repair patch will increase the structural stiffness, the fatigue frequency of a repaired structure will double or even triple the frequency of the original structure. For a repaired aircraft structure that vibrates at 600 Hz, it will experience over two million cycles for every one hour of flight.

A conservative approach is to design the damped repairs to achieve zero crack growth, i.e., by reducing the maximum stress intensity factor below the material's fatigue crack growth threshold. In some cases, however, such an approach can be overly conservative. This is particularly true when the high stress cycles have an extremely low rate of occurrence. In this case, repairs are only required to reduce fatigue crack growth rate below a certain level in order to restore the structural integrity of a damaged structure. Since acoustic loading is a random process involving an extremely large number of cycles, the conventional cycle-by-cycle-based crack growth analysis is often impractical. Consequently fatigue crack growth rates are commonly correlated using the root-mean-square value (with respect to time) of the crack-tip stress intensity factor (K_{rms}). However, such an approach has been found to lead to considerable overestimation of the crack growth rate under narrow band random loading (Byrne, 1975). This overestimation can be attributed to two major mechanisms. First, some of the cycles in the random time history may be below crack growth threshold and hence do not contribute to the propagation of the crack. Secondly and more importantly, plasticity-induced crack closure (Elber, 1970) causes the stress cycles below the crack closure level to not affect crack growth.

For a given structural response to a random acoustic excitation, the probability density distribution of the peak stress intensity factor of each loading cycle, K_p, is assumed to be given by a distribution $\chi(K_p)$. As an example, the probability density distribution of the peak stress intensity factor, K_p, for narrow band random acoustic loading (Byrne, 1975) is a truncated Rayleigh distribution,

$$\chi(K_p) = \frac{K_p}{2K_{rms}^2} e^{-K_p^2/2K_{rms}^2} \quad K_p < K_M \tag{12.47}$$

where K_M denotes the maximum stress intensity factor in the time history. For convenience, let us denote the ratio K_M/K_{rms} as α, i.e.,

$$\alpha = K_M/K_{rms} \tag{12.48}$$

which can range between 3.75 (Byrne, 1975) and 5.0 (Callinan et al., 2006).

Let us now denote the crack growth rate for the parent structure as

$$\frac{da}{dN} = F(\Delta K_{eff}) \tag{12.49}$$

where $\Delta K_{eff} = K_p - K_{op}$ denotes the range of the effective stress intensity factor, with K_{op} denoting the crack-opening stress intensity factor. Since it is impractical to track the crack closure behaviour on a cycle-by-cycle basis for random loadings, it is not unreasonable to assume that the crack opening stress is a constant fraction of K_M, the maximum stress intensity factor of a loading spectrum,

$$K_{op} = \beta K_M \tag{12.50}$$

In this case, the average crack growth rate per cycle (total crack growth per block of random loading divided by the number of cycles in the block) can be obtained by integrating the product of χ and F:

$$\frac{da}{dn} = \int_{\alpha\beta K_{rms}}^{\alpha K_{rms}} F(K_p - \alpha\beta K_{rms})\chi(K_p)dK_p \tag{12.51}$$

Once the fatigue crack growth relation is known for a material, the crack growth per block can be readily determined by numerical integration.

For the damped repair shown in Figure 12.3, it is necessary to consider the contributions of both the membrane and the bending stress intensity factor. In this regard, Duong and Wang (2004) have found that the following equivalent stress intensity factor provides a satisfactory correlation with experimental results (see Equation (11.10)),

$$K_{eq} = K_m^{rms} + K_b^{rms} + (1-\sqrt{3})\frac{K_b^{rms}}{K_m^{rms} + K_b^{rms}}\sqrt{(K_m^{rms})^2 + (K_b^{rms})^2/3} \tag{12.52}$$

Consequently, the spectrum peak stress intensity factor K_p in Equations (12.49)–(12.52) should be replaced by the equivalent stress intensity factor K_{eq}.

12.5 Optimization of Damped Repairs

Since the loss factors of the skin and the patch are generally much less than unity, a good approximation to the model loss factor, expression (12.30), is,

$$\eta_{\mathrm{m}} \approx \eta_0 + \eta_{\mathrm{t}} \tag{12.53}$$

In this case, it can be shown that the mth mode loss factor attains its maximum value ($\mathrm{d}\eta_{\mathrm{m}}/\mathrm{d}g_{\mathrm{m}} = 0$) when the shear parameter (12.27) equals to the following:

$$g_{\mathrm{m,opt}} = \frac{1}{\sqrt{(1+Y)(1+\eta_{\mathrm{g}}^2)}} \tag{12.54}$$

where Y and η_{g} are given, respectively, by Equations (12.15) and (12.24). At this optimal loss condition, the model loss factor is given by,

$$\eta_{\mathrm{m,max}} = \frac{\eta_{\mathrm{g}} Y}{(2+Y) + 2\sqrt{(1+Y)(1+\eta_{\mathrm{g}}^2)}} + \eta_{\mathrm{t}} \tag{12.55}$$

From Equation (12.27) it is clear that the wave number, k_{m}, the geometric factor, Y, and the shear loss factor, η_{g}, need to satisfy the following condition to achieve maximum damping:

$$k_{\mathrm{mx}}^2 + k_{\mathrm{my}}^2 = g'\sqrt{(1+Y)(1+\eta_{\mathrm{g}}^2)} \tag{12.56}$$

For a given structure to be repaired, determination of the optimal damping configuration involves a multi-parameter optimization. Since the extensional stiffness of a repair patch needs to match that of the structure being repaired, it is important to select a repair material that meets the constraint $E_{\mathrm{s}}t_{\mathrm{s}} = E_{\mathrm{p}}t_{\mathrm{p}}$.

12.6 An Illustrative Example

Consider a square panel (thickness = 1 mm, edge length = 200 mm) made of aluminium alloy. The panel is subjected to an overall sound pressure level of 160 db. The modulus and thickness of the repair patch are respectively 140 GPa and 0.5 mm. If the patch is adhesively bonded to the panel without a damping layer, like a conventional repair, the root-mean-square values of the membrane stress and the bending stress at the centre of a fixed edge are approximately 11 and 13 MPa, respectively. Now consider the case of damped repair incorporating a layer of Dyad 609 viscoelastic material (thickness = 1 mm). The shear modulus and the loss factor of Dyad 609 are shown in Figures 12.8 and 12.9. It is clear that this particular viscoelastic material attains its maximum damping at a temperature of 80 °C. For temperatures below 10 °C, the material behaves very much like an elastic material. Therefore, a damped repair using Dyad 609 will only show significant damping at high temperatures. The maximum membrane and bending stresses at the centre of a clamped edge are presented in Figure 12.10.

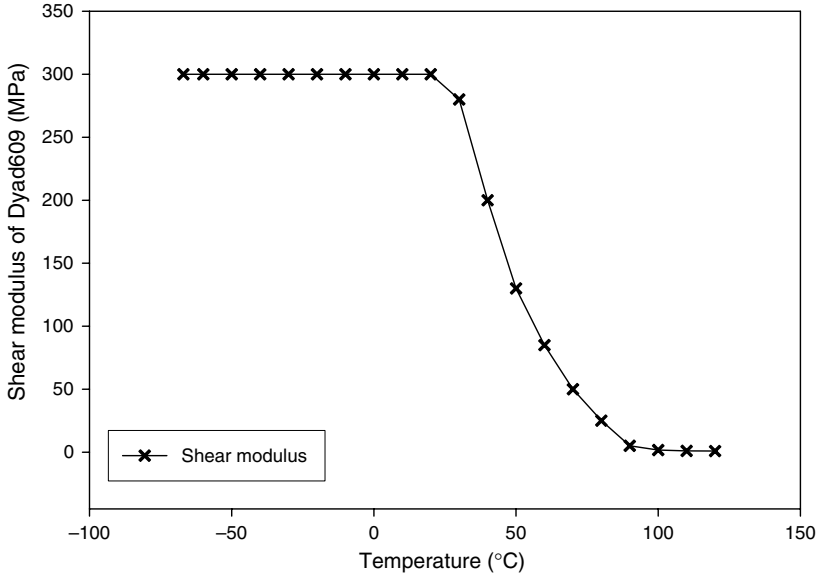

Fig. 12.8. Shear modulus of Dyad 609.

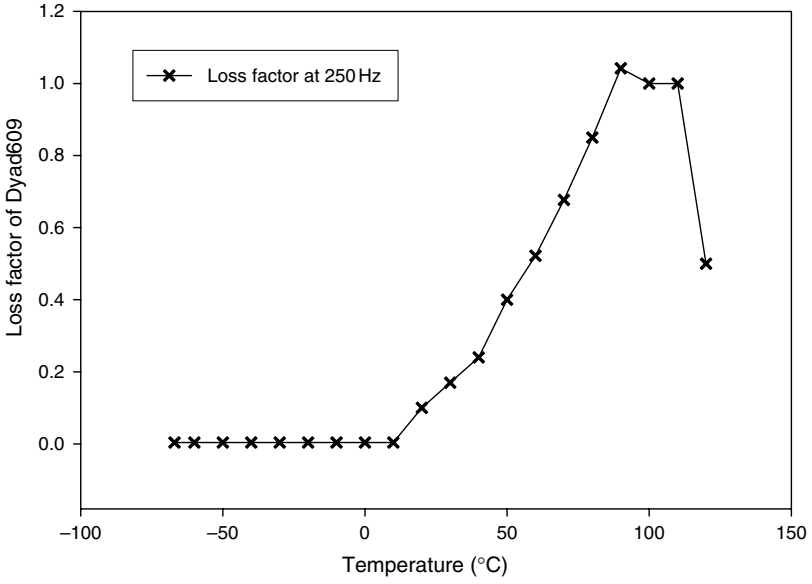

Fig. 12.9. Loss factor of Dyad 609 at 250 Hz.

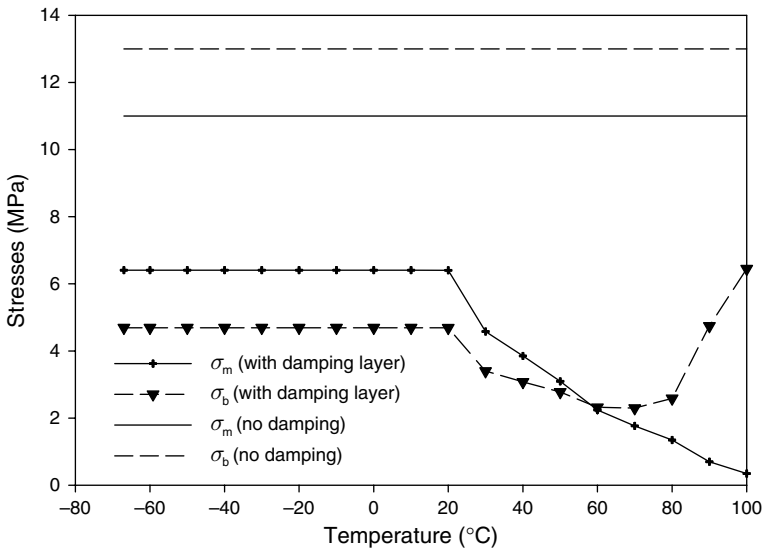

Fig. 12.10. Membrane and bending stresses at the centre of a clamped edge of a square panel.

The stress distributions at three different temperatures are presented in Figure 12.11. Comparing with the case of conventional bonded repair without a damping layer, the damped repair configuration achieves a significant reduction in stresses. At temperatures below 10 °C, the stress reduction by the damped repair is primarily due to the presence of the core, which considerably increases the total bending stiffness of the repaired region. As the temperature increases, as shown in Figure 12.10, the damping effect of the core becomes increasingly effective. The membrane stress decreases from 6.4 MPa at 10 °C to 0.33 MPa at 100 °C. Because the shear stiffness of the core decreases with temperature, the skin panel and the patch become eventually uncoupled as the temperature increases above 60 °C. As a result, the membrane stress monotonically decreases while the bending stress initially decreases then increases with temperature.

Figure 12.12 shows stress intensity factors for a 50 mm crack located at the centre of a clamped edge. Both the membrane and the bending stress intensity factors remain approximately constant at temperatures below 20 °C. As the temperature increases, the membrane stress intensity factor monotonically decreases while the bending stress intensity factor reaches its minimum at 80 °C. The equivalent stress intensity factor, Equation (12.52), followed a similar trend as the membrane stress intensity factor, due to the relative small contribution of the bending component.

Clearly the crack size has a significant effect on the stress intensity factors. In the case of uniform stresses along the crack path, the stress intensity factors would asymptotically approach their upper bound values. In the present case, however, the stress intensity factors initially increase with crack length then decrease with crack length. This is illustrated in Figure 12.13 for three different temperatures. This is primarily due to the non-uniform distribution of the membrane and bending stresses shown in Figure 12.11.

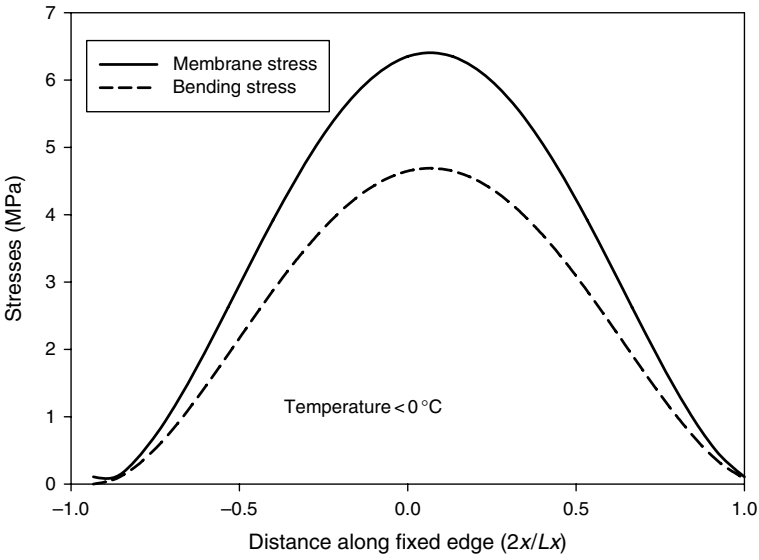

(a)

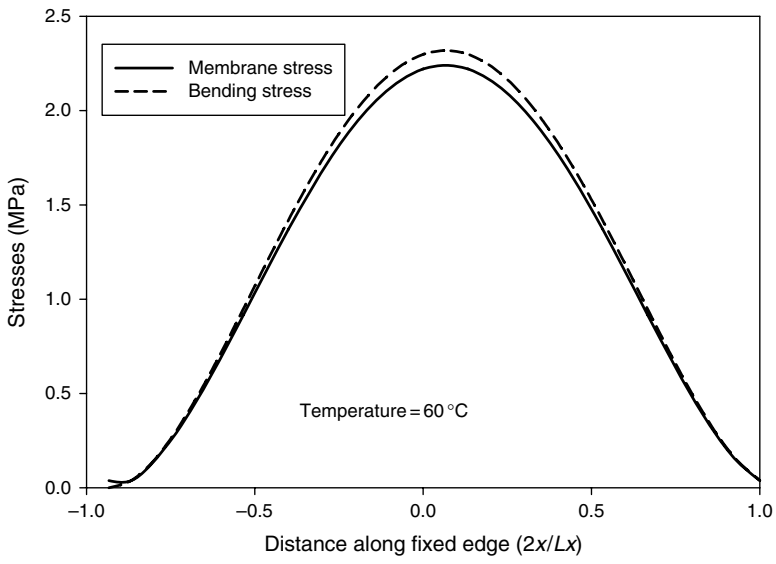

(b)

Fig. 12.11. Stress distributions along a fixed edge.

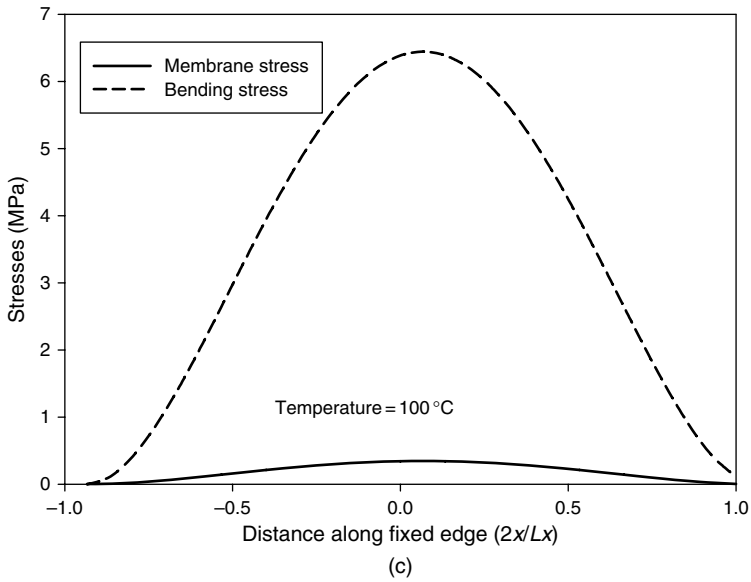

Fig. 12.11. (Continued)

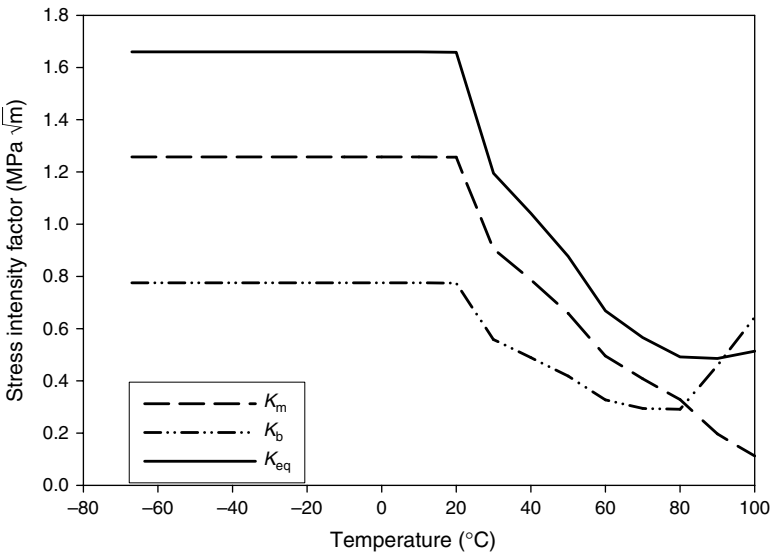

Fig. 12.12. Membrane and bending stress intensity factors (half crack length = 25 mm). The equivalent value K_{eq} is determined via Equation (12.52).

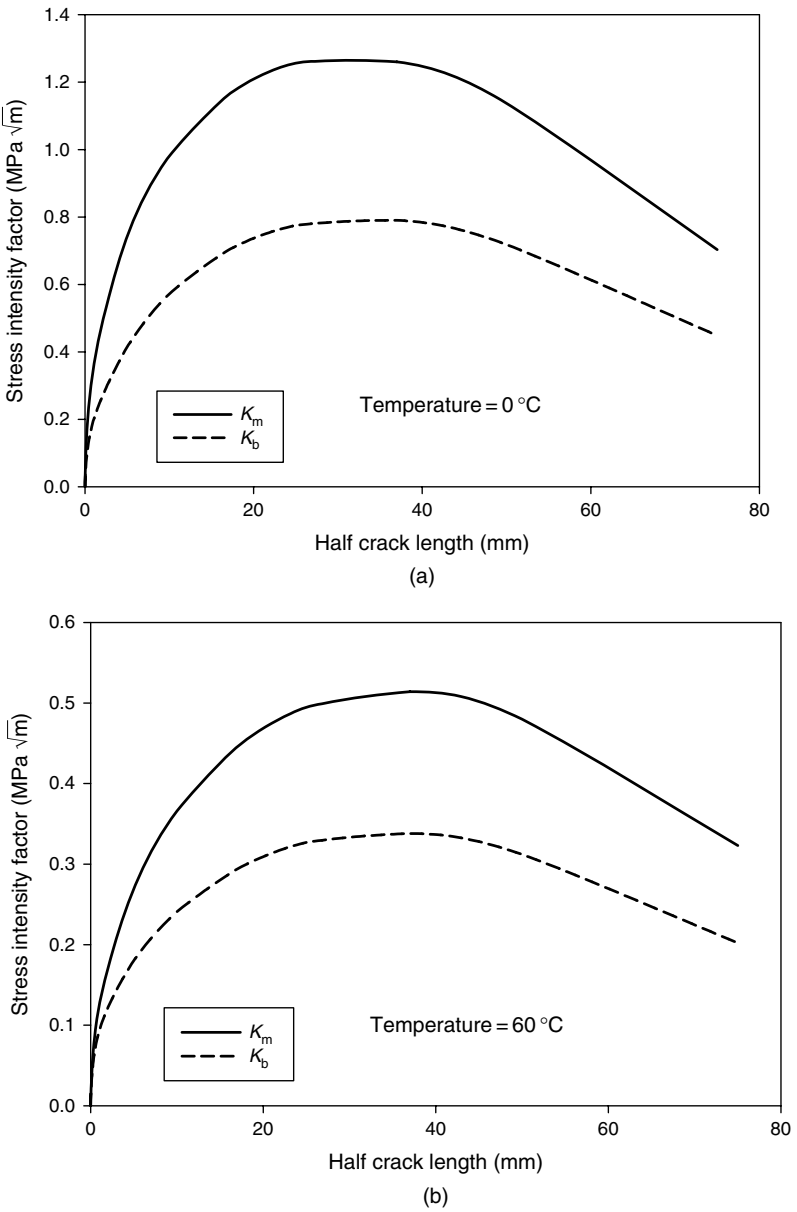

Fig. 12.13. Stress intensity factors for varying crack lengths at three different temperatures.

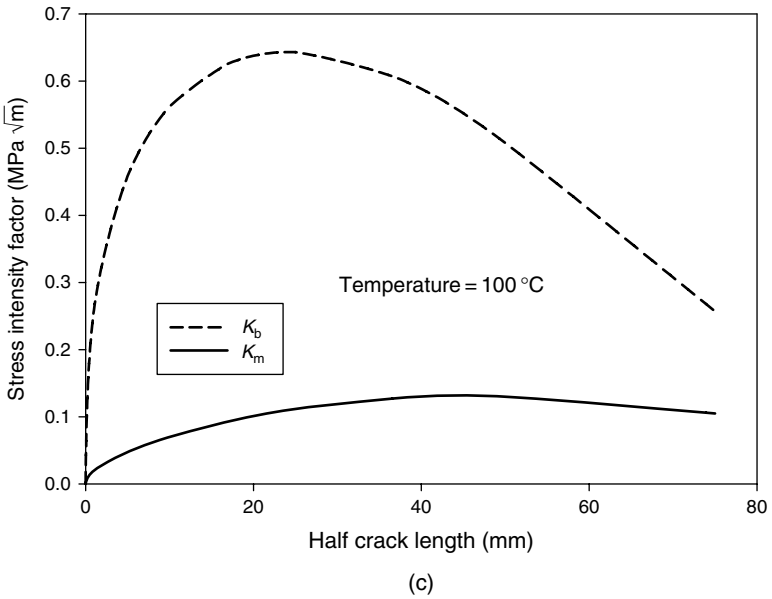

Fig. 12.13. (Continued)

It is worth noting that this is consistent with the observed deviation of acoustic fatigue cracks away from clamped edges after reaching a certain length (Byrne, 1977). To accurately determine the influence of crack-tip deflection on the repair efficiency would require detailed computation using the FE method. However, from the viewpoint of designing damped repair to acoustic fatigue cracks, it suffices to consider the maximum stress intensity factor of edge cracks.

CHAPTER 13

Repair Analysis Methods Accounting for Secondary Effects

The preceding chapters do not completely address all effects pertaining to the bonded repair. Some effects are secondary in nature and they do not fit well within the logical framework of those chapters. This chapter is therefore devoted to a brief discussion of the remaining effects, not included in the preceding chapters for one reason or another.

13.1 Effect of Tapering on Load Attraction of Bonded Patches

In Chapters 3 and 4, all solutions for the load attraction pertain to patches of uniform thickness. However, in practice, all patches are tapered at their edge to avoid the adhesive failure there. Nevertheless, results from FE analyses indicate that the tapering effect on the stress level in the skin around and under the patch is normally quite small for patches repaired on thin structures such as fuselage skin and skin of the wing's lower and upper surfaces (6–10 ply patch with a taper ratio from 10:1 to 30:1), where the volume fraction of the tapering region is smaller than 20% of the total volume fraction of the patch. Thus, the use of results given in Chapters 3 and 4 is justified for these patches.

On the other hand, repair of a thick skin such as a frame structure may require thicker patches with higher taper ratio. In such cases, the volume fraction of the tapering region may be much larger than 20% of the total volume fraction of the patch since the size of the patch cannot be increased in proportion to its thickness due to the existence of the surrounding structure which limits the availability of the repair space. The effect of patch tapering on load attraction is thus inevitable for such cases. This effect therefore will be addressed in this section using the multi-inclusion model, following closely the work by Li (2000) for thermoelastic behavior of composites with functionally graded interphase. For simplicity, only tapered elliptical patches under far-field-tensile load are considered in the present analysis, as the one illustrated in Figure 13.1. A similar analysis can be carried out for a combined thermo-mechanical loading. However, the latter analysis is omitted from this chapter for reason of clarity.

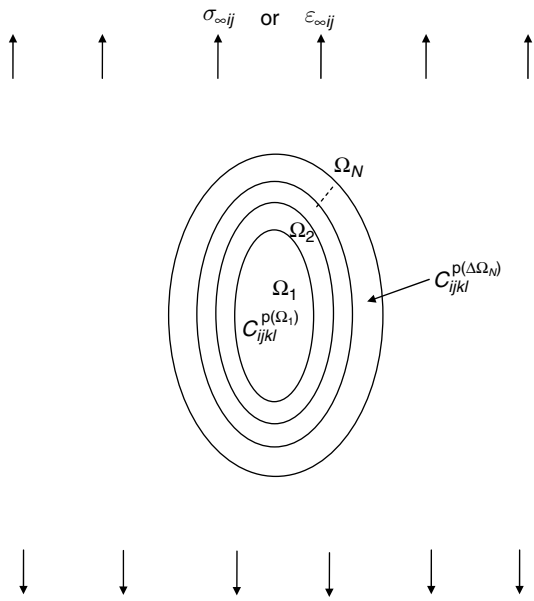

Fig. 13.1. Geometry of a tapered patch with concentric and similar ellipses.

Consider a tapered elliptical patch shown in Figure 13.1. This tapered patch will be analyzed as a uniformly thick patch of the same external dimensions but with effective elastic moduli. These effective elastic moduli will be derived based on the averaging method widely used in micromechanics for determining the macroscopic properties of heterogeneous materials (Mura, 1998; Nemat-Nasser and Hori, 1993; Li, 2000). Let us denote the concentric ellipses of the patched or overlap region as $\Omega_r\,(r = 1, \ldots, N)$ such that Ω_1 be the full thickness region of the patch, and the annulus between two successively concentric ellipses of the tapering region of the patch be $\Delta\Omega_r = \Omega_r - \Omega_{r-1}\ (r = 2, \ldots, N)$ with a uniform patch thickness of $t_{\mathrm{p}}^{(\Delta\Omega_r)}$. Furthermore, as in Chapters 3 and 4, the patch is also assumed to be rigidly bonded to the skin and it is therefore considered to be an integral part of the skin in the overlap region. The overlap region is then treated as an inhomogeneity, which is composed of an elliptical region Ω_1 and $(N-1)$ annulus, each region with different elastic moduli. For convenience, in the following development, we will adopt the following notation for Ω_1, i.e., $\Delta\Omega_1 \equiv \Omega_1$. The constitutive relations for annulus regions $\Delta\Omega_r$ and elliptical region Ω_1 can be expressed as

$$\begin{aligned} \sigma_{ij}^{\mathrm{I}(\Delta\Omega_r)} &= C_{ijkl}^{\mathrm{I}(\Delta\Omega_r)} \varepsilon_{kl}^{\mathrm{I}(\Delta\Omega_r)} \\ \varepsilon_{ij}^{\mathrm{I}(\Delta\Omega_r)} &= C_{ijkl}^{\mathrm{I}(\Delta\Omega_r)-1} \varepsilon_{kl}^{\mathrm{I}(\Delta\Omega_r)} \end{aligned} \qquad (r = 1, \ldots, N) \tag{13.1}$$

where $C_{ijkl}^{\mathrm{I}(\Delta\Omega_i)}$ is the elasticity tensor of the patch–skin combination in the overlap region $\Delta\Omega_r$, superscripts I and $(\Delta\Omega_r)$ signify, respectively, the inhomogeneity problem and the

overlap region $\Delta\Omega_r$. $C_{ijkl}^{\mathrm{I}(\Delta\Omega_i)}$ can be evaluated by using Equation (4.31) or equivalently in compact notation by Equation (6.47) as

$$C_{ijkl}^{\mathrm{I}(\Delta\Omega_r)} = \frac{1}{t_{\mathrm{s}}}\left(t_{\mathrm{s}}C_{ijkl}^{\mathrm{s}} + t_{\mathrm{p}}^{(\Delta\Omega_r)}C_{ijkl}^{\mathrm{p}(\Delta\Omega_r)}\right) \tag{13.2}$$

where $C_{ijkl}^{\mathrm{p}(\Delta\Omega_r)}$, $t_{\mathrm{p}}^{(\Delta\Omega_r)}$ are the elastic moduli and thickness of the patch in region $\Delta\Omega_r$, and t_{I} in Equation (4.31) and (6.47) has been set to equal t_{s}.

The average stress and strain fields inside the inhomogeneous region of the inhomogeneity problem can be determined by the equivalent inclusion method described in Chapter 4. However, since the inhomogeneity now composes of concentric and similar ellipses, the corresponding equivalent inclusion problem must also compose of these ellipses. As in Chapter 4, the inclusion problem is a homogeneous problem in which the constitutive relation for the medium is given by the usual elasticity formula as

$$\sigma_{ij}^{\mathrm{H}} = C_{ijkl}^{\mathrm{s}}\varepsilon_{kl}^{\mathrm{H}} \tag{13.3}$$

However, each annulus region $\Delta\Omega_r$ $(r = 1, \ldots, N)$ of the inclusion will be prescribed by a different average eigenstrain field. This type of inclusion problem will be referred to as a multi-inclusion problem, and it then will be solved by the multi-inclusion model.

According to the multi-inclusion model, for an inclusion composing of concentric and similar ellipses, subjected to average eigenstrain fields $\left\langle \varepsilon_{ij}^{*(\Delta\Omega_r)} \right\rangle$ $(r = 1, \ldots, N)$ in each sub-region $\Delta\Omega_r$, the average field in the annulus embedded in an infinite medium only depends on the shapes and orientation of the ellipses. Furthermore, when all ellipses of the inclusion are concentric and similar in shape, the average strain in the annulus is given by

$$\left\langle \varepsilon_{ij}^{\mathrm{H}(\Delta\Omega_r)} \right\rangle = S_{ijkl}\left\langle \varepsilon_{kl}^{*(\Delta\Omega_r)} \right\rangle \tag{13.4}$$

and the average stress is

$$\left\langle \sigma_{ij}^{\mathrm{H}(\Delta\Omega_r)} \right\rangle = C_{ijkl}^{\mathrm{s}}\left(S_{klmn} - \delta_{kl}\delta_{mn}\right)\left\langle \varepsilon_{mn}^{*(\Delta\Omega_r)} \right\rangle \tag{13.5}$$

where S_{ijkl} is Eshelby tensor, which is a function of the elastic moduli C_{ijkl}^{s} of the infinite medium and the inclusion shape, δ_{ij} is the Kronecker delta, the superscript H denotes the homogeneous or inclusion problem, and $\langle \bullet \rangle \equiv \frac{1}{\Delta\Omega_r}\int_{\Delta\Omega_r}(\bullet)\,\mathrm{d}A$. For 2-D elliptical inclusion in an infinite isotropic medium, S_{ijkl} is given by a fourth equation of (6.4) in Chapter 6. Since elliptical regions $\Omega_1, \ldots, \Omega_N$ are concentric and similar, S_{ijkl} is the same for all regions $\Delta\Omega_r$ and it can be calculated by Equation (6.4) of Chapter 6 using geometrical dimensions of Ω_1. So far the multi-inclusion has been assumed to be subjected only to the eigenstrain field. When the inclusion is also under a uniform stress and strain field applied at the far field in addition to the mentioned eigenstrain, Equations (13.4) and (13.5) become

$$\begin{aligned}\left\langle \varepsilon_{ij}^{\mathrm{H}(\Delta\Omega_r)} \right\rangle &= S_{ijkl} \left\langle \varepsilon_{kl}^{*(\Delta\Omega_r)} \right\rangle + \varepsilon_{\infty ij} \\ \left\langle \sigma_{ij}^{\mathrm{H}(\Delta\Omega_r)} \right\rangle &= C_{ijkl}^{\mathrm{s}} \left[(S_{klmn} - \delta_{kl}\delta_{mn}) \left\langle \varepsilon_{mn}^{*(\Delta\Omega_r)} \right\rangle + \varepsilon_{\infty ij} \right]\end{aligned} \tag{13.6}$$

On the other hand, as in Chapter 4 and from Equation (4.1), the equivalency condition of the equivalent inclusion method requires that

$$\begin{aligned}\varepsilon_{ij}^{\mathrm{I}(\Delta\Omega_r)} &= \varepsilon_{ij}^{\mathrm{H}(\Delta\Omega_r)} \\ \sigma_{ij}^{\mathrm{I}(\Delta\Omega_r)} &= \sigma_{ij}^{\mathrm{H}(\Delta\Omega_r)}\end{aligned} \qquad (r = 1, \ldots, N) \tag{13.7}$$

Applying condition (13.7) above to the average strain and stress fields, one obtains

$$\begin{aligned}\left\langle \varepsilon_{ij}^{\mathrm{I}(\Delta\Omega_r)} \right\rangle &= \left\langle \varepsilon_{ij}^{\mathrm{H}(\Delta\Omega_r)} \right\rangle \\ \left\langle \sigma_{ij}^{\mathrm{I}(\Delta\Omega_r)} \right\rangle &= \left\langle \sigma_{ij}^{\mathrm{H}(\Delta\Omega_r)} \right\rangle\end{aligned} \qquad (r = 1, \ldots, N) \tag{13.8}$$

Following the procedure outlined in Section 4.1 of Chapter 4 and assuming that the strain fields in the inclusion and inhomogeneity problems are composed of two parts, one from a uniform far field $\varepsilon_{\infty ij}$ and the other from the disturbance field induced by the eigenstrain or inhomogeneity, one finally arrives at the following equations upon substitution of Equations (13.1), (13.3), and (13.6) into (13.8) (see Equation (4.5)):

$$\begin{aligned}\Delta C_{ijkl}^{(\Delta\Omega_r)} S_{klmn} \left\langle \varepsilon_{mn}^{*(\Delta\Omega_r)} \right\rangle - C_{ijkl}^{\mathrm{s}} \left\langle \varepsilon_{kl}^{*(\Delta\Omega_r)} \right\rangle &= -\Delta C_{ijkl}^{(\Delta\Omega_r)} \varepsilon_{\infty kl} \\ \Delta C_{ijkl}^{(\Delta\Omega_r)} &= C_{ijkl}^{\mathrm{s}} - C_{ijkl}^{\mathrm{I}(\Delta\Omega_{\mathrm{r}})}\end{aligned} \qquad (r = 1, \ldots, N) \tag{13.9}$$

The first equation of (13.9) can be rearranged by multiplying both sides of the equation with $\Delta C_{ijkl}^{(\Delta\Omega_r)-1}$ to yield

$$\left\langle \varepsilon_{ij}^{*(\Delta\Omega_r)} \right\rangle = \Lambda_{ijkl}^{(\Delta\Omega_r)} \varepsilon_{\infty kl} \tag{13.10}$$

where

$$\Lambda_{ijkl}^{(\Delta\Omega_r)} = \left(\Delta C_{iijmn}^{(\Delta\Omega_r)-1} C_{mnkl}^{s} - S_{ijkl} \right)^{-1} \qquad (r = 1, \ldots, N) \tag{13.11}$$

With the equivalent eigenstrain known, the average stress and strain field in the annulus regions $\Delta\Omega_r$ and elliptical region Ω_1 of the inhomogeneity can be obtained from Equations (13.6), (13.8), and (13.10) as

$$\begin{aligned}\left\langle \varepsilon_{ij}^{\mathrm{I}(\Delta\Omega_r)} \right\rangle &= \left(S_{ijkl} \Lambda_{klmn}^{(\Delta\Omega_r)} + \delta_{ij}\delta_{mn} \right) \varepsilon_{\infty mn} \\ \left\langle \sigma_{ij}^{\mathrm{I}(\Delta\Omega_r)} \right\rangle &= C_{ijkl}^{\mathrm{s}} \left[(S_{klmn} - \delta_{kl}\delta_{mn}) \Lambda_{mnpq}^{(\Delta\Omega_r)} + \delta_{ij}\delta_{pq} \right] \varepsilon_{\infty pq}\end{aligned} \qquad (r = 1, \ldots, N) \tag{13.12}$$

The average field in the whole inhomogeneity can be determined by summing weighted contributions from all regions, $\Delta\Omega_r$, and dividing the result by its total area, i.e., Ω_N, thus,

$$\begin{aligned}\left\langle \varepsilon_{ij}^{\mathrm{I}} \right\rangle &= \frac{1}{\Omega_N}\sum_{r=1}^{N}\Delta\Omega_r\left\langle \varepsilon_{ij}^{\mathrm{I}(\Delta\Omega_r)} \right\rangle = \left(\sum_{r=1}^{N} f_r\left[S_{ijkl}\Lambda_{klmn}^{(\Delta\Omega_r)} + \delta_{ij}\delta_{mn}\right]\right)\varepsilon_{\infty mn} \\ \left\langle \sigma_{ij}^{\mathrm{I}} \right\rangle &= \frac{1}{\Omega_N}\sum_{r=1}^{N}\Delta\Omega_r\left\langle \sigma_{ij}^{\mathrm{I}(\Delta\Omega_r)} \right\rangle = \left(\sum_{r=1}^{N} f_r C_{ijkl}^{s}\left[\left(S_{klmn} - \delta_{kl}\delta_{mn}\right)\Lambda_{mnpq}^{(\Delta\Omega_r)} + \delta_{ij}\delta_{pq}\right]\right)\varepsilon_{\infty pq}\end{aligned} \tag{13.13}$$

where $f_r = \frac{\Delta\Omega_r}{\Omega_N}$ is the volume fraction of the annulus region $\Delta\Omega_r$. By defining the effective elastic moduli $C_{ijkl}^{\mathrm{I(effective)}}$ of the inhomogeneity shown in Figure 13.1 as $\left\langle \sigma_{ij}^{I} \right\rangle = C_{ijkl}^{\mathrm{I(effective)}}\left\langle \varepsilon_{kl}^{\mathrm{I}} \right\rangle$, it is very easy to show from Equation (13.13) that

$$C_{ijkl}^{\mathrm{I(effective)}} = C_{ijmn}^{\mathrm{s}}\left[\left(S_{mnpq} - \delta_{mn}\delta_{pq}\right)\Lambda_{pqrs} + \delta_{mn}\delta_{rs}\right]\left[S_{kltu}\Lambda_{turs} + \delta_{kl}\delta_{rs}\right]^{-1} \tag{13.14}$$

where $\Lambda_{ijkl} = \sum_{r=1}^{N} f_r \cdot \Lambda_{ijkl}^{(\Delta\Omega_r)}$.

13.2 Effect of Patches in Proximity on Load Attraction

Bonding a patch on aircraft skin results in an area that is locally stiffened compared to the surrounding skin. This attracts proportionally higher load per unit width of the skin than at an un-patched area of the skin. When another patch is introduced into the proximity of the first, there will be an interaction between the two patches. This interaction tends to raise the stress levels in the neighboring patch. Limited FE studies were conducted to investigate that effect for two patches of the same stiffness in the proximity (Atluri, 1997; Callinan et al., 1998; Muller and Fredell, 1999; Vlot et al., 2000; and Duong, 2003a). From these FE studies, it was found that the effect of the patch proximity was most pronounced when two patches aligned vertically (with the far-field load in the vertical direction). On the other hand, patches aligned horizontally have very little influence on each other. The results of the FE studies can also be summarized as follows. Referring to Figure 13.2, the proximity effect on the subjected patch is negligible for any proximate patch located outside the shaded area of Figure 13.2. Furthermore, the effect of the proximate patch located inside the shaded area can be conservatively estimated using the curves given in Figure 13.3, which represent the most severe case, i.e., when two patches are aligned vertically. However, the interaction curve in Figure 13.3 had been determined only for a special case when two patches having the same stiffness ratio of 1. For the general case, this interaction can be predicted analytically for two non-identical patches in the proximity by expanding the equivalent inclusion method described in Chapter 4 for a case of a single inhomogeneity to that of two inhomogeneities, following the work of Moschovidis and Mura (1975; Mura, 1998). To illustrate this method, for simplicity, let us consider two elliptical inhomogeneities Ω_1 and Ω_2 in an infinite skin with elastic moduli of C_{ijkl}^{s}, as shown in Figure 13.4. For convenience, x_i and $\overline{x}_i$ coordinate systems are taken at the center of Ω_1 and Ω_2, respectively, and tensor components referring to the

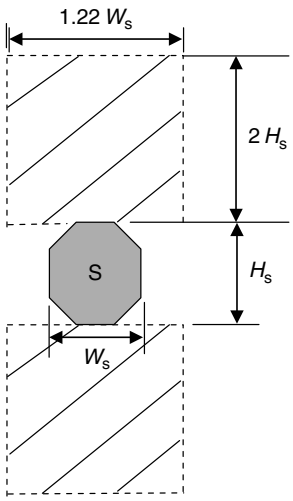

Fig. 13.2. Region of influence by the proximate patch as shown in shaded area.

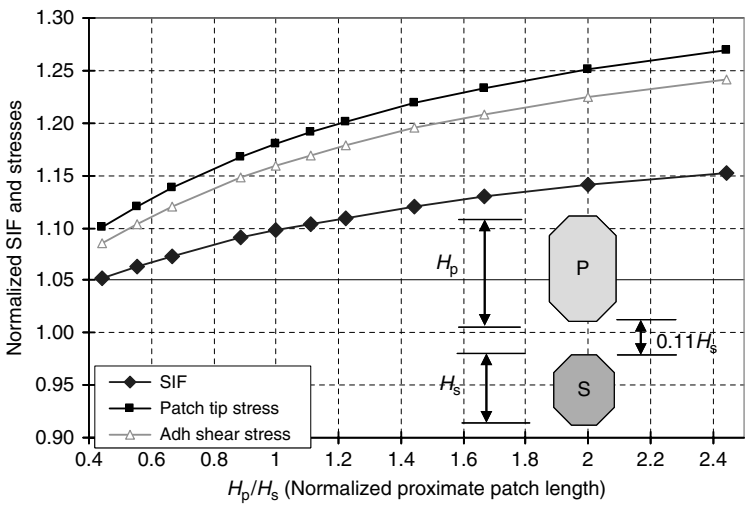

Fig. 13.3. The proximity effect on the subjected patch when two patches have the same stiffness ratio equal to 1 and are aligned vertically. In the figure, P and S denote the subjected and proximate patches, respectively.

$\overline{x}_i$ coordinate system will be denoted by bars in the development followed. Furthermore, the two coordinate systems are related by the following coordinate transformation law:

$$\begin{aligned} x_i - r_i &= T_{ij}\overline{x}_j \\ \overline{x}_j &= T_{ji}\left(x_j - r_j\right) \end{aligned} \tag{13.15}$$

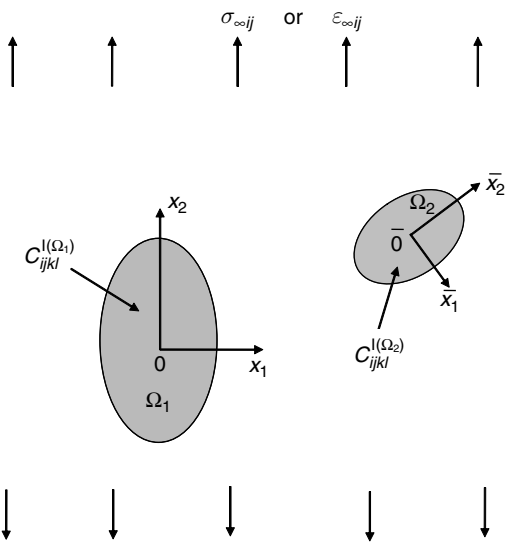

Fig. 13.4. Two elliptical inhomogeneities under far-field-uniformstresses or strains.

where T_{ij} is the direction cosine between the x_i-axis and $\bar{x}_j$-axis, and r_i is the x_i-coordinate of the origin $\bar{\mathbf{0}}$ in Ω_2. As before, the overlap regions of the two patches in proximity will be idealized as two inhomogeneities with equivalent elastic moduli. Applying the equivalent inclusion method leads to the following equivalency equations in subdomains Ω_1 and Ω_2:

$$\begin{aligned} C_{ijkl}^{\mathrm{I}(\Omega_r)}\left(\varepsilon_{\infty kl}+\Delta\varepsilon_{kl}^{\mathrm{I}}\right) &= C_{ijkl}^{\mathrm{s}}\left(\varepsilon_{\infty kl}+\Delta\varepsilon_{kl}^{\mathrm{H}}-\varepsilon_{kl}^{*(\Omega_r)}\right) \\ \Delta\varepsilon_{kl}^{\mathrm{I}} &= \Delta\varepsilon_{kl}^{\mathrm{H}} \end{aligned} \qquad \text{in } \Omega_r,\ r=1,2 \tag{13.16}$$

where superscripts I and (Ω_r) again signify, respectively, the inhomogeneity problem and the inhomogeneity Ω_r, while the superscript H denotes the homogeneous or the equivalent inclusion problem. Thus, $C_{ijkl}^{\mathrm{I}(\Omega_r)}$ is the elasticity tensor of the inhomogeneity Ω_r. Furthermore, $\Delta\varepsilon_{ij}^{\mathrm{H}}$ or $\Delta\sigma_{ij}^{\mathrm{H}}$ and $\Delta\varepsilon_{ij}^{\mathrm{I}}$ or $\Delta\sigma_{ij}^{\mathrm{I}}$ are disturbance strain or stress fields due to eigenstrain field in the equivalent inclusion problem and disturbance strain or stress field due to the inhomogeneity in the inhomogeneity problem, respectively. These fields define disturbance strain or stress at every point in the domain, both interior and exterior to subdomains Ω_1 and Ω_2. It is worthy to note that the total strain fields $\varepsilon_{ij}^{\mathrm{H}}$ and $\varepsilon_{ij}^{\mathrm{I}}$ were employed in all previous formulations for the inclusion and inhomogeneity problems. However, for simplicity, the present formulation will employ the disturbance strain fields $\Delta\varepsilon_{ij}^{\mathrm{H}}$ and $\Delta\varepsilon_{ij}^{\mathrm{I}}$ instead, and they are related to the corresponding total strain fields by $\varepsilon_{ij}^{\mathrm{H\ or\ I}}=\Delta\varepsilon_{ij}^{\mathrm{H\ or\ I}}+\varepsilon_{\infty ij}$. Let us further assume the equivalent eigenstrain fields in Ω_1 and Ω_2 to be

$$\begin{aligned}\varepsilon_{ij}^{*(\Omega_1)} &= F_{ij}^{(\Omega_1)} + F_{ijk}^{(\Omega_1)} x_k + F_{ijkl}^{(\Omega_1)} x_k x_l + \cdots \\ \overline{\varepsilon}_{ij}^{*(\Omega_2)} &= \overline{F}_{ij}^{(\Omega_2)} + \overline{F}_{ijk}^{(\Omega_2)} \overline{x}_k + \overline{F}_{ijkl}^{(\Omega_2)} \overline{x}_k \overline{x}_l + \cdots\end{aligned} \tag{13.17}$$

and the corresponding disturbance strain fields due to each of these two eigenstrain fields to be represented in the respective coordinate systems x_i and $\overline{x}_i$ by

$$\begin{aligned}\Delta\varepsilon_{ij}^{\mathrm{H}(\Omega_1)} &= S_{ijkl}^{(\Omega_1)}(\mathbf{x}) F_{kl}^{(\Omega_1)} + S_{ijklm}^{(\Omega_1)}(\mathbf{x}) F_{klm}^{(\Omega_1)} + S_{ijklmn}^{(\Omega_1)}(\mathbf{x}) F_{klmn}^{(\Omega_1)} + \cdots \\ \Delta\overline{\varepsilon}_{ij}^{\mathrm{H}(\Omega_2)} &= \overline{S}_{ijkl}^{(\Omega_2)}(\overline{\mathbf{x}}) \overline{F}_{kl}^{(\Omega_2)} + \overline{S}_{ijklm}^{(\Omega_2)}(\overline{\mathbf{x}}) \overline{F}_{klm}^{(\Omega_2)} + \overline{S}_{ijklmn}^{(\Omega_2)}(\overline{\mathbf{x}}) \overline{F}_{klmn}^{(\Omega_2)} + \cdots\end{aligned} \tag{13.18}$$

for all $\mathbf{x} \in \Re$, $\overline{\mathbf{x}} \in \Re$, where $\Re$ is an infinite domain including Ω_1 and Ω_2.

Since $\Delta\varepsilon_{ij}^{\mathrm{H}(\Omega_1)}$ and $\Delta\overline{\varepsilon}_{ij}^{\mathrm{H}(\Omega_2)}$ are the respective strain fields caused by $\varepsilon_{ij}^{*(\Omega_1)}$ and $\overline{\varepsilon}_{ij}^{*(\Omega_2)}$, and tensor components of $\Delta\overline{\varepsilon}_{ij}^{\mathrm{H}(\Omega_2)}$ are given in the coordinate system $\overline{x}_i$, the strain field $\Delta\varepsilon_{ij}^{\mathrm{H}}$ given in Equation (13.16) is the sum of $\Delta\varepsilon_{ij}^{\mathrm{H}(\Omega_1)}$ and $\Delta\overline{\varepsilon}_{ij}^{\mathrm{H}(\Omega_2)}$ after appropriate coordinate transformation. For elliptical regions Ω_1 and Ω_2, it was shown in Mura (1998) that Eshelby tensors $S^{(\Omega_1)}$'s and $\overline{S}^{(\Omega_2)}$'s given in Equations (13.18) are a polynomials of the spatial coordinates of the same degree as their corresponding eigenstrain field inside the respective regions Ω_1 and Ω_2. In particular, $S_{ijkl}^{(\Omega_r)}$, which is the Eshelby tensor corresponding to the constant eigenstrain $F_{kl}^{(\Omega_r)}$ in Ω_r, is also the constant tensor in Ω_r, while $S_{ijklmn}^{(\Omega_r)}$, which is the Eshelby tensor corresponding to the second-degree polynomial eigenstrain, is the second-degree polymonial of the spatial coordinates in Ω_r. Thus, the Eshelby tensors $S^{(\Omega_1)}$'s and $\overline{S}^{(\Omega_2)}$'s in their respective elliptical regions Ω_1 and Ω_2 are represented exactly by the following equations (after consideration of symmetry):

$$\begin{aligned}S_{ijkl}^{(\Omega_1)}(\mathbf{x}) &= S_{ijkl}^{(\Omega_1)}(\mathbf{0}) \\ S_{ijklm}^{(\Omega_1)}(\mathbf{x}) &= \frac{\partial}{\partial x_q} S_{ijklm}^{(\Omega_1)}(\mathbf{0})\, x_q \\ S_{ijklmn}^{(\Omega_1)}(\mathbf{x}) &= S_{ijklmn}^{(\Omega_1)}(\mathbf{0}) + \frac{1}{2}\frac{\partial^2}{\partial x_p \partial x_q} S_{ijklmn}^{(\Omega_1)}(\mathbf{0})\, x_p x_q \\ \overline{S}_{ijkl}^{(\Omega_2)}(\overline{\mathbf{x}}) &= \overline{S}_{ijkl}^{(\Omega_2)}\left(\overline{\mathbf{0}}\right) \\ \overline{S}_{ijklm}^{(\Omega_2)}(\overline{\mathbf{x}}) &= \frac{\partial}{\partial \overline{x}_{\mathrm{q}}} \overline{S}_{ijklm}^{(\Omega_2)}\left(\overline{\mathbf{0}}\right) \overline{x}_q \\ \overline{S}_{ijklmn}^{(\Omega_2)}(\overline{\mathbf{x}}) &= \overline{S}_{ijklmn}^{(\Omega_2)}\left(\overline{\mathbf{0}}\right) + \frac{1}{2}\frac{\partial^2}{\partial \overline{x}_p \partial \overline{x}_q} \overline{S}_{ijklmn}^{(\Omega_2)}\left(\overline{\mathbf{0}}\right) \overline{x}_p \overline{x}_q\end{aligned} \tag{13.19}$$

for $\mathbf{x} \in \Omega_1$ and $\overline{\mathbf{x}} \in \Omega_2$.

However, the Eshelby tensors $S^{(\Omega_1)}$'s and $S^{(\Omega_2)}$'s are not polynomials of $\mathbf{x}$ and $\overline{\mathbf{x}}$ outside Ω_1 and Ω_2 or inside Ω_2 and Ω_1, respectively. Thus, the disturbance strain fields $\Delta\varepsilon_{ij}^{\mathrm{H}(\Omega_1)}$ and $\Delta\overline{\varepsilon}_{ij}^{\mathrm{H}(\Omega_2)}$ inside the respective region Ω_2 and Ω_1 due to the eigenstrain $\varepsilon_{kl}^{*(\Omega_1)}$ and $\overline{\varepsilon}_{kl}^{*(\Omega_2)}$ can only be approximated by a polynomials of $\overline{\mathbf{x}}$ or $\mathbf{x}$ by Taylor series expansion around points $\overline{\mathbf{0}}$ or $\mathbf{0}$, respectively, and appropriate coordinate transformation as:

$$\begin{aligned}\Delta\overline{\varepsilon}_{ij}^{(\Omega_1)}(\overline{\mathbf{x}}) &= T_{ri}T_{sj}\left[S_{rskl}^{(\Omega_1)}(\overline{\mathbf{0}}) + T_{pu}\frac{\partial}{\partial x_p}S_{rskl}^{(\Omega_1)}(\overline{\mathbf{0}})\overline{x}_u + \frac{1}{2!}T_{pu}T_{qv}\frac{\partial^2}{\partial x_p\partial x_q}S_{rskl}^{(\Omega_1)}(\overline{\mathbf{0}})\overline{x}_u\overline{x}_v\right]F_{kl} + \cdots \\ &+ T_{ri}T_{sj}\left[S_{rsklm}^{(\Omega_1)}(\overline{\mathbf{0}}) + T_{pu}\frac{\partial}{\partial x_p}S_{rsklm}^{(\Omega_1)}(\overline{\mathbf{0}})\overline{x}_u + \frac{1}{2!}T_{pu}T_{qv}\frac{\partial^2}{\partial x_p\partial x_q}S_{rsklm}^{(\Omega_1)}(\overline{\mathbf{0}})\overline{x}_u\overline{x}_v\right]F_{klm} + \cdots \\ &+ T_{ri}T_{sj}\left[S_{rsklmn}^{(\Omega_1)}(\overline{\mathbf{0}}) + T_{pu}\frac{\partial}{\partial x_p}S_{rsklmn}^{(\Omega_1)}(\overline{\mathbf{0}})\overline{x}_u + \frac{1}{2!}T_{pu}T_{qv}\frac{\partial^2}{\partial x_p\partial x_q}S_{rsklmn}^{(\Omega_1)}(\overline{\mathbf{0}})\overline{x}_u\overline{x}_v\right]F_{klmn} + \cdots\end{aligned} \tag{13.20}$$

$$\begin{aligned}\Delta\overline{\varepsilon}_{ij}^{(\Omega_2)}(\mathbf{x}) &= T_{ir}T_{js}\left[\overline{S}_{rskl}^{(\Omega_2)}(\mathbf{0}) + T_{up}\frac{\partial}{\partial\overline{x}_p}\overline{S}_{rskl}^{(\Omega_2)}(\mathbf{0})x_u + \frac{1}{2!}T_{up}T_{vq}\frac{\partial^2}{\partial\overline{x}_p\partial\overline{x}_q}\overline{S}_{rskl}^{(\Omega_2)}(\mathbf{0})x_ux_v\right]\overline{F}_{kl} + \cdots \\ &+ T_{ir}T_{js}\left[\overline{S}_{rsklm}^{(\Omega_2)}(\mathbf{0}) + T_{up}\frac{\partial}{\partial\overline{x}_p}\overline{S}_{rsklm}^{(\Omega_2)}(\mathbf{0})x_u + \frac{1}{2!}T_{up}T_{vq}\frac{\partial^2}{\partial\overline{x}_p\partial\overline{x}_q}\overline{S}_{rsklm}^{(\Omega_2)}(\mathbf{0})x_ux_v\right]\overline{F}_{klm} + \cdots \\ &+ T_{ir}T_{js}\left[\overline{S}_{rsklmn}^{(\Omega_2)}(\mathbf{0}) + T_{up}\frac{\partial}{\partial\overline{x}_p}\overline{S}_{rsklmn}^{(\Omega_2)}(\mathbf{0})x_u + \frac{1}{2!}T_{up}T_{vq}\frac{\partial^2}{\partial\overline{x}_p\partial\overline{x}_q}\overline{S}_{rsklmn}^{(\Omega_2)}(\mathbf{0})x_ux_v\right]\overline{F}_{klmn} + \cdots\end{aligned}$$

for $\mathbf{x}\in\Omega_1$ and $\overline{\mathbf{x}}\in\Omega_2$.

It is worthy to note that in the above equation $S_{ijkl}^{(\Omega_1)}(\overline{\mathbf{0}})$, $S_{ijklm}^{(\Omega_1)}(\overline{\mathbf{0}})$ and $S_{ijklmn}^{(\Omega_1)}(\overline{\mathbf{0}})$ are the Eshelby tensors of the inclusion Ω_1 due to the eigenstrain $\varepsilon_{kl}^{*(\Omega_1)}$ evaluated at point $(\overline{\mathbf{0}})$ inside Ω_2 with their components referring to x_i-coordinates while $\Delta\overline{\varepsilon}_{ij}^{H(\Omega_1)}(\overline{\mathbf{x}})$ is the disturbance strain due to the eigenstrain $\varepsilon_{kl}^{*(\Omega_1)}$ but evaluated at an arbitrary point $\overline{\mathbf{x}}$ inside Ω_2 and with their tensor components referring to $\overline{x}_i$-coordinates. Similarly, $\overline{S}_{ijkl}^{(\Omega_2)}(\mathbf{0})$, $\overline{S}_{ijklm}^{(\Omega_2)}(\mathbf{0})$ and $\overline{S}_{ijklmn}^{(\Omega_2)}(\mathbf{0})$ are the Eshelby tensors of the inclusion Ω_2 due to eigenstrain $\varepsilon_{kl}^{*(\Omega_2)}$ evaluated at point $\mathbf{0}$ inside Ω_1 with their components referring to $\overline{x}_i$-coordinates, and $\Delta\varepsilon_{ij}^{H(\Omega_2)}(\mathbf{x})$ is the corresponding disturbance strain evaluated at point $\mathbf{x}$ inside Ω_1 with tensor components referring to x_i-coordinates.

Substituting Equations (13.17)–(13.20) into Equation (13.16), noting that $\Delta\varepsilon_{ij}^{\mathrm{H}}$ is the sum of $\Delta\varepsilon_{ij}^{\mathrm{H}(\Omega_1)}$ and $\Delta\overline{\varepsilon}_{ij}^{\mathrm{H}(\Omega_2)}$, and equating the coefficients of the power series of the right-and left-hand sides of the resulting equation yield the following system of algebraic equations for solving the equivalent eigenstrains $F^{(\Omega_1)}$'s and $\overline{F}^{(\Omega_2)}$'s:

$$\begin{aligned}&\Delta C_{stmn}^{\mathrm{I}(\Omega_1)}\left\{\left[S_{mnij}^{(\Omega_1)}(\mathbf{0})F_{ij}^{(\Omega_1)} + S_{mnijkl}^{(\Omega_1)}(\mathbf{0})F_{ijkl}^{(\Omega_1)} + \cdots\right]\right. \\ &\quad\left. + T_{mc}T_{nh}\left[\overline{S}_{chij}^{(\Omega_2)}(\mathbf{0})\overline{F}_{ij}^{(\Omega_2)} + \overline{S}_{chijk}^{(\Omega_2)}(\mathbf{0})\overline{F}_{ijk}^{(\Omega_2)} + \overline{S}_{chijkl}^{(\Omega_2)}(\mathbf{0})\overline{F}_{ijkl}^{(\Omega_2)} + \cdots\right]\right\} \\ &\quad - C_{stmn}^{\mathrm{s}}F_{mn}^{(\Omega_1)} = -\Delta C_{stmn}^{\mathrm{I}(\Omega_1)}\varepsilon_{\infty mn}\end{aligned}$$

$$\Delta C^{\mathrm{I}(\Omega_1)}_{stmn}\left\{\left[\frac{\partial}{\partial x_p}S^{(\Omega_1)}_{mnijk}(\mathbf{0})F^{(\Omega_1)}_{ijk}+\cdots\right]\right.$$

$$\left.+T_{mc}T_{nh}T_{pf}\left[\frac{\partial}{\partial \overline{x}_f}\overline{S}^{(\Omega_2)}_{chij}(\mathbf{0})\overline{F}^{(\Omega_2)}_{ij}+\frac{\partial}{\partial \overline{x}_f}\overline{S}^{(\Omega_2)}_{chijk}(\mathbf{0})\overline{F}^{(\Omega_2)}_{ijk}+\frac{\partial}{\partial \overline{x}_f}\overline{S}^{(\Omega_2)}_{chijkl}(\mathbf{0})\overline{F}^{(\Omega_2)}_{ijkl}+\cdots\right]\right\}$$

$$-C^{\mathrm{s}}_{stmn}F^{(\Omega_1)}_{mnp}=0$$

$$\frac{1}{2!}\Delta C^{\mathrm{I}(\Omega_1)}_{stmn}\left\{\left[\frac{\partial^2}{\partial x_p\partial x_q}S^{(\Omega_1)}_{mnijk}(\mathbf{0})F^{(\Omega_1)}_{ijk}+\cdots\right]+T_{mc}T_{nh}T_{pf}T_{qg}\right.$$

$$\left.\left[\frac{\partial^2}{\partial \overline{x}_f\partial \overline{x}_g}\overline{S}^{(\Omega_2)}_{chij}(\mathbf{0})\overline{F}^{(\Omega_2)}_{ij}+\frac{\partial^2}{\partial \overline{x}_f\partial \overline{x}_g}\overline{S}^{(\Omega_2)}_{chijk}(\mathbf{0})\overline{F}^{(\Omega_2)}_{ijk}+\frac{\partial^2}{\partial \overline{x}_f\partial \overline{x}_g}\overline{S}^{(\Omega_2)}_{chijkl}(\mathbf{0})\overline{F}^{(\Omega_2)}_{ijkl}+\cdots\right]\right\}$$

$$-C^{\mathrm{s}}_{stmn}F^{(\Omega_1)}_{mnpq}=0 \tag{13.21}$$

$$\Delta C^{\mathrm{I}(\Omega_2)}_{stmn}\left\{T_{cm}T_{hn}\left[S^{(\Omega_1)}_{chij}(\overline{\mathbf{0}})F^{(\Omega_1)}_{ij}+S^{(\Omega_1)}_{chijk}(\overline{\mathbf{0}})F^{(\Omega_1)}_{ijk}+S^{(\Omega_1)}_{chijkl}(\overline{\mathbf{0}})F^{(\Omega_1)}_{ijkl}+\cdots\right]\right.$$

$$\left.+\left[\overline{S}^{(\Omega_2)}_{mnij}(\overline{\mathbf{0}})\overline{F}^{(\Omega_2)}_{ij}+\overline{S}^{(\Omega_2)}_{mnijkl}(\overline{\mathbf{0}})\overline{F}^{(\Omega_2)}_{ijkl}+\cdots\right]\right\}$$

$$-C^{\mathrm{s}}_{stmn}\overline{F}^{(\Omega_2)}_{mn}=-\Delta C^{\mathrm{I}(\Omega_2)}_{stmn}\varepsilon_{\infty mn}$$

$$\Delta C^{\mathrm{I}(\Omega_2)}_{stmn}\left\{T_{cm}T_{hn}T_{fp}\left[\frac{\partial}{\partial x_f}S^{(\Omega_1)}_{chij}(\overline{0})F^{(\Omega_1)}_{ij}+\frac{\partial}{\partial x_f}S^{(\Omega_1)}_{chijk}(\overline{\mathbf{0}})F^{(\Omega_1)}_{ijk}\right.\right.$$

$$\left.\left.+\frac{\partial}{\partial x_f}S^{(\Omega_1)}_{chijkl}(\overline{\mathbf{0}})F^{(\Omega_1)}_{ijkl}+\cdots\right]+\left[\frac{\partial}{\partial \overline{x}_f}\overline{S}^{(\Omega_2)}_{mnijkl}(\overline{\mathbf{0}})\overline{F}^{(\Omega_2)}_{ijkl}+\cdots\right]\right\}$$

$$-C^{\mathrm{s}}_{stmn}\overline{F}^{(\Omega_2)}_{mnp}=0$$

$$\frac{1}{2!}\Delta C^{\mathrm{I}(\Omega_2)}_{stmn}\left\{T_{cm}T_{hn}T_{fp}T_{gq}\left[\frac{\partial^2}{\partial x_f\partial x_g}S^{(\Omega_1)}_{chij}(\overline{\mathbf{0}})F^{(\Omega_1)}_{ij}+\frac{\partial^2}{\partial x_f\partial x_g}S^{(\Omega_1)}_{chijk}(\overline{\mathbf{0}})F^{(\Omega_1)}_{ijk}\right.\right.$$

$$\left.\left.+\frac{\partial^2}{\partial x_f\partial x_g}S^{(\Omega_1)}_{chijkl}(\overline{\mathbf{0}})F^{(\Omega_1)}_{ijkl}+\cdots\right]+\left[\frac{\partial^2}{\partial \overline{x}_p\partial \overline{x}_q}\overline{S}^{(\Omega_2)}_{mnijkl}(\overline{\mathbf{0}})\overline{F}^{(\Omega_2)}_{ijkl}+\cdots\right]\right\}$$

$$-C^{\mathrm{s}}_{stmn}\overline{F}^{(\Omega_2)}_{mnpq}=0$$

Once the eigenstrains are determined, the stress and strain fields in the equivalent inclusion problem and thus in the inhomogeneity problem can be evaluated by Equations (13.16) and (13.18). The stresses and strains in the patch and in the skin under the patch can be determined from the strain field $\varepsilon^{\mathrm{I}}_{ij}$ in a similar manner as in Chapter 4

by using the classical laminate theory applying to the skin–patch combination. The original problem of two inhomogeneities in proximity is therefore completely solved.

13.3 Effect of Adherend Shear Deformation on Repair Efficiency

One effect related to thick patches is the effect of shear deformations in the skin and patch on the repair efficiency. In Chapter 3, the stress intensity factor is estimated for a supported one-sided or two-sided repair by using either an energy argument or a crack bridging model. In either way, pertinent results from theory of bonded joints and doublers presented in Chapter 2 are used in that estimate. However, for simplicity, only classical solutions of these bonded joints and doublers are developed in Chapter 2, and they ignore the shear deformations in the adherends. The adhesive layer can sustain significant shear stresses during load transfer. These large shear stresses would also be present at the interface between the adherend and the adhesive, and they would cause the adherend shear deformations. For thick patches with low transverse shear modulus such as laminated composite patches, their shear deformations will be significant, which will reduce the efficiency of the repair. This section is therefore devoted to address the effect of adherend shear deformation on the repair efficiency. However, for demonstration purpose, this effect will only be examined in detail within the context of the crack bridging model delineated in Section 3.3.4 for a two-sided or a supported one-sided repair.

It was shown in Section 3.3.4 that the constraint imposed by the bonded patch on the opening of the crack is simulated by a distribution of springs across the crack surfaces. These springs have a spring constant Λ given by

$$\sigma_0 = E_s \Lambda \bar{u}_s \tag{13.22}$$

where σ_0 is the stress in the skin at the perspective crack location of an uncracked geometry, E_s and $\bar{u}_s$ are the Young's modulus and the crack opening displacement (averaging through the thickness) of the skin, respectively. Equivalently, Λ can be defined in terms of the complementary energy via the following relation:

$$U_c = \frac{1}{2}\sigma_0 \bar{u}_s = \frac{1}{2}\frac{\sigma_0^2}{E_s \Lambda} \tag{13.23}$$

In the first approach, Λ will be derived from the stress analysis of a double-strap joint using Equation (13.22), accounting for the adherend shear deformations. This analysis follows the work of Tsai et al. (1998). Let us consider a double-strap joint shown in Figure 13.5. From equilibrium consideration of differential elements of the skin, patch, and adhesive, one obtains

$$\begin{aligned} \frac{dN_p}{dx} - \tau^{(A)} &= 0 \\ \frac{dN_s}{dx} + \tau^{(A)} &= 0 \end{aligned} \tag{13.24}$$

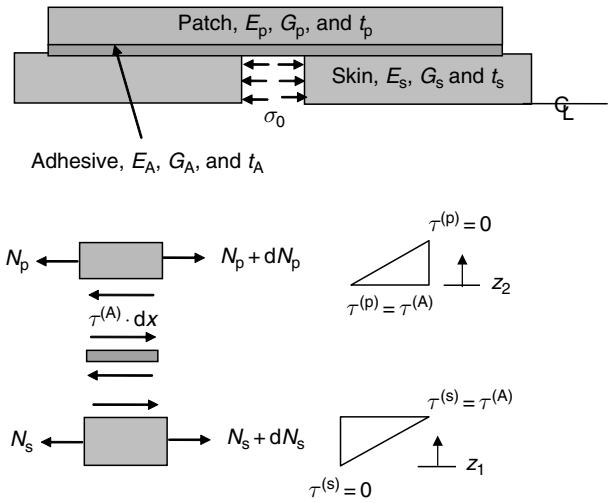

Fig. 13.5. Geometry of a semi-infinite double-strap joint used to derive the spring constant of the crack-bridging model, accounting for adherend shear deformations.

where N is the normal stress resultant, τ_A is the adhesive shear stress which is assumed to be uniform across the adhesive thickness, subscripts s and p indicate skin and patch, respectively. Shear deformations of the skin and the patch are accounted for in the present formulation by assuming that the shear stress or strain distribution through the thickness of the skin or patch is linear. It then follows that

$$\begin{aligned} \tau^{(s)} &= \frac{\tau^{(A)} z_1}{t_s} \quad \gamma^{(s)} = \frac{\tau^{(A)} z_1}{G_s t_s} \\ \tau^{(p)} &= \tau^{(A)} \left(1 - \frac{z_2}{t_p}\right) \quad \gamma^{(p)} = \frac{\tau^{(A)}}{G_p} \left(1 - \frac{z_2}{t_p}\right) \end{aligned} \tag{13.25}$$

where G and t are the shear modulus and thickness, respectively, and the rest have been previously defined. The axial displacement in the skin is obtained from the kinematics relation and (13.25) as

$$\begin{aligned} u_s(z_1) &= \int \frac{du_s}{dz_1} dz_1 = \int \gamma^{(s)} dz_1 = u_{so} + \int_0^{z_1} \gamma^{(s)}(z_1') \, dz_1' \\ &= u_{so} + \frac{\tau^{(A)} z_1^2}{2 G_s t_s} \end{aligned} \tag{13.26}$$

By defining u_{si} as the skin displacement at the skin–adhesive interface, from Equation (13.26),

$$u_{si} = u_s(z_1 = t_s) = u_{so} + \frac{\tau^{(A)} t_s}{2 G_s} \tag{13.27}$$

Thus, Equation (13.26) can be rewritten as

$$u_{\mathrm{s}} = u_{\mathrm{si}} - \frac{\tau^{(\mathrm{A})} t_{\mathrm{s}}}{2G_{\mathrm{s}}} + \frac{\tau^{(\mathrm{A})} z_1^2}{2G_{\mathrm{s}} t_{\mathrm{s}}} \tag{13.28}$$

Similarly, the displacement of the patch is given by

$$\begin{aligned} u_{\mathrm{p}} &= u_{\mathrm{pi}} + \int_0^{z_2} \gamma^{(\mathrm{p})}(z_2')\mathrm{d}z_2' \\ &= u_{\mathrm{pi}} + \frac{\tau^{(\mathrm{A})}}{G_{\mathrm{p}}}\left(z_2 - \frac{z_2^2}{2t_{\mathrm{p}}}\right) \end{aligned} \tag{13.29}$$

where $u_{\mathrm{pi}} \equiv u_{\mathrm{p}}\,(z_2 = 0)$ is the patch displacement at the patch–adhesive interface. On the other hand, constitutive relations of the skin and patch, Equations (13.28) and (13.29) provide

$$\begin{aligned} N_{\mathrm{s}} &= E_{\mathrm{s}}' \int_0^{t_{\mathrm{s}}} \frac{\mathrm{d}u_{\mathrm{s}}}{\mathrm{d}x}\mathrm{d}z_1 = E_{\mathrm{s}}' t_{\mathrm{s}}\left(\frac{\mathrm{d}u_{\mathrm{si}}}{\mathrm{d}x} - \frac{1}{3}\frac{t_{\mathrm{s}}}{G_{\mathrm{s}}}\frac{\mathrm{d}\tau^{(\mathrm{A})}}{\mathrm{d}x}\right) \\ N_{\mathrm{p}} &= E_{\mathrm{p}}' \int_0^{t_{\mathrm{p}}} \frac{\mathrm{d}u_{\mathrm{p}}}{\mathrm{d}x}\mathrm{d}z_2 = E_{\mathrm{p}}' t_{\mathrm{p}}\left(\frac{\mathrm{d}u_{\mathrm{pi}}}{\mathrm{d}x} + \frac{1}{3}\frac{t_{\mathrm{p}}}{G_{\mathrm{p}}}\frac{\mathrm{d}\tau^{(\mathrm{A})}}{\mathrm{d}x}\right) \end{aligned} \tag{13.30}$$

where $E_{\mathrm{s,p}}' = \frac{E_{\mathrm{s,p}}}{1-\nu_{\mathrm{s,p}}^2}$. Similarly, the kinematics and constitutive relations of the adhesive are given by

$$\begin{aligned} \gamma^{(\mathrm{A})} &= \frac{1}{t_{\mathrm{A}}}\left(u_{\mathrm{pi}} - u_{\mathrm{si}}\right) \\ \tau^{(\mathrm{A})} &= \frac{G_{\mathrm{A}}}{t_{\mathrm{A}}}\left(u_{\mathrm{pi}} - u_{\mathrm{si}}\right) \end{aligned} \tag{13.31}$$

Thus,

$$\frac{\mathrm{d}\tau^{(\mathrm{A})}}{\mathrm{d}x} = \frac{G_{\mathrm{A}}}{t_{\mathrm{A}}}\left(\frac{\mathrm{d}u_{\mathrm{pi}}}{\mathrm{d}x} - \frac{\mathrm{d}u_{\mathrm{si}}}{\mathrm{d}x}\right) \tag{13.32}$$

Substitution of Equation (13.30) for $\frac{\mathrm{d}u_{\mathrm{si}}}{\mathrm{d}x}$ and $\frac{\mathrm{d}u_{\mathrm{pi}}}{\mathrm{d}x}$ into (13.32) results in the following equation.

$$\frac{\mathrm{d}\tau^{(\mathrm{A})}}{\mathrm{d}x} = \frac{G_{\mathrm{A}}}{t_{\mathrm{A}}}\left[\frac{N_{\mathrm{p}}}{E_{\mathrm{p}}' t_{\mathrm{p}}} - \frac{N_{\mathrm{s}}}{E_{\mathrm{s}}' t_{\mathrm{s}}} - \frac{\mathrm{d}\tau^{(\mathrm{A})}}{\mathrm{d}x}\left(\frac{t_{\mathrm{p}}}{3G_{\mathrm{p}}} + \frac{t_{\mathrm{s}}}{3G_{\mathrm{s}}}\right)\right] \tag{13.33}$$

Differentiating Equation (13.33) with respect to x and substituting Equation (13.24) into the resulting equation for $\frac{\mathrm{d}N_{\mathrm{p}}}{\mathrm{d}x}$ and $\frac{\mathrm{d}N_{\mathrm{s}}}{\mathrm{d}x}$ yield

$$\frac{\mathrm{d}^2\tau^{(\mathrm{A})}}{\mathrm{d}x^2}\left[1 + \frac{G_{\mathrm{A}}}{t_{\mathrm{A}}}\left(\frac{t_{\mathrm{p}}}{3G_{\mathrm{p}}} + \frac{t_{\mathrm{s}}}{3G_{\mathrm{s}}}\right)\right] - \frac{G_{\mathrm{A}}}{t_{\mathrm{A}}}\left(\frac{1}{E_{\mathrm{p}}' t_{\mathrm{p}}} + \frac{1}{E_{\mathrm{s}}' t_{\mathrm{s}}}\right)\tau^{(\mathrm{A})} = 0 \tag{13.34}$$

or

$$\frac{\mathrm{d}^2\tau^{(\mathrm{A})}}{\mathrm{d}x^2} - \tilde{\beta}_{\mathrm{A}}^2\tau^{(\mathrm{A})} = 0 \tag{13.35}$$

where

$$\tilde{\beta}_{\mathrm{A}}^2 = \frac{\frac{G_{\mathrm{A}}}{t_{\mathrm{A}}}\left(\frac{1}{E_{\mathrm{p}}' t_{\mathrm{p}}} + \frac{1}{E_{\mathrm{s}}' t_{\mathrm{s}}}\right)}{1 + \frac{G_{\mathrm{A}}}{t_{\mathrm{A}}}\left(\frac{t_{\mathrm{p}}}{3G_{\mathrm{p}}} + \frac{t_{\mathrm{s}}}{3G_{\mathrm{s}}}\right)} \tag{13.36}$$

Equation (13.35) is similar to Equation (2.5) of the classical theory, except that the inverse load transfer length β_{A} has been modified to become $\tilde{\beta}_{\mathrm{A}}$ as given by (13.36). For a semi-infinite domain, the solution of Equation (13.35) is given by

$$\tau^{(\mathrm{A})} = \tau_{\max}^{(\mathrm{A})} \mathrm{e}^{-\tilde{\beta}_{\mathrm{A}} x} \tag{13.37}$$

$\tau_{\max}^{(\mathrm{A})}$ in Equation (13.37) then can be determined from the following boundary condition:

$$\int_0^{\infty} \tau^{(\mathrm{A})} \mathrm{d}x = -\sigma_0 t_{\mathrm{s}} \tag{13.38}$$

which essentially states that the total shear load in the adhesive layer must be equal to the total load in the skin at the joint end before transferring all of it to the patch. Substituting Equation (13.37) into (13.38) and performing the integration yield

$$\begin{aligned} \tau_{\max}^{(\mathrm{A})} &= -\sigma_0 t_{\mathrm{s}} \tilde{\beta}_{\mathrm{A}} \\ \tau^{(\mathrm{A})} &= -\sigma_0 t_{\mathrm{s}} \tilde{\beta}_{\mathrm{A}} \mathrm{e}^{-\tilde{\beta}_{\mathrm{A}} x} \end{aligned} \tag{13.39}$$

It remains now to determine the average displacement of the skin through its thickness at the joint end, i.e., $x = 0$. From Equation (13.28) and the second equation of (13.31), by noting that $u_{\mathrm{pi}}(x = 0) = 0$ due to symmetry, it is very easy to show that

$$\begin{aligned} u_{\mathrm{s}}(x = 0) &= u_{\mathrm{si}}(0) - \frac{\tau^{(\mathrm{A})}(0)\, t_{\mathrm{s}}}{2G_{\mathrm{s}}} + \frac{\tau^{(\mathrm{A})}(0)\, z_1^2}{2G_{\mathrm{s}} t_{\mathrm{s}}} \\ u_{\mathrm{si}}(0) &= -\frac{t_{\mathrm{A}}}{G_{\mathrm{A}}}\tau^{(\mathrm{A})}(0) \end{aligned} \tag{13.40}$$

or

$$u_{\mathrm{s}}(x = 0) = -\frac{t_{\mathrm{A}}}{G_{\mathrm{A}}}\tau^{(\mathrm{A})}(0) - \frac{\tau^{(\mathrm{A})}(0)\, t_{\mathrm{s}}}{2G_{\mathrm{s}}} + \frac{\tau^{(\mathrm{A})}(0)\, z_1^2}{2G_{\mathrm{s}} t_{\mathrm{s}}} \tag{13.41}$$

Evaluation of the second equation of (13.39) at $x = 0$ and substitution of the result for $\tau^{(\mathrm{A})}(0)$ into the above equation yield

$$u_{\mathrm{s}}(x = 0) = \sigma_0 t_{\mathrm{s}} \tilde{\beta}_{\mathrm{A}} \left[\frac{t_{\mathrm{A}}}{G_{\mathrm{A}}} + \frac{t_{\mathrm{s}}}{2G_{\mathrm{s}}} - \frac{z_1^2}{2G_{\mathrm{s}} t_{\mathrm{s}}}\right] \tag{13.42}$$

With that, the average displacement of the skin at the joint end through its thickness is found to be

$$\overline{u}_{\mathrm{s}}(0)=\frac{1}{t_{\mathrm{s}}}\int_{0}^{t_{\mathrm{s}}}u_{\mathrm{s}}(x=0,z_1)\,\mathrm{d}z_1=\sigma_0 t_{\mathrm{s}}\tilde{\beta}_{\mathrm{A}}\left[\frac{t_{\mathrm{s}}}{3G_{\mathrm{s}}}+\frac{t_{\mathrm{A}}}{G_{\mathrm{A}}}\right] \tag{13.43}$$

The spring constant Λ of the crack-bridging model is finally determined from Equations (13.22) and (13.43) as

$$\Lambda=\frac{1}{E_{\mathrm{s}}t_{\mathrm{s}}\tilde{\beta}_{\mathrm{A}}\left[\frac{t_{\mathrm{s}}}{3G_{\mathrm{s}}}+\frac{t_{\mathrm{A}}}{G_{\mathrm{A}}}\right]} \tag{13.44}$$

It is clear from Equation (13.44) that the spring constant Λ will have a smaller numerical value than that predicted by the classical theory since $\tilde{\beta}_{\mathrm{A}}>\beta_{\mathrm{A}}$ and $\frac{t_{\mathrm{s}}}{3G_{\mathrm{s}}}+\frac{t_{\mathrm{A}}}{G_{\mathrm{A}}}>\frac{t_{\mathrm{A}}}{G_{\mathrm{A}}}$. Thus, according to the double-strap joint model that accounts for the adherend shear deformation, a patch will be less effective in restraining the crack-opening displacement than it would be based on the classical model since the system of springs idealizing the patch based on the former model are softer or more compliant than those derived based on the latter model.

It was pointed out by Chalkley and Rose (1998, 2001) that the above approach to determine the spring constant may not always give a conservative estimate for Λ. For a conservative estimate of a spring constant Λ, another approach based on Chalkley and Rose's work which in turn is an extension of the Hashin variational method should be employed. A brief discussion of this variational approach will be presented here. Chalkley and Rose's analysis begins by assuming the stress states in the skin, patch, and adhesive can be expressed in term of a single stress potential $\tilde{\phi}$ as

Skin

$$\begin{aligned}\sigma_{xx}^{(\mathrm{s})}&=-\sigma_0\tilde{\phi}(x)\\ \sigma_{zx}^{(\mathrm{s})}&=\sigma_0\tilde{\phi}'(x)\,z\\ \sigma_{zz}^{(\mathrm{s})}&=\frac{1}{2}\sigma_0\tilde{\phi}''(x)\left[t_{\mathrm{s}}\left(t_{\mathrm{s}}+t_{\mathrm{p}}\right)-z^2\right]\end{aligned} \tag{13.45}$$

Patch

$$\begin{aligned}\sigma_{xx}^{(\mathrm{p})}&=\frac{t_{\mathrm{s}}}{t_{\mathrm{p}}}\sigma_0\tilde{\phi}(x)\\ \sigma_{zx}^{(\mathrm{p})}&=\frac{t_{\mathrm{s}}}{t_{\mathrm{p}}}\sigma_0\tilde{\phi}'(x)\left(t_{\mathrm{s}}+t_{\mathrm{p}}+t_{\mathrm{A}}-z\right)\\ \sigma_{zz}^{(\mathrm{p})}&=\frac{1}{2}\frac{t_{\mathrm{s}}}{t_{\mathrm{p}}}\sigma_0\tilde{\phi}''(x)\left[t_{\mathrm{s}}+t_{\mathrm{p}}+t_{\mathrm{A}}-z\right]^2\end{aligned} \tag{13.46}$$

Adhesive

$$\begin{aligned}\sigma_{xx}^{(\mathrm{A})} &= 0\\ \sigma_{zx}^{(\mathrm{A})} &= \sigma_0 t_\mathrm{s}\tilde{\phi}'(x)\\ \sigma_{zz}^{(\mathrm{A})} &= \frac{1}{2}\sigma_0 t_\mathrm{s} t_\mathrm{p}\tilde{\phi}''(x)\end{aligned} \tag{13.47}$$

It is worthy to note that the above assumed stress states ensure continuity of the σ_{xz} and σ_{zz} stresses across the patch/adhesive and skin/adhesive interfaces. For a semi-infinite joint, the complementary energy is given by

$$2U_\mathrm{c} = \int_0^{t_\mathrm{s}+t_\mathrm{A}+t_\mathrm{p}} \mathrm{d}z \int_0^{\infty} W(x,z)\mathrm{d}x \tag{13.48}$$

where $W(x,z)$ is the strain energy density. $W(x,z)$ can be expressed in terms of stresses as

$$W(x,z) = \frac{1}{2}\left(\frac{\sigma_{xx}^2}{E'} + \frac{\sigma_{zz}^2}{E'} + \frac{\sigma_{xz}^2}{G} - 2\frac{\nu}{E'}\sigma_{xx}\sigma_{zz}\right) \tag{13.49}$$

Substituting Equations (13.45)–(13.47) and (13.49) into (13.48) and performing the first integration through the thickness lead to

$$2U_\mathrm{c} = \sigma_0^2 t_\mathrm{s}^2 \int \left(A_0\tilde{\phi}^2(x) + A_1\tilde{\phi}'(x)^2 + A_2\phi(x)\tilde{\phi}'(x) + A_3\tilde{\phi}''(x)^2\right)\mathrm{d}x \tag{13.50}$$

where

$$\begin{aligned}A_0 &= \frac{1}{E'_\mathrm{s}t_\mathrm{s}} + \frac{1}{E'_\mathrm{p}t_\mathrm{p}}\\ A_1 &= \frac{t_\mathrm{A}}{G_\mathrm{A}} + \frac{t_\mathrm{s}}{3G_\mathrm{s}} + \frac{t_\mathrm{p}}{3G_\mathrm{p}}\\ A_2 &= \frac{1}{3E_\mathrm{s}E_\mathrm{p}}\left[\left(2t_\mathrm{s}+3t_\mathrm{p}\right)E_\mathrm{p}\nu_\mathrm{s}\left(1+\nu_\mathrm{s}\right) - t_\mathrm{p}E_\mathrm{s}\nu_\mathrm{p}\left(1+\nu_\mathrm{p}\right)\right]\\ A_3 &= \frac{t_\mathrm{s}}{4E'_\mathrm{s}}\left(\frac{8}{15}t_\mathrm{s}^2 + \frac{4}{3}t_\mathrm{s}t_\mathrm{p} + t_\mathrm{p}^2\right) + \frac{t_\mathrm{p}^3}{20E'_\mathrm{p}} + \frac{t_\mathrm{p}^2 t_\mathrm{A}}{4E'_\mathrm{A}}\end{aligned} \tag{13.51}$$

The governing differential equation for the stress potential ϕ can be derived by minimizing U_c given by Equation (13.50) through a variational analysis as

$$A_3\tilde{\phi}'''' + \left(A_2 - A_1\right)\tilde{\phi}'' + A_0\phi = 0 \tag{13.52}$$

The boundary conditions for Equation (13.52) are determined from the stress condition of the skin at the joint end, i.e.,

$$\sigma_{xx}^{(\mathrm{s})}(x=0) = -\sigma_0 \quad \text{or} \quad \tilde{\phi}(0) = 1 \tag{13.53}$$

and

$$\sigma_{xz}^{(s)}(x=0)=0 \quad \text{or} \quad \tilde{\phi}'(0)=0 \tag{13.54}$$

The solution of Equation (13.52) over the semi-infinite domain that satisfies boundary conditions (13.53) and (13.54) is

$$\phi(x)=-\frac{\beta_{\mathrm{A}}^{(\mathrm{II})}}{\beta_{\mathrm{A}}^{(\mathrm{I})}-\beta_{\mathrm{A}}^{(\mathrm{II})}}\mathrm{e}^{-\beta_{\mathrm{A}}^{(\mathrm{I})}x}+\frac{\beta_{\mathrm{A}}^{(\mathrm{I})}}{\beta_{\mathrm{A}}^{(\mathrm{I})}-\beta_{\mathrm{A}}^{(\mathrm{II})}}\mathrm{e}^{-\beta_{\mathrm{A}}^{(\mathrm{II})}x} \tag{13.55}$$

where

$$\begin{aligned}\beta_{\mathrm{A}}^{(\mathrm{I})}&=\sqrt{\frac{1}{2A_3}}\sqrt{(A_1-A_2)-\sqrt{(A_1-A_2)^2-4A_0A_3}}\\ \beta_{\mathrm{A}}^{(\mathrm{II})}&=\sqrt{\frac{1}{2A_3}}\sqrt{(A_1-A_2)+\sqrt{(A_1-A_2)^2-4A_0A_3}}\end{aligned} \tag{13.56}$$

Once the stress potential is determined, stresses in the skin, patch, and adhesive can be obtained from Equations (13.45)–(13.47) while the complementary energy can be evaluated from Equation (13.50) as

$$U_{\mathrm{c}}=\sigma_0^2t_{\mathrm{s}}^2\left[\frac{\left(\beta_{\mathrm{A}}^{(\mathrm{I})}\beta_{\mathrm{A}}^{(\mathrm{II})}\right)^2\left(A_1-A_2+A_3\beta_{\mathrm{A}}^{(\mathrm{I})}\beta_{\mathrm{A}}^{(\mathrm{II})}\right)+4A_0\left(\beta_{\mathrm{A}}^{(\mathrm{I})2}+3\beta_{\mathrm{A}}^{(\mathrm{I})}\beta_{\mathrm{A}}^{(\mathrm{II})}+\beta_{\mathrm{A}}^{(\mathrm{II})2}\right)}{4\beta_{\mathrm{A}}^{(\mathrm{I})}\beta_{\mathrm{A}}^{(\mathrm{II})}\left(\beta_{\mathrm{A}}^{(\mathrm{I})}+\beta_{\mathrm{A}}^{(\mathrm{II})}\right)}\right] \tag{13.57}$$

With that, the spring constant Λ finally can be easily derived from Equation (13.23) with U_{c} given by Equation (13.57).

CHAPTER 14

Concluding Remarks

As mentioned in Chapter 1, the goal of this book is to provide a theoretical foundation for the design and analysis of bonded repairs and bonded doublers. The preceding 13 chapters addressed various important issues pertinent to the repairs and at the same time introduced to the reader many powerful mathematical techniques borrowed from various branches of mechanics such as micromechanics of composite or heterogeneous materials, elasticity, plate theory, and fracture mechanics. However, the book is not complete since not all topics relevant to the field of bonded repairs are covered. These omissions are intended for one reason or another to limit the length of the book. One important topic that has been omitted from the book is the composite repair to composite structures, including a scarf repair. The topic does not fit well within the logical framework of the present book and perhaps it shall be included in another book which is devoted entirely to the subject of composite repairs to composite structures. Nevertheless, some of the methods and approaches developed herein clearly can be extended to include these latter repairs. For example, even though the formulation for the load attraction problem of an anisotropic skin bonded with an anisotropic patch under general loading may be simpler by using a new method known as Stroh formalism (Ting, 1996; Cheng and Reddy, 2004), the two-stage analysis approach delineated in Chapter 6 can be applied similarly to the composite repair of cut-out or grind-out cavity in a laminated skin (Wang and Duong, 2003). Similarly, the bond-line analysis developed in Chapter 7 can also be modified to analyze scarf joints or scarf repair within a one-dimensional approximation.

This book has been based mostly on the recent works by the authors during the last 10 years, and it was inspired by the original and significant contribution of Rose during the 1980s. The authors' works were carried out at the Boeing Company through a USAF contract entitled Composite Repair of Aircraft Structure (CRAS) and at the Defence Science and Technology Office (DSTO), respectively. These works have provided an analytical capability that (after implementation into software) not only yields a quick and easy way to design and analyze the bonded repairs but also explains the physics of the behavior of the repairs in general. However, as in any other major research programs, due to the limited budgets and/or beyond the scopes of these works, some

other important aspects of the bonded repairs still remain unaddressed and therefore require further research. Among them is the following short list:

- Investigating the failure mechanism and developing a test-validated failure criterion for patches in compression;
- Identifying design and analysis issues associated with thick structures and developing methods which will be validated through test to address these issues;
- Expanding existing repair methodologies to stress corrosion cracking and composite repairs to composite structures;
- Applications and demonstrations of the existing analytical methods on large and sub-components such as curved panels, heavy frames, bulkhead, and wing spars.

At the time this book was completed, some of these aspects were under investigation with a low level of funding effort, and few of them were addressed partially in Chapter 13. New results obtained from the current and future studies on these topics will be certainly incorporated into our book in the future when there is an opportunity for a book revision.

Appendix: Introduction to CRAS Software

Composite Repair of Aircraft Structures is an analysis/design software application for bonded composite repairs over damaged metallic structures. The repairs to be analyzed by CRAS may be a crack patching or a corrosion repair. CRAS provides users three main tools: an initial design tool based on simple closed-form solutions for an elliptical patch and results from 1-D bonded joint theory, a refined closed-form analysis tool where varying degrees of complexity are included in the formulation, and a rapid FE modeling tool. The repairs of complex structures, which are aircraft-specific such as splice joints, using the CRAS software are demonstrated in the appendices of Duong et al.'s report (2003a). Both design guidelines and FE techniques for these complex repairs are also provided there.

A.1 Brief Descriptions of CRAS Design and Analysis Tools

(a) Initial design

The CRAS initial design tool provides an initial design of the repaired patch based on user's inputs for the skin, patch and adhesive materials, design and fatigue loads, damage configuration (crack length, corrosion grind-out diameter and depth, hole), maximum number fatigue cycles, and preferred patch shape (octagon, ellipse or rectangle). CRAS designs a patch under biaxial loading, following the approaches described in Chapters 9 and 10. As mentioned in those two chapters, the effect of out-of-plane bending is not considered in the initial design.

(b) Refined closed-form analysis

The CRAS refined closed-form analysis tool provides the user with a quick, alternative method (without relying on FE analysis), to estimate the skin stresses at critical locations near the edge of the patch, K_I in crack patching, and K_t at the bottom of the corrosion cavity in corrosion repair. This analysis tool has a wide range of capabilities that were derived from various analytical models developed in Chapters 3–7. In particular, different analytical models developed in Chapters 3–7 to address various effects pertinent to a bonded repair were implemented into Fortran codes, and these Fortran codes were integrated into CRAS software as modules. The sources of these codes can also be found in the software package and they can be run independently with proper input files. The availability of

Table A.1. A sample list of analysis modules or Fortran codes used in CRAS analysis tool.

CRAS analysis module/Fortran code	Capability	Method
JMPSYY	Analysis of load attraction of a polygonal patch in a fully supported one-sided or two-sided repair	Equivalent inclusion method with second-ordered eigenstrain described in Chapter 4
STAGE2	Fracture analysis or stage II analysis of Rose's two-stage analysis procedure for a polygonal patch in a fully supported one-sided or two-sided repair	Displacement compatibility method and elasticity by complex stress function described in Chapter 4
JAMXX1	Analysis of load attraction of a polygonal patch in an unsupported one-sided repair	Plate inclusion model described in Chapter 5
BENDING	Fracture analysis or stage II analysis of Rose's two-stage analysis procedure for a polygonal patch in an unsupported one-sided repair	Crack-bridging model described in Chapter 5
JMPSYYCA	Two-stage analysis of a corrosion repair with a polygonal patch	Equivalent inclusion method with second ordered eigenstrain described in Chapter 6
CONSTHRM	Plane stress analysis of residual thermal stresses of a circular patch due to curing in a circular plate of finite size and with constrained edge	Wang et al. curing model described in Chapter 4
SINGLE	Plate-bending analysis of residual thermal stresses of a circular patch due to curing in a circular plate of finite size and with constrained edge	Wang et al. curing model described in Chapter 5
JOINT	Bond-line analysis near the end of a tapered patch	A unified approach for geometrically nonlinear analysis of bonded joints described in Chapter 7

these codes is intended to give a greater flexibility in using CRAS. Table A.1 lists a sample of the analysis modules or Fortran codes used in the CRAS analysis tool, along with their corresponding capability and their corresponding analytical model as described in Chapters 3–7.

(c) Rapid finite element modeler – PatchGen

PatchGen is a program designed to facilitate the creation of FE models of patch repairs of skin structure. It creates a session file that can then be played by

MSC/PATRAN (2001). The session file creates a bulk data deck that is the input for the MSC/NASTRAN solver (2001). After the solver has completed, the results file can be read back into MSC/PATRAN (2001) to view the results. PatchGen was used initially during the development phase of CRAS project to validate the formulations and predictions of the analytical methods discussed in Chapters 4–7 with FE results.

A.2 How to Use the CRAS Software Application

This section describes the use of the CRAS software application. The program is a PC-based Windows software application that is user-friendly with online help. For a detailed description of the software, the reader should refer to CRAS User Manual (2003). An example problem is also given there.

A.2.1 Starting the program

After installation, select the CRAS application from the Start Programs menu, or double-click on the first icon illustrated in Figure A.1 to start the CRAS program.

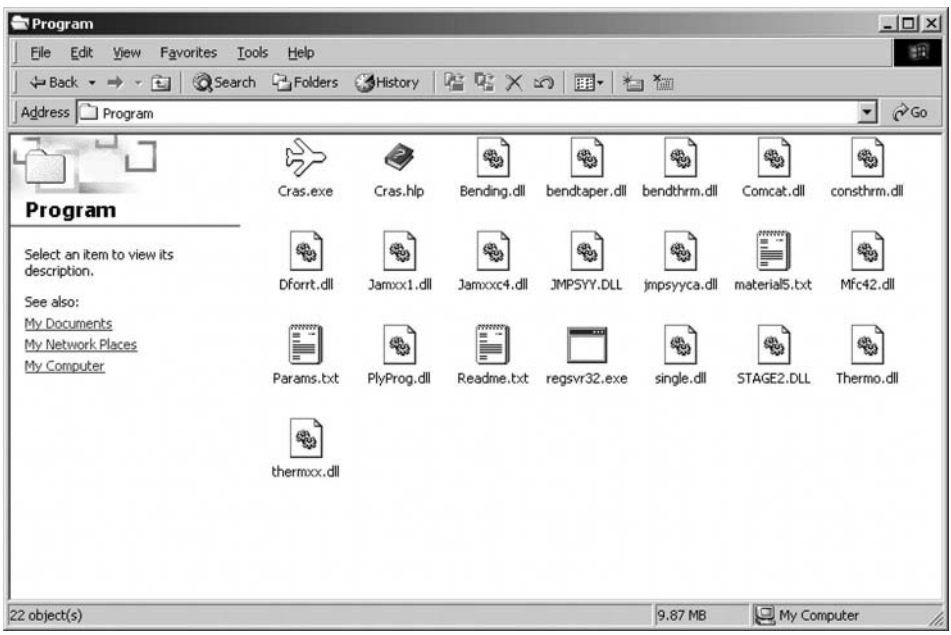

Fig. A.1. Program Windows directory.

The view shown in Figure A.2 is displayed as the opening screen:

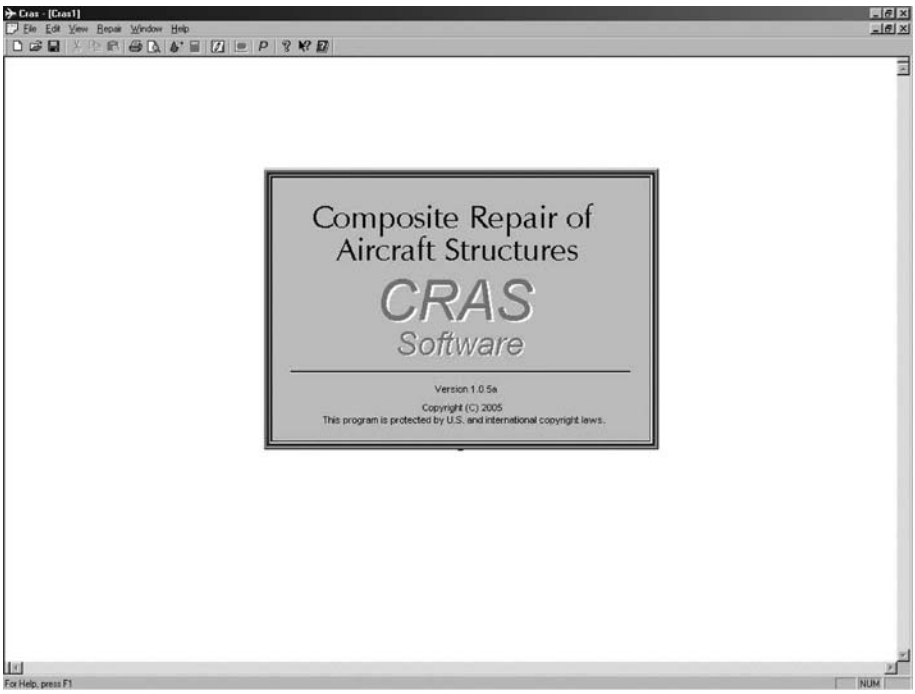

Fig. A.2. Opening screen.

The user may enter information about the repair design by selecting the Repair command on the menu bar. Six dialog commands are available (Figure A.3).

(1) Design Wizard: The advisory mode dialog wizard guides the user to design a repair patch

(2) Analysis: The dialog to execute the analytical programs for the repair patch

(3) Design: The advanced mode dialog allows users who are familiar with the program to quickly select and enter data to design a repair patch

(4) PatchGen Only: The dialog allows the user to create an MSC/PATRAN session file of a repair patch without CRAS calculating the design; this executes PatchGen only

(5) User Specified Material: The dialog to allow the user to enter skin, laminate, and/or adhesive material data

(6) Load Constant N: The dialog to initialize the load constant N (default is 5)

Also, two measurement unit options are available:

(1) English – Displays the measurement units in the English units

(2) Metric – Displays the measurement units in the metric units

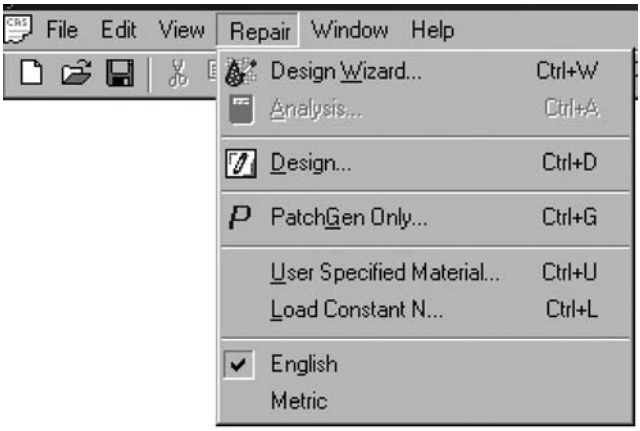

Fig. A.3. Repair menu commands.

By selecting the appropriate icon button on the toolbar, some of the Repair menu commands may also be activated (Figure A.4).

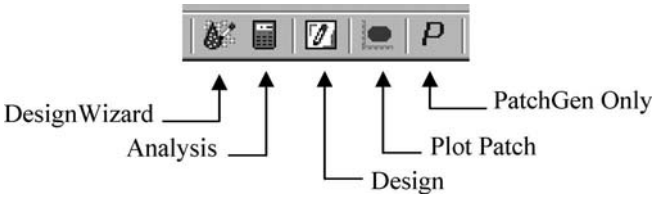

Fig. A.4. Dialog commands in the toolbar.

For some of the menu commands and toolbar buttons, they may initially appear dimmed or grayed. This indicates that the menu command is not yet available for input. For example, the Repair→Analysis and View → Patch Design menu commands will not be enabled until a valid repair patch is designed via the Repair→Design or Repair→Design Wizard dialog.

A.2.2 User Specified Material Dialog

The user may enter their own skin, laminate, and/or adhesive material data by providing the information in the Repair→User Specified Material dialog (Figure A.5). By selecting the appropriate tab, the data may be entered for the new material.

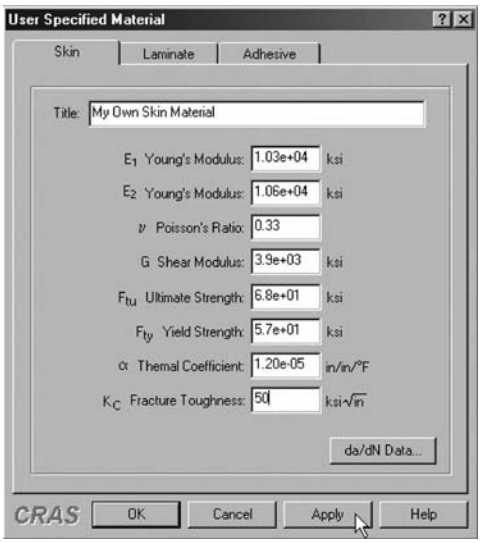

Fig. A.5. Repair→User Specified Material dialog box.

The new material will be added to the end of the drop-down list of the appropriate skin, laminate, or adhesive material combo box in the Repair→Design and Repair→Design Wizard dialogs for the user to select (Figure A.6).

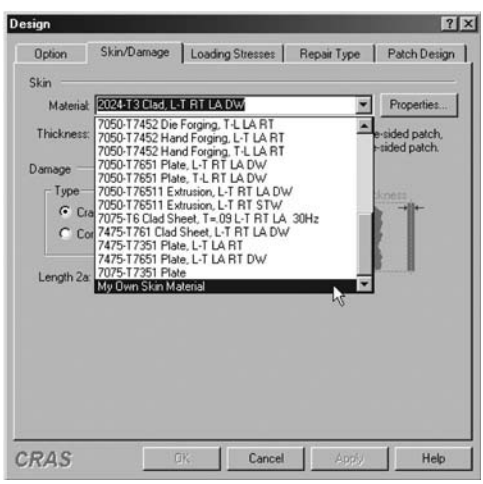

Fig. A.6. Selecting the user specified skin material.

For the da/dN data of the user specified skin material (Figure A.7), the following limitations apply:

1. Only one set of da/dN data with a maximum of 30 values in ascending order.
2. A maximum of six different R ratio values in ascending order; minimum of one set of R ratio.
3. A maximum of 30 delta K values for each R ratio in ascending order.
4. First delta K value of each R ratio must be in descending order.
5. The number of delta K values for each R ratio must equal the number of da/dN values.
6. For the English units, the delta K values are in ksi sqrt in., and da/dN values are in inches/cycle; for metric units, the delta K values are in MPa sqrt mm., and da/dN values are in mm/cycle.

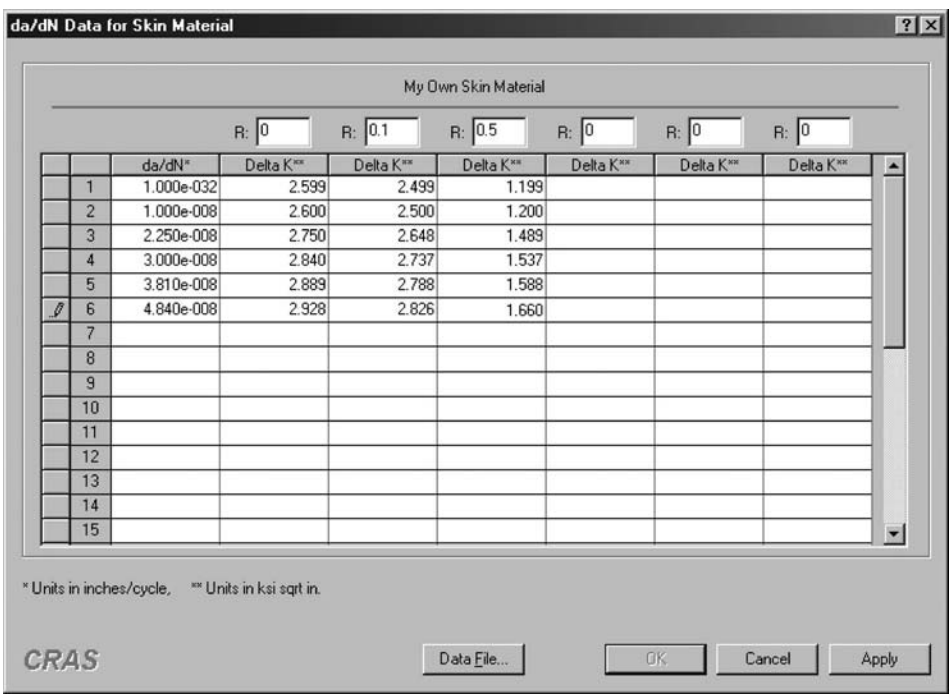

Fig. A.7. User specified skin material da/dN data dialog.

Also, a data file may be read in with its values populated in the cells of the da/dN grid. The file may be selected by clicking on the Data File . . . button on the da/dN data dialog. The dialog shown in Figure A.8 will be displayed to allow the user to select and/or enter the data file name.

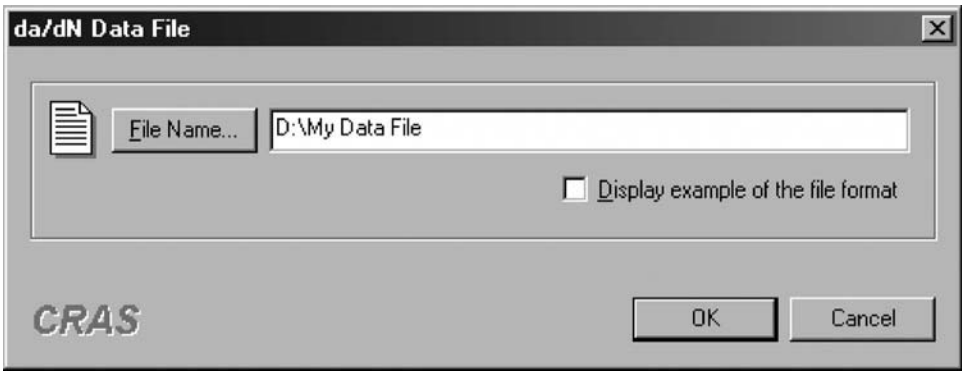

Fig. A.8. da/dN data file dialog.

The user may click on the File Name . . . button to select the da/dN data file in the dialog shown in Figure A.9.

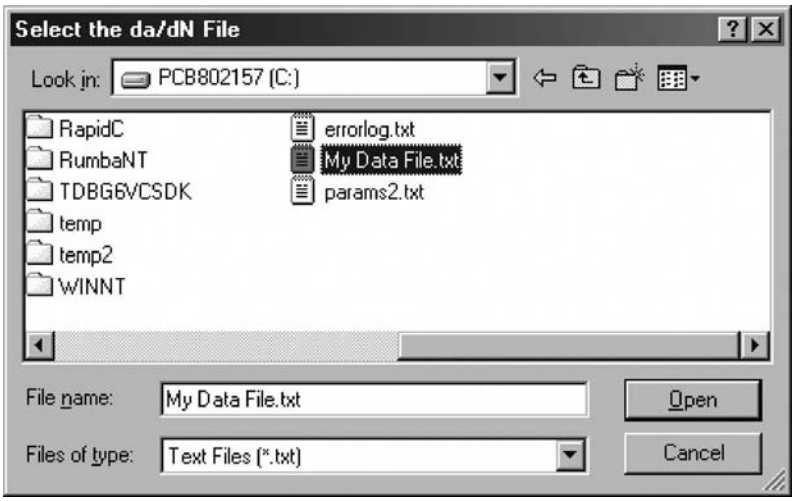

Fig. A.9. da/dN data file selection dialog.

An example of the file format for the da/dN data file is given in Figure A.10.

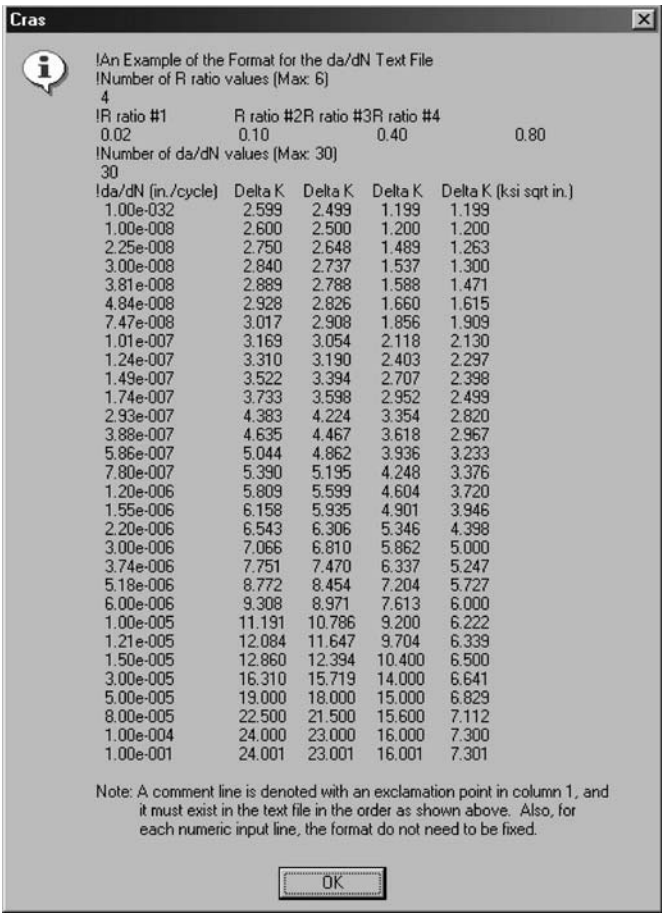

Fig. A.10. An example of the da/dN file format.

A.2.3 Load Constant N dialog

For CRAS to calculate the initial design of a repair patch, the user must provide the load constant N value. The default is set to 5 (Figure A.11).

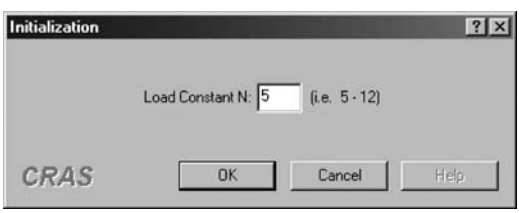

Fig. A.11. Repair→Load Constant N dialog.

A.2.4 Design Wizard dialog

By using the Repair→Design Wizard dialog, the user is guided through the design process of a repair patch in a sequenced order (Figure A.12). It contains five pages with advisory help on the right side of the page. The advisory help describes the purpose of the page and its inputs.

The pages allow the user to enter information grouped by common characteristics. The pages are listed as follows:

1. Design Option
2. Skin/Damage
3. Loading Stresses
4. Repair Type
5. Patch Design

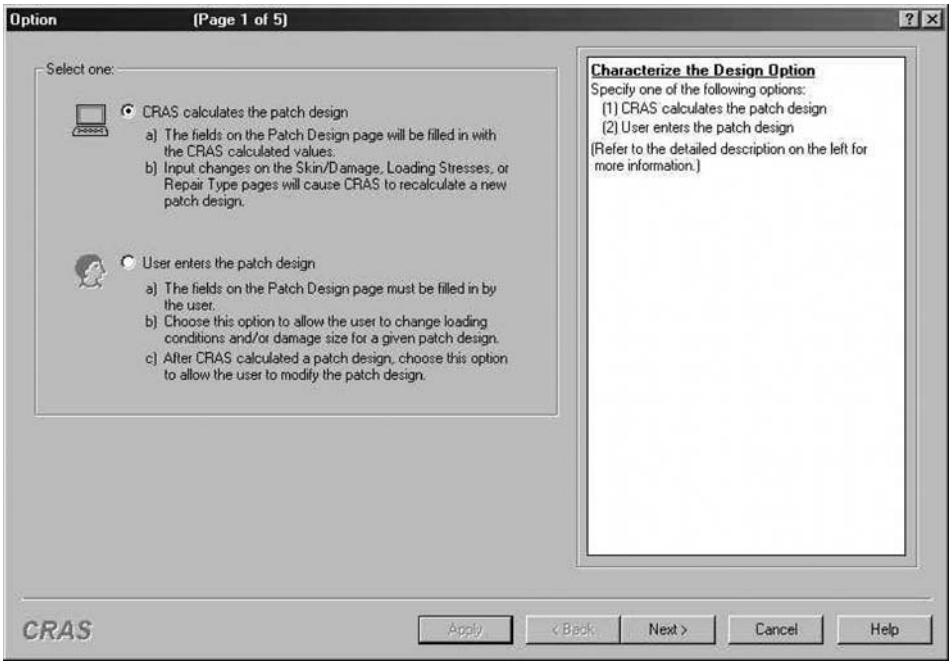

Fig. A.12. Repair→Design Wizard dialog.

CRAS allows the user to (1) Have CRAS calculate the patch design, or (2) Enter their own patch design. The default option is to have CRAS calculate the patch design. No matter which option is selected, the following three pages of the design dialog allow the user to enter information about the skin/damage, loading stresses and repair type.

If the user had selected to have CRAS calculate the patch design, then the fields on the fifth page are filled with the values of the CRAS calculated patch design (Figure A.13). The fields are grayed to indicate that the user may not change the values on the page, except by selecting an alternative CRAS calculated patch design.

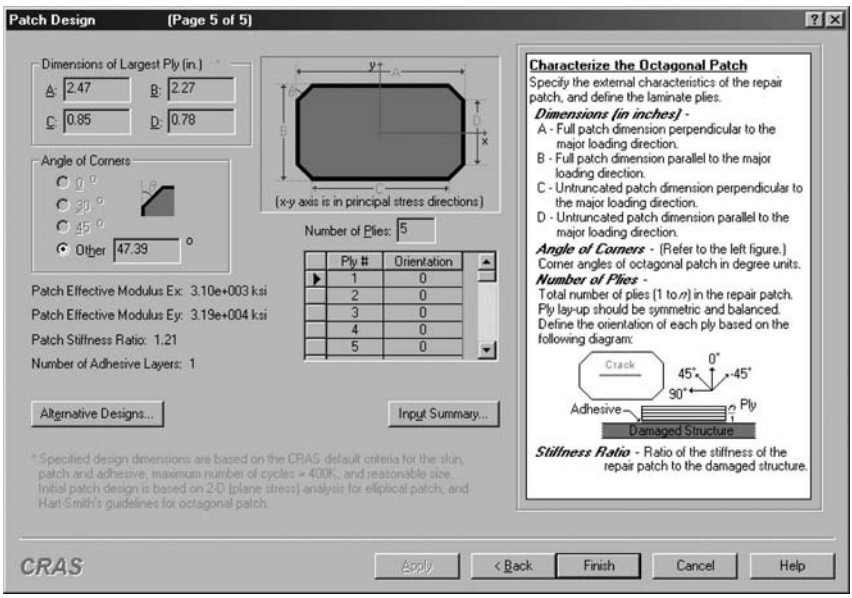

Fig. A.13. CRAS calculates patch design via Repair→Design Wizard.

CRAS will try to calculate up to four more alternative patch designs (Figure A.14). Each design is at least 10% greater in volume than the previous design. If alternative designs were also calculated, then the Alternative Designs . . . button will be enabled for the user to select; otherwise, the button will not be enabled.

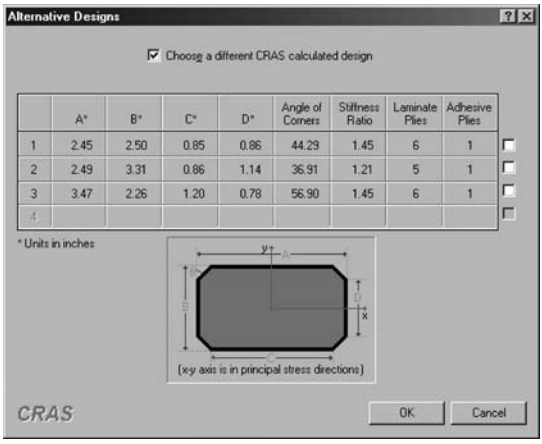

Fig. A.14. Alternative designs dialog.

Also, if the user makes changes to the input of the previous three pages in either the Repair→Design or Repair→Design Wizard dialogs, then CRAS will calculate a new patch design and alternative designs based on the input of those three pages.

For more information on how the user may enter their own patch design, refer to Section 4.6.

A.2.5 Design dialog

By using the Repair→Design dialog, the user may enter the same data as the Repair→Design Wizard, but by selecting the appropriate tabs (Figure A.15). This allows the user to fill in the information and yet skip certain pages entirely.

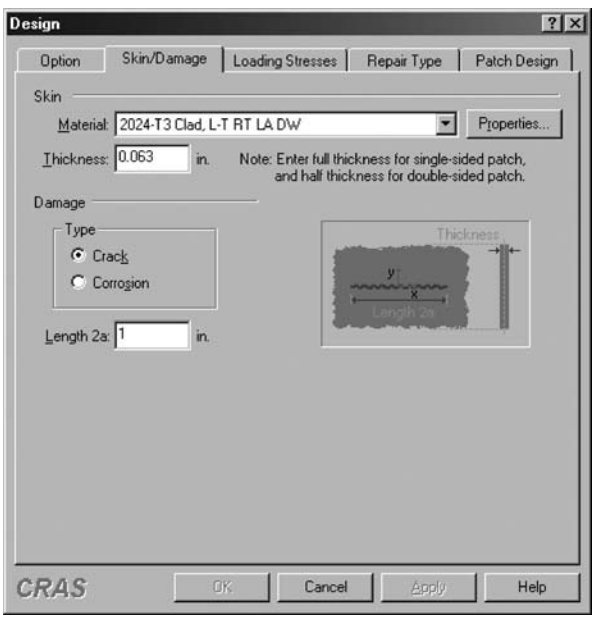

Fig. A.15. Repair→Design Dialog.

Although this gives the user more flexibility, it should be noted that if the user selects to allow CRAS to calculate an initial patch design, the Patch Design tab must be selected to have the fields populated with the calculated dimensions. That is, by activating the Patch Design tab, the initial patch design will be calculated with the information provided in the previous three tabs and the load constant dialog (Figure A.16). Note that the edit

fields containing the design parameters are initially grayed, which indicates that the user may not change its values.

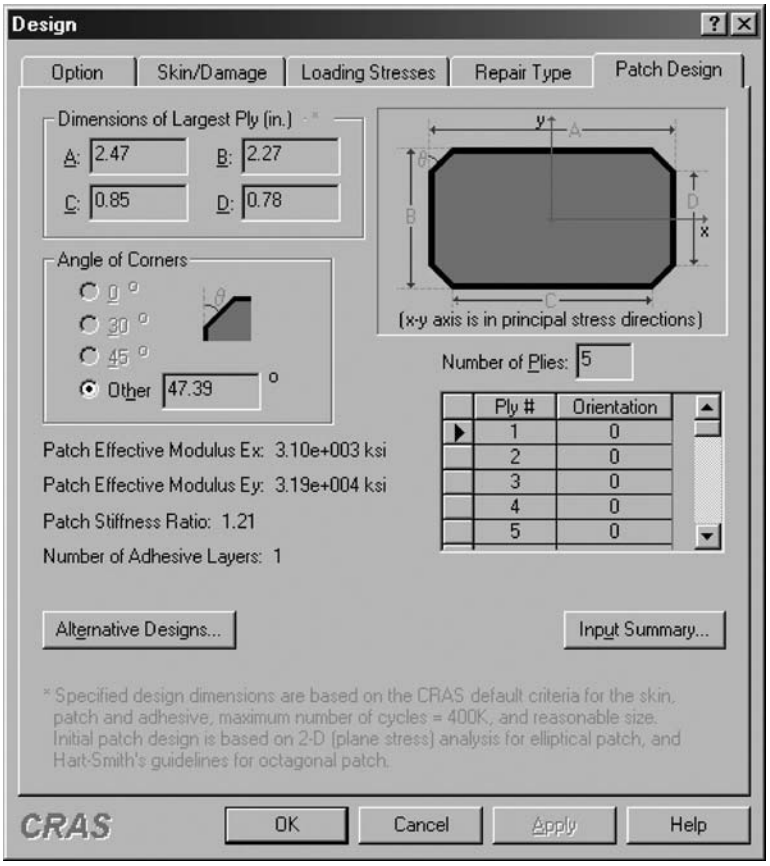

Fig. A.16. CRAS calculated patch design via Repair→Design.

A.2.6 User enters the patch design option

By selecting User Enters the Patch Design from the Design or Design Wizard dialog, the user may enter their own patch design without having CRAS calculate an initial design (Figure A.17).

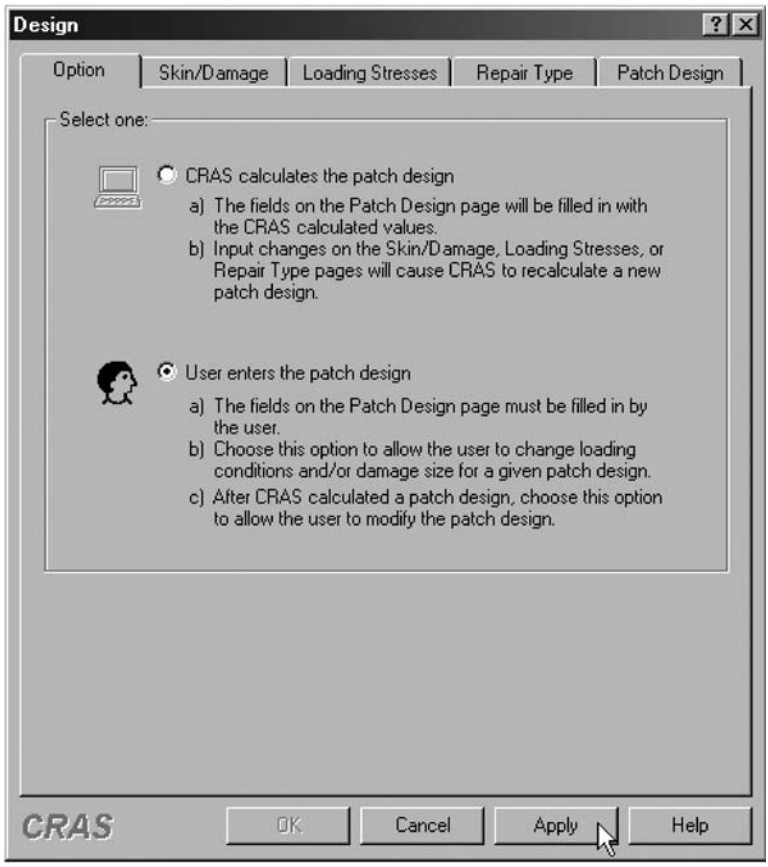

Fig. A.17. Option to allow user to enter patch design.

In the next three pages of the dialog, the user enters the skin/damage, loading stresses and repair type data. The user must then also specify the patch design in the last page that is titled Patch Design. The fields on this page are enabled for the user to enter the information about their patch design (Figure A.18).

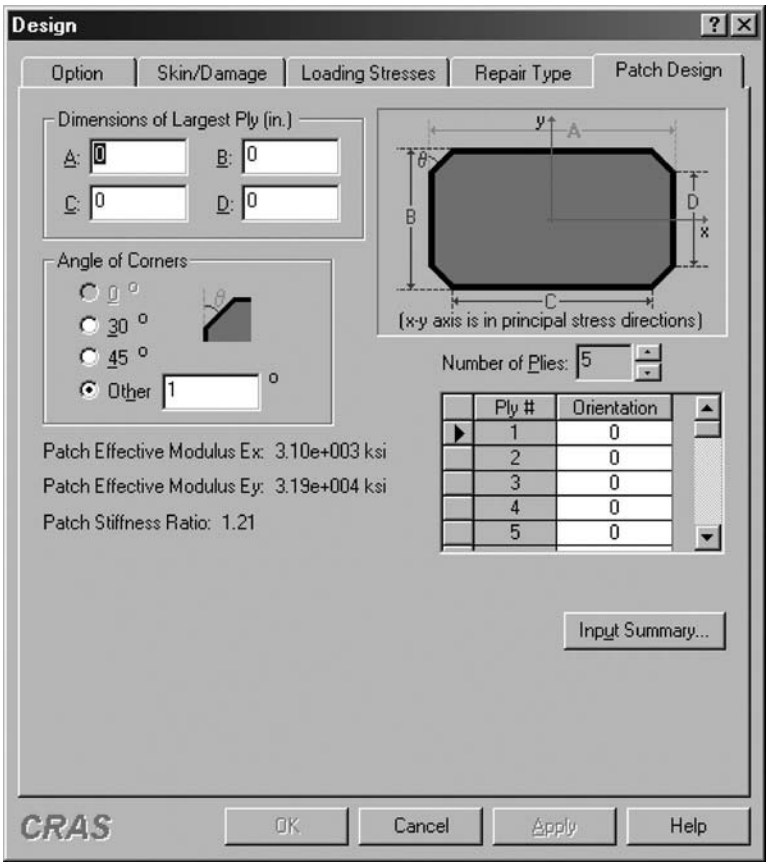

Fig. A.18. User enters own patch design via Repair→Design.

Also, it should be noted that the user can select to have CRAS calculate an initial patch design, and the fields on the fifth page will be filled with the values of the patch design. After CRAS calculates the initial patch design, the user may change the design parameters by selecting the User enters the patch design option on the Options tab. The edit controls are then enabled on the Patch Design tab to allow the user to make any changes. Note that the Alternative Designs . . . button will no longer be available for the user to select (Figure A.19).

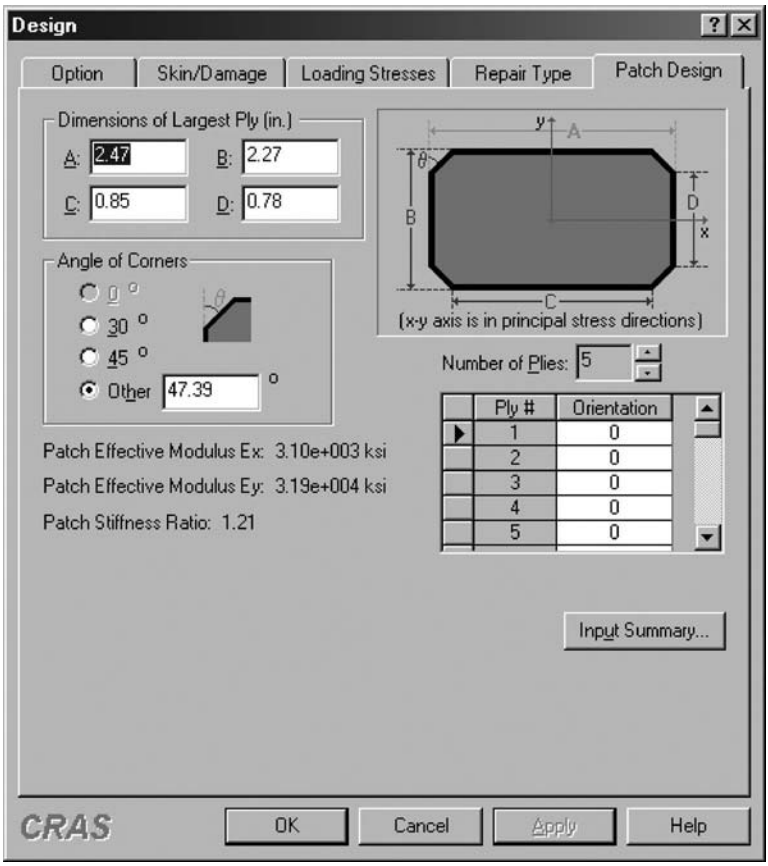

Fig. A.19. Modify original CRAS calculated patch design.

For an octagonal patch, if the user modifies the patch dimensions of the last ply, CRAS will recalculate the corresponding angle. If the user modifies the patch angle, then CRAS will recalculate dimension C of the patch design's largest ply.

A.2.7 Analysis dialog

Analysis is performed on the patch design of the last page of the Repair→Design or Repair→Design Wizard dialogs. The Repair→Analysis menu command is enabled when the repair patch design is specified (Figure A.20). The user may select to have CRAS analyze

- A crack with either an octagonal, elliptical, or rectangular patch
  - The stresses in and around the patch
  - The stress intensity factor

  - The adhesive shear strain and stress
  - The ply-by-ply stresses
- A corrosion with either an octagonal, an elliptical, or a rectangular patch
  - The stresses in and around the patch
  - The adhesive shear strain and stress
  - The ply-by-ply stresses

or generate a session file using PatchGen. If PatchGen is selected, then the Options button will be enabled to allow the user to select to enter data

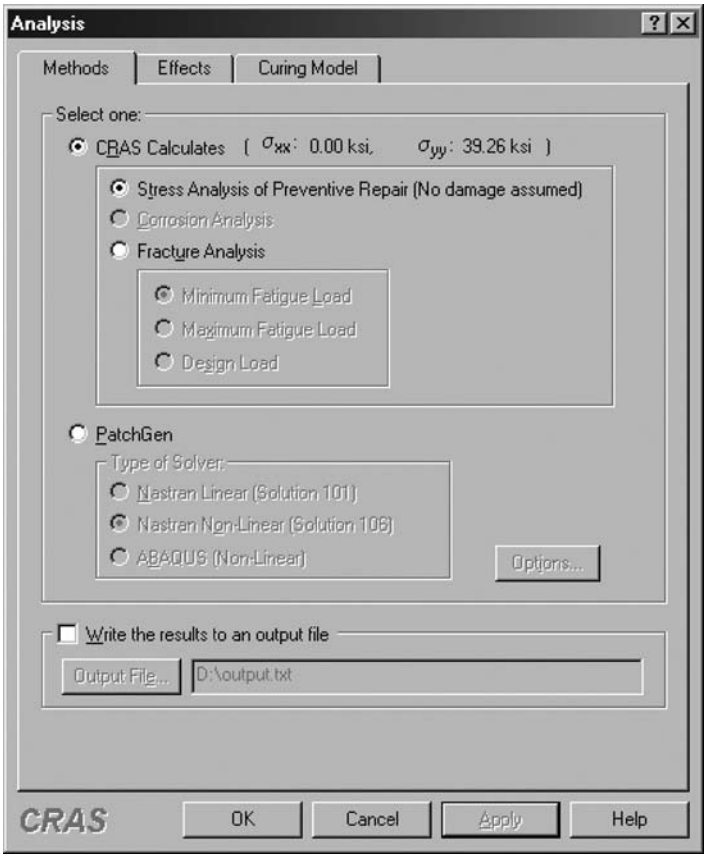

Fig. A.20. Repair→Analysis dialog.

A.2.8 PatchGen Only dialog

By using the Repair→PatchGen Only dialog, the user can create an FE model of patch repair (Figure A.21). After selecting the type of file to be generated and the type of solver to be used on the first dialog, the user needs to enter data on eight more pages. The

eight pages request information about the input/output files, panel, loading, boundary condition, stiffeners, coordinate transformation, damage, and patch (Figure A.22).

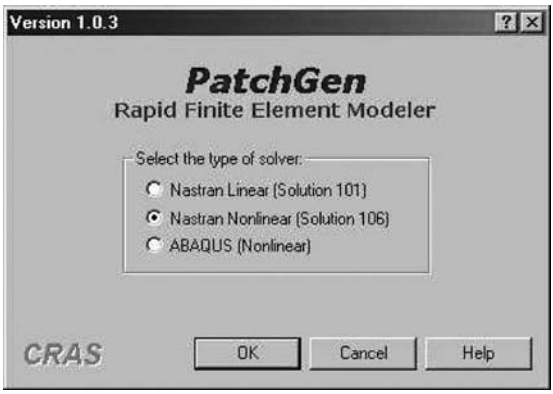

Fig. A.21. Repair→PatchGen Only dialog.

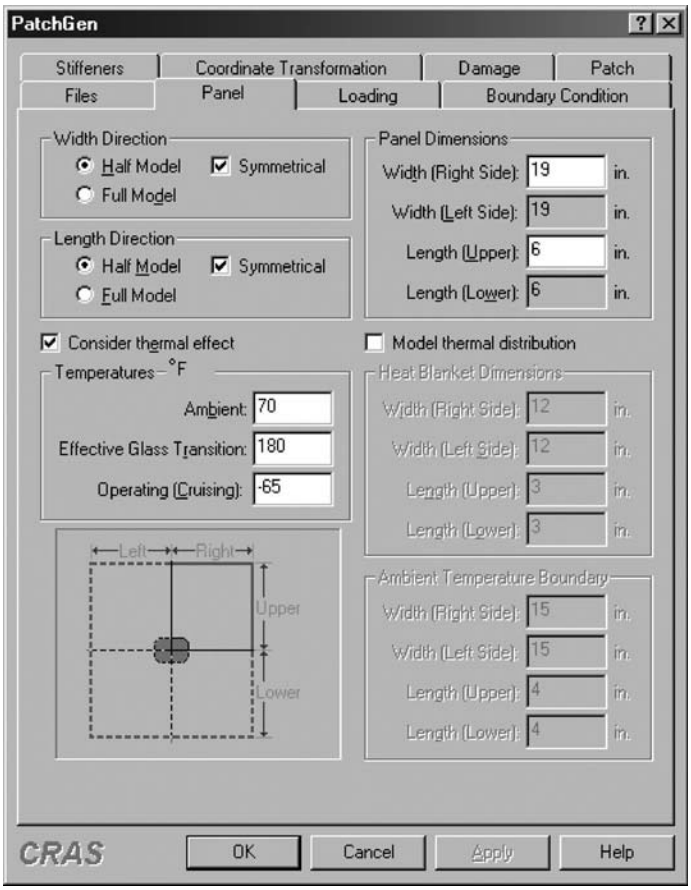

Fig. A.22. PatchGen dialog.

A.2.9 Dialog buttons

At the bottom of the dialog box, the buttons control the changes of the input and provide help if requested (Figure A.23). For the Repair→Design Wizard, the Back, Next, and Finish buttons allow the user to navigate through the dialog boxes for the input sequence (Figure A.24).

The OK button will close the dialog box and save any changes made.

The Cancel button will close the dialog box without saving any changes.

The Apply button will keep the input change for that page.

The Help button provides assistance about the active page or dialog box.

Fig. A.23. Dialog buttons.

Fig. A.24. Repair→Design Wizard dialog buttons.

At the upper right corner of the dialog box, the *question mark* button will provide help on an item of that page. Click on the *question mark* button, and click on the item to bring up help information. Also, the X button will close the dialog box without saving any changes (Figure A.25).

Fig. A.25. Help and Cancel buttons.

A.2.10 Different types of help

The Windows interface of the CRAS software provides many types of on-screen help and user hints (Figure A.26). First, the advisory mode, which is invoked by selecting the Repair→Design Wizard, steps an inexperienced user through sequenced dialog pages to design a repair patch using the input data. Secondly, on-line help may be invoked by using either the *Help* menu or the dialog button. Also, context-sensitive help may be invoked by clicking on the *question mark* button in the upper right corner of the dialog box, and then click on the item to bring up the control's help information. Or the user

may right-click the control item and select What's This? to bring up the help information on that control item. Finally, the CRAS application's main window status bar provides variable on-screen cues at the lower edge of the program window. The on-screen cues provide a short textual indicator of the program action corresponding to the position of the mouse cursor. That is, whenever the user moves the cursor over an enabled control in a dialog box, a brief help message describing the functionality of the control appears in the status bar. In addition, each time the cursor is positioned over an icon in the tool bar, a short icon descriptor is displayed adjacent to the cursor. By volunteering this flyby help, it hopes to aid the user's progress.

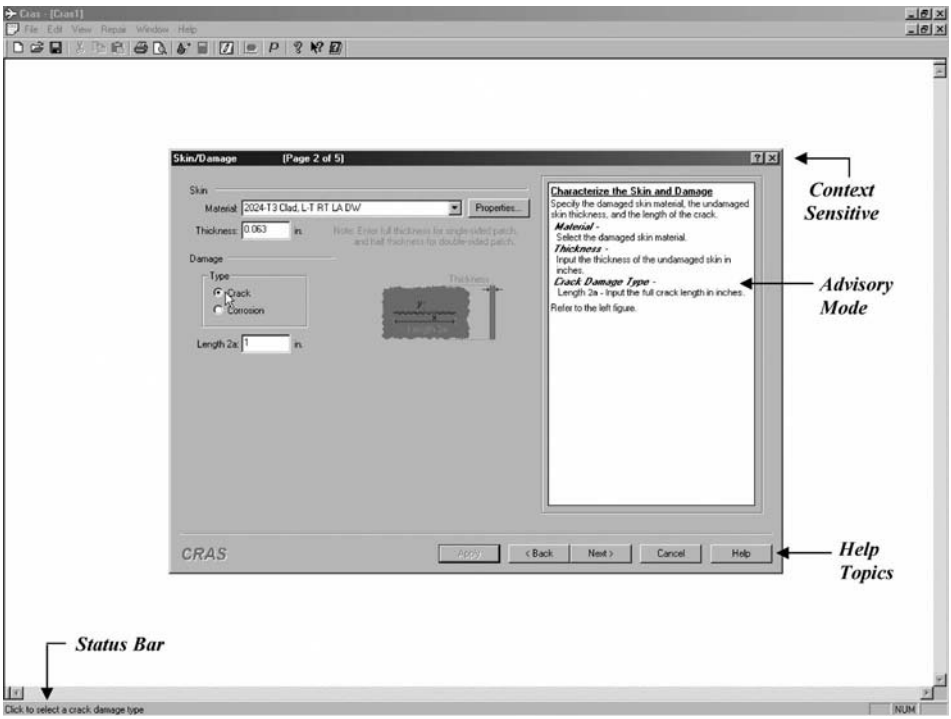

Fig. A.26. Help in the CRAS software.

A.2.11 Document/View

After the analysis is complete, the output will be displayed on the view document as shown in Figure A.27. It may be saved into a file by selecting File→Save As . . .

A plot of the repair patch may be viewed by selecting View→Patch Design from the menu bar, or clicking the graph icon on the toolbar (Figure A.28).

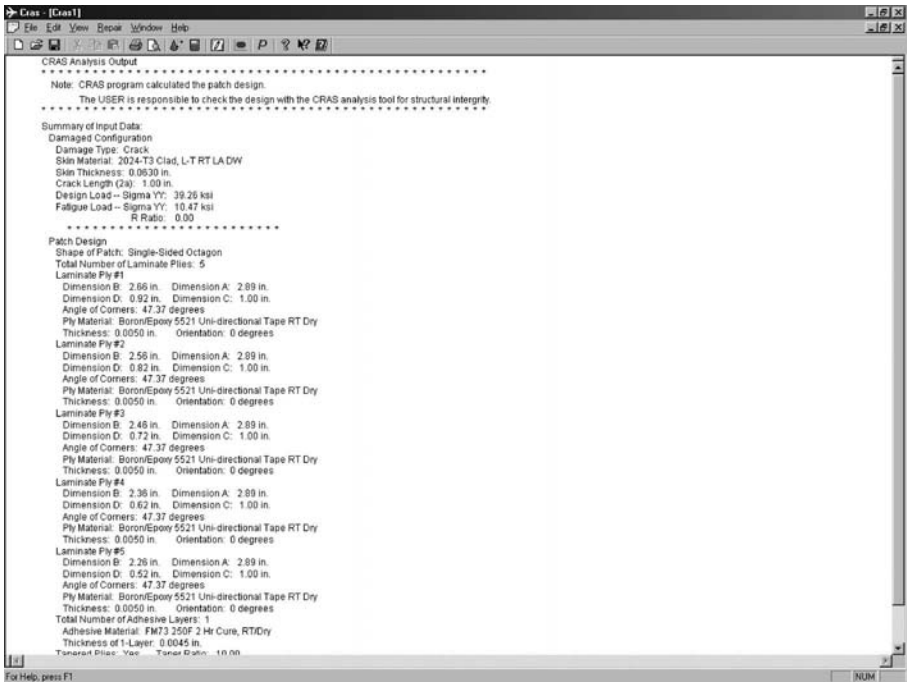

Fig. A.27. CRAS analysis output.

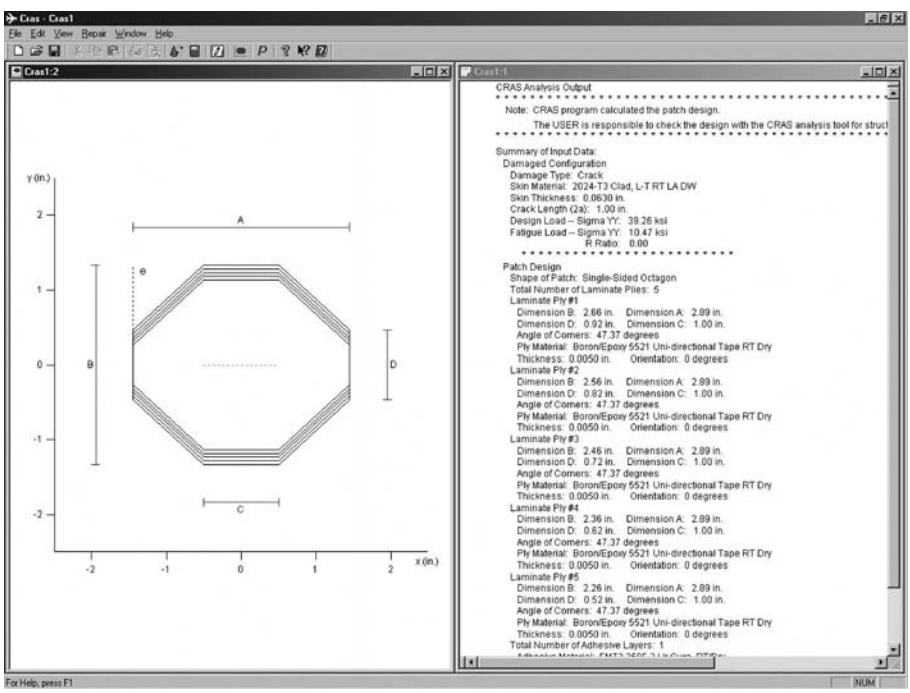

Fig. A.28. CRAS analysis output with plot.

References

ABAQUS (1997) *User's manual*, Version 5.6, Hibbitt, Karlsson and Sorensen, Inc, Rhode Island.

Adams, R. D., Atkins, R. W., Harris, J. A., and Kinloch, A. J. (1986) Stress analysis and failure properties of carbon-fibre-reinforced-plastics/steel double-lap joints. *Journal of Adhesion*, 20, 29–53.

Adams, R. D., Comyn, J., and Wake, W. C. (1997) *Structural Adhesive Joints in Engineering*. Chapman & Hall, London.

Adams, R. D. and Harris, J. A. (1987) The influence of local geometry on the strength of adhesive joints. *International Journal of Adhesion and Adhesive*, 7, 69–80.

Adams, R. D. and Peppiatt, N. A. (1974) Stress analysis of adhesive-bonded lap joints. *Journal of Strain Analysis*, 9, 185–196.

Adams, R. D. (1989) Strength predictions for lap joints, especially with composite adherends, a review. *Journal of Adhesion*, 30, 219–242.

Adams, R. D. (1992) Strength predictions in bonded joints – current thoughts and research at the University of Bristol, UK. *Journal of Adhesion*, 37, 47–50.

Akisanya, A. R. and Fleck, N. A. (1997) Interfacial cracking from the free-edge of a long bi-material strip. *International Journal of Solids and Structures*, 34, 1645–1665.

Allman, D. J. (1977) A theory for elastic stresses in adhesive bonded lap joints. *Quarterly Journal of Mechanics and Applied Mathematics*, 30, 415–436.

Arendt, C. and Sun, C.T. (1994) Bending effects of unsymmetric adhesively bonded composite repairs on cracked aluminum panels. *Proceedings of FAA/NASA International Symposium on Advanced Structural Integrity Methods for Airframe Durability and Damage Tolerance*, NASA Conference Publication 3274, part 1, 33–48.

Atluri, S. N. (1992) *Composite Repairs of Cracked Metallic Aircraft Structures*. DOT Report No. DOT/FAA/CT-92/93.

Atluri, S. N. (1997) *Structure Integrity and Durability*. Tech Science Press, USA.

Baker, A. A. (1988) Crack patching: Experimental studies, practical applications. In *Bonded Repair of Aircraft Structures*, A. A. Baker and R. Jones (eds). Martinus Nijhoff.

Baker, A. A. (1996) Fatigue studies related to certification of composite crack patching for primary metallic structure, *Proceedings of the FAA/NASA Symposium on Continued Airworthiness of Aircraft Structures*, Atlanta, USA, 313–330.

Baker, A. A. and Jones, R. (eds) (1988) *Bonded Repair of Aircraft Structures*. Martinus Nijhoff Publishers, Dordretcht.

Baker, A. A., Jones, R., and Rose, L. R. F. (2002) *Advances in the Bonded Composite Repair of Metallic Aircraft Structures*. Elsevier Publisher, The Netherlands, Amsterdam.

Barneveld, W. M. Th. Van, (1994) Theoretical Analysis of in-Field Bonded Repair of Cracked, Orthotropic Aircraft Structures. Final Thesis, Delft Technical University, The Netherlands.

Barut, A., Hanauska, J., Madenci, E., and Ambur, D. R. (2002) Analysis method for bonded patch repair of a skin with a cutout. *Composite Structures*, 55, 277–294.

Belason, B. E. and Buccolo, M. (1995) Mechanical Properties of boron/epoxy composites. Textron Specialty Materials (Manufacturer Material Data).

Bennett, W. F. (1972) Non-destructive testing of adhesive bonding, *Paper presented at the 9th Conference on Non-destructive Testing*, Loughborough University, UK.

Beom, H. G. (1998) Analysis of a plate containing an elliptic inclusion with eigencurvatures. *Archive of Applied Mechanics*, 68, 422–432.

Beom, H. G. and Earmme, Y. Y. (1999) The elastic field of an elliptic cylindrical inclusion in a laminate with multiple isotropic layers. *Journal of Applied Mechanics*, 66, 165–171.

Bigwood, D. A. and Crocombe, A. D. (1990) Non-linear adhesive bonded joint design analyses. *International Journal of Adhesion and Adhesives*, 10, 31–41.

Bogy, D. B. (1971) Two edge-bonded elastic wedges of dissimilar materials and wedge angles under surface traction. *Journal of Applied Mechanics*, 38, 377–386.

Bottega, W. J. and Loia, M. A. (1996) Edge debonding in patched cylindrical panels. *International Journal of Solids and Structures*, 33, 3755–3777.

Bottega, W. J. and Loia, M. A. (1997) Axisymmetric edge debonding in patched plates. *International Journal of Solids and Structures*, 34, 2255–2289.

Boykett, R. and Walker, K. (1996) F-111C Lower Wing Skin Bonded Composite Repair Substantiation Testing. DSTO-TR-0480, Aeronautical and Maritime Research Laboratory, Melbourne, Australia.

Bowden, P. B. and Jukes, J. A. (1972) The plastic flow of isotropic polymers. *Journal of Materials Science*, 7, 52–63.

Brewer, T. K. (1994) A/B/C/D Aircraft Lower Nacelle Skin Acoustic and Strain Measurements and Sonic Fatigue Analysis. McDonnell Douglas Aerospace, MDC 94B0044.

Broek, D. (1987) *Elementary Engineering Fracture Mechanics*. Martinus Nijhoff Publisher, Dordretcht.

Budiansky, B. and Hutchinson, J. W. (1978) Analysis of closure in fatigue crack growth. *Journal of Applied Mechanics*, 45, 267–275.

Byrne, K. P. (1975) Bending-induced crack propagation in a 4% Cu-Al alloy with reference to acoustically propagated fatigue cracks. *Journal of Sound and Vibration*, 42, 337–355.

Byrne, K. P. (1977) On the growth rate of bending induced edge cracks in acoustically excited panels. *Journal of Sound and Vibration*, 53, 505–528.

CalcuRep 2001 Manual (2001). USAF Academy, draft version.

Callinan, R. J., Chiu, W. K., and Galea, S. C. (1998) Optimization of a Composite Repair to Cracked Panels Subjected to Acoustic Excitation. Paper A98-31631 21st ICAS Congress 13–18 September 1998, Melbourne, Australia.

Callinan, R. J., Ferrarotto, P., Geddes, R., Stoyanokski, I., and Tejeddor, S. (2005) Flight Trial of Dosimeter on F/A-18 to Determine the Acoustic Environment and the Effectiveness of the Highly Damped Patch, DSTO Report DSTO-RR-0284, AR 013–232.

Callinan, R. J., Galea, S. C., and Sanderson, S. (1997a) Finite element analysis of bonded repairs to edge cracks in panels subjected to acoustic excitation. *Composite Structures*, 38, 649–660.

Callinan, R., Rose, L. R. F., and Wang, C. H. (1997b) Three dimensional stress analysis of crack patching. *Advances in Fracture*, 4, 2151–2158, Pergamon Press.

Callinan, R., Rose, L. R. F. and Sanderson, S. (1998) Analysis of the Interaction Effect for Bonded Repairs. *Defence Science and Technology Organisation Report DSTO-TR-0715*, Australia.

Callinan, R. J., Wang, C. H., Galea, S. C., Sanderson, S., and Rose, L. R. F. (1999) Analytical solution for the stress intensity factor in bonded repairs to panels subjected to acoustic excitation. 1999 Joint FAA/DoD/NASA Conference on Aging aircraft.

Callinan, R. J., Sanderson, S., Wang, C. H., and Galea, S. (2006) Generic design procedures for the repair of acostic fatigue damage. DSTO-RR-0283.

Carnahan, B., Luther, H. A., and Wilkes, J. O. (1969) *Applied Numerical Method*, John Wiley and Sons.

Chalkley, P. and Rose, L. R. F. (1998) Variational Bounds for the Equivalent Spring Constants for Bonded Repairs. Defence Science and Technology Organisation Report DSTO-RR-0139.

Chalkley, P. and Rose, F. (2001) Stress analysis of double-strap joints using a variational method. *International Journal of Adhesion and Adhesives*, 21, 241–247.

Cheng, Z-. Q. and Reddy, J. N. (2004) Laminated anisotropic thin plate with an elliptic inhomogeneity. *Mechanics of Materials*, 36, 647–657.

Clark, J. D and Mcgregor, I. J. (1993) Ultimate tensile stress over a zone: a new failure criterion for adhesive joints. *Journal of Adhesion*, 42, 227–245.

Clarkson, B. L. (1968) Stresses in skin panels subjected to random acoustic loading. *The Aeronautical Journal of the Royal Aeronautical Society*, 72, 1000–1010.

CRMS-Guidelines for Composite Repair to Metallic Structure (1998). AFRL-WP-TR-1998-4113.

Cornell, R. W. (1953) Determination of stresses in cemented lap joints. *Journal of Applied Mechanics*, 20, 355–364.

Cox, B. N. and Rose, L. R. F. (1994) Time- or cycle dependent crack bridging. *Mechanics of Materials*, 19, 39–57.

Composite Repair of Aircraft Structures (CRAS) Design Manual (2003) Cooperative Agreement Final Report, Addendum 2. Submitted to U.S. Air Force Research Laboratory, Wright Patterson, OH.

Composite Repair of Aircraft Structures (CRAS) (2003) Software User Manual, version 1.0.1.

Davis, M. J. (1995) Composite Materials and Adhesive Bonded Repairs. RAAF Standard Engineering C5033.

De Koning, A. U. (1980) A Simple Crack Closure Model for Prediction of Fatigue Crack Growth Rates Under Variable Amplitude Loading. NRL MP 80006.

Dill, H. D. and Saff, C. R. (1976) Analysis of Crack Growth Following Compressive High Loads Based on Crack Surface Displacements and Contact Analysis. MCAIR 76-006, McDonnel Aircraft Compnay.

DTDH (1972) Damage Tolerant Design Handbook, a compilation of fracture and crack-growth data for high-strength alloys, Metals and Ceramics Information Centre, MCIC-HB-01.

Dugdale, D. S. (1960) Yielding of steel sheets containing slits. *Journal of Mechanics and Physics of Solids*, 8, 100–104.

Duong, C. N. (2003a) Composite Repair of Aircraft Structures, Program Report, Volume II: *Theoretical Manual and Illustrative Solutions*. Submitted to U.S. Air Force Research Laboratory, Wright Patterson, OH.

Duong, C. N. (2003b) Composite Repair of Aircraft Structures, Program Report, Volume III: *Tests and Method Validations*. Submitted to U. S. Air Force Research Laboratory, Wright Patterson, OH.

Duong, C. N. (2004) An engineering approach to geometrically nonlinear analysis of a one-sided composite repair under thermo-mechanical loading. *Composite Structures*, 64, 13–21.

Duong, C. N. (2006) A unified approach to geometrically nonlinear analysis of tapered bonded joints and doublers. *International Journal of Solids and Structures*, 43, 3498–3526.

Duong, C. and Knauss, W. G. (1995) A nonlinear thermoviscoelastic stress and fracture analysis of an adhesive bond. *Journal of Mechanics and Physics of Solids*, 43, 1505–1549.

Duong, C. N. and Wang, C. H. (2004) On the characterization of fatigue crack growth in one-sided bonded repair. *Journal of Engineering Materials and Technology*, 136, 192–198.

Duong, C. N. and Yu, J. (1997) The stress intensity factor for a cracked stiffened sheet repaired with an adhesively bonded composite patch. *International Journal of Fracture*, 84, 37–60.

Duong, C. N. and Yu, J. (2002a) An analytical estimate of thermal effects in a composite bonded repair: Plane stress analysis. *International Journal of Solids and Structures*, 39, 1003–1014.

Duong, C. N. and Yu, J. (2002b) Stress analysis of a bonded repair over a corrosion grind-out using an inclusion model with a second ordered eigenstrain theory. *International Journal of Engineering Science*, 40, 347–365.

Duong, C. N. and Yu, J. (2003a) Analysis of a plate containing a polygon-shape inclusion with a uniform eigencurvature. *Journal of Applied Mechanics*, 70, 404–407.

Duong, C. N. and Yu, J. (2003b) Thermal stresses in a one-sided bonded repair by plate inclusion model. *Journal of Thermal Stresses*, 26, 457–466.

Duong, C. N. and Yu, J. (2003c) Thermal stresses in one-sided bond repair: Geometrically nonlinear analysis. *Theoretical and Applied Fracture Mechanics*, 40, 197–209.

Duong, C. N., Wang J. J., and Yu, J. (2001a) An approximate algorithmic solution for the elastic fields in bonded patched sheets. *International Journal of Solids and Structures*, 38, 4685–4699.

Duong, C. N., Hart-Smith, L. J., and Yu, J. (2001b) Analytical approach to bonded repair of elliptical dent, corrosion grind-out, and cut-out. *Theoretical and Applied Fracture Mechanics*, 36, 187–193.

Duong, C. N., Hart-Smith, L. J., Grip, R., Kubo, M., and Anderson, B. (2002) CRAS design and analysis software for bonded composite repair. *Proceeding of the 6th Aging Aircraft Conference*, September 2002, San Francisco, California.

Duong, C. N., Hart-Smith, L. J., Heaton, P., Beier, T., Tom, J., and Anderson, B. (2003) Composite Repair of Aircraft Structures, Program Report, Volume I: Program Overview. Submitted to U. S. Air Force Research Laboratory, Wright Patterson, OH.

Duong, C. N., Verhoeven, S., and Guijt, C. B. (2006) Analytical and experimental study of load attraction and fatigue crack growth in two-sided bonded repair. *Composite Structures*, 73, 394–402.

Edde, F. and Verreman, Y. (1992) On the fracture parameters in a clamped cracked lap shear adhesive joint. *International Journal of Adhesion and Adhesive*, 12, 43–48.

Edwards, P. R. and Newman, J. C., Jr. (1990) An AGARD supplemental test programme on the behaviour of short cracks under constant amplitude and aircraft spectrum loading. AGARD Report 767.

Elber, W. (1970) Fatigue crack closure under cyclic loading. *Engineering Fracture Mechanics*, 2, 37–45.

Engels, H. and Becker, W. (2002) Closed-form analysis of external patch repairs of laminates. *Composite Structures*, 56, 259–268.

Engineering Sciences Data Unit (ESDU), http://www.esdu.com

Erdogan, F. and Arin, K. (1972) A sandwich plate with a part-through and a debonding crack. *Engineering Fracture Mechanics*, 4, 449–458.

Ervin, V. J. and Stephan, E. P. (1992) Collocation with Chebychev polynomials for a hyper-singular integral equation in an interval. *Journal of Computational and Applied Mathematics*, 43, 221–229.

ESDU (1986) Design against fatigue: vibration of structures under acoustic or aerodynamic excitation, *Item 86025*, ESDU International plc.

ESDU (1996) The relation between sound pressure level and R. M. S. fluctuating pressure, *Item 66018*, ESDU International.

Eshelby, J. D. (1957) The determination of the elastic field of an ellipsoidal inclusion and related problems. *Proceeding of Royal Society* (London) A241, 376–396.

Fernlund, G. and Spelt, J. K. (1991a) Analytical method for calculating adhesive joint fracture parameters. *Engineering Fracture Mechanics*, 40, 119–132.

Fernlund, G. and Spelt, J. K. (1991b) Failure load prediction of structural adhesive joints, part 1: analytical method. *International Journal of Adhesion and Adhesives*, 11, 213–220.

Fredell, R. S. (1994) Damage Tolerant Repair Techniques for Pressurized Aircraft Fuselages. Ph.D. Thesis, Delft Technical University, Netherlands.

Frenkel, A. (1983) A Chebyshev expansion of singular integrodifferential equations with a $\partial^2 \ln|s-t|/\partial s \partial t$ kernel. *Journal of Computational Physics*, 51, 335–342.

Gilbert, Y. and Rigolot, A. (1988) Determination of stress distribution in double-lap joints, matched asymptotic expansions and conformal mapping. *Adhesively Bonded Joints: Analysis and Design, ASTM STP 981*, American Society for Testing and Materials, Philadelphia. 145–159.

Goland, M. and Reissner, E. (1944) The stresses in cemented joints. *Journal of Applied Mechanics*, 11, A17–A27.

Golberg, M. A. (1983) The convergence of several algorithms for solving integral equations with finite-part integrals. *Journal of Integral Equations*, 5, 329–340.

Golberg, M. A. (1985) The convergence of several algorithms for solving integral equations with finite-part integrals, II. *Journal of Integral Equations*, 9, 267–275.

Gordon, R. W., Hollkamp, J. J., Liguore, S., and Callinan, R. J. (2001) An Experimental Investigation of Damped Repairs for Sonic Fatigue. *Fifth Joint NASA/FAA/DoD Conference on Aging Aircraft*, Orlando.

Gradshteyn, L. S. and Ryzhik, I. M. (1965) *Table of Integrals, Series, and Products*. Academic Press, New York.

Groth, H. L. (1988). Stress singularities and fracture at interface corners in bonded joints. *International Journal of Adhesion and Adhesives*, 8, 107–113.

Guideline for Composite Repair of Metallic Structure (CRMS), AFRL-WP-TR-1998-4113.

Guo, W., Wang, C. H., and Rose, L. R. F. (1998) On the influence of cross sectional thickness on fatigue crack growth. *Fatigue and Fracture of Engineering Materials and Structures*, 22, 437–444.

Hadamard, J. (1952) *Lectures on Cauchy's Problem in Linear Partial Differential Equations*. Dover Publications Inc., New York.

Harris, J. A. and Fay, P. A. (1992) Fatigue life evaluation of structural adhesives for automotive applications. *International Journal of Adhesion and Adhesives*, 12, 9–18.

Hart-Smith, L. J. (1973a) Adhesive-Bonded Double-Lap Joints. NASA CR-112235.

Hart-Smith, L. J. (1973b) Adhesive-Bonded Single-Lap Joints. NASA CR-112236.

Hart-Smith, L. J. (1973c) Adhesive-Bonded Scarf and Stepped-Lap joints. NASA CR-112237.

Hart-Smith, L. J. (1974) Analysis and Design of Advanced Composite Bonded Joints. NASA CR 2218.

Hart-Smith, L. J. (1982) Induced Peel Stresses in Adhesively Bonded Joints, Douglas Aircraft Company, MDC J9422A.

Hart-Smith, L. J. (1999) Nonlinear closed-form analyses of stresses and deflections in bonded one-sided splices and patches. *The Proceedings of the 3rd Aging Aircraft Conference*, New Mexico.

Hart-Smith, L. J. (2001a) Recent expansions in the capabilities of Rose's closed-form analyses for bonded crack patching. *9th Australian International Aerospace Congress*, Canberra, Australia.

Hart-Smith, L. J. (2001b) Extension of the Rose bonded crack patching analysis to orthotropic composite patches, also accounting for residual thermal stresses. *Proceeding of the 5th Aging Aircraft Conference on September 10–13 in Kissimmee*, Florida.

Hart-Smith, L. J. (2005a) The Goland and Reissner bonded lap joint analysis revisited yet again- but this time essentially validated. To be published.

Hart-Smith, L. J. (2005b) Analyses of adhesive peel and shear stresses in bonded single strap joints and one-sided patches and doublers, accounting for thermal mismatch effects. To be published.

Hart-Smith, L. J. and Duong, C. N. (2005) Use of bonded crack-patching analysis tools to design repairs for non-crack-like (corrosion) damage. To be published.

Hart-Smith, L. J. and Wilkins, K. (2000) Analyses of bending deformations in adhesively bonded one-sided doublers and patches over skin crack. *Proceeding of the 4th Aging Aircraft Conference*, St Louis.

Hui, C. Y. and Zehnder, A. T. (1993) A theory for the fracture of thin plates subjected to bending and twisting moments. *International Journal of Fracture*, 61, 211–229.

Hylands, R. W. and Sidwell, E. H. (1980) The effect of glue-line thickness on bonded steel-to-steel joints. *Journal of Adhesion*, 10, 203–218.

Hein, V. L. and Erdogan, F. (1971) Stress singularities in a two-material wedge. *International Journal of Fracture Mechanics*, 7, 317–330.

Ikegami, R., Haugse, E. and Trego, A. (2001) Structural Technology and Analysis Program. AFRL-VA-WP-TR-2001-3037.

Imanaka, M., Fukuchi, Y., Kishimoto, W., Okita, K., Nakayama, N., and Nagai, H. (1988) Fatigue life estimation of adhesively bonded lap joints. *Journal of Engineering Material and Technology*, 110, 350–354.

James, M. L., Smith, G. M., and Wolford, J. C. (1977) *Applied Numerical Methods for Digital Computation with Fortran and CSMP*. Harper & Row Publishers, New York.

Johnson, W. S. (1986) Stress Analysis of the Cracked Lap Shear Specimen: An ASTM Round Robin. NASA Technical Memorandum 89006.

Johnson, W. S and Mall, S. (1985) A fracture mechanics approach for designing adhesively bonded joints. In W. S. Johnson (ed.), *Delamination and Debonding of Materials, ASTM STP 876*, American Society for Testing and Materials, Philadelphia, 189–199.

Johnson, W. C., Earmme, Y. Y., and Lee, J. K. (1980a) Approximation of the strain field associated with an inhomogeneous precipitate, part 1: Theory. *Journal of Applied Mechanics*, 47, 775–780.

Johnson, W. C., Earmme, Y. Y., and Lee, J. K. (1980b) Approximation of the strain field associated with an inhomogeneous precipitate, part 2: The cuboidal inhomogeneity. *Journal of Applied Mechanics*, 47, 781–788.

Joint Service Specification Guide (JSSG) (1998) USAF JSSG-2006.

Jones, R. (1975) An approximate expression for the fundamental frequency of vibration of elastic plates. *Journal of Sound and Vibration*, 38, 503–504.

Jones, R. (1988) Crack patching: Design aspects. In *Bonded Repair of Aircraft Structures*, edited by A. A. Baker and R. Jones, Martinus Nijhoff Publishers, Dordretcht, pp. 40–76.

Jones, R., Chiu, W. K. and Paul, J. (1993) Designing for damage tolerant composite joints. *Composite Materials*, 25, 201–207.

Jones, R. M. (1975) *Mechanics of Composite Materials*. McGraw-Hill, Washington DC.

Joseph, P. F. and Erdogan, F. (1987) Plates and Shells Containing a Surface Crack Under General Loading Conditions. NASA Contractor Report 178323, NASA Langley Research Centre, USA.

Joseph, P. F. and Erdogan, F. (1989) Surface crack problems in plates. *International Journal of Fracture*, 41, 105–131.

Kairouz, K. C. and Matthews, F. L. (1993) Strength and failure modes of bonded single lap joints between cross-ply substrates. *Composites*, 24, 475–484.

Kalnins, A. (1964) Analysis of shell of revolutions subjected to symmetrical and non-symmetrical loads. *Journal of Applied Mechanics*, 31, 1355–1365.

Karlsson, A. M. and Bottega, W. J. (2000a) On the behaviour of a class of patched plates during cooling. *International Journal of Non-Linear Mechanics*, 35, 543–566.

Karlsson, A. M. and Bottega, W. J. (2000b) On thermal buckling of patched beam plates. *International Journal of Solids and Structures*, 37, 4655–4690.

Kaya, A. C. and Erdogan, F. (1987) On the solution of integral equations with strongly singular kernels. *Quarterly of Applied Mathematics*, 45, 105–122.

Keer, L. M., Lin, C. T., and Mura, T. (1976) Fracture analysis of adhesively bonded sheets. *Journal of Applied Mechanics*, 43, 652–656.

Kinloch, A. J. (1987) *Adhesion and Adhesives: Science and Technology*. Chapman & Hall, London.

Klug, J. C. and Sun, C. T. (1998) Large deflection effects of cracked aluminum plates repaired with bonded composite patches. *Composite Structures*, 42, 291–296.

Krenk, S., Jonsson, J., and Hansen, L. P. (1996) Fatigue analysis and testing of adhesive joints. *Engineering Fracture Mechanics*, 53, 839–872.

Krylov, V. I. (1962) *Approximate Calculation of Integrals*. Macmillan Company, New York.

Lekhnitskii, S. G. (1968) *Anisotropic Plates*. Gordon & Breach, New York.

Li, J. Y. (2000) Thermoelastic behavior of composites with functionally graded interphase: a multi-inclusion model. *International Journal of Solids and Structures*, 37, 5579–5597.

Liguore, S. L. Beier, T. H., Gordon, R. W., and Hollkamp, J. J. (2001) Design and analysis of damped repairs for sonic fatigue cracking, *The 2001 USAF Aircraft Structural Integrity Program Conference*, 11–13 December: Williamsburg, Virginia, USA.

Liguore, S. L., Hunter, K., Perez, R., and Beier, T. H. (1999) Flight test evaluation of damped composite repairs for sonic fatigue. *Sonic Fatigue Session of the 40th AIAA/ASME/ASCE/AHS SDM Conference*, 12–15 April. St. Louis, MO, 1498–1508.

Losi, G. U. and Knauss, W. G. (1992) Free volume theory and nonlinear thermoviscoelasticity. *Polymer Engineering and Science*, 32, 542–557.

Piessens, R. and de Doncker, E. (1983) *QUADPACK: A Subroutine Package For Automatic Integration*. Springer Verlag, New York.

MacMillan, W. D. (1958) *The Theory of the Potential*. Dover Publication, New York.

Mall, S., Johnson, W. S., and Everett, R. A. Jr. (1982) Cyclic Debonding of Adhesively Bonded Composites. NASA Technical Memorandum 84577.

MIL-HDBK-5G (1997) CD-ROM, AFRL/MLSC, WPAFB.

Mead, D. J. and Markus, S. (1970) Loss factors and resonant frequencies of encastre damped sandwich beams. *Journal of Sound and Vibration*, 12, 99–112.

Miles, J. W. (1954) On structural fatigue under random loading. *Journal of Aeronautical Science*, 21, 753–762.

Mortensen, F. and Thomsen, O. T. (1997) Simplified linear and non-linear analysis of stepped and scarfed lap adhesive joints between composite laminates. *Composite Structures*, 38, 281–294.

Mortensen, F. and Thomsen, O. T. (2002) Analysis of adhesive bonded joints: a unified approach. *Composites Science and Technology*, 62, 1011–1031.

Moschovidis, Z. A. (1975) Two Ellipsoidal Inhomogeneities and Related Problems Treated by the Equivalent Inclusion Method. Ph.D. Dissertation, Northwestern University, Evanston.

Moschovidis, Z. A. and Mura, T. (1975) Two ellipsoidal inhomogeneities by the equivalent inclusion method. *Journal of Applied Mechanics*, 42, 847–851.

MSC/NASTRAN (2001) Reference Manual. The MacNeal-Schwendler Corporation, California.

MSC/PATRAN (2001) User Guides and Reference Manuals. The MacNeal-Schwendler Corporation, California.

Muller, R. and Fredell, R. (1999) Analysis of multiple bonded patch interaction – Simple design guidelines for multiple bonded repairs in close proximity. *Applied Composite Materials*, 6, 217–237.

Mura, T. (1998) *Micromechanics of Defects in Solids*, 2nd edition. Kluwer Acadamic Publisher, Dordretcht.

Muskhelishvili, N. I. (1953) *Some Basic Problems of the Mathmetical Theory of Elasticity*. Noordhoff, Groningen, The Netherlands.

Nemat-Nasser, S. and Hori, M. (1987) Toughening by partial or full bridging of cracks in ceramics and fibre reinforced composites. *Mechanics of Materials*, 6, 245–269.

Nemat-Nasser, S. and Hori, M. (1993) *Micromechanics: Overall Properties of Heterogeneous Materials*. Elsevier, North-Holland, Amsterdam.

Newman, J. C., Jr. (1984) A crack-opening stress equation for fatigue crack growth. *International Journal of Fracture*, 24, R131–R135.

Newman, J. C., Jr. (1981) A crack-closure model for predicting fatigue crack growth under aircraft spectrum loading. In *Methods and Models for Predicting Fatigue Crack Growth under Random Loading*, Chang, J. B. and Hudson, C. M. (eds). ASTM STP 748, 53–84.

Newman, J. C., Jr. (1982) Prediction of fatigue-crack growth under variable amplitude and spectrum loading using a closure model. In *Design of Fatigue and Fracture Resistant Structures*, Abelkis, P. R. and Hudson, C. M. (eds). ASTM STP 761, 255–277.

Newman, J. C., Jr. (1992) FASTRANII – A Fatigue Crack Growth Structural Analysis Program. NASA Technical Memorandum 104195, NASA Langley Research Centre.

Newman, J. C., Jr., Crews, J. H., Jr., Biglew, C. A., and Dawicke, D. S. (1995) Variations of a global constraint factor in cracked bodies under tension and bending loading, *Constraint Effects in Fracture Theory and Applications: Second Volume*, ASTM STP 1244, M. Kirk and A. Baker (eds.), American Society for Testing and Materials, Philadelphia.

Nozaki, H. and Taya, M. (1997) Elastic fields in a polygon-shaped inclusion with uniform eigenstrains. *Journal of Applied Mechanics*, 64, 495–502.

Oplinger, D. W. (1994) Effects of adherend deflections in single-lap joints. *International Journal of Solids and Structures*, 31, 2565–2587.

Oterkus, E., Barut, A., Madenci, E., and Ambur, D. R. (2005) Nonlinear analysis of a composite panel with a cutout repaired by a bonded tapered composite patch. *International Journal of Solids and Structures*, 42, 5274–5306.

PAFEC Users' Manual (1995) PAFEC Limited, Strelley Hall, Nottingham, United Kingdom.

RAAF Engineering Standard DEF(AUST) 9005-A, *Design of Bonded Repairs, 2006*.

Raizenne, M. D., Heath, J. B. R., and Benak, T. (1988) TTCP PTP-4 Collaborative Test Program – Variable Amplitude Loading of Thin Metallic Materials Repaired with Composite Patches. Laboratory Technical Report, LTR-ST-1662, National Aeronautical Establishment, Ottawa, Canada.

Ratwani, M. M. (1974) Analysis of cracked adhesively bonded laminated structures. *AIAA Journal*, 17, 988–994.

Ratwani, M. M. (1980) A parametric study of fatigue crack growth behavior in adhesively bonded metallic structures. *Journal of Engineering Materials and Technology*, 100, 46–51.

Ratwani, M. M. and Kan, H. P. (1982) *Development of Composite Patches to Repair Complex Cracked Metallic Structures*. Vol. I, Final Report NADC-80161-60, U.S Navy, Naval Air Development Center.

Reedy, E. D., Jr (1990). Intensity of the stress singularity at the interface corner between a bonded elastic and rigid layer. *Engineering Fracture Mechanics*, 36, 575–583.

Reedy, E. D., Jr (1993) Free-edge stress intensity factor for a bonded ductile layer subjected to shear. *Journal of Applied Mechanics*, 60, 715–720.

Reedy, E. D., Jr and Guess, R. T. (1997) Interface corner failure analysis of joint strength: effect of adherend stiffness. *International Journal of Fracture*, 88, 305–314.

Reissner, E. (1947) On bending of elastic plates. *Quarterly Journal of Applied Mathematics*, 5, 55–68.

Rice, J. R. and Levy, N. (1972) The part-through surface crack in an elastic plate. *Journal of Applied Mechanics*, 39, 185–194.

Roark, R. J. and Young, W. C. (1989) *Roark's Formulas for Stress and Strain*, 6th edition. McGraw-Hill, New York.

Roberts, T. M. (1989). Shear and normal stresses in adhesive joints. *Journal of Engineering Mechanics*, 115, 2460–2479.

Rodin, G. J. (1996) Eshelby's inclusion problem for polygons and polyhedra. *Journal of Mechanics and Physics of Solids*, 44, 1977–1995.

Rogers, L., Maly, J., Searle, I. R., Begami, R. I., Owen, W., Smith, D., Gordan, R. W., and Conley, D. (1997) Durability patch: Repair and life extension of high-cycle fatigue damage on secondary structure of ageing aircraft, *1st Joint DOD/FAA/NASA Conference on Aging Aircraft*, Ogden, Utah, 8–10 July, 595–623.

Rose, L. R. F. (1981) An application of the inclusion analogy. *International Journal of Solids and Structures*, 17, 827–838.

Rose, L. R. F. (1982) A cracked plate repaired by bonded reinforcements. *International Journal of Fracture*, 18, 135–144.

Rose, L. R. F. (1987a) Crack reinforcement by distributed springs. *Journal of the Mechanics and Physics of Solids*, 35, 383–405.

Rose, L. R. F. (1987b) Influence of debonding on the efficiency of crack patching. *Theoretical and Applied Fracture Mechanics*, 7, 125–132.

Rose, L. R. F. (1988) Theoretical analysis of crack patching. In *Bonded Repair of Aircraft Structure*, A. A. Baker and R. Jones (eds). Kluwer Academic Publisher, Dordretcht, 77–106.

Rose, L. R. F. and Wang, C. H. (2001) Closure analysis of small fatigue cracks with a self-similar plastic wake. *Journal of the Mechanics and Physics of Solids*, 49, 401–429.

Sendeckyj, G. P. (1967) Ellipsoidal Inhomogeneity Problem. Ph.D. Dissertation, Northwestern University, Evanston.

Spigel, B. S., Buckingham, J., and Wieland, R. D. (1998) Composite Doubler Design Optimization (CDDO) and Thermally Compatible Repair Material (TCRM). Final Report. SwRI Project No. 06-8311, Southwest Research Institute.

Sun, C. T. and Chin, H. (1988) Analysis of asymmetric composite laminates. *AIAA Journal*, 26, 714–718.

Sun, C. T., Klug, J., and Arendt, C. (1996) Analysis of cracked aluminum plates repaired with bonded composite patches. *AIAA*, 34, 369–374.

Swenson, D. and James, M. (1997) FRANC2D/L: A Crack Propagation Simulator for Plane Layered Structures, Version 1.4 User's Guide. Kansas State University.

Tada, H., Paris, P. C. and Irwin, G. R. (1985) *The Stress Analysis of Cracks Handbook*. Del Research Corporation, St Louis, Missouri.

Tanaka, K. and Nakai, Y. (1983) Mechanics of growth threshold of small fatigue cracks. *Fatigue Crack Growth Threshold Concepts*, D. L. Davidson and S. Suresh (eds), The Metallurgical Society of AIME, 497–516.

Thomsen, O. T. (1992) Elasto-static and elasto-plastic stress analysis of adhesive bonded tubular lap joints. *Composite Structures*, 21, 249–259.

Thomsen, O. T., Rits, W., and Eaton, D. C. G. (1996) Ply drop-off effects in CFRP/honeycomp sandwich panels – theory. *Composites Science and Technology*, 56, 407–422.

Timoshenko, S. and Woinowsky-Krieger, S. (1959) *Theory of Plates and Shells*. McGraw-Hill, New York.

Timoshenko, S. P. and Goodier, J. N. (1970) *Theory of Elasticity*. McGraw-Hill Book Company, New York.

Ting, T. C. T. (1996) *Anisotropic Elasticity: Theory and Applications*. Oxford University Press, New York.

Tong, L. and Steven, G. P. (1999) *Analysis and Design of Structural Bonded Joints*. Kluwer Academic Publishers, MA.

Tsai, M. Y. and Morton, J. (1994) An evaluation of analytical and numerical solutions to the single-lap joint. *International Journal of Solids and Structures*, 18, 2537–2563.

Tsai, M. Y., Oplinger, D. W., and Morton, J. (1998) Improved theoretical solutions for adhesive lap joints. *International Journal of Solids and Structures*, 35, 1163–1185.

Vlot, A., Verhoeven, S., Ipenburg, G., Siwpersad, D. R. C., and Woerden, H. J. M. (2000) Stress concentration around bonded repairs. *Fatigue and Fracture of Engineering Material and Structures*, 23, 263–276.

Volkensen, O. (1938) Die niektraftverteiling in zugbeansprunchten mit konstanten laschenquerscritten. *Luftfahrforsch*, 15, 41–47.

Wang, C. H. (1997) Analysis of cracks in constrained layers. *International Journal of Fracture*, 83, 1–17.

Wang, C. H. (1998) On the fracture of constrained layers. *International Journal of Fracture*, 93, 227–246.

Wang, C. H. (1999) Fatigue crack closure analysis of bridged cracks representing composite repairs. *Fatigue and Fracture of Engineering Materials and Structures*, 23, 477–488.

Wang, C. H. and Chalkley, P. (2000) Plastic yielding of a film adhesive under multiaxial stresses. *International Journal of Adhesion and Adhesive*, 20, 155–164.

Wang, C. H. and Erjavec, D. (2000) Geometrically linear analysis of the thermal stresses in one-sided composite repairs. *Journal of Thermal Stresses*, 23, 833–851.

Wang, C. H. and Rose, L. R. F. (1997a) Determination of triaxial stresses in bonded joints. *International Journal of Adhesion and Adhesive*, 17, 17–25.

Wang, C. H. and Rose, L. R. F. (1997b) Failure analysis of adhesively bonded joints. *Advances in Fracture Research*, 6, 3057–3064, Pergamon Press, Sydney.

Wang, C. H. and Rose, L. F. R. (1998) Bonded repair of cracks under mixed mode loading. *International Journal of Solids and Structures*, 35, 2749–2773.

Wang, C. H. and Rose, L. R. F. (1999) A crack bridging model for bonded plates subjected to tension and bending. *International Journal of Solids and Structure*, 36, 1985–2014.

Wang, C. H. and Rose, L. R. F. (2000) Compact solutions for the corner singularity in bonded lap joints. *International Journal of Adhesion and Adhesives*, 20, 145–154.

Wang, C. H., Heller, M., and Rose, L. R. F. (1998a) Substrate stress concentrations in bonded lap joints. *Journal of Strain Analysis*, 33, 331–346.

Wang, C. H., Callinan, R. J., and Rose, L. R. F. (1998b) Analysis of out-of-plane bending of one-sided repair. *International Journal of Solids and Structures*, 35, 1653–1675.

Wang, C. H., Rose, L. R. F., and Baker, A. A. (1998c) Modelling of the fatigue growth behaviour of patched cracks. *International Journal of Fracture*, 88, L65–L70.

Wang, C. H., Rose, L. R. F., Callinan, R., and Baker, A. A. (2000) Thermal stresses in a plate with a circular reinforcement. *International Journal of Solids and Structures*, 37, 4577–4599.

Wang, J. J. and Duong, C. N. (2003) Analytical solutions for load increase factors in bonded composite repairs. *Proceeding of SAMPE Conference*, SAMPE 2003 Symposium and Exhibition, Long Beach, California, May 11–15.

Williams, M. L. (1952) Stress singularities resulting from various boundary conditions in angular corners of plates in extension. *Journal of Applied Mechanics*, 19, 526–528.

Wolfram, S. (1991) *Mathematica*. Addison-Wesley, Boston.

Index

* Page numbers in *italics* refer to illustrations.

This Page Intentionally Left Blank